Transactions of the ASME, Journal of Heat Transfer (ISSN 0022-1481) is published bi-monthly (Feb., Apr., June, Aug., Oct., Dec.) by The American Society of Mechanical Engineers, Three Park Avenue, New York, NY 10016. Periodicals postage paid at New York, NY and additional mailing offices. POSTMASTER: Send address changes to Transactions of the ASME, Journal of Heat Transfer, c/o THE AMERICAN SOCIETY OF MECHANICAL ENGINEERS, 22 Law Drive, Box 2300, Fairfield, NJ 07007-2300.
CHANGES OF ADDRESS must be received at Society headquarters seven weeks before they are to be effective. Please send old label and new address.
STATEMENT from By-Laws. The Society shall not be responsible for statements or opinions advanced in papers or ... printed in its publications (B7.1, Para. 3), **COPYRIGHT © 2004** by The American Society of Mechanical Engineers. For authorization to photocopy material for internal or personal use under those circumstances not falling within the fair use provisions of the Copyright Act, contact the Copyright Clearance Center (CCC), 222 Rosewood Drive, Danvers, MA 01923, tel: 978-750-8400, *www.copyright.com*. Request for special permission or bulk copying should be addressed to Reprints/Permission Department. **INDEXED** by Applied Mechanics Reviews and Engineering Information, Inc. Canadian Goods & Services Tax Registration #126148048.

Journal of Heat Transfer

Published Bimonthly by ASME

VOLUME 126 • NUMBER 6 • DECEMBER 2004

(**Contents continued on inside back cover**)

This journal is printed on acid-free paper, which exceeds the ANSI Z39.48-1992 specification for permanence of paper and library materials. ♾™
♻ 85% recycled content, including 10% post-consumer fibers.

The ASME Journal of Heat Transfer is abstracted and indexed in the following: *Applied Science and Technology Index, Chemical Abstracts, Chemical Engineering and Biotechnology Abstracts (Electronic equivalent of Process and Chemical Engineering), Civil Engineering Abstracts, Compendex (The electronic equivalent of Engineering Index), Corrosion Abstracts, Current Contents, E & P Health, Safety, and Environment, Ei EncompassLit, Engineered Materials Abstracts, Engineering Index, Enviroline (The electronic equivalent of Environment Abstracts), Environment Abstracts, Environmental Engineering Abstracts, Environmental Science and Pollution Management, Fluidex, Fuel and Energy Abstracts, Index to Scientific Reviews, INSPEC, International Building Services Abstracts, Mechanical & Transportation Engineering Abstracts, Mechanical Engineering Abstracts, METADEX (The electronic equivalent of Metals Abstracts and Alloys Index), Petroleum Abstracts, Process and Chemical Engineering, Referativnyi Zhurnal, Science Citation Index, SciSearch (The electronic equivalent of Science Citation Index), Theoretical Chemical Engineering*

2003 Max Jacob Memorial Award Lecture

Heat Exchanger Design for the Process Industries

Kenneth J. Bell
e-mail: kjbell@okstate.edu
School of Chemical Engineering,
Oklahoma State University,
Stillwater, OK 74078-5021

The design process for heat exchangers in the process industries and for similar applications in the power and large-scale environmental control industries is described. Because of the variety of substances (frequently multicomponent, of variable and uncertain composition, and changing phase) to be processed under wide ranges of temperatures, pressures, flow rates, chemical compatibility, and fouling propensity, these exchangers are almost always custom-designed and constructed. Many different exchanger configurations are commercially available to meet special conditions, with design procedures of varying degrees of reliability. A general design logic can be applied, with detailed procedures specific to the type of exchanger. The basis of the design process is first a careful and comprehensive specification of the range of conditions to be satisfied, and second, organized use of a fundamentally valid and extrapolatable rating method. The emphasis in choosing a design method is upon rational representation of the physical processes, rather than upon high accuracy. Finally, the resultant design must be vetted in detail by the designer and the process engineer for operability, flexibility, maintainability, and safety. [DOI: 10.1115/1.1833366]

Introduction

''Shock and awe'' accurately describe my reaction when I opened the letter from Jack Howell, Chairman of the Max Jakob Memorial Award Committee, informing me that I had been selected to receive the Jakob Award for 2003. A glance at the list of awardees is sufficient to demonstrate that the award has traditionally been given to distinguished researchers, most of them academically connected, whose publications have typically numbered in the hundreds. The only recipient whose career was primarily in industrial practice was Karl Gardner, the importance of whose technical publications on fin efficiency and mean temperature difference greatly outweighed their modest numbers. No way can my research contributions stand in this company. Had I been aware that one of my former Ph.D. students, Amanie Abdelmessih, was circulating a nomination form, I would have tried to gently but firmly discourage her. But that option was not given to me, and I certainly do not wish to disparage the collective wisdom of the Award Committee.

The Charter for the Award states ''The Award shall be bestowed in recognition of eminent achievement or distinguished service in the area of heat transfer.'' This provides a very large net to catch a variety of fish, and perhaps my career activities in bringing the research results of others into industrial practice and bringing the realities of industrial practice into the lab and the classroom may rise to that standard. Max Jakob himself devoted much of the second volume of *Heat Transfer* to applications including whole chapters on ''Ordinary Heat Exchangers (Recuperators),'' ''Regenerators,'' and ''Cooling Towers.'' Figure 1 of this paper is a pretty schematic example of a ''recuperator.'' This example would be identified in the trade as a Tubular Exchangers Manufacturers Association, Inc. (TEMA) AEL 1-2 shell-and-tube heat exchanger [1], typical of the central subject of this paper.

Historically, my bifurcated career between academe and industry was launched on the day I entered graduate school at the University of Delaware. I was asked to assist Allan Colburn with some calculations he needed for a paper he would give to receive the James Clayton Award from the Institution of Mechanical Engineers. The paper was to be presented at The General Discussion on Heat Transfer in London in 1951, a meeting now generally considered to be the first International Heat Transfer Conference. This assignment led to my serving as Colburn's Teaching Assistant and my doctoral research on the ASME-sponsored Cooperative Research Program on Shell-and-Tube Heat Exchangers, of which Colburn and Olaf Bergelin were Co-Principal Investigators. The Advisory Committee for the Project included Bill McAdams of MIT, Al Mueller of du Pont, Karl Gardner of Griscom-Russell, and Townsend Tinker of Ross Heater. A few years later, close associations developed with Don Kern, with Jerry Taborek and Joe Palen of Heat Transfer Research, Inc. (HTRI), and Geoff Hewitt of Heat Transfer and Fluid Flow Services (HTFS). Early academic connections included Jim Knudsen, Warren Rohsenow, Art Bergles, and Ralph Webb, all well-connected with the industrial practice of heat transfer. With these people to work with and steal from, and particularly to introduce me around the heat exchanger industrial establishment, it is hard to see how my professional interests could have gone any other direction.

The Challenge of the Design Process

Heat exchangers designed for the process industries and for similar applications in the power and large-scale environmental control industries are usually custom-designed and constructed. The design process must accommodate the wide variety of substances (frequently mixtures, and often of uncertain composition and properties) to be handled under extremes of temperature, pressure, and chemical compatibility. Single-phase and phase-change processes, both vaporization and condensation, must be included, often occurring in the same equipment, sometimes sequentially in the same stream. The design conditions specified must consider possible future operational changes, intentional and accidental, and the construction features selected must meet both present and plausible future safety and environmental requirements. The equipment must satisfy the mechanical design codes and applicable industrial standards, be compatible with other process units, and be maintainable, especially with regard to fouling and corrosion. The thermal/hydraulic design methods developed to fulfill these requirements start with whatever fundamental correlations are available in the literature, but must also incorporate the necessary additional information and procedures required to cover the gaps, limitations, and simplifications in those correlations, and make provision for the designer to enter any special information that he/she has access to.

Contributed by the Heat Transfer Division for publication in the JOURNAL OF HEAT TRANSFER. Manuscript received by the Heat Transfer Division June 28, 2004; revision received October 6, 2004.

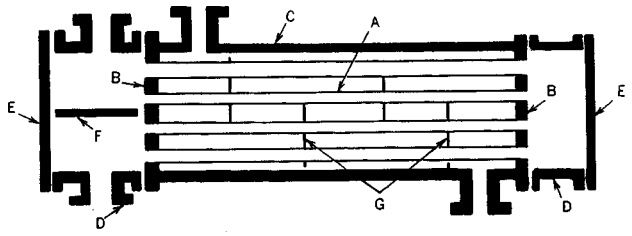

Fig. 1 Schematic of a typical shell-and-tube heat exchanger: TEMA AEL, with fixed tubesheets and channel heads with Removable covers. A: Tubes, B: Tubesheets, C: Shell, D: Tube-side channels and nozzles, E: Channel covers, F: Tube-side pass divider, G: Baffles (or tube supports) (see Ref. [2]).

This paper offers a brief survey of the logic of the design process for this equipment, together with some observations of present and future trends.

The Basic Design Equation

For the usual process heat exchanger, two fluids exchange heat (sensible, latent, or some combination) across a solid interface. The basic thermal design equation for this case is

$$dA^* = dQ/U^*(T-t) \tag{1}$$

which may be formally integrated over the total heat duty of the exchanger, Q_T, to give

$$A_T^* = \int_{Q=0}^{Q=Q_T} dQ/U^*(T-t) \tag{2}$$

where A_T^* is the required total heat transfer area of the exchanger, dQ is the local rate of heat transfer across the differential area dA^*, Q_T is the total heat transfer rate (or ''duty'') required for the exchanger, U^* is the local overall heat transfer coefficient referenced to area A^*, and T and t are the local temperatures of the hot and cold streams in the heat exchanger, respectively. T and t are functions of the quantity of heat that has been transferred from the start of the calculation, as computed by heat balances and equilibrium relationships. U^* is also indirectly a function of the heat transferred as local flow conditions and thermal properties change with T and t.

The overall heat transfer coefficient U^* for a typical heat exchanger with two fluids exchanging heat across a solid surface (''wall,'' which may be a plain or corrugated sheet, or the wall of a plain or finned cylindrical tube) with fouling on both sides of the wall, is given by Eq. (3):

$$U^* = 1/[(A^*/h_1A_1) + (R_{f1}A^*/A_1) + (X_wA^*/A_{wm}k_w) + (A^*/h_2A_2) + (R_{f2}A^*/A_2)] \tag{3}$$

In Eq. (3), h_1 and h_2 are the film heat transfer coefficients for fluids 1 and 2, respectively; A_1 and A_2 are the corresponding heat transfer areas for the two surfaces, R_{f1} and R_{f2} are the fouling resistances for the two fluids, X_w is the thickness of the wall, and k_w is the thermal conductivity of the wall. If extended surfaces (''fins'') are used on one or both sides of the wall, a ''surface effectiveness,'' E_f, must be incorporated into the corresponding area terms to account for the additional conductive resistance of the fin. More elaborate formulations of this equation must be used for special situations, such as tubes with liners. Correlations for calculating the film heat transfer coefficients are provided in many references, of which the Heat Exchanger Design Handbook—1998, G. F. Hewitt, editor, [3] is the most comprehensive.

The ''reference heat transfer area'' must be carefully defined, especially for heat exchangers using some form of extended surface (usually fins attached to the prime surface). Essentially any convenient surface can be used for this purpose: For a shell and tube exchanger with plain tubes, the outside heat transfer area of the tubes is commonly used. But for a typical crossflow air-cooled heat exchanger using high-finned tubes, either the outside surface area of the tubes including fins or the inside tube surface area may be used; In this case, there is about a 20:1 ratio between the two areas, and there is unlikely to be any confusion, but other cases are not so obvious. If there is any possible question, the reference area basis should be carefully defined and used consistently in any citing of the coefficient.

Under certain assumptions, Eq. (2) can be analytically integrated to give equations of the form

$$A_T^* = Q_T/U^*(\mathrm{MTD}) \tag{4}$$

where MTD, or ''mean temperature difference,'' can be calculated from analytically derived equations (or graphical representations) using the terminal temperatures of the two streams and the flow geometry of the streams (e.g., cocurrent, counter-current, crossflow, etc.) These mean temperature difference methods are treated extensively in textbooks and handbooks and work well enough for many routine cases. In practice, however, the assumptions are often too restrictive, and computer programs for the numerical integration of the equation are almost always used.

For example, for condensation of a single component vapor in the presence of a noncondensable gas, the vapor-side heat transfer coefficient changes from one dominated by a standard condensing correlation to one dominated by a diffusive mass transfer correlation, while the heat duty is first dominated by the latent heat of condensation of the vapor but later is due mainly to sensible cooling of the condensate and the noncondensable gas. Starting from one end of the heat exchanger, the local compositions, temperatures, and phase distributions are calculated as functions of the quantity of heat transferred from the entrance (usually assuming local phase equilibrium to calculate the relative amounts of each phase, which is of course an approximation that needs to be carefully considered for its possible impact on the performance). U^* is then calculated using the local conditions (including the two-phase flow pattern) and the appropriate correlations, and the integral numerically evaluated.

Some types of exchangers can accommodate more than two streams: Gasketed or welded plate heat exchangers can be configured for three streams in a single pack, while some plate-fin type exchangers used in air-separation services are designed for 10 or 12 streams. Most of these types are designed and manufactured by only a few companies, and they have developed both the basic correlations and the design programs for these equipments.

The Logical Structure of the Thermal/Hydraulic Design Procedure

The basic logical structure of the process heat exchanger design process is diagrammed in Fig. 2. The fundamental goal of any such process is to find the ''optimal'' design among the infinite set of designs that could satisfy the thermal/hydraulic and mechanical requirements. Because of the large number of qualitative (but vital) factors that enter into the selection process and the inherent uncertainties in even the quantitative factors in the design calculations, optimal needs to be understood broadly and defined not too rigidly.

Generally, the design programs are looking for the least costly (which usually, but not always, translates into the smallest) heat exchanger of a given type that will meet the required thermal duty within the allowed pressure drops and satisfy mechanical code requirements. But, for example, there may be piping, structural limitations, or necessary maintenance capabilities that require a less than optimal flow configuration, and hence, a larger exchanger. To the extent possible, these requirements should be communicated to the exchanger designer in the inquiry documents, but in any event the final design quoted should be carefully vetted by the customer engineer.

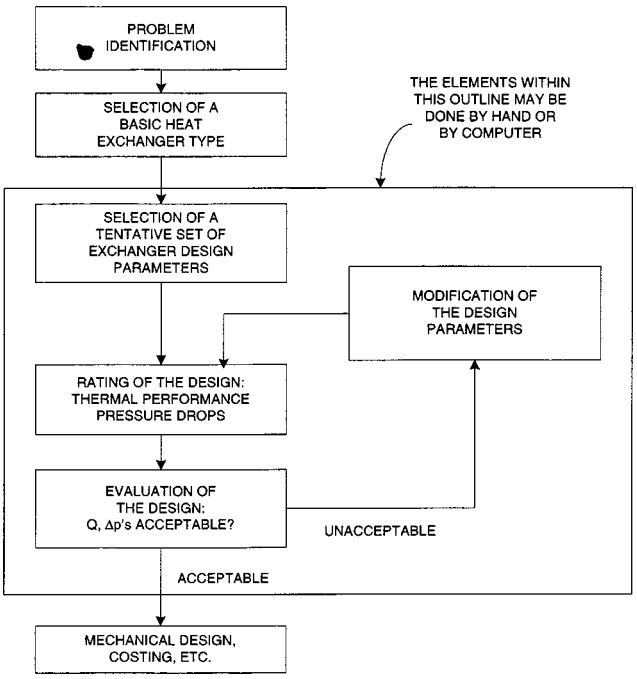

Fig. 2 Basic logical structure of the process heat exchanger design procedure

The first step in the design procedure is to completely and unambiguously define the problem and provide the designer (who is usually employed by the engineer/contractor or the exchanger manufacturer/vendor, rather than the customer) with all of the data required to solve the problem. This will include, but is not limited to, the flow rates, compositions, temperatures, and pressures of the streams in the exchanger. Unless the streams are single-component well-known substances, it will usually be necessary to also provide the usual thermodynamic and thermophysical properties over the range of temperatures and pressures to be encountered. Design fouling resistances must also be provided, preferably by the customer, based on experience with the same or similar materials; If the designer has to provide the fouling resistances, any thermal guarantee on equipment performance is severely compromised. (Fouling is discussed in greater detail later in this paper.) Finally, there may be additional requirements or limitations on diameter, length, weight, piping connections, supports, and construction features intended to facilitate maintenance. Alternative design features or variant performance specifications may be requested.

The next block shown in Fig. 2 is ''selection of a basic heat exchanger type,'' e.g., a shell-and-tube versus a welded plate, etc. In fact, this decision is usually prefigured in arriving at some of the specifications listed in the previous paragraph and in the selection of vendors requested to provide bids. For many—perhaps most—services, the decision is practically automatic: It is easy to go straight to a shell-and-tube exchanger for service involving two streams at high temperatures and high pressures, for example. But even here, there are specialized options available—diffusion-bonded printed circuit or Monobloc™ constructions, for example. For most applications, there is an increasingly wide choice of exchanger configurations available, and some of the established practices should be at least re-examined to see if there might be attractive alternatives. Among the factors to be taken into consideration, besides first cost, are:

1. Level of confidence in the design method—is the method backed up by solid performance data either from the laboratory or the field?

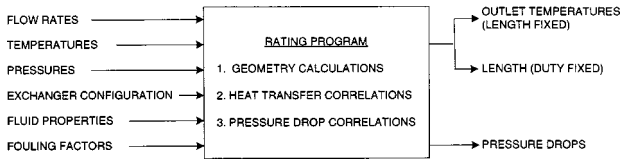

Fig. 3 The rating program: Core block of the heat exchanger design process

2. Level of confidence in the fabrication techniques—does the equipment have a good service experience record? What lifetime can be expected?
3. Level of confidence in plant operating and maintenance personnel with respect to this equipment—do they know the characteristics of this equipment, and are they able to maintain and clean it?
4. Operational flexibility—can this equipment or its operating conditions be adjusted or modified to meet likely changes in plant requirements?

This step is interactive with the problem identification step, but it must take place before selecting the bid list of vendors.

The next set of logic blocks actually carry out the thermal/hydraulic design of the chosen equipment. As Fig. 2 indicates, these steps can be carried out either by hand (and head) methods, or—in practice, almost all the time—by computer methods. Acceptable hand methods exist for all major types of heat exchangers—''acceptable'' meaning in this instance that a reasonably close design can be obtained in a reasonable time period by using handbook correlations, a hand calculator (or even a slide rule!), and a knowledgeable designer. In practice, hand design is limited to pedagogical exercises or highly specialized applications for which there is no commercially available, reliable computer design method.

In any case, the next step is to select a tentative but sufficient set of exchanger design parameters to allow the rating procedure to work. If one already has an existing heat exchanger whose performance in a new service is to be evaluated, the parameters of that exchanger are simply fed into the program and the output examined for acceptability.

However, for the usual design case where a new exchanger is required, reasonable starting values must be supplied. For the case of a shell-and-tube heat exchanger, these would include (in addition to the process specifications) the three-letter TEMA exchanger configuration identifier, the shell diameter, the tube diameter and wall thickness, tube layout, baffle type, baffle spacing and cut, and the tube length (if known). Additional information would include nozzle orientation data, maximum allowable diameter and/or length, type of bypass sealing devices if required, and (usually) the requirement that TEMA construction standards for such items as tube-to-baffle clearance would be met. If a hand design method is to be used, these values should be estimated as closely as possible a priori in order to minimize the calculation time. A method for making those estimates is given in Section 3.1.4 of Hewitt, HEDH-1998 [3].

If a computer method is used, the program itself will provide the starting estimates for shell diameter and baffle cut and spacing. Usually, the largest allowable values are chosen, resulting in the minimum shell-side pressure drop. These parameters and others such as number of tube-side passes are later modified in the design modification step in order to close in on the optimal design.

The next step is to ''rate'' the performance of the starting design for the specified service. Figure 3 illustrates the function of the rating program: It takes the specified streams and their input conditions and calculates the changes in temperature and pressure effected on those streams by the specified heat exchanger. A more detailed look at how a typical rating program is developed is given later. The thermal rating output is either the outlet tempera-

tures and corresponding thermal duty of the exchanger if the length has been specified, or the length required for the otherwise specified exchanger to satisfy the thermal duty given in the input data. The pressure drops of each stream are also calculated. If one is rating an existing exchanger, these output values should be sufficient to determine the feasibility of using that exchanger in the prescribed service. If, however, a new exchanger is being designed, the process has only started.

In the design case, the heat duty is compared to that required and the pressure drops to those allowed. If the duty is sufficient and both pressure drops are near but below the allowed values, the thermal/hydraulic design is complete and the designer can move on to cleaning up and verifying the mechanical design, cost estimation, etc. If not all of those conditions are satisfied, the designer (if by hand) or the program (if by fully integrated computer program) moves on to the design modification program.

The purpose of this step is to examine the output of the rating program and determine what is good and acceptable and what was unacceptable in the case that was rated. Then, the designer or the program must select what can be changed to most efficiently correct the deficiency without too badly upsetting that which was good. Here, the designer by hand has the intellectual advantage because she or he has been able to observe the outcome of each step in the calculation and can concentrate immediately and directly upon those changes (unlike the computer, the person can make several changes at once) likely to have the desired effect. Indeed, the designer may have aborted the rating calculation early on when it was evident that the final results would be unacceptable.

The design modification program in the computer is quite rigid and must follow a very logical diagram to ensure that it is making changes that will move in the right direction, are physically realizable, and adhere to accepted manufacturing and mechanical code standards. Convergence to a final result from a wide range of input conditions is critical. Such a program taxes the knowledge, logical ability, and programming skill of the best designers and programmers in the business. An early version of a shell-and-tube design modification code involved about 40 binary decisions, allowing 2^{40} (about $1.1\times10^{12}=35{,}000$ years at 1 computation per second) different logical (or illogical) paths through the program. One error in the logic, or failure to close a decision point, is a potential Trojan horse. (In fact, an early version of this program out for testing refused to allow a design with more than two tube-side passes, because of a word-length difference between the computer it was developed on and the computers that most of the user companies had.)

A weak point in the rigid computer logic is its no-tolerance policy on the allowable pressure drop. First, the allowable pressure drop is there to be used to the fullest to obtain the best possible design. There are no prizes given either for wasting pressure drop on poor design features or for failing to use as much of the allowable drop as possible. Second, the allowable pressure drops are usually specified by the process engineer based on experience and a reasonable allocation of the total available pressure difference between major processing units: Other than in vacuum or low-pressure gas systems, the pressure drops are rarely optimized nor are they usually a major cost or operational feasibility factor. Third, the best exchanger design methods have a typical uncertainty of $\pm30\%$ on the calculated pressure drop when clean, and a much higher and more uncertain value under many fouling conditions. Therefore, after the program has converged on the optimal design, it is common practice to print out the major parameters for the last three or four rating cases for examination by the designer and for consideration as alternate designs by the process engineer.

As a final point, every major heat exchanger design produced by a computer program needs to be carefully examined by both an experienced designer and an experienced process engineer for basic reasonableness in the context of the application. Too often, the output of a computer design program is accepted without question by an inexperienced engineer who has no basic understanding of the fluid-mechanical or thermal processes occurring in the heat exchanger nor an awareness of the uncertainties in the basic data or the design assumptions built into the program.

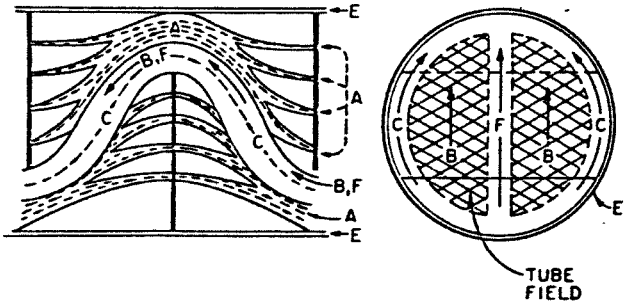

Fig. 4 Idealized diagram of shell-side flow streams (see Refs. [4,5])

History of the Development of a Rating Method

Since the rating program is the key block in the design method logic, it will be instructive to retrace the steps by which one such a program evolved. The so-called ''stream analysis method'' for shell-and-tube heat exchangers in shell-side sensible heat transfer service is chosen because of its importance and the author's long involvement in this work. Prior to Tinker's publication in 1951 [4], the design calculations were largely based on a highly idealized flow pattern of crossflow in a series of ideal tube banks connected by window regions of flow parallel to the tubes. This neglected the presence and the effect on both heat transfer and pressure drop of several tube bundle bypass and baffle leakage streams due to necessary construction features of the exchanger. This tended to overestimate both the heat transfer coefficient and the pressure drop.

Tinker [4] presented a diagram, shown here (in modified form) in Fig. 4, which identified the five basic streams that occur on the shell side of a typical exchanger. Stream B is the nominal main stream that flows across the tube bank and through the next window to the next tube bank. (''Nominal'' is used here because in fact this stream is often less than half of the total flow in the exchanger.) Stream A is the tube-to-baffle leakage stream, flowing through the small but necessary clearances between the tubes and the baffles. Stream A thus short-circuits part of the heat transfer surface but it is a high velocity stream in close contact with heat transfer surface, so it does not represent a major penalty against thermal performance. Stream E similarly flows through the shell-to-baffle clearances, but away from any heat transfer surface. It causes a major loss in the thermal performance, especially in laminar flow. These clearances are limited by TEMA [1] manufacturing standards, but cannot be eliminated entirely in practical heat exchangers.

Stream C is the bypass stream flowing between the tube bundle and the shell. In fixed tubesheet or U-tube bundle design, this stream can be minimized by careful matching of the tube layout to shell inside diameter. However, there are significant clearances required by the various floating head designs employed when thermal stress between shell and tube bundle is a problem. In those cases, seal strips around the periphery of the bundle should be used to partially block the bypass stream and force it back into the tube field. Finally, and this is a later addition to the Tinker diagram, there is an internal bypass stream, F, which exists whenever there are tubes omitted to accommodate the pass partition plates used in the tube-side headers to allow multiple tube-side passes. Ordinarily, care would be taken to position these clearances perpendicular to the shell-side flow direction (unlike that shown in the diagram), but they would almost certainly occur with six or

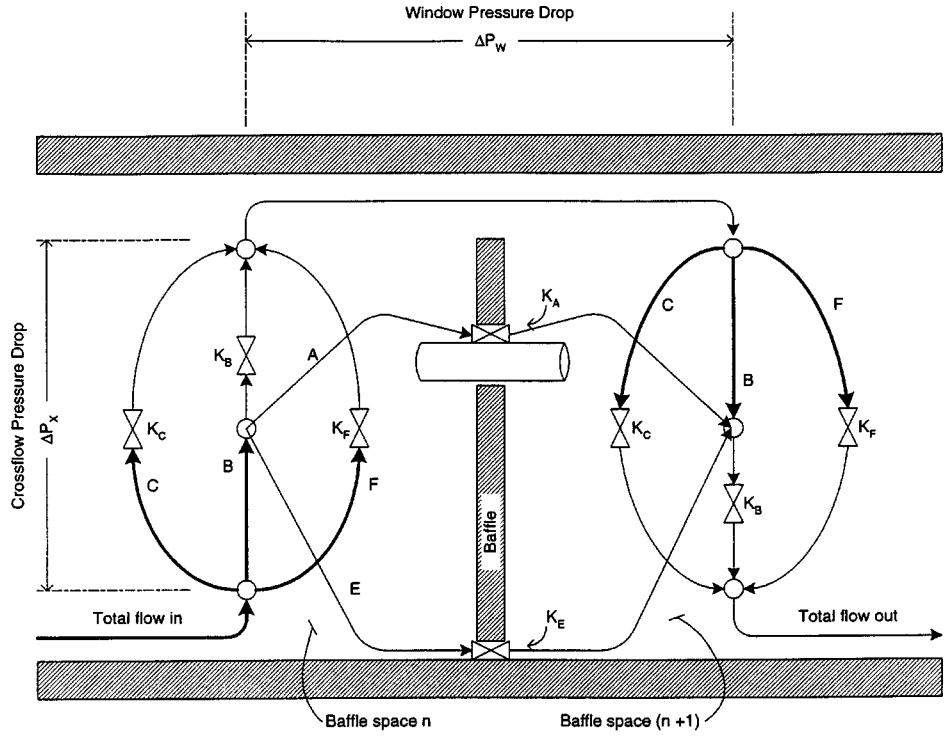

Fig. 5 Schematic model of shell-side flow paths and resistances across one baffle space (see Ref. [5])

more passes, and often with four passes. This stream is not as detrimental as the C stream because it flows nearer to the main heat transfer surface. It may be partially blocked by seal strips or internal tie rods.

Having identified the streams, Tinker then set up a system of pressure nodal points similar to that shown in Fig. 5, taken from a later paper by Palen and Taborek [5]. Since streams extending from one nodal point to another must undergo the same pressure loss, Tinker developed the equations for flow through the various paths using friction factors for flow across the tube banks, through the windows, and through the bundle bypass clearance. He also wrote the equations for the leakage flows using annular orifice coefficients. The friction factors were of course functions of geometry and Reynolds number.

This elaborate system of equations had to be solved by hand, the computer being in its infancy, and the method was too time-consuming for practical use. Also, there were few friction factor and orifice coefficient data available, and attempts to estimate constant values proved unsatisfactory. And there were few reliable experimental data on commercial exchangers available to verify the predictions.

Simultaneously, however, Professor Allan Colburn and Professor Olaf Bergelin were working with ASME, TEMA, Esso (Exxon), du Pont, York, Downingtown Iron Works, Andale, and other interested parties to establish and fund a research program in the Department of Chemical Engineering at the University of Delaware for a systematic study of shell-and-tube heat exchangers. This program came into being in 1947 and continued until the issuance of the Final Report in 1963. The program started with the determination of friction factors and Colburn *j* factors for seven ideal tube banks over a Reynolds number range from (eventually) 1 to 8000; These tube banks were later modified by removing tubes adjacent to one wall in order to obtain friction and heat transfer data for bypass flows. The next study was of a small but carefully scaled cylindrical exchanger in which the leakage paths could be sealed off (by a technique not feasible in industrial service) and the baffle cut and spacing varied. Subsequent studies selectively removed the baffle sealing and varied the leakage clearances. A larger cylindrical exchanger was designed and tested to validate and extend the data gathered on the small exchanger, and to allow bypass studies by removing the outermost tubes. Along the way, a detailed study of annular orifice coefficients for the full range of baffle leakage geometries was carried out [6].

The results of the Delaware project were fully reported in three reports of the University of Delaware Engineering Experiment Station [7–9]. A design method still suitable for hand use (and subsequently, hand-held programmable calculators) was first published in 1960 (Bell, 1960) [10] and is readily accessible in a number of references, notably Section 3.3 by Taborek in Hewitt, HEDH-1998 [3].

Two further developments in this time frame were occurring that would eventually converge to bring shell-and-tube design to a practical and reliable level. The first—and continuing—development was in fast, large-scale, user-friendly computing. The second was the formation of Heat Transfer Research, Inc. (HTRI) in 1961. HTRI is a cooperative proprietary research organization funded by the member companies, which include most of the large petroleum and chemical processors, engineer/contractor firms and heat exchanger manufacturers. Dr. Jerry Taborek was the first Technical Director, and I early on became a consultant to the organization. [We should also note that Heat Transfer and Fluid Flow Services (HTFS) was founded shortly thereafter in the United Kingdom, with a similar charter and Dr. Geoff Hewitt as the chief technical person. In spite of a certain air of competitiveness between the two organizations, the principals developed close personal and professional relationships.] HTRI acquired a large-scale test facility and an extensive data bank of test data on commercial exchangers from C. F. Braun and Co., and augmented this data bank with tests on carefully designed commercial-sized test heat exchangers.

Thus, about 1961, all the pieces came together to bring Tinker's concept to fruition: The detailed fundamental data were available from the Delaware project, the technical staff and resources to analyze the data and develop the computer algorithms were avail-

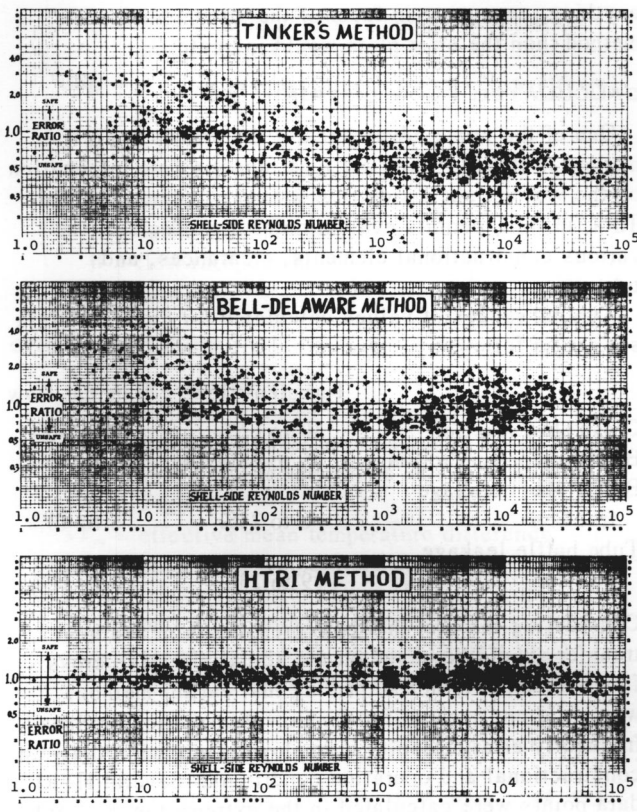

Fig. 6 Pressure drop error ratios for three shell-side rating methods (see Ref. [5]). (Reproduced with permission. Copyright © 1969 AIChE.)

able at HTRI, computing capabilities were adequate to the computational task, and the large-scale data were available to validate the output. There were, however, gaps in the data—*f* and *j* correlations for some of the basic tube layouts as functions of Reynolds number were simply nonexistent, and how to deal with the distortion of the temperature profile by the leakage and bypass streams, for example. Most of these gaps were filled in by what can be described as very informal work sessions among Taborek, Palen, Mueller, and the author around Jerry's swimming pool, giving rise to the legend of the Taborek Three Martini Correlation. In the event, the results validated the techniques.

Palen and Taborek [5] give a general description of the stream analysis method at that date, and show a comparison of the heat transfer and pressure drop data against the large experimental data bank covering a wide range of shell-and-tube exchanger size, flow rate, and fluid properties. The comparison charts for the approximately 1300 shell-side pressure drop and 1000 heat transfer data points for the three best (at that date) design methods are given here as Figs. 6 and 7. (My apologies—the figures shown here are copied directly from the published paper and are difficult to read. The original figures have been lost.) For the pressure drop, the ordinate is the ratio of the computed pressure drop to that actually measured, so a value greater than 1.00 is ''safe.'' It can be seen that the stream analysis method (''HTRI method'') is the most accurate, but still has error bounds of about $\pm 30\%$ for the bulk of the data. For heat transfer, the comparison is made on the basis of the ratio of the heat duty predicted for the exchanger to that actually transferred, so a value greater than 1.00 is ''unsafe.'' The bulk of the heat transfer results fall within about $\pm 20\%$ of the actual value.

The stream analysis method has been considerably expanded in the last 30 years to include a number of additional design types such as ''No Tubes in the Window'' (NTIW) and finned tubes, but no major change in the underlying model has been made. The results have met with general industry acceptance by experienced engineers, who understand and can deal with the uncertainty and know the obstacles to obtaining a step improvement.

How About Using Computational Fluid Dynamics (CFD)?

A question that will occur to any engineer familiar with the current state of the art in fluid mechanics is, ''Why not use CFD methods to get the right answer?'' The answer is that they have been used with some success to obtain certain results: Prithiviraj and Andrews [11] used a three-dimensional program, HEATX, to calculate the shell-side pressure drop in 12 heat exchangers (nine full bundles and 3 NTIW) whose pressure drop had been measured, and obtained agreement within about $\pm 10\%$. Kistler [12] says that HTRI has used CFD methods in studying flow distribution in manifolds and air flow in the vicinity of air-cooled heat exchangers. Ljubicic [13] says that CFD has been used to calculate the heat transfer and pressure drop inside the Twisted Tube® used in shell-and-tube heat exchangers designed and built by Brown Fintube (see further description later).

A basic difficulty in using current CFD methods for the shell side of shell-and-tube exchangers is that the methods require that the flow field be entirely laminar or entirely turbulent and have no criteria for selecting or changing flow regime during a computation. Further, additional information is required to select the proper turbulence model, and CFD methods do not exist for transition flow. Shell-side flows have a wide transition range (or perhaps they are simply ''disturbed''), and evidently little has been done to characterize the turbulent flow characteristics in tube banks and the even less regular geometries found in the peripheral regions.

Turning to the heat transfer problem, one must consider the distortion of the temperature profile caused by the leakage and bypass streams and their incomplete mixing with the main stream. This requires in principle that the thermal balance be carried out on each stream and related (through the local overall heat transfer coefficient) to the temperature change of the other stream. Even if the fundamental mechanisms were well understood (and they are not), the computational effort would, in the author's opinion, be too cumbersome to consider for the repetitive calculations that are part of the design process. If available, a validated CFD method would be useful for a detailed evaluation of a proposed final or near-final design, or for trouble shooting. The effort to develop a comprehensive, validated CFD program, including the fundamental studies and evaluation of the stream mixing phenomena and the generation of accurate large-scale test data for validation would likely have a price tag on the order of $10 million, and there is simply no support in sight for that kind of expenditure. But CFD will certainly have a continuing role to play in specialized applications such as those mentioned, and those applications will expand enormously if a reliable two-phase (liquid-gas/vapor) program were to become available.

New Developments in Heat Exchanger Construction

Any discussion of heat exchanger design must recognize that the options available to the designer are constantly expanding. Even the old standbys are being dressed up with new possibilities. Looking at the tube side of shell-and-tube exchangers, both internal and external enhancements are in common use. Externally, low finned tubes are commonly used with low coefficient fluids (like gases) on the shell side to increase the h_0A_0 value and reduce the overall size of the exchanger. Internal tube enhancements like internal fins (straight and spiraled), twisted tapes, wire inserts, and artificial roughness are employed to increase the area and/or the coefficient, and in some cases, to minimize the fouling.

Several developments are improving the shell-side performance. The helically baffled heat exchanger (Kral et al. [14]),

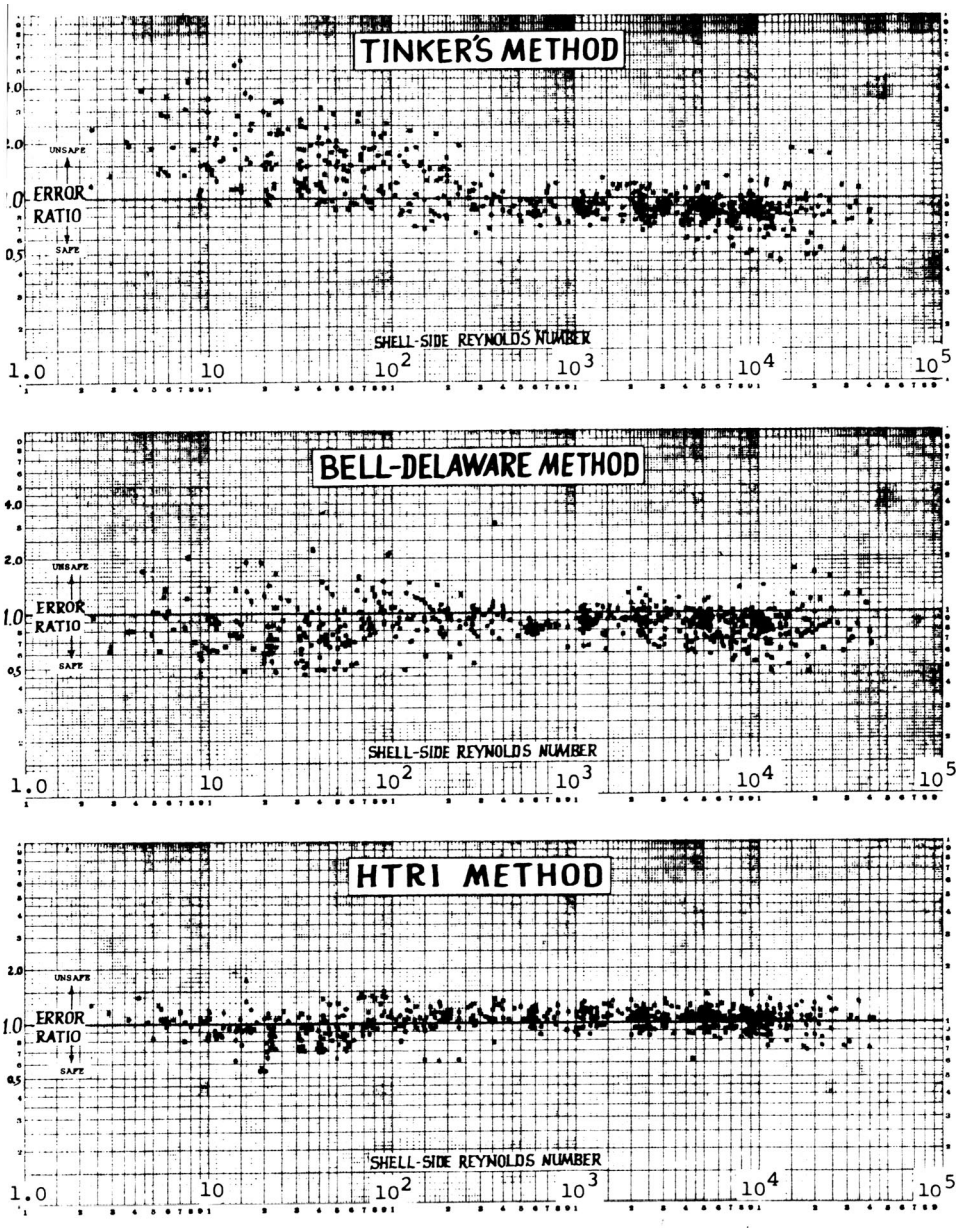

Fig. 7 Heat flux error ratios for three shell-side rating methods (see Ref. [5].) (Reproduced with permission. Copyright © 1969 AIChE.)

shown in Fig. 8, substantially alters the shell-side flow pattern by inducing a swirling pattern with a velocity component parallel to the tubes. As might be expected, this improves the heat transfer to pressure drop ratio, with an apparently optimal helix angle of 40 deg. Without access to the proprietary design procedures, one might reasonably have questions about temperature and velocity profiles from the center to the periphery. However, the design has been accepted into standard practice and is commercially available as the Helichanger in the US.

Another shell-side design used in Europe and only recently reintroduced to the US scene is the disk-and-donut configuration (see Ref. [15]), shown schematically in Fig. 9. This design essentially eliminates the C (bundle bypass) stream while preserving the clearance required for floating head designs.

The Twisted Tube® configuration shown in Fig. 10 is especially interesting from both shell-side and tube-side aspects. Developed in Sweden and marketed in this country by Brown Fintube, this tube is self-supporting against vibration and sagging, without the

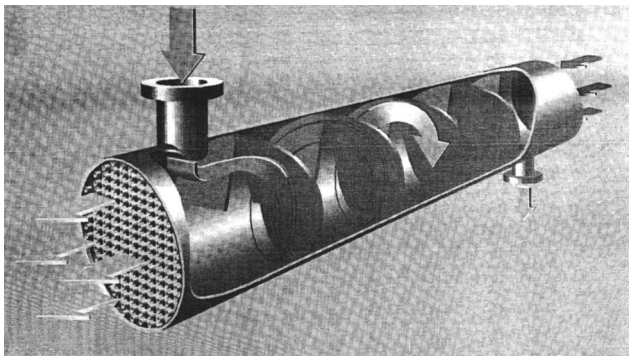

Fig. 8 Schematic diagram of the shell-side flow in a helically baffled heat exchanger (see Ref. [14]). (Courtesy, ABB Lummus Heat Exchanger, Bloomfield, NJ.)

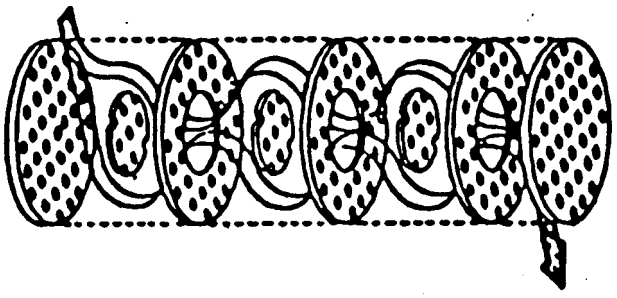

Fig. 9 Schematic diagram of a disk-and-donut heat exchanger (see Ref. [15])

use of shell-side tube supports (baffles). The tortuous but essentially constant cross-sectional (and hence, nonseparating) flow paths provide secondary flow patterns on both sides, with particular enhancement of heat transfer in laminar flow, and true countercurrent flow in 1-1 exchangers. It is necessary to shroud the tube bundle to minimize bypass flow around the periphery.

Turning to other exchanger types, the various configurations of the plate heat exchanger are becoming competitive in applications never before possible. The original design (Fig. 11) relied upon gaskets to seal the fluids against leaking to the atmosphere, and this severely limited the process temperatures and pressures for which plate heat exchangers could be considered. Further, the narrow spacing between plates effectively eliminated plate exchangers from consideration for low density gases and most condensation and vaporization services. The development of plates welded together in pairs allowed much higher pressures in one stream, and the all-welded construction allowed both higher pressures and higher temperatures in both streams. Plate redesign to allow higher spacing, while retaining the mutually self-supporting feature, permitted application to some gas and liquid-vapor phase changes duties that were formerly off-limits. However, the all-

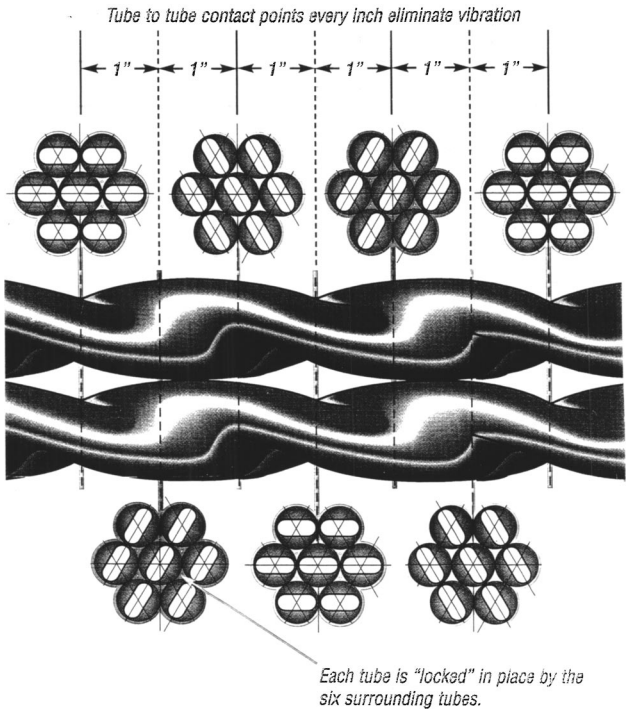

Fig. 10 Diagram of two Twisted Tubes®, showing how tubes are mutually self-supporting. (Courtesy, Brown Fintube Co., Houston, TX.)

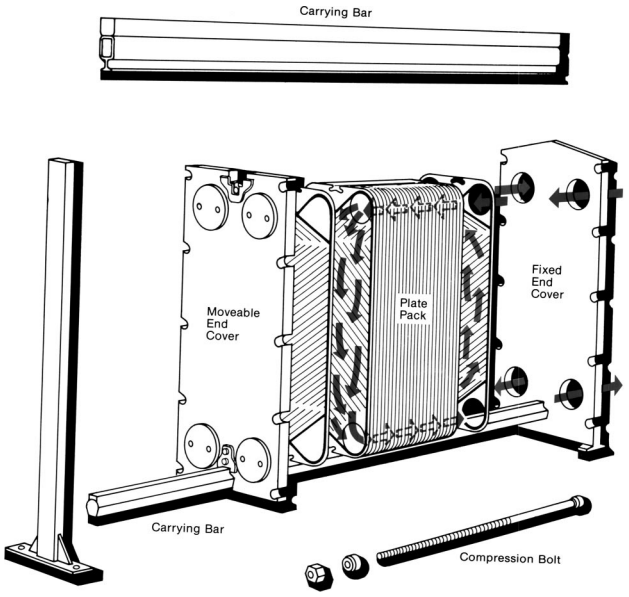

Fig. 11 Exploded diagram of a gasketed plate heat exchanger. (Reproduced with permission of Alfa Laval Inc.)

welded design forfeits the flexibility of quickly and easily changing the number of plates and/or the configuration to meet changed process requirements, which had always been a feature of the plate exchanger concept.

In recent years, ''printed circuit'' exchangers have been introduced and provide very compact heat transfer surface. These exchangers are formed from plates on which multiple parallel fine channels (typically 1–4 mm deep and wide) are formed by techniques similar to those used for printed circuit boards. The plates are then bonded together to form a monolithic block and inlet and outlet channels welded on. The small diameter, relatively short channels give high heat transfer coefficients even in the usual laminar flow mode, and the construction gives high heat transfer areas per unit volume. These exchangers must be protected against plugging by particulate matter, usually by upstream strainers, but they have proved useful in such services as high-pressure gas processing on ocean platforms.

The earlier citations are only a small sampling of the ingenuity being brought to bear upon the manifold problems of process heat transfer technology.

Fouling: The Greatest Unsolved Problem in Process Heat Transfer

''Fouling'' refers to any unwanted deposit of material on a heat transfer surface, or by extension, to any deposit that alters the desired fluid flow pattern. Fouling creates an additional resistance to heat transfer and increases pressure drop by narrowing or closing off flow passages. Fouling may arise from many different sources, among them deposition of suspended particulate matter, corrosion of the surface, formation of polymeric materials from or decomposition of process fluids (coking, caramelization, tar formation, etc.), crystallization or precipitation (especially of inverse solubility substances like calcium sulfate), and biological growths from algae to mussels. Only a few services can generally be regarded as free from fouling or, for other reasons, little affected by the usually encountered degree of fouling: Air and other clean gases, saturated light hydrocarbons, and ultra-pure water systems are examples. Some fouling is self-limiting: For example, some deposits weaken as they get thicker or age, and the increasing fluid shear stress is sufficient to remove (on the average) fouling about as fast as it is formed. Other types of fouling increase without practical limit until the only option is to shut the equipment

down and clean. Both chemical and mechanical (brushing, water jets, drilling) cleaning methods are available, depending upon the nature of the fouling.

Fouling is usually provided for through the incorporation into Eq. (3) of fouling resistances, either estimated by the customer based on past experience or selected from various tables of recommended values. These are at best rough guesses and primarily intended to buy some additional operating time before having to shut down for cleaning. Using a fixed value neglects the fact that fouling is usually a transient phenomenon. A problem that occasionally arises from this is that the start-up of a clean exchanger may result in higher than designed-for heat transfer (and higher surface temperatures) and consequent premature initiation and rapid growth of the fouling. Nesta and Bennett [16] have just published a paper emphasizing some quantitative guidelines in designing shell-and-tube exchangers to limit the fouling effects to an acceptable asymptotic value.

Recognizing that fouling has become the primary source of uncertainty in heat exchanger design, research in this area has recently become fashionable, even in universities. The literature on fouling has correspondingly exploded, though much of it tends to be anecdotal and difficult to develop into a coherent body of understanding of mechanisms. One exception to this is the many years of work on cooling tower water and its treatment, carried out by HTRI under the guidance of J. G. Knudsen. Unfortunately, much of this work is proprietary. The most comprehensive single source of information is by Bott [17]. Because of space limitations in this paper, I can only suggest combing the literature for the many contributions made by N. Epstein, A. P. Watkinson, H. Muller-Steinhagen, E. F. C. Somerscales, and C. B. Panchal, to name a few of the past and present pioneers in this very difficult, but vital, aspect of heat exchanger design.

Closing Comment

Even given its basis in science, heat exchanger design for the process industries is still a highly subjective and selective art form. Undoubtedly, it will become more rationalized and quantified as more is learned of the basic processes and practical means evolved to utilize that learning in the design process. All of this has been and will continue to be great good fun.

References

[1] Tubular Exchanger Manufacturers Association, Inc., 1999, *Standards, 8th ed.*, Tarrytown, New York.

[2] Bell, K. J., 1970, Process Heat Transfer Class Notes, Oklahoma State University, Stillwater, Oklahoma.

[3] *Heat Exchanger Design Handbook-1998, (HEDH-1998)*, 1998, G. F. Hewitt, ed., Begell House, New York.

[4] Tinker, T., 1951, ''Shell Side Characteristics of Shell and Tube Heat Exchangers, Parts I, II, III,'' *Proceedings of the General Discussion on Heat Transfer*, Institution of Mechanical Engineers, London, pp. 89–116.

[5] Palen, J. W., and Taborek, J., 1969, ''Solution of Shell Side Flow Pressure Drop and Heat Transfer by Stream Analysis Method,'' *CEP Symp. Ser.*, **65**(92), *Heat Transfer—Philadelphia*, pp. 53–63.

[6] Bell, K. J., and Bergelin, O. P., 1957, ''Flow Through Annular Orifices,'' Trans. ASME, **79**, pp. 593–603.

[7] Bergelin, O. P., Colburn, A. P., and Hull, H. L., 1950, ''Heat Transfer and Pressure Drop During Viscous Flow Across Unbaffled Tube Banks,'' *Bulletin No. 2, University of Delaware Engineering Experiment Station*, Newark, Delaware.

[8] Bergelin, O. P., Leighton, M. D., Lafferty, W. L., Jr., and Pigford, R. L., 1958, ''Heat Transfer and Pressure Drop During Viscous and Turbulent Flow Across Baffled and Unbaffled Tube Banks,'' *Bulletin No. 4, University of Delaware Engineering Experiment Station*, Newark, Delaware.

[9] Bell, K. J., 1963, ''Final Report of the Cooperative Research Program on Shell and Tube Heat Exchangers,'' *Bulletin No. 5, University of Delaware Engineering Experimental Station*, Newark, Delaware.

[10] Bell, K. J., 1960, ''Exchanger Design—Based on the Delaware Research Program,'' Petro/Chem Engineer, October, pp. C-26–C-40c.

[11] Prithiviraj, M., and Andrews, M. J., 1999, ''Comparison of a Three-Dimensional Numerical Model With Existing Methods for Prediction of Flow in Shell-and-Tube Heat Exchangers,'' Heat Transfer Eng., **20**(2), pp. 15–19.

[12] Kistler, S., 2004 (personal communication).

[13] Lubicic, B., 2004 (personal communication).

[14] Kral, D., Stehlik, P., Van Der Ploeg, H. J., and Master, B. I., 1996, ''Helical Baffles in Shell-and-Tube Heat Exchangers, Part I: Experimental Verification,'' Heat Transfer Eng., **17**(1), pp. 93–101.

[15] Taborek, J., 2004, ''Pressure Drop to Heat Transfer Conversion in Shell-and-Tube Heat Exchangers With Disc-and-Donut Baffles,'' paper presented at AICHE Spring Meeting, 2004, New Orleans, LA.

[16] Nesta, J., and Bennett, C. A., 2004, ''Mitigation of Fouling in Shell and Tube Heat Exchangers'' (unpublished).

[17] Bott, T. R., 1995, *Fouling of Heat Exchangers*, Elsevier, Amsterdam.

Contact Resistance Measurement and Its Effect on the Thermal Conductivity of Packed Sphere Systems

W. W. M. Siu

S. H.-K. Lee*
Associate Professor,
Mem. ASME

Department of Mechanical Engineering, Hong Kong University of Science and Technology, Clear Water Bay, Kowloon, Hong Kong

There has been a growing interest in porous systems with a smaller length-scale modeling requirement on the order of each particle, where the existing tools tend to be inadequate. To address this, a Discrete Conduction Model was recently proposed to allow for the transient temperature calculation of 3D random packed-sphere systems for various microstructures. Since many of the motivating applications involve contacting spheres and since there has been a limited number of contact-resistance studies on spheres undergoing elastic deformation, the objective of this study is to obtain measurements of the contact resistances between metallic spheres in elastic contact, as well as to quantify their influence on the effective thermal conductivity. To accomplish this, an experiment was constructed utilizing air and interfacial resistance to replace the functions of the guard heater and vacuum chamber, and in so doing, enabled transient observations. The overall uncertainty was estimated to be ±6%, and the results were benchmarked against available data. A correlation was obtained relating the contact resistance with the contact radius, and results showed the contact resistance to have minimal transient behavior. The results also showed that the neglect of contact resistance could incur an error in the effective thermal conductivity calculation as large as 800%, and a guideline was presented under which the effect of the contact resistance may be ignored. A correlation accounting for the effect of contact resistance on the effective thermal conductivity was also presented.
[DOI: 10.1115/1.1795231]

Introduction

Heat transfer in a porous medium is an area rich in practical applications and has for decades attracted numerous researchers. By and large, most of the earlier pioneering studies were driven by large length-scale applications, such as geothermal heating, and therefore, the typical assumption of a continuous, macroscopic system with effective thermal properties was generally adequate. More recently, however, there has been a growing interest in modeling porous systems with a smaller length-scale requirement on the order of each particle, and for these applications, the existing tools are generally inadequate (c.f. [1,2]). To address this shortcoming, a Discrete Conduction Model was recently proposed [1], which, when combined with a packing algorithm [3], allows for the transient temperature calculation of three-dimensional (3D) random packed-sphere systems for various microstructures. From these results, correlations were obtained for the determination of any packed bed's effective thermal conductivity given the relevant microstructural parameters (i.e., the coordination number N_c and the contact area ratio, γ).

However, many of the motivating applications involve contacting spheres, which have imperfect contacts similar to those between nominally flat surfaces (Fig. 1). This gives rise to a temperature jump when heat is transferred across the contact, and since this is due to the existence of the contact, the associated resistance is often referred to as the contact resistance. Since, in general, the actual contacting area may be as low as 0.1% of the nominally contacting area [4], the effect of contact resistance may be important, particularly for contacting spheres where the nominal contact area is small to begin with. This can also be inferred from an earlier experimental study [5], where the results showed the effective thermal conductivity of a packed-sphere system to increase with increasing compression force. Still, it is unclear how much of this change was due to changes in the contact resistance and how much was due to changes in the microstructure, specifically the contact area ratio, of the packed bed. In this regard, it has already been demonstrated that even assuming perfect contacts, changes in the contact area ratio affects the overall thermal conductivity by changing the constriction resistance within the spheres [1].

How important is the contact resistance in a packed-sphere system? What is the extent of this effect? How does it hinder the numerical modeling efforts? Questions such as these are not only important, fundamentally, but practically as well since application-oriented studies have found the existing heat transfer tools ''appreciably over-predicts the hot spot'' [6]. Unfortunately, there have only been a limited number of studies on spheres, and most of these were generally applicable only for spherical surfaces undergoing plastic deformation (c.f. [7–10]). For the elastic deformation range, there is a shortage of data. Therefore, the objectives of the present study are to measure the contact resistance (with air gap) for the appropriate deformation range, to study its effect on the overall thermal conductivity, and then, finally, to quantify it through an appropriate correlation.

Experiment

Overview and Experimental Procedures. Most of the existing measurement techniques utilize guard heaters in measuring contact resistances, as it ensures a one-dimensional temperature distribution in the reference materials [11]. The drawback of this approach is that it interferes with the stated objective of transient measurements. Therefore, to accomplish our stated objectives, a

*Corresponding author. e-mail: shklee@ust.hk
Contributed by the Heat Transfer Division for publication in the JOURNAL OF HEAT TRANSFER. Manuscript received by the Heat Transfer Division May 8, 2003; revision received May 24, 2004. Associate Editor: B. Farouk.

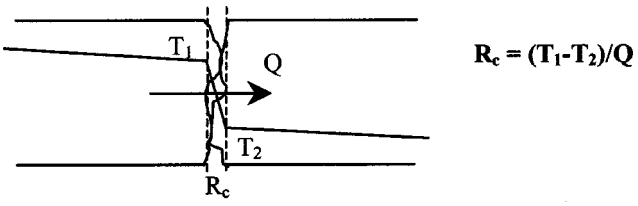

Fig. 1 Schematic showing the temperature jump due to imperfect contact between two surfaces

new experimental arrangement is needed, which is shown in Fig. 2. The focus of this experiment is the sphere for which the contact-resistance measurement was made. On the left and right side of this sphere are the hot and cool pistons, respectively. The sphere in-between these two pistons is pressurized through a compression screw acting on the right-hand side of the cool piston, while the resulting force is measured by a force transducer located on the left-hand side of the hot piston. Besides exerting a force on the sphere, the two pistons also provide a heat-flow through the sphere, which was accomplished by maintaining the two pistons at different temperatures through circulating water baths.

Prior to taking the data, the specimens were cleaned in an ultrasonic alcohol bath, their surface roughness was measured at 20 locations on each sphere (Tencor Alpha-Step 200 surface-profile system), and then they were loaded into the test section maintaining contact only with the hot piston. After the temperatures of both the hot piston and specimen reached steady state, the cool piston was immediately brought into contact through the compression screw and temperature measurements were taken from thermocouples embedded within the two pistons at intervals of 15 s until steady state was reached. Within each piston, temperature was measured at seven locations, of which four were used to calculate the heat flow and extrapolate the contact temperature (linear extrapolation), and the remaining three were used to monitor for heat loss in the radial direction. In this way, the contact temperature and heat flow were determined from the hot and cool pistons. As given below in Eq. (1), the difference between these two contact temperatures were used as the driving potential and

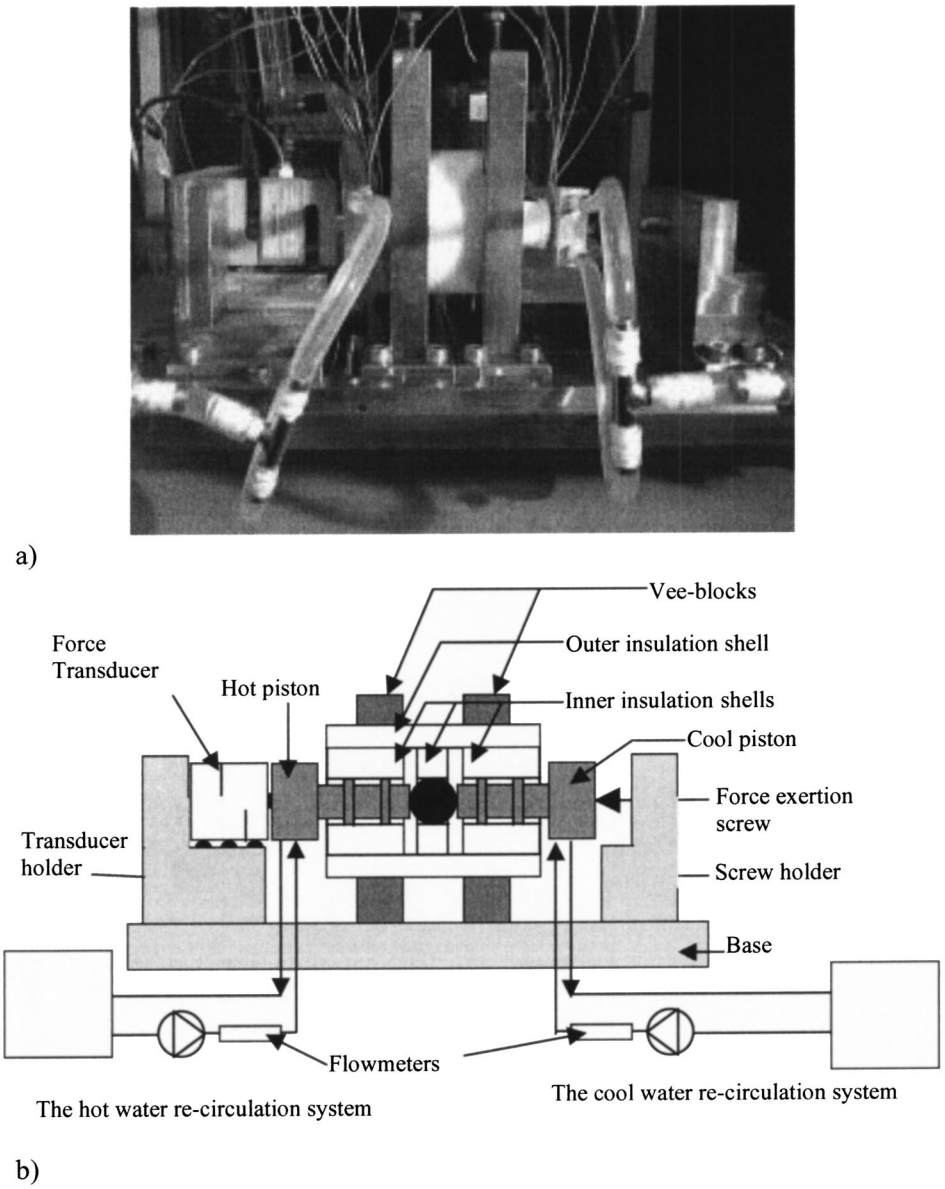

Fig. 2 Experimental setup shown in *a*) photo and *b*) schematic

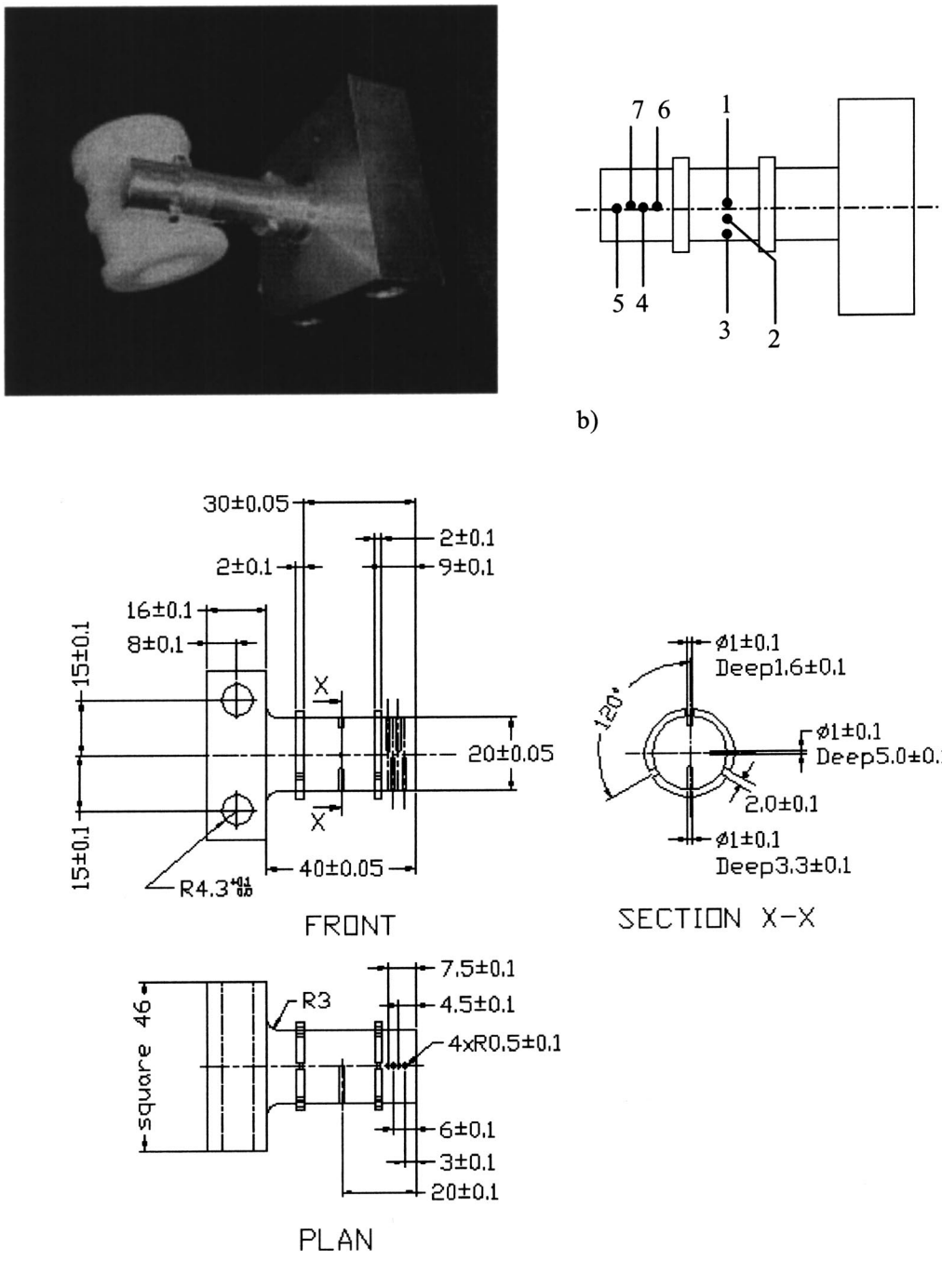

Fig. 3 Illustration showing *a*) picture of the piston, *b*) the location of the thermocouple placement positions, and *c*) the piston

this was, in turn, divided by the average of the two heat flows to determine the total resistance between the two pistons

$$R_T = \frac{(T_{c,hot} - T_{c,cool})}{\frac{1}{2}(Q_{hot} + Q_{cool})} \tag{1}$$

For measurements involving only one sphere between the two pistons, this total resistance consists of the constriction resistance within the sphere and the contact resistances between the sphere and the pistons. For measurements involving two spheres in between the pistons, the total resistance will additionally contain the contact resistance between the two spheres and the associated constriction resistance. Therefore, the contact resistance between the two spheres can be obtained by subtracting the total resistance with one sphere from the total resistance with two spheres, and then finally subtracting the constriction resistances between the two contacting spheres. This is given below in Eq. (2*a*), where $R_{T,2}$ represents the total resistance for 2 spheres, $R_{T,1}$ represents that for 1 sphere, and R_k is the constriction resistance given in Eq. (2*b*) [11]:

$$R_c = R_{T,2} - R_{T,1} - R_k \tag{2a}$$

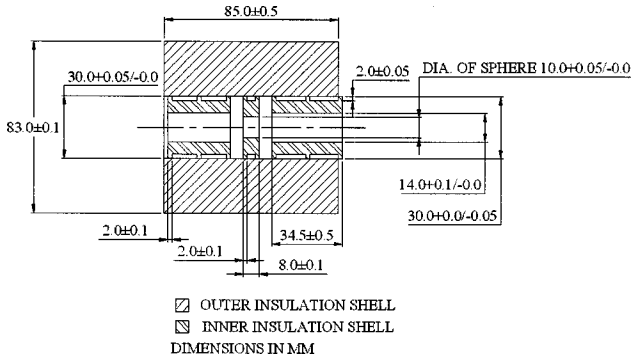

Fig. 4 Schematic showing the placement of the inner and outer shells

$$R_k = \frac{1}{2kr_c} \tag{2b}$$

$$r_c = \left[\frac{3}{4}\frac{(1-\nu^2)}{E} F r_s\right]^{1/3} \tag{2c}$$

Equation (2*b*) requires knowledge of the contact radius r_c, which was determined using the Hertz relation [Eq. (2*c*)], given by Timoshenko and Goodier [12] for spheres subject to a compressive force F and undergoing elastic deformation. This force was measured by the force transducer located on the left-hand side of the hot piston, and to verify for elastic deformation, the spheres were tested using a UTM machine (MTS Sintech 10/D).

Detail Setup

Piston Assembly. The pistons were machined out of aluminum 6061-T6 (167.27 W/m-K) to a dimension of 10 ± 0.05 mm in diameter and 40 ± 0.05 mm in length. As shown in Fig. 3, two fin structures, measuring 2 ± 0.1 mm in width and 2 ± 0.05 mm in height were also machined into each piston in order to create a 2 ± 0.05 mm insulating air gap between the surface of the piston and the inner insulation shell. The thickness of this air gap was chosen to ensure that the Rayleigh number was less than 1700, and thus the air became a nonconvecting medium with a thermal conductivity of 0.026 W/m-K.

To maintain the temperature of the piston, water was circulated between the piston and constant-temperature water tanks, in which 1.5 kg of stainless steel screens was placed to provide thermal capacitance. To ensure turbulent heat transfer, the water was circulated within the 8 ± 0.1 mm dia opening at a controlled flow rate of 5 l/min and a corresponding Reynolds number of 3800. Each water tank was made out of 10 mm nominally thick acrylic, and the internal volume was 0.027 m^3 (300 mm×300 mm×300 mm). Immersed in the hot-water tank was a 450-ohm resistor connected to an electric current source through an Omega CN9000 temperature controller (accuracy of ±0.5°C), operating in an on/off mode. The temperature of the hot-water tank was monitored and confirmed to be within ±0.25°C of the set point. Besides the hot-water tank, the temperature of the cool-water tank was also maintained at 0.5 ± 0.2°C by the usage of an ice bath.

As shown in Fig. 3(*b*), a total of seven openings were created at various locations of each piston. Four openings (1 ± 0.1 mm in diameter and 5 ± 0.1 mm in depth) were precisely machined along the centerline of the piston, in order to provide temperature measurements in the axial direction, which were used to extrapolate the contact temperature (with the sphere) and to compute the axial heat flow. The centers of these four openings were located 1.5 ± 0.1 mm from each other, and the center of the first opening was located 3 ± 0.1 mm from the end of the piston. In addition, three openings were also precisely machined at various angular locations in order to provide radial temperature measurements. These three openings (1 ± 0.1 mm in diameter) were created at the same axial location, but spaced apart at 90 ± 0.1 deg and with respective depths of 1.6 ± 0.1 mm, 3.3 ± 0.1 mm, and 5 ± 0.1 mm. The net effect is that these three openings allowed temperature measurements to be made 1.6 ± 0.1 mm from each other and 1.6 ± 0.1 mm from the surface of the piston. These three temperature measurements were used to compute the heat loss in the radial direction.

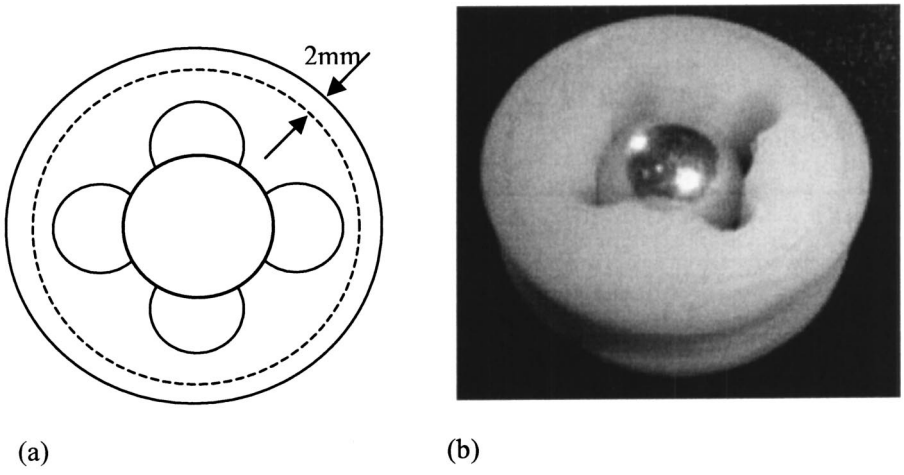

Fig. 5 *a*) Schematic and *b*) photo of the sphere-shell utilized to insulate the sphere

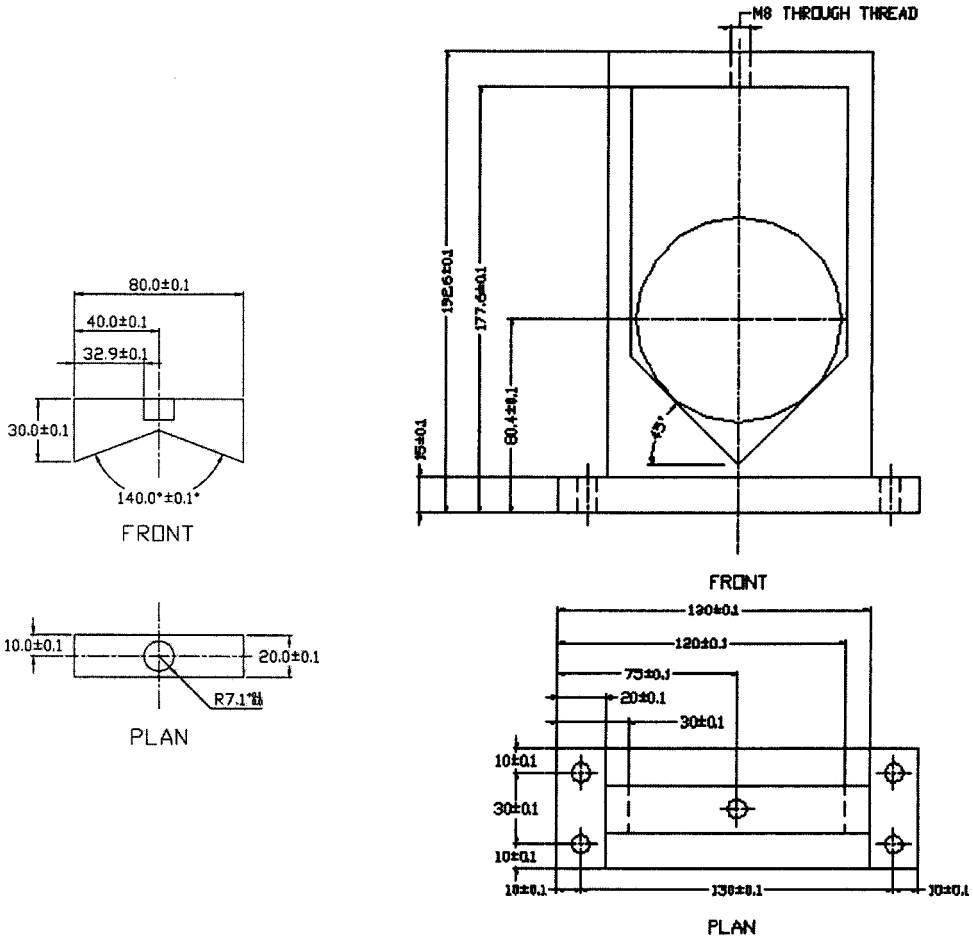

Fig. 6 Schematic of *a*) the upper Vee-block and *b*) the lower Vee-block

Inserted within the openings, along with OmegaTherm-201 heat-sink compounds, were 0.254 mm (nominal diameter) type-T thermocouples (nominal outer diameter including insulation layers of 1 mm). These thermocouples were connected to an Omega DP 41-TC (accuracy of $\pm 0.005\%$) read-out through a silver-plated Omega OSW5-39 thermocouple-selector switch. All the thermocouples were calibrated over the range of 0–100°C against a set of NIST-traceable mercury-in-glass thermometers (accuracy of ± 0.025°C). The measurements showed these thermocouples to have an accuracy of $\pm 0.01\%$ over the range of 0–100°C.

Insulation and Alignment. Figure 2(*b*) shows the piston and spheres to be enclosed within a composite shell structure. This shell structure serves the function of aligning the pistons and the sphere as well as providing the necessary thermal insulation. The latter function is particularly important in light of the absence of a guard heater. Further examination of Fig. 2(*b*) shows one outer shell and three inner shells. The outer shell was machined out of ABS (k=0.27 W/m-K) [13] to a length of 85 ± 0.5 mm, an inner diameter of $30 + 0.1/-0$ mm and an outer diameter of 83 ± 0.1 mm. Contained within this outer shell were three inner shells, two of which housed the hot and cool pistons and the third housed the sphere. These three inner shells were separated into noncontacting units in order to accommodate different sphere sizes and to minimize any axial heat flow between them.

The two inner shells that housed the pistons were identical and are called piston shells, while the inner shell that housed the sphere is called the sphere shell. Similar to the outer shell, all three inner shells were machined out of ABS, and as shown in Fig. 4, they were utilized here in order to introduce air gaps (2 ± 0.05 mm) and thus minimize any heat flow to the outer shell. In addition, additional air gaps were introduced between the piston and piston shell and between the sphere and the sphere shell. To create the air gap in the piston, large sections of the piston and the inner surface of the sphere shell (Fig. 5) were machined away, leaving a clover pattern for the sphere shell and finlike structures on the pistons. In order to preserve the alignment of the pistons within the piston shell, the spacing between these finlike structures was typically at least equal to the inner diameter of the piston shells.

The composite shell structure was mounted within two identical, carbon-steel Vee-blocks, which, as shown in Fig. 6, consisted of a movable upper jaw (subtended angle of 140 deg$\pm$0.1 deg) and a stationary lower jaw (subtended angle of 90 deg$\pm$0.1 deg). To align the Vee-blocks, they were fitted onto a base, which was machined out of medium carbon steel to a tolerance of ± 0.05 mm. Also attached to the base were the force transducer (Omega LCCB-200) and the compression screw, and these were aligned with the Vee-blocks with an overall misalignment of less than 0.2 mm, so as to minimize the contact force between the pressurized spheres and the shells. The overall misalignment is estimated to yield a force measurement with a maximum uncertainty of 0.08%. The force transducer was connected to a digital readout (Omega DP2000) and calibrated against an electronic balance to an accuracy of ± 0.5 N. Furthermore, to minimize the uncertainty from friction, the force transducer was also mounted on roller bearings to enable free movement.

Results and Discussion

Verification, Error Analyses and Benchmarking. A total of two sphere sizes, made out of three different materials, were uti-

lized in this study, and for each size, a total of 10 spheres were used. As shown in Table 1, the roughness measurement for each sphere size exhibited sufficient uniformity to enable meaningful measurements. Besides roughness measurements, the spheres were also subjected to elastic deformation tests, and the results in Fig. 7 showed the smaller aluminum sphere to exhibit the greatest deformation ($<0.3\%$) under a 100 N compression loading. Using 20% safety margin, a loading condition of 80 N was determined to produce elasticlike deformation. Consequently, all the contact-resistance measurements were made under a maximum loading condition of 80 N, and all the spheres were discarded after the measurement.

Besides verifying for maximum loading condition, experiments were carried out to estimate the error in determining the heat flow through the spheres. From the discussion preceding Eq. (1), it is noted that seven thermocouples were embedded within each piston for the purpose of determining the appropriate temperature gradients. From Fig. 8, the radial temperature gradients in both pistons were found to be small, and thus the measurements at each axial location were taken to represent the respective planar temperatures. From these, the axial temperature gradients and heat flows were estimated for both the hot and cool pistons for various temperature settings. As shown in Table 2, the results show the heat-flow measurements at the hot and cool pistons to be different, and this difference varies according to the temperature settings. Selecting the optimum temperature setting for the cold and hot water baths to be 0°C and 50°C, respectively, it is noted that there is a 12% difference in the heat-flow measurement. Detailed consideration of the experimental setup reveals this difference to come from three possible sources. That is, the hot piston may be interacting with the environment, the heat flow through the spheres may escape through the contacts with the cylindrical shells, and finally, the cool piston may be interacting with the environment. Considering the hot piston first, it is noted that the axial temperature gradients were measured at locations downstream of the piston flanges where heat losses would occur. Consequently, the measured axial gradient already accounts for the heat losses at the flanges, and since the radial temperature gradients were very small, it can be reasonably concluded that this axial heat flow in the piston is essentially the heat entering the contacting spheres. However, not all of this heat will successfully pass through the spheres toward the cool piston, as the spheres could lose heat by conducting to the cylindrical shell. Consequently, the measured heat flow in the hot piston would likely overestimate the heat flow between the two pistons. As for the cool piston, it is noted that the flange that could pick up heat from the environment is located downstream of the axially embedded thermocouples. As a result, this would tend to lower the axial temperature gradient and cause an underestimation of the axial heat flow. Since the hot-piston measurement is an overestimate and the cool-piston measurement is an underestimate, the average of these two measurements were utilized in calculating the thermal resistance in Eq. (1).

Based on the above discussion, a reasonable estimate of the uncertainty in measuring the contact resistance can be determined through the expression in Eq. (3) [14]. For a typical measurement, the temperature difference between the hot and cool pistons was set at 50°C, with an associated error of less than 0.1°C, and this combined with the previously discussed 12% uncertainty in estimating the heat flow gives an overall uncertainty in the resistance measurement of 12%. Since the measured resistance was calculated based on the averaged heat flows measured from the hot and cool pistons, this 12% uncertainty can be reasonably translated as $\pm 6\%$.

Table 1 Properties of experimental specimens

	Materials		
	A1 1100	Brass	Chrome Steel
Sphere diameter (mm)	12.19	11.11	11.11
Mean Surface Roughness (μm)	0.689	0.146	0.137
Standard Deviation (μm)	0.384	0.021	0.061
Young's modulus (GPa)	71	105	200
Tensile strength (MPa)	70–180	482.8	2241.56
Yield strength (MPa)	28–165	331.06	3034.65
Thermal conductivity (W/m-K)	240	117.15	44.77
Density (kg/m^3)	2700	8414.69	7833.41
Hardness (Rockwell)	B 54-72	B 75-81	C 62-66

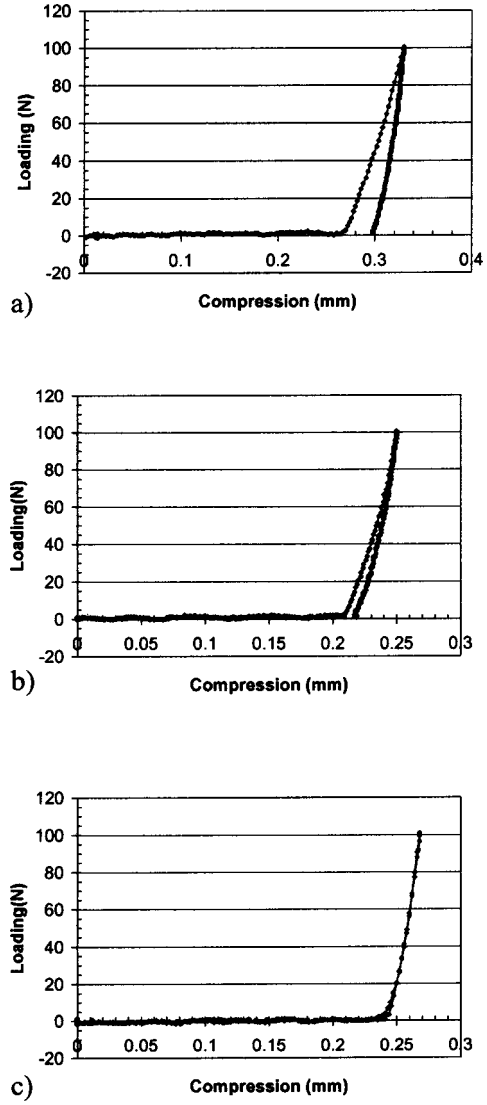

Fig. 7 Plot of the compression deformation for *a*) 12.19 mm diam aluminum sphere, *b*) 11.11 mm diam brass sphere, and *c*) 11.11 mm diam chrome steel sphere

$$\delta R = \frac{\partial R}{\partial(\Delta T)} * \delta(\Delta T) + \frac{\partial R}{\partial Q} * \delta Q$$

$$= \frac{1}{Q} * \delta(\Delta T) + \frac{\Delta T}{Q^2} * \delta Q$$

$$\Rightarrow \frac{\delta R}{R}$$

$$= \frac{\delta(\Delta T)}{\Delta T} + \frac{\delta Q}{Q}$$

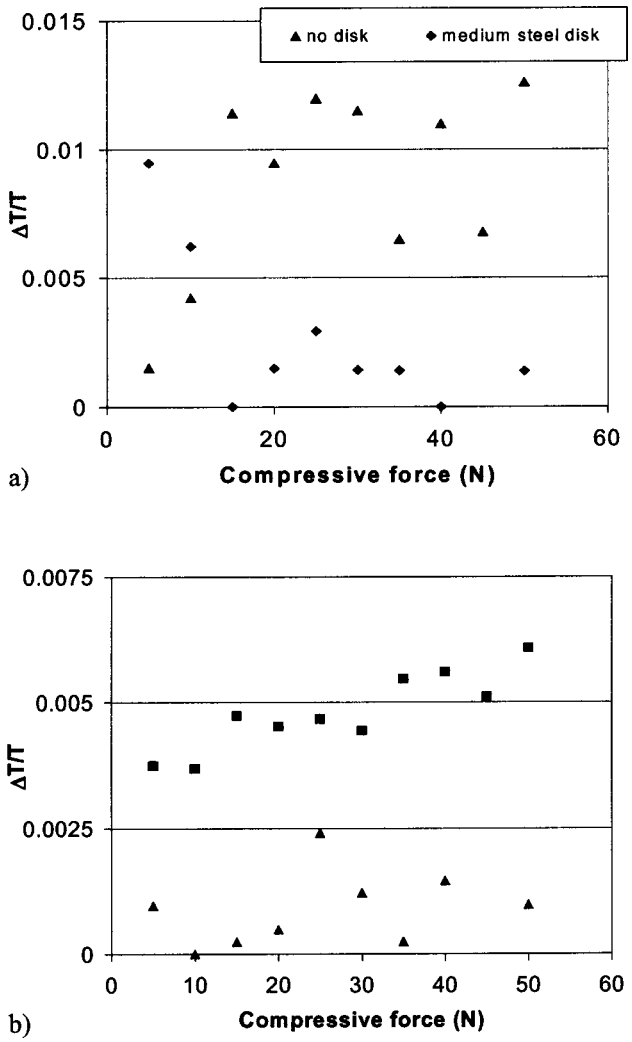

Fig. 8 Temperature measurements showing uniform radial distribution in the *a*) cool piston and *b*) hot piston

$$= \frac{\delta T + \delta T}{\Delta T} + 12\%$$

$$= \frac{0.1 + 0.1}{50} + 12\% \approx 12\%$$

$$\Rightarrow \pm 6\% \tag{3}$$

For benchmarking purpose, the present experiment was utilized to measure the thermal conductivity of a 5 mm thick aluminum (6061-T6) disc sandwiched between the hot and cool pistons. By subtracting the measured resistance from that, obtained by pushing the two pistons together, the thermal conductivity was back calculated, which, as shown in Fig. 9(*a*), is within the published range. Finally, as shown in Fig. 9(*b*) the contact resistance measured by placing the two aluminum pistons in direct contact was in excellent agreement with available contact resistance values of aluminum [15].

Table 2 Percentage difference of heat flow between the hot and cool pistons (%)

Number of trial	0 vs 25°C	0 vs 30°C	0 vs 40°C	0 vs 50°C	0 vs 60°C
1	17	16	10	10	16
2	12	26	17	14	13
3	10	11	14	11	15
Average	13	18	14	12	15

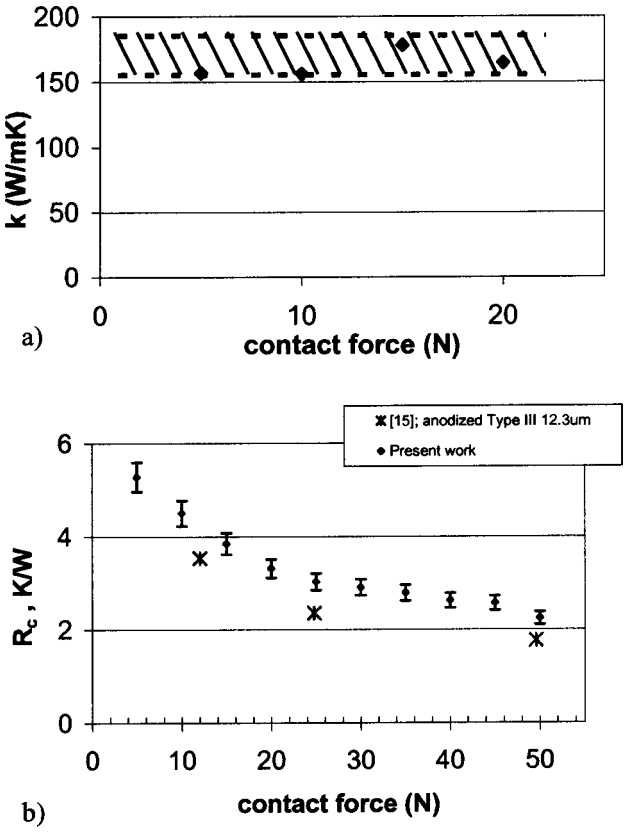

Fig. 9 Comparison of *a*) the back-calculated thermal conductivity of aluminum against the range of expected range 155–185 W/m-K between the dotted line and *b*) the measured thermal resistance value between aluminum surfaces

Contact Resistance. Given in Table 3 is the experimental matrix for which contact resistance was determined. The results for aluminum, brass, and chrome-steel spheres are shown in Fig. 10, and as expected, the trends show the chrome steel to have the highest contact resistance and the aluminum to have the lowest for a given compressive force. Replotting these results against the contact radius, these data can be seen in Fig. 11 to have the potential of collapsing onto a single curve. Given in Eq. (4) is the expression for the best-fit polynomial correlation with an associated correlation coefficient of 0.8, where r_c is expressed in units of meters and R_c is expressed in units of K/W.

Thus, this is one of the first correlations to be presented in this contact radius range, and also perhaps one of the few to show that, surface roughness being equal, different materials exhibit different contact resistance due to differences in the contact radius.

Table 3 Experimental matrix for the current measurements

Material	Sphere diameter (mm)	Number of spheres	Compressive force, N
A1 1100	12.19	1	1–80
A1 1100	12.19	2	1–80
Brass	11.11	1	1–80
Brass	11.11	2	1–80
Chrome steel	11.11	1	1–80
Chrome steel	11.11	2	1–80

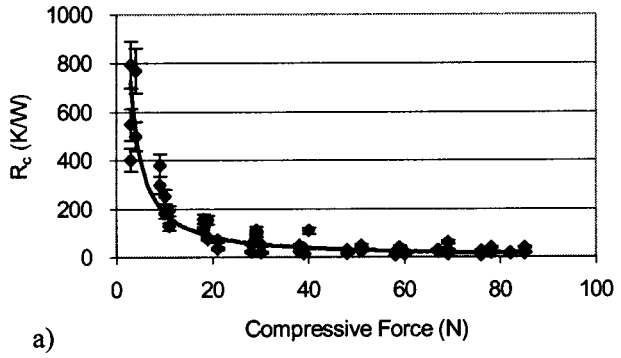

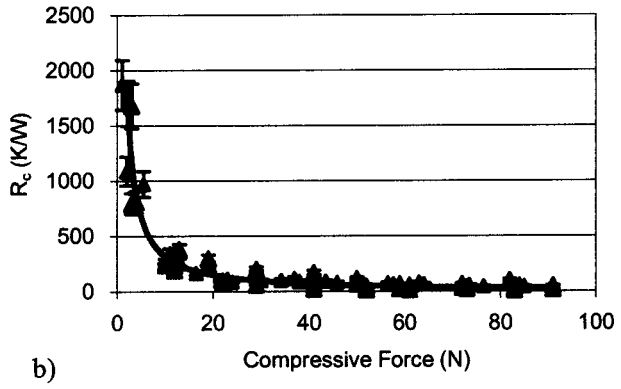

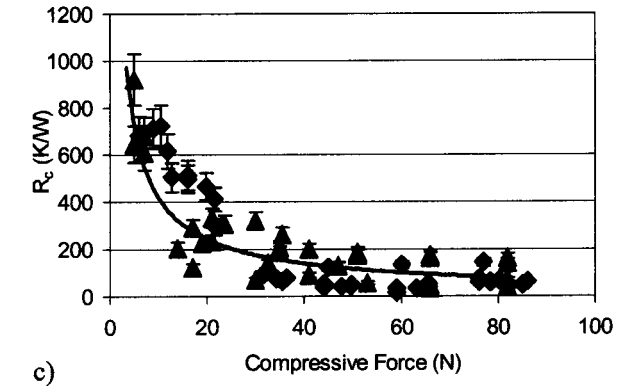

Fig. 10 Contact resistance measurements for *a*) aluminum, *b*) brass, and *c*) chrome-steel spheres

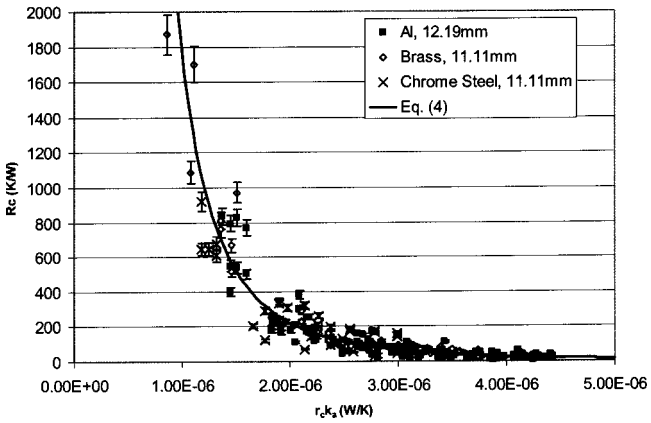

Fig. 11 Correlation of the contact resistance data for a large number of sphere types and sizes

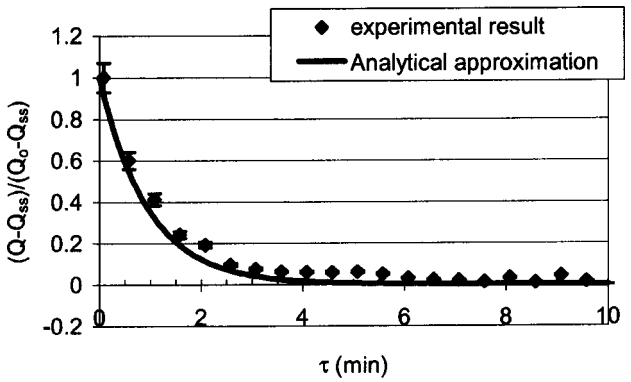

Fig. 12 Comparison of the measured and predicted transient response of a sphere in contacts with hot and cool pistons

$$R_c = \frac{1.75\times 10^{-15}\ [\mathrm{W^2\,K^{-2}}]}{(r_c k_a)^3\ [\mathrm{W^3\,K^{-3}}]} \tag{4}$$

Besides the steady-state contact-resistance measurement, this apparatus was also designed to render transient measurements, and so an interesting side question is whether the contact resistances may vary with time. Shown in Fig. 12 is the transient heat-flow measurement plotted together with the analytically predicted transient heat flow assuming the presence of a steady-state contact resistance. The agreement between the analytical prediction and the transient measurement seems to indicate that the transient component of the contact resistance, if it exists, is very small relative to its steady-state value.

Effective Conductivity. To quantify the effect of the contact resistance on the effective thermal conductivity, the presently obtained contact-resistance data were coupled with the Discrete Conduction Model [1] for 3D regular and random packed-sphere systems. The regular packed-sphere system (Face-center Cubic, Body-center Cubic, and Simple Cubic) consisted of 2 mm AISI-SS304 spheres, while the random packed-sphere system consisted of 2 mm AISI-SS304 spheres with mean coordination numbers between 4.8 and 5.5 and mean contact radius ratios between 5% and 20%. The contact resistance for these spheres were obtained through Eq. (4), which has been assumed to be applicable for spheres of different materials so long as they have similar average surface roughness and contact radius ratio as those measured in this experiment. The resulting temperature of each sphere was utilized to compute the planar-averaged temperature, which inturn was used to compute the overall effective thermal conductivity, herein denoted as ω.

As shown in Fig. 13, the results for the regular packed sphere system indicate the contact resistance to significantly affect the effective thermal conductivity of the packed bed, ω. Specifically, Fig. 13(*a*) shows the contact resistance to be a significant portion of the total resistance, particularly for highly conducting spheres (Cu) or spheres with low contact radius. Focusing only on 2 mm spheres ($r_c = 0.03$ mm), the results in Fig. 13(*b*) further show the neglect of contact resistance to produce an effective thermal conductivity value up to eight times higher than what it should be, and this effect is particularly prominent for spheres with large thermal conductivity. However, from this figure it is also apparent that the contact resistance can be reasonably neglected for certain range of contact radius and/or sphere conductivity. From our data, we obtained the condition given in Eq. (5) under which the neglect of contact resistance would produce an error in the effective thermal conductivity less than or equal to 10%. That is, so long as the ratio of sphere conductivity to the square of the contact radius is less than $7\times 10^8\ [\mathrm{Wm^{-3}\,K^{-1}}]$, the neglect of contact resistance may be acceptable.

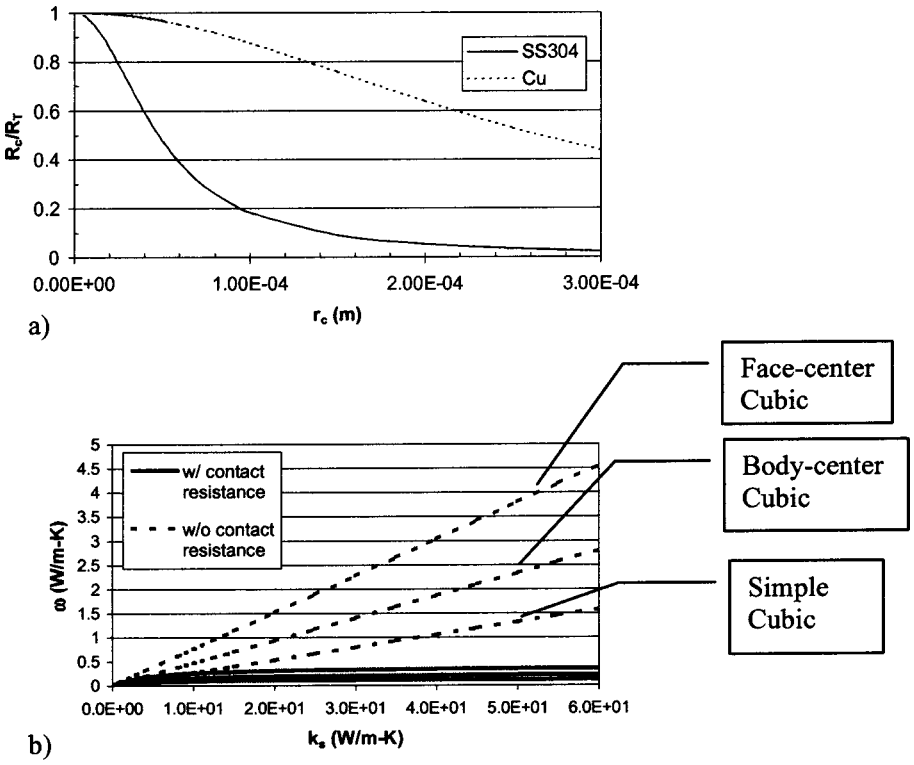

Fig. 13 Plot showing *a*) the ratio of contact resistance to the total resistance against contact radius for spheres in a Face-center Cubic arrangement and *b*) the effect of neglecting contact resistance in calculating the effective conductivity for increasing sphere conductivity

$$\frac{k_s}{r_c^2} < 7\times 10^8 \ [\mathrm{Wm^{-3}\,K^{-1}}] \tag{5}$$

For situations where the contact resistance cannot be neglected, the effective thermal conductivity needs to be adjusted accordingly. Denoting ω_0 as the effective thermal conductivity assuming perfect contacts, the adjustment is presented below in Eq. (6) where R_k and R_c, respectively, represent the constriction and contact resistances based on the mean contact radius ratio of the packing.

$$\omega = \frac{(\omega_0)R_k}{(R_c+R_k)} \tag{6}$$

Combining our earlier findings [1] for ω_0 and R_k along with the current measurement on R_c, Eq. (6) can be equivalently expressed below in Eq. (7). In Eq. (7*a*), the effective thermal conductivity of the packed bed, ω, is expressed in units of W/m-K, while γ and N_c represent the mean contact radius ratio and the mean coordination number and are dimensionless.

$$\omega_0 = (0.0125N_c^2 + 0.0716N_c)k_s\gamma \tag{7a}$$

Table 4 Comparison of the effective conductivity computed with Discrete Conduction Model and Eq. (7)

	Mean N_c	Mean γ (%)	R_c/R_T	ω from Discrete Conduction Model	ω computed from Eq. (7*b*)	Relative difference (%)
1	4.8452	5	0.491	0.221	0.224	1.36
2	5.3785	10	0.195	0.792	0.797	0.63
3	5.5418	20	0.056	1.928	1.929	0.05

$$\omega = \frac{\omega_0 R_k}{(R_c+R_k)} = \frac{(0.0125N_c^2+0.0716N_c)k_s\gamma R_k}{(R_c+R_k)} \tag{7b}$$

$$R_k = \frac{0.57588}{k_s r_c}\left(1 - \frac{1.0920\times 10^{-3}}{\gamma} + \frac{3.0187\times 10^{-5}}{\gamma^2} - \frac{1.202\times 10^{-7}}{\gamma^3}\right) \tag{7c}$$

$$R_c = \frac{1.75\times 10^{-15}\ [\mathrm{W^2\,K^{-2}}]}{(r_c k_a)^3\ [\mathrm{W^3\,K^{-3}}]} \tag{7d}$$

Finally, to verify the appropriateness of Eq. (7), the effective thermal conductivities for three random packed beds were calculated both through using Eq. (7) and the Discrete Conduction Model (contact resistance added). The comparison, given in Table 4, shows excellent agreement.

Conclusion

An experiment was designed and constructed to measure the contact resistance between spheres in elastic deformation. In particular, this design did not rely on the usage of a guard heater and was thus capable of rendering transient measurements. The experimental uncertainty was estimated to be ±6%, and the results were benchmarked against available data. A correlation was obtained relating the contact resistance with the contact radius, and results also showed the contact resistance to have minimal transient behavior. The effect of the contact resistance on the effective thermal conductivity of a packed bed was also studied, and the results showed that under certain situations, the neglect of contact resistance could incur an error in the effective thermal conductivity calculation as large as 800%. A guideline was, thus, presented under which the effect of the contact resistance may be ignored,

and for cases where the contact resistance cannot be ignored, a correlation for the effective thermal conductivity was also presented.

Acknowledgment

The authors would like to acknowledge the financial support from the Department of Mechanical Engineering at HKUST and the Research Grant Council of Hong Kong (Grants No. HKUST6237/00E and No. HKUST6192/03E).

Nomenclature

E = Young's Modulus, Pa
F = force, N
k = thermal conductivity, W/m-K
N_c = number of contacting spheres or the coordination number, dimensionless
Q = rate of heat transfer, W
Q_o = initial rate of heat transfer, W
R = thermal resistance, K/W
r = radius, m; r_c is contact radius
T = temperature, K

Greek

ν = Poisson ratio
γ = ratio of contact radius to sphere radius, r_c/r_s
τ = time, s
ω = effective conductivity, W/m-K
ω_o = effective conductivity with assumption of perfect contact, W/m-K

Subscript

a = air
c = contact
k = constriction
s = sphere, or length scale with r_s
ss = steady state
T = total

References

[1] Siu, W. W. M., and Lee, S. H.-K., 2004, ''Transient Temperature Computation of Spheres in Three-Dimensional Random Packings,'' Int. J. Heat Mass Transfer, **47**(5), pp. 887–898.
[2] Kaviany, M., 1995, *Principle of Heat Transfer in Porous Media*, Springer, New York.
[3] Wu, A. K. C., and Lee, S. H.-K., 2000, ''Sphere Packing Algrithm for Heat Transfer Studies,'' Numer. Heat Transfer, Part A, **37**(6), pp. 631–652.
[4] Snaith, B., Probert, S. D., and O'Callaghan, P. W., 1986, ''Thermal Resistances of Pressed Contacts,'' Appl. Energy, **22**, pp. 31–84.
[5] Peterson, G. P., and Fletcher, L. S., 1988, ''Thermal Contact Conductance of Packed Beds in Contact With a Flat Surface,'' ASME J. Heat Transfer, **110**, pp. 38–41.
[6] Kamiuto, K., and Saitoh, S., 1995, ''Simultaneous Heat and Mass Transfer in Packed Bed Catalytic Reactors,'' J. Thermophys. Heat Transfer, **9**(3), pp. 524–530.
[7] Fisher, N. J., and Yovanovich, M. M., 1989, ''Thermal Constriction Resistance of Sphere/Layer Flat Contacts: Theory and Experiment,'' ASME J. Heat Transfer, **111**, pp. 249–256.
[8] Sridhar, M. R., and Yovanovich, M. M., 1993, ''Elastoplastic Constriction Resistance of Sphere/Flat Contacts: Theory and Experiment,'' ASME HTD-Vol. 263, *Enhanced Cooling Techniques for Electronics Applications*, ASME, New York, pp. 123–134.
[9] Lambert, M. A., and Fletcher, L. S., 1997, ''Thermal Contact Conductance of Spherical Rough Metals,'' ASME J. Heat Transfer, **119**, pp. 684–690.
[10] Nishino, K., Yamashita, S., and Torii, K., 1995, ''Thermal Contact Conductance Under Low Applied Load in a Vacuum Environment,'' Exp. Therm. Fluid Sci., **10**, pp. 258–271.
[11] Madhusudana, C. V., 1995, *Thermal Contact Conductance*, Springer, New York.
[12] Timoshenko, S., and Goodier, J. N., 1951, *Theory of Elasticity*, McGraw-Hill, New York.
[13] Maccni, R. R., 1988, ''Characteristics Crucial to the Application of Engineering Plastics,'' *Engineering Materials Handbook—Vol. 2 Engineering Plastics*, ASM, Metals Park, OH.
[14] Beckwith, T. G., Buck, N. L., and Maragoni, R. D., 1982, *Mechanical Measurement*, Addison Wesley, Reading, MA.
[15] Lambert, M. A., Marotta, E. E., and Fletcher, L. S., 1993, ''The Thermal Contact Conductance of Hard and Soft Coat Anodized Aluminum,'' ASME HTD-Vol. 263, *Enhanced Cooling Technique for Electronics Applications*, ASME, New York, pp. 135–141.

Modeling Thermal Contact Resistance: A Scale Analysis Approach

M. Bahrami
Research Assistant Professor,
Mem. ASME

J. R. Culham
Associate Professor,
Mem. ASME

M. M. Yovanovich
Professor,
Fellow ASME

Microelectronics Heat Transfer Laboratory,
Department of Mechanical Engineering,
University of Waterloo, Waterloo, ON,
Canada N2L 3G1

A compact analytical model is developed for predicting thermal contact resistance (TCR) of nonconforming rough contacts of bare solids in a vacuum. Instead of using probability relationships to model the size and number of microcontacts of Gaussian surfaces, a novel approach is taken by employing the "scale analysis method." It is demonstrated that the geometry of heat sources on a half-space for microcontacts is justifiable for an applicable range of contact pressure. It is shown that the surface curvature and contact pressure distribution have no effect on the effective microthermal resistance. The present model allows TCR to be predicted over the entire range of nonconforming rough contacts from conforming rough to smooth Hertzian contacts. A new nondimensional parameter, i.e., ratio of the macro- over microthermal resistances, is introduced as a criterion to identify three regions of TCR. The present model is compared to collected TCR data for SS304 and showed excellent agreement. Additionally, more than 880 experimental data points, collected by many researchers, are summarized and compared to the present model, and relatively good agreement is observed. The data cover a wide range of materials, mechanical and thermophysical properties, micro- and macrocontact geometries, and similar and dissimilar metal contacts. [DOI: 10.1115/1.1795238]

Introduction

Heat transfer through interfaces formed by mechanical contact of rough solids has many important applications, such as in microelectronics chip cooling, spacecraft structures, and nuclear fuel-temperature prediction. Heat transfer across the interface can take place by three different modes: i) conduction at the microcontacts, ii) conduction through the interstitial fluid in the gap between the contacting solids, and iii) thermal radiation across the gap. The radiation heat transfer remains small and can be neglected when surface temperatures are not too high [1]. The mean separation between contacting bodies is sufficiently large (of order micrometers) that nanoscale effects influencing radiation heat transfer can be neglected. An order-of-magnitude analysis of the controlling heat transfer modes in the gap between contacting bodies indicates that the heat flux attributed to Stefan-Boltzman radiation is small and can also be neglected.

The interstitial fluid is assumed to be absent, thus the only remaining heat transfer mode is conduction through the microcontacts. In addition, the thermal rectification is not considered in this paper. This is the phenomenon in which thermal resistance is larger in one direction than in the other due to dissimilar materials.

Engineered or real surfaces have roughness and surface curvature/out-of-flatness simultaneously. Due to surface roughness, contact between two surfaces occurs only over microscopic contacts, which are located in the ''contact plane.'' The real area of contact, i.e., the total area of microcontacts, is a small fraction of the nominal contact area, typically a few percent [2,3]. As illustrated in Fig. 1, the macrocontact area—the area where microcontacts are distributed—is formed as a result of surface curvature of contacting bodies. Heat flow is constricted to pass through the macrocontact and then microcontacts. This phenomenon is observed through a relatively high temperature drop across the interface. Here an example is given to show the magnitude and relative importance of TCR versus the ''bulk resistance.'' Consider two 3 cm^2 flat SS plates with a thickness of 5 mm and surface roughness of 1 μm. The TCR for the bare joint in a vacuum under 0.1 MPa contact pressure, is approximately 30 K/W compared to the plate bulk resistance of 0.2 K/W.

Bahrami et al. [4] reviewed the existing theoretical TCR models. They divided TCR modeling procedures into geometrical, mechanical, and thermal analyses and discussed aspects of each component of the analysis in detail. Comparing to more than 400 experimental data points, Bahrami et al. [4] showed that the existing analytical models are applicable only to the limiting cases, namely, conforming rough contacts and smooth sphere-flat contacts and do not cover the entire range of TCR. Therefore, the need for a theoretical model that can predict TCR over the entire range of contacts still exists.

The objective of this study is to develop a compact analytical model for predicting TCR over the entire range of nonconforming rough contacts, i.e., from conforming rough to smooth sphere-flat contact. A novel approach is taken by employing scale analysis methods to achieve this goal.

Theoretical Background

Analytical, experimental, and numerical models have been developed to predict TCR since the 1930s. A large number of publications on TCR exist in the literature, which shows that the development of a general predictive model is difficult, to name a few Clausing and Chao [5], Lambert and Fletcher [6], and Nishino et al. [7]. A comprehensive review of the literature can be found in Bahrami et al. [4]. In this study, only a short review of the materials used to develop the present model is given.

According to the examination of the microgeometry of rough surfaces, surface asperities have small slopes and curved shapes at their summits [8,9]. It is a common methodology to simplify the contact of two Gaussian rough surfaces by the contact of a smooth plane with a random rough surface that has equivalent surface characteristics. The equivalent surface roughness σ and surface slope m can be found from

$$\sigma = \sqrt{\sigma_1^2 + \sigma_2^2} \quad \text{and} \quad m = \sqrt{m_1^2 + m_2^2} \tag{1}$$

Cooper et al. [10] showed that the microcontacts can be assumed

Contributed by the Heat Transfer Division for publication in the JOURNAL OF HEAT TRANSFER. Manuscript received by the Heat Transfer Division October 17, 2003; revision received June 11, 2004. Associate Editor: G. Chen.

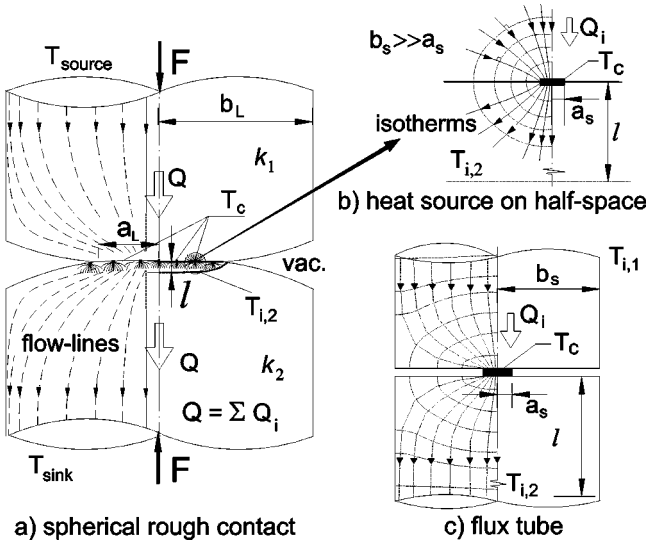

Fig. 1 Schematic geometry of spherical rough contact in vacuum, heat source on half-space, and flux tube geometries

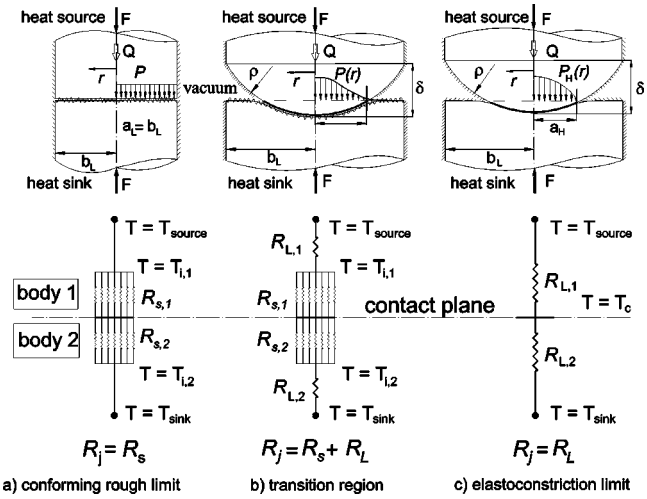

Fig. 2 Conforming rough, elastoconstriction, and transition regions

isothermal provided the thermal conductivity in each body is independent of direction, position, and temperature.

Thermal spreading resistance is defined as the difference between the average temperature of the contact area and the average temperature of the heat sink/source, divided by the total heat flow rate Q [1], i.e., $R=\Delta T/Q$. The real shapes of microcontacts can be a wide variety of singly connected areas, depending on the local profile of the contacting asperities. Yovanovich et al. [11] studied the steady-state thermal constriction resistance of a singly connected planar contact of arbitrary shape. They proposed a definition for thermal constriction resistance based on the square root of the contact area. Square root of the contact area was found to be the characteristic dimension and a nondimensional constriction resistance based on the square root of area was proposed, which varied by less than 5% for all shapes considered. Therefore, the real shape of the microcontacts would be a second-order effect, and an equivalent circular contact, which has the same area, can represent the microcontacts.

Yovanovich and Hegazy [12] showed through experiments that the surface microhardness is much higher than the bulk hardness and that the microhardness decreases as the indentation depth increases, until the bulk hardness is reached. They proposed a correlation for determining the microhardness,

$$H_{mic}=c_1(d_v/\sigma_0)^{c_2} \tag{2}$$

where d_v μm, c_1 GPa, c_2, and $\sigma_0=1$ μm are the Vickers indentation diagonal, correlation coefficients determined from the Vickers microhardness measurement, and a reference value, respectively. Microhardness depends on several parameters: roughness, mean absolute slope of asperities, method of surface preparation, and applied pressure. Sridhar and Yovanovich [13] suggested empirical relations to estimate Vickers microhardness coefficients, using the bulk hardness of the material. Two least-squares cubic fit expressions were reported

$$\begin{aligned} c_1&=H_{BGM}(4.0-5.77\kappa+4.0\kappa^2-0.61\kappa^3)\\ c_2&=-0.57+0.82\kappa-0.41\kappa^2+0.06\kappa^3 \end{aligned} \tag{3}$$

where $\kappa=H_B/H_{BGM}$, H_B is the Brinell hardness of the bulk material, and $H_{BGM}=3.178$ GPa. The above correlations are valid for the range $1.3\leqslant H_B\leqslant 7.6$ GPa; the RMS percent difference between data and calculated values was reported: 5.3% and 20.8% for c_1, and c_2, respectively. Milanez et al. [14] investigated the effect of microhardness coefficients on TCR by comparing the TCRs computed from the measured versus the estimated [from Eq. (3)] microhardness coefficients. They concluded that despite the difference between the measured and estimated values of microhardness coefficients, the TCRs predicted by both methods are in good agreement.

As shown in Fig. 1, there are two geometries that can be used as basic elements to model the thermal constriction/spreading resistance of the microcontacts, i) heat source on a half-space in which microcontacts are assumed to be located far from each other, where thermal constriction/spreading resistance of a circular microcontact of radius a_s can be found from

$$R_{mic,\text{half-space}}=\frac{1}{2k_s a_s} \tag{4}$$

where $k_s=2k_1k_2/(k_1+k_2)$, and ii) the flux tube geometry, considering the effect of neighboring microcontacts. Cooper et al. [10] proposed a simple accurate correlation for determining the flux tube constriction/spreading resistance,

$$R_{mic,\text{flux tube}}=\frac{\psi(\varepsilon_s)}{2k_s a_s} \tag{5}$$

where $\psi(\varepsilon_s)=(1-\varepsilon_s)^{1.5}$ and $\varepsilon_s=a_s/b_s$.

For smooth spherical contacts, Hertzian theory can be used to calculate the radius of the macrocontact area a_H. Hertz replaced the geometry of two spheres by a flat surface and an equivalent sphere, where the effective radius of curvature is $1/\rho=1/\rho_1+1/\rho_2$. Hertz derived a relationship for the radius of the contact area

$$\begin{aligned} a_H&=\left(\frac{3F\rho}{4E'}\right)^{1/3}\\ \frac{1}{E'}&=\frac{1-\upsilon_1^2}{E_1}+\frac{1-\upsilon_2^2}{E_2} \end{aligned} \tag{6}$$

where E, υ, and E' are the Young's modulus, Poisson ratio, and effective elastic modulus, respectively. Clausing and Chao [5] modeled the surface out-of-flatness by a spherical profile. For surfaces with large radii of curvature (approaching flat), they proposed an approximate relationship between radius of curvature and surface out-of-flatness as $\rho=b_L^2/2\delta$, where δ is the maximum out-of-flatness of the surface (see Fig. 2). Using the flux tube correlation [Eq. (5)] and neglecting the effect of surface roughness, the joint resistance for the smooth sphere-flat contact (i.e., elastoconstriction limit [15]) can be determined from

$$R_{j,\mathrm{EC}}=\frac{(1-a_H/b_L)^{1.5}}{2k_s a_H} \tag{7}$$

Comparison between the elastoconstriction model [i.e., Eq. (7)] and the smooth sphere-flat experimental data shows good agreement [4], thus the flux tube solution can be employed for determining the macrothermal resistance.

Macro- and Microthermal Resistances

As illustrated in Fig. 1, when the heat flow rate Q is transferred from a heat source at T_{source} to a heat sink at T_{sink}, it experiences the macrothermal constrictions $R_{L,1}$ and $R_{L,2}$, which arose due to the macrocontact area. Heat is then passed through n_s (parallel) microcontacts in the contact plane, which is called the effective microcontact resistance R_s. Therefore, TCR of a nonconforming rough joint in a vacuum can be written as

$$R_j=R_L+R_s \tag{8}$$

where $R_{\mathrm{L}}=R_{\mathrm{L},1}+R_{\mathrm{L},2}$, $R_{\mathrm{s}}=R_{\mathrm{s},1}+R_{\mathrm{s},2}$, and

$$\frac{1}{R_{\mathrm{s},1\ \mathrm{or}\ 2}}=\sum^{n_s}\frac{1}{R_{\mathrm{mic},1\ \mathrm{or}\ 2}}$$

where $R_{\mathrm{mic},1\ \mathrm{or}\ 2}$ is the sum of thermal constriction and spreading resistances of a single microcontact in body 1 or 2.

Equation (8) is a general expression and applicable to all spherical rough contacts; it was used by many researchers, such as Clausing and Chao [5], Nishino et al. [7], and Lambert and Fletcher [6]. A proof of Eq. (8) is given as follows. Assuming circular isothermal microcontacts, at T_c, that have a mean radius in the order of $a_s\sim\mu$m, isothermal planes must exist at intermediate temperatures $T_{i,1}$ and $T_{i,2}$ (i.e., $T_{\mathrm{source}}<T_{\mathrm{i},1}<T_c<T_{i,2}<T_{\mathrm{sink}}$) at some location l above/below the contact plane in body 1 and 2, respectively. If the microcontacts are considered as heat sources on a half-space the distance between these intermediate isothermal planes and the contact plane $l=40a_s\sim40\ \mu$m [1]. As microcontacts grow in size and number, they start to affect each other (the flux tube geometry) and l decreases, $l\sim b_s$ [16]. Consequently, macrothermal constriction/spreading resistances $R_{\mathrm{L},1}$ and $R_{L,2}$ are in series between the heat source and the isothermal plane $T_{i,1}$ and the isothermal plane $T_{\mathrm{i},2}$ and the heat sink, respectively. Also microcontacts provide n_s parallel paths for transferring heat between two isothermal planes $T_{\mathrm{i},1}$ and $T_{\mathrm{i},2}$.

Two limiting cases can be distinguished for Eq. (8): i) the conforming rough limit (i.e., contact of flat rough surfaces where the surface curvatures are very large thus macrothermal resistance R_L is negligible and microthermal resistance R_s is the controlling part), ii) the elastoconstriction limit where the radii of curvature of contacting bodies are small and surfaces are smooth, thus the macrothermal resistance R_L is predominant and R_s is negligible, and iii) transition region or general contact in which both R_L and R_s exist and have the same order of magnitude. Figure 2 shows the abovementioned regions and their corresponding thermal resistance networks. Later, a nondimensional parameter will be introduced, and a criterion will be proposed to specify these limits.

The Present Model

Due to the random nature of the surface roughness, studying the deformation and heat transfer of each single asperity is impossible; instead a representative (modeled) asperity is chosen and studied. Surface roughness is modeled by assuming a Gaussian distribution of asperities. The RMS surface roughness σ is a measure for the mean surface asperity heights.

In this section, using scale analysis, first an expression is derived for TCR of conforming rough contacts R_s. Then, the nonconforming macrocontact area is divided into infinitesimal surface elements where the conforming rough model relation can be applied. By integrating the local conductance over the macrocontact, an effective microcontact resistance R_s is found. Using the flux-tube correlation, the macrocontact resistance R_L is computed. Finally, superimposing the macro- and microthermal resistances [i.e., Eq. (8)] the joint resistance is determined.

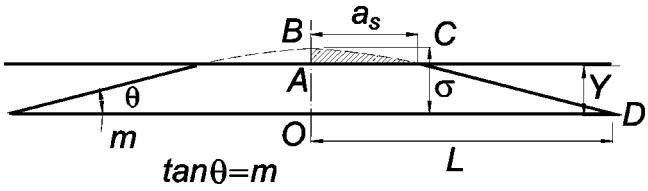

Fig. 3 Schematic geometry of microcontact

TCR of the Conforming Rough Limit. Surface roughness can be visualized as shallow valleys and hills with small slopes where asperities have spherical shapes at their summits. Figure 3 illustrates a model asperity, which represents the equivalent rough surface characteristics σ and m, placed in contact with a smooth plate at a mean separation Y. Using the equivalent rough surface simplification and considering that the mean surface slope m is small, one can assume that the microcontacts are flat and in the same contact plane. As discussed previously, the shape of microcontacts can be assumed circular. Figure 3 also illustrates a schematic geometry of a representative microcontact and proportionalities between the mean microcontact radius a_s and the surface roughness σ and slope m. In triangles ΔOBD and ΔABC, one can write $AC\propto OD$ from similar triangles. We also know that $AC=a_s$ and $OD=L=\sigma/m$, which leads to $a_s\propto\sigma/m$. This is in agreement with Kimura [17] who proposed that the ratio of roughness to asperity slope σ/m, instead of roughness itself, should be recognized as the parameter characterizing the geometrical property of the surface.

Considering n_s circular microcontacts with the mean radius of a_s within the macrocontact area, the real contact area is $A_r\propto\pi n_s a_s^2\propto\pi n_s(\sigma/m)^2$. The microcontacts are assumed to deform plastically, i.e., each microcontact can be visualized as a small microhardness indenter. The empirical correlation proposed by Yovanovich and Hegazy [12], see Eq. (2), is used to estimate the microhardness. Preserving the microcontact area (i.e., $A_v=\pi a_s^2$), where A_v is the projected area of the Vickers microhardness test, the Vickers indentation diagonal d_v can be related to the mean radius of microcontacts a_s, $d_v=\sqrt{2\pi}a_s$, microhardness becomes

$$H_{mic}\propto H^*\equiv c_1\left(\frac{\sigma}{m\sigma_0}\right)^{c_2} \tag{9}$$

Assuming plastic deformation of microcontacts, external force can be related to the real contact area and surface microhardness through a force balance,

$$F=A_r H_{mic}\propto\pi n_s\left(\frac{\sigma}{m}\right)^2 H^* \tag{10}$$

where H_{mic} is the microhardness of the softer material in contact. From Eq. (10) the number of microcontacts can be determined

$$n_s\propto\frac{F}{\pi(\sigma/m)^2 H^*} \tag{11}$$

It can be seen from Eq. (11) that an increase in load creates new microcontacts, while the mean size of microcontacts remains constant (i.e., $a_s\propto\sigma/m$). It should be noted that the size of microcontacts already in contact will increase as the load increases, or the mean separation Y decreases. However, the mean size of microcontacts, including new microcontacts generated, remains essentially constant. This is in agreement with Greenwood and Williamson [3] and also satisfies the proportionality $A_r\propto F$ reported by Tabor [2].

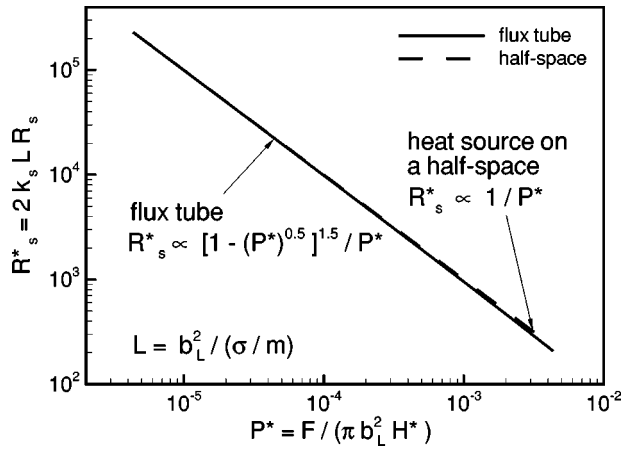

Fig. 4 Comparison between half-space and flux tube solutions

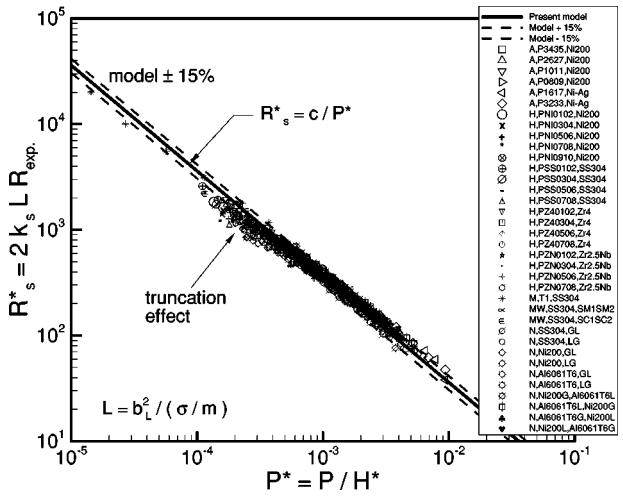

Fig. 5 Comparison between scale analysis model and data, conforming rough limit

The thermal model is based on the premise that n_s heat channels, covering the nominal contact area, form a set of parallel paths for transferring heat flow. If the half-space assumption is considered [see Fig. 1(*b*)] TCR can be found from

$$R_{s,\text{half-space}}=\frac{1}{2k_s n_s a_s}\propto\frac{1}{2k_s n_s(\sigma/m)} \tag{12}$$

Many researchers including Cooper et al. [10] modeled the microthermal constriction/spreading resistance using the flux tube geometry, thus TCR is

$$R_{s,\text{flux tube}}=\frac{\psi(\varepsilon_s)}{2k_s n_s a_s}\propto\frac{\psi(\varepsilon_s)}{2k_s n_s(\sigma/m)} \tag{13}$$

where $\psi(\cdot)$ is the constriction alleviation factor given in Eq. (5). The apparent contact area is covered by flux tubes with a mean radius b_s, and the relative size of microcontacts can be found from $\varepsilon_s=a_s/b_s=\sqrt{A_r/A_a}$, where $A_a=\pi b_L^2$. Substituting A_r and A_a one obtains

$$\varepsilon_s\propto\sqrt{\frac{F/\pi b_L^2}{H^*}}\equiv\sqrt{P^*} \tag{14}$$

where P^* is a nondimensional parameter that can be interpreted as the ratio of the nominal contact pressure to the pressure at the microcontacts. The number of microcontacts can be expressed in terms of P^* from Eq. (11)

$$n_s\propto\frac{b_L^2}{(\sigma/m)^2}P^* \tag{15}$$

We find the TCR for conforming rough surfaces by using the nondimensional parameter P^* and the flux tube solution

$$R_{s,\text{flux tube}}\propto\frac{(\sigma/m)(1-\sqrt{P^*})^{1.5}}{2k_s b_L^2 P^*} \tag{16}$$

or in the non-dimensional form

$$R^*_{s,\text{flux tube}}=2k_s L R_s\propto\frac{(1-\sqrt{P^*})^{1.5}}{P^*} \tag{17}$$

where $L=b_L^2/(\sigma/m)$ is the conforming rough limit length scale. The TCR for conforming rough surfaces, using the heat source on a half-space solution, can be found by substituting Eq. (15) into Eq. (12)

$$R^*_{s,\text{half-space}}\propto\frac{1}{P^*} \tag{18}$$

Figure 4 shows the comparison between Eqs. (17) and (18). It can be seen that over a wide range of P^*, they are almost identical and show very good agreement. However, as expected, at relatively large values of P^* the half-space relationship [Eq. (18)] shows slightly higher resistances than the flux tube. The RMS relative difference between two relationships is less than 4%. Therefore, the microcontacts can be modeled as heat sources on a half-space, and Eq. (18) is chosen for thermal analysis of microcontacts.

Using scale analysis techniques we derived Eq. (18), which illustrates that the TCR of microcontacts is inversely proportional to the dimensionless pressure (or external load). To find the equality or exact relationship, Eq. (18) must be multiplied by the scale-analysis constant c, which can be found through comparison with experimental data, i.e.,

$$R^*_s=\frac{c}{P^*} \tag{19}$$

The dimensional forms of thermal resistance and conductance using $h_s=1/(R_s A_a)$ are

$$R_s=\frac{\pi c(\sigma/m)H^*}{2k_s F}$$
$$h_s=\frac{2}{\pi c}k_s\left(\frac{m}{\sigma}\right)\frac{P}{H^*} \tag{20}$$

where c and $P=F/(\pi b_L^2)$ are the scale-analysis constant and nominal contact pressure, respectively. From Eqs. (20) and (10), it can be seen that the effective microthermal resistance is inversely proportional to the real contact area, i.e., $R_s\propto(\sigma/m)/(k_s A_r)$.

Approximately 610 experimental data points collected by Antonetti [18], Hegazy [19], Milanez et al. [20], McWaid [21], and Nho [22] are summarized, nondimensionalized, and plotted along with Eq. (19) in Fig. 5 with $c=0.36$. Minimizing the RMS difference between the model [Eq. (19)] and the experimental data, the constant of the scale analysis c was found to be $c=0.36$. The relative RMS and the mean absolute difference between the data and the relationship are 14.1% and 10.9%, respectively. Table 1 indicates the researchers and the specimen materials used in the experiments. Table 2 lists the data set number (the number that was originally assigned to the experimental data set by the researchers); the geometrical, mechanical, and average contact temperature, and the thermophysical properties of the experimental data, as reported.

Table 1 Researchers and specimen materials used in comparisons

Ref.	Researcher	Material(s)
A	Antonetti [18]	Ni 200 Ni 200-Ag
Bah	Bahrami [25]	SS 304
Blo	Bloom [28]	SS 17-4 PH
B	Burde [27]	SPS 245, CS
CC	Clausing and Chao [30]	Al 2024 T4 Brass Anaconda Mg AZ 31B SS303
CM	Cassidy and Mark [29]	SS 416
F	Fisher [31]	Ni 200-Carbon Steel
FG	Fletcher and Gyorog [32]	Brass 360 Mg Az 31B SS 304
G	Gyorog [33]	SS 304
H	Hegazy [19]	Ni 200 SS 304 Zircaloy 4 Zr-2.5%wt Nb
K	Kitscha [34]	Steel 1020-CS
MM	McMillan and Mikic [35]	SS 303
MR	Mikic and Rohsenow [16]	SS 305
M	Milanez et al. [20]	SS 304
MW	McWaid [21]	SS 304
N	Nho [22]	Al 6061 T6 Ni 200 SS 304 Ni⇆Al
SG	Smuda and Gyorog [36]	SS 304

Nho [22] studied the contact of ground with lapped surfaces. He showed that the grinding process generates near-Gaussian surface heights distributions. The surface slope was estimated from $m=\sqrt{m_{\min}m_{\max}}$, where $m_{\min}$ and $m_{\max}$ are the minimum and maximum surface slopes measured by the profilometer. Nho [22] carried out an extensive experimental program with similar and dissimilar metals (i.e., aluminum alloy 6061 T6, nickel 200, and SS 304 pairs) over a broad range of thermophysical properties and contact pressure. The [22] data are named to show the heat flow direction and the surface preparation method, for example, "N, Ni200-G, Al6061T6-L" means that the experiment was conducted between ground nickel 200 and lapped aluminum 6061 T6, and the heat flow direction was from nickel to aluminum specimen. As can be seen in Fig. 5, Nho's data show a negligible directional effect for similar metals. Additionally, the directional effect is not observed in nickel 200 and aluminum 6061 T6 pairs, but for nickel 200 and SS 304 pairs a large deviation from the predicted TCR is observed; those data are not included in the comparison.

As can be observed in Fig. 5, a common trend can be recognized in most of the conforming rough data sets. Experimental data show a lower resistance at relatively light loads compared with the model; the data approach the model as the load increases. This phenomenon, which is called the *truncation effect* [20], is important at light loads when surfaces are relatively rough. A possible explanation for this trend is the Gaussian assumption of the surface asperities, which implies that asperities with "infinite" heights exist. Milanez et al. [20] experimentally studied the truncation effect and proposed correlations for maximum asperities heights as functions of surface roughness.

Yovanovich [23] proposed an accurate correlation for determining the thermal conductance of conforming rough contacts based on the analytical model of Cooper et al. [10]

$$h_c=1.25k_s\left(\frac{m}{\sigma}\right)\left(\frac{P}{H_{mic}}\right)^{0.95} \tag{21}$$

Comparison of Eq. (20) with $[c=0.36]$ and Eq. (21) reveals that the present model and the Yovanovich [23] correlation are in good agreement over moderate and high loads, $1\times10^{-4}\leqslant P/H_{mic}\leqslant 2\times10^{-2}$; for relatively light loads, $P/H_{mic}\leqslant 1\times10^{-4}$, Eq. (20) predicts higher resistances.

General Model. Bahrami et al. [24] studied mechanical contact of spherical rough surfaces. Assuming elastic bulk deformation and plastic deformation for microcontacts, a general contact pressure distribution was proposed that covers nonconforming contacts ranging from spherical rough to smooth Hertzian contacts. A simple correlation was proposed for calculating the radius of the macrocontact as a function of two nondimensional parameters,

$$a_L=1.80a_H\frac{\sqrt{\alpha+0.31\tau^{0.056}}}{\tau^{0.028}} \tag{22}$$

where $\alpha=\sigma\rho/a_H^2$ and $\tau=\rho/a_H$ are the roughness parameter introduced by Johnson [9] and the geometric parameter, respectively.

The thermal macroresistance can be found by using the flux tube correlation [Eq. (5)] and the radius of the macrocontact area given by Eq. (22)

$$R_L=\frac{(1-a_L/b_L)^{1.5}}{2k_sa_L} \tag{23}$$

In Eq. (23), it is assumed that the radii of two contacting bodies are the same (i.e., $b_{L,1}=b_{L,2}=b_L$). In the general case where $b_{L,1}\neq b_{L,2}$, thermal spreading resistance will be $R=\psi(a/b)/4ka$.

The macrocontact area is a circle, thus the heat transferred in a nonconforming rough contact under vacuum conditions can be calculated from

$$Q=2\pi\Delta T_s\int_0^{a_L}h_s(r)rdr \tag{24}$$

where $h_s(r)$ and $\Delta T_s=T_{i,1}-T_{i,2}$ are the local thermal conductance, and the effective temperature difference for microcontacts, respectively. The effective microthermal conductance for a joint can be defined as $h_s=Q/A_a\Delta T_s$. Therefore, the effective microcontact thermal resistance, where $R=1/hA_a$ is

$$R_s=\frac{1}{2\pi}\left[\int_0^{a_L}h_s(r)rdr\right]^{-1} \tag{25}$$

Assuming constant pressure in the surface elements dr, one can calculate the local thermal conductance at r from Eq. (20)

$$h_s(r)=\frac{2}{c\pi}k_s\left(\frac{m}{\sigma}\right)\frac{P(r)}{H^*} \tag{26}$$

where $P(r)$ is the local contact pressure at r. Substituting Eq. (26) into Eq. (25), one obtains

$$R_s=\frac{cH^*(\sigma/m)}{4k_s}\left[\int_0^{a_L}P(r)rdr\right]^{-1} \tag{27}$$

From a force balance, we know that $F=2\pi\int_0^{a_L}P(r)rdr$, therefore, Eq. (27) simplifies to

$$R_s=\frac{c\pi H^*(\sigma/m)}{2k_sF} \tag{28}$$

Table 2 Summary of geometrical, mechanical and thermo-physical properties, conforming rough contacts

Reference, test # and material	E'	σ/m	c_1/c_2	k_s	b_L	$\overline{T}_c$
	GPa	μm	GPa	W/mK	mm	°C
A,P3435,Ni200	112.09	8.48/0.344	6.3/−0.26	67.1	14.3	110
A,P2627,Ni200	112.09	1.23/0.139	6.3/−0.26	64.5	14.3	150
A,P1011,Ni200	112.09	4.27/0.237	6.3/−0.26	67.7	14.3	100
A,P0809,Ni200	112.09	4.29/0.240	6.3/−0.26	67.3	14.3	108
A,P1617,Ni-Ag	63.90	4.45/0.255	0.39/0	100.0	14.3	195
A,P3233,Ni-Ag	63.90	8.03/0.349	0.39/0	100.0	14.3	190
H,PNI0102,Ni200	112.08	0.90/0.110	6.3/−0.26	75.3	12.5	120
H,PNI0304,Ni200	112.08	3.43/0.190	6.3/−0.26	76.0	12.5	115
H,PNI0506,Ni200	112.08	4.24/0.188	6.3/−0.26	75.9	12.5	110
H,PNI0708,Ni200	112.08	9.53/0.228	6.3/−0.26	75.7	12.5	115
H,PNI0910,Ni200	112.08	13.94/0.233	6.3/−0.26	75.8	12.5	115
H,PSS0102,SS304	113.74	0.48/0.072	6.3/−0.26	19.2	12.5	140
H,PSS0304,SS304	113.74	2.71/0.116	6.3/−0.26	19.1	12.5	145
H,PSS0506,SS304	113.74	5.88/0.146	6.3/−0.26	18.9	12.5	130
H,PSS0708,SS304	113.74	10.95/0.19	6.3/−0.26	18.9	12.5	125
H,PZ40102,Zircaloy4	57.26	0.61/0.049	3.32/−0.15	16.6	12.5	130
H,PZ40304,Zircaloy4	57.26	2.75/0.148	3.32/−0.15	17.5	12.5	155
H,PZ40506,Zircaloy4	57.26	3.14/0.129	3.32/−0.15	18.6	12.5	155
H,PZ40708,Zircaloy4	57.26	7.92/0.207	3.32/−0.15	18.6	12.5	160
H,PZN0102,Zr2.5Nb	57.26	0.92/0.083	5.88/−0.27	21.3	12.5	165
H,PZN0304,Zr2.5Nb	57.26	2.50/0.162	5.88/−0.27	21.2	12.5	170
H,PZN0506,Zr2.5Nb	57.26	5.99/0.184	5.88/−0.27	21.2	12.5	165
H,PZN0708,Zr2.5Nb	57.26	8.81/0.200	5.88/−0.27	21.2	12.5	160
M,T1,SS304	113.74	0.72/0.041	6.27/−0.23	18.8	12.5	39
MW,SS304,SM1SM2	113.74	1.34/0.105	4.8/0	16.0	12.7	52
MW,SS304,SC1SC2	113.74	1.44/0.089	4.5/0	16.0	12.7	52
N,SS304,GL	113.74	0.97/0.061	5.12/−0.29	19.5	12.5	175
N,SS304,LG	113.74	0.97/0.061	5.12/−0.29	19.5	12.5	185
N,Ni200,GL	112.08	0.87/0.050	4.6/−0.21	68.9	12.5	195
N,Ni200,LG	112.08	0.87/0.050	4.6/−0.21	69.4	12.5	185
N,Al6061T6,GL	39.11	0.86/0.058	0.9/−0.006	211.4	12.5	223
N,Al6061T6,LG	39.11	0.86/0.058	0.9/−0.006	211.5	12.5	227
N,Ni200-G,Al6061T6-L	56.23	0.90/0.048	1.1/−0.008	104.3	12.5	168
N,Al6061T6-L,Ni200-G	56.23	0.90/0.048	1.1/−0.008	102.7	12.5	210
N,Al6061T6-G,Ni200-L	56.23	1.20/0.057	1.03/−0.001	108.1	12.5	135
N,Ni200-L,Al6061T6-G	56.23	1.20/0.057	1.03/−0.001	108.8	12.5	125

Equations (20) and (28) are identical, which implies that the effective thermal microresistance R_s is not a function of the surface curvature. Additionally, the pressure-distribution profile does not affect the thermal microresistance. Through experiments, it can be observed that the joint resistance R_j increases as surface curvature decreases from the conforming $\rho\to\infty$ toward nonconforming contacts, if all other input contact parameters remain constant. This increase arises due to the formation of the macrocontact area and, consequently, the macroresistance R_L. It should be noted that the effective microthermal resistance R_s remains unchanged as surface curvature varies [Eq. (28)].

By superimposing the macro- and the microresistances [Eq. (8)], the thermal joint resistance for a spherical rough contact is obtained

$$R_j=\frac{0.565H^*(\sigma/m)}{k_sF}+\frac{(1-a_L/b_L)^{1.5}}{2k_sa_L} \tag{29}$$

From Eq. (29) one can conclude that i) the effective microthermal resistance, except for the thermal conductivity, is only a function of the contact microscale characteristics (i.e., surface roughness σ, slope m, microhardness H^*, and the load F), and ii) on the other hand, the macrothermal resistance is a function of the macroscale contact parameters, the macrocontact radius a_L, and size of the contacting bodies b_L. The macrocontact radius is a function of the effective elasticity modulus E', radius of curvature ρ, surface roughness σ, and the load F [Eq. (22)].

The applied load and surface roughness appear to play important roles in both macro- and microthermal resistances. The effect of surface roughness on the macroresistance is limited to the macrocontact radius a_L. The applied load is the connecting bridge between the macro- and micromechanical analyses, since the force balance must be satisfied in both analyses.

Equation (29) is a general relationship that covers both limiting cases and the transition region. It can be easily seen that in the conforming rough limit where $a_L\to b_L$, the macroresistance $R_L\to 0$, and Eq. (29) yields Eq. (20). Also, in the elastoconstriction limit where $\sigma\to 0$, the microresistance $R_s\to 0$ and $a_L\to a_H$, and Eq. (29) is reduced to Eq. (7).

Dividing both sides of Eq. (29) by R_s, one obtains

$$\frac{1.77k_sF}{H^*(\sigma/m)}R_j=1+\Theta \tag{30}$$

where Θ is the ratio of the macro- to microthermal resistances

$$\Theta=\frac{F(1-a_L/b_L)^{1.5}}{1.13H^*(\sigma/m)a_L} \tag{31}$$

Θ is a nondimensional parameter that includes the applied load, macro- and microgeometrical parameters (i.e., σ, m, ρ, and b_L) as well as the elastic and plastic mechanical properties of the contacting bodies E' and H^*. Based on this nondimensional parameter, a criterion can be defined for the elastoconstriction and conforming rough limits,

$$\begin{cases}\Theta\ll 1 & \text{conforming rough}\\ \Theta\gg 1 & \text{elastoconstriction}\end{cases} \tag{32}$$

As expected, Θ is independent of the thermal conductivity.

Equation (29) can be nondimensionalized with respect to the conforming rough limit length scale L and rewritten

$$R_j^*=2k_sLR_j=\frac{0.36}{P^*}+\frac{L(1-a_L/b_L)^{1.5}}{a_L} \tag{33}$$

where $L=b_L^2/(\sigma/m)$ and $P^*=F/(\pi b_L^2H^*)$.

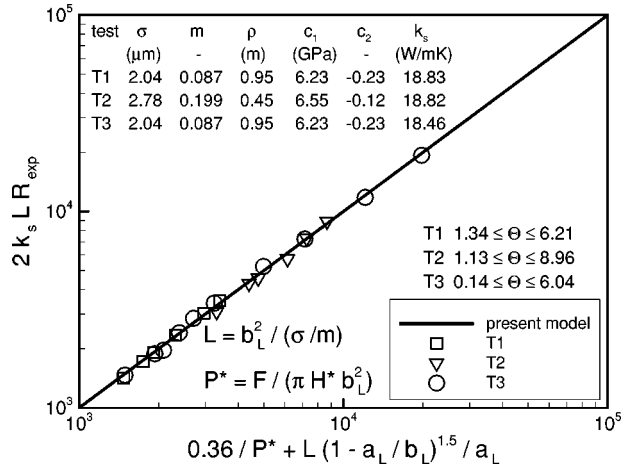

Fig. 6 Comparison between data [25] and present model

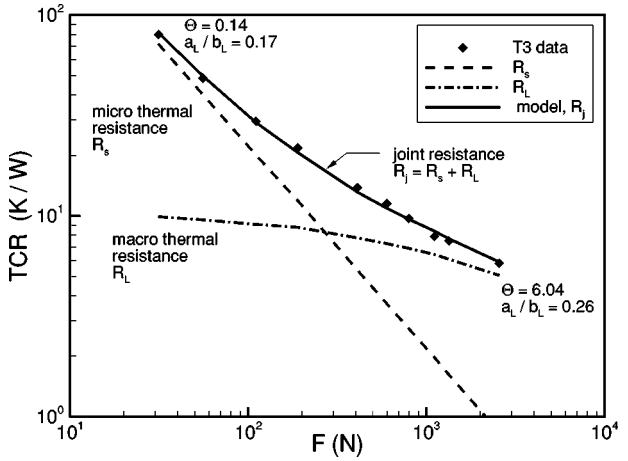

Fig. 7 Micro-, macro-, and joint thermal resistances for data set T3

Comparison With Experimental Data

To verify the general model, an experimental program was conducted to obtain data for nonconforming rough contacts in a vacuum [25]. The contact assembly included a bead-blasted flat specimen placed in contact with a smooth, polished, spherical sample in series with an ARMCO iron flux meter in a vacuum chamber. Both the flat and spherical specimens were made of SS304, $E=207$ GPa and $\nu=0.3$. Samples were machined into cylindrical shapes of 25 mm diam and 45 mm length. Both contact specimens and the flux meter were prepared for placement of six thermocouples by drilling holes that were 0.64 mm diam and 2.5 mm deep. Thermocouples were placed along the samples length so that the temperature distribution within each section could be determined. These thermocouples were located 5 mm apart with the first one 10 mm from the contact surface. The thermal conductivity of the ARMCO iron flux meter was known and used to measure the heat flow rate transferred through the contact. Also, separate tests were conducted to correlate the thermal conductivity of SS304 specimens as a function of temperature. The temperature distributions within the flat and spherical specimens were used to determine the contact temperature drop by extrapolating to the contact plane.

The flatness deviation of the flat specimens was checked using an optical flat, before bead-blasting. In general, the out-of-flatness deviation was less than 0.3 μm. The surface roughness and slope of the flat samples were measured using a Taylor-Hobson ST3 Plus Talysurf profilometer. Eight randomly selected traces of surface height profile were taken from each bead-blasted specimen. Each trace was approximately 1 cm long. The average values of surface roughness and slope are shown in Fig. 6, the RMS difference between the mean values and the measurements is approximately 6%.

Three sets of data were collected as indicated by Tests 1–3. Two radii of curvature were chosen for spherical samples, 0.45 and 0.95 m. Radii of curvature of spherical samples were measured using a Mitutoyo BHN 305 coordinate measuring machine. For each spherical sample, five separate radii of curvature were measured; the averaged values are shown in Fig. 6. The maximum relative difference between the average radii and measurements is less than 3.5%.

Mean contact temperatures of tests were recorded in the range of 45 to 145°C. The applied load was varied from 28 to 2600 N. The measured thermal joint resistance values were nondimensionalized and compared to the general model [i.e., Eq. (33)] in Fig. 6. A comprehensive uncertainty analysis based on a differential error analysis method [26] is performed in [25] to estimate the uncertainty of the collected data. The accuracy of the experimental data is approximately 5.8%. The maximum relative difference between the model and the data is 6.84%; the RMS difference between the model and data sets T1, T2, and T3 are 2.43, 4.13, and 3.84%, respectively.

The experimental program was designed to study and cover the transition region where the magnitude of the micro- and macrothermal resistances are comparable. Since a large number of reliable TCR data are available for the conforming rough and the elastoconstriction limits, no tests were conducted in these limiting regions. The values chosen for radii of curvature, load, and surface roughness provides TCR data over a relatively wide range of the transition region, $0.14\leqslant\Theta\leqslant 8.96$, see Fig. 6. To verify the reproducibility of experiments, Test 3 was conducted with the same radius of curvature and surface roughness of Test 1; new specimens were used over a wider range of applied load compared to T1. The relative importance of the micro- and macrothermal resistances is shown in Fig. 7 for the data set T3, as the applied load increases. The ratio of a_L/b_L varies from 0.17 to 0.26 as the load increases from 28 to 2561.5 N. Also the microresistance becomes smaller and the macroresistance dominates the joint resistance by increasing the load. Observe that, even at relatively large load of 2561.5 N, the radius of the macrocontact area covers only 26% of samples radius b_L. The spherical specimens have large radii of curvature, e.g. $\rho=0.95$ m, or equivalently the maximum out-of-flatness of 82 μm for T3. These samples seem flat, and

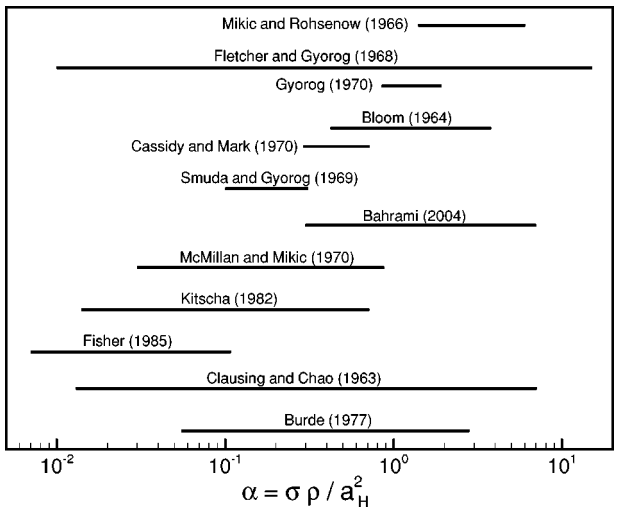

Fig. 8 Range of roughness parameter α for experimental data used in comparison

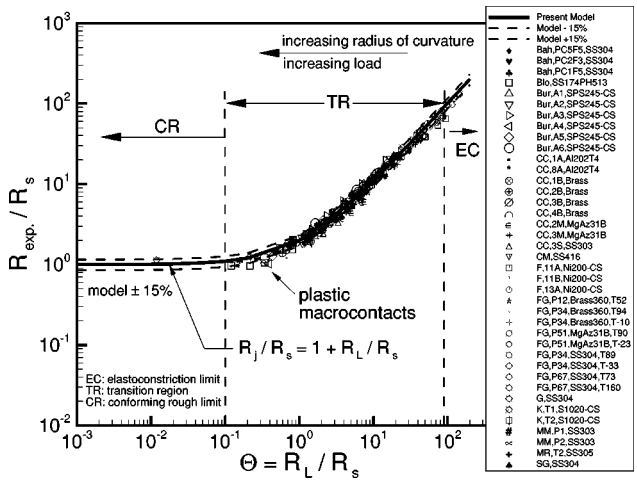

Fig. 9 Comparison between general model and nonconforming rough data

their surface curvatures cannot be detected by the naked eye, yet surface curvatures cause a relatively large thermal resistance even at high loads. This clearly shows the significance and impact of the surface curvature (out-of-flatness) on TCR.

Approximately 260 experimental data points collected by Burde [27], Bloom [28], Cassidy and Mark [29], Clausing and Chao [30], Fisher [31], Fletcher and Gyorog [32], Gyorog [33], Kitscha [34], McMillan and Mikic [35], Mikic and Rohsenow [16], and Smuda and Gyorog [36] are summarized through a comprehensive literature review. The nondimensional roughness parameter $\alpha = \sigma\rho / a_H^2$ is an important mechanical parameter for the spherical rough contacts. As the roughness parameter approaches zero the contact pressure and the macrocontact radius approaches the Hertzian values. The roughness parameter may be reduced by i) increasing the load, ii) decreasing surface roughness, and iii) decreasing the radius of curvature. Figure 8 summarizes the range of the roughness parameter for the experimental data used in the comparison. As shown, the above data sets cover a wide range of the roughness parameter.

The collected data were nondimensionalized and compared with the model [Eq. (30)] in Fig. 9. The three regions of TCR are also shown in the plot. The present model illustrates good agreement with the data; the RMS and mean absolute relative difference between the model and data are approximately 11.7% and 9.4%, respectively. Table 1 lists the researchers and the specimen materials used in the experiments. Table 3 lists the data set number (the number which was originally assigned to the experimental data set by the researchers); the geometrical, mechanical, and average contact temperature, and the thermophysical properties of the experimental data, as reported.

As the external load increases beyond the elastic limit of the contacting bodies, elastoplastic and plastic deformations may occur. The plastic macrocontact radius a_P is larger than the radius a_L (elastic) (i.e., $a_P > a_L$). Consequently, lower TCR will be measured; this trend can be clearly seen in the Fisher [31] data set "F,11A,Ni200-CS" (see Figs. 9 and 10).

More than 880 experimental data points (data sets used in comparisons in Figs. 5–9) are combined, nondimensionalized, and compared to the present model [Eq. (33)] in Fig. 10. The present model shows good agreement over the entire range of the comparison with the experimental data, which cover a wide range of the input parameters (see Table 4). The data include the contact between dissimilar metals, such as Ni 200-Al 6061 T6, Ni 200-Ag, and SS-CS.

Table 3 Summary of geometrical, mechanical and thermophysical properties, nonconforming contacts

Reference, test # and material	E'	σ/m	ρ	c_1/c_2	k_s	b_L	$\overline{T_c}$
	GPa	μm	m	GPa	W/mK	mm	°C
Blo,SS17,4PH,513	107.69	2.71/0.15	31.63	4.33/0	15.2	25.4	−60
Bur,A1,SPS245,CS	113.74	0.63/0.04	0.0143	3.93/0	40.7	7.15	70
Bur,A2,SPS245-CS	113.74	1.31/0.07	0.0143	3.92/0	40.7	7.15	70
Bur,A3,SPS245-CS	113.74	2.44/0.22	0.0143	3.92/0	40.7	7.15	70
Bur,A4,SPS245-CS	113.74	2.56/0.08	0.0191	4.44/0	40.7	7.15	70
Bur,A5,SPS245-CS	113.74	2.59/0.10	0.0254	4.44/0	40.7	7.15	70
Bur,A6,SPS245-CS	113.74	2.58/0.10	0.0381	4.44/0	40.7	7.15	70
CC,1A,Al2024T4	37.86	0.43/0.06	13.80	1.72/−0.04	136.8	12.7	104
CC,8A,Al2024T4	38.66	2.26/0.14	14.66	1.73/−0.04	141.4	12.7	110
CC,1B,Brass	49.62	0.47/0.06	3.87	3.02/−0.17	125.0	12.7	171
CC,2B,Brass	49.62	0.50/0.06	4.07	3.02/−0.17	125.0	12.7	129
CC,3B,Brass	51.92	0.50/0.06	3.34	3.02/−0.17	101.5	12.7	71
CC,4B,Brass	49.62	0.50/0.06	4.07	3.02/−0.17	125.0	12.7	127
CC,2M,MgAz31B	25.64	0.11/0.03	30.32	0.41/0	96.0	12.7	100
CC,3M,MgAz31B	25.64	0.11/0.03	12.41	0.41/0	96.0	12.7	100
CC,3S,SS303	113.74	0.11/0.03	21.17	4.59/−0.13	17.8	12.7	118
CM,SS416	106.04	0.126/0.08	13.44	2.62/0	24.9	12.7	
F,11A,Ni200-CS	112.62	0.12/0.04	0.0191	4.00/0	57.9	12.5	40
F,11B,Ni200-CS	112.62	0.12/0.04	0.0381	4.00/0	57.9	12.5	40
F,13A,Ni200-CS	112.62	0.06/0.03	0.0381	4.00/0	58.1	12.5	40
FG,P12,Brass360,T52	54.13	0.07/0.02	28.91	1.08/0	107.0	12.7	52
FG,P34,Brass360,T94	53.56	2.21/0.14	2.56	1.13/0	112.0	12.7	94
FG,P34,Brass360,T-10	55.84	2.21/0.14	2.56	1.13/0	98.0	12.7	−10
FG,P51,MgAz31B,T90	23.36	0.16/0.03	0.8077	0.47/0	88.0	12.7	90
FG,P51,MgAz31B,T-23	26.21	0.16/0.03	0.8077	0.62/0	70.0	12.7	−23
FG,P34,SS304,T89	106.04	1.17/0.10	9.62	2.06/0	15.9	12.7	89
FG,P34,SS304,T−33	106.04	1.17/0.10	9.62	2.85/0	13.5	12.7	−33
FG,P67,SS304,T73	106.04	0.11/0.03	0.4019	2.85/0	15.6	12.7	73
FG,P67,SS304,T160	106.04	0.11/0.03	0.4019	2.85/0	16.6	12.7	160
G,SS304	106.04	0.79/0.08	72.00	4.00/0	16.2	12.7	155
K,T1,Steel1020-CS	113.74	0.76/0.08	0.0130	4.00/0	48.0	12.7	
K,T2,Steel1020-CS	113.74	0.13/0.03	0.0130	4.00/0	51.4	12.7	
MM,P1,SS303	113.74	2.70/0.07	0.1180	4.00/0	17.3	12.7	
MM,P2,SS303	113.74	1.75/0.07	2.44	4.00/0	22.0	12.7	
MR,T2,SS305	107.14	3.87/0.21	39.69	4.2/0	19.9	12.7	
SG,SS304	106.04	0.14/0.03	70.74	4.00/0	16.2	12.7	143

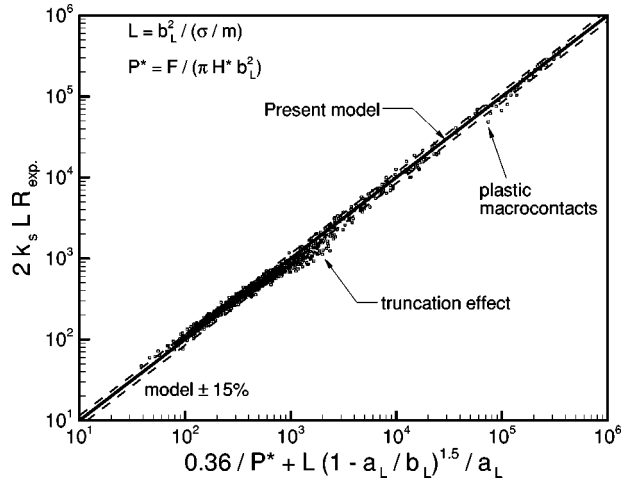

Fig. 10 Comparison of general model with all data

The surface slope m has not been reported by Clausing and Chao [30], Kitscha [34], Fisher [31], and Mikic and Rohsenow [16]. It was estimated using a correlation proposed by Lambert and Fletcher [6], $m=0.076\sigma^{0.52}$, where σ is in micrometer. Because of the abovementioned approximation to account for unreported data, the accuracy of the comparison is difficult to assess. However, the RMS and the mean absolute difference between the model and data for the entire set of data are approximately 13.8% and 10.4%, respectively. A $\pm 15\%$ bound is included in Fig. 10; 730 out of 880 data points fall into the $\pm 15\%$ bound. The accuracy of experimental data were reported by some of researchers, such as Antonetti [18], Fisher [31], and Hegazy [19], to be 8.1, 5, and 7%, respectively.

Summary and Conclusion

We show that the joint resistance is the superposition of the macro- and microthermal resistances in a vacuum. It is shown that the heat source on a half-space assumption for the geometry of microcontacts is justifiable. In other words, microcontacts are located far (enough) from each other that they do not interfere and can be considered as heat sources on a half-space. In this study, instead of using probability relationships, the scale analysis method is used and a compact TCR model is developed for the conforming rough contacts. The scale relationship satisfies the observed physical proportionality and shows the trends of the experimental data. The constant of the scale relationship is determined through comparison with experimental data. The effective microthermal resistance is observed to be inversely proportional to the real contact area and directly proportional to the surface parameter σ/m.

The scale analysis relationship derived for the conforming rough contacts is integrated over the macrocontact area to extend the scale analysis model to cover the general contact or the transition region. It is shown that the effective microthermal resistance component of the joint resistance R_s is not a function of the surface curvature/out-of-flatness. Additionally, the profile of the effective contact pressure distribution does not affect the effective microthermal resistance. The macrothermal resistance is determined using the flux tube correlation in which the radius of the macrocontact proposed by Bahrami et al. [24] is employed. Superimposing the macro- and microthermal resistances a general relationship for TCR is derived. This expression covers the entire TCR ranging from the conforming rough to the spherical smooth bare joints in a vacuum.

A new nondimensional parameter is introduced that represents the ratio of the macro- to the microthermal resistances. Based on this nondimensional parameter, a criterion is proposed for specifying the three regions of TCR (i.e., the conforming rough limit, the elastoconstriction limit, and the transition region).

Three sets of collected data for SS304 are compared to the present model, and very good agreement is observed. In addition, the present model is compared to 75 data sets, more than 880 TCR data points collected by many researchers during last 40 years that cover a wide range of surface characteristics, thermal and mechanical properties, and mean contact temperature. The RMS difference between the model and data is approximately 13.8% over the entire range of the comparison.

Table 4 Range of parameters for experimental data

Parameter
$7.15 \leqslant b_L \leqslant 14.28$ mm
$25.64 \leqslant E' \leqslant 114.0$ GPa
$7.72 \leqslant F \leqslant 16763.9$ N
$16.6 \leqslant k_s \leqslant 227.2$ W/m K
$0.04 \leqslant m \leqslant 0.34$
$0.12 \leqslant \sigma \leqslant 13.94$ μm
$-60 \leqslant \bar{T}_c \leqslant 195$ C
$0.0127 \leqslant \rho \leqslant 120$ m

Acknowledgments

The authors gratefully acknowledge the financial support of the Center for Microelectronics Assembly and Packaging (CMAP) and the Natural Sciences and Engineering Research Council of Canada (NSERC).

Nomenclature

A = area, m^2
a = radius of contact, m
b = flux tube radius, m
c = scale analysis constant
c_1 = Vickers microhardness coefficient, GPa
c_2 = Vickers microhardness coefficient
d_v = Vickers indentation diagonal, μm
dr = increment in radial direction, m
E = Young's modulus, GPa
E' = effective elastic modulus, GPa
F = external force, N
h = contact conductance, W/m^2 K
H_{mic} = microhardness, GPa
H^* = $c_1(\sigma/\sigma_0 m)^{c_2}$, GPa
k = thermal conductivity, W/m K
L = length scale$\equiv b_L^2/(\sigma/m)$, m
m = effective mean absolute surface slope
n_s = number of microcontacts
P = pressure, Pa
P^* = nondimensional pressure$\equiv F/(\pi H^* b_L^2)$
Q = heat flow rate, W
R = thermal resistance, K/W
R^* = nondimensional thermal resistance
T = temperature, K
Y = mean surface plane separation, m

Greek

α = nondimensional parameter$\equiv \sigma\rho/a_H^2$
δ = maximum surface out-of-flatness, m
ε = flux tube relative radius, a/b
θ = angle of the surface asperities, rad
Θ = nondimensional parameter$\equiv R_L/R_s$
κ = H_B/H_{BGM}
ψ = spreading resistance factor
ρ = radius of curvature, m
σ = RMS surface roughness, μm

σ_0 = roughness reference value=1 μm
τ = nondimensional parameter$\equiv\rho/a_H$
v = Poisson ratio

Subscripts

0 = value at origin
1, 2 = surface 1, 2
a = apparent
EC = elastoconstriction
H = Hertz
j = joint
L = large
mic = microcontact
P = plastic deformation
r = real
s = small, solids
v = Vickers

References

[1] Yovanovich, M. M., and Marotta, E. E., 2003, *Thermal Spreading and Contact Resistances*, chap. 4, Heat Transfer Handbook, Editors: A. Bejan and D. Kraus, Wiley, New York.
[2] Tabor, D., 1951, *The Hardness of Metals*, Oxford University Press, London.
[3] Greenwood, J. A., and Williamson, B. P., 1966, ''Contact of Nominally Flat Surfaces,'' Proc. R. Soc. London, Ser. A, **295**, pp. 300–319.
[4] Bahrami, M., Culham, J. R., Yovanovich, M. M., and Schneider, G. E., 2003, ''Review of Thermal Joint Resistance Models for Non-Conforming Rough Surfaces in a Vacuum,'' Paper No. HT2003-47051, ASME Heat Transfer Conference, Las Vegas.
[5] Clausing, A. M., and Chao, B. T., 1965, ''Thermal Contact Resistance in a Vacuum Environment,'' ASME J. Heat Transfer, **87**, pp. 243–251.
[6] Lambert, M. A., and Fletcher, L. S., 1997, ''Thermal Contact Conductance of Spherical Rough Metals,'' ASME J. Heat Transfer, **119**(4), pp. 684–690.
[7] Nishino, K., Yamashita, S., and Torii, K., 1995, ''Thermal Contact Conductance Under Low Applied Load in a Vacuum Environment,'' *Experimental Thermal and Fluid Science*, Elsevier, New York, Vol. 10, pp. 258–271.
[8] Francois, R. V., 2001, ''Statistical Analysis of Asperities on a Rough Surface,'' Wear, **249**, pp. 401–408.
[9] Johnson, K. L., 1985, *Contact Mechanics*, Cambridge University Press, Cambridge, England.
[10] Cooper, M. G., Mikic, B. B., and Yovanovich, M. M., 1969, ''Thermal Contact Conductance,'' Int. J. Heat Mass Transfer, **12**, pp. 279–300.
[11] Yovanovich, M. M., Burde, S. S., and Thompson, C. C., 1976, ''Thermal Constriction Resistance of Arbitrary Planar Contacts With Constant Flux,'' AIAA, Paper No. 76-440, Vol. 56, pp. 126–139.
[12] Yovanovich, M. M., and Hegazy, A., 1983, ''An Accurate Universal Contact Conductance Correlation for Conforming Rough Surfaces With Different Micro-Hardness Profiles,'' AIAA, Paper No. 83-1434.
[13] Sridhar, M. R., and Yovanovich, M., 1996, ''Empirical Methods to Predict Vickers Microhardness,'' Wear, **193**, pp. 91–98.
[14] Milanez, F. H., Culham, J. R., and Yovanovich, M. M., 2003, ''Comparisons Between Plastic Contact Hardness Models and Experiments,'' AIAA Paper No. 2003-0160, 41th AIAA Aerospace Meeting and Exhibit, Reno.
[15] Yovanovich, M. M., 1986, ''Recent Developments In Thermal Contact, Gap and Joint Conductance Theories and Experiment,'' ASME, Keynote Paper Delivered at 8th Int. Heat Transfer Conference, San Francisco, pp. 35–45.
[16] Mikic, B. B., and Rohsenow, W. M., 1966, ''Thermal Contact Conductance,'' Tech. Rep., Dept. of Mech. Eng. MIT, NASA Contract No. NGR 22-009-065.
[17] Kimura, Y., 1970, ''Estimation of the Number and the Mean Area of Real Contact Points on the Basis of Surface Profiles,'' Wear, **15**, pp. 47–55.
[18] Antonetti, V. W., 1983, ''On the Use of Metallic Coatings to Enhance Thermal Conductance,'' Ph.D. thesis, University of Waterloo, Dept. of Mech. Eng., Waterloo, Canada.
[19] Hegazy, A. A., 1985, ''Thermal Joint Conductance of Conforming Rough Surfaces: Effect of Surface Micro-Hardness Variation,'' Ph.D. thesis, University of Waterloo, Dept. of Mech. Eng., Waterloo, Canada.
[20] Milanez, F. H., Yovanovich, M. M., and Mantelli, M. B. H., 2003, ''Thermal Contact Conductance at Low Contact Pressures,'' J. Thermophys. Heat Transfer, **18**, pp. 37–44.
[21] McWaid, T. H., 1990, ''Thermal Contact Resistance Across Pressed Metal Contact in a Vacuum Environment,'' Ph.D. thesis, University of California Santa Barbara, Dept. of Mech. Eng.
[22] Nho, K. M., 1990, ''Experimental Investigation of Heat Flow Rate and Directional Effect on Contact Conductance of Anistropic Ground/Lapped Interfaces,'' Ph.D. thesis, University of Waterloo, Dept. of Mech. Eng., Waterloo, Canada.
[23] Yovanovich, M. M., 1982, ''Thermal Contact Correlations,'' AIAA Paper No. 81-1164, *Progress in Aeronautics and Aerodynamics: Spacecraft Radiative Transfer and Temperature Control*, T. E. Horton, ed., Vol. 83, pp. 83–95.
[24] Bahrami, M., Culham, J. R., Yovanovich, M. M., and Schneider, G. E., 2004, ''Thermal Contact Resistance of Non-Conforming Rough Surfaces, Part 1: Mechanical Model,'' J. Thermophys. Heat Transfer, **18(2)**, pp. 209–217.
[25] Bahrami, M., 2004, ''Modeling of Thermal Joint Resistance for Rough Sphere-Flat Contact in a Vacuum,'' Ph.D. thesis, University of Waterloo, Dept. of Mech. Eng., Waterloo, Canada.
[26] Holman, J. P., and Gajda, W. J., 1994, *Experimental Methods for Engineers*, McGraw-Hill, New York.
[27] Burde, S. S., 1977, *Thermal Contact Resistance Between Smooth Spheres and Rough Flats*, Ph.D. thesis, University of Waterloo, Dept. of Mech. Eng., Waterloo, Canada.
[28] Bloom, M. F., 1964, ''Thermal Contact Conductance in a Vacuum Environment,'' Douglas Aircraft Company Report SM-47700.
[29] Cassidy, J. F., and Mark, H., 1970, ''Thermal Contact Resistance Measurements at Ambient Pressure of One Atmosphere to 3×10 E-12 mm Hg and Comparison With Theoretical Predictions,'' *Progress in Aeronautics-Themophysics: Applications to Thermal Design Aircraft*, J. T. Bevans, ed., Vol. 23, pp. 23–37.
[30] Clausing, A. M., and Chao, B. T., 1963, ''Thermal Contact Resistance in a Vacuum Environment,'' Tech. Report, University of Illinois, Urbana, Report ME-TN-242-1.
[31] Fisher, N. F., 1987, ''Thermal Constriction Resistance of Sphere/Layered Flat Contacts: Theory and Experiment,'' Master's thesis, University of Waterloo, Dept. of Mech. Eng., Waterloo, Canada.
[32] Fletcher, L. S., and Gyorog, D. A., 1970, ''Heat Transfer Between Surfaces in Contact; An Analytical and Experimental Study of Thermal Contact Resistance of Metallic Interfaces,'' AIAA, Paper No. 70-852.
[33] Gyorog, D. A., 1970, ''Investigation of Thermal Isolation Materials for Contacting Surfaces,'' AIAA 8th. Aerospace Science Meeting, New York.
[34] Kitscha, W., 1982, ''Thermal Resistance of the Sphere-Flat Contact,'' Master's thesis, University of Waterloo, Dept. of Mech. Eng., Waterloo, Canada.
[35] McMillan, R., and Mikic, B. B., 1970, ''Thermal Contact Resistance With Non-Uniform Interface Pressures,'' Tech. Report, Dept. of Mech. Eng. MIT, NASA Contract No. NGR 22-009-(477).
[36] Smuda, P. A., and Gyorog, D. A., 1969, ''Thermal Isolation With Low-Conductance Interstitial Materials Under Compressive Loads,'' AIAA, Paper No. 69-25, AIAA 7th Aerospace Science Meeting, New York.

Film Condensation of Saturated Vapor Over Horizontal Noncircular Tubes With Progressively Increasing Radius of Curvature Drawn in the Direction of Gravity

Arijit Dutta

S. K. Som
e-mail: sksom@mech.iitkgp.ernet.in

P. K. Das

Department of Mechanical Engineering,
Indian Institute of Technology,
Kharagpur

A theoretical study has been made to determine the heat transfer coefficient in film condensation of slowly downward flowing saturated vapor over horizontal noncircular tubes with progressively increasing radius of curvature drawn in the direction of gravity. The noncircular tube profile considered for the present work, is an equiangular spiral described by a curve in polar coordinate as $R_p = ae^{m\theta}$ (a and m being parametric constants). Nusselt number in case of noncircular tube has been determined on the basis of an equivalent diameter of a circular tube that equals the surface area of the noncircular tube with that of the circular one. It has been recognized that both the local Nusselt number (Nu_θ) and average Nusselt number ($\overline{Nu}$) become a function of m, $(Ra/Ja)^{1/4}$ and N_σ $(=\sigma/(\rho-\rho_g)R^2)$. An enhancement in heat transfer coefficient has been observed in case of a noncircular tube over that of a circular tube of same surface area because of the combined effect of gravity force component and surface tension driven favourable pressure gradient in the direction of flow of the liquid film. The relative weightage of both the components in the enhancement of heat transfer has been reported. An estimation of pressure drop of cooling liquid flowing through the circular and noncircular tubes of same surface area has been made to compare the values against the enhancement in heat transfer rate. [DOI: 10.1115/1.1798891]

Keywords: Condensation, Enhancement, Film, Heat Transfer, Phase Change, Surface Tension

Introduction

The phenomenon of condensation on outer or inner surfaces of horizontal tubes is largely associated with various fields of engineering like thermal power plant, refrigeration, air-conditioning units and many chemical process industries. Most of the condensers for ''Commercial purposes'' use circular tubes carrying cooling water through them, which causes condensation of vapor flowing over the tubes. An augmentation in the rate of heat transfer in condensation dictates the use of smaller condenser tubes for a given duty in achieving a reduction in the cost. The tube profile plays a pertinent role in this regard. If the tubes are made non circular in a sense that the tube profiles are drawn in the direction of gravity with increasing radius of curvature, then the combined effects of gravity force component and surface tension driven favourable pressure gradient in the direction of flow help in draining out the condensate from the tube surface much faster. This results in a reduction of liquid film thickness on tube surface, and hence in an augmentation in the rate of heat transfer in condensation.

The pioneering work in the field of condensation is due to Nusselt [1] who predicted, from a simplified theoretical analysis, the heat transfer coefficient in film condensation over horizontal circular tubes. Later, Dhir and Lienhard [2] proposed a generalized analysis of laminar film condensation in a nonuniform gravity field on surfaces of varying slope. They introduced a term called effective gravity which was the component of gravity in the direction of film flow. They finally predicted the Nusselt number for various axisymmetric bodies and rotating plates. The problem of laminar film condensation over noncircular tubes has also received considerable attention in recent times. The important works in the area are due to Cheng and Tao [3], Yang and Chen [4], Fiez and Roetzel [5], Yang and Hsu [6,7], Asbik et al. [8] and Mosaad [9]. However, all those works referred to elliptical tubes only and predicted the condensation heat transfer coefficient as a function of ellipticity of the tube surface. A recent work of Asbik et al. considered the forced convection laminar film condensation of downward flowing vapor on a small horizontal elliptic cylinder and bank of elliptical tubes. They predicted the heat transfer coefficient as a function of eccentricity of the elliptical profile and the interspace of the elliptical tubes which agreed well with the experimental data.

The concept of enhancement in the rate of heat transfer in condensation over tubes having profiles with increasing radius of curvature in the direction of gravity has not yet been explored in literature. The present work proposes a theoretical model in this regard and determines the weightage of both effective gravity and surface tension driven pressure gradient in the enhancement of heat transfer in condensation over noncircular tubes with progressively increasing radius of curvature. Moreover, an estimation of pressure drop of the cooling liquid flowing through the circular and noncircular tubes of same surface area have been made to compare the values against the enhancement in heat transfer rate.

Theoretical Formulation

The central theme of the present work is to investigate the condensation heat transfer phenomenon over a tube surface whose

Contributed by the Heat Transfer Division for publication in the JOURNAL OF HEAT TRANSFER. Manuscript received by the Heat Transfer Division June 4, 2003; revision received June 24, 2004. Associate Editor: J. N. Chung.

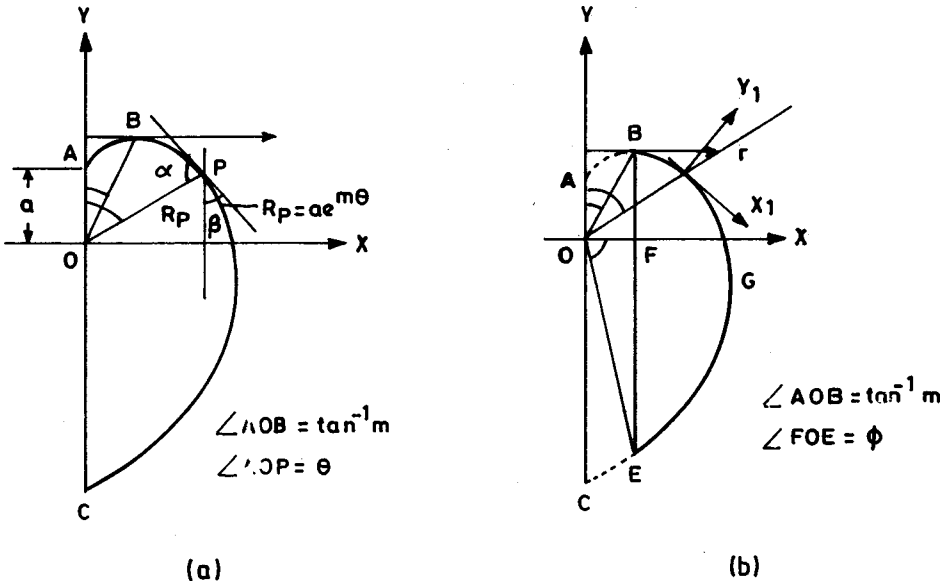

Fig. 1 An equiangular spiral curve generated on vertical axis: (a) symmetrical half of an equiangular spiral; and (b) symmetrical half of a polar surface.

profile has an increasing radius of curvature in the direction of gravity. The profile given by the polar curves of equiangular spiral type $R_p = ae^{m\theta}$ generated symmetrically about its vertical axis (Fig. 1(a)) has been considered in this context. However, the entire symmetrical half of the polar curve shown in Fig. 1(a) cannot be taken as the tube surface for the purpose. The reason behind this is described as follows: A polar curve described by $R_p = ae^{m\theta}$ has always a positive slope in the first quadrant in XY plane from $\theta=0$ to $\theta=\tan^{-1}\mathrm{m}$ (the portion AB as shown in Fig. 1(a)). The condensate over the solid surface has to always flow in the form of a thin liquid film due to gravity along the surface of the tube. But this cannot happen in the upward sloping part AB (Fig. 1(a)) of the profile $R_p = ae^{m\theta}$. This leads to the consideration of a surface formed by the segment of the polar profile $R_p = ae^{m\theta}$ described on a vertical chord BE as shown in Fig. 1(b). The segment BGE represents the half of the tube surface with chord BE as the axis of symmetry. The surface thus described will be referred to as "polar surface".

Growth of Liquid Film Thickness. The growth of liquid film thickness along the tube surface is found out from the conservation of momentum and mass of a liquid element in the film.

Conservation of Momentum. The equation of motion of a liquid element is written in a local coordinate system (x_1, y_1) (Fig. 1(b)) with axes parallel and perpendicular to the surface in consideration of the following assumptions:

- The film is very thin and moving with very low velocity such that the nonlinear inertia terms can be neglected and the flow can be considered as laminar. The consideration of laminar flow will be justified later on from the results of the model.
- Vapor phase is either quiescent or moves downward with almost a negligible velocity that does not have any influence on the motion of the liquid film.

Therefore it follows:

$$\mu \frac{d^2 v_{x_1}}{dy_1^2} = -(\rho - \rho_v) g \cos\beta + \frac{dP_\sigma}{dx_1} \tag{1}$$

where β is the angle a tangent makes with the downward vertical direction (direction of gravity), and dp_σ/dx_1 is the pressure gradient due to surface tension.

It follows from geometry (Fig. 1(a))

$$\beta = \pi - \alpha - \theta. \tag{2}$$

For an equiangular spiral curve $R_p = ae^{m\theta}$, the angle α (Fig. 1(a)) that a radius vector R_p makes with the tangent at any point is constant and is given by $\alpha = \cot^{-1}\mathrm{m}$. Therefore Eq. (2) can be written as

$$\beta = \pi - \cot^{-1}\mathrm{m} - \theta = \pi/2 + \tan^{-1}\mathrm{m} - \theta. \tag{3}$$

The surface tension pressure p_σ can be written as

$$p_\sigma = \frac{\sigma}{R_c} \tag{4}$$

$$\frac{dp_\sigma}{dx_1} = -\left(\frac{\sigma}{R_c^2}\right)\left(\frac{dR_c}{d\theta}\right)\left(\frac{d\theta}{dx_1}\right) \tag{5}$$

where R_c is the radius of curvature and is given by

$$R_c = \frac{\left\{R_p^2 + \left(\frac{dR_p}{d\theta}\right)^2\right\}^{3/2}}{\left\{R_p^2 + 2\left(\frac{dR_p}{d\theta}\right)^2 - R_p\frac{d^2R_p}{d\theta^2}\right\}} \tag{6}$$

It is apparent from Eq. (5) that the surface tension imposes a favorable pressure gradient in the flow of liquid film. Therefore, a liquid element is acted upon by the effective gravity force component along with the favourable pressure force and the resistive viscous force.

For the profile $R_p = ae^{m\theta}$, Eq. (6) becomes

$$R_c = (1+m^2)^{1/2} ae^{m\theta} \tag{7}$$

again,

$$\frac{dx_1}{d\theta} = \sqrt{R_p^2 + \left(\frac{dR_p}{d\theta}\right)^2} = a(1+m^2)^{1/2} e^{m\theta} \quad (\text{since, } R_p = ae^{m\theta}) \tag{8}$$

With the help of Eqs. (7) and (8), Eq. (5) can be written as

$$\frac{dp_\sigma}{dx_1} = -\frac{\sigma m e^{-2m\theta}}{a^2(1+m^2)} \tag{9}$$

Substituting β from Eq. (3) and dp_σ/dx_1 from Eq. (9) in Eq. (1) , one gets

$$\frac{d^2v_{x_1}}{dy_1^2}=-\frac{(\rho-\rho_v)g}{\mu}\left[\cos(\pi/2+\tan^{-1}m-\theta)+\frac{\sigma m e^{-2m\theta}}{g(\rho-\rho_v)a^2(1+m^2)}\right] \tag{10}$$

Upon integrating the Eq. (10) twice, we have

$$v_{x_1}=-\frac{(\rho-\rho_v)g}{2\mu}y_1^2\left[\cos(\pi/2+\tan^{-1}m-\theta)+\frac{\sigma m e^{-2m\theta}}{g(\rho-\rho_v)a^2(1+m^2)}\right]+c_1y_1+c_2 \tag{11}$$

where the constants c_1 and c_2 are determined from the boundary conditions

$$\text{At } y_1=0, \quad v_{x_1}=0$$

$$\text{At } y_1=\delta, \quad \frac{\partial v_{x_1}}{\partial y_1}=0$$

Finally, it follows:

$$v_{x_1}=\frac{(\rho-\rho_v)g}{\mu}y_1\left(\delta-\frac{y_1}{2}\right)\left[\cos(\pi/2+\tan^{-1}m-\theta)+\frac{\sigma m e^{-2m\theta}}{(\rho-\rho_v)ga^2(1+m^2)}\right] \tag{12}$$

Conservation of Mass. In consideration of a control volume within the liquid film, the equation for conservation of mass can be written as

$$\dot{m}_{x_1+dx_1}-\dot{m}_{x_1}=\dot{m}_c dx_1$$
$$\frac{d}{d\theta}\left[\int_0^\delta \rho v_{x_1}dy_1\right]\frac{d\theta}{dx_1}=\dot{m}_c \tag{13}$$

where $\dot{m}_c$ is the mass influx from the liquid-vapor interface due to condensation.

The Rate of Condensation. The rate of condensation $\dot{m}_c$ is determined by the temperature gradient in the liquid film at the interface with the vapor phase. Since the velocity of liquid film is very small, one can neglect the convective effect in the liquid film. Hence, the heat transfer in the film is purely by conduction. Therefore, in consideration of the film to be very thin and the vapor outside the film at saturated state with a temperature of T_s, we can write for the temperature distribution within the film as

$$T=T_\omega+(T_s-T_\omega)\frac{y_1}{\delta}$$
$$\dot{m}_c=\frac{\left|-k\frac{\partial T}{\partial y_1}\right|}{h_{fg}} \tag{14}$$

or,

$$\dot{m}_c=\frac{k(T_s-T_\omega)}{\delta h_{fg}} \tag{15}$$

With the help of Eqs. (15) and (8), Eq. (13) can be written after some rearrangement as

$$\frac{\delta^4}{3}\left[\sin(\pi/2+\tan^{-1}m-\theta)-2\frac{\sigma m e^{-2m\theta}}{(\rho-\rho_v)ga^2(1+m^2)}\right]+\delta^3\frac{d\delta}{d\theta}\left[\cos(\pi/2+\tan^{-1}m-\theta)+\frac{\sigma m e^{-2m\theta}}{(\rho-\rho_v)ga^2(1+m^2)}\right]=M(1+m^2)^{1/2}e^{m\theta}. \tag{16}$$

where

$$M=\frac{\mu k(T_s-T_\omega)a}{\rho(\rho-\rho_v)gh_{fg}}$$

Equation (16) is reduced to the following form by changing the variable as $z=\delta^4$

$$\frac{dz}{d\theta}+\frac{4}{3}z\left[\frac{\left\{\sin(\pi/2+\tan^{-1}m-\theta)-2\frac{\sigma m e^{-2m\theta}}{(\rho-\rho_v)ga^2(1+m^2)}\right\}}{\left\{\cos(\pi/2+\tan^{-1}m-\theta)+\frac{\sigma m e^{-2m\theta}}{(\rho-\rho_v)ga^2(1+m^2)}\right\}}\right]=4\frac{M(1+m^2)^{1/2}e^{m\theta}}{\left\{\cos(\pi/2+\tan^{-1}m-\theta)+\frac{\sigma m e^{-2m\theta}}{(\rho-\rho_v)ga^2(1+m^2)}\right\}} \tag{17}$$

Equation (17) is solved for z, and then substituting z by δ^4, we get after some rearrangement

$$\delta=\left[4M(1+m^2)^{1/2}\int_{\tan^{-1}m}^{\theta}e^{m\theta}\left[\cos(\pi/2+\tan^{-1}m-\theta)+\frac{\sigma m e^{-2m\theta}}{(\rho-\rho_v)ga^2(1+m^2)}\right]^{1/3}\times d\theta\left[\cos(\pi/2+\tan^{-1}m-\theta)+\frac{\sigma m e^{-2m\theta}}{(\rho-\rho_v)ga^2(1+m^2)}\right]^{4/3}\right]^{1/4} \tag{18}$$

Heat Transfer Coefficient. The local heat transfer coefficient h_{x_1} is defined as

$$h_{x_1}=\frac{\left|-k\frac{\partial T}{\partial y_1}\right|_{y_1=0}}{(T_s-T_\omega)}$$

with the help of Eq. (14), it becomes

$$h_{x_1}=\frac{k}{\delta} \tag{19}$$

Substituting the value of δ from Eq. (18) into Eq. (19), we get

$$h_{x_1}=k\left[\frac{\left[\cos(\pi/2+\tan^{-1}m-\theta)+\dfrac{\sigma m e^{-2m\theta}}{(\rho-\rho_v)ga^2(1+m^2)}\right]^{4/3}}{\left[4M(1+m^2)^{1/2}\displaystyle\int_{\tan^{-1}m}^{\theta}e^{m\theta}\left[\cos(\pi/2+\tan^{-1}m-\theta)+\dfrac{\sigma m e^{-2m\theta}}{(\rho-\rho_v)ga^2(1+m^2)}\right]^{1/3}d\theta\right]}\right]^{1/4} \tag{20}$$

It can be mentioned in this context that by putting $m=0$, as a special case, in Eqs. (18) and (19), the expressions for δ and h_{x_1} become identical to those predicted by Nusselt [1] in case of a circular tube surface. In this situation a represents the radius of the circular tube.

The local and average Nusselt numbers are defined as

$$\mathrm{Nu}_{x_1}=\frac{h_{x_1}(2R)}{k} \tag{21}$$

$$\overline{\mathrm{Nu}}=\frac{\overline{h}(2R)}{k} \tag{22}$$

where R is the radius of an equivalent circular tube which has the same surface area as that of the polar surface under consideration. It is important to note that in defining the Nusselt number in this way, one can compare the heat transfer rate for a non-circular tube with that for a circular tube having the same surface area. Different tube surface profiles with same surface area, as studied in the present work, are shown in Fig. 2.

Therefore, one has to obtain the relationship between a and R by equating the semi perimeters S_p of the polar curve with πR as

$$\begin{aligned}S_p&=\int_{\tan^{-1}m}^{\pi/2+\phi}[a(1+m^2)^{1/2}e^{m\theta}]d\theta\\&=a\left[\frac{(1+m^2)^{1/2}}{m}(e^{(\pi/2+\phi)}-e^{m\tan^{-1}m})\right]\\&=\pi R\end{aligned} \tag{23}$$

which finally gives

$$a=\frac{\pi R}{\left[\dfrac{(1+m^2)^{1/2}}{m}(e^{(\pi/2+\phi)m}-e^{m\tan^{-1}m})\right]}. \tag{24}$$

The profile BGE (Fig. 1(b)) described by the chord BE is bounded by the polar angles $\tan^{-1}m$ to $\pi/2+\phi$. The angle ϕ is determined as follows: from Fig. 1,

$$\mathrm{OB}=ae^{m\tan^{-1}m}.$$

$$\mathrm{OF}=ae^{m\tan^{-1}m}\sin(\tan^{-1}m).$$

$$\mathrm{OE}=ae^{m(\pi/2+\phi)}.$$

therefore,

$$\cos\phi=\frac{ae^{m\tan^{-1}m}\sin(\tan^{-1}m)}{ae^{m(\pi/2+\phi)}}.$$

With the help of Eq. (24) and following Eqs. (20), (21), and (22) the expressions for Nu_{x_1} and Nu for the polar surface can be written as

$$\begin{aligned}\mathrm{Nu}_{x_1}&=[G_1(m)]^{1/4}\left(\frac{\mathrm{Ra}}{\mathrm{Ja}}\right)^{1/4}\\&\times\left[\frac{[G_2(m)+N_\sigma G_3(m)]^{4/3}}{2[\int_{\tan^{-1}m}^{\theta}G_4(m)[G_2(m)+N_\sigma G_3(m)]^{1/3}d\theta]}\right]^{1/4}\end{aligned} \tag{25}$$

where

$$\mathrm{G_1(m)}=\frac{\left[(e^{(\pi/2+\phi)m}-e^{m\tan^{-1}m})\dfrac{(1+m^2)^{1/2}}{m}\right]}{\pi(1+m^2)^{1/2}}$$

$$\mathrm{G_2(m)}=\cos(\pi/2+\tan^{-1}\mathrm{m}-\theta)$$

$$\mathrm{G_3(m)}=\frac{me^{-2m\theta}}{(1+m^2)}\frac{\left[(e^{(\pi/2+\phi)m}-e^{m\tan^{-1}m})\dfrac{(1+m^2)^{1/2}}{m}\right]^2}{\pi^2}$$

$\mathrm{G_4(m)}=e^{m\theta}$.

The average Nusselt number can be obtained as

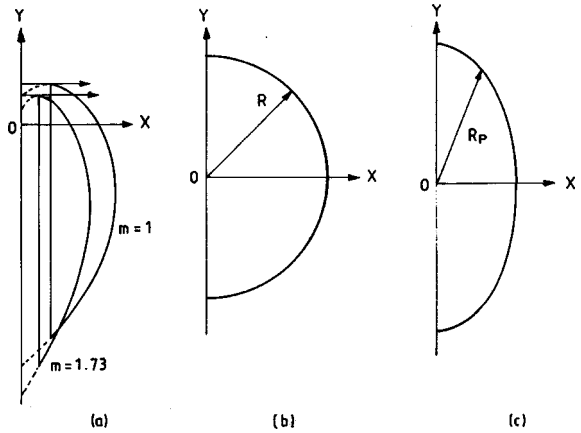

Fig. 2 Different surface profiles of same surface area: (a) polar surface; (b) circular surface; and (c) elliptical surface.

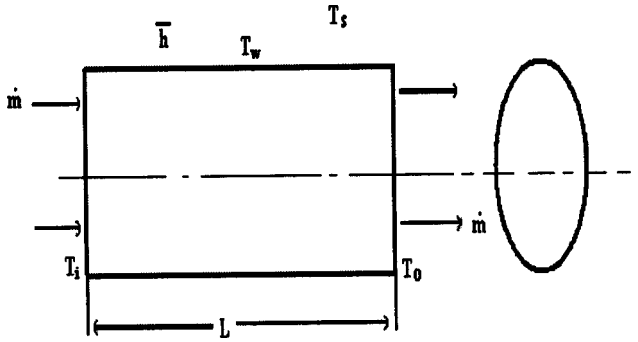

Fig. 3 Schematic diagram of a tube with an arbitrary shape of the surface

$$\overline{\mathrm{Nu}}=\frac{1}{\pi R}\left[\int_{\tan^{-1}m}^{\pi/2+\phi}\frac{\mathrm{Nu}_{x_1}\pi R(1+m^2)^{1/2}e^{m\theta}}{\left\{(e^{(\pi/2+\phi)m}-e^{m\tan^{-1}m})\dfrac{(1+m^2)^{1/2}}{m}\right\}}d\theta\right] \tag{26}$$

where

$$\mathrm{a}=\frac{\rho(\rho-\rho_v)g(2R)^3c_p}{\mu k}\ \text{(Rayleigh Number)}. \tag{27}$$

$$\mathrm{Ja}=\frac{c_p(T_s-T_w)}{h_{fg}}\ \text{(Jacob Number)}. \tag{28}$$

$$N_\sigma=\frac{\sigma}{(\rho-\rho_v)gR^2}\ \text{(Non-dimensional surface tension force)}. \tag{29}$$

In Tube Pressure Drop—A Comparison Between Non-circular and Circular Tubes of Identical Surface Area

Circular tubes have the largest cross-sectional area for a given length of perimeter. When a tube profile is changed for a better film drainage, reduction in cross-sectional areas adversely affects the inside pressure drop.

The heat transferred by a vapor due to its condensation over a tube surface is carried away by the cooling liquid flowing through the tube. Since, pressure drop in the flow of cooling liquid is an important design parameter, the enhancement in the rate of condensation heat transfer on non-circular tubes from that over a circular tube of same surface area has been compared with the consequential increase in the pressure drop values.

The Fig. 3 shows the schematic diagram of a tube with an arbitrary shape of the surface which may be circular or non-circular. However, the length and perimeter of the tube are kept fixed while the cross-sectional area varies according to the choice of the surface profile.

From an energy balance over the entire length of the tube (Fig. 3)

$$\overline{h}PL(T_s-T_w)=\dot{m}c_p(T_o-T_i)$$

or,

$$\dot{m}=\frac{\overline{h}PL(T_s-T_w)}{c_p(T_o-T_i)}. \tag{30}$$

Two separate cases have been considered.

Case I. Let the temperature difference (T_o-T_i) of the cooling liquid remains the same while $\dot{m}$ varies accordingly.

Then, from Eq. (30),

$$\dot{m}=K_1\overline{h} \tag{31}$$

where,

$$K_1=\frac{PL(T_s-T_w)}{c_p(T_o-T_i)}$$

again,

$$\Delta P=f\frac{L}{D_h}\rho\frac{v^2}{2}=\frac{1}{8}f\frac{PL}{\rho A^3}\dot{m}^2=\frac{K_2f\dot{m}^2}{A^3} \tag{32}$$

where, A=the cross-sectional area of the tube, f=friction factor and

$$K_2=\frac{1}{8}\frac{PL}{\rho}$$

In consideration of a fully developed turbulent flow, the law of resistance can be written as,

$$f=K\,\mathrm{Re}^{-n}=K\left(\frac{4\dot{m}}{P\mu}\right)^{-n}=K_3\dot{m}^{-n}. \tag{33}$$

where, K and n are constants, and

$$K_3=\left(\frac{4}{P\mu}\right)^{-n}$$

Equation (32) can be written with the help of Eqs. (31) and (33) as

$$\Delta P=K_2K_3K_1^{2-n}\left(\frac{\overline{h}^{2-n}}{A^3}\right)=K_4\frac{\overline{h}^{2-n}}{A^3} \tag{34}$$

$$\text{where,}\quad K_4=K_1^{2-n}K_2K_3$$

In the light of Eq. (34), we can write therefore,

$$\frac{\Delta P}{\Delta P_C}=\left(\frac{\overline{h}}{h_C}\right)^{2-n}\left(\frac{A_C}{A}\right)^3=\left(\frac{\overline{\mathrm{Nu}}}{\mathrm{Nu}_C}\right)^{2-n}\left(\frac{A_C}{A}\right)^3. \tag{35}$$

where subscript c denotes the quantities for a circular tube.

Case II. Let the mass flow rate $\dot{m}$ of the coolant remains the same and the temperature difference (T_o-T_i) varies accordingly.

From Eqs. (31) and (32), one can write under the situation,

$$\frac{\Delta P}{\Delta P_C}=\left(\frac{A_C}{A}\right)^3 \tag{36}$$

The variations in physical properties of the coolant with the variations in the mean temperature of flow for the circular and noncircular tubes are neglected.

Determination of Cross-Sectional Area Ratio A_c/A for the Same Perimeter

For any polar curve, cross-sectional area is given by

$$A=\int\int r\,dr\,d\theta=2\int_0^{\pi}\int_0^{R_p}r\,dr\,d\theta=2\int_0^{\pi}\frac{R_p^2}{2}d\theta \tag{37}$$

Polar Profile. From Eq. (24) and Eq. (37),

$$A_{\text{polar}}=\left(\frac{\pi R}{\left[\dfrac{(1+m^2)^{1/2}}{m}(e^{(\pi/2+\phi)m}-e^{m\tan^{-1}m})\right]}\right)^2\times\left\{\frac{1}{2m}(e^{2m(\pi/2+\phi)}-e^{2m\tan^{-1}m})\right\}$$

Further,

$$\frac{A_{\text{polar}}}{A_c}=\frac{\left(\dfrac{\pi R}{\left[\dfrac{(1+m^2)^{1/2}}{m}(e^{(\pi/2+\phi)m}-e^{m\tan^{-1}m})\right]}\right)^2\left\{\dfrac{1}{2m}(e^{2m(\pi/2+\phi)}-e^{2m\tan^{-1}m})\right\}}{\pi R^2} \tag{38}$$

Elliptical Profile. An estimation of pressure drop ΔP for elliptical tubes has also been made to compare the values against the enhancement in heat transfer rate as a function of ellipticity for an horizontal elliptic tube with the major axis being vertical, as reported by Mosaad [9] In consideration of an elliptic profile with the length of semi-major axis as a and eccentricity (ellipticity) of e, we can write equating the perimeter of the ellipse with that of a circle of radius R as

$$a=\frac{\pi R}{\displaystyle\int_0^{\pi}\frac{(1-e^2)}{(1-e^2\sin^2\phi)^{3/2}}d\phi} \tag{39}$$

where ϕ=angle made by the tangent at any point on the elliptical surface with the horizontal direction. Hence,

$$A_{\text{ellipse}}=\frac{\pi\left(\dfrac{\pi R}{\displaystyle\int_0^{\pi}\frac{(1-e^2)}{(1-e^2\sin^2\phi)^{3/2}}d\phi}\right)^2(1-e^2)^{1/2}}{2}$$

therefore,

$$\frac{A_{\text{ellipse}}}{A_c}=\frac{\left(\dfrac{\pi R}{\displaystyle\int_0^{\pi}\frac{(1-e^2)}{(1-e^2\sin^2\phi)^{3/2}}d\phi}\right)^2(1-e^2)^{1/2}}{R^2} \tag{40}$$

Results and Discussion

It is already established that the pertinent dimensionless parameters influencing the Nusselt number are $(\text{Ra/Ja})^{1/4}$, m and N_{σ}.

Figure 4 shows the variations in average Nusselt number Nu with $(\text{Ra/Ja})^{1/4}$ for different values of m at a fixed value of N_{σ} for polar tube surfaces. The variation of $\overline{\text{Nu}}$ for a circular tube surface has also been shown in the figure by the curve with $m=0$. It is observed that for any given value of $(\text{Ra/Ja})^{1/4}$, the average Nusselt numbers (Nu) for non-circular tube surfaces are always more than that of a circular tube having the same surface area, and increase with an increase in m. However, the gain in Nu decreases with an increase in m.

The enhancement in heat transfer coefficients takes place due to the combined effect of gravity force component and surface tension driven favorable pressure gradient along the tube surface. The enhancement in average Nusselt number (Nu) for a polar tube surface due to the effective gravity force only is shown in Fig. 5.

The Fig. 6 shows the relative gain in the average Nusselt number for a polar tube surface over that of a cylindrical surface of same surface area. As the value of m becomes large, a tends to a very small value. In a limiting case of $m\to\infty$ and $a\to 0$, a polar surface becomes identical to a vertical plate. It is observed accordingly in Fig. 6 that the ratio of $\text{Nu}_{\text{polar}}/\text{Nu}_{\text{circular}}$ increases asymptotically to a value of 1.3 which equals to $\text{Nu}_{\text{vertical plate}}/\text{Nu}_{\text{circular}}$ for the given value of $(\text{Ra/Ja})^{1/4}$.

Table 1 shows the quantitative figures for the enhancement in average Nusselt number specifying the relative weightage of effective gravity and the additional contribution due to surface tension component coupled with gravity for a polar tube surface over the circular one having the same surface area. The values of Nu have been found out for $(\text{Ra/Ja})^{1/4}=230$ and $N_{\sigma}=0.19$, which are the typical values in consideration of saturated steam at 1 atm pressure condensing over a tube surface at 40°C. It is observed that the gravity plays the dominant role in enhancing the Nusselt number for a polar tube surface.

It can be mentioned in this context that though the values of Nusselt number are quite high corresponding to the typical values of input parameters as stated above, the flow of liquid film is

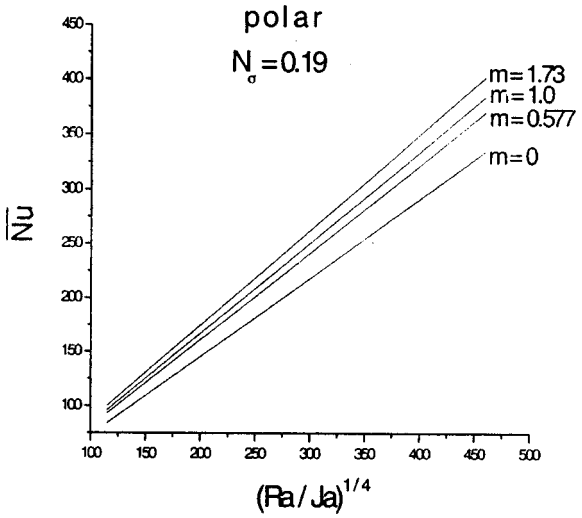

Fig. 4 Variations of $\overline{\text{Nu}}$ with $(\text{Ra/Ja})^{1/4}$ for different values of m of a polar surface

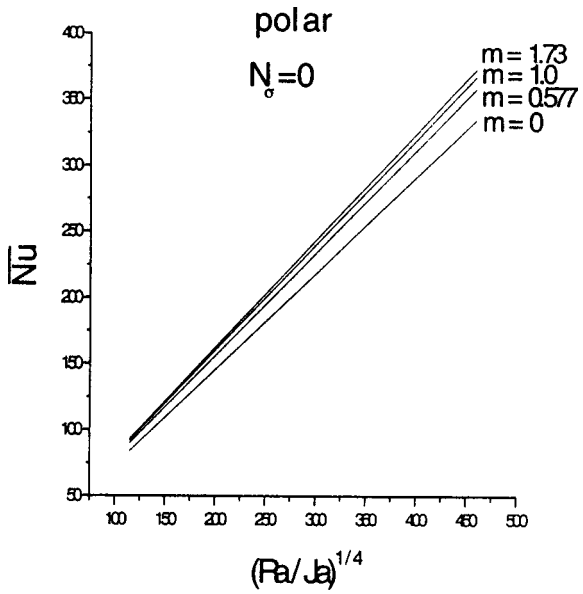

Fig. 5 Variations of $\overline{\text{Nu}}$ with $(\text{Ra/Ja})^{1/4}$ for different values of m of a polar surface due to gravity only

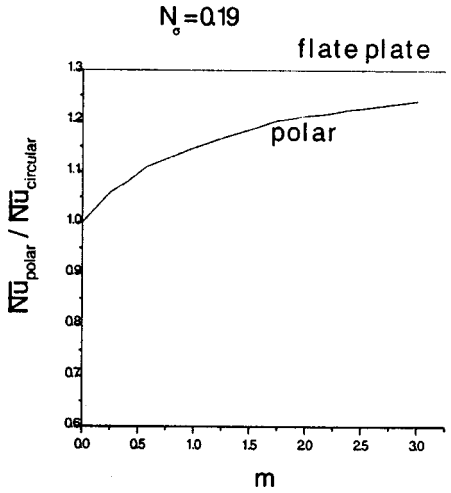

Fig. 6 Variations of $(\bar{Nu}_{polar}/\bar{Nu}_{circular})$ with m for given values of $(Ra/Ja)^{1/4}$ and N_σ

laminar. The Fig. 7 shows the variation of film Reynolds number Re along a polar tube surface and depicts that the values of Re are well below the critical one ($Re_{cr}=1800$) for the onset of turbulent flow as stated in Ozisik [10].

The Fig. 8 shows the variations of local Nusselt number for a polar tube surface with m=1. The curve for $m=0$ in Fig. 8 represents the variation of local Nusselt number for a circular tube surface whose surface area is same as that of polar tube surface with $m=1$.

Table 1 Enhancement in average Nusselt number for polar tube over that of a circular one with same surface area ($(Ra/Ja)^{1/4}=230$, $N_\sigma=0.19$)

	Polar tube surface		
m	Enhancement due to gravity (%)	Additional enhancement due to the coupling of surface tension with gravity (%)	Total enhancement (%)
0.577	7.07	3.53	10.6
1.0	9.61	5.08	14.69
1.73	11.4	8.52	19.92

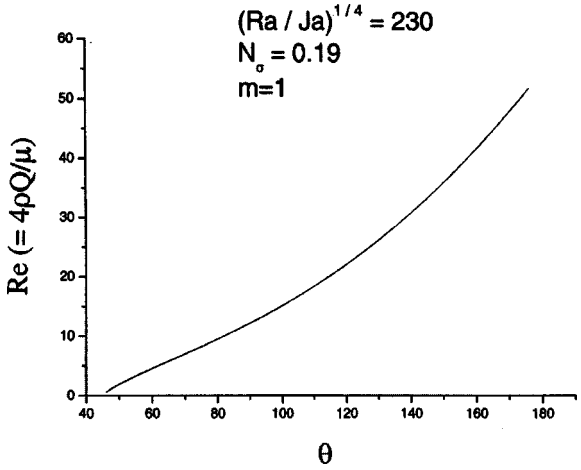

Fig. 7 Variation of Reynolds number with θ

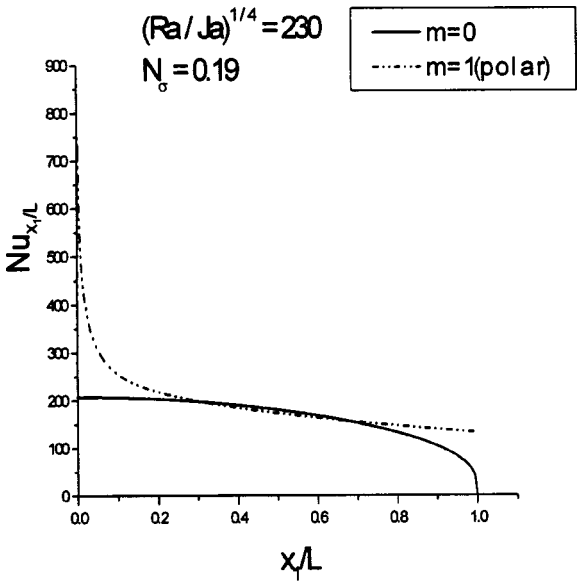

Fig. 8 Variations of local Nusselt number with x_1/L for different values of m

The comparisons of coolant pressure drop for different noncircular tubes of same area against the enhancement in condensation heat transfer have been presented in Figs. 9 and 10. Tubes with different surface profiles, namely polar and elliptic have been considered. For all the cases the in-tube pressure drop and the Nusselt number due to condensation have been normalized by dividing them by the corresponding quantities of a circular tube with the same surface area.

While calculating $\Delta P/\Delta P_c$ from Eq. (35), the value of n has been taken as 0.25 in accordance with Blassius law of frictional resistance for a fully developed turbulent flow through a pipe.

Figures 9 and 10 show the variations in $\Delta P/\Delta P_c$ with Nu/Nu_c for noncircular tubes of polar and elliptic surfaces. The values of

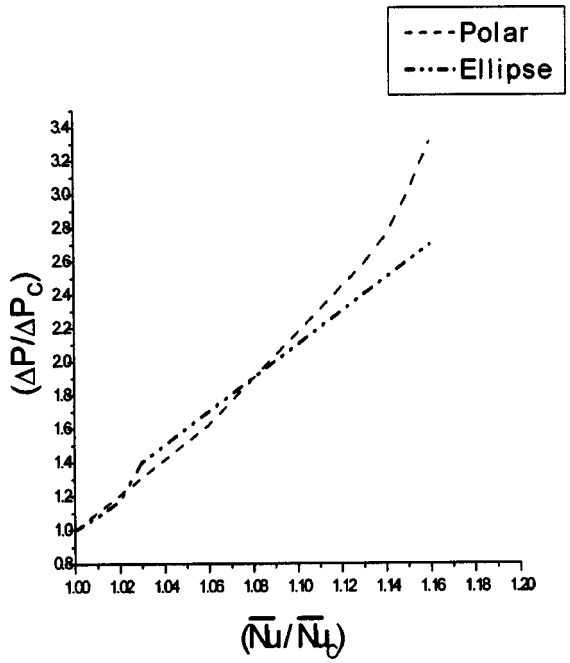

Fig. 9 $(\Delta P/\Delta P_c)$ versus $(\bar{Nu}/\bar{Nu}_c)$ of different noncircular tubes for same value of (T_o-T_i)

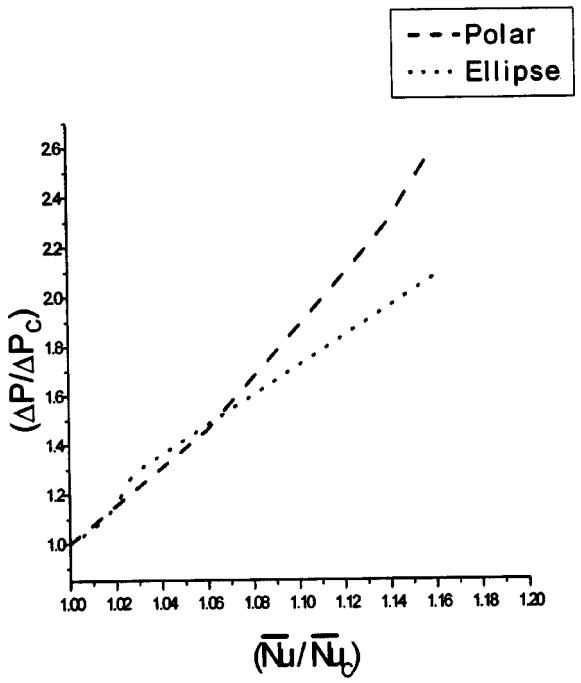

Fig. 10 $(\Delta P/\Delta P_c)$ versus $(\bar{Nu}/\bar{Nu}_c)$ of different noncircular tubes for same value of $\dot{m}$

$\bar{\mathrm{Nu}}/\bar{\mathrm{Nu}}_c$ as a function of ellipticity for elliptic tubes in case of free convection have been taken from Mosaad [9], while the corresponding values of $\Delta P/\Delta P_c$ are calculated from Eqs. (35) and (36) with the help of Eq. (40) in the present paper. It is observed from Figs. 9 and 10 that for any given rate of condensation heat transfer at outer surface, the coolant flow inside the tube experiences almost the same pressure drop for tubes with both polar and elliptic surface profiles. However, beyond a certain value of Nu, the polar surface profile shows relatively worst performance resulting in higher pressure drop values compared to those by elliptic tubes. For any given value of $\bar{\mathrm{Nu}}/\bar{\mathrm{Nu}}_c$, the value of $\Delta P/\Delta P_c$ is always higher in case of constant temperature difference $(T_o - T_i)$ of the cooling liquid (Fig. 9) than that in case of constant mass flow rate $\dot{m}$ of the cooling liquid (Fig. 10). This is obvious since, for a constant value of $(T_o - T_i)$, the value of $\dot{m}$ increases with an increase in the rate of heat transfer, and at the same time, the cross-sectional areas of noncircular tubes are reduced from that of a circular one of same surface area.

It appears from Figs. 9 and 10, that the enhancement in heat transfer for tubes with polar and elliptic surfaces over the circular ones take place at the cost of increased pressure drop as compared to that in a circular tube. This implies that for a given heat transfer rate, though the circular tube requires the highest surface area as compared to noncircular tubes, the pressure drop of the coolant inside the tube is lowest.

Finally, the choice of a tube surface for a compact condenser towards a cost effective process of condensation lies in the trade off between a gain in the rate of heat transfer and a loss in the pumping power subjected to the constraint of ease of manufacturing.

Conclusion

• Heat transfer coefficient in film condensation over noncircular tubes with progressively increasing radius of curvature in the direction of gravity has been evaluated theoretically. A polar surface comprising a segment of an equiangular spiral curve generated symmetrically on a vertical chord has been considered.

• The average Nusselt number $(\bar{\mathrm{Nu}})$ for a polar tube surface is higher than that for a circular one of same surface area. The gravity plays the dominant role in enhancing the average Nusselt Number (Nu).

• An increase in m (the parameter defining the equiangular spiral curve) increases Nu for a polar surface. The average Nusselt number (Nu) increases monotonically with m to an asymptotic value which equals to the value of Nu for a vertical plate.

• For a given condensation rate, the pressure drop in circular tube is the lowest, while those in tubes with polar and elliptic surfaces are almost equal.

Nomenclature

a = parametric constant of polar curve $R_p = ae^{m\theta}$
c_p = specific heat of condensate at mean film temperature
f = friction factor
g = acceleration due to gravity
h_{x_1} = local heat transfer coefficient
$\bar{h}$ = average heat transfer coefficient
h_{fg} = latent heat due to condensation
Ja = Jacob number, $c_p(T_s - T_w)/h_{fg}$
k = thermal conductivity of condensate at mean film temperature
L = length of semi perimeter of any polar curve
m = parametric constant of polar curve $R_p = ae^{m\theta}$
$\dot{m}$ = mass flow rate of cooling liquid flowing through the tube
$\dot{m}_c$ = mass flux of condensate
N_σ = nondimensional surface tension force, $\sigma/(\rho - \rho_v)gR^2$
Nu_{x_1} = local Nusselt number, $h_{x_1}(2R)/k$
$\bar{\mathrm{Nu}}$ = average Nusselt number, $\bar{h}(2R)/k$
P_σ = pressure due to surface tension
P = perimeter of the tube surface
Q = condensate volume flow rate per unit width of the surface
R = radius of an equivalent circle having same surface area to that of the polar curve
R_p = radius vector of polar curve
R_c = radius of curvature
Ra = Rayleigh number, $\rho(\rho - \rho_v)g(2R)^3 c_p/\mu k$
S_p = semi perimeter of the tube surface
T_s = saturation temperature of vapor
T_w = wall temperature
T_i = bulk mean coolant temperature at inlet to the tube
T_o = bulk mean coolant temperature at outlet to the tube
v_{x_1} = condensate velocity along tangential direction of the tube surface

Greek Symbols

α = angle between radius vector and tangent at any point on tube surface
β = angle between tangent and direction due to gravity at any point on tube surface
δ = liquid film thickness
θ = polar angle
ρ = density of condensate at mean film temperature
ρ_v = density of vapor at its saturation temperature
μ = dynamic viscosity of condensate at mean film temperature
σ = surface tension coefficient

Subscripts

x_1 = tangential direction along the tube surface
y_1 = normal direction at any point to the tube surface
v = vapor phase

References

[1] Nusselt, W., 1916, ''Des Oberflachenkondensation des Wasserdamfes,'' Z. Vereines Deutsch. Ing., **60**, pp. 541–564, 569–575.

[2] Dhir, V., and Lienhard, J., 1971, ''Laminar Film Condensation on Plane and Axisymmetric Bodies in Nonuniform Gravity,'' ASME J. Heat Transfer, **93**, pp. 97–100.

[3] Cheng, S., and Tao, J., 1988, ''Study of Condensation Heat Transfer in Elliptical Pipes in a Stationary Saturated Vapor,'' ASME J. Heat Transfer, **96**, pp. 405–408.

[4] Yang, S., and Chen, C., 1994, ''Laminar Film Condensation on a Horizontal Elliptical Tube With Variable Wall Temperature,'' Int. J. Heat Mass Transfer, **116**, pp. 3155–3141.

[5] Fieg, G. P., and Roetzel, W., 1994, ''Calculation of Laminar Film Condensation in/on Inclined Elliptical Tubes,'' Int. J. Heat Mass Transfer, **37**, pp. 619–624.

[6] Yang, S., and Hsu, C., 1997, ''Mixed-Convection Laminar Film Condensation on a Horizontal Elliptical Tube With Uniform Surface Heat Flux,'' Numer. Heat Transfer, **32**, pp. 85–95.

[7] Yang, S., and Hsu, C., 1997, ''Free and Forced Convection Film Condensation From a Horizontal Elliptic Tube With a Vertical Plate and Horizontal Tube as Special Cases,'' Int. J. Heat Mass Transfer, **18**, pp. 567–574.

[8] Asbik, M., Hadda, D., Zeghmati, B., and Khmou, A., 2000, ''Forced Convection Laminar Film Condensation of Downward Flowing Vapor on a Single Horizontal Elliptical Cylinder or a Bank of Elliptical Tubes,'' Numer. Heat Transfer, **37**, pp. 511–544.

[9] Mosad, M., 2001, ''Mixed-Convection Laminar Film Condensation on an Inclined Elliptical Tube,'' ASME J. Heat Transfer, **123**, pp. 294–300.

[10] Ozisik, M. N., 1985, *Heat Transfer A Basic Approach*, McGraw-Hill Book Company (International Edition).

Effect of Boundary Wall Conditions on Heat Transfer for Fully Opened Tilted Cavity

Walid Chakroun
e-mail: chakroun@kuc01.kuniv.edu.kw
Center of Research for Experimental Thermal Sciences,
Mechanical Engineering Department,
P.O. Box 5969,
Safat 13060, Kuwait

An experimental investigation was performed to study the effect of wall conditions as well as the tilt angle on heat transfer for fully opened tilted cavity. The cavity has a rectangular shape with a square cross section. One side is fully opened to the ambient, permitting air to flow inside the cavity by virtue of buoyancy. The cavity was selected to be long enough to simulate two-dimensional natural convection. Seven cases with different wall configurations were examined: (a) three of which with only one wall heated and the other two were insulated, (b) three of which with two walls heated and the other one was insulated, and (c) a case with all walls were heated. The heated walls were maintained at constant heat flux, which correspond to a constant Grashof number of 1.3×10^8. In each case, the cavity was rotated over a range of ±90 deg (measured from the vertical direction) in 15 deg increments. It was concluded that tilt angle, wall configuration, and the number of heated walls are all factors that strongly affect the convective heat transfer coefficient between the cavity and the ambient air. Empirical correlations were provided to predict the average Nusselt number at different inclination angles for all seven cases. It was found that the correlations could predict the result to within 4 to 10 percent, depending on the inclination angle and the case considered. [DOI: 10.1115/1.1798931]

Keywords: Cavity Flows, Heat Transfer

Introduction

Buoyancy-driven natural convection is an essential mechanism for a wide range of engineering applications. Among those, many processes involve the flow of a fluid in rectangular enclosures. Practical applications of such configurations can be found in the solar engineering field; e.g., passive solar heating and solar concentrating receivers. They also have a fundamental importance in cooling of electronic equipment, fire research, brake-housing systems on aircraft, optimizing energy conservation, and understanding climatic conditions in buildings. The buoyant flow in such enclosures is similar in nature to that of rectangular cavity.

In general, rectangular cavities are classified to be either closed or opened from one side to the surrounding. Figure 1, that was taken from Chakroun et al. [1], illustrates the main features of a tilted partially opened cavity. The tilt angle of rotation (α) is measured in the clockwise direction with respect to the vertical axis. The rate of heat transferred from the cavity to the surrounding is influenced by the following geometrical parameters (see Fig. 1): the tilt angle (α), the aspect ratio ($AR=H/B$) which is the cavity height to width ratio, the opening ratio ($OR=a/H$) which is the ratio of the opening height to the cavity height, and the opening displacement ratio ($DR=d/H$) which is the ratio of the center aperture height to the height of the cavity. The configuration and number of the heated walls are also important parameters in the determination of heat transfer in cavities.

Cavities with different boundary conditions have received substantial attention during the past two decades. Many researchers have both numerically and experimentally examined cavities with different boundary conditions in an attempt to better understand the heat transfer mechanism involved. For example, Doria [2] studied the natural convection in open cavities to predict the fire spread in a room. Jacobs et al. [3,4] studied the buoyancy-induced flows in open cavities to model the circulation of air above city streets and geothermal reservoirs. Natural convection in a shallow open cavity was studied by Chan and Tien [5–7] to model pipes with one end connected to a reservoir and the other to a closed valve. Chen et al. [8], Sernas and Kyriakides [9] did experimental studies in modeling solar concentrating receivers. Sezai and Mohamad [10] have concluded that as Rayleigh number increases the difference between two and three dimensional prediction increases. Their work was performed in a three-dimensional cubic cavity. More work on three-dimensional natural convection in an inclined cubic cavity was performed by Lee and Lin [11]. Table 1 (adapted with modification from Chakroun et al. [1]) is a summary of the previous work done on fully/partially open cavities. It can be noticed that the boundary conditions are presented by letters. A cavity is considered type *A* when all its walls are isothermal at T_h. A cavity of type *B* is characterized by having walls 1 and 2 at T_h and wall 3 at T_∞. A type *C* cavity has wall 1 at T_h and the other two walls are adiabatic. In cavity of type *D* wall 1 is maintained at T_c ($T_c<T_\infty<T_h$) and the other walls are adiabatic. A type E cavity is when one wall is maintained at constant heat flux and the other walls are adiabatic. A type F cavity is when two of its walls are maintained at constant heat flux and the other one is adiabatic. A type *G* cavity is when three walls are maintained at constant heat flux. Table 2 explains the various types of wall boundary conditions considered in Table 1. Each of those boundary conditions finds an application in the real world.

It is clear from the tables that no work is performed to study the effect of different heated wall arrangements (and different tilt angles) on the heat transfer mechanism in fully opened cavities. The main purpose of this study is to provide further information on the heat transfer coefficient in rectangular cavities where different wall conditions can exist. This class of flows, which may occur either by design or natural circumstances, is related to air entrainment into heated open cavities, particularly when the cavities are inclined. Several examples may be found in the environment and in many engineering systems such as natural convection flows over valleys, solar receiver tracing systems, electronic systems where cavities are formed in spaces between discrete circuit devices, tilted double glazed window, and tilted thermoelectric cooling or heating elements. Considerable differences exist in the

Contributed by the Heat Transfer Division for publication in the JOURNAL OF HEAT TRANSFER. Manuscript received by the Heat Transfer Division June 26, 2003; revision received June 16, 2004. Associate Editor: S. Acharya.

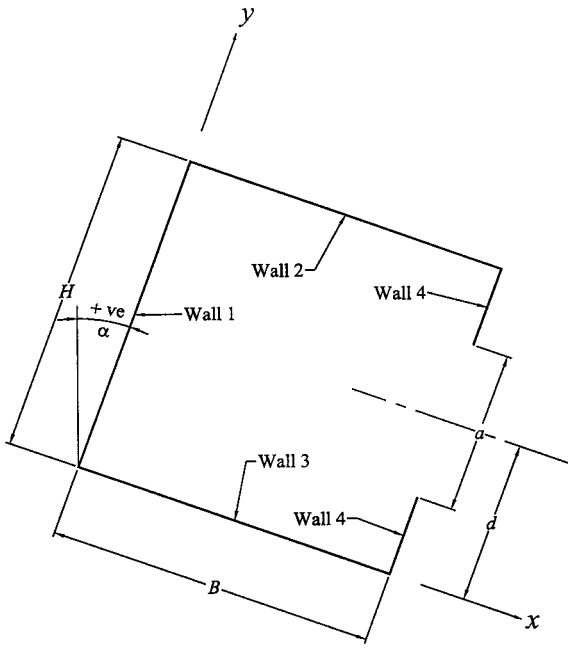

Fig. 1 Geometry of a partially open cavity

heat transfer, where different boundary conditions are applied. In this study, seven cases with different wall configurations were examined: (a) three cases in which one wall is heated and the other two are insulated, (b) three cases in which two walls are heated and the other one is insulated, and (c) one case in which all walls are heated (see Fig. 2). The heated walls were maintained at constant heat flux. Referring to Fig. 2, although cases I and III look the same (because of the symmetry between them), a profound difference between them is realized when studying the heat transfer mechanism. This will be discussed in the result section. The same can be said when comparing case IV to case VI. Depending on the angle of inclination α, the heated wall(s) may be located either at the upper side (cases I and IV) or at the lower side (cases III and VI) of the cavity. The effect of changing the inclination angle is thoroughly explored in the results and discussion section. The experiments were carried out for an aspect ratio (AR) and an opening ratio (OR) of one. All tests were conducted at a constant heat flux Grashof number, Gr_B^* of 1.3×10^8 ($\mathrm{Gr}_B^* = g\beta q''_{\mathrm{conv}} B^4/k_a\nu^2$). In each case, the cavity was rotated over a range of angles from -90 to $+90$ deg (where α is measured from the vertical direction) in 15 deg increments.

There are many applications that can be modeled as a cavity with different wall conditions. The current study can be applied to the area of solar energy by analyzing the effect of solar radiation on the environment inside buildings. Depending on the solar altitude angle, one or more walls may be subjected to heating at the same time. That is, in the same building, the influence of solar heat gain may vary from one room to another, depending on the location of the room. A room in the top floor of a building can be subjected to solar heating from one side wall (as in cases I and III at $\alpha=+90$ deg), only from the roof (as in case II at $\alpha=+90$ deg)

Table 2 Explanation for the types of boundary conditions given in Table 1

B. C. Type	Boundary condition on walls			
	1	2	3	4
A	T_h	T_h	T_h	T_h
B	T_h	T_h	T_∞	N/A
C	T_h	a	a	a
D	T_c	a	a	a
E	q''	a	a	a
	a	q''	a	a
	a	a	q''	a
F	q''	q''	a	a
	q''	a	q''	a
	a	q''	q''	a
G	q''	q''	q''	a

Note: $T_c<T_\infty<T_h$, a=adiabatic, N/A not applicable, and q''=constant heat flux on the wall.

Table 1 Review of previous work on fully/partially open cavities (refer to Table 2 for what A, B, C, D, E, F, and G mean)

Reference	Geometry		DR	B.C.	α	Pr	Gr or Ra
	AR	OR					
LeQueare et al. [12]	1	1	0.5	A	0, 20, 45	0.73	$10^4\leqslant \mathrm{Gr_H}\leqslant 10^7$
	0.5, 2	1	0.5	A	0	0.73	$\mathrm{Gr_H}=10^7$
Penot [13]	1	1	0.5	A	0, $\pm$45, 90	0.7	$10^3\leqslant \mathrm{Gr_H}\leqslant 10^7$
Miyamoto et al. [14]	1	0.5, 1	0.5	A	$-45\leqslant\alpha\leqslant80$	0.7	$7\times10^3\leqslant \mathrm{Ra_B}\leqslant 7\times10^4$
	1	0.5, 1	0.5	A	0	0.7	$1\leqslant \mathrm{Ra_B}\leqslant 7\times10^5$
Showole and Tarasuk [15]	0.25, 0.5, 1	1	0.5	A	$-90\leqslant\alpha\leqslant-30$	0.7	$10^4<\mathrm{Ra_B}<5\times10^5$
	1	1	0.5	A	-90, -45	0.7	$10^3<\mathrm{Ra_B}<5\times10^5$
Angirasa et al. [16]	1	1	0.5	A	0	0.7	$10^4<\mathrm{Ra_B}<5\times10^5$
Sernas and Kyriakides [9]	1	1	0.5	B	0	0.7	$\mathrm{Gr_H}=10^7$
Hess and Henze [17]	1	0.5, 1	0.5	C	0	7	$3\times10^{10}\leqslant \mathrm{Ra_H}<2\times10^{11}$
Chan and Tien [5]	1, 0.143	1	0.5	C	0	1, 7	$10^3<\mathrm{Ra_B}\leqslant10^7$
Chan and Tien [7]	0.143	1	0.5	C	0	8.7	$10^6<\mathrm{Ra_B}\leqslant10^8$
Angirasa et al. [18]	1	1	0.5	C	0	0.1<Pr<1	$10^2<\mathrm{Ra_B}\leqslant10^8$
Lin and Xin [19]	1	1	0.5	C	0	0.7	$\mathrm{Ra_B}=10^{10}$, 10^{11}
Mohamad [20]	0.5, 2, 1	1	0.5	C	$-80\leqslant\alpha\leqslant0$	0.7	$10^3\leqslant \mathrm{Ra_H}\leqslant10^7$
Chakroun et al. [1]	0.25, 0.5, 1	0.25, 0.5, 1	0.5	E	$-90\leqslant\alpha\leqslant90$	0.7	$\mathrm{Gr_h}=5.5\times10^8$
Elsayed et al. [21]	1	1	0.5	C	$-60\leqslant\alpha\leqslant90$	0.71	$10^2\leqslant \mathrm{Gr_H}\leqslant10^5$
Elsayed [22]	1	1	0.5	D	0	0.72	$\mathrm{Gr_h}=10^5$, 10^7, 10^{10}
Elsayed and Chakroun [23]	1	0.25, 0.5, 0.74	0<DR<1	E	$-90\leqslant\alpha\leqslant90$	0.7	$\mathrm{Gr_h}=5.5\times10^8$
Present	1	1	0.5	E	$-90\leqslant\alpha\leqslant90$	0.7	$\mathrm{Gr}^*=1.3\times10^8$
Present	1	1	0.5	F	$-90\leqslant\alpha\leqslant90$	0.7	$\mathrm{Gr}^*=1.3\times10^8$
Present	1	1	0.5	G	$-90\leqslant\alpha\leqslant90$	0.7	$\mathrm{Gr}^*=1.3\times10^8$

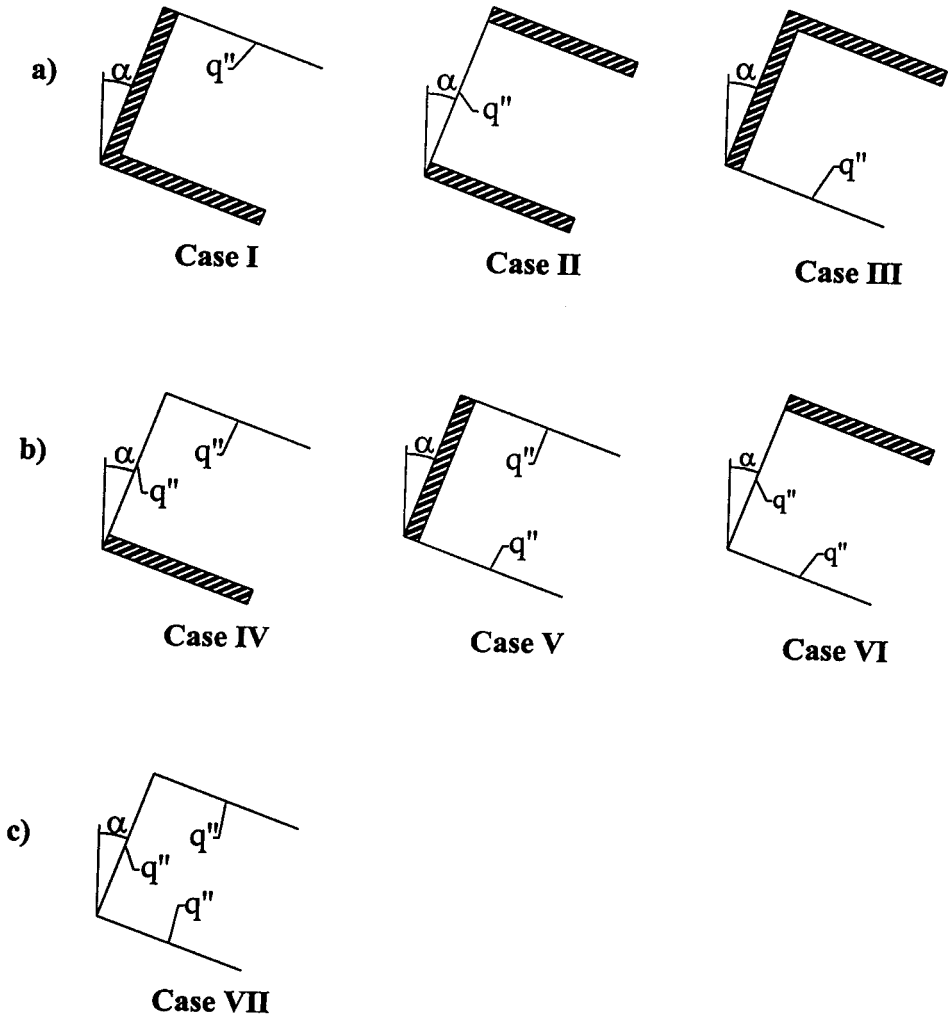

Fig. 2 Schematic diagram of the cavity showing all seven cases considered: (a) cavity with one wall heated and the other two walls are adiabatic; (b) cavity with two walls heated and the other one wall are adiabatic; and (c) cavity with all three walls heated

or from both the side wall and the roof (as in cases IV and VI at $\alpha=+90$ deg). For those buildings adjacent to modern skyscrapers decorated with reflective glass, incident solar radiation received by the building comes directly from the sun as well as from the rays being reflected from the neighboring skyscrapers (as in cases V and VII at $\alpha=+90$ deg).

Experimental Setup

Figure 3 (taken with modification from Chakroun et al. [1] illustrates the main features of the experimental setup. The cavity has dimensions of $a=B=H=14.85$ cm and $L=91.45$ cm, yielding an aspect ratio ($AR=H/B$) of 1.0 and an opening ratio ($OR=a/H$) of 1.0 as well. The length of the cavity (L) was selected to be more than six times its side length (B) to achieve two-dimensional flow of air inside the cavity. The heated walls were chosen to be made out of thin aluminum plates (14.85 cm×91.45 cm and 0.6 cm thick) because of their high thermal conductivity and light weight. The adiabatic walls were composed of Plexiglas (14.85 cm×91.45 cm and 0.6 cm thick) with thermal conductivity of 0.18 W/m K to serve as insulating material to prevent heat from dissipating to the adjacent walls.

Figure 4 shows a cross sectional view of a heated wall of the cavity. The first layer is the aluminum plate. Next is the heating

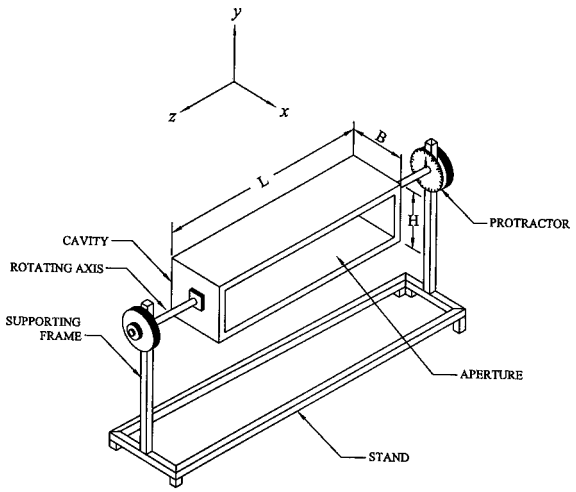

Fig. 3 Schematic diagram of the experimental setup showing the rotating mechanism of the cavity

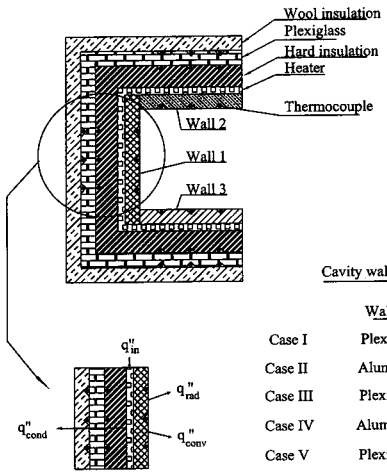

Cavity wall material for different cases

	Wall 1	Wall 2	Wall 3
Case I	Plexiglass	Aluminium	Plexiglass
Case II	Aluminium	Plexiglass	Plexiglass
Case III	Plexiglass	Plexiglass	Aluminium
Case IV	Aluminium	Aluminium	Plexiglass
Case V	Plexiglass	Aluminium	Aluminium
Case VI	Aluminium	Plexiglass	Aluminium
Case VII	Aluminium	Aluminium	Aluminium

Fig. 4 Cross sectional view and energy balance of the heated wall of the cavity

pad layer that supplied a constant heat flux to the cavity. The third layer is the hard insulation, made out of Polystyrene with a thickness of 3 cm. This is followed by the fourth layer which is the Plexiglas plate with a thickness of 0.9 cm. The Plexiglas plate was used to measure the heat loss by conduction from the backside of the heaters. A thin layer of glass wool insulation was placed last.

Each aluminum plate was electrically heated separately by flexible silicone rubber self-adhesive heating pads. The number of pads used depended on the case performed, e.g., if one wall was heated, only nine pads were turned on, if two walls were heated, eighteen pads were on, and if all three walls were heated, all twenty-seven pads were turned on. The pads were evenly distributed on the wall to provide constant heat flux. If one wall is heated, a plexiglass sheet to eliminate conduction from wall to wall replaces the aluminum plate on the other two walls.

The heat input to the pads was controlled by an electric circuit composed of a 240 V power supply and a manual voltage regulator. The output of the voltage regulator was directly coupled to the heating pads via a distribution board. All pads were connected in parallel; hence, they received the same power. The power supplied to the pads was calculated from the current and the voltage supplied.

The surface temperature of the aluminum plates was measured using copper-Constantan thermocouples (gauge 30), equally spaced to accurately monitor the temperature of the heated wall. All thermocouples used to measure the wall temperature, were imbedded inside a small groove and high conductive epoxy was place on the top to smoothen the wall in order to eliminate the disturbance of the flow at the wall.

Each thermocouple was connected to a digital temperature controller to ensure that the temperature of the walls was always less than the maximum working temperature of the pads (120°C), hence preventing them from burning out. For each run, steady state condition was achieved when the temperature did not vary by more than ± 0.2°C/1h.

Nusselt Number Data Reduction Equation

The results are presented in terms of average Nusselt number $\overline{\mathrm{Nu}}$, defined as

$$\overline{\mathrm{Nu}} = \frac{\overline{h}B}{k_a} \tag{1}$$

where $\overline{h}$ is the average convection coefficient between the cavity and the ambient air, B is the width of the cavity, and k_a is the thermal conductivity of air within the cavity. In terms of the local heat transfer coefficient h, Eq. (1) is rewritten in the following form:

$$\overline{Nu} = \frac{B}{k_a}\frac{1}{H}\int_0^H h\,dy \tag{2}$$

where H and y are as defined in Fig. 1. When one wall is at constant heat flux, the local heat transfer coefficient is given by the equation

$$h = \frac{q''_{\mathrm{conv}}}{(T_w - T_\infty)} \tag{3}$$

where q''_{conv} is the energy loss by convection from the heated wall to the ambient air, T_w is the local temperature of the wall, and T_∞ is the ambient temperature measured away from the cavity. The local temperature of the wall was measured by thermocouples placed at the three middle sections of the wall. Dividing the wall into three equal segments, Eqs. (2) and (3) are combined to give

$$\overline{\mathrm{Nu}} = \frac{B}{3k_a}\sum_{i=1}^{3}\frac{q''_{\mathrm{conv}}}{(T_{wi} - T_\infty)} \tag{4}$$

where i is the order of the various sections on the heated wall. The convection heat flux for each wall q''_{conv}, is determined by applying an overall energy balance to the heated wall (see Fig. 4). The energy balance reveals

$$q''_{\mathrm{in}} = q''_{\mathrm{cond}} + q''_{\mathrm{conv}} + q''_{\mathrm{rad}} \tag{5}$$

where q''_{in} is the constant heat flux supplied by the heating elements, q''_{cond} is the energy loss by conduction transported from the heating elements to the back layers of the cavity, q''_{conv} and q''_{rad} are the energy loss by convection and radiation from the heated wall to the ambient air, respectively.

The amount of electrical power input per unit area to the heating elements represents the heat flux q''_{in} to the cavity. This can be written as

$$q''_{\mathrm{in}} = \frac{1}{n}\sum_{j=1}^{n}\frac{I_j V_j}{A_j} \tag{6}$$

where n is the number of heated walls, j is the wall identification number, I and V are the current and voltage difference across the heating elements, respectively, and A_j is the area of the heated wall ($A_j = H \times L = B \times L$, since $B = H$). For cases where two or three walls are heated, the flux input to all heated walls remains the same since the electric power and the area always increase by the same ratio.

The conduction heat flux is measured by the aid of a Plexiglas plate provided with three thermocouples mounted on each side, as mentioned earlier. The plate is located behind the heating elements and the hard insulation (Polystyrene), as shown in Fig. 4. The conduction heat flux is expressed as

$$q''_{\mathrm{cond}} = \frac{k_p}{H}\sum_{j=1}^{n}\int_0^s (T_{j,i} - T_{j,o})\frac{ds}{t_j} \tag{7}$$

where j is the wall identification number, n is the number of heated walls, k_p is the thermal conductivity of the Plexiglas wall, t_j is the thickness of the Plexiglas wall, s is the incremental distance across which it is integrated along the walls, and $T_{j,i}$ and $T_{j,o}$ are the local temperatures on the inner and outer surfaces of the jth wall, respectively.

The radiation heat flux from the heated wall is modeled by

$$q''_{\mathrm{rad}} = \frac{\sigma[(\overline{T}_w + 273)^4 - (T_\infty + 273)^4]}{\dfrac{1-\varepsilon}{\varepsilon} + \dfrac{1}{F_{ia}}} \tag{8}$$

Table 3 Constants for the sigmoidal function used in Eq. (18)

Case	a	b	c	α_o	$\overline{\mathrm{Nu}}_o$
1	1.991×10	−1.796×10	2.921×10	6.134×10	1.378×10
2	2.814×10	−2.635×10	4.969×10	1.413×10^{2}	3.089
3	6.034×10	−3.288×10	1.562×10	2.089×100	−2.668×10
4	2.201×10	−2.604×10	4.090×10	1.266×100	6.609
5	3.258×10	−3.767×10	1.100	7.961×10	−1.912
6	1.245×10^{2}	−1919×10	5.002×10^{-2}	1.061×10	−9334×10
7	2.668×10	−2.523×10	1.372	5.769×10	9.563×10^{-1}

where σ is the Stefan-Boltzmann constant, $\overline{T_w}$ is the average wall temperature of one wall (obtained by averaging the temperatures of the three middle thermocouples mounted on the wall to avoid the z direction side-effects), T_∞ is the temperature of the ambient air sufficiently far from the cavity, ε is the emissivity of the aluminum plate, and F_{ia} is the view factor between the surface of wall i and the surrounding, calculated from the analytical expression given by Gross et al. [24]. As mentioned earlier, for cases with two or three heated walls, the radiation heat flux is calculated by summing the individual radiation flux from each heated wall and dividing that by the total area.

It follows that, rearranging Eq. (5) for each heated wall as

$$q''_{\mathrm{conv}} = q''_{\mathrm{in}} - q''_{\mathrm{cond}} - q''_{\mathrm{rad}} \tag{9}$$

and substituting it in Eq. (4) gives

$$\overline{\mathrm{Nu}} = \frac{B}{3k_a}\sum_{i=1}^{3}\frac{q''_{\mathrm{in}} - q''_{\mathrm{cond}} - q''_{\mathrm{rad}}}{(T_{wi} - T_\infty)} \tag{10}$$

or, by substituting from Eqs. (6), (7), and (8),

$$\overline{\mathrm{Nu}} = \frac{B}{3k_a}\sum_{i=1}^{3}\frac{\dfrac{1}{n}\Sigma_{j=1}^{n}\dfrac{I_j V_j}{A_j} - \dfrac{k_p}{H}\Sigma_{j=1}^{n}\int_0^s (T_{j,i} - T_{j,o})\dfrac{ds}{t_j} - \dfrac{\sigma[(\overline{T_w}+273)^4 - (T_\infty+273)^4]}{\dfrac{1-\varepsilon}{\varepsilon} + \dfrac{1}{F_{ia}}}}{(T_{wi} - T_\infty)} \tag{11}$$

The above expression shows explicitly all the variables involved in the experimental determination of $\overline{\mathrm{Nu}}$.

The constant heat flux Grashof number for this experiment was defined as

$$\mathrm{Gr}_B^* = g\beta\frac{q''_{\mathrm{conv}} B^4}{k_a \nu^2} \tag{12}$$

where g is the gravitational acceleration, β is the coefficient of thermal expansion of air, q''_{conv} is the energy loss by convection from the heated wall, B is the width of the cavity, k_a is the thermal conductivity of air, and ν is the kinematic viscosity of air.

The uncertainties in the experimentally determined Nusselt number and Grashof number are estimated based on the ANSI/ASME Standard on Measurement Uncertainty [25] following the procedures of Coleman and Steele [26].

The total uncertainty U in the measured value of either Nusselt number or Grashof's number is expressed as follows:

$$U = (E_b^2 + E_p^2)^{1/2} \tag{13}$$

where E_b and E_p are the bias and the precision limits in the measured quantities. The expressions used in the determination of Nusselt number and Grashof number are given in Eqs. (11) and (12), respectively. These expressions can be expressed in the form

$$\overline{\mathrm{Nu}} = f(v_1, v_2, v_3, \ldots, v_m) \tag{14}$$

and

$$\mathrm{Gr}_B^* = f(v_1, v_2, v_3, \ldots, v_m) \tag{15}$$

where m is the number of variables involved in each equation. The expression for E_b and E_p are, respectively, given as follows:

$$E_p^2 = \sum_{i=1}^{m}\left(\frac{\partial\overline{\mathrm{Nu}}}{\partial r_i}e_{pi}\right)^2 \tag{16}$$

$$E_b^2 = \sum_{i=1}^{m}\left(\frac{\partial\overline{\mathrm{Nu}}}{\partial r_i}e_{bi}\right)^2 + 2\left(\frac{\partial\overline{\mathrm{Nu}}}{\partial r_1}\right)\left(\frac{\partial\overline{\mathrm{Nu}}}{\partial r_2}\right)e'_{b1}e'_{b2} \tag{17}$$

where e_{pi} is the precision limit error in the variable r_i, e_{bi} is the bias limit error in the variable r_i, and $e'_{bi}e'_{bj}$ are the correlated bias error in the variable ri and rj. Similar equation can be used for the Grashof number where the Nusselt number ($\overline{\mathrm{Nu}}$) is substituted by the Grashof number (Gr_B^*) in Eqs. (16) and (17). A computer program was prepared to determine all the partial derivatives in order to calculate the uncertainties in the measured variables using Eq. (13). Chakroun et al. [1] have reported a detailed procedure on estimating the uncertainties. The same technique is used in the present paper.

The overall uncertainty of Nusselt number in the present work ranges from 4 to 10 percent depending on the number of heated walls and the inclination angle α. When the cavity is facing upward, the total uncertainty is minimum. As the cavity is tilted downward the uncertainty starts increasing to reach a value of 10 percent at an angle of +90°. At this angle, the heat is transferred only by conduction and steady state takes a long time to be achieved. The total uncertainty is mostly bias errors so the data can be compared from case to case with each other with good

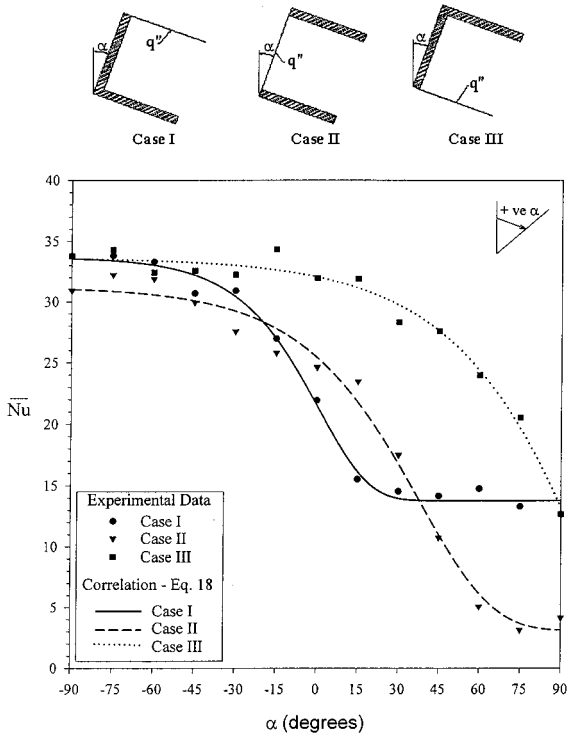

Fig. 5 Comparison of the average Nusselt number for cases I, II, and III

degree of accuracy. The total uncertainty of Grashof's number ranges from 2.5 percent to about 7.3 percent depending on the case investigated and the inclination angle α.

Results and Discussion

The results for the seven cases introduced earlier are presented here. For each case, the cavity was rotated over a range of ± 90 deg (measured from the vertical direction) in 15 deg increments. The data was collected at $\mathrm{Gr}_B^* = 1.3 \times 10^8$.

The results for each case were correlated using a sigmoid function with five parameters expressed as

$$\overline{\mathrm{Nu}} = \overline{\mathrm{Nu}}_o + \frac{a}{[1 + e^{-(\alpha - \alpha_o/b)}]^c} \tag{18}$$

where α_o, $\overline{\mathrm{Nu}}_o$, a, b, and c are constants that can be obtained from Table 3. The correlations are presented on Figs. 5, 7, and 9 for easy comparison with the experimental result of each case. The regression provides a single equation for all the cases where the objective is to obtain the heat transfer at intermediate angles. This correlation can be used in any computer application to represent the result. The maximum standard deviation for the correlation was obtained to be 10.2.

Even though the data was collected for constant heat flux, the temperature of the walls of the cavity at each angle was found to be constant to within ± 0.25°C. So according to the temperature data of the walls in this work, Grashof number for constant heat flux of 1.3×10^8 would correspond to Grashof number of constant wall temperature between of 0.24×10^7 and 0.76×10^7 depending on the angle of rotation and the case being considered. The Nusselt number for angle 0 deg in case II can be compared to that obtained by Angirasa et al. [18]. For this angle, Grashof number of constant wall temperature will have a value of 0.4×10^7. In the present work the value of Nu for this angle was 24.6 compared to 23 as obtained by Angirasa et al. [18]. The difference is within the reported uncertainty. Also case VII at zero angle of rotation was compared to Angirasa et al. [16] where all three walls are heated. Grashof number based on constant wall temperature for this case was 0.66×10^7. The value of Nusselt number here was equal to 24. The closest Grashof number reported by Angirasa et al. [16] was 1×10^7 and Nusselt number for this configuration was 32. The difference between the two values is caused by the variation in the Grashof number.

Figure 5 presents the variation of average Nusselt number with tilt angle for case I, II, and III. Case I represents the data for the setup where one wall (namely, wall number 3) is maintained at a constant heat flux and the other two walls are adiabatic. Referring to the schematic sketch included in the figure, the cavity rotates in a clockwise direction with respect to the vertical axis. Starting at an inclination angle α of $+90$ deg, $\overline{\mathrm{Nu}}$ was found to be the lowest. This is expected since the cavity is facing downward and the heat transfer process is inhibited. It is noticed that in this case, $\overline{\mathrm{Nu}}$ remains almost constant for further inclination angles (from $+90$ deg to $+15$ deg). This can be rationalized as follows: when the cavity is rotated (by increments of 15 deg) over this range, the heated wall is always located on top of the heated air. So the heated air is trapped in a region between the heated wall and the adjacent insulated wall. Of course, the nearby air keeps on rising until it gets stratified within the upper corner of the cavity, which can be resembled as a dome capturing the heated air. As a result, the buoyancy force is suppressed and the rate of increase in $\overline{\mathrm{Nu}}$ is minimal. As 0 deg inclination angle is reached, a sudden flow instability takes place. The previously trapped heated air finds a path to exit the cavity, allowing for cooler air to replace it, hence enhancing the mechanism of heat transfer by natural convection. This can be seen from the noticeable jump in $\overline{\mathrm{Nu}}$ at an inclination angle of 0 deg. The value of $\overline{\mathrm{Nu}}$ increases thereafter from 0 deg to -30 deg. The inclination angle of the cavity seems to have a little effect from -30 deg to -90 deg, yielding a constant value for $\overline{\mathrm{Nu}}$. Since the aperture of the cavity faces upward, the buoyancy driven flow finds no obstacles, resulting in a constant heat transfer.

Data for case II where the middle wall (wall number 1) of the cavity is maintained under a constant heat flux is also presented. The average Nusselt number increases as the tilt angle decreases. The rate at which $\overline{\mathrm{Nu}}$ increases is high between $+60$ to 0 deg and relatively mild between 0 to -60 deg. The difference in the rate of heat transfer is due to the sensitivity of $\overline{\mathrm{Nu}}$ to tilt angle in the range from $+60$ to 0 deg. The change of inclination angle in the ranges between $+90$ to $+60$ deg and between -60 to -90 deg appears to have little effect on $\overline{\mathrm{Nu}}$.

The experimental results for case III where one wall (namely wall number 2) is maintained at a constant heat flux and the other two walls are adiabatic is also presented. The minimum value of $\overline{\mathrm{Nu}}$ is seen at $+90$ deg. A rapid increase in $\overline{\mathrm{Nu}}$ is noticed in the subsequent angles (from $+75$ deg to 0 deg). As the cavity is rotated, the heated wall (wall number 2) is always beneath the air enclosed in the cavity, supporting the buoyancy-driven flow. At about zero tilt angle, the value of $\overline{\mathrm{Nu}}$ is the highest. This confirms that the average Nusselt number is maximized when the heated wall is placed horizontally as the lower wall of the cavity. $\overline{\mathrm{Nu}}$ stays approximately constant in the angles to follow because, as mentioned in the foregoing cases, the buoyancy force is free from any constraints in these angles. This comparison is made to analyze the behavior of the heat transfer in the cavity when only one wall is heated as a function of inclination angle as well as the location of the heated wall. For cases I and III, the value of $\overline{\mathrm{Nu}}$ at $+90$ deg is the same for both. That is due to the symmetry between the two cases at that angle. But unlike case I, case III experiences a sudden increase in $\overline{\mathrm{Nu}}$ in the subsequent angles (from $+75$ deg to 0 deg). As the cavity (in case III) is rotated, the heated wall (wall number 3) is located beneath the air enclosed in the cavity, supporting the buoyancy-driven flow. At about zero tilt angle, the value of $\overline{\mathrm{Nu}}$ is the highest in case III among all preceding cases ($\overline{\mathrm{Nu}} = 34.35$). This confirms that when the heated wall forms the lower wall of the cavity, heat transfer, and hence aver-

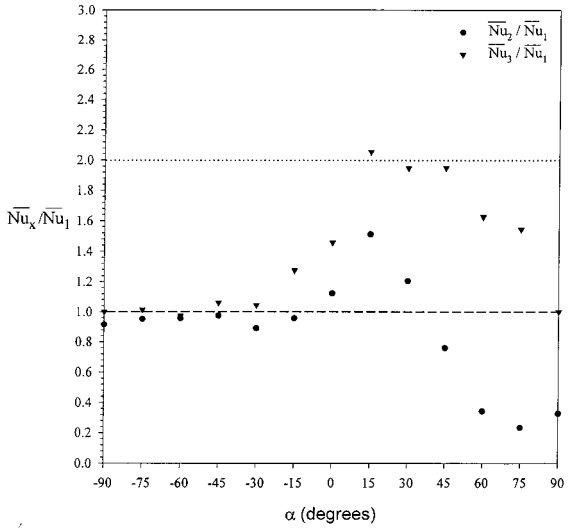

Fig. 6 Comparison for the average Nusselt number for cases II, and III to that of case I

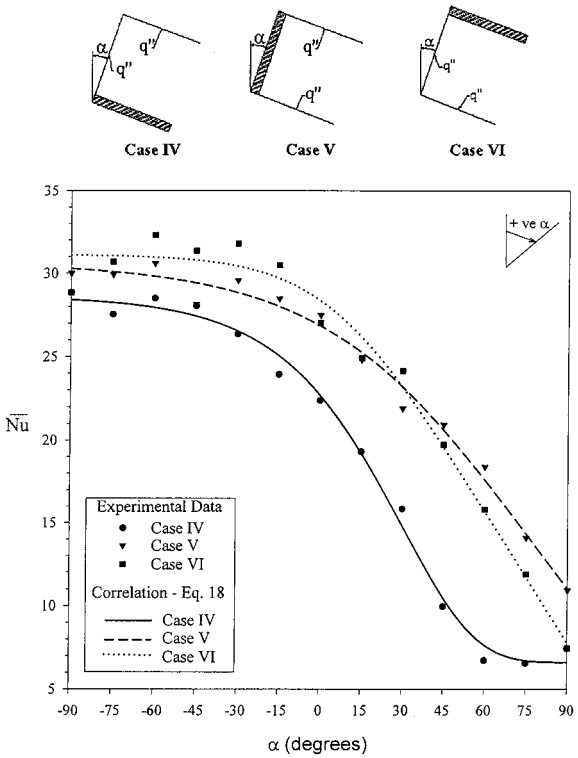

Fig. 7 Comparison of the average Nusselt number for cases IV, V, and VI

age Nusselt number is maximized. For cases I and III, the maximum divergence in $\overline{Nu}$ occurs at an angle of +15 deg where convection heat transfer is doubled. It is also noticed that $\overline{Nu}$ in case III is superior in the range from +75 to −15 deg.

It is also noticed that for case II, the Nusselt number at the stratification angle of $\alpha=+90$ deg is a much lower value than for cases I and III at the same angle. That is because the heated wall is in a horizontal position located on top of the heated air, hence further air suppression took place. This conclusion is confirmed when comparing $\overline{Nu}$ of all three cases at an inclination angle of 0 deg. At that angle, case I (with the heated wall located at the upper-horizontal position) has a value of $\overline{Nu}=21.93$, case II (with the heated wall located at the side-vertical position) has a value of $\overline{Nu}=24.62$ and case III (with the heated wall located at the lower horizontal position) has a value of $\overline{Nu}=31.95$. Obviously, case III has a better heat transfer owing to the location of the heated wall.

At $\alpha=-90$ deg, $\overline{Nu}$ is identically the same ($\overline{Nu}=33.79$) for cases I and III because of the symmetry of those cases at such an angle. For case II however, $\overline{Nu}=30.92$, which is slightly less than that of cases I and III. This is an indication that in case II, as the heated air (guarded by buoyancy force) is trying to escape vertically from the cavity, cooler (ambient) air is retarding it, hence slowing the heat transfer process.

Figure 6 presents the same information as before (in Fig. 5) in the form of ratios of $\overline{Nu}_2$ and $\overline{Nu}_3$ to that of $\overline{Nu}_1$. It is shown that $\overline{Nu}_3/\overline{Nu}_1$ is always greater than or equal to unity. This ratio is maximized between angles +75 and −15 deg and approaches one from angles −30 to −90 deg. The behavior of $\overline{Nu}_2/\overline{Nu}_1$ is different, however, especially in the range from +90 to −30 deg. At +90 deg, this ratio starts at a value relatively lower than one and stays almost constant for angles +75 and +60 deg, then increases linearly from +60 to +15 deg, after which it starts decreasing until an angle of −30 deg is reached. The ratio is in the neighborhood of one from −30 to −90 deg. Obviously, both ratios converge to unity in the range from −30 to −90 deg, showing that $\overline{Nu}$ for all three cases is almost the same at those angles, where the aperture of the cavity faces upward.

Figure 7 presents the results for cases IV, V, and VI on one figure for comparison. Case IV represents the set up where walls 1 and 3 kept at constant heat flux. $\overline{Nu}$ is almost constant with a value of about 7 from inclination angles of +90 to +60 deg, increases steadily from +60 to −60 deg and then remains constant from −60 to −90 deg at a value of about 28. The low rate of heat transfer at inclination angle +90, +75 and +60 deg is due to the down-facing aperture with both heated walls on top. The results for case V where walls 2 and 3 are subjected to constant heat flux is also presented. At +90 deg, $\overline{Nu}=10.91$, which is relatively high. $\overline{Nu}$ gradually increases until an inclination angle of −30 deg is reached. Any change in α beyond −30 deg appears to cause little 1 change in $\overline{Nu}$. Case VI where walls 1 and 2 are subjected to constant heat flux is also presented. Obviously, $\overline{Nu}$ rapidly increases as α is decreased from +90 to −15 deg, since both heated walls are located in the lower side of the cavity, allowing a higher buoyancy force to be generated. $\overline{Nu}$ remains almost the same from −15 deg to −90 with a value of about 30. When comparing cases IV, V and VI, it is clear that the data for case VI is shifted upward giving a higher $\overline{Nu}$ in comparison with case IV for all tilt angles (except at +90 and −90 deg). This behavior can be predicted since the heated walls in case VI are located under the air enclosed in the cavity, hence enforcing the buoyancy force; but located on top of the air in case IV, leading to suppression in the buoyancy force. In both cases, the aperture of the cavity is facing either downward or upward at angle +90 and −90 deg, respectively. Because of the analogy between those cases at such angles, $\overline{Nu}$ is the same, i.e., $\overline{Nu}=7.44$ at +90 deg and 28.83 at −90. Comparing cases V and VI, $\overline{Nu}$ for case V is higher than case VI in the range from +90 to 0 deg, but lower from −15 to −75 deg.

Figure 8 shows the ratio of $\overline{Nu}$ for cases V and VI over case IV. It is clear from the figure that cases V and VI always have a higher $\overline{Nu}$ than case IV, especially at $\alpha=+60$ deg, where it is about 2.8 times higher in case V than it is in case IV and about 2.4 higher as high in case VI than it is in case IV.

Figure 9 presents the variation of average Nusselt number $\overline{Nu}$ with tilt angle α for case VII, where all three walls are kept at constant heat flux. Steady-state condition (at $\alpha=+90$ deg) was achieved over a period of twelve hours resulting in $\overline{Nu}=4.03$. In the range from +90 to +15 deg, $\overline{Nu}$ increases as α decreases, showing that heat transfer is strongly affected by inclination angle in this range. Conversely, any change in α has little impact on $\overline{Nu}$

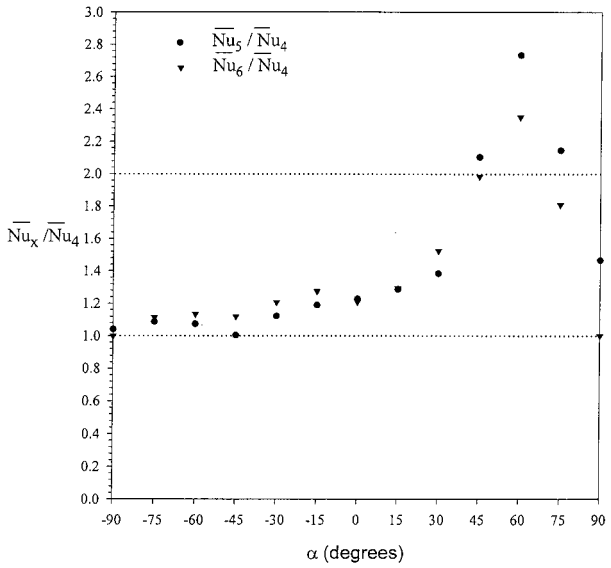

Fig. 8 Comparison of the average Nusselt number for cases V, and VI to that of case IV

in the range of angles from +15 to −90 deg. It should be noted that in general, $\overline{Nu}$ for case VII is almost the lowest among all other cases between 0 and −90 deg. This can be explained by the small value of temperature difference when three walls are heated. The temperature difference among the walls is the prime mover of the heat transfer mechanism. Therefore, case VII faces the least value of temperature difference since three walls are heated. In the range of +90 to 0 deg, case II has the lowest value of $\overline{Nu}$. The heat transfer mechanism for case VII in this range is aided by the presence of the heated wall at the bottom of the cavity; hence, it has a better value of $\overline{Nu}$ than case II. Considering cases III, VI, and VII, where one, two and three heated walls respectively are present; the heated walls are located on the lower side of the cavity. Comparison is better made when the range of inclination angles is divided into two ranges, from +90 deg to 0 deg and

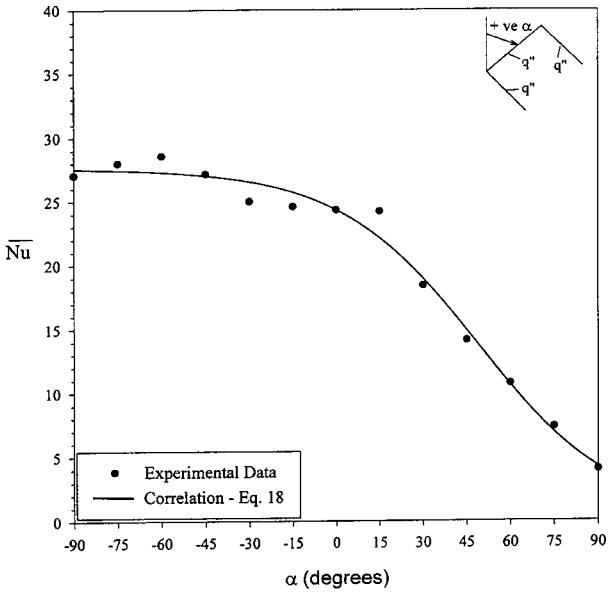

Fig. 9 Variation of average Nusselt number with tilt angle for case VII

from 0 deg to −90 deg. In the range from +90 to 0 deg, the value of $\overline{Nu}$ is the highest in case III because, as stated earlier, the heated wall lies at the bottom side of the cavity enhancing the heat transfer to take place. Although case VI has a heated wall at the bottom, it also has a heated wall at the top that is suppressing the buoyancy force. Case VII has a heated wall at the bottom, but two heated walls at the top, hence further suppression takes place and $\overline{Nu}$ is minimum. From 0 to −90 deg, case III having a higher $\overline{Nu}$ value than case VI and case VII. Since the prime mover of air within the cavity is the temperature difference between the walls. In that range (from 0 to −90 deg), as the hot air in case VII leave the vicinity of the lower heated wall, it is slowed down by the two upper heated walls. The situation is less drastic in case VI where only one heated wall is at the top; hence, the temperature difference between the walls is higher. Case III (from 0 to −90 deg) only has one heated wall at the bottom and no heated walls at the top, so the temperature difference is maximized and convection currents develop in the enclosure of the cavity, hence natural convection is maximized.

Conclusions

The experimental evidence provided in this study indicates that the convection heat transfer coefficient in fully open cavities is strongly affected by the inclination angle, the number of heated walls, and the wall configuration. Seven cases with different wall conditions were thoroughly investigated. The work was carried out at a constant heat flux with a Grashof number $Gr_B^* = 1.3 \times 10^8$.

In all cases, the average Nusselt number $\overline{Nu}$ decreases with the increase of tilt angle. The effect of buoyancy gets stronger when the angle of rotation decreases from 90 deg to −90 deg. As expected, $\overline{Nu}$ had the highest value at a tilt angle of −90 deg (upward facing cavity) where the buoyancy force is enhanced and the heated fluid rises from all over the cavity. At +90 deg (downward facing cavity) $\overline{Nu}$ was minimum and the buoyancy force is suppressed. The flow trapped inside the cavity and heat can transfer only by conduction.

For the case where cavity has one heated wall and the remaining two kept adiabatic, the heat transfer for case III dominates. The heated wall for this case was always located in the lower side of the cavity, hence supporting the buoyancy-driven flow. For cases I and II, the increase or decrease in heat transfer depends on the tilt angle. Three different regions can be classified: Between tilt angles +90 and +45 deg case II resulted in less $\overline{Nu}$, since the heated wall was horizontally positioned on top of the hot enclosed air, hence further suppression took place. In the range between +30 to about 0 deg, the heated wall for case I now is at the top resulted in less heat transfer for this case over case II. Between −15 deg and −90 deg, $\overline{Nu}$ in cases I and III is higher than that of case II.

The analysis is more complex when considering two heated walls cavities. Case IV always has the lowest $\overline{Nu}$ value over the entire range of tilt angles. This is because the heated walls are always located at the topside of the cavity, hence working against the buoyancy force. For cases V and VI, which one has higher heat transfer depends on the angle of rotation and no general statement can be made in this regard.

Considering case VII, the value of $\overline{Nu}$ was relatively the lowest among all cases. Since the prime mover of air within the cavity is the temperature difference between the walls, case VII, with all its walls heated, has the least temperature difference, hence very few convection currents develop in the enclosure of the cavity and natural convection is minimized.

Nomenclature

A = heated wall area (m^2)
a = height of aperture (m)
AR = cavity aspect ratio ($AR = H/B$)

B = width of the cavity (m)
DR = opening displacement ratio ($DR = d/H$)
d = distance from the centerline of the opening to the base of the cavity (m)
F_{ia} = configuration factor between the heated wall i and the surroundings
g = gravitational acceleration (m/s^2)
Gr = Grashof number
Gr* = constant heat flux Grashof number
H = height of the cavity (m)
$\underline{h}$ = local value of heat transfer coefficient (W/m^2·K)
$\overline{h}$ = average convection heat transfer coefficient (W/m^2·K)
I = electric current (A)
j = wall identification number
k_a = thermal conductivity of air (W/m·K)
k_p = thermal conductivity of Plexiglas plate (W/m·K)
L = length of the cavity (m)
$\overline{\mathrm{Nu}}$ = average Nusselt number
$\overline{\mathrm{Nu}}_x$ = average Nusselt number of case x
n = number of heated walls
OR = cavity opening ratio ($OR = a/H$)
P = power supply to heating pads (W)
Pr = Prandtl number
q''_{cond} = conduction heat flux (energy loss) from the heating pads (W/m^2)
q''_{conv} = convection heat flux (energy loss) from the heated wall (W/m^2)
q''_{in} = constant heat flux supplied to the heated wall (W/m^2)
q''_{rad} = radiation heat flux (energy loss) from the heated wall (W/m^2)
s = distance along a wall (m)
T_c = temperature of cold wall (C)
$\underline{T_h}$ = temperature of hot wall (C)
$\overline{T}_{\mathrm{in}}$ = average temperature of Plexiglas plate closer to the heating pads (C)
$\overline{T}_{\mathrm{out}}$ = average temperature of Plexiglas plate further from the heating pads (C)
$\overline{T}_w$ = average temperature of the heated wall (C)
T_∞ = Ambient temperature (C)
t = thickness of Plexiglas plate (m)
V = voltage difference across the heating pads (V)
x, y, z = rectangular coordinates (m)
α = inclination angle (degrees)
β = coefficient of thermal expansion of air (C^{-1})
ε = emissivity of heated wall (aluminum plate)
σ = Stefan-Boltzmann constant (W/m^2·K^4)
υ = kinematic viscosity of air (m^2/s)

References

[1] Chakroun, W., Elsayed, M. M., and Al-Fahed, S. F., 1997, "Experimental Measurements of Heat Transfer Coefficient in a Partially/Fully Open Tilted Cavity," ASME J. Sol. Energy Eng., **119**, pp. 298–303.

[2] Doria, M. L., 1974, "A Numerical Model for the Prediction of Two-Dimensional Unsteady Flows of Multi-Component Gases With Strong Buoyancy Effects and Recirculation," *Notre Dame Report*, TR-37191-74-4.

[3] Jacobs, H. R., Mason, W. E., and Hikida, W. T., 1974, "Natural Convection in Open Rectangular Cavities," *Proc. Fifth International Heat Transfer Conference*, Tokyo, Japan, **3**, pp. 90–94.

[4] Jacobs, H. R., and Mason, W. E., 1976, "Natural Convection in Open Rectangular Cavities With Adiabatic Side Walls," *Proc. 1976 Heat Transfer and fluid Mechanics Inst.*, pp. 33–46. Stanford University Press, Stanford.

[5] Chan, Y. L., and Tien, C. L., 1985, "A Numerical Study of Two-Dimensional Laminar Natural Convection in Shallow Open Cavities," ASME J. Heat Transfer, **28**, pp. 603–612.

[6] Chan, Y. L., and Tien, C. L., 1985, "A Numerical Study of Two-Dimensional Laminar Natural Convection in Square Open Cavities," Numer. Heat Transfer, **8**, pp. 65–80.

[7] Chan, Y. L., and Tien, C. L., 1986, "Laminar Natural Convection in Shallow Open Cavities," ASME J. Heat Transfer, **108**, pp. 305–309.

[8] Chen, K. S., Humphrey, J. A. C., and Sherman, F. S., 1985, "Experimental Investigation of Thermally Driven Flow in Open Cavities of Rectangular Cross-Section," Philos. Trans. R. Soc. London, Ser. A, **316**, pp. 57–84.

[9] Sernas, V., and Kyriakides, I., 1982, "Natural Convection in an Open Cavity," *Proc. Seventh International Heat Transfer Conference*, Munchen, Germany, **2**, pp. 275–286.

[10] Sezai, I., and Mohamad, A. A., 1998, "Three-Dimensional Simulation of Natural Convection in Cavities With Side Opening," Int. J. Numer. Methods Heat Fluid Flow, **8**(8), pp. 800–813.

[11] Lee, T. L., and Lin, T. F., 1995, "Three-Dimensional Natural Convection of Air in an Inclined Cubic Cavity," Numer. Heat Transfer, Part A, **27**, pp. 681–703.

[12] LeQuere, P., Humphrey, J. A. C., and Sherman, F. S., 1981, "Numerical Calculation of Thermally Driven Two-Dimensional Unsteady Laminar Flow in Cavities of Rectangular Cross Section," Numer. Heat Transfer, **4**, pp. 249–283.

[13] Penot, F., 1982, "Numerical Calculation of Two-Dimensional Natural Convection in Isothermal Open Cavities," Numer. Heat Transfer, **5**, pp. 421–437.

[14] Miyamoto, M., Keuhn, T. H., Goldstein, R. J., and Katoh, Y., 1989, "Two-Dimensional Laminar Natural Convection Heat Transfer From a Fully or Partially Open Square Cavity," Numer. Heat Transfer, Part A, **15**, pp. 411–430.

[15] Showole, R. A., and Tarasuk, J. D., 1993, "Experimental and Numerical Studies of Natural Convection With Flow Separation in Upward-Facing Inclined Open Cavities," ASME J. Heat Transfer, **115**, pp. 592–605.

[16] Angirasa, D., Eggels, I. G., and Nieuwstadt, F. T. M., 1995, "Numerical Simulation of Transient Natural Convection From an Isothermal Cavity Open on a Side," Numer. Heat Transfer, Part A, **28**, pp. 755–768.

[17] Hess, C. F., and Henze, R. H., 1984, "Experimental Investigation of Natural Convection Losses From Open Cavities," ASME J. Heat Transfer, **106**, pp. 333–338.

[18] Angirasa, D., Pourquie, M. J. B. M., and Nieuwstadt, F. T. M., 1992, "Numerical Study of Transient and Steady Laminar Buoyancy-Driven Flows and Heat Transfer in a Square Open Cavity," Numer. Heat Transfer, Part A, **22**, pp. 223–239.

[19] Lin, C. X., and Xin, M. D., 1992, "Transient Turbulence Free Convection in an Open Cavity," Inst. Chem. Eng. Symp. Ser., **1**, pp. 515–521.

[20] Mohamad, A. A., 1995, "Natural Convection in Open Cavities, and Slots," Numer. Heat Transfer, Part A, **27**, pp. 705–716.

[21] Elsayed, N. M., Al-Najem, M. M., El-Refaee, M. M., and Noor, A. A., 1999, "Numerical Study in Fully Open Tilted Cavities," Heat Transfer Eng., **20**, pp. 73–85.

[22] Elsayed, M. M., 1989, "Infiltrationload in Cold Rooms," HVAC&R Res., **4**(2), pp. 179–202.

[23] Elsayed, M. M., and Chakroun, W., 1999, "Effect of Aperture Geometry on Heat Transfer in Tilted Partially Open Cavities," ASME J. Heat Transfer, **121**, pp. 819–827.

[24] Gross, U., Spindler, R., and Hahne, E., 1981, "Shape Factor Equations for Radiation Heat Transfer Between Plane Rectangular Bodies," Lett. Heat Mass Transfer, **8**, pp. 219–227, (reported in J. R. Howell, 1982, *Catalog of Radiation Configuration Factor*, Howell, J. R., 1982, McGraw-Hill, New York, p. 97.)

[25] ASME, 1986, Measurement Uncertainty, ANSI/ASME PTC 19.1-1985, Part 1.

[26] Coleman, H. W., and Steele, W. G., 1989, *Experimental and Uncertainty Analysis for Engineers*, John Wiley and Sons, New York.

Fluid Flow and Heat Transfer in a Lid-Driven Cavity Due to an Oscillating Thin Fin: Transient Behavior

Xundan Shi
Graduate Student

J. M. Khodadadi
e-mail: khodajm@auburn.edu
Professor,
ASME Member

Mechanical Engineering Department,
Auburn University,
201 Ross Hall, Auburn,
Alabama 36849-5341, USA

A finite-volume-based computational study of transient laminar flow and heat transfer (neglecting natural convection) within a lid-driven square cavity due to an oscillating thin fin is presented. The lid moves from left to right and a thin fin positioned perpendicular to the right stationary wall oscillates in the horizontal direction. The length of the fin varies sinusoidally with its mean length and amplitude equal to 10 and 5 percent of the side of the cavity, respectively. Two Reynolds numbers of 100 and 1000 for a $Pr=1$ fluid were considered. For a given convection time scale (t_{conv}), fin's oscillation periods (τ) were selected in order to cover both slow ($\tau/t_{conv}>1$) and fast ($\tau/t_{conv}<1$) oscillation regimes. This corresponded to a Strouhal number range of 0.005 to 0.5. The number of the cycles needed to reach the periodic state for the flow and thermal fields increases as τ/t_{conv} decreases for both Re numbers with the thermal field attaining the periodic state later than the velocity field. The key feature of the transient evolution of the fluid flow for the case with $Re=1000$ with slow oscillation is the creation, lateral motion and subsequent wall impingement of a CCW rotating vortex within the lower half of the cavity. This CCW rotating vortex that has a lifetime of about 1.5τ brings about marked changes to the temperature field within a cycle. The dimensionless time for the mean Nusselt numbers to reach their maximum or minimum is independent of the frequency of the fin's oscillation and is dependent on the distance between the oscillating fin and the respective wall, and the direction of the primary CW rotating vortex. The phase lag angle between the oscillation of the fin and the mean Nusselt number on the four walls increases as the distance between the fin and the respective wall increases. [DOI: 10.1115/1.1833362]

Introduction

Modification of flow and heat transfer in a rectangular cell by vertical or horizontal plate fins is of great interest because the introduction of thin fins is one way to control heat transfer in various engineering applications. Laminar natural convection in differentially heated cavities with internal fins (partitions) has been studied extensively, for example [1], among others. The high packaging density and increasing heat flux from electronic modules have necessitated the use of forced convection in electronic cooling practices. The existence of chips or boards in a rectangular cell could have a significant effect on the resulting flow field and heat transfer. No attention has been given to the investigation of a shear-driven cavity with isothermal fins [2]. Such problems are, however, commonly encountered, e.g. the estimation of heat loss of electronic packages in a closed cavity, the design of various drying devices and decreasing the heat loss in various engineering applications. Besides being a simple benchmark geometry for the study of complex flow phenomena, a cavity system can simulate a lubricating groove between sliding plates or approximate the separated flow in a surface cavity with an external stream flowing over it. A great number of studies have focused on this problem and an excellent review paper was recently reported by Shankar and Deshpande [2]. In general, interest has focused on low Reynolds number laminar regime for square cavities ([3], among many others who assumed 2-D flow). The authors [4] have reported results of a parametric study of steady laminar flow and heat transfer within a lid-driven square cavity due to a single thin fin. Fins with lengths of 5, 10 and 15 percent of the side, positioned at 15 locations on the stationary walls were examined for Re=500, 1000, 2000, and Pr=1. Placing a fin on the right wall brings about multi-cell recirculating vortices compared to the case without a fin that exhibits a primary vortex and two small corner cells. A fin positioned near the top right corner of the cavity can reduce heat transfer most effectively. Placing a fin on the right wall—compared to putting a fin on the left and bottom walls—can always enhance heat transfer on the left wall and at the same time, reduce heat transfer on the bottom, right and top walls.

Given the extensive work on steady-state behavior of stationary thin fins in various geometries and in a square lid-driven cavity [4] in particular, the next challenge is to investigate the transient evolution and periodic characteristics of a cavity with an *oscillating* thin fin. Because of the limitation on computing capacity, this topic is still untouched by most researchers. Some related research relevant to the present study has been reported. Flow and heat transfer in a channel due to the presence of very thin fins swinging back and forth normal to the flow direction was investigated by Fu and Yang [5,6]. The Arbitrary Lagrangian–Eulerian (ALE) method was adopted to handle the moving fins. The boundary layers attaching on the fins were contracted and disturbed. The parameters of the velocities of the fluid and the swinging speed of the fins were employed to investigate the evolving flow and thermal fields. Variations of the average Nusselt number on the fin with time for various cases showed that the swinging of the fin results in a significant heat transfer enhancement.

The objective of this study was to determine the transient evolution of the flow and thermal fields en route to the periodic state due to an oscillating thin fin attached to a wall of a square lid-driven cavity. Given the existing thorough knowledge of the steady 2-D laminar flow in lid-driven cavities, it is appropriate that the effect of an oscillating fin on the flow and thermal fields

Contributed by the Heat Transfer Division for publication in the JOURNAL OF HEAT TRANSFER. Manuscript received by the Heat Transfer Division November 8, 2003; revision received June 1, 2004. Associate Editor: S. Pratap Vanka.

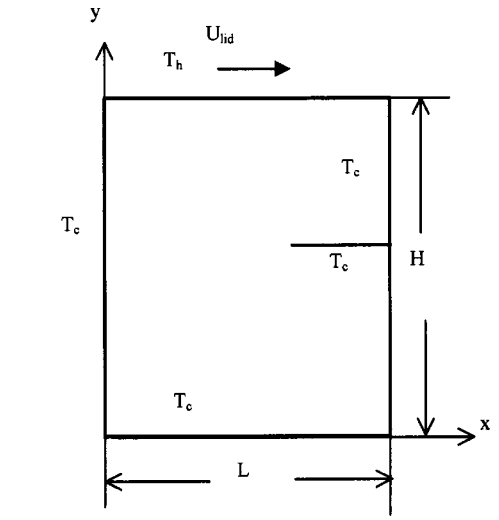

(a)

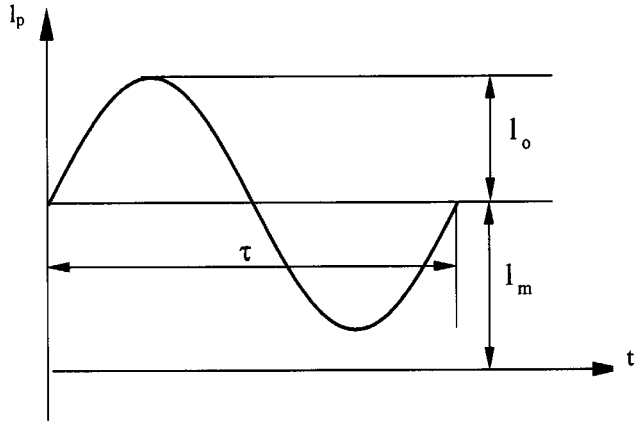

(b)

Fig. 1 Model of a square lid-driven cavity: (*a*) geometry and the coordinate system; (*b*) oscillating length of the fin

first be elucidated for such a system. Knowledge of the dynamic behavior, such as the time to reach the periodic state, the transient characteristics of the fluid flow, temperature fields and Nusselt numbers on the four walls are the key points in design of similar systems.

Problem Formulation

The proposed physical model for a two-dimensional lid-driven cavity (height H and length L) is shown in Fig. 1(*a*). For the present study it is assumed that $H=L$. The top wall is moving at the speed of U_{lid} from left to right, whereas the remaining three walls are stationary. The moving wall is maintained at a temperature (T_h) different from the remaining walls of cavity (T_c), with $T_h > T_c$. Based on the earlier findings of the authors [4], a thin fin is attached to the middle of the right wall. The fin is made of a highly-conductive material, so the Biot number is much smaller than 1. The fin can move back and forth horizontally and its length is:

$$l_p = l_m + l_o \sin 2\pi ft, \tag{1}$$

where f is the frequency of the fin's oscillation. Quantities l_m and l_o ($l_m \geq l_o$) are the mean and oscillating lengths of the fin, respectively. Figure 1(*b*) shows the time dependent variation of the length of the fin, with the period of oscillation τ equal to $1/f$. The dimensionless horizontal velocity of the fin can be expressed as:

$$U_p = \frac{u_p}{U_{\text{lid}}} = -2\pi \cdot \frac{l_o f}{U_{\text{lid}}} \cdot \cos 2\pi ft = -2\pi \cdot \text{St} \cdot \cos 2\pi ft, \tag{2}$$

where $\text{St} = l_o f / U_{\text{lid}}$ is the Strouhal number. The vertical velocity of the fin is zero. The effect of natural convection is neglected, so the ratio Gr/Re^2 is taken to be much smaller than 1.

Dimensionless Form of the Governing Equations. The fluid within the enclosure is an incompressible fluid and the fluid properties are constant. The flow within the enclosure is assumed to be laminar. The gravity effect and viscous dissipation are neglected. The dimensionless form of the governing equations can be obtained via introducing dimensionless variables:

$$X = \frac{x}{H}, \quad Y = \frac{y}{H}, \quad U = \frac{u}{U_{\text{lid}}}, \quad V = \frac{v}{U_{\text{lid}}},$$

$$P = \frac{p}{\rho U_{\text{lid}}^2}, \quad \theta = \frac{T - T_c}{T_h - T_c}, \quad t^* = \frac{U_{\text{lid}} t}{H}. \tag{3}$$

The governing equations of continuity, momentum, and thermal energy are then written in dimensionless form:

$$\frac{\partial U}{\partial X} + \frac{\partial V}{\partial Y} = 0, \tag{4}$$

$$\frac{\partial U}{\partial t^*} + U\frac{\partial U}{\partial X} + V\frac{\partial U}{\partial Y} = -\frac{\partial P}{\partial X} + \frac{1}{\text{Re}}\left(\frac{\partial^2 U}{\partial X^2} + \frac{\partial^2 U}{\partial Y^2}\right), \tag{5}$$

$$\frac{\partial V}{\partial t^*} + U\frac{\partial V}{\partial X} + V\frac{\partial V}{\partial Y} = -\frac{\partial P}{\partial Y} + \frac{1}{\text{Re}}\left(\frac{\partial^2 V}{\partial X^2} + \frac{\partial^2 V}{\partial Y^2}\right), \tag{6}$$

$$\frac{\partial \theta}{\partial t^*} + U\frac{\partial \theta}{\partial X} + V\frac{\partial \theta}{\partial Y} = \frac{1}{\text{Pr Re}}\left(\frac{\partial^2 \theta}{\partial X^2} + \frac{\partial^2 \theta}{\partial Y^2}\right). \tag{7}$$

The Reynolds number is defined as $\text{Re} = U_{\text{lid}} H/\nu$ and the Prandtl number is $\text{Pr} = \nu/\alpha$. For $t^* > 0$, the dimensionless form of the boundary conditions can be expressed as follows:

$$\text{At } X = 0,1 \text{ and } Y = 0: \quad U = V = 0, \theta = 0,$$

$$\text{At } Y = 1: \quad U = 1, V = 0, \theta = 1, \tag{8}$$

$$\text{On the moving fin:} \quad U = -2\pi\ \text{St}\cos(2\pi ft), V = 0, \theta = 0.$$

Therefore, Re, Pr and St are the dimensionless groups that govern this problem. The Reynolds numbers of 100 and 1000 were studied and the Prandtl number of the fluid is fixed to 1. Given the results of [4], l_m and l_o were assigned 0.1H and 0.05H, respectively. The time scales for convection and diffusion are given as

$$t_{\text{conv}} = \frac{H}{U_{\text{lid}}}, \quad t_{\text{diff}} = \frac{H^2}{\nu}. \tag{9}$$

The ratio of t_{diff} over t_{conv} equals Re. The ratio of the period of the fin's oscillation τ over t_{conv} is defined as TR. TR bigger than 1 corresponds to *slow oscillation*, whereas TR smaller than 1 signifies *fast oscillation*. Note that:

$$\text{TR} = \frac{\tau}{t_{\text{conv}}} = \frac{U_{\text{lid}}}{f \cdot H} = \frac{l_o}{H}\frac{1}{\text{St}}. \tag{10}$$

With $l_o/H = 0.05$, TR values of 10, 2, 1, 0.5 and 0.1 were investigated that correspond to Strouhal numbers of 0.005, 0.025, 0.05, 0.1 and 0.5, respectively.

Computational Details. The unsteady governing equations were solved by the finite-volume-method using Patankar's [7] SIMPLE algorithm. A two-dimensional uniformly-spaced staggered grid system was used. Hayase et al.'s [8] QUICK scheme was utilized for the convective terms, whereas the central differ-

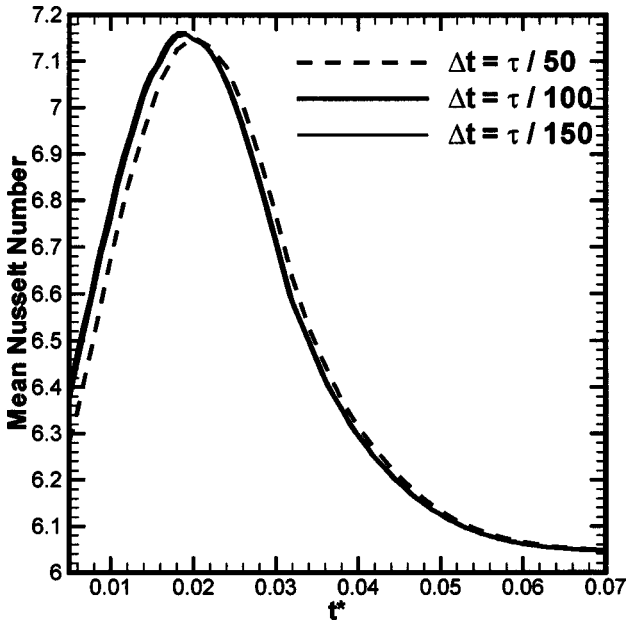

Fig. 2 A comparison of the mean Nusselt number of the system for various time steps (Re=1000, TR=0.1)

ence scheme was used for the diffusive terms. In order to keep consistent accuracy over the entire computational domain, a third-order-accurate boundary condition treatment suggested by Hayase et al. [8] was adopted. The moving fin is within the calculation domain and the FAVOR (Fractional Area/Volume Obstacle Representation) method (Hirt and Sicilian [9] and Tsukiyama et al. [10]) was used to treat the moving fin in this problem.

Details of a grid independence test using seven different grid densities (40×40, 60×60, 80×80, 100×100, 120×120, 150×150 and 240×240) was given by Shi and Khodadadi [4] for the steady version of this problem. The code was tested and verified extensively via comparing the results with the benchmark problems of Ghia et al. [3] and Torrance et al. [11]. Upon comparing critical quantities like the minimum value of the stream function of the primary vortex and the drag coefficients to benchmark data and considering both the accuracy and the computational time, the present calculations were all performed with a 150×150 uniformly-spaced grid system. Greater details can be found elsewhere [12].

Parameters for Numerical Simulations. The steady-state fluid flow and temperature fields of a lid-driven cavity with a fin that has length l_m and is attached to the middle of the right wall [4] are treated as the initial fields in this study. For the unsteady computations, tolerance of the normalized residuals upon convergence is set to 10^{-6} for every calculation case. The under-relaxation parameters for u, v, and T are all set to 0.6, whereas the under-relaxation parameter for pressure correction is set to 0.3. The three-time-level-method that is a 2nd order implicit scheme is used for approximating the unsteady terms. Three different time steps $\Delta t=\tau/50$, $\tau/100$ and $\tau/150$ for Re=1000 and TR=0.1 were adopted for the time step independence test. The variations of the mean Nusselt number $\overline{\mathrm{Nu}}$ of the system with dimensionless time are shown in Fig. 2. The results for $\tau/100$ and $\tau/150$ are identical. The deviations among the predictions with different time steps were quantified. For example, the deviations of the mean Nusselt number of the system for time steps of $\tau/50$, $\tau/100$ and $\tau/150$ evaluated at $t^*=0.012$ was less than 1.5 percent. To save computational time, the time step $\Delta t=\tau/100$ was used for all the cases in this study.

Table 1 Number of cycles needed to reach the periodic states for fluid flow (N_f) and temperature fields (N_t)

	N_f, N_t				
	St=0.5 TR=0.1	St=0.1 TR=0.5	St=0.05 TR=1	St=0.025 TR=2	St=0.005 TR=10
Re=100	8, 13	6, 8	4, 5	3, 4	3, 3
Re=1000	64, 95	52, 56	31, 35	20, 28	7, 11

Results and Discussions

The mean and oscillating lengths of the fin were $l_m/H=0.1$ and $l_o/H=0.05$, respectively. For $t<0$, the fin's length was equal to l_m/H. For $t\geq0$, the length of the thin fin varies according to Eq. (1). After a certain period of time, the fluid flow and temperature fields will reach their periodic states. The evolution of the fluid flow and temperature fields and the transient response of the average Nusselt numbers on the four walls is discussed here.

Time Required to Reach the Periodic State. Due to uncoupling of the momentum and energy equations, the fluid flow and temperature fields could reach their respective periodic states at different times. The cycle-to-cycle variations of the fluid flow and temperature fields were quantitatively defined and strictly monitored [12], exhibiting monotonic decay with time. Comparing the Re=100 and 1000 cases, it was observed that it takes fewer cycles to reach the periodic state for the lower Reynolds number. For a given Reynolds number, it took more cycles to reach the periodic state when TR is smaller (i.e. the Strouhal number is greater). For all the cases investigated, it takes fewer cycles for the flow field to reach the periodic state in comparison to the temperature field. Adopting a very stringent criteria [12], the number of cycles needed to reach the periodic state (N_f and N_t) are summarized in Table 1. The difference between N_t and N_f increases as TR decreases.

Transient Evolution of the Flow Fields. The instantaneous streamlines during the first, second and fifth cycles are shown in Figs. 3(*a*)–(*c*), respectively, for Re=1000 and TR=10. Before the start of oscillations, the steady flow field is characterized by a clockwise-rotating (CW) primary vortex in the upper half of the cavity and a counter-clockwise-rotating (CCW) vortex in the lower half of the cavity. During the first quarter of the first cycle (i.e. $t/\tau\leq0.25$), as the fin is getting longer, the center of the CCW rotating vortex moves from left to right. In addition, three small vortices are formed above the fin, under the fin and at the right bottom corner. The length of the fin decreases within the second and third quarters of the cycle and the CCW rotating vortex is squeezed and it moves toward the left and is pushed against the left wall. Two of the three vortices formed during $t/\tau\leq0.4$ that are below the fin start growing and an interesting quadru-cell structure is observed at $t/\tau=0.6$. By the time the fin has attained its shortest length at $t/\tau=0.75$, the original CW primary vortex has merged with the bottom right corner vortex and effectively touches the bottom plate of the cavity. It should be noted that other small vortices have also formed during the $0.4\leq t/\tau\leq0.8$ time period under the fin and at the bottom left corner. Within the last quarter of the first cycle, the fin gets longer and the CCW rotating vortex near the left wall is getting weaker whereas the CCW rotating vortex close to the fin is getting stronger. The vertical extent of the CW rotating primary vortex varies appreciably in one cycle.

During the first quarter of the second cycle (Fig. 3(*b*)), the CCW rotating vortex near the left wall gets smaller after it impinges on the wall. By $t/\tau=1.2$, it has totally disappeared. The other CCW rotating vortex anchored to the fin that was created during the third quarter of the previous cycle is already in motion

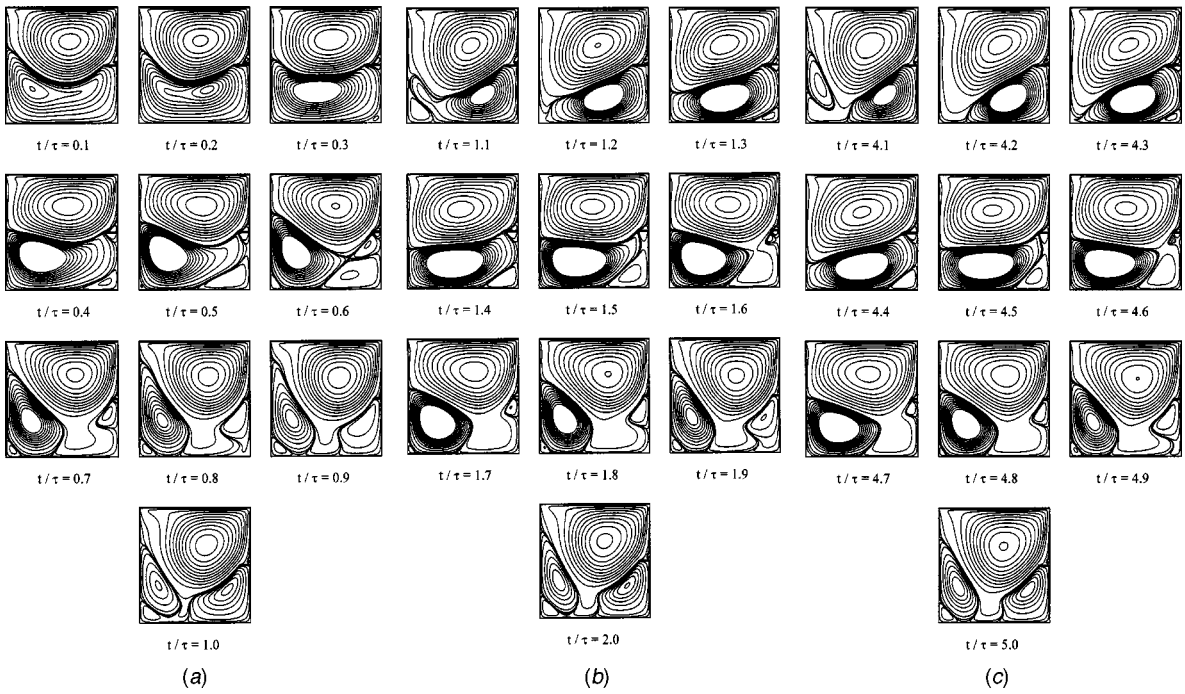

Fig. 3 Transient evolution of the flow field (Re=1000, TR=10) during the (*a*) first, (*b*) second and (*c*) fifth cycles

from the right toward the left wall. The flow field during the rest of the second cycle is similar to the flow field in the first cycle and subsequent cycles.

Comparing the flow fields in the third, fourth and fifth cycles, identical evolutions were observed, suggesting that for Re=1000 and TR=10, the periodic state was achieved after 4 cycles (quantitatively this number is 7 as given in Table 1). Upon attaining the periodic state (Fig. 3(*c*)), the most remarkable feature of flow field within a cycle is the emergence, lateral motion, wall impingement and disappearance of the CCW rotating vortex within the lower half of the cavity. The lifetime of this CCW rotating vortex is about one and a half periods of the fin's oscillation. This implies that the emergence, movement and disappearance of this CCW rotating vortex are closely dependent on the oscillation of the fin. Since the lifetime of the CCW vortex is greater than the period of the motion of the fin, there are generally two CCW vortices within the lower half of the cavity at a given instant. These two CCW vortices can be found at different stages of their lifetime. The cycle-to-cycle changes of the flow field of the other nine cases studied were not as varied as the case detailed above. The flow field variations for these cases were generally localized in regions of the order of a quarter of the cavity.

Transient Evolution of the Temperature Fields. Figure 4 shows the transient evolution of the temperature fields for the Re=1000 and TR=10 case during the eleventh cycle. The temperature distribution in the lower half of the cavity depends on the cyclic creation and movement of the CCW rotating vortex that is formed near the oscillating fin and the right wall within the third quarter of the cycle. Since both the fin and the right wall are cold, the temperature within the CCW rotating vortex is also low. But during the lateral movement of the vortex, the CCW vortex is in contact with the CW rotating primary vortex above it and absorbs heat from it. As a result, the temperature in the CCW rotating vortex increases while moving from the right wall to the left wall. When it impinges on the left wall, the local temperature gradient is steepened markedly.

The temperature distribution within the upper half varies periodically because of the heat exchange between the CW rotating primary vortex and the CCW rotating vortex. Within the first quar

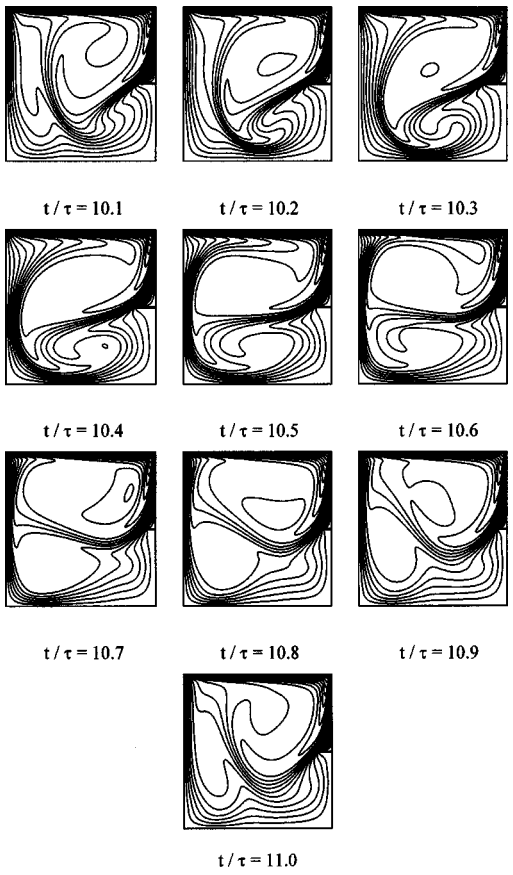

Fig. 4 Transient evolution of the temperature field (Re=1000, TR=10) during the eleventh cycle (contour level increment of 0.05)

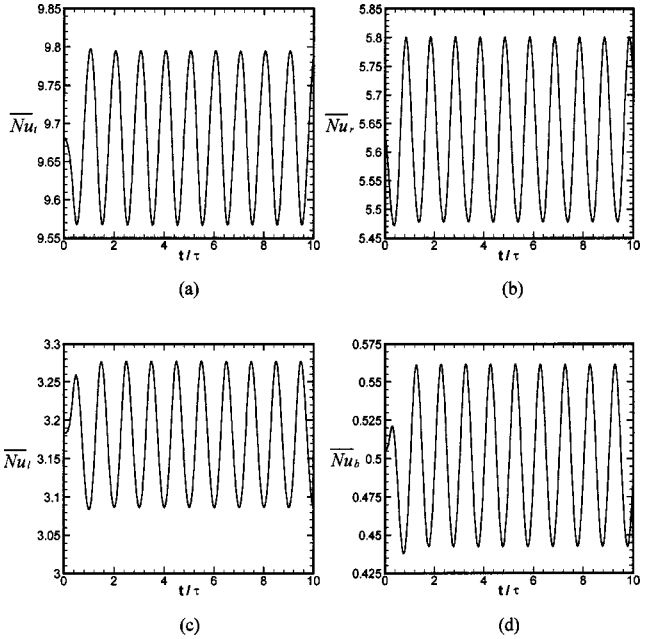

Fig. 5 Transient response of the mean Nusselt numbers on four walls: (*a*) $\overline{\mathrm{Nu}}_t$, (*b*) $\overline{\mathrm{Nu}}_r$, (*c*) $\overline{\mathrm{Nu}}_l$ and (*d*) $\overline{\mathrm{Nu}}_b$ for Re=100 and TR=10

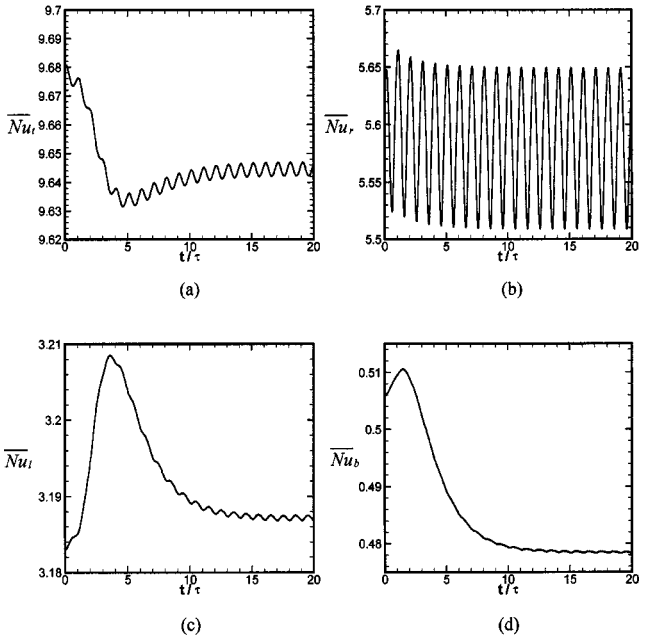

Fig. 6 Transient response of the mean Nusselt numbers on four walls: (*a*) $\overline{\mathrm{Nu}}_t$, (*b*) $\overline{\mathrm{Nu}}_r$, (*c*) $\overline{\mathrm{Nu}}_l$ and (*d*) $\overline{\mathrm{Nu}}_b$ for Re=100 and TR=1

ter, one CCW rotating vortex near the left wall vanishes, however the other CCW rotating vortex is following its lateral motion. During the first quarter, the contact area between the CCW rotating vortex and the primary CW vortex is relatively small and the heat absorbed from the top moving wall accumulates mainly within the primary CW vortex. As a result, the temperature within the primary CW vortex increases within the second quarter. As the CCW rotating vortex moves from the right wall to the left wall within the second and third quarters, it is in contact with the primary vortex and absorbs heat from it, thus giving rise to the decrease of the temperature in the zone covered by the primary vortex.

Transient Evolution of the Mean Nusselt Number on Four Walls. Figures 5, 6, and 7 show the transient evolution of the instantaneous mean Nusselt number on four walls for Re=100 and TR=10, 1 and 0.1, respectively. The definitions of the instantaneous mean Nusselt numbers on the walls are given as integrals of the instantaneous local Nusselt numbers, i.e.:

$$\overline{\mathrm{Nu}_i}(t^*) = \int_0^1 \mathrm{Nu}_i(s,t^*)\,ds, \tag{11}$$

with the subscript i denoting b, l, r or t and variable s being X or Y. As TR increases, one can observe that the oscillations of the mean Nusselt numbers on four walls are easily recognizable. This is due to the long period of oscillation in relation to the convective time scale. In other words, as the fin oscillates slowly, convection has enough time to transmit the oscillation of the fin to every point within the cavity. For the case of TR=10 that corresponds to the slowest oscillation of the fin considered, the maximum and minimum values of the mean Nusselt number on each wall match very closely to the steady-state values for fins with length 0.05 and 0.15, respectively [4,12]. As the fin oscillates faster, the time for the fluid to travel from one side to another side is greater than the period of the fin's oscillation. This brings about the confinement of the fin's oscillation within the area near the fin.

The mean Nusselt number on the top wall reaches a periodic state within several cycles when TR$\geqslant$1. This implies that with slow oscillation, the periodic thermal state is readily achieved. For TR$<$1, it takes more cycles to reach a periodic state. After comparing the variation of $\overline{\mathrm{Nu}}_t$ in Figs. 5–7, one can conclude that there is a minimum value for $\overline{\mathrm{Nu}}_t$ during the transient process. It takes more cycles to reach the minimum when TR is small. However, if we calculate the dimensionless time t^*, it is observed that the minimum was reached almost at the same time, that is $t^*=5$. The value of the minimum of $\overline{\mathrm{Nu}}_t$ is lowered as TR decreases. This is because the *equivalent* length of an oscillating fin increases as it oscillates faster. The equivalent length can be defined as the length of a fixed fin for a system under steady-state condition that has the same mean Nusselt number of a system with an oscillating

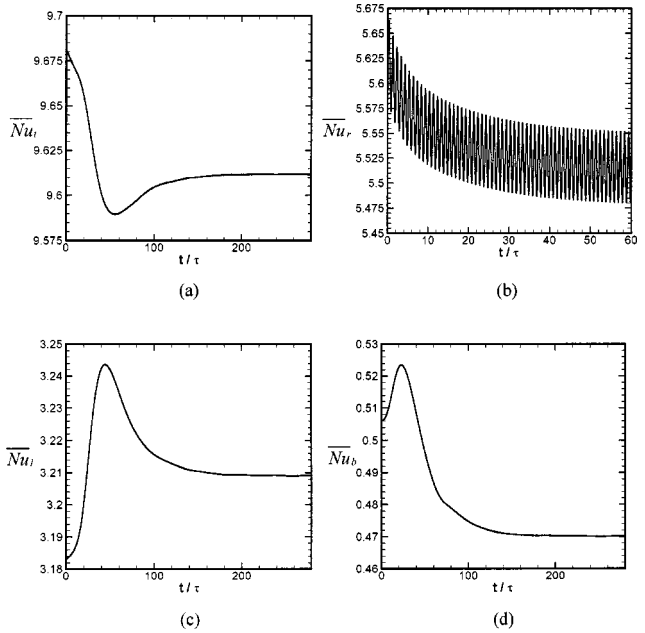

Fig. 7 Transient response of the mean Nusselt numbers on four walls: (*a*) $\overline{\mathrm{Nu}}_t$, (*b*) $\overline{\mathrm{Nu}}_r$, (*c*) $\overline{\mathrm{Nu}}_l$ and (*d*) $\overline{\mathrm{Nu}}_b$ for Re=100 and TR=0.1

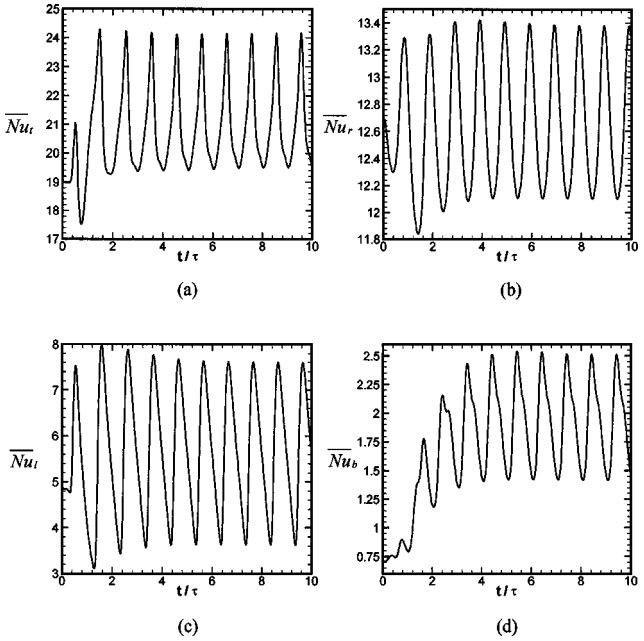

Fig. 8 Transient response of the mean Nusselt numbers on four walls: (*a*) $\overline{\mathrm{Nu}}_t$, (*b*) $\overline{\mathrm{Nu}}_r$, (*c*) $\overline{\mathrm{Nu}}_l$ and (*d*) $\overline{\mathrm{Nu}}_b$ for Re=1000 and TR=10

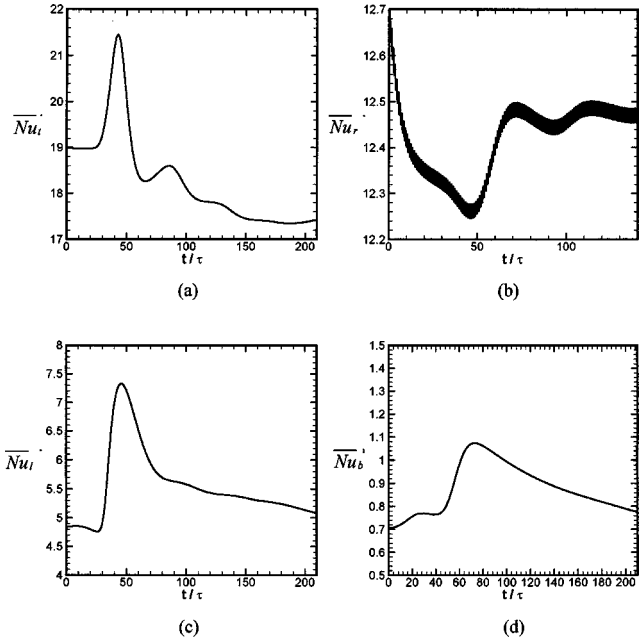

Fig. 9 Transient response of the mean Nusselt numbers on four walls: (*a*) $\overline{\mathrm{Nu}}_t$, (*b*) $\overline{\mathrm{Nu}}_r$, (*c*) $\overline{\mathrm{Nu}}_l$ and (*d*) $\overline{\mathrm{Nu}}_b$ for Re=1000 and TR=0.1

fin when $t\rightarrow\infty$. The mean value of the fluctuations of $\overline{\mathrm{Nu}}_t$ decreases as TR decreases. This is also because the equivalent length of an oscillating fin increases as it oscillates faster. The amplitude of the fluctuations of $\overline{\mathrm{Nu}}_t$ diminishes as TR decreases. The oscillations are completely damped when TR=0.1.

As for the variation of the mean Nusselt number on the right wall, since the fin is attached to the middle of the right wall, it is heavily affected by the oscillation of the fin. For all the cases studied, $\overline{\mathrm{Nu}}_r$ reaches a periodic state after a period of time. Similar to $\overline{\mathrm{Nu}}_t$, the mean value and amplitude of the fluctuations of $\overline{\mathrm{Nu}}_r$ decrease as the fin oscillates faster.

In regard to the transient evolution of the mean Nusselt number on the left and bottom walls, they attain a steady state for TR =0.1 (fast oscillation) and reach a periodic state for the other cases we studied. There exists a maximum during the transient process and $\overline{\mathrm{Nu}}_b$ reaches its maximum earlier than $\overline{\mathrm{Nu}}_l$. Similar to $\overline{\mathrm{Nu}}_t$, the dimensionless time t^* for both $\overline{\mathrm{Nu}}_l$ and $\overline{\mathrm{Nu}}_b$ to reach their respective maxima is independent of the frequency of the fin's oscillation. $\overline{\mathrm{Nu}}_l$ and $\overline{\mathrm{Nu}}_b$ reach their maxima at $t^*=3.5$ and 1.5, respectively. One can see that the time for $\overline{\mathrm{Nu}}_l$, $\overline{\mathrm{Nu}}_t$ and $\overline{\mathrm{Nu}}_b$ to reach their maximum or minimum is dependent on the distance between the oscillating fin and the respective wall and the direction of the primary CW vortex. Since the primary vortex is rotating in the clockwise direction, the bottom wall is on the downstream end. It takes a short time for the bottom wall to be affected by the fin. Since the top wall is on the upstream end, it takes a longer time for the top wall to be affected by the fin. The amplitude of the fluctuations of $\overline{\mathrm{Nu}}_l$ and $\overline{\mathrm{Nu}}_b$ decreases with the decreasing of TR. As TR decreases, the mean value of the fluctuation of $\overline{\mathrm{Nu}}_b$ decreases, whereas it increases for $\overline{\mathrm{Nu}}_l$. This is because the fin is attached at the middle of the right wall. Therefore, based on steady-state results [4,12], this will improve the heat transfer on the left wall.

Figures 8 and 9 show the transient evolution of the instantaneous mean Nusselt number on four walls for Re=1000 and TR =10 and 0.1, respectively. After comparing the corresponding cases for Re=100 and 1000, one can see that $\overline{\mathrm{Nu}}_t$, $\overline{\mathrm{Nu}}_l$ and $\overline{\mathrm{Nu}}_b$ reach periodic states for TR>1 and steady state for TR$\leqslant$1. This implies that the ratio of the period of the oscillation to the convection time scale plays a very important role in this system. The amplitude of the oscillation of $\overline{\mathrm{Nu}}_t$, $\overline{\mathrm{Nu}}_l$ and $\overline{\mathrm{Nu}}_b$ decreases faster with a decrease of TR for cases with Re=1000 compared to Re =100. This indicates that the oscillation of the fin has less effect on the heat transfer on the left, top and bottom walls when the Reynolds number is greater. This is because the primary vortex is stronger when the Reynolds number is greater. This makes the fluctuation from the oscillating fin harder to diffuse to the area far from the fin. As for $\overline{\mathrm{Nu}}_r$, it reaches a periodic state after a period of time for all the cases we studied.

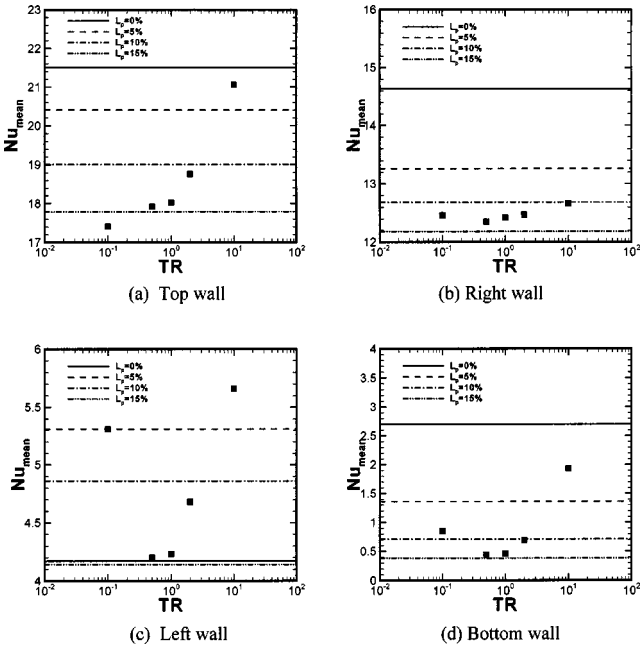

Fig. 10 Variations of the steady-state and time-averaged mean Nusselt numbers on the four walls for Re=1000

Table 2 Phase lag for the mean Nusselt number on the four walls (Re=100, 1000 with TR=10 and $10 \leq t/\tau \leq 11$)

	Phase Lag, β (degrees)			
	Left wall	Bottom wall	Right wall	Top wall
Re=100	90	10.8	212.4	291.6
Re=1000	144	61.2	237.6	111.6

The dependence of the time-averaged mean Nusselt numbers (Nu_{mean}) on the four walls for Re=1000 are shown in Fig. 10 as a function of TR. The steady-state mean Nusselt numbers on those walls for the cases with no fin and fins with length of 5, 10 and 15 percent of the side are also shown, indicating enhanced heat transfer on the left wall and diminished heat transfer on the remaining three walls [4]. As for the influence of TR on the time-averaged mean Nusselt number, the general trend of the rise of the equivalent fin length for faster oscillations (TR decreasing) is clearly observed. Attainment of minima values for the mean Nusselt number on different walls suggest a resonance for the system for the range of TR from 0.5 to 1.

Based on the foregoing discussions, the mean Nusselt numbers on the four walls reach their periodic state when Re=100, 1000 and TR=10. The phase lag between the fin's oscillation and the mean Nusselt number should be studied for these two cases of slow oscillation in order to see how the oscillation of fin affects the mean Nusselt number on the four walls. The phase lag angle β is defined as

$$\beta = \frac{t_1 - t_2}{\tau} \cdot 2\pi, \tag{12}$$

where t_1 and t_2 are the times when the fin's length and the mean Nusselt number reach their maximum values, respectively. The phase lag for the mean Nusselt number on the four walls for the cases with Re=100, 1000 and TR=10 that is computed during the tenth cycle is summarized in Table 2. In general, the phase lag angle β increases as the distance between the fin and the respective wall increases. This is because the fin is attached at the middle of the right wall and the primary vortex is rotating clockwise. The oscillations reach the bottom wall first and reach the top half of the right wall last. But the variation of β for $\overline{Nu}_t$ when Re=1000 and TR=10 cannot be explained by this reasoning. This may be because the heat transfer on the fin is enhanced as the Reynolds number increases. The fin can absorb more heat as the fin's length gets longer and the system needs more heat from the top wall since it is the only hot wall for the system. This increases the Nusselt number at the top wall and decreases the phase lag angle β for $\overline{Nu}_t$.

Conclusions

1. The number of the cycles needed to reach the periodic state for the flow (N_f) and thermal (N_t) fields increases as the TR decreases for both Re numbers. The thermal field attains the periodic state later than the velocity field. The difference between N_f and N_t increases as TR decreases.

2. The key feature of the transient evolution of the fluid flow for the case with Re=1000 and TR=10 is the creation, lateral motion and subsequent wall impingement of a CCW rotating vortex within the lower half of the cavity. The lifetime of this CCW rotating vortex is about one and a half period of the fin's oscillation. This CCW rotating vortex brings about marked changes to the temperature field within a cycle.

3. The dimensionless time for $\overline{Nu}_l$, $\overline{Nu}_t$, and $\overline{Nu}_b$ to reach their maximum or minimum is independent of the frequency of the fin's oscillation and dependent on the distance between the oscillating fin and the respective wall, and the direction of the primary CW rotating vortex.

4. The phase lag angle between the oscillation of the fin and the mean Nusselt number on the four walls increases as the distance between the fin and the respective wall increases.

Nomenclature

l_p = length of the fin, m
$\overline{Nu}$ = average or mean Nusselt number, defined by Eq. (11)
T_c = temperature of the left, bottom and right walls, K
T_h = temperature of the moving lid, K
U_{lid} = velocity of the moving lid, m/s

Greek Symbols

θ = dimensionless temperature, i.e. $(T-T_c)/(T_h-T_c)$

Subscripts

b, l, r, t = related to the bottom, left, right and top walls

References

[1] Yamaguchi, Y., and Asako, Y., 2001, "Effect of Partition Wall on Natural Convection Heat Transfer in a Vertical Air Layer," ASME J. Heat Transfer, **123**, pp. 441–449.

[2] Shankar, P. N., and Deshpande, M. D., 2000, "Fluid Mechanics in the Driven Cavity," Annu. Rev. Fluid Mech., **32**, pp. 93–136.

[3] Ghia, U., Ghia, K. N., and Shin, C. T., 1982, "High-Re Solutions for Incompressible Flow Using the Navier-Stokes Equations and a Multigrid Method," J. Comput. Phys., **48**, pp. 387–411.

[4] Shi, X., and Khodadadi, J. M., 2002, "Laminar Fluid Flow and Heat Transfer in a Lid-Driven Cavity Due to a Thin Fin," ASME J. Heat Transfer, **124**, pp. 1056–1063.

[5] Fu, W.-S., and Yang, S.-J., 2001, "A New Model of Heat Transfer of Fins Swinging Back and Forth in a Flow," Int. J. Heat Mass Transfer, **44**, pp. 1687–1697.

[6] Fu, W.-S., and Yang, S.-J., 2001, "A Numerical Study of Effects of the Swinging Amplitude of Fins on Heat Transfer Characteristics in a Flow," Heat Mass Transfer, **38**, pp. 55–63.

[7] Patankar, S. V., 1980, *Numerical Heat Transfer and Fluid Flow*, Hemisphere Pub. Co., Washington, D.C.

[8] Hayase, T., Humphrey, J. A. C., and Grief, R., 1992, "A Consistently Formulated QUICK Scheme for Fast and Stable Convergence Using Finite-Volume Iterative Calculation Procedures," J. Comput. Phys., **98**, pp. 108–118.

[9] Hirt, C. W., and Sicilian, J. M., 1985, "A Porosity Technique for the Definition of Obstacles in Rectangular Cell Meshes," *Proceedings of the 4th Int. Conf. Ship Hydrodynamics*, Washington, D.C.

[10] Tsukiyama, H., Tajima, Y., Yao, M., and Arai, H., 1993, "Solution Method of the Time Transient Moving Boundary Problems Using Generalized Porous Media Technique—FAVORITE (FAVOR ImitaTE) Program," J. Wind. Eng. Ind. Aerodyn., **46–47**, pp. 381–391.

[11] Torrance, K., Davis, R., Eike, K., Gill, P., Gutman, D., Hsui, A., Lyons, S., and Zie, H., 1972, "Cavity Flows Driven by Buoyancy and Shear," J. Fluid Mech., **51**, pp. 221–231.

[12] Shi, X., 2003, "Forced and Natural Convection Heat Transfer within Enclosures with Fixed and Moving Fins and Partitions," Ph.D. thesis, Department of Mechanical Engineering, Auburn University.

N. Ranc
e-mail: nicolas.ranc@u-paris10.fr

V. Pina

L.E.E.E., E.A.387, Université de Paris X Nanterre, 1, Chemin Desvallières, 92410 Ville d'Avray, France
Tel.: +33-1-47-09-70-13; Fax: +33-1-47-09-16-45

G. Sutter

S. Philippon

L.P.M.M., U.M.R. C.N.R.S. n°7554, I.S.G.M.P., Université de Metz, Ile du Saulcy, 57045 Metz, France

Temperature Measurement by Visible Pyrometry: Orthogonal Cutting Application

The working processes of metallic materials at high strain rate like forging, stamping and machining often induce high temperatures that are difficult to quantify precisely. In this work we, developed a high-speed broad band visible pyrometer using an intensified CCD camera (spectral range: 0.4 μm–0.9 μm). The advantage of the visible pyrometry technique is to limit the temperature error due to the uncertainties on the emissivity value and to have a good spatial resolution (3.6 μm) and a large observation area. This pyrometer was validated in the case of high speed machining and more precisely in the orthogonal cutting of a low carbon steel XC18. The cutting speed varies between 22 ms^{-1} and 60 ms^{-1}. The experimental device allows one to visualize the evolution of the temperature field in the chip according to the cutting speed. The maximum temperature in the chip can reach 730°C and minimal temperature which can be detected is around 550°C.
[DOI: 10.1115/1.1833361]

1 Introduction

To understand and model more precisely the transformation processes of metallic materials like forging, stamping and machining, it is necessary to take into account a majority of the various phenomena or parameters occurring during these processes. In most cases, they generate friction and high plastic deformations which dissipate a major part of the mechanical energy into heat.

Temperature is one of the most significant parameters, particularly in high speed processes. One can assume that the thermal phenomena are adiabatic because the heat has not enough time to spread in the material. The temperature rises can be significant and completely modify the manufacturing process. For example the behavior law of materials and the friction coefficient strongly depend on the temperature. To validate the analytical and numerical models, it is necessary to determine the temperature in experiments.

An application, in which the temperature plays an essential role, is machining and more particularly high speed machining [1,2]. Hasting et al. [3] analyze the cutting process from a theory in which the properties of the work piece material depend on the temperature and the strain-rate. Indeed, this manufacturing process generates great strain located mainly in the primary deformation zone and an intense friction on tool-chip interface [4,5]. The temperature in the chip can reach 800–900°C [6]. The optimization of the cutting conditions, as well as the tools damage, depends mainly on the maximum temperature reached. Indeed an increase in the temperature on the tool–chip interface reduces the friction coefficient and thus the cutting pressures, but it affects the tool life [7] and it can also generate a modification of the workpiece material characteristics. The objective of this study is to develop an experimental device to measure the temperature which can be used for transformation processes of metallic materials and validate it for high speed orthogonal cutting. For this purpose, we chose to design and realize a fast pyrometer.

The radiation emitted by the surface of a material depends on its temperature and the wavelength (Planck law [8]) and is also proportional to a factor called emissivity which is a surface characteristic. The dependence of this radiation with the temperature is the principle of pyrometry. Compared with conventional temperature sensors such as thermocouples, this measurement technique has the advantage of being nonintrusive and having a very short response time [9]. It also allows to visualize temperature cartographies. However, the pyrometry presents difficulties related to uncertainty on the surface emissivity. Although measurement techniques eliminating the emissivity have been developed [10,11], they are not easily usable for our study.

The design of a pyrometer consists in choosing a spectral range, which is linked to the measured temperature and the spectral sensitivity of the selected detector. If the spectral bandwidth is reduced to a few tens of nanometers (limited by an interference filter for instance) we consider that the pyrometry is monochromatic [6]. On the contrary if the bandwidth is broad, we will use the polychromatic pyrometry technique [12].

The spectral band associated with the thermal radiation is commonly limited to wavelengths ranging between 0.1 μm and 100 μm. In this range, the behavior of electromagnetic waves strongly depends on their wavelength. This spectral band is divided into several regions: ultraviolet ray, visible, near infrared, mid-infrared, and far infrared (Fig. 1). By taking account of the atmosphere absorption, the visible and near infrared fields are cutting out in three observation spectral bands (band I: 0.5–2 μm; band II: 3–5 μm; band III: 8–12 μm). Detectors are used to measure the power radiated by a surface. Their operation principle can be very different but we can distinguish two principal families: thermal detectors and quantum detectors.

1.1 Thermal Detectors. In the case of the thermal detectors, incident radiation causes an increase in temperature of the detector surface. The measurement of this temperature variation allows one to quantify the received energy. This type of detector has a constant spectral sensitivity in relatively broad spectral bands. However its principal drawback is the relatively long response time (approximately 10^{-3} s).

1.2 Quantum Detectors. The quantum detectors are made of materials which absorb incident radiation by producing free or semi free charge carriers (photovoltaic or photoconductor detector) or by ejecting an electron by photo emission (photoemissive detector). The principal semiconductors used in the photovoltaic and photoconductive detectors are silicon (Si), germanium (Ge), the indium antimonide (InSb) and the mercury cadmium telluride (HgCdTe also noted MCT) (Table I). The photovoltaic detectors are generally more sensitive and faster than the photoconductors. To obtain a better detectivity, these detectors are often cooled at the liquid nitrogen temperature (77 K).

Contributed by the Heat Transfer Division for publication in the JOURNAL OF HEAT TRANSFER. Manuscript received by the Heat Transfer Division October 9, 2003; revision received August 17, 2004. Associate Editor: B. Farouk.

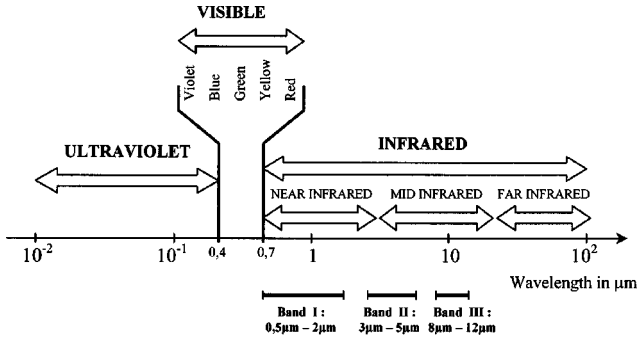

Fig. 1 Thermal radiation spectrum

The photoemissive detectors are composed of a photocathode placed in a vacuum. When this photocathode is struck by an incident photon it causes the expulsion of an electron in vacuum. The released electron is then accelerated towards the anode and contributes to create a current. This type of detector is rather sensitive to short wavelengths (ultraviolet, visible, and near infrared), because the energy of the incident photon must be sufficient to eject the electron. The materials used to carry out the photocathode and their spectral sensitivity are given in Table I. In a photomultiplier, the signal can also be amplified by a succession of dynodes (polarized electrodes) allowing starting from an emitted electron, to release several from them. On the same principle, an intensified charge-coupled-device (CCD) camera consists of a slightly glass substrate with millions of parallel traversing channels of few ten micrometers of diameter containing a secondary electron emitter. Electrons generated by the photocathode are driven through the channels by a constant field from a high voltage applied to the microchannel plate. An electron passing through strikes the walls, causing the formation of more electrons. A single entering electron can produce several thousands of electrons that finally exit from the plate.

Pyrometry techniques are often used for the study of the dynamic behavior of materials: Ravichandran et al. use a matrix of 8×8 HgCdTe Infrared detectors [13] to measure the field of temperature in an adiabatic shear band (between 30°C and 100°C) [14] or at the head of the crack [15]. The spatial resolution of their device is about one hundred micrometers with a response time of about a microsecond. In a previous study, we measured the maximum temperature reached in adiabatic shear bands in the visible range using a monochromatic pyrometer at 0.634 μm [16]. With this technique, it is possible to obtain only one thermography with an aperture time of 6 μs and a spatial resolution of 5 μm.

Many authors were interested in the temperature measurements during high speed machining [6]. More recently we have determined the temperature field in the cutting zone during an orthogonal high speed machining operation of 42CD4 steel [6]. We used a monochromatic pyrometer with an interference filter at 0.8 μm to study the influence of the cutting speed and the chip thickness on the temperature profile.

In this article, we develop a broad band visible pyrometer particularly adapted with high speed machining of low carbon steel XC18. This steel forms a continuous chip and the temperature is about 500°C (lower than for the 42CD4 steel). A broad band pyrometer allows one to detect lower temperature than a monochromatic pyrometer. After some remarks on the solid radiation in Sec. 2, we will justify our choices in the design of the broadband pyrometer. The thermographies obtained in this work and in particular the influence of the cutting speed on the temperature field are presented in Sec. 4. The measurement errors due to emissivity values are also discussed.

Table 1 Principal photosensitive materials

Photosensitive material	Range of sensibility	Sensor type
Si	0.4 μm–1.1 μm	Photovoltaic
InSb	1 μm–5.5 μm	Photovoltaic
HgCdTe	2 μm–14 μm	Photovoltaic Photoconductor
PbS	1.3 μm–3 μm	Photoconductor
Bialkali coating (Sb–Rb–Cs;Sb–K–Cs)	0.15 μm–0.65 μm	Photoemissive
Multialkali coating S_{20} (Na–K–Sb–Cs)	0.15 μm–0.85 μm	Photoemissive
AsGa (GEN III)	0.3 μm–0.9 μm	Photoemissive

2 Pyrometry Technique

2.1 Radiation of Solids. The intensity is the power radiated in a direction $\boldsymbol{\delta}$ by a unit surface in a solid angle of one steradian. The radiation dP emitted by a surface dS with a normal $\mathbf{n}$ in a solid angle $d\Omega$ of direction $\boldsymbol{\delta}$ is related to the intensity I:

$$dP = I(\boldsymbol{\delta})\boldsymbol{\delta}\cdot\mathbf{n}d\Omega dS \tag{1}$$

The intensity depends on the radiation wavelength. We can also define the spectral intensity noted I_λ by the following relation:

$$I_\lambda = \frac{\partial I}{\partial \lambda} \tag{2}$$

A blackbody absorbs completely any incident radiation, whatever its wavelength. The spectral intensity of a blackbody noted I_λ^0 at the temperature T is given by Planck's law [17]:

$$I_\lambda^0(\lambda,T) = \frac{C_1\lambda^{-5}}{\exp\left(\frac{C_2}{\lambda T}\right)-1} \tag{3}$$

With $C_1 = 2hc^2$ and $C_2 = hc/k$ the first and second radiation constants, $k = 1.380\,662.10^{-23}\,\mathrm{J\,K^{-1}}$ the Boltzman constant, $h = 6.626\,176.10^{-34}\,\mathrm{J\,s}$ the Planck constant and $c = 2.998.10^8\,\mathrm{ms^{-1}}$ the light celerity in vacuum.

Generally for the short wavelengths ($\lambda T \ll C_2 = 14{,}388\,\mu\mathrm{m\,K}$), we use the Wien approximation:

$$\exp\left(\frac{C_2}{\lambda T}\right) \gg 1 \tag{4}$$

With this approximation, the Planck law becomes then

$$I_\lambda^0(\lambda,T) = \frac{C_1\lambda^{-5}}{\exp\left(\frac{C_2}{\lambda T}\right)} \tag{5}$$

For a given temperature, the spectral intensity of the blackbody shows a maximum for a wavelength λ_{max} (Fig. 2). This wavelength is given by the Wien law:

$$\lambda_{max} = \frac{C_2}{5}\frac{1}{T} \tag{6}$$

For a temperature of 700°C this maximum is in the near infrared band at a wavelength of 2.96 μm. When the temperature decreases this maximum of intensity is shifted towards the big wavelengths (infrared range).

Another significant quantity is the radiance sensitivity to the temperature variations. This sensitivity is characterized by the ratio $(1/I_\lambda^0)(\partial I_\lambda^0/\partial T)$. For a blackbody we have:

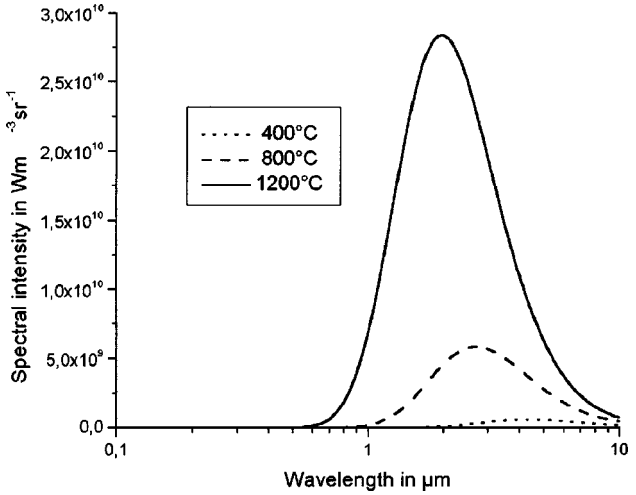

Fig. 2 Blackbody spectral intensity for the temperatures of 400°C, 800°C, and 1200°C

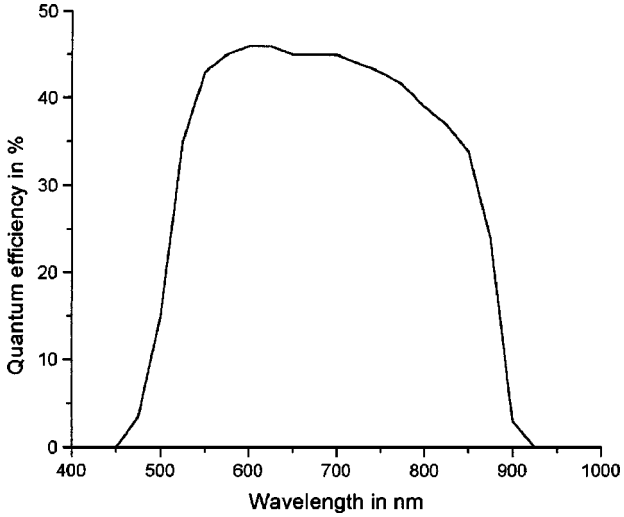

Fig. 4 Quantum efficiency of the intensified camera

$$\frac{1}{I_\lambda^0}\frac{\partial I_\lambda^0}{\partial T}=\frac{C_2}{\lambda T^2}\frac{\exp\left(\frac{C_2}{\lambda T}\right)}{\exp\left(\frac{C_2}{\lambda T}\right)-1} \tag{7}$$

This sensitivity is represented in Fig. 3 for the temperatures of 400°C, 800°C, and 1200°C according to the wavelength. We can observe that this sensitivity becomes very high for the short wavelengths (ultraviolet field).

The behavior of a real surface is different from a blackbody's. We can express its intensity as

$$I_\lambda(\lambda,T)=\varepsilon_\lambda(\lambda,T)I_\lambda^0(\lambda,T)$$

$$\text{with } \varepsilon_\lambda(\lambda,T) \text{ the spectral emissivity} \tag{8}$$

The emissivity characterizes the radiation of a real surface compared to the radiation of a blackbody at the same temperature and placed under the same conditions. This factor always lies between 0 and 1 (the case $\varepsilon=1$ corresponds to the blackbody). Moreover, the surface emissivity depends on the material [18–22]; the surface roughness [21–23]; the physical state of material (solid or liquid) [19,21,24]; the surface temperature [19–21]; the direction for emission [22,23,25]; the wavelength [18,20,21].

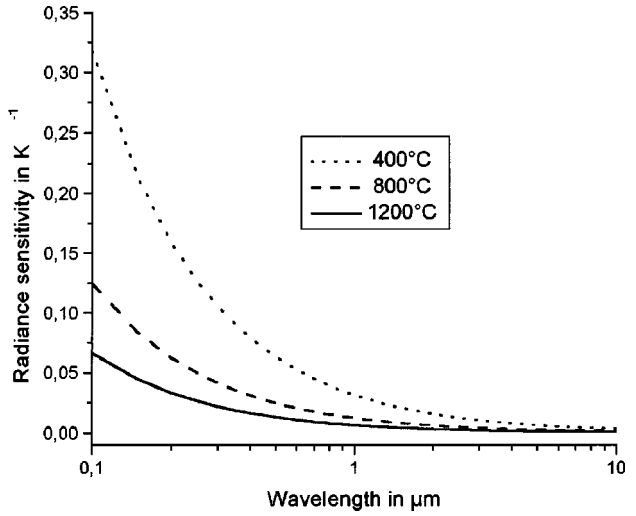

Fig. 3 Radiance sensitivity to the temperature variations for the temperatures of 400°C, 800°C, and 1200°C

2.2 Principle of Pyrometry. The measurement technique by pyrometry is achieved through measuring the power radiated by a surface using a detector in order to deduce its temperature. If we make the assumption that the surface behaves like a blackbody, we can determine a radiance temperature (T_λ) also called the blackbody equivalent temperature. This radiance temperature is always lower or equal to the real temperature of the surface. If we need to know the real temperature, it is necessary to determine the surface emissivity.

In this article, we try to minimize the difference between the real temperature and radiance temperature. Indeed, Fig. 3 shows that the shorter the wavelength is, the higher the sensitivity to variations in temperature is, and the weaker the error between the real temperature and the radiance temperature will be. The advantage of this technique is that the dependence of temperature on emissivity is greatly reduced.

3 Experimental Device

3.1 Choice of the Detector and the Optical Device. The choice of the wavelength of the pyrometer is a compromise between a maximum sensitivity and a sufficient level of radiated power which can be detected. For this study, we chose an intensified camera whose spectral band is located in the visible (0.4 μm to 0.9 μm). Figure 4 represents the quantum efficiency $\eta(\lambda)$ of the camera according to the wavelength which is given by the manufacturer. In order to collect the maximum of the radiated power, the entire spectral band of the camera was used. The aperture time can vary between 5 ns and a few milliseconds. We carried out only one image during an orthogonal cutting test because the refresh time of the CCD is much larger than the machining duration.

To focus the maximum of energy, we use an objective with a 50 mm focal length. This optical device enables one to obtain a very good resolution: a pixel corresponds to approximately 3.6 μm and the surface observed is a square of 3.7×3.7 mm.

3.2 Temperature Determination: Calibration Curves The pyrometer is calibrated on a blackbody for temperatures between 500°C and 900°C. Three aperture times of 150 μs, 200 μs, and 600 μs were selected. They correspond to the durations of complete machining of the specimen for speeds of 60 ms^{-1}, 38 ms^{-1}, and 22 ms^{-1}. Figure 5(a) represents the measured level of a pixel Si for different blackbody temperatures and for each aperture time. The blackbody temperature varies between 500°C and

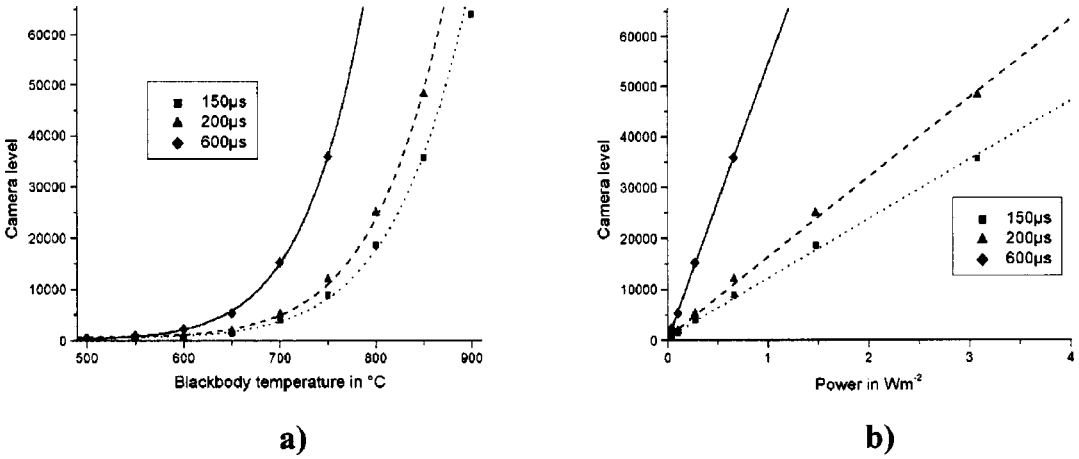

Fig. 5 Calibration curves. (a) Representation according to the temperature. (b) Representation according to the power

900°C with an increment of 50°C. In Fig. 5(b), we draw the level of pixel versus the power received by the detector $E(T)$:

$$E(T)=\int_0^\infty \eta(\lambda) I_\lambda^0(\lambda,T)\,d\lambda \tag{9}$$

We can consider that the relation between Si and $E(T)$ is linear. Then we have:

$$\mathrm{Si}=\mathrm{Si}^0+k\cdot E(T) \tag{10}$$

Si^0 and k are two calibration constants, which depend on the camera, the optical device and the acquisition chain. To identify them simply, we represent the evolution of Si according to $E(T)$ and we determine the parameters Si^0 and k by a linear regression. Also, the evolution of the pixel level is also traced according to the temperature for each aperture time in Fig. 5(a).

3.3 A Technical Application: A High Speed Machining. To validate the pyrometer presented above, we performed an application to the measurement of the temperature field during a high speed machining process. The mechanical device of machining was developed by Sutter et al. [26], to investigate high cutting speed allowing to reach 100 m/s and perfectly reproduces orthogonal cutting conditions. This device reduces the problems observed in the conventional machine tools (for example the maximum cutting speed, parasite vibrations). Dry cutting conditions are chosen according to the future orientation in machining. The great accessibility for photographic recordings allows an easy adaptation of the device for optical temperature measurement. Vernaza-Pena et al. [27] also observed experimentally the temperature distribution during orthogonal cutting of an aluminum alloy with HgCdTe infrared detectors.

The parallelepipedal specimen is placed on a projectile and is cut out by two fixed tools (Fig. 6). The two tools are symmetrically positioned to balance the force during machining and to ensure a constant depth of cut. The projectile is animated with a translatory motion in the launch tube by the relaxation of compressed air. The launch tube ensures a precise guiding of the projectile and the specimen. At the end of the launch tube, the specimen is machined by the tools. A second tube, called a receiving tube, supports the tools and drives the projectile towards a shock absorber after machining.

A wide range of cutting speed is possible with this device (from 10 to 100 ms^{-1}). The speed is measured by photodiodes and a time counter. All tests are carried out using carbide tools without a chip-breaker. The rake angle, α, can vary with slope of the tool but all the tests presented here were made with $\alpha=0$ deg. To neglect the wear effects, the tools are changed for each shot. Before and after each test, the length of the specimen is measured to determine the chip thickness t_1. This value is confirmed by the photographic recordings which allow a measurement of t_1 during the chip formation [Figs. 7(a) and 7(b)].

4 Results and Discussion

4.1 Presentation of Thermographies. The aperture time of the camera is slightly lower than the duration of specimen machining. The difference between the aperture time and the machining duration are 146 μs, 63 μs, and 16 μs, respectively for the speed of 22 ms^{-1}, 38 ms^{-1}, and 60 ms^{-1}. During this aperture time, the temperature field in chip is supposed to be stationary. After analysis of the images recorded for the different cutting speeds and also taking into account the corresponding calibration curves, we obtain the thermographies presented in Fig. 8. The effect of the cutting speed on the maximum temperature level in the chip can also be studied. We observe an increase in the maximum of temperature with the cutting speed. This increase in temperature is more significant for low speed than for high speeds. Between 22 ms^{-1} and 38 ms^{-1}, there is an increment of 80°C, whereas between 38 ms^{-1} and 60 ms^{-1} we have an increment of only 15°C. A similar tendency was already observed for another steel [6] and other cutting conditions like oblique turning process with a localized temperature measurement at the tool–chip interface [28].

One of the advantages of this device is to record the chip formation without changing the camera and the visualization zone. The chip is enlightened with a flash and the camera is opened

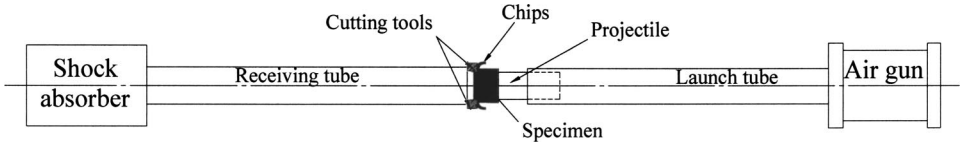

Fig. 6 Mechanical device of orthogonal cutting

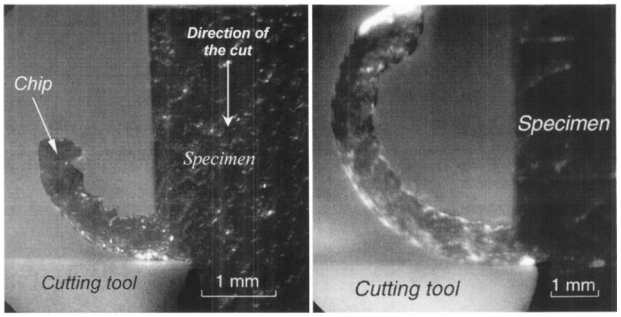

Fig. 7 Photographic recording of chip formation during the process of orthogonal cutting. (a) $t_1=0.49$ mm, $V_c=17$ ms^{-1}, $\alpha=0$ deg; (b) $t_1=0.54$ mm, $V_c=60$ ms^{-1}, $\alpha=0$ deg

during approximately one microsecond. We performed the images presented in Figs. 7(a) and 7(b). We can notice that the chip remains continuous and does not segment. We showed that the field of temperature in the zone of machining can be regarded as stationary during machining [6]. Therefore we can consider that the temperature in the chip remains constant during the aperture time.

4.2 Error Measurement on *T*. As we said previously, the approximation between the real temperature and the radiance temperature introduces errors related to the emissivity. During machining, this factor varies because it depends on the temperature and the roughness of the surface of specimen. During the plastic deformation, there is an increase in the surface roughness and therefore in the emissivity.

At first, to estimate these errors, we make the assumption that for the weak variations of roughness and measured temperature (between 600°C and 700°C), the emissivity varies little. We can determine the surface radiance temperature T_λ with the relation (10) according to the signal Si:

$$T_\lambda = E^{-1}\left(\frac{\mathrm{Si}-\mathrm{Si}^0}{k}\right) \tag{11}$$

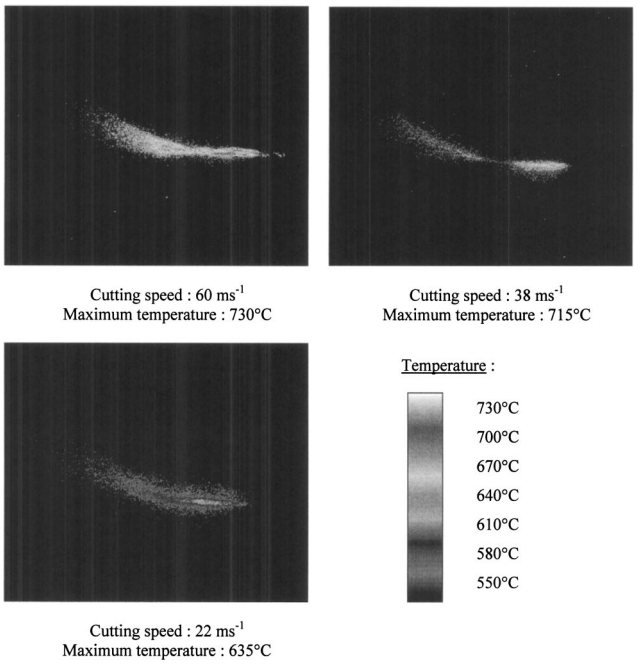

Fig. 8 Chip thermography for different cutting speeds

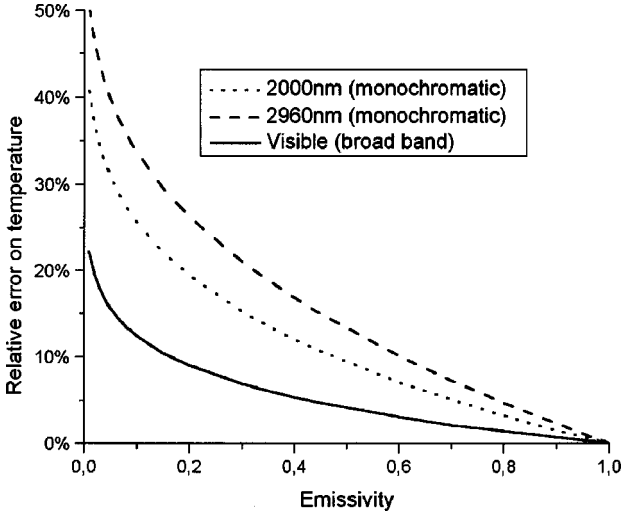

Fig. 9 Error on the temperature measurement according to the emissivity at a temperature of 800°C

The inverse function E^{-1} will be calculated numerically.

The real surface temperature can be expressed according to the detector signal and the emissivity:

$$\mathrm{Si}=\mathrm{Si}^0+k\cdot E'(T) \quad \text{with} \quad E'(T)=\int_0^\infty \eta(\lambda)\varepsilon_\lambda(\lambda,T)I^0_\lambda(\lambda,T)d\lambda \tag{12}$$

If we consider that the emissivity is constant in the spectral band of the camera (0.4 μm–0.9 μm), we obtain

$$\mathrm{Si}=\mathrm{Si}^0+k\varepsilon_\lambda\cdot E(T) \tag{13}$$

We can express the error as:

$$\Delta T=T-T_\lambda=E^{-1}\left(\frac{\mathrm{Si}-\mathrm{Si}^0}{k\varepsilon_\lambda}\right)-E^{-1}\left(\frac{\mathrm{Si}-\mathrm{Si}^0}{k}\right) \tag{14}$$

The quantification of the error consists of estimating the value of the emissivity, either using bibliographical data [29], or by a direct measurement during a static test in a vacuum chamber. The knowledge of the emissivity values allows us to limit its evolution range.

The relative error between the real temperature and the radiance temperature is represented in Fig. 9 versus emissivity at a temperature of 800°C for infrared and visible domains. In the visible spectral band, the order of magnitude of emissivity is 0.4 [29]. It increases with the roughness and the temperature. The maximum relative error is then 5.3%. A variation of 10% of the emissivity causes a relative error of 0.5% on temperature.

In the case of monochromatic infrared pyrometry at 2.96 μm wavelength and with a band width of 10 nm, the order of magnitude of emissivity is generally lower than in the visible and the uncertainty on the temperature is around 21% for an emissivity of 0.3. A variation of 10% of the emissivity causes a relative error of 1.3% on temperature. These error values are indeed higher in infrared than in the visible. The relative error on temperature is represented in Fig. 10 versus temperature for an emissivity value of 0.4 in the visible domain (0.4 μm–0.8 μm) and 0.3 in the infrared domain (2.96 μm–2.00 μm).

5 Conclusion

The working processes of metallic materials at high strain rate often induce high temperatures that it is necessary to quantify precisely. The knowledge of these temperatures is an invaluable help to understand the mechanisms which take place during the industrial process. In this article, we developed a high-speed

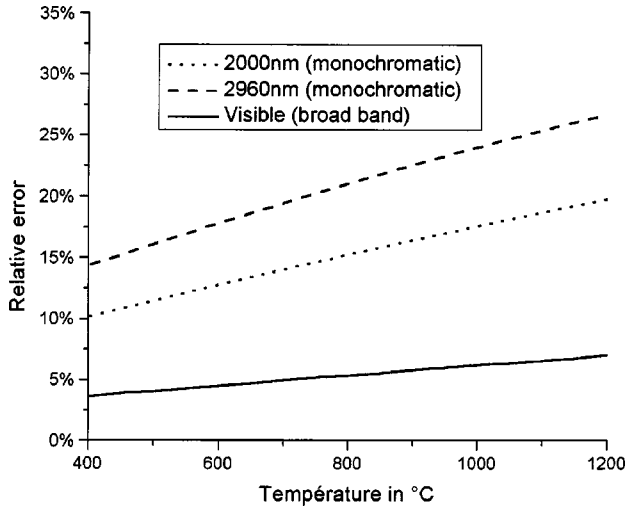

Fig. 10 Error on the temperature measurement according to the temperature for a fixed emissivity

broad band pyrometer. Its visible spectral range is particularly adapted to the temperature range of this type of process. The spectral band between 0.4 μm and 0.9 μm was chosen in order to obtain a maximum sensitivity and a sufficient radiated power which can be detected. The choice of a maximum sensitivity and thus a smallest possible wavelength allows one to limit the error due to the emissivity.

Another advantage of the visible pyrometer is to have a good spatial resolution (3.6 μm). The broad band pyrometry allows one to measure lower temperature than monochromatic pyrometry at 0.8 μm wavelength and to keep the same sensitivity. In Fig. 10 the temperature errors for broad band and monochromatic pyrometry are equal.

This pyrometer was validated in the case of high speed machining and more precisely in orthogonal cutting. This experimental device allows one to visualize the evolution of the temperature field in the chip according to the cutting speed.

References

[1] Milton, C., and Shaw, M. C., 1984, *Metal Cutting Principles*, Clarendon Press, Oxford Science Publication, UK.

[2] Loewen, E. G., and Shaw, M. C., 2000, ''On the Analysis of Cutting Tool Temperature,'' Trans. Am. Soc. Mech. Engrs., **71**, pp. 217–231.

[3] Hastings, W. F., Mathews, P., and Oxley, P. L. B., 1980, ''A Machining Theory for Predicting Chip Geometry, Cutting Forces Etc. From Material Properties and Cutting Conditions,'' Proc. R. Soc. London, Ser. A, **371**, pp. 569–587.

[4] Doyle, E. D., Homme, J. G., and Tabor, D., 1979, ''Frictional Interaction Between Chip and Rake Face in Continuous Chip Formation,'' Proc. R. Soc. London, Ser. A, **3666**, pp. 176–183.

[5] Grzesik, W., 2003, ''Friction Behavior of Heat Isolating Coating in Machining: Mechanical, Thermal and Energy-Based Considerations,'' Int. J. Mach. Tools Manuf., **43**, pp. 145–150.

[6] Sutter, G., Faure, L., Molinari, A., Ranc, N., and Pina, V., 2003, ''An Experimental Technique for the Measurement of Temperature Fields for the Orthogonal Cutting in High Speed Machining,'' Int. J. Mach. Tools Manuf., **43**, pp. 671–678.

[7] Ay, H., and Yang, W. J., 1998, ''Heat Transfer and Life of Metal Cutting Tools in Turning,'' Int. J. Heat Mass Transfer, **43**, pp. 613–623.

[8] Planck, M., 1901, ''Distribution of Energy,'' Ann. Phys. (N.Y.), **4**, 3, pp. 553–563.

[9] Childs, P. R. N., Greenwood, J. R., and Long, C. A., 2000, ''Review of Temperature Measurement,'' Rev. Sci. Instrum., **71**, 8, pp. 2959–2978.

[10] Murray, T. P., 1967, ''Polaradiometer: A New Instrument for Temperature Measurement,'' Rev. Sci. Instrum., **38**, pp. 791–798.

[11] Hervé, P., 1983, ''Mesure simultanée de la température de surface et de son émissivité,'' Measurement, **485**, pp. 20–24.

[12] Duvaut, T., Georgeault, D., and Beaudoin, J. L., 1995, ''Multiwavelength Infrared Pyrometry: Optimization and Computer Simulations,'' Infrared Phys. Technol., **36**, pp. 1089–1103.

[13] Zehnder, A. T., Guduru, P. R., Rosakis, A. J., and Ravichandran, G., 2000, ''Million Frames Per Second Infrared Imaging System,'' Rev. Sci. Instrum., **71**, 10, pp. 3762–3768.

[14] Guduru, P. R., Ravichandran, G., and Rosakis, A. J., 2001, ''Observation of Transient High Vortical Microstructures in Solids During Adiabatic Shear Banding,'' Phys. Rev. E, **64**, pp. 1–6.

[15] Guduru, P. R., Zehnder, A. T., Rosakis, A. J., and Ravichandran, G., 2001, ''Dynamic Full Field Measurements of Crack Tip Temperatures,'' Eng. Fract. Mech., **68**, pp. 1535–1556.

[16] Ranc, N., Pina, V., and Hervé, P., 2000, ''Optical Measurements of Phase Transition and Temperature in Adiabatic Shear Bands in Titanium Alloys,'' J. Phys. IV, **10**, pp. 347–352.

[17] Modest, M. F., 1993, *Radiative Heat Transfert*, McGraw–Hill, New York.

[18] Palik, E. D., 1985, *Handbook of Optical Constants*, Academic, New York.

[19] Piriou, B., 1973, ''Mise au point sur les facteurs d'émission,'' Rev. Int. Hautes Temp. Refract., **10**, pp. 283–295.

[20] Hampartsoumian, E., Hainsworth, D., Taylor, J. M., and Williams, A., 2001, ''The Radiant Emissivity of Some Materials at High Temperatures-Review,'' J. Inst. Energy, **74**, pp. 91–99.

[21] Hiernaut, J. P., Beukers, R., Hoch, M., Matsui, T., and Ohse, R. W., 1986, ''Determination of the Melting Point and of the Spectral and Total Emissivities of Tungsten, Tantalum and Molybdenum in the Solid and Liquid States With a Six-Wavelength,'' High Temp. - High Press., **18**, pp. 627–633.

[22] Dunkle, R. V., 1960, ''Thermal Radiation Characteristics of Surfaces,'' Theory and fundamental research in heat transfer: Proceedings of the Annual Meeting of the American Society of Mechanical Engineers, New York.

[23] Hervé, P., 1977, ''Influence de l'état de surface sur le rayonnement thermique des matériaux solides,'' Ph.D. thesis, Paris VI.

[24] Antoni Zdziobek, A., Pina, V., Hervé, P., and Durand, F., 1997, ''A Radiative Thermal Analysis Method for Phase Change Determination of Strictly Controlled Refractory Alloys,'' High Temp. Mater. Sci., **37**, pp. 97–114.

[25] Birkebak, R. C., and Eckert, E. R. G., 1965, ''Effects of Roughness of Metal Surfaces on Angular Distribution of Monochromatic Reflected Radiation,'' ASME J. Heat Transfer, **87**, pp. 85–94.

[26] Sutter, G., Molinari, A., Faure, L., Klepaczko, J. R., and Dudzinski, D., 1998, ''An Experimental Study of High Speed Orthogonal Cutting,'' ASME J. Manuf. Sci. Eng., **12**, pp. 169–172.

[27] Vernaza-Pena, K. M., Mason, J. J., and Li, M., 2001, ''Experimental Study of the Temperature Field Generated During Orthogonal Machining of an Aluminum Alloy,'' Exp. Mech., **42**, 2, pp. 221–229.

[28] Muller, B., 2001, ''Temperature Measurements With a Fibre-Optic Two-Color Pyrometer,'' Scientific Fundamentals of High Speed Cutting, edited by H. Schulz, Carl Hanser Verlag, München-Wien, pp. 181–186.

[29] Touloukian, Y. S., and DeWitt, D. P., 1970, *Thermophysical Properties of Matter—Thermal Radiative Properties*, IFI/Plenum, New York, Washington, Vol. 7.

Anahita Ayasoufi

Theo G. Keith
Professor
ASME Fellow

Ramin K. Rahmani

Department of Mechanical, Industrial and Manufacturing Engineering, University of Toledo, Toledo, OH

Application of the Conservation Element and Solution Element Method in Numerical Modeling of Three-Dimensional Heat Conduction With Melting and/or Freezing

The conservation element and solution element (CE/SE) method, an accurate and efficient explicit numerical method for resolving moving discontinuities in fluid mechanics problems, is used to solve three-dimensional phase-change problems. Several isothermal phase-change cases are studied and comparisons are made to existing analytical solutions. The CE/SE method is found to be accurate, robust, and efficient for the numerical modeling of phase-change problems. [DOI: 10.1115/1.1795235]

Introduction

The range of scientific and industrial applications of heat flow with solid-liquid phase change is so broad that, in many fields, one has little difficulty finding a phase-change process. Migration and solidification of magma in geology, planet's core solidification in astrophysics, global weather modeling, formation of ice on the oceans as well as on aircraft surfaces, casting and welding of metals, water purification through freezing, usage of latent heat-storage systems in temperature control, ablation of bodies during reentry, destroying cancer cells in cryosurgery, melting of electrical fuses, and preserving food through deep freezing are some examples of phase-change-related phenomena and industries [1,2]. Because of its importance, then, accurate and robust methods of modeling phase-change problems are of great interest.

The challenge one is faced with, in modeling phase-change processes, lies in the determination of the unknown location of the phase interface. This geometric nonlinearity [3] leads to classification of the phase-change problems, along with similar problems in molecular diffusion, friction and lubrication, inviscid flow, etc., in the category of moving (free) boundary problems. Overviews of such problems may be found in [4–6].

There exist two principal approaches for modeling phase-change problems: 1) Phase front fitting in which explicit tracking of the phase-change boundary is followed by using moving grid schemes. One example of these methods is the method introduced in [7], which is based on using set spatial steps while the time step floats. Another example is the isotherm migration method [6], which is based on using a set time step with two distinct and time-varying space steps for the two phases. A survey of front-tracking methods appears in [6]. The phase front fitting methods, however, often require complicated starting solutions [8] and are inapplicable for materials that change phase over a temperature interval rather than at a single specified temperature. Moreover, these methods are difficult to extend to multidimensional problems. 2) Phase front capturing methods, which automatically determine the location of the phase front as part of the solution of the problem. These methods offer a more suitable approach for modeling a general phase-change problem. The most prominent of the phase capture schemes is the enthalpy method, which is based on the method of weak solutions [9,10] and, by incorporating the latent heat of fusion in the formulation, provides the location of the liquid/solid interface as an integral part of the solution [11]. Numerical application of these methods, however, produces better results when the phase change occurs within a temperature range. For situations where the phase change occurs at a single temperature, the phase front is a moving discontinuity. Consequently, all of these methods need regularization and special adjustments in order to achieve convergence and stability of the numerical solution [12] and to avoid oscillations in the location of the interface.

The method of space-time conservation element and solution element (CE/SE) was developed by Chang [13–15] at the NASA Glenn Research Center in order to solve the conservation laws. Since its inception, the method has been found capable of accurately resolving shock waves and contact discontinuities without introducing numerical oscillations [16]. The CE/SE method has been used to obtain highly accurate numerical solutions for solving two-dimensional and axisymmetric inviscid flows [17,18], quasi-one-dimensional inviscid flows [19], and two- and three-dimensional viscous flows [20,21]. In particular, problems involving shock waves, rarefaction waves, acoustic waves, vortices, ZND detonation waves, shock/acoustic wave/vortex interactions, a dam-break, and a hydraulic jump [22] have been investigated using the method. A mathematical discussion on the convergence and error bound analysis of the CE/SE method applied to a one-dimensional, time-dependent, convection-diffusion equation is given in [23]. It has been shown that the CE/SE method is genuinely robust, i.e., unlike many other shock capturing schemes, the accuracy of the CE/SE results is achieved without resorting to special treatment for each individual case [24].

This new framework for solving conservation laws differs substantially in both concept and methodology from the traditional methods, i.e., finite difference, finite volume, finite element, and spectral methods. Among the above methods, finite difference, finite element, and spectral methods are designed to solve the differential form of the conservation laws. The differential forms are obtained from the integral forms with the assumption that the physical solution is smooth. This assumption becomes a difficulty in the presence of discontinuities. Thus, a method designed to obtain a numerical solution to the differential form without enforcing flux conservation has a fundamental disadvantage in mod-

Contributed by the Heat Transfer Division for publication in the JOURNAL OF HEAT TRANSFER. Manuscript received by the Heat Transfer Division August 8, 2003; revision received June 18, 2004. Associate Editor: S. P. Vanka.

eling discontinuities [25]. Advantages of the CE/SE method compared to traditional methods are discussed in detail in [25].

The CE/SE method is developed on the basis of local and global flux conservation in a space-time domain in which space and time are treated in a unified manner [26]. This method is designed to enforce flux conservation in space and time, both locally and globally. This feature is the key to the CE/SE method's capability to accurately capture discontinuities. Among the traditional methods, the finite volume method is designed to enforce flux conservation. However, this method requires flux evaluation on the interface of neighboring cells, which is accomplished using interpolation or extrapolation and generally requires an ad hoc choice of a special flux model among many existing models. In the CE/SE method, flux conservation is achieved without complexity, since flux evaluation is an integral part of the solution procedure. Among finite element methods, discontinuous Galerkin (DG) methods [27–29] are also known to be able to resolve discontinuities without spurious oscillations. The CE/SE method used here is explicit, and therefore, it is computationally efficient. Moreover, it is conceptually simple, easy to implement, and extendable to higher dimensions. Despite its second-order accuracy, this method possesses low dispersion and dissipation errors. These distinguishing features of this newly designed method suggest it would be a good alternative for numerical simulation of isothermal phase change problems. The application of the present method, however, is not limited to isothermal phase change cases. The present scheme can readily be applied to cases where the change of phase occurs over a temperature range.

The CE/SE method was applied by the authors to two-dimensional [30] and axisymmetric [31] phase-change problems and was found to be effective and accurate for these applications. The method is now extended to numerically model three-dimensional heat conduction problems with solid/liquid phase change.

In this paper, the problem formulation using the enthalpy method is briefly presented and then the CE/SE method is described for numerical simulation of phase change problems using unstructured meshing, which is selected because of its flexibility for handling complex geometries. To provide a clear geometric description of the four-dimensional space time involved in cases with three spatial dimensions, an analogy with the two-dimensional formulation is most helpful. Therefore, both two- and three-dimensional formulations are presented. Several cases are studied to validate the numerical results. The error behavior of the scheme and its accuracy are also studied numerically for different time steps and different grid sizes.

Governing Equation, Enthalpy Method

The enthalpy method is used for modeling heat conduction with phase-change phenomenon. This method gives the solid-liquid interface as a part of the solution without explicit tracking. The governing equation, i.e., the conservation of energy, with the assumption of constant thermophysical properties within each phase is the Fourier-Biot equation that for a three-dimensional Cartesian coordinate system with no energy generation is written as

$$\rho c \frac{\partial T}{\partial t} = \frac{\partial}{\partial x}\left(k \frac{\partial T}{\partial x}\right) + \frac{\partial}{\partial y}\left(k \frac{\partial T}{\partial y}\right) + \frac{\partial}{\partial z}\left(k \frac{\partial T}{\partial z}\right) \tag{1}$$

where T is the absolute temperature, t denotes time, and c, k, and ρ are specific heat, thermal conductivity, and density of the material, respectively. The left-hand side of Eq. (1) is related to the change of enthalpy. The specific enthalpy may be defined as

$$\overline{h} = \int_0^T c\, dT + \phi L_f \tag{2}$$

where L_f is the latent heat of fusion and ϕ equals 1 for liquids and 0 for solids. Using the above definition, Eq. (1) can be written as

$$\frac{\partial H}{\partial t} = \frac{\partial}{\partial x}\left(k \frac{\partial T}{\partial x}\right) + \frac{\partial}{\partial y}\left(k \frac{\partial T}{\partial y}\right) + \frac{\partial}{\partial z}\left(k \frac{\partial T}{\partial z}\right) \tag{3}$$

where $H=\rho\overline{h}$ is the enthalpy per unit volume. To use Eq. (3) when both solid and liquid phases are involved, procedures are needed for both choosing the thermal conductivity and calculating the temperature field from the enthalpy field. Since c is assumed to be constant within each phase, the enthalpy of the liquid and solid, for a material that changes phase at a single temperature T_f, can be calculated from Eq. (2) as

$$H_S = \rho_S\left(\int_0^T c_S dT\right) = \rho_S c_S T$$
$$H_L = \rho_L\left(\int_0^{T_f} c_S dT + \int_{T_f}^T c_L dT + L_f\right) = \rho_L(c_S T_f + c_L(T-T_f) + L_f) \tag{4}$$

where subscripts L and S refer to liquid and solid phases, respectively. Therefore, the temperature field can be calculated using Eq. (4) as follows:

$$T = \begin{cases} \dfrac{H}{\rho_S c_S} & H \leqslant H_{Sf} \\ T_f & H_{Sf} \leqslant H \leqslant H_{Lf} \\ \dfrac{(H-H_{Lf})}{\rho_L c_L} + T_f & H \geqslant H_{Lf} \end{cases} \tag{5}$$

where $H_{Lf}=\rho_L(c_S T_f + L_f)$ and $H_{Sf}=\rho_S c_S T_f$ are enthalpies per unit volume of the fusion liquid and the fusion solid, respectively. These values can also be used in the numerical approach for determining whether each grid element is solid, liquid, or undergoing melting/freezing. Corresponding thermal conductivities are then chosen for that grid element. For elements that are undergoing phase change, an average thermal conductivity is used.

Numerical Method: CE/SE

Two-Dimensional Formulation. Define vector $\vec{U}$ as

$$\vec{U} = (F, G, H) \tag{6}$$

where H is enthalpy per unit volume and

$$F = -k\frac{\partial T}{\partial x}, \quad G = -k\frac{\partial T}{\partial y} \tag{7}$$

are referred to as the flux functions. Considering (x,y,t) as the coordinates of a three-dimensional Euclidean space-time, the computational grid that is used here can be explained as follows. The spatial projection of the grid is a two-dimensional, unstructured mesh, which consists of Delaunay triangulation on the xy plane that, considering the time axis as the third dimension, makes prisms perpendicular to the xy plane. The computational molecule of this grid is shown in Fig. 1(a), where nodes V_1, V_2, and V_3 determine vertices of a triangular cell j at time level $n-1/2$, with C as its centroid, while points C_1, C_2, and C_3 denote the centroids of three neighboring cells j_1, j_2, and j_3, respectively. The neighbors are named in a way that any vertex V_k, k=1, 2, and 3, of cell j faces the side shared by cell j and its neighbor j_k. Primed points represent the same spatial nodes one-half time step later. For each cell, the integral form of the governing equation may be applied to the octahedral element that is the union of three tetragonal prisms: $CV_2C_1V_3V_3'C'V_2'C_1'$, $CV_3C_2V_1V_1'C'V_3'C_2'$, and $CV_1C_3V_2V_2'C'V_1'C_3'$. The octahedron will be called the *Conservation Element* (CE) of cell j. The integral conservation law will then be

$$\int_{S(CE)} \vec{U}\cdot\hat{n}\, ds = 0 \tag{8}$$

where $S(CE)$ denotes the boundary of the conservation element while $\hat{n}[=(n_x,n_y,n_t)]$ and ds, respectively, denote the unit outward normal vector and the area of a surface element on $S(CE)$. In order to perform the above surface integration, $\vec{U}$ may be replaced by a first-order Taylor series approximation about a suitably chosen node, (called *a solution point*), where the discretized values of $\vec{U}$ and its derivatives are saved. In this method both $\vec{U}$ and its first-order derivatives are considered the independent variables that must be determined. By "suitably chosen," as will be shown shortly, it is intended that solution points are selected such that the method is explicit. Let (x_j',y_j') represent the spatial coordinates of the solution point related to cell j. Therefore, components of $\vec{U}$ may be approximated as

$$H(x,y,t;j,n)=H_j^n+(H_x)_j^n(x-x_j')+(H_y)_j^n(y-y_j')+(H_t)_j^n(t-t^n) \tag{9}$$

where H_j^n, $(H_x)_j^n$, $(H_y)_j^n$, and $(H_t)_j^n$ are constant coefficients associated with the solution point (x_j',y_j',t^n). The same approach may be used for F and G. Further, the derivatives of F and G can be found from Eq. (7), i.e.,

$$(F_x)_j^n=-k(T_{xx})_j^n,\quad (F_y)_j^n=-k(T_{xy})_j^n,\quad (F_t)_j^n=-k(T_{xt})_j^n \tag{10}$$
$$(G_x)_j^n=-k(T_{yx})_j^n,\quad (G_y)_j^n=-k(T_{yy})_j^n,\quad (G_t)_j^n=-k(T_{yt})_j^n$$

where the coefficients $(T_{xx})_j^n$, $(T_{xy})_j^n$, $(T_{xt})_j^n$, $(T_{yx})_j^n$, $(T_{yy})_j^n$, and $(T_{yt})_j^n$ will be calculated later in the section of second-order derivatives.

In Eq. (9), the notation $H(x,y,t;j,n)$ [32] means the value of H at the point (x,y,t) is evaluated using the nodal values saved at the solution point (x_j',y_j',t^n). The reason these need to be defined can be understood by considering the fact that each point on any of the surfaces indicated in Fig. 1(a) may be evaluated using different discrete values, e.g., the value of $\vec{U}$ at a point on the $CV_1V_1'C'$ plane may be found using the expansion point of cell j at time level n as well as time level $n-1/2$. Also, the value of $\vec{U}$ at a point on the $CV_1C_1V_3$ plane may be found using the expansion point of cell j at time level $n-1/2$ as well as that of the neighboring cell j_1 at the same time level. To assign a unique value to each surface point while integrating, each surface needs to be related to one and only one (j,n) entity, which is called a *solution element* (SE). Consequently, solution elements must be defined so that each component surface on the boundary of any conservation element belongs to an assigned solution element. Figure 1(b) shows two of four solution elements related to the cell j, i.e., SE (j,n), which consists of the hexagon $C_1'V_3'C_2'V_1'C_3'V_2'$ combined with three vertical rectangular planes cutting through it; SE $(j_3,n-1/2)$, which consists of the hexagon CV_1ABDV_2 combined with three vertical rectangular planes cutting through it, where A, B, and D are related to the neighbor j_3 of cell j (not shown); and two other SEs $(j_1,n-1/2)$ and $(j_2,n-1/2)$ that are built the same way. Using the notation convention introduced in [33], consider the SE $(j_1,n-1/2)$. The two lateral faces related to this SE, i.e., $C_1V_2V_2'C_1'$ and $C_1V_3V_3'C_1'$ [see Fig. 1(a)] will be referred to as $S(1,1)$ and $S(2,1)$, respectively. Furthermore, the areas of $S(1,1)$ and $S(2,1)$ will be referred to as $S^{(1,1)}$ and $S^{(2,1)}$, respectively, while $\hat{n}^{(1,1)}$, and $\hat{n}^{(2,1)}$ represent the unit normals of the above lateral faces, outward with respect to the octahedron. Furthermore, spatial coordinates of the centroid of each of these faces will be referred to as $(x_c^{(1,1)},y_c^{(1,1)})$ and $(x_c^{(2,1)},y_c^{(2,1)})$, respectively. Also the surface $C_1V_3CV_2$, that is the horizontal plane related to this SE, will be called $S(1)$, while its area and will be referred to as $S^{(1)}$. The unit outward normal to this surface is $(0,0,-1)$.

In general, for SE $(j_k,n-1/2)$, $k=1,2,3$, the lateral faces will be called $S(l,k)$, while their area, unit outward normal, and the spatial coordinates of their centroid will be referred to as $S^{(l,k)}$, $\hat{n}^{(l,k)}=(n_x^{(l,k)},n_y^{(l,k)},0)$, and $(x_c^{(l,k)},y_c^{(l,k)})$, $l=1,2$, respectively. Also the corresponding horizontal plane will be denoted by $S(k)$, while its area, and the spatial coordinates of its centroid will be represented by $S^{(k)}$ and $(x_c^{(k)},y_c^{(k)})$, respectively. Note that the so-called horizontal planes form the bottom of the octahedron. The horizontal planes that contain the top of the octahedron, however, belong to SE (j,n). The area and spatial coordinates of the centroid of the top surfaces are equal to those of the bottom surfaces but their unit outward normal is $(0,0,+1)$. Using the above conventions and performing the inner products, Eq. (8) can be written as

$$\begin{aligned}\int_{S(\mathrm{CE})}\vec{U}\cdot\hat{n}ds=\sum_{k=1}^{3}\Bigg\{&\int_{S(k)}H(x,y,t;j,n)(+1)ds\\&+\int_{S(k)}H(x,y,t;j_k,n-1/2)(-1)ds\\&+\sum_{l=1}^{2}\int_{S(l,k)}[F(x,y,t;j_k,n-1/2)n_x^{(l,k)}\\&+G(x,y,t;j_k,n-1/2)n_y^{(l,k)}]ds\Bigg\}\end{aligned} \tag{11}$$

where the first and second integrals are performed over the top and bottom surfaces, respectively, and the third integral is related to the lateral faces of the octahedral CE.

Using Eq. (9), the third integral of Eq. (11) can be evaluated as follows

$$\begin{aligned}I^{(l,k)}=&\int_{S(l,k)}[F(x,y,t;j_k,n-1/2)n_x^{(l,k)}\\&+G(x,y,t;j_k,n-1/2)n_y^{(l,k)}]ds\\=&\int_{S(l,k)}\{[F_{j_k}^{n-1/2}+(F_x)_{j_k}^{n-1/2}(x-x_{j_k}')+(F_y)_{j_k}^{n-1/2}(y-y_{j_k}')\\&+(F_t)_{j_k}^{n-1/2}(t-t^{n-1/2})]n_x^{(l,k)}\\&+[G_{j_k}^{n-1/2}+(G_x)_{j_k}^{n-1/2}(x-x_{j_k}')+(G_y)_{j_k}^{n-1/2}(y-y_{j_k}')\\&+(G_t)_{j_k}^{n-1/2}(t-t^{n-1/2})]n_y^{(l,k)}\}ds\end{aligned}$$

Rearranging leads to

$$\begin{aligned}I^{(l,k)}=&\int_{S(l,k)}ds\{[F_{j_k}^{n-1/2}-(F_x)_{j_k}^{n-1/2}x_{j_k}'-(F_y)_{j_k}^{n-1/2}y_{j_k}'\\&-(F_t)_{j_k}^{n-1/2}t^{n-1/2}]n_x^{(l,k)}+[G_{j_k}^{n-1/2}-(G_x)_{j_k}^{n-1/2}x_{j_k}'\\&-(G_y)_{j_k}^{n-1/2}y_{j_k}'-(G_t)_{j_k}^{n-1/2}t^{n-1/2}]n_y^{(l,k)}\}+[(F_x)_{j_k}^{n-1/2}n_x^{(l,k)}\\&+(G_x)_{j_k}^{n-1/2}n_y^{(l,k)}]\int_{S(l,k)}xds+[(F_y)_{j_k}^{n-1/2}n_x^{(l,k)}\\&+(G_y)_{j_k}^{n-1/2}n_y^{(l,k)}]\int_{S(l,k)}yds+[(F_t)_{j_k}^{n-1/2}n_x^{(l,k)}\\&+(G_t)_{j_k}^{n-1/2}n_y^{(l,k)}]\int_{S(l,k)}tds\end{aligned}$$

But $\int_{S(l,k)}ds$ is the area of the corresponding lateral face and the rest of the above integrals may be evaluated using the space-time coordinates of its centroid. Therefore, the integral becomes

$$\begin{aligned}I^{(l,k)}=\{&F(x_c^{(l,k)},y_c^{(l,k)},t^n-\Delta t/4;j_k,n-\tfrac{1}{2})n_x^{(l,k)}+G(x_c^{(l,k)},y_c^{(l,k)},t^n\\&-\Delta t/4;j_k,n-\tfrac{1}{2})n_y^{(l,k)}\}S^{(l,k)}\end{aligned} \tag{12}$$

Following a similar procedure, the first and second integrals of Eq. (11) become

$$\int_{S(k)} H(x,y,t;j,n)(+1)ds = S^{(k)}[H_j^n + (H_x)_j^n(x_c^{(k)} - x_j') + (H_y)_j^n(y_c^{(k)} - y_j')] \quad (13)$$

and

$$\int_{S(k)} H(x,y,t;j_k,n-1/2)(-1)ds = -S^{(k)}[H_{j_k}^{n-1/2} + (H_x)_{j_k}^{n-1/2}(x_c^{(k)} - x_{j_k}') + (H_y)_{j_k}^{n-1/2}(y_c^{(k)} - y_{j_k}')] = -S^{(k)}H(\dot{x}_c^{(k)}, y_c^{(k)}, t^{n-1/2}; j_k, n-\tfrac{1}{2}) \quad (14)$$

respectively.

Equation (11), after substitution of the evaluated integrals, provides an expression for H_j^n. The expression contains three unknowns H_j^n, $(H_x)_j^n$, and $(H_y)_j^n$, but examination of the expressions that contain $(H_x)_j^n$ and $(H_y)_j^n$ suggests that they may be eliminated, resulting in an explicit method, provided the solution point is chosen at the centroid of the hexagon $C_1V_3C_2V_1C_3V_2$ formed by the vertices of cell j and the centroids of its three neighbors. Using this, the equation for H_j^n can be written in a convenient manner. Note that despite the apparent complexity, the equation for H_j^n is in fact composed of three similar parts, each related to one of the neighboring cells.

$$H_j^n = \sum_{k=1}^{3} R^{(k)} \Big/ \sum_{k=1}^{3} S^{(k)} \quad (15)$$

where

$$R^{(k)} = S^{(k)}H(x_c^{(k)}, y_c^{(k)}, t^{n-1/2}; j_k, n-\tfrac{1}{2}) - \sum_{l=1}^{2} I^{(l,k)}$$

and $I^{(l,k)}$ is evaluated using Eq. (12).

The above formulation has the important attribute of being able to handle nonlinearities that may exist in the definition of functions H, F, and G.

Once the values of enthalpy are updated over the entire domain, Eq. (5) can be used to obtain the temperature field, and the first and second order derivatives of the field parameters may be calculated as described in the following sections.

First-Order Derivatives. As described in detail in [32], the first-order derivatives of the field parameters can be evaluated from

$$(\Psi_x)_j^n = \frac{\sum_{k=1}^{3} |\theta_m\theta_p|^{\tilde{\alpha}}\Psi_x^{(k)}}{\sum_{k=1}^{3} |\theta_m\theta_p|^{\tilde{\alpha}}}, \quad (\Psi_y)_j^n = \frac{\sum_{k=1}^{3} |\theta_m\theta_p|^{\tilde{\alpha}}\Psi_y^{(k)}}{\sum_{k=1}^{3} |\theta_m\theta_p|^{\tilde{\alpha}}} \quad (16)$$

where

$$\theta_k = \sqrt{(\Psi_x^{(k)})^2 + (\Psi_y^{(k)})^2}, \quad k=1,2,3$$

and, for any given integer, $k=1, 2, 3$, $\{k\}\cup\{m,p\}=\{1,2,3\}$. Parameters $\Psi_x^{(k)}$ and $\Psi_y^{(k)}$ are calculated solving the following three systems, each containing two equations and two unknowns. Parameter Ψ can be either H or T.

$$(x_{j_k}' - x_j')\Psi_x^{(1)} + (y_{j_k}' - y_j')\Psi_y^{(1)} = \Psi_{j_k}^n - \Psi_j^n, \quad k=2,3$$

$$(x_{j_k}' - x_j')\Psi_x^{(2)} + (y_{j_k}' - y_j')\Psi_y^{(2)} = \Psi_{j_k}^n - \Psi_j^n, \quad k=1,3$$

$$(x_{j_k}' - x_j')\Psi_x^{(3)} + (y_{j_k}' - y_j')\Psi_y^{(3)} = \Psi_{j_k}^n - \Psi_j^n, \quad k=1,2$$

The constant $\tilde{\alpha}$, in Eq. (16), is usually set equal to 1. The above weighted average provides the necessary numerical damping [34]. Note that, to avoid dividing by zero, in practice a small positive number (e.g., 10^{-20}) is added to the denominators in Eq. (16).

Second-Order Derivatives. As explained in [34], once the first-order derivatives of the temperature field are known, expanding $(T_x)_{j_k}^{n-1/2}$, $k=1, 2, 3$, which is saved at the solution point $(S_k, n-1/2)$ about the space-time solution point (S,n), results in three equations

$$(x_{j_k}' - x_j')(T_{xx})_j^n + (y_{j_k}' - y_j')(T_{xy})_j^n - \frac{\Delta t}{2}(T_{xt})_j^n = (T_x)_{j_k}^{n-1/2} - (T_x)_j^n, \quad k=1,2,3$$

These may be solved simultaneously for $(T_{xx})_j^n$, $(T_{xy})_j^n$, and $(T_{xt})_j^n$. A similar system gives $(T_{yx})_j^n$, $(T_{yy})_j^n$, and $(T_{yt})_j^n$. Using this technique, the mesh values of second-order derivatives of T can be evaluated in order to be used in Eq. (10). The first-order derivatives of flux functions, evaluated from Eq. (10), can then be used in Eq. (15).

Three-Dimensional Formulation. In three spatial dimensions, Eq. (6) becomes

$$\vec{U} = (F,G,P,H) \quad (17)$$

where

$$F = -k\frac{\partial T}{\partial x}, \quad G = -k\frac{\partial T}{\partial y}, \quad P = -k\frac{\partial T}{\partial z} \quad (18)$$

and H is the enthalpy per unit volume.

Considering (x,y,z,t) as coordinates of a four-dimensional Euclidean space-time, Eq. (8) will still be valid. The spatial projection of the unstructured grid used here consists of tetrahedral elements. To provide a clear geometric description of the CE, an analogy with the 2D formulation is helpful. As described in the previous sections, the integrations involved in the 2D case are performed on the CE's top, bottom, and lateral faces that are 2D surfaces. Similarly, the integrations for the 3D case are performed on the CE's top, bottom, and lateral faces that are 3D volumes.

Top/Bottom Faces. These faces are constant-time faces. Consider a tetrahedral element "cell j" at time level $n-1/2$, e.g., the tetrahedron $V_1V_2V_3V_4$ depicted in Fig. 2. Let nodes V_1, V_2, V_3, and V_4 represent vertices of cell j while its four neighboring cells are referred to as cells j_1, j_2, j_3, and j_4. The neighbors are named in a way that any vertex V_k, $k=1$, 2, 3, and 4, of cell j faces the side shared by cell j and its neighbor j_k. Further, let point C denote the centroid of cell j while C_k represents the centroid of the neighboring cell j_k. The 3D analogue of hexagon $V_1C_2V_3C_1V_2C_3$ of Fig. 1(*a*) can be visualized as follows. For each face of tetrahedral cell j, a hexahedron can be constructed using vertices of that face, the centroid of cell j, and the centroid of the corresponding neighbor. These hexahedra, i.e., $CV_2V_3V_4C_1$, $CV_1V_3V_4C_2$, $CV_1V_2V_4C_3$, and $CV_1V_2V_3C_4$, are 3D analogues of the 2D bottom faces $CV_2V_3C_1$, $CV_3V_1C_2$, and $CV_1V_2C_3$ depicted in Fig. 1(*a*). The hexahedron related to neighbor j_1, i.e., $CV_2V_3V_4C_1$, is depicted in Fig. 2. The union of these four hexahedra is a polyhedron with 12 triangular faces. The centroid of this polyhedron is the solution point of cell j, and its spatial coordinates will be referred to as x_j', y_j', and z_j'. This polyhedron is the 3D analogue of the bottom face of the hexagonal prism depicted in Fig. 1(*a*). A similar polyhedron represents the top face of the 3D case's CE.

Adopting a notation convention similar to that introduced in [33], the volume of each of the four hexahedra introduced above will be referred to as $V^{(k)}$, $k=1$, 2, 3, and 4, where $V^{(k)}$ is volume

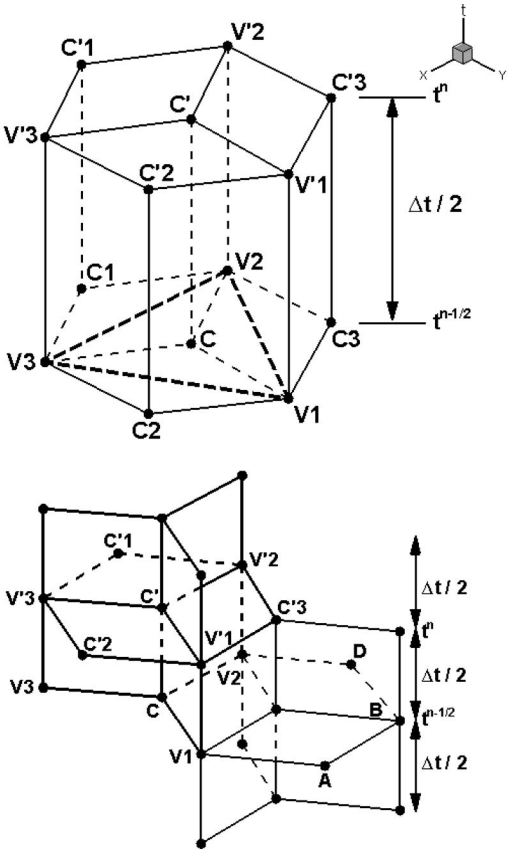

Fig. 1 Computational molecule of CE/SE method, *a*) CEs and *b*) SEs

of the hexahedron related to neighbor j_k. Further, let coordinates of the centroid of the hexahedra be represented by $x_c^{(k)}$, $y_c^{(k)}$, and $z_c^{(k)}$ where $k=1$, 2, 3, and 4. The unit outward normals for top and bottom faces are (0,0,0,1) and (0,0,0,−1), respectively.

Lateral Faces. These faces simply connect the top and bottom faces in the fourth-dimension. Therefore, there are three lateral faces (which are in fact 3D volumes) associated with each neighbor. To visualize these faces, note that three lateral faces associated with neighbor j_1 are volumes $C_1V_2V_3C_1'V_2'V_3'$, $C_1V_3V_4C_1'V_3'V_4'$, and $C_1V_2V_4C_1'V_2'V_4'$, where the primed nodes refer to the same spatial position as the corresponding unprimed nodes, but at the new time level n. The volume of these lateral faces will be referred to as $V^{(l,k)}$ where $l=1$, 2, 3 and $k=1$, 2, 3, 4 refer to the associated neighbor. The centroid of each lateral face is represented by the space-time point $(x_c^{(l,k)}, y_c^{(l,k)}, z_c^{(l,k)}, t^n - \Delta t/4)$. The unit outward normal of each lateral face is represented by $\hat{n}^{(l,k)}=(\hat{n}_x^{(l,k)}, \hat{n}_y^{(l,k)}, \hat{n}_z^{(l,k)}, 0)$. These unit normals are defined outward with respect to the hexahedra introduced in the previous section.

Analogous to the 2D case, each lateral face represented by $V(l,k)$, as well as each bottom face represented by $V(k)$, is associated with SE $(j_k, n-1/2)$, $k=1$, 2, 3, 4. The top face is associated with SE (j,n). Using the three-dimensional analogue of Eq. (9), i.e.,

$$H(x,y,t;j,n)=H_j^n+(H_x)_j^n(x-x_j')+(H_y)_j^n(y-y_j')+(H_z)_j^n(z-z_j')+(H_t)_j^n(t-t^n)$$

and with integrations similar to the 2D case, the 3D analogue of Eq. (15) becomes

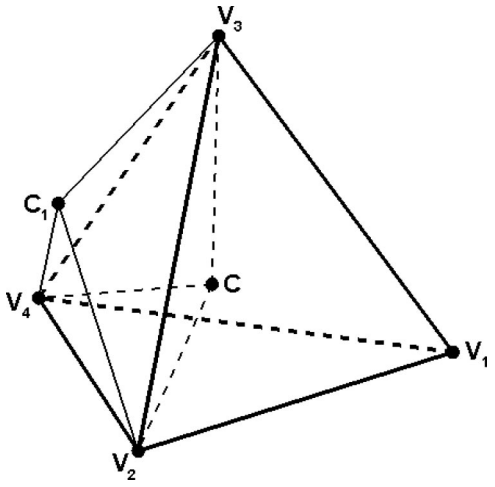

Fig. 2 Geometry for 3D formulation

$$H_j^n=\sum_{k=1}^{4} R^{(k)} \Big/ \sum_{k=1}^{4} V^{(k)} \tag{19}$$

where

$$R^{(k)}=V^{(k)}H(x_c^{(k)}, y_c^{(k)}, z_c^{(k)}, t^{n-1/2}; j_k, n-\tfrac{1}{2}) - \sum_{l=1}^{3} \{F(x_c^{(l,k)}, y_c^{(l,k)}, z_c^{(l,k)}, t^n-\Delta t/4; j_k, n-\tfrac{1}{2})n_x^{(l,k)} + G(x_c^{(l,k)}, y_c^{(l,k)}, z_c^{(l,k)}, t^n-\Delta t/4; j_k, n-\tfrac{1}{2})n_y^{(l,k)} + P(x_c^{(l,k)}, y_c^{(l,k)}, z_c^{(l,k)}, t^n-\Delta t/4; j_k, n-\tfrac{1}{2})n_z^{(l,k)}\}V^{(l,k)}$$

First-Order Derivatives. Using an approach similar to the 2D case, the process of determining the first-order derivatives of the field parameters can be summarized in solving the following four linear systems, each having three equations and three unknowns.

$$(x_{j_k}'-x_j')\Psi_x^{(1)}+(y_{j_k}'-y_j')\Psi_y^{(1)}+(z_{j_k}'-z_j')\Psi_z^{(1)}=\Psi_{j_k}^n-\Psi_j^n, \quad k=2,3,4$$

$$(x_{j_k}'-x_j')\Psi_x^{(2)}+(y_{j_k}'-y_j')\Psi_y^{(2)}+(z_{j_k}'-z_j')\Psi_z^{(2)}=\Psi_{j_k}^n-\Psi_j^n, \quad k=1,3,4$$

$$(x_{j_k}'-x_j')\Psi_x^{(3)}+(y_{j_k}'-y_j')\Psi_y^{(3)}+(z_{j_k}'-z_j')\Psi_z^{(3)}=\Psi_{j_k}^n-\Psi_j^n, \quad k=1,2,4$$

$$(x_{j_k}'-x_j')\Psi_x^{(4)}+(y_{j_k}'-y_j')\Psi_y^{(4)}+(z_{j_k}'-z_j')\Psi_z^{(4)}=\Psi_{j_k}^n-\Psi_j^n, \quad k=1,2,3$$

The above systems can be solved for $\Psi_x^{(k)}$, $\Psi_y^{(k)}$, and $\Psi_z^{(k)}$, where $k=1$, 2, 3, and 4. A weighted average may then be used to calculate $(\Psi_x)_j^n$, $(\Psi_y)_j^n$, and $(\Psi_z)_j^n$ as follows

$$(\Psi_w)_j^n=\frac{\sum_{k=1}^{3} |\theta_m\theta_q\theta_r|^{\tilde{\alpha}}(\Psi_w)_{O_k}^n}{\sum_{k=1}^{3} |\theta_m\theta_q\theta_r|^{\tilde{\alpha}}}$$

where

$$\theta_k=\sqrt{(\Psi_x^{(k)})^2+(\Psi_y^{(k)})^2+(\Psi_z^{(k)})^2}, \quad k=1,2,3,4$$

and, for any given integer, $k=1$, 2, 3, 4, $\{k\}\cup\{m,q,r\}=\{1,2,3,4\}$. Variable w can be each of x, y, or z while parameter Ψ represents either H or T. The constant $\tilde{\alpha}$ is usually set equal to 1. Note that, to avoid dividing by 0, in practice a small positive number, such as 10^{-20}, is added to the above denominators.

Second-Order Derivatives. Using an approach similar to the 2D case, the process of determining the second-order derivatives can be summarized in solving the following three linear systems, each having four equations and four unknowns.

$$(x'_{j_k}-x'_j)(T_{wx})^n_j+(y'_{j_k}-y'_j)(T_{wy})^n_j+(z'_{j_k}-z'_j)(T_{wz})^n_j-\frac{\Delta t}{2}(T_{wt})^n_j$$
$$=(T_w)^{n-1/2}_{j_k}-(T_w)^n_j, \quad k=1,2,3,4$$

These may be solved simultaneously for second-order derivatives of temperature, i.e., $(T_{wx})^n_j$, $(T_{wy})^n_j$, $(T_{wz})^n_j$, and $(T_{wt})^n_j$ where w can be x, y, or z. Using this technique, the mesh values of second-order derivatives of T can be evaluated and used in the solution procedure which is similar to that of the 2D case.

In order to treat the boundary conditions, a ghost cell is defined for each boundary cell. Geometrically, the ghost cell is the mirror image of the corresponding boundary cell with respect to the boundary. The 3D case's reflecting boundary conditions are derived using a technique similar to that described in [32] for the 2D case. Phase-change related details of both constant temperature and convective boundary conditions are described in [31].

Results and Discussion

To assess the accuracy and effectiveness of the CE/SE method applied to conduction problems with phase change, several 2D and axisymmetric classical cases were studied by the authors. The results were compared to analytical solutions, and the method was found to be accurate, robust, and efficient. Details of the 2D scheme, numerical analysis of error behavior, and the application of the method to the limit of small Stefan numbers are presented in [30], while the development of the axisymmetric formulation, its validation cases, and error behavior are discussed in [31].

In order to validate the computer program for 3D cases and study the error behavior of the numerical scheme, the following two cases were designed and applied to a unit cube, with unit conductivity.

$$\text{Case 1.} \quad H=T \quad \text{and} \quad T=x+y+z+\text{const.} \tag{20}$$

$$\text{Case 2.} \quad H=T \quad \text{and} \quad T=x^2+y^2+z^2+6t \tag{21}$$

As can be seen, the above temperature distributions satisfy the governing equation.

Case 1. This case is a steady first-order problem for which it can be easily shown that the CE/SE formulation is exact, in the sense that no truncation error exists. Therefore, the spatial grid is not an issue in this case. On the other hand, the time-step issue needs to be studied. Equation (20) was applied on the boundaries, with an initially imposed error distribution over the entire domain. The results confirmed that, after a period of time, the temperature converges to the accurate distribution everywhere in the field. Figure 3 shows the absolute error (which is defined as the infinity norm of the difference between the numerical and exact solutions) depicted versus the iterations for different time steps. The errors vanish to the order of machine zero.

Using this case, the error behavior was studied for different time steps. Since the present method is explicit, there are stability restrictions on the time step. Usage of a time step larger than the spatial grid size leads to divergence. By reducing the time step, it was found that the numerical errors grow, but there is an upper bound for this growth. Further reduction of the time step results in stable accurate solutions, for which, the errors vanish to the order of machine zero (Fig. 3). Based on the above results, the procedure of choosing the right time step for a spatial grid, may be summarized as starting from a large time step and reducing it until stable, time-step independent results are achieved. As can be seen, the fastest convergence rate is achieved by using the largest time step that falls within this category.

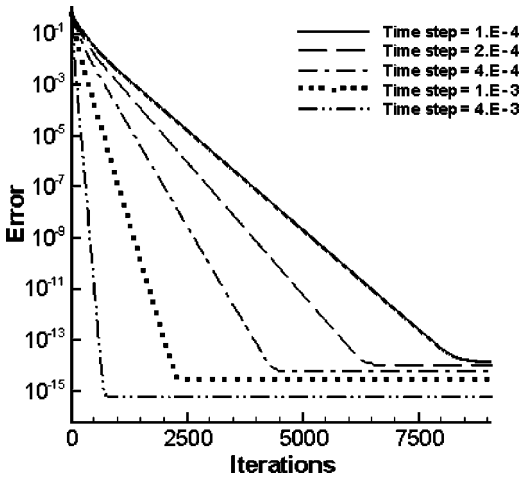

Fig. 3 Vanishing errors for Case 1

Case 2. For this transient problem [see Eq. (21)], unlike the previous case, there is a mesh-dependent error associated with second-order accuracy of the CE/SE method. Clearly, this error should decrease by using finer spatial grids. Different spatial grids were used for this case. A grid that has nine nodes on each edge of the unit cube will be referred to as the coarse grid, while the so-called medium grid consists of 21 nodes on each edge of the unit cube. The grid referred to as fine grid contains 31 nodes on each edge of the unit cube. Equation (21) was applied on the boundaries. Both exact solution and a uniform error distribution were used as initial conditions. The absolute average errors (defined as the arithmetic average of the difference between the numerical and exact solutions, for all cells) are shown in Fig. 4. In Fig. 5, the absolute average errors are plotted versus the spatial mesh spacing for different grids. This figure confirms the second-order accuracy of the scheme.

Case 3: Freezing of a Finite Slab. Consider a slab of thickness L with the initial state assumed to be liquid at the fusion temperature T_f. At $t=0$, the temperature of the surface at $x=0$

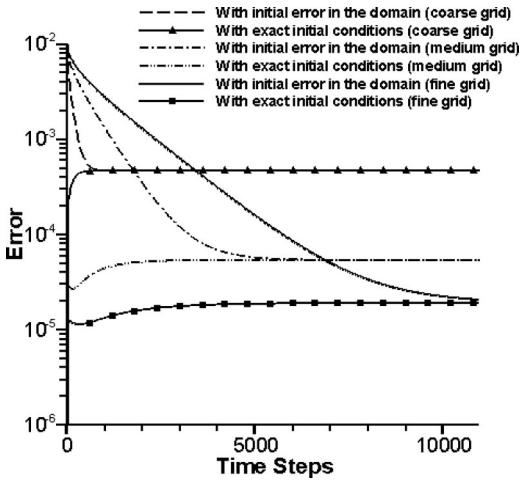

Fig. 4 Grid size effects for Case 2

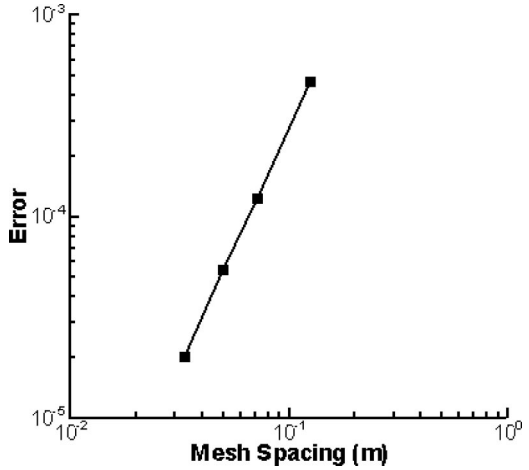

Fig. 5 Demonstration of the CE/SE scheme's second-order accuracy

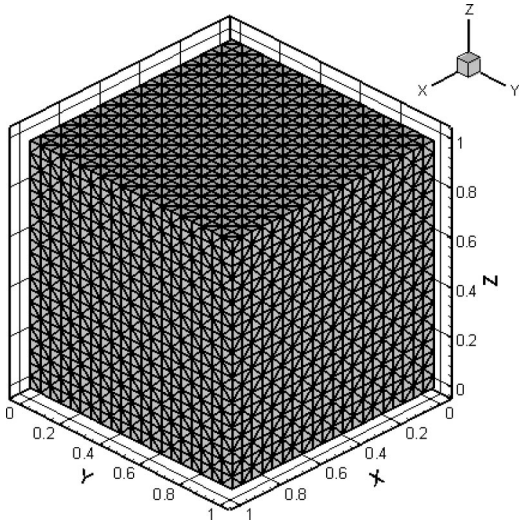

Fig. 6 Spatial grid for the unit cube

drops to T_W and is held there. The surface at $x=L$ is effectively insulated. The analytical solution of this problem (from [35]) determines the phase-change interface to be at

$$x_{\text{int.}} = 2\gamma\sqrt{\alpha_s t}$$

where α_s is the thermal diffusivity of the solid phase and γ is determined by solving

$$\gamma e^{\gamma^2}\,\text{erf}(\gamma) = \frac{c_s(T_f - T_W)}{L_f\sqrt{\pi}}$$

where c_s denotes the specific heat of the solid phase and L_f is the latent heat of fusion. Also the temperature in the solid region is determined from

$$T = T_W + \frac{T_f - T_W}{\text{erf}(\gamma)}\,\text{erf}(\eta)$$

where $\eta = x/2\sqrt{\alpha_s t}$.

In order to model this one-dimensional problem using the three-dimensional code, all sides of the unit cube are assumed to be insulated, except one side, (plane $y=0$), which acts like the $x=0$ wall of the problem stated above.

This problem is studied for $S_t=4$ where $S_t = c_s(T_f - T_W)/L_f$ is the Stefan number. Other parameters are $T_W = -1.0°\text{C}$, $T_f = 0.0°\text{C}$, while the thermal diffusivity and specific heats are set equal to unity. An example of the spatial mesh for the unit cube is given in Fig. 6. Figure 7 shows the position of phase-change interface compared to the analytical solution versus time. The temperature distribution in the y direction at time $t=0.14\,\text{s}$ is also compared to the analytical solution in Fig. 8. No changes occur in either the x or z directions. As can be seen, accurate results are obtained.

This case is also solved using another commonly used fixed domain scheme from [36]. The error percentages within the domain are depicted in Fig. 9, for both CE/SE method and the method of [36], using identical time step and spatial grid spacing. As can be seen, the error associated with the CE/SE method is more uniform over the domain, compared the method of [36]. The mean values and standard deviations associated with Fig. 9 are given in Table 1.

Case 4: Thawing of a Cube. Consider a unit cube that is initially frozen at the fusion temperature T_f. At time $t=0$, the temperature of all outer surfaces are raised to T_W and held there. This case is studied for $S_t=4$, $T_W=1.0°\text{C}$, and $T_f=0.0°\text{C}$, while the thermal diffusivity and specific heats are set equal to unity. Figure 10(*a*) shows the frozen core of the cube at different times. These graphs are generated using a shaded view of the frozen cells in the mesh. Figure 10(*b*) shows the xy view of the phase-change interface location at different times. The plots are generated using constant enthalpy contours ranging from H_{sf} to H_{Lf}. The top graph also contains the xy view of the spatial mesh from

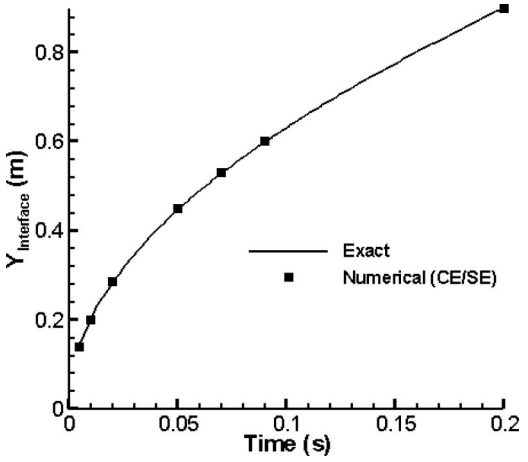

Fig. 7 Location of the phase change interface for Case 3

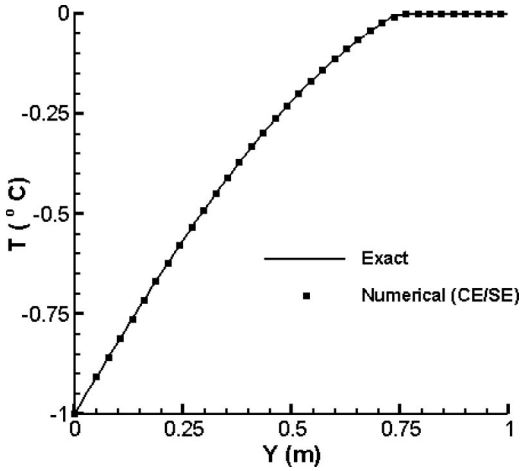

Fig. 8 Temperature distribution at $t=0.14$ s for Case 3

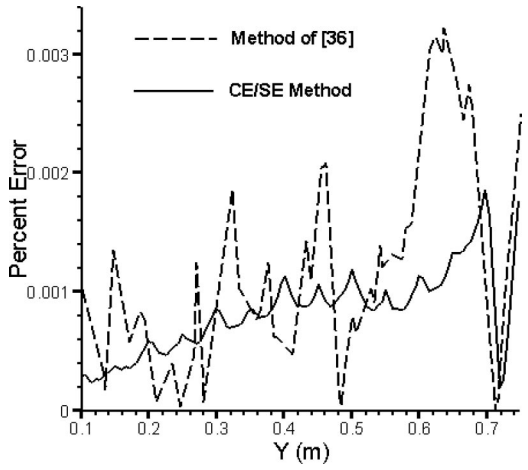

Fig. 9 Comparison of the errors at $t=0.14$ s for Case 3

Table 1 Statistical parameters associated with Fig. (9)

	CE/SE	Method of [36]
Mean Error (%)	0.000836	0.001275
Standard Deviation	0.000521	0.001227

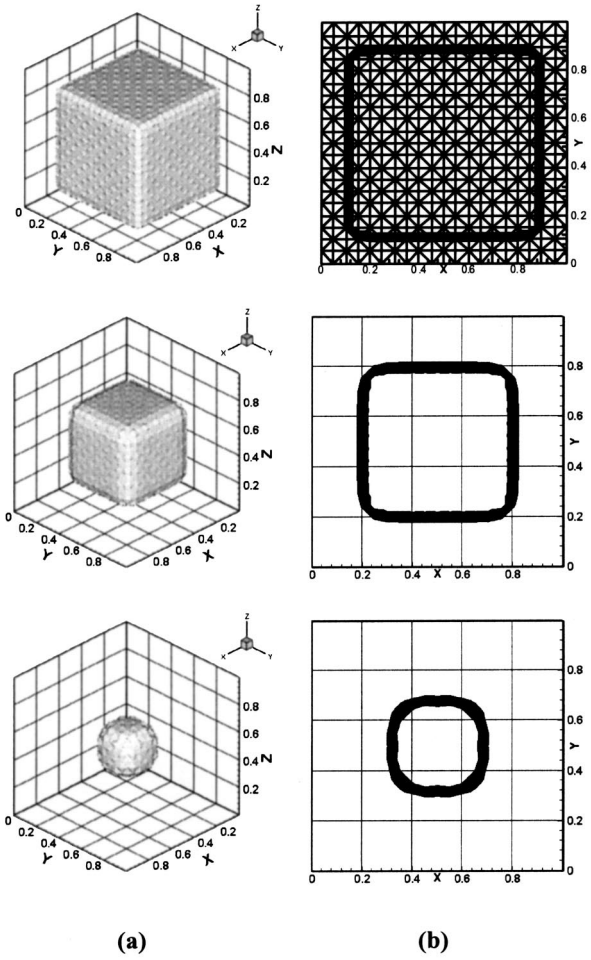

Fig. 10 The thawing cube, (Case 4), at $t=0.005$, 0.02, and 0.05 s

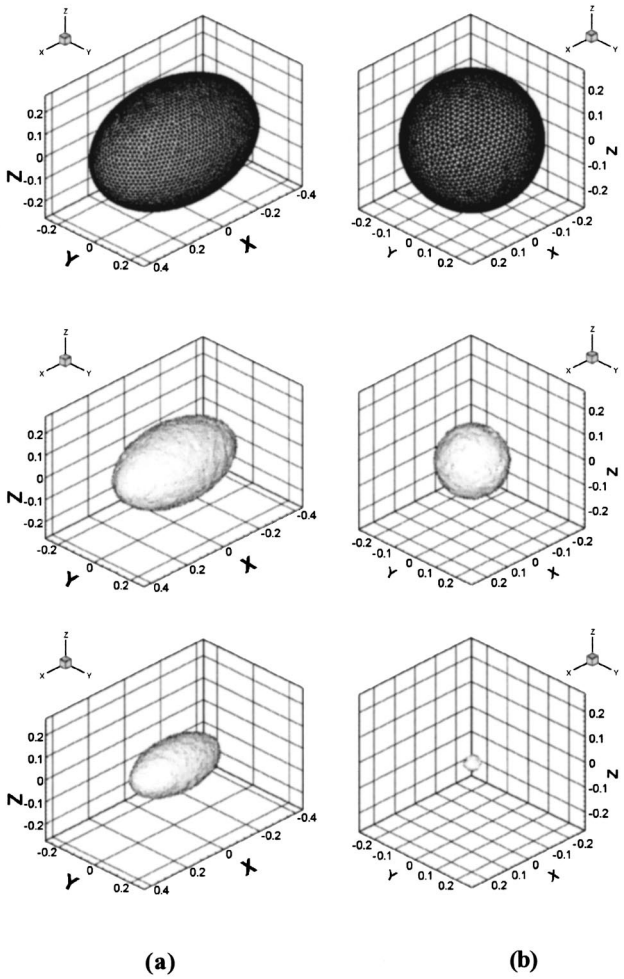

Fig. 11 (*a*) Thawing ellipsoid, (Case 5), at $t=0$, 0.0035, and 0.0085 s, (*b*) Thawing sphere, (Case 6), at $t=0$, 0.0025, and 0.0065 s

which the interface width is observed to be roughly equal to one cell's size. This demonstrates the ability of the CE/SE method for capturing the discontinuities sharply.

Case 5: Thawing of an Ellipsoid. Consider a prolate ellipsoid that is initially frozen at the fusion temperature T_f. At time $t=0$, the temperature of its outer surface is raised to T_W and held there. This case is studied for $S_t=1$, $T_W=1.0°C$, and $T_f=0.0°C$, while the thermal diffusivity and specific heats are set equal to unity. The geometry has a half major axis equal to 0.4 m and a half minor axis of 0.25 m. The frozen core is represented in Fig. 11(*a*) at different times. The top graph shows both the spatial mesh and the initial frozen ellipsoid.

By reducing the eccentricity of the original ellipse, the above case approaches the case of a thawing sphere, for which, approximations for the total melting time are available in [3]. It is worthwhile, therefore, to also study this limiting case of a thawing sphere.

Case 6: Thawing of a Sphere. Consider a sphere that is initially frozen at the fusion temperature T_f. At time $t=0$, the temperature of its outer surface is raised to T_W and held there. This case is studied for $S_t=1$, 2, 3, and 4. The thermal diffusivity and specific heats are set equal to unity while $T_W=1.0°C$, and $T_f=0.0°C$. The radius of the sphere is taken to be 0.25 m. The frozen core is represented in Fig. 11(*b*) at different times, for a

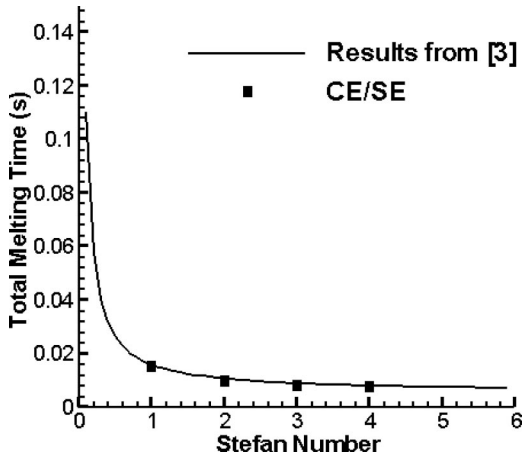

Fig. 12 Total melting time for the thawing sphere of Case 6

case where $S_t = 4$. The top graph shows both the spatial mesh and the initial frozen sphere. The total melting times, as shown in Fig. 12, agree with the results from [3]. However, for the freezing slab case, the error associated with the approximate relations given in [3], is reported to be 5%, while the comparison of CE/SE results with the exact solution of that case shows a maximum error of about 1%. A similar relation between the errors can then be expected for the thawing sphere case.

Conclusions

The CE/SE method, an accurate and efficient method for resolving discontinuities in fluid mechanics problems, was used by the authors as a new alternative for solving three-dimensional phase-change problems. Comparison of the results to existing analytical solutions verified the ability of the method to capture moving phase fronts without incurring oscillations.

The CE/SE method is computationally efficient since it is explicit and requires no iterations to achieve convergence within the same time step. This efficiency becomes a very important advantage when dealing with problems in three spatial dimensions. The 3D CE/SE formulation was developed for phase-change problems. Several cases were studied and the accuracy and efficiency of the method was verified for this application.

References

[1] Sulfredge, C. D., Chow, L. C., and Tagavi, K. A., 1992, ''Void Formation in Radial Solidification of Cylinders,'' ASME J. Sol. Energy Eng., **114**, pp. 32–39.

[2] Sarler, B., 1995, ''Stefan's Work on Solid-Liquid Phase Change,'' Eng. Anal. Boundary Elem., **16**, pp. 83–92.

[3] Alexiades, V., and Solomon, A. D., 1993, *Mathematical Modeling of Melting and Freezing Processes*, Hemisphere, Washington, DC.

[4] Rubinstein, L. I., 1971, *The Stefan Problem, Translations of Mathematical Monographs, 27*, American Mathematical Society, Providence.

[5] Elliott, C. M., and Ockendon, J. R., 1982, *Weak and Variational Methods for Moving Boundary Problems*, Pitman, New York.

[6] Crank, J., 1984, *Free and Moving Boundary Problems*, Clarendon Press, Oxford.

[7] Douglas, J., and Gallie, T., 1955, ''On the Numerical Integration of a Parabolic Differential Equation Subject to a Moving Boundary Condition,'' Duke Math. J., **22**, pp. 557–571.

[8] Boley, B. A., 1968, ''A General Starting Solution for Melting and Solidifying Slabs,'' Int. J. Eng. Sci., **6**, 89.

[9] Atthey, D. R., 1975, ''A Finite Difference Scheme for Melting Problems Based on the Method of Weak Solutions,'' *Moving Boundary Problems in Heat Flow and Diffusion*, J. R., Ockendon, and W. R., Hodgkins, eds., Clarendon Press, Oxford, p. 182.

[10] Ockendon, J. R., 1975, ''Techniques of Analysis,'' *Moving Boundary Problems in Heat Flow and Diffusion*, J. R., Ockendon, and W. R., Hodgkins, eds., Clarendon Press, Oxford, p. 138.

[11] Voller, V., and Cross, M., 1981, ''Accurate Solutions of Moving Boundary Problems Using the Enthalpy Method,'' Int. J. Heat Mass Transfer, **24**, pp. 545–556.

[12] Celentano, D., and Pérez, E., 1996, ''A Phase-Change Temperature-Based Formulation Including General Latent Heat Effects,'' Int. J. Numer. Methods Heat Fluid Flow, **6**(8), pp. 71–79.

[13] Chang, S. C., and To, W. M., 1991, ''A New Numerical Framework for Solving Conservation Laws—The Method of Space-Time Conservation Element and Solution Element,'' NASA TM 104495.

[14] Chang, S. C., Wang, X. Y., and Chow, C. Y., 1999, ''The Space-Time Conservation Element and Solution Element Method: A New High Resolution and Genuinely Multidimensional Paradigm for Solving Conservation Laws,'' J. Comput. Phys., **156**, pp. 89–136.

[15] Chang, S. C., Wang, X. Y., and To, W. M., 2000, ''Application of the Space-Time Conservation Element and Solution Element Method to One-Dimensional Convection-Diffusion Problems,'' J. Comput. Phys., **165**, pp. 189–215.

[16] Wang, X. Y., Chow, C. Y., and Chang, S. C., 1998, ''The Space-Time Conservation Element and Solution Element Method—A New High-Resolution and Genuinely Multidimensional Paradigm for Solving Conservation Laws II, Numerical Simulation of Shock Waves and Contact Discontinuities,'' NASA/TM-1998-208844.

[17] Loh, C. Y., Hultgren, L. S., and Chang, S. C., 2001, ''Wave Computation in Incompressible Flow Using the Space-Time Conservation Element and Solution Element Method,'' AIAA J., **39**(5), pp. 794–801.

[18] Loh, C. Y., and Zaman, K. B. M. Q., 2002, ''Numerical Investigation of 'Transonic Resonance' With a Convergent-Divergent Nozzle,'' AIAA J., **40**(12), pp. 2393–2401.

[19] Wang, X. Y., Chang, S. C., and Jorgenson, P. C. E., 2000, ''Prediction of Sound Waves Propagating Through a Nozzle Without/With a Shock Wave Using the Space-Time CE/SE Method,'' AIAA Paper 2000-0222, presented at 38th AIAA Aerospace Sciences Meeting, Reno.

[20] Guo, Y., Hsu, A. T., Wu, J., Yang, Z., and Oyedrian, A., 2000, ''Extension of CE/SE Method to 2D Viscous Flows,'' *36th AIAA/ASME/SAE/ASEE Joint Propulsion Conference and Exhibit*, July 17–19, 2000.

[21] Chen, K. H., and Liu, N. S., 2000, ''Navier-Stokes Solution of the FLUX Code: A Module for the NCC Solver Using the Concept of Space-Time Conservation Element and Solution Element,'' AIAA 2000-0455.

[22] Molls, T., and Molls, F., 1998, ''Space-Time Conservation Method Applied to Saint Venant Equations,'' J. Hydraul. Eng., **125**(5), pp. 501–508.

[23] Yang, D., Yu, S. T., and Zhao, J., 2001, ''Convergence and Error Bound Analysis for the Space-Time CESE Method,'' Numer. Methods Partial Differ. Equ., **17**, pp. 64–78.

[24] Liu, N. S., and Chen, K. H., 1999, ''FLUX: An Alternative Flow Solver for the National Combustion Code,'' AIAA Paper, 99–1079.

[25] Chang, S. C., 1995, ''The Method of Space-Time Conservation Element and Solution Element—A New Approach for Solving the Navier-Stokes and Euler Equations,'' J. Comput. Phys., **119**, pp. 295–324.

[26] Chang, S. C., Yu, S. T., Himansu, A., Wang, X. Y., Chow, C. Y., and Loh, C. Y., 1996, *The Method of Space-Time Conservation Element and Solution Element—A New Paradigm for Numerical Solution of Conservation Laws*, Computational Fluid Dynamics Review, UK.

[27] Cockburn, B., 1999, ''Discontinuous Galerkin Methods for Convection Dominate Problems,'' *High-Order Methods for Computational Physics*, T. J., Barth, and H., Deconinck, eds., Springer, Berlin, pp. 69–224.

[28] Babuška, I., Baumann, C. E., and Oden, J. T., 1999, ''A Discontinuous hp Finite Element Method for Diffusion Problems: 1-D Analysis,'' Comput. Math. Appl., **37**, pp. 103–122.

[29] Engel, G., Garikipati, K., Hughes, T. J. R., Larson, M. G., Mazzei, L., and Taylor, R. L., 2002, ''Continuous/Discontinuous Finite Element Approximations of Fourth-Order Elliptic Problems in Structural and Continuum Mechanics With Applications to Thin Beams and Plates, and Strain Gradient Elasticity,'' Comput. Methods Appl. Mech. Eng., **191**, pp. 3669–3750.

[30] Ayasoufi, A., and Keith, T. G., 2003, ''Application of the Conservation Element and Solution Element Method in Numerical Modeling of Heat Conduction With Melting and/or Freezing,'' Int. J. Numer. Methods Heat Fluid Flow, **13**(4), pp. 448–472.

[31] Ayasoufi, A., and Keith, T. G., 2004, ''Application of the Conservation Element and Solution Element Method in Numerical Modeling of Axisymmetric Heat Conduction With Melting and/or Freezing,'' JSME Int. J., Ser. B, **47**(1), pp. 115–125.

[32] Wang, X. Y., and Chang, S. C., 1999, ''A 2D Non-Splitting Unstructured Triangular Mesh Euler Solver Based on the Space Time Conservation Element and Solution Element Method,'' Comput. Fluid Dyn. J., **8**(2), pp. 309–325.

[33] Zhang, Z. C., Yu, S. T., and Chang, S. C., 2002, ''A Space-Time Conservation Element and Solution Element Method for Solving the Two- and Three-Dimensional Unsteady Euler Equations Using Quadrilateral and Hexahedral Meshes,'' J. Comput. Phys., **175**, pp. 168–199.

[34] Liu, N. S., and Chen, K. H., 2001, ''An Alternative Flow Solver for the NCC—The FLUX Code and Its Algorithm,'' 39th AIAA Aerospace Sciences Meeting and Exhibit, Reno, NV.

[35] Lunardini, V. J., 1981, *Heat Transfer in Cold Climates*, Van Nostrand Reinhold, New York.

[36] Voller, V. R., and Swaminathan, R., 1991, ''General Source-Based Method for Solidification Phase Change,'' Numer. Heat Transfer, Part B, **19**, pp. 175–189.

Submicron Heat Transport Model in Silicon Accounting for Phonon Dispersion and Polarization

Sreekant V. J. Narumanchi
National Revewable Energy Laboratory,
1617 Cole Boulevard,
Golden, CO 80401

Jayathi Y. Murthy
School of Mechanical Engineering,
Purdue University,
585 Purdue Mall,
West Lafayette, IN 47907

Cristina H. Amon
Institute for Complex Engineered Systems and
Department of Mechanical Engineering,
Carnegie Mellon University,
5000 Forbes Avenue,
Pittsburgh, PA 15213

In recent years, the Boltzmann transport equation (BTE) has begun to be used for predicting thermal transport in dielectrics and semiconductors at the submicron scale. However, most published studies make a gray assumption and do not account for either dispersion or polarization. In this study, we propose a model based on the BTE, accounting for transverse acoustic and longitudinal acoustic phonons as well as optical phonons. This model incorporates realistic phonon dispersion curves for silicon. The interactions among the different phonon branches and different phonon frequencies are considered, and the proposed model satisfies energy conservation. Frequency-dependent relaxation times, obtained from perturbation theory, and accounting for phonon interaction rules, are used. In the present study, the BTE is numerically solved using a structured finite volume approach. For a problem involving a film with two boundaries at different temperatures, the numerical results match the analogous exact solutions from radiative transport literature for various acoustic thicknesses. For the same problem, the transient thermal response in the acoustically thick limit matches results from the solution to the parabolic Fourier diffusion equation. In the acoustically thick limit, the bulk experimental value of thermal conductivity of silicon at different temperatures is recovered from the model. Experimental in-plane thermal conductivity data for silicon thin films over a wide range of temperatures are also matched satisfactorily. [DOI: 10.1115/1.1833367]

Keywords: Conduction, Electronics, Heat Transfer, Microscale, Modeling, Nanoscale

Introduction

In recent years, the extreme miniaturization of integrated circuits has led to increasing concerns about the steady and unsteady thermal performance of microelectronic devices. It is now well-established that conventional Fourier analysis leads to erroneous thermal predictions when the mean free path of heat carriers is comparable to or larger than the characteristic domain size. This is also true when the time scale of interest is smaller than the relaxation time of the carriers [1,2]. When the system length scale is comparable to the carrier mean free path but larger than the carrier wavelength, and phase coherence effects are unimportant, the Boltzmann transport equation in the relaxation time approximation can be employed [3–6]. Phonons, which are quantized lattice vibrations [7,8], are the predominant energy carriers in semiconductors at room temperature.

Studies illustrating non-local spatial [9–11] and temporal [12,13] effects have been reported. A number of studies have employed the gray phonon Boltzmann transport equation (BTE) to study thermal transport in thin films [5,14,15] and superlattices [6,16–18]. The molecular dynamics approach is viable when the system consists of a few layers of atoms, and has been employed to study thermal transport in nanostructures [6]. Considerable effort has also been devoted to measure and predict in-plane thermal conductivity of single crystalline silicon thin films [6,19–23]. Studies have also been performed to examine Joule heating effects in semiconductor devices. Thermal predictions in submicron transistor thin films have been reported [24–26] by employing the two-fluid approach [27,28] to solve the phonon BTE. In this approach, the phonons are divided into propagating and reservoir modes. The propagating mode is responsible for energy transport, while the reservoir mode functions in a purely capacitative mode. Energy exchange between branches is restricted to interactions between the reservoir and propagating modes. However, this model is primarily a gray model in the sense that only a single phonon relaxation time and velocity are used. The unsteady hot spot problem with a gray assumption was recently studied [29].

The problem of self-heating in submicron transistors involves energy transfer between the energetic electrons and the acoustic and optical phonons. One issue of recent focus has been the proportion of energy transmitted by the electrons to the optical phonons and the acoustic phonons [30]. Pop et al. [31,32] have performed Monte Carlo studies simulating the energy deposition from the electrons to the different phonon branches. These studies are still not fully coupled [31,32], since the fully coupled electron and phonon BTE are not solved.

Two-dimensional simulations of concurrent electrical and thermal transport in semiconductor devices (GaAs metal–semiconductor field effect transistors and Si metal–oxide–semiconductor field effect transistors) have been reported [33–36]. The approach is to consider hydrodynamic equations for electron transport [37] and energy conservation equations for electrons and the different phonon modes (polarization branches). The equations are derived by taking moments of the Boltzmann equations, and are, hence, lower-order approximations. Again, frequency-dependent relaxation times are not considered. Additionally, an important simplifying assumption in these studies is that heat propagation by acoustic phonons is assumed to be through diffusion (Fourier law).

Studies have been presented on the phonon heat conduction in a free-standing quantum well [38] and semiconductor nanowires [39]. These studies incorporate modification of phonon dispersion due to phonon confinement effects and the resultant changes in the group velocities and relaxation times. The details of phonon-phonon interactions (three-phonon processes) are considered. However, they work with the bulk expression for the thermal conductivity, incorporating an average modified group velocity and a modified relaxation time.

Recently, a Monte Carlo study of steady state phonon transport

Contributed by the Heat Transfer Division for publication in the JOURNAL OF HEAT TRANSFER. Manuscript received by the Heat Transfer Division August 4, 2003; revision received September 28, 2004. Associate Editor: G. Chen.

in silicon thin films including phonon dispersion and polarization effects has appeared in the literature [40]. However, this study neglects the interaction between optical phonons and acoustic phonons. In semiconductors such as silicon, the group velocity of optical phonons is small and, hence, their contribution to thermal transport is negligible. However, the interaction between optical and acoustic phonons alters the effective relaxation rates of acoustic phonons [41], and hence, optical phonons must be considered even in steady state thermal predictions. In transient predictions, if optical phonons are assumed to act purely capacitatively, the inclusion of scattering to acoustic phonons is essential to allow them to recover the correct steady state behavior.

It is clear therefore that full phonon dispersion effects in submicron thermal transport have not been considered in the literature. In this study, we present a model based on the BTE which accounts for transverse and longitudinal acoustic phonons as well as optical phonons. The interactions among the different phonon branches and frequencies are described by frequency-dependent relaxation times. These relaxation times have been presented in the literature [42–44] and are obtained by perturbation theory techniques. The energy interchange among the different branches/frequencies is dictated by energy and wave vector conservation rules [38,42–44]. The BTE is solved by a structured finite volume approach. The results from the model are compared to exact solutions of the BTE. Bulk thermal conductivity of silicon is also predicted by the model and shown to match experimental values reasonably well. Also, in-plane thermal conductivity of doped and undoped silicon thin films of varying thicknesses are predicted over a range of temperatures and are shown to satisfactorily match experimental data.

The full phonon dispersion model has been applied to study the problem of self-heating in a submicron silicon on insulator transistor [45]. The thermal predictions are compared to those obtained from other simpler BTE-based models from the literature and considerable discrepancies are found [45]. The differences in model predictions are a result of simpler models not accounting adequately for the spectrum of relaxation times associated with self-heating. Energy due to self-heating must be scattered from the optical modes to the acoustic modes for transport. Energy is scattered preferentially to high-frequency longitudinal acoustic (LA) and transverse acoustic (TA) modes, and the predicted hot-spot temperature depends on the group velocity with which these phonons transport the energy away. Thus, dispersion and polarization effects as well as frequency-dependant relaxation times are critical for thermal predictions in applications where the phonon groups are substantially out of equilibrium with each other. In addition, the thermal problem associated with the transient electrostatic discharge phenomena [25] has been considered [46,47]. In these studies [46,47], the results from the full phonon dispersion model are compared to those obtained from Fourier diffusion and other simpler BTE-based models from the literature. Considerable discrepancies are found [46,47]. Simpler semi-gray models [24] have assigned optical and transverse acoustic phonons into a reservoir or capacitative mode, while longitudinal acoustic phonons have been assigned to a propagating mode. These choices govern the capacitance of the material being modeled and determine the temporal response in unsteady problems. Again, accounting for phonon polarization and dispersion is the only way to accurately capture the correct capacitance of the system.

Theory

Model Based on Boltzmann Transport Equation. The model is based on the solution to the BTE in the relaxation time approximation. In this approximation, the BTE may be written as [5]

$$\frac{\partial f_w}{\partial t} + \vec{v}_w \cdot \nabla f_w = \frac{f_w^0 - f_w}{\tau_w} \tag{1}$$

where w is the frequency, f_w is the frequency-dependent distribution function of phonons, $\vec{v}_w$ is the group velocity vector of the phonons, f_w^0 is the equilibrium distribution function, and τ_w is the frequency-dependent relaxation time of phonons. Defining the following quantities [26]

$$e_w'''(\vec{r},\hat{s},w) = \hbar w f_w D(w); \quad e_w'' = \int_{\Delta w_i} e_w''' dw$$
$$e_w = \int_{4\pi} e_w'' d\Omega; \quad e_w^0 = \frac{1}{4\pi}\int_{4\pi} e_w'' d\Omega = \frac{1}{4\pi} e_w \tag{2}$$

where e_w''' is the volumetric energy density per unit frequency per unit solid angle (J s/m^3 sr rad), e_w'' is the volumetric energy density per unit solid angle (J/m^3 sr) for a given frequency band, $\vec{r}$ is the position vector, and $\hat{s}$ is the unit direction vector. The quantity e_w is the volumetric energy density (J/m^3) in the band, and e_w^0 is the associated equilibrium volumetric energy density. $\hbar$ is the reduced Planck constant, and $D(w)$ is the phonon density of states. The frequency integration is done over a discrete frequency band Δw_i.

The bulk phonon dispersion curves for silicon at 300 K are shown in Fig. 1 for the [001] direction [48,49]. The phonon dispersion curves are different in different directions. In this study, as an approximation, the dispersion curves are assumed to be isotropic. The dispersion curves in the [001] direction are assumed to hold over all directions in k space, similar to assumptions made in earlier studies on thermal conductivity. In a given symmetry direction, silicon has three acoustic branches and three optical branches. Of the three acoustic branches, one is longitudinal and

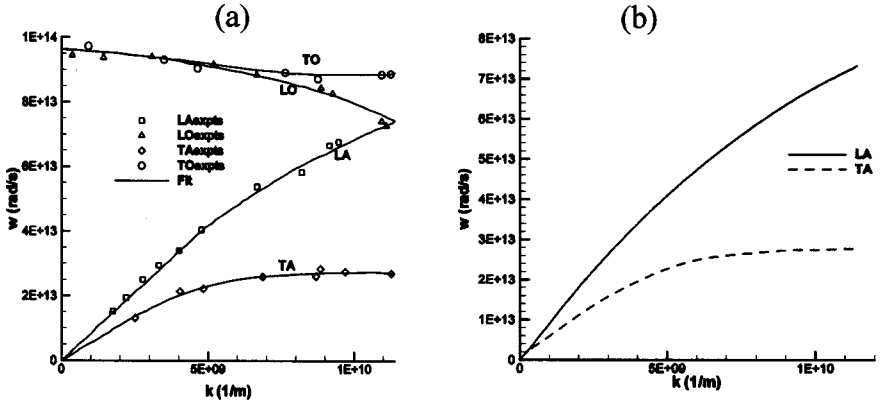

Fig. 1 (*a*) Experimental dispersion curve in the [001] direction in silicon at 300 K [48]; (*b*) spline curve fit to the LA and TA branches

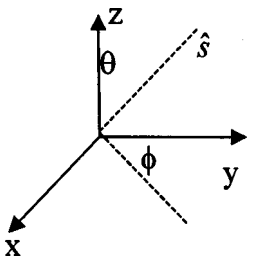

Fig. 2 Coordinates axes and representative phonon direction

two are degenerate transverse branches. Similarly, there is one longitudinal optical phonon branch and two degenerate transverse optical phonon branches. In the proposed model, only one frequency band is used for the optical phonon branch, while there are N_{LA} and N_{TA} bands in the LA and TA branches, respectively. The experimental dispersion curves for the LA and TA branches are fit by cubic splines and all relevant dispersion curve information (e.g., phonon group velocity, density of states) is extracted from these fits.

The optical mode for silicon has a negligible group velocity and therefore the ballistic term in Eq. (1) is absent. The BTE for the optical mode can be written as

$$\frac{\partial e_o}{\partial t} = \sum_{j=1}^{N\mathrm{bands}-1} \left(\int_{T_{\mathrm{ref}}}^{T_{oj}} C_o dT - e_o \right) \gamma_{oj} + q_{\mathrm{vol}} \tag{3}$$

where $e_o = \int_{T_{\mathrm{ref}}}^{T_o} C_o dT$, $\gamma_{oj} = \overline{(1/\tau_{oj})} = (1/\Delta w_o) \int_{\Delta w_o} (1/\tau_{oj}) dw$ is the band-averaged inverse relaxation time for the interaction between the optical phonons and the jth band of an acoustic branch, C_o is the optical mode specific heat, and the term q_{vol} is the volumetric heat generation. In microelectronics applications, it (q_{vol}) would represent the transfer of energy from the energetic electrons to the optical phonons (Joule heating). The optical mode corresponds to $j = N\mathrm{bands}$, and the summation on the right-hand side (rhs) of Eq. (3) represents the interaction with all acoustic bands.

In the development that follows, a number of ''temperatures'' are defined. Since thermodynamic temperature cannot be defined for systems that are not in equilibrium, these temperatures must properly be interpreted as measures of the corresponding energy. In this spirit, T_o is the temperature of the optical mode, T_{ref} is the reference temperature, T_{oj} is an *interaction* temperature specific to the optical mode and the jth band of the acoustic modes (either LA or TA) and is defined in Eq. (11). The significance of T_{oj} is that if the optical branch and the jth band of the acoustic branches (LA or TA) were the only bands exchanging energy, and ballistic and storage effects were absent, T_{oj} would be equilibrium ''temperature'' achieved by both bands.

The BTE for the ith frequency band of the acoustic branches (valid for both LA and TA) in the direction $\hat{s}$ (Fig. 2) is written as

$$\frac{\partial e_i''}{\partial t} + \nabla \cdot (v_i \hat{s} e_i'') = (e_i^0 - e_i'') \gamma_{ii} + \sum_{\substack{j=1 \\ j \neq i}}^{N\mathrm{bands}} \left\{ \left(\frac{1}{4\pi} \int_{T_{ref}}^{T_{ij}} C_i dT - e_i'' \right) \gamma_{ij} \right\} \tag{4}$$

$$v_i = \frac{1}{\Delta w_i} \int_{\Delta w_i} v_w dw; \quad C_i = \int_{\Delta w_i} C_{wi} dw;$$

$$e_i'' = \int_{\Delta w_i} \hbar w f_w D(w) dw; \tag{5}$$

$$\gamma_{ii} = \overline{(1/\tau_{ii})} = \frac{1}{\Delta w_i} \int_{\Delta w_i} \frac{1}{\tau_{ii}} dw; \quad \gamma_{ij} = \overline{(1/\tau_{ij})} = \frac{1}{\Delta w_i} \int_{\Delta w_i} \frac{1}{\tau_{ij}} dw$$

where v_i is the band-averaged group velocity, C_{wi} is the specific heat per unit frequency in band i, C_i is the band integrated specific heat, e_i'' the band integrated energy density per unit solid angle, γ_{ii} is the band-averaged inverse relaxation time for interaction of band i with itself, and γ_{ij} is the band-averaged inverse relaxation time for interaction of band i with band j. The first term on the rhs of Eq. 14 depicts scattering within a given frequency band, but across directions (elastic scattering). Physically, processes such as impurity scattering (described in detail in a later section) may be described by such a term. The second term on the rhs depicts the scattering from the ith band of the acoustic band considered to all other bands in all branches except to itself. T_{ij} again signifies an *interaction* temperature that the two bands i and j would attain if they were the only two bands exchanging energy. In order to satisfy energy conservation, the following two conditions are also satisfied

$$T_{ij} = T_{ji}; \quad \text{and} \quad \int_{\Delta w_i} \frac{1}{\tau_{ij}} dw = \int_{\Delta w_j} \frac{1}{\tau_{ji}} dw \tag{6}$$

where i is any frequency band in a given phonon branch and j is any other band in the same or different branch with which energy is being exchanged.

The equilibrium energy density is defined as

$$e_i^0 = \frac{1}{4\pi} \int_{4\pi} e_i'' d\Omega = \frac{1}{4\pi} \int_{T_{ref}}^{T_i} C_i dT = \frac{e_i}{4\pi} \tag{7}$$

where T_i is the temperature associated with the ith band of the branch considered.

Energy Conservation. In this section, we demonstrate that the model satisfies energy conservation. Integrating Eq. (4) over a solid angle of 4π and over all the frequency bands in the acoustic branches, and adding to Eq. (3), we obtain

$$\frac{\partial e_o}{\partial t} + \sum_{i=1}^{N\mathrm{bands}-1} \left(\frac{\partial e_i}{\partial t} + \nabla \cdot \vec{q}_i \right) - q_{\mathrm{vol}} = \sum_{j=1}^{N\mathrm{bands}-1} \left\{ \left(\int_{T_{ref}}^{T_{oj}} C_o dT - e_o \right) \gamma_{oj} \right\} + \sum_{i=1}^{N\mathrm{bands}-1} \sum_{\substack{j=1 \\ j \neq i}}^{N\mathrm{bands}} \left\{ \left(\frac{1}{4\pi} \int_{T_{\mathrm{ref}}}^{T_{ij}} C_i dT - e_i'' \right) \gamma_{ij} \right\} \tag{8}$$

where the flux associated with the ith band of any one of the acoustic branches is

$$\vec{q}_i = \int_{4\pi} v_i \hat{s} e_i'' d\Omega \tag{9}$$

For the optical band, the flux is zero. The left-hand side (lhs) of Eq. (8) may be written as

$$\frac{\partial e_{\mathrm{total}}}{\partial t} + \nabla \cdot \vec{q}_{\mathrm{total}} - q_{\mathrm{vol}} \quad \text{where} \quad e_{\mathrm{total}} = e_o + \sum_{i=1}^{N\mathrm{bands}-1} e_i;$$

$$\vec{q}_{\mathrm{total}} = \sum_{i=1}^{N\mathrm{bands}-1} \vec{q}_i \tag{10}$$

From the first law of thermodynamics, the lhs of Eq. (8) is zero, hence, the rhs of Eq. (8) should be zero. Thus

$$\int_{T_{\mathrm{ref}}}^{T_{ij}} \left(\frac{C_i}{\Delta w_i} + \frac{C_j}{\Delta w_j} \right) dT = \int_{T_{\mathrm{ref}}}^{T_i} \frac{C_i}{\Delta w_i} dT + \int_{T_{\mathrm{ref}}}^{T_j} \frac{C_j}{\Delta w_j} dT \tag{11}$$

This is satisfied for i and j band combinations including the optical phonon band. An overall lattice temperature, T_L may be de-

fined as follows. From the expression for e_{total} *in Eq.* (10):

$$e_{\text{total}} = \int_{T_{\text{ref}}}^{T_L} C_{\text{total}} dT = \int_{T_{\text{ref}}}^{T_o} C_o dT + \sum_{i=1}^{N\text{bands}-1} \left(\int_{T_{\text{ref}}}^{T_i} C_i dT \right) \tag{12}$$

where C_{total} is the total specific heat of the solid.

Acoustically Thick Limit Behavior. In this section, we derive the acoustically thick limit behavior of the model. In the spatially thick limit, the lhs of Eq. (4) is close to zero. Hence, we may write

$$e_i'' \left\{ \sum_{j=1}^{N\text{bands}} \gamma_{ij} \right\} \approx e_i^0 \gamma_{ii} + \sum_{\substack{j=1 \\ j \neq i}}^{N\text{bands}} \left\{ \left(\frac{1}{4\pi} \int_{T_{\text{ref}}}^{T_{ij}} C_i dT \right) \gamma_{ij} \right\} \tag{13}$$

Summing Eq. (13) over all solid angles (4π), we get

$$e_i \left\{ \sum_{j=1}^{N\text{bands}} \gamma_{ij} \right\} \approx e_i \gamma_{ii} + \sum_{\substack{j=1 \\ j \neq i}}^{N\text{bands}} \left\{ \left(\int_{T_{\text{ref}}}^{T_{ij}} C_i dT \right) \gamma_{ij} \right\} \tag{14}$$

Writing similar equations for each band in the acoustic branch and solving the equations in conjunction with Eq. (11), we obtain $T_i \approx T_{ij} \approx T_j \approx T_L$, for all i and j (see Appendix A). The spatial gradient of the energy density may be approximated as

$$\nabla e_i'' \approx \nabla e_i^0 = \nabla T_L \nabla_{T_L} e_i^0 = \nabla T_L \frac{C_i(T_L)}{4\pi} \tag{15}$$

Thus, Eq. (4) for a band i in one of the acoustic branches may be written as

$$\frac{\partial e_i''}{\partial t} + \nabla T_L \cdot \left(v_i \hat{s} \frac{C_i(T_L)}{4\pi} \right) = (e_i^0 - e_i'') \gamma_{ii} + \sum_{\substack{j=1 \\ j \neq i}}^{N\text{bands}} \left\{ \left(\frac{1}{4\pi} \int_{T_{\text{ref}}}^{T_{ij}} C_i dT - e_i'' \right) \gamma_{ij} \right\} \tag{16}$$

Multiplying Eq. (16) by $v_i \hat{s}$ and integrating over 4π yields

$$\frac{\partial \vec{q}_i}{\partial t} + \nabla T_L \cdot \left(v_i^2 \frac{C_i(T_L)}{4\pi} \frac{4\pi}{3} \delta \right) = -\vec{q}_i \left(\sum_{j=1}^{N\text{bands}} \gamma_{ij} \right) \tag{17}$$

where $\int_{4\pi} \hat{s}\hat{s} d\Omega = (4\pi/3)\delta$, δ is a unit tensor [50].

In the temporally thick limit, the time scale of interest is $t \gg \tau$, with τ being an estimate of the relaxation time of a frequency band i. The relaxation time of a band τ_i is defined as $1/\tau_i = \Sigma_{j=1}^{N\text{bands}} \gamma_{ij}$. In the temporally thick limit, $\partial \vec{q}_i / \partial t \ll \vec{q}_i / \tau$, implying that the transient term on the lhs of Eq. (17) may be dropped, yielding

$$\nabla T_L \cdot \left(v_i^2 \frac{C_i(T_L)}{4\pi} \frac{4\pi}{3} \delta \right) = -\vec{q}_i \left(\sum_{j=1}^{N\text{bands}} \gamma_{ij} \right) \tag{18}$$

Hence, the total heat flux may now be obtained by summing over all the acoustic phonon band fluxes, $\vec{q}_i$:

$$\vec{q}_{\text{total}} = \sum_{i=1}^{N\text{bands}-1} \vec{q}_i = -K \nabla T_L$$

where

$$K = \sum_{i=1}^{N\text{bands}-1} \frac{1}{3} \frac{v_i^2 C_i(T_L)}{\left(\sum_{j=1}^{N\text{bands}} \gamma_{ij} \right)} \tag{19}$$

Thus, in the spatially and temporally thick limit, the energy conservation equation [Eq. (8)] reduces to the form

$$C_{\text{total}} \frac{\partial T_L}{\partial t} = \nabla \cdot (K \nabla T_L) + q_{\text{vol}} \tag{20}$$

This is simply the parabolic Fourier diffusion equation.

Volumetric Specific Heat. The contribution of the acoustic phonons to the energy density of a solid may be expressed as [7]:

$$u = \sum_p \frac{d\vec{k}}{(2\pi)^3} \frac{\hbar w}{(e^{\hbar w / k_B T} - 1)} \tag{21}$$

where $d\vec{k}$ denotes the elemental Brillouin zone volume, k_B is the Boltzmann constant, T is temperature in K, and the summation p is over the acoustic phonon branches. Assuming the Brillouin zone is a sphere of radius k, $d\vec{k} = 4\pi k^2 dk$ and the specific heat C is

$$C = \frac{du}{dT} = \sum_p \int \frac{\hbar^2 w^2 k^2 e^{\hbar w / k_B T} dk}{2\pi^2 k_B T^2 (e^{\hbar w / k_B T} - 1)^2} \tag{22}$$

The contribution to the specific heat due to a band i in any acoustic branch may be expressed as

$$C_i = \int_{\Delta k} \frac{\hbar^2 w^2 k^2 e^{\hbar w / k_B T} dk}{2\pi^2 k_B T^2 (e^{\hbar w / k_B T} - 1)^2} \tag{23}$$

where Δk is the width of the wavevector corresponding to the frequency limits (Δw) of that particular band. For the total specific heat due to acoustic modes in silicon, the k range extends from zero to k_{edge}, where $k_{\text{edge}} (= 1.139\,57 \times 10^{10}\ \text{m}^{-1})$ is the phonon wave vector value at the edge of the Brillouin zone [Fig. 1(*b*)]. The frequency of the LA branch at the edge of the zone is $w_L = 7.46 \times 10^{13}$ rad/s, while for the TA branch $w_T = 2.7856 \times 10^{13}$ rad/s. The optical band is considered to be centered at a frequency of 9.0×10^{13} rad/s with $\Delta w = 1.5 \times 10^{13}$ rad/s. As mentioned earlier, a spline fit is used to obtain a w-k representation of the experimental dispersion curve. This equation is used to obtain C_i for each band in the acoustic branch, and hence the total C due to the acoustic modes. The contribution of the three optical phonon modes in the Einstein approximation [7] is

$$C_o = \int_{\Delta w_o} C_{wo} dw = 3 \frac{k_B}{V} \left(\frac{\hbar w_o}{k_B T} \right)^2 \frac{e^{\hbar w_o / k_B T}}{(e^{\hbar w_o / k_B T} - 1)^2} \tag{24}$$

where w_o is the frequency chosen for the optical mode (9.0×10^{13} rad/s in this study), C_{wo} is the volumetric specific heat of the optical modes per unit frequency, and V is the volume of a primitive cell, given by $V = (a^3/4)$, and $a = 5.43\,A^0$ for silicon [7]. Figure 3 shows the computed specific heat (total, LA, TA, and O contribution). The experimental specific heats [51] are also plotted. A good match is obtained over a wide range of temperatures.

Relaxation Rates

Impurity Scattering. The impurity or isotope scattering mechanism arises from the presence of atoms with different mass. The relaxation time for this type of scattering is given by [42,43,52–54]:

$$\frac{1}{\tau_I} = \frac{\pi}{6} \Gamma V D(w) w^2; \quad \Gamma = \sum_i f_i [1 - (M_i / M)]^2 \tag{25}$$

where M_i is the mass of an atom, M is the mass of the host atom, f_i is the fractional content of atoms with mass M_i, which is different from M, the scattering parameter $\Gamma = 2.64 \times 10^{-4}$ [38] for the three Si isotopes, V is the volume per host atom, and $D(w)$ is the phonon density of states. Impurity scattering is an elastic scattering process, i.e. the frequency of the scattered phonon remains unaltered. This type of scattering is included in the term γ_{ii} in Eq. (4) by averaging Eq. (25) over the frequency band.

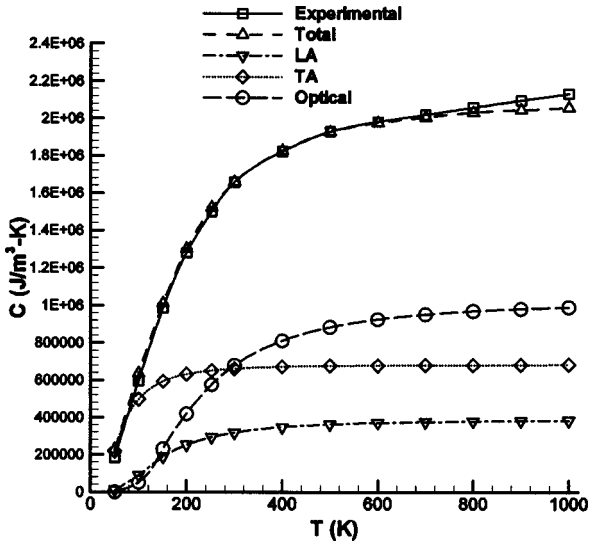

Fig. 3 Volumetric specific heat of silicon at different temperatures

Three-Phonon Interactions. There are two types three phonon processes—Normal (*N*) processes and Umpklapp (*U*) processes. There is a considerable literature on the role of these processes in thermal conductivity [42,43]. *U* processes pose direct thermal resistance while *N* processes influence thermal resistance by altering the phonon distribution. Three-phonon processes must satisfy energy (frequency) and wave vector (momentum) conservation rules [42–44]. Energy and momentum conservation are expressed by

$$w+w'=w'' \quad (\text{energy or frequency})$$
$$k+k'=k'' \quad (N \text{ processes}); \quad k+k'=k''+b \quad (U \text{ processes}) \tag{26}$$

where w, w', and w'' are phonon frequencies, k, k', and k'' are the phonon wave vectors and b is the reciprocal lattice vector.

At higher temperatures (room temperature and above) in silicon, *U* processes are expected to be dominant [43]. In a semiconductor like silicon, the following three-phonon processes are believed to be important

$$\text{L+T}\leftrightarrow\text{L}; \quad \text{T+T}\leftrightarrow\text{L}; \quad \text{T+L}\leftrightarrow\text{L}$$
$$\text{L+T}\leftrightarrow\text{O}; \quad \text{L+L}\leftrightarrow\text{O}; \quad \text{T+L}\leftrightarrow\text{O} \tag{27}$$

where L denotes LA, T denotes TA, and O the optical mode.

Expressions for the relaxation rates for some of the *U* processes in Eq. (27) have been presented in Ref. [44] and have also been employed in Ref. [38]. The relaxation time associated with the energy exchange between frequencies i and j for processes of the type L+T↔L and T+T↔L is given by

$$\frac{1}{\tau_{ij}} \approx \frac{2\gamma^2\hbar}{3\pi\rho v_{\text{ph}}^2 v_g} w_i w_T w_j r_c^2 \left[\frac{1}{(e^{\hbar w_T/k_B T}-1)} - \frac{1}{(e^{\hbar w_j/k_B T}-1)}\right] \tag{28}$$

where i refers to the first mode (e.g., mode L on the lhs in L+T↔L) and j refers to the resultant mode (e.g., mode L on the rhs in L+T↔L), v_{ph} is the phase velocity of the thermal mode (the mode with frequency w_i), $v_g=|\partial w_j/\partial q_j|$ at $w_j=w_i+w_T$ in the direction of the reciprocal lattice vector b, γ is the Gruneisen constant and is an adjustable parameter, ρ is the density of the solid, w_i is the frequency of the thermal mode, w_T is the frequency of the transverse branch at the edge of the first Brillouin zone, T is the lattice temperature in K. A single γ, which is independent of polarization and wave vector, is used. The treatment of r_c is the same as in Ref. [44]. It is important to note that in principle these terms can be employed at any temperature [38]; however, the computation of r_c in Ref. [38] is valid only for low to intermediate temperatures. For example, in Eq. (28), the T mode in the process L+T↔L is taken to be at the edge of the Brillouin zone [38,44]. This assumption is valid only if the wavevector of the L mode in the lhs of L+T↔L is low. In order to conserve momentum (or wave vector) for this *U* process, the second mode (T) must lie at the edge of the zone boundary. This assumption is not in general valid at high temperatures, but relaxing it would require the direct implementation of energy and momentum conservation rules, and is not attempted here. The relaxation rate for energy exchange between bands i and j for processes of the type T+L↔L is given by

$$\frac{1}{\tau_{ij}} \approx \frac{\gamma^2\hbar}{3\pi\rho v_{\text{ph}}^2 v_g} w_i w_j w_L r_c^2 \left[\frac{1}{(e^{\hbar w_j/k_B T}-1)} - \frac{1}{(e^{\hbar w_L/k_B T}-1)}\right] \tag{29}$$

where i refers to the T mode on the lhs in T+L↔L, and j refers to mode L on LHS in T+L↔L, v_{ph} is the phase velocity of the thermal mode (mode T), and v_g is the group velocity evaluated at $w_j=w_L-w_i$. Here w_i is the frequency of the thermal mode and w_L is the frequency of the longitudinal mode at the edge of the first Brillouin zone (the mode L on the rhs in T+L↔L). The relaxation rate expression for processes of the type T+L↔O, L+L↔O and L+T↔O is [44]

$$\frac{1}{\tau_{ij}} \approx \frac{\gamma^2\hbar}{3\pi\rho v_{\text{ph}}^2 v_g^3} w_i w_j^3 w_o \left[\frac{1}{(e^{\hbar w_j/k_B T}-1)} - \frac{1}{(e^{\hbar w_o/k_B T}-1)}\right] \tag{30}$$

where i refers to the first mode and j refers to the second mode on the lhs of the interactions T+L↔O, L+L↔O, L+T↔O, v_{ph} is the phase velocity of the thermal mode (mode i), $v_g=|\partial w_j/\partial q_j|$ at $w_j=w_o-w_i$, and w_o is the optical mode frequency. The expressions in Eqs. (28)–(30) involve discrete frequencies. In the present model, the BTE is solved for frequency bands of finite width. Hence, the expressions are integrated and then averaged over appropriate frequency bands. The procedure is explained in Appendix B. All possible interactions between the two bands i and j through any of the processes described in Eq. (27) are considered.

Numerical Solution

The finite volume method [55–57] is employed to solve the two-dimensional (2D) BTE. The spatial domain is discretized into rectangular control volumes, with the angular domain at any spatial point discretized into nonoverlapping control angles; the centroid of each control angle is denoted by the direction vector $\hat{s}$ (Fig. 2). Each octant is divided into $N_\theta X N_\phi$ control angles. The details of the discretization procedure are described in Refs. [56], [57]. The transient term in the BTE [Eqs. (3) and (4)] is treated using a fully implicit scheme, while the third order accurate SMART scheme [58,59] is used to treat the ballistic term. Each discrete angular direction in each frequency band results in a linear set of algebraic equations, which are solved using the tridiagonal matrix algorithm [55]. The directions themselves are solved sequentially using Picard iteration.

Boundary Conditions. The treatment of specular and diffuse boundaries is similar to that described in Refs. [29], [46]. In this study, boundary scattering is considered elastic, implying that the phonons in one frequency band remain in that band upon reflection.

Results

Steady One-Dimensional Transport Between Parallel Plates. To test the model, comparisons are made between the steady state solution to the BTE and the published literature [50] for the problem of one-dimensional (1D) radiation between parallel plates. In

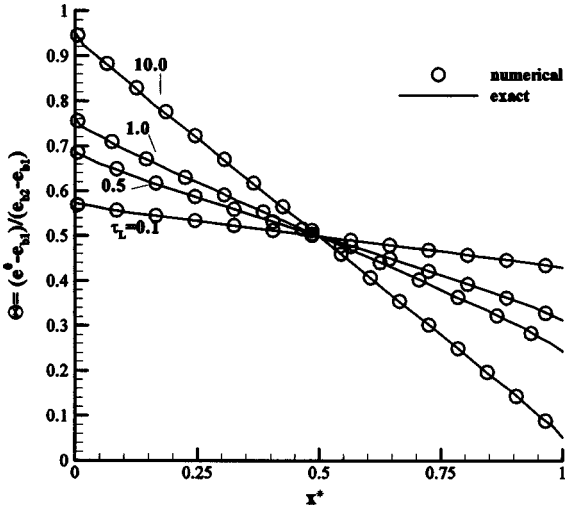

Fig. 4 Steady 1D transport between parallel plates

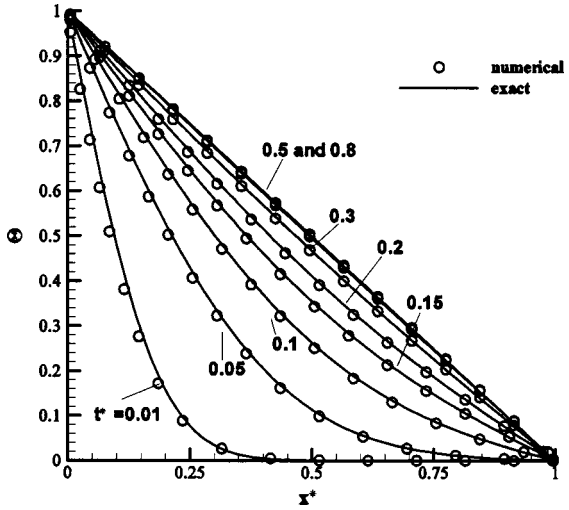

Fig. 5 1D transient diffusion with one spectral band

the solution to the BTE, only one band is considered and its interaction with the other bands/branches is turned off. This is done so that the BTE resembles the radiative transfer equation. The radiation problem involves two infinite black parallel plates, maintained at different constant temperatures T_1 and T_2, containing an absorbing emitting medium in between them. The results for the nondimensionalized energy densities, $\Theta=(e^0-e_{b1})/(e_{b2}-e_{b1})$ is plotted in Fig. 4 for a range of acoustic thicknesses ($\tau_L=L/v\tau$). A mesh of 100 spatial cells is used and the angular resolution is 8×8 in the octant. Refinement of the spatial and angular discretization does not alter results by more than 0.5%. The numerical solution matches well with exact solutions [50] for a wide range of acoustic thicknesses.

1D Transient Diffusion. In order to study the limiting behavior of the model, the 1D transient BTE is solved in the spatially and temporally thick limit. The results should match those obtained from the 1D transient parabolic Fourier diffusion equation given by

$$C\frac{\partial T}{\partial t}=K\frac{\partial^2 T}{\partial x^2} \tag{31}$$

where C is the total volumetric specific heat (J/m^3 K) (Fig. 3), and K is the thermal conductivity obtained from Eq. (19). The results presented here are for the case of one band and the case 3×3×1 bands (i.e., three LA, three TA, and one optical band). In the first case, since only one band is considered, cross-band interaction terms are absent [Eq. (4)]. For the second case (3×3×1), however, crossband interactions are present.

Single Band Case. In this case, the parameters are chosen so the acoustic thickness of the problem is 100. The time step is chosen to be $0.001\tau_{\text{diff}}$, where $\tau_{\text{diff}}=L^2C/K$ is the diffusion time constant. The time step is chosen to satisfy $\tau\ll\Delta t\ll\tau_{\text{diff}}$. As before, 100 spatial cells are used and the angular resolution is 8×8 in the octant. In Fig. 5, results at nondimensionalized time instants $t^*(=t/\tau_{\text{diff}})$ are shown. The results indicate a good match between solutions to the BTE and the exact solution to Eq. (31) for all the time instants. The small discrepancies, especially at the earlier time instants ($t^*=0.01$) may be ascribed to the finite acoustic thickness used in the BTE simulations.

Multiple Bands (3×3×1). This is a case in which there are three LA bands, three TA bands, and one optical band. The relaxation times are chosen so that each frequency band has an acoustic thickness greater than 80 and the reciprocity prescribed by Eq. (6) is satisfied. The effective inverse relaxation time for a frequency band is given by $1/\tau_i=\Sigma_{j=1}^{N\text{bands}}\gamma_{ij}$, and the acoustic thickness for the band is $\tau_{Li}=L/v_i\tau_i$, where v_i is the band-averaged group velocity obtained from the actual phonon dispersion curve (Fig. 1). Again the time step chosen is $0.001\tau_{\text{diff}}$ and satisfies $\tau\ll\Delta t\ll\tau_{\text{diff}}$, with τ representing the effective relaxation time. Spatial and angular resolution is the same as for the one-band case. Figure 6 compares the solutions obtained from the BTE to the exact solutions. A good match is obtained between the solutions to the BTE and the exact solutions at all time instants. The seven band temperatures (three LA, three TA, and one optical) along with the overall lattice temperature are plotted in Fig. 6. At each time instant, all the band temperatures are seen to have collapsed onto the lattice temperature, as predicted by the analysis in the spatially and temporally thick limit. The slight discrepancy with respect to the exact solutions may again be ascribed to the finite acoustic thickness of the problem.

Bulk Silicon Thermal Conductivity. It is important to note that in the results presented up to this point, the relaxation times have been prescribed so as to yield the desired acoustic thickness. In this section, the aim is to predict the variation of bulk thermal conductivity of silicon with temperature. The relaxation times are obtained by the model described in Eqs. (25)–(30). A single value of the Gruneisen constant (γ) of 0.59 is assumed here. Since a pure sample of single crystal silicon is considered, isotope scat-

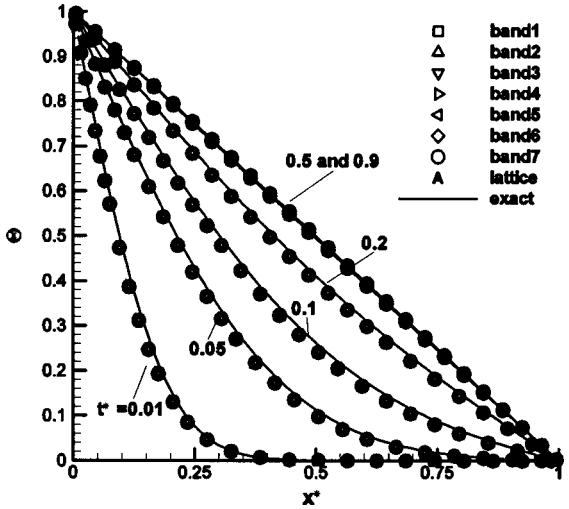

Fig. 6 1D transient diffusion, with 3×3×1 spectral bands

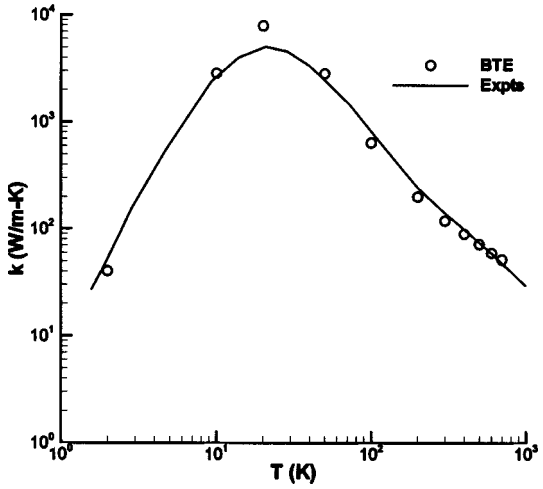

Fig. 7 Bulk thermal conductivity of silicon at different temperatures; experimental data from Holland [49]

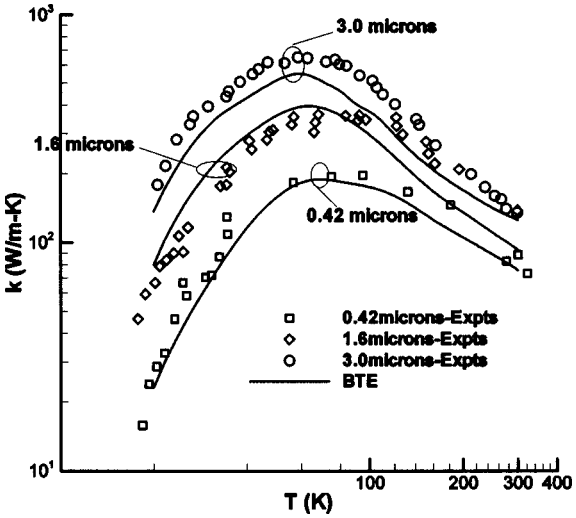

Fig. 8 Undoped silicon thin film in-plane thermal conductivity; experimental data are from Asheghi et al. [20] (for the 0.42 and 1.6 μm films), and from Asheghi et al. [21] (for the 3.0 μm film)

tering [42,43,52,53] is the only form of impurity scattering considered [Eq. (25)]. *U* processes are the only three-phonon processes considered [Eqs. (28)–(30)]. The details of the relaxation time treatment has been described in the earlier sections. For the thermal conductivity computations, 150 spatial cells are used; the angular resolution in the octant is 8×8. The number of frequency bands is 6×6×1. This frequency band discretization yields results with a numerical accuracy of about 3%. The boundary scattering treatment is similar to that presented in Ref. [49]. The relaxation time due to boundary scattering is incorporated as [49]

$$\frac{1}{\tau_b} = \frac{v}{LF} \tag{32}$$

where $v = 6400\ \mathrm{ms}^{-1}$, $L = 0.716$ cm, $F = 0.8$ [49]. L is to be construed as an equivalent sample size [$L = (2/\sqrt{\pi})\sqrt{l_1 l_2}$, where $l_1 l_2$ is the sample cross section area [49], $l_1 = l_2 = 0.00635$ m], and F is a geometric factor. The factor F represents a correction due to both the smoothness of the surface and the finite length to thickness of the sample [49]. A frequency-dependent group velocity was employed in Eq. (32), and the results were well within 1% of the results obtained from using a single velocity of 6400 ms^{-1} in Eq. (32). Boundary scattering is incorporated by adding the term $[(e_i^0 - e_i'')/\tau_b]$ on the rhs of Eq. (4). If boundary scattering were to be modeled more rigorously, a three-dimensional simulation of the bulk silicon sample would be required. Such an approach would be intensive computationally. Hence, as an approximation, boundary scattering is incorporated as a volumetric scattering term. The thermal conductivity is extracted by computing the total phonon energy flux at the boundary, and is presented in Fig. 7 for a wide range of temperatures. A reasonable match is found with experimental data [49]. The relaxation times for three-phonon processes are strictly appropriate only for temperatures>300 K ($T > 0.5T_{\mathrm{Debye}}$ for silicon [43]), since *U* processes are the only three-phonon processes considered. Nevertheless, the computations are seen to match low-temperature data quite well. This is because, at low temperatures, the thermal conductivity is dominated by isotope and boundary scattering processes.

Undoped Silicon Thin Films. The model is used to predict in-plane thermal conductivity for undoped silicon thin films for which experimental data have been reported in [20–23]. A 2D domain is considered. The top and bottom boundary of the domain are considered reflecting. The degree of specularity is given by a factor p; $p = 1.0$ indicates a completely specular interface, while $p = 0$ indicates a completely diffuse interface. A small temperature difference is maintained across the side boundaries, which are maintained at constant temperature. Thermal conductivity is extracted by computing the phonon energy flux across the boundaries. For the BTE simulations, 100 cells are used in the in-plane direction. The angular discretization is 8×8 in the octant, while the frequency discretization is 6×6×1. This numerical mesh yields an accuracy of 3%–4%. Figure 8 shows the thermal conductivity data for three different films of thicknesses 0.42, 1.6, and 3.0 μm, along with the predictions from the numerical solution to the full phonon dispersion BTE model. The experimental data for the 0.42 and 1.6 μm films are taken from Ref. [20], while the 3.0 μm film data comes from Ref. [21]. A specularity parameter of $p = 0.4$ appears to give a reasonable match between the BTE results and the experimental data for all three films over a range of temperatures. Mazumder and Majumdar [40] have used a p value of 0.6 to obtain a match between their numerical results and experimental data for the undoped 3.0-μm-thick silicon film.

Doped Silicon Thin Films. We now attempt to match the experimental thermal conductivity data of boron-doped 3.0-μm-thick silicon films [21]. We follow the same simplified approach for the additional dopant impurity scattering as Mazumder and Majumdar [40]. The relaxation time for dopant scattering is given

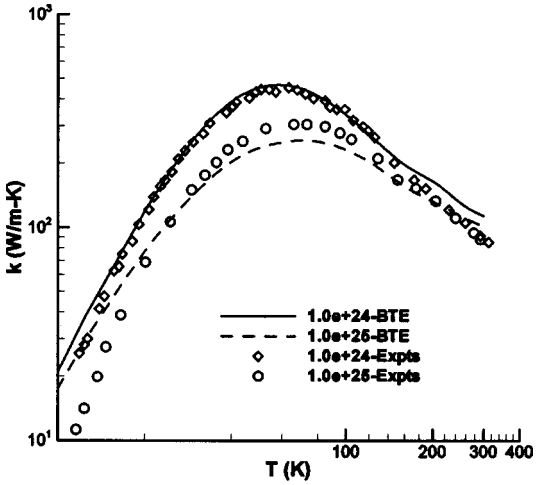

Fig. 9 Doped 3.0 μm silicon thin film in-plane thermal conductivity; experimental data are from Asheghi et al. [21]

by $\tau^{-1}=\alpha\sigma\rho v_g$, where α is a constant which is empirically determined to give the best fit to the experimental data, σ is the scattering cross section [40], ρ is the density of the solid, and v_g is the phonon group velocity. The value of the constant we use is 50. This value differs from that used in Ref. [40] because of the differences in other relaxation times used in the two studies. The numerical mesh is the same as for the case of undoped thin films. The corresponding results are shown in Fig. 9. We show results for two different dopant (boron) concentrations—$1.0e+24$ and $1.0e+25$ atoms/m^3. Given the approximate nature of the relaxation time expression for dopant impurity scattering, the match between experimental data and the BTE results over a wide range of temperatures is fair.

Summary and Conclusions

A comprehensive model based on the solution to the BTE has been presented. This model incorporates longitudinal acoustic, transverse acoustic and optical phonons, and considers the interactions between them via frequency-dependent relaxation times. Selection rules involving frequency (energy) conservation have been incorporated and the model satisfies energy conservation. The limiting behavior of the model has been examined. Numerical results from the model compare favorably with exact solutions for both steady and transient cases. The numerical results for the bulk thermal conductivity of silicon compare well with experimental data over a wide range of temperatures. In-plane experimental thermal conductivity data for doped and undoped silicon thin films of varying thicknesses are matched satisfactorily over a wide range of temperatures. The model can be applied to a wide variety of problems involving heat conduction at micro/nanoscales, particularly in problems where the phonon groups are substantially out of equilibrium with each other.

Acknowledgments

One of the authors (S.N.) acknowledges helpful comments by Dr. P. G. Klemens regarding relaxation times in silicon. The authors gratefully acknowledge the support of the NSF Grant Nos. CTS-0103082, CTS-0312420, and CTS-0219008, and the Pennsylvania Infrastructure Technology Alliance (PITA), a partnership of Carnegie Mellon University, Lehigh University and the Commonwealth of Pennsylvania's Department of Community and Economic Development.

Nomenclature

a = Lattice constant (m)
b = Reciprocal lattice vector (m^{-1})
C = Total volumetric heat capacity (J/m^3 K)
C_w = Volumetric specific heat per unit frequency (J s/m^3 K)
$D(w)$ = Phonon density of states (m^{-3})
e_{total} = Total energy (J/m^3)
f_i = Fraction of atoms with mass M_i
f_w = Phonon distribution function
$\hbar$ = Reduced Planck's constant [$=h/(2\pi)$,1.054 $\times 10^{-34}$ J s]
$\vec{k}$ = Wave vector
k_B = Boltzmann's constant ($1.38e-23$ J/K)
k, k', k'' = Phonon wave vectors (m^{-1})
K = Thermal conductivity (W/m K)
M_i = Mass of atom i different from host atom
N_{LA}, N_{TA} = Number of frequency bands in LA and TA branches
Nbands = Total number of frequency bands ($N_{\text{LA}}+N_{\text{TA}}+1$)
N_θ, N_ϕ = Number of θ and ϕ divisions in an octant
q_{vol} = Volumetric heat generation (W/m^3)
$\vec{r}$ = Position vector (m)
r_c = Parameter describing area of interacting surface (m)
$\hat{s}$ = Unit direction vector
t = Time (s)
T = Temperature (K)
u = Volumetric energy density (J/m^3)
v = Phonon velocity (m/s)
V = Volume of a primitive cell (m^3)
w = Phonon frequency (rad/s)
x = Distance along the x direction (m)

Greek symbols

Δw = Frequency bandwidth (rad/s)
Δt = Time step (s)
Δk = Width of wave vector band (m^{-1})
δ = Unit tensor
Γ = Scattering parameter
ϕ = Azimuthal angle
γ = Gruneisen constant
γ_{ij} = Band-averaged inverse relaxation time for interaction (s^{-1})
ρ = Density of solid (kg/m^3)
τ = Relaxation time of a phonon (s)
θ = Polar angle (deg)
Θ = Dimensionless temperature, energy density

Subscripts

$b1$, $b2$ = Boundaries
i = ith frequency band
ij = Property specific to bands i and j
L = Lattice
o = Optical mode
P = Propagating mode
R = Reservoir mode
w = Phonon frequency

Superscripts

0 = Equilibrium condition

Appendix A

The lhs of Eq. (4) is small in the acoustically thick limit. Dropping the lhs and integrating over all solid angles, the equation for a frequency band i may be written as

$$\left(\int_{T_{\text{ref}}}^{T_i} C_i dT\right)\left\{\sum_{j=1}^{N\text{bands}} \gamma_{ij}\right\} \approx \left(\int_{T_{\text{ref}}}^{T_i} C_i dT\right)\gamma_{ii} + \sum_{\substack{j=1 \\ j\neq i}}^{N\text{bands}} \left\{\left(\int_{T_{\text{ref}}}^{T_{ij}} C_i dT\right)\gamma_{ij}\right\} \tag{A1}$$

From Eq. (11)

$$\int_{T_{\text{ref}}}^{T_{ij}}\left(\frac{C_i}{\Delta w_i}+\frac{C_j}{\Delta w_j}\right)dT = \int_{T_{\text{ref}}}^{T_i}\frac{C_i}{\Delta w_i}dT + \int_{T_{\text{ref}}}^{T_j}\frac{C_j}{\Delta w_j}dT, \quad \text{i}\neq\text{j} \tag{A2}$$

Defining the variables

$$\beta_i = \int_{T_{\text{ref}}}^{T_i} C_i dT; \quad \beta_{ij} = \int_{T_{\text{ref}}}^{T_{ij}} C_i dT \tag{A3}$$

Equations (A1)–(A2) may be written for all bands, leading to a homogeneous set of equations in β_i and β_{ij}:

$$A\beta = 0 \tag{A4}$$

Here $\beta=(\beta_1,\beta_{12},\beta_{13},\ldots\beta_{1N\text{bands}},\ldots\beta_i,\beta_{i2},\beta_{i3},\ldots\beta_{iN\text{bands}},\ldots)^T$.

Since $|A| \neq 0$, the only solution to Eq. (*A*4) is $\beta_i = \beta_{ij} = 0$ for all i and j with $i \neq j$. Since $C_i \neq 0$, $T_i = T_{ij} = T_j$. From Eq. (12), it follows that $T_i = T_{ij} = T_j = T_L$, for all $i, j, i \neq j$.

Appendix B

As an example, consider the computation of the band-averaged relaxation time for a frequency band i due to a process of the type L+T↔L. Here, the frequency band i is on the LA branch (on the lhs of L+T↔L), the band j is on the LA branch (on the rhs of L+T↔L) and the highest frequency band of the TA branch-constitutes the third interacting band (the mode T in L+T↔L). The frequency-dependent relaxation time is given by Eq. (28). Recall that conservation rules require

$$w_j = w_i + w_T \tag{B1}$$

Thus, only those frequencies in bands i and j can interact for which Eq. (*B*1) is satisfied.

The contribution of this interaction to the relaxation time of the ith band is computed as

$$\frac{1}{\tau} = \int_{\Delta w_{\text{overlap}}} \frac{2\gamma^2 \hbar}{3\pi\rho v_{\text{ph}}^2 v_g} w_i w_T (w_i + w_T) r_c^2 * \left[\frac{1}{(e^{\hbar w_T / k_B T} - 1)} - \frac{1}{(e^{\hbar (w_i + w_T)/k_B T} - 1)} \right] dw_i \tag{B2}$$

Here, $\Delta w_{\text{overlap}}$ represents that portion of the band Δw_i which overlaps band Δw_j when band Δw_i is translated by w_T. This is also considered a contribution to the relaxation time of band j, as well as to the relaxation time of the highest frequency band in the TA branch. Contributions of this type are obtained for all such possible processes. The net band-averaged inverse relaxation time for all three-phonon interactions between bands i and j is found from

$$\gamma_{ij} = \frac{1}{\Delta w_i} \sum \frac{1}{\tau} \tag{B3}$$

Equation (*B*3) assumes parallel channels for energy exchange between the bands (Mathiessen's rule).

References

[1] Flik, M. I., Choi, B. I., and Goodson, K. E., 1992, "Heat Transfer Regimes in Microstructures," ASME J. Heat Transfer, **114**, pp. 666–674.

[2] Majumdar, A., 1998, "Microscale Energy Transport in Solids," in *Microscale Energy Transport*, Tien, C.-L., Majumdar, A., and Gerner, F. M., eds., Taylor and Francis, Washington, D.C., pp. 1–94.

[3] Chen, G., 1999, "Phonon Wave Heat Conduction in Thin Films and Superlattices," J. Heat Transfer, **121**, pp. 945–953.

[4] Chen, G., 2000, "Particularities of Heat Conduction in Nanostructures," J. Nanopart. Res., **2**, pp. 199–204.

[5] Majumdar, A., 1993, "Microscale Heat Conduction in Dielectric Thin Films," ASME J. Heat Transfer, **115**, pp. 7–16.

[6] Cahill, D. G., Ford, W. K., Goodson, K. E., Mahan, G. D., Majumdar, A., Maris, H. J., Merlin, R., and Phillpot, S. R., 2003, "Nanoscale Thermal Transport," J. Appl. Phys., **93**(2), pp. 793–818.

[7] Ashcroft, N. W., and Mermin, N. D., 1976, *Solid State Physics*, Saunders, Philadelphia.

[8] Kittel, C., 1996, *Introduction to Solid State Physics*, Wiley, New York.

[9] Mahan, G. D., and Claro, F., 1988, "Nonlocal Theory of Thermal Conductivity," Phys. Rev. B, **38**(3), pp. 1963–1969.

[10] Claro, F., and Mahan, G. D., 1989, "Transient Heat Transport in Solids," J. Appl. Phys., **66**(9), pp. 4213–4217.

[11] Chen, G., 1996, "Nonlocal and Nonequilibrium Heat Conduction in the Vicinity of Nanoparticles," ASME J. Heat Transfer, **118**, pp. 539–545.

[12] Qiu, T. Q., and Tien, C. L., 1993, "Heat Transfer Mechanisms During Short-Pulse Laser Heating of Metals," ASME J. Heat Transfer, **115**, pp. 835–841.

[13] Qiu, T. Q., and Tien, C. L., 1994, "Femtosecond Laser Heating of Multi-Layer Metals—I. Analysis," Int. J. Heat Mass Transfer, **37**(17), pp. 2789–2797.

[14] Joshi, A. A., and Majumdar, A., 1993, "Transient Ballistic and Diffusive Phonon Transport in Thin Films," J. Appl. Phys., **74**(1), pp. 31–39.

[15] Goodson, K. E., 1996, "Thermal Conduction in Nonhomogeneous CVD Diamond Layers in Electronic Microstructures," ASME J. Heat Transfer, **118**, pp. 279–286.

[16] Chen, G., 1997, "Size and Interface Effects on Thermal Conductivity of Superlattices and Periodic Thin-Film Structures," J. Heat Transfer, **119**, pp. 220–229.

[17] Chen, G., 1998, "Thermal Conductivity and Ballistic-Phonon Transport in the Cross-Plane Direction of Superlattices," Phys. Rev. B, **57**(23), pp. 14958–14973.

[18] Chen, G., and Neagu, M., 1997, "Thermal Conductivity and Heat Transfer in Superlattices," Appl. Phys. Lett., **71**(19), pp. 2761–2763.

[19] Cahill, D. G., Goodson, K. E., and Majumdar, A., 2002, "Thermometry and Thermal Transport in Micro/Nanoscale Solid-State Devices and Structures," ASME J. Heat Transfer, **124**, pp. 223–241.

[20] Asheghi, M., Touzelbaev, M. N., Goodson, K. E., Leung, Y. K., and Wong, S. S., 1998, "Temperature-Dependent Thermal Conductivity of Single-Crystal Silicon Layers in SOI Substrates," J. Heat Transfer, **120**, pp. 30–36.

[21] Asheghi, M., Kurabayashi, K., Kasnavi, R., and Goodson, K. E., 2002, "Thermal Conduction in Doped Single-Crystal Silicon Films," J. Appl. Phys., **91**(8), pp. 5079–5088.

[22] Ju, Y. S., and Goodson, K. E., 1999, "Phonon Scattering in Silicon Thin Films With Thickness of Order 100 nm," Appl. Phys. Lett., **74**(20), pp. 3305–3307.

[23] Goodson, K. E., and Ju, Y. S., 1999, "Heat Conduction in Novel Electronic Films," Annu. Rev. Mater. Sci., **29**, pp. 261–293.

[24] Ju, Y. S., 1999, "Microscale Heat Conduction in Integrated Circuits and Their Constituent Films," Ph.D. thesis, Department of Mechanical Engineering, Stanford University.

[25] Sverdrup, P. G., 2000, "Simulation and Thermometry of Sub-Continuum Heat Transport in Semiconductor Devices," Ph.D. thesis, Department of Mechanical Engineering, Stanford University.

[26] Sverdrup, P. G., Ju, Y. S., and Goodson, K. E., 2001, "Sub-Continuum Simulations of Heat Conduction in Silicon-on-Insulator Transistors," ASME J. Heat Transfer, **123**, pp. 130–137.

[27] Armstrong, B. H., 1981, "Two-Fluid Theory of Thermal Conductivity of Dielectric Crystals," Phys. Rev. B, **23**(2), pp. 883–899.

[28] Armstrong, B. H., 1985, "N Processes, the Relaxation-Time Approximation, and Lattice Thermal Conductivity," Phys. Rev. B, **32**(6), pp. 3381–3390.

[29] Narumanchi, S. V. J., Murthy, J. Y., and Amon, C. H., 2003, "Simulation of Unsteady Small Heat Source Effects in Sub-Micron Heat Conduction," ASME J. Heat Transfer, **125**(5), pp. 896–903.

[30] Duncan, A., Ravaioli, U., and Jakumeit, J., 1998, "Full-Band Monte Carlo Investigation of Carrier Trends in the Scaling of Metal-Oxide Semiconductor Field-Effect Transistors," IEEE Trans. Electron Devices, **45**, pp. 867–876.

[31] Pop, E., Banerjee, K., Sverdrup, P. G., Dutton, R., and Goodson, K. E., "Localized Heating Effects and Scaling of Sub-0.18 Micron CMOS Devices," IEEE Intern. Electron Devices Meeting (IEDM), Dec. 2001, Washington D.C. pp. 31.1.1–31.1.4.

[32] Pop, E., Sinha, S., and Goodson, K. E., 2003, "Detailed Phonon Generation Simulations Via the Monte Carlo Method," *Proceedings—ASME Summer Heat Transfer Conference, Las Vegas, NV*, Paper No. HT2003-47312.

[33] Majumdar, A., Fushinobu, K., and Hijikata, K., 1995, "Effect of Gate Voltage on Hot-Electron and Hot-Phonon Interaction and Transport in a Submicrometer Transistor," J. Appl. Phys., **77**(12), pp. 6686–6694.

[34] Fushinobu, K., Hijikata, K., and Majumdar, A., 1995, "Heat Generation in Sub-Micron GaAs MESFETs," Proceedings—International Intersociety Electronic Packaging Conference EEP-Vol. 10-2, Advances in Electronic Packaging, pp. 897–902.

[35] Fushinobu, K., Majumdar, A., and Hijikata, K., 1995, "Heat Generation and Transport in Submicron Semiconductor Devices," ASME J. Heat Transfer, **117**, pp. 25–31.

[36] Lai, J., and Majumdar, A., 1996, "Concurrent Thermal and Electrical Modeling of Sub-Micrometer Silicon Devices," J. Appl. Phys., **79**(9), pp. 7353–7361.

[37] Blotekjaer, K., 1970, "Transport Equations for Electrons in Two-Valley Semiconductors," IEEE Trans. Electron Devices, **ED-17**(1), pp. 38–47.

[38] Balandin, A., and Wang, K. L., 1998, "Significant Decrease of the Lattice Thermal Conductivity Due to Phonon Confinement in a Free-Standing Semiconductor Quantum Well," Phys. Rev. B, **58**(3), pp. 1544–1549.

[39] Zou, J., and Balandin, A., 2001, "Phonon Heat Conduction in a Semiconductor Nanowire," J. Appl. Phys., **89**(5), pp. 2932–2938.

[40] Mazumder, S., and Majumdar, A., 2001, "Monte Carlo Study of Phonon Transport in Solid Thin Films Including Dispersion and Polarization," ASME J. Heat Transfer, **123**, pp. 749–759.

[41] Ecsedy, D. J., and Klemens, P. G., 1977, "Thermal Resistivity of Dielectric Crystals Due to Four-Phonon Processes and Optical Modes," Phys. Rev. B, **15**(12), pp. 5957–5962.

[42] Klemens, P. G., 1958, "Thermal Conductivity and Lattice Vibrational Modes," in *Solid State Physics*, Seitz, F. and Thurnbull, D., eds., Academic Press, New York, pp. 1–98.

[43] Klemens, P. G., 1969, "Theory of Thermal Conductivity of Solids," in *Thermal Conductivity*, Tye, R. P., ed., Academic Press, London, pp. 1–68.

[44] Han, Y.-J., and Klemens, P. G., 1993, "Anharmonic Thermal Resistivity of Dielectric Crystals at Low Temperatures," Phys. Rev. B, **48**, pp. 6033–6042.

[45] Narumanchi, S. V. J., Murthy, J. Y., and Amon, C. H., 2003, "Simulations of Heat Conduction in Sub-Micron Silicon-on-Insulator Transistors Accounting for Phonon Dispersion and Polarization," *ASME International Mechanical Engineering Congress and Exposition, Washington, DC*, Paper No. IMECE2003-42447.

[46] Narumanchi, S. V. J., 2003, ''Heat Transport in Sub-Micron Conduction,'' Ph.D. thesis, Department of Mechanical Engineering, Carnegie Mellon University.
[47] Narumanchi, S. V. J., Murthy, J. Y., and Amon, C. H., 2004, ''Heat Transport During Transient Electrostatic Discharge Events in a Sub-Micron Transistor,'' *Proceedings—ASME Heat Transfer/Fluids Engineering Summer Conference, Charlotte, NC*, Paper No. HT-FED2004-56252.
[48] Brockhouse, B. N., 1959, ''Lattice Vibrations in Silicon and Germanium,'' Phys. Rev. Lett., **2**(6), pp. 256–259.
[49] Holland, M. G., 1963, ''Analysis of Lattice Thermal Conductivity,'' Phys. Rev., **132**(6), pp. 2461–2471.
[50] Modest, M. F., 1993, *Radiative Heat Transfer*, McGraw-Hill, New York.
[51] Touloukian, Y. S., and Buyco, E. H., 1970, ''Specific Heat: Nonmetallic Solids,'' in *Thermophysical Properties of Matter*, IFI/Plenum, New York.
[52] Klemens, P. G., 1951, ''The Thermal Conductivity of Dielectric Solids at Low Temperatures,'' Proc. R. Soc. London, Ser. A, **208**(1092), pp. 108–133.
[53] Klemens, P. G., 1955, ''The Scattering of Low Frequency Lattice Waves by Lattice Imperfections,'' Proc. Phys. Soc., London, Sect. A, **68**, pp. 1113–1128.
[54] Tamura, S., 1983, ''Isotope Scattering of Dispersive Phonons in Ge,'' Phys. Rev. B, **27**, pp. 858–866.
[55] Patankar, S. V., 1980, *Numerical Heat Transfer and Fluid Flow*, Taylor & Francis, London.
[56] Chai, J. C., Lee, H. S., and Patankar, S. V., 1994, ''Finite Volume Method for Radiation Heat Transfer,'' J. Thermophys. Heat Transfer, **8**(3), pp. 419–425.
[57] Murthy, J. Y., and Mathur, S. R., 1998, ''Finite Volume Method for Radiative Heat Transfer Using Unstructured Meshes,'' J. Thermophys. Heat Transfer, **12**(3), pp. 313–321.
[58] Gaskell, P. H., and Lau, A. K. C., 1988, ''Curvature-Compensated Convective Transport: Smart, a New Boundedness-Preserving Transport Algorithm,'' Int. J. Numer. Methods Fluids, **8**, pp. 617–641.
[59] Darwish, M. S., and Moukalled, F. H., 1994, ''Normalized Variable and Space Formulation Methodology for High-Resolution Schemes,'' Numer. Heat Transfer, Part B, **26**, pp. 79–96.

Optimal Spacings for Mixed Convection

T. Bello-Ochende

A. Bejan

Department of Mechanical Engineering and Materials Science,
Duke University,
Box 90300, Durham, NC 27708-0300

This paper completes the description of geometry optimization in stacks of parallel plates that generate heat. The spacing between plates, or the number of plates in a fixed volume, has been maximized in two limits: pure natural convection and pure forced convection. In this paper, the in-between regime of mixed convection is modeled numerically. After simulating the flow and temperature fields in configurations with a variety of spacings, this paper reports the optimal spacings and the dimensionless groups that govern them (Rayleigh number, pressure drop number, mixed convection ratio). It shows that the numerical results match the results in the limits of natural convection and forced convection. The paper constructs a correlation that bridges the gap between the two limits, and provides a single formula for optimal spacings covering the entire domain, from natural convection to forced convection. [DOI: 10.1115/1.1833363]

Keywords: Constructal Theory, Forced Convection, Mixed Convection, Natural Convection, Intersection of Asymptotes Method

1 Introduction

A current research trend in heat transfer is the optimization of flow structure, or the generation of flow geometry in flow systems with global objective and global constraints [1]. In heat exchangers and electronics cooling, for example, the global objective is the maximization of heat transfer density. Compactness and miniaturization are driven by the need to install more and more heat transfer (or ''augmentation'') in the available volume. When the flow structure is free to ''morph'', the objective and constraints drive the structure towards an architecture that performs at the highest level from a global (system level) point of view.

In heat transfer, there are many examples of the generation of geometry based on the principle of global objective and constraints. The simplest are the optimal spacings for heat generating volumes cooled through channels formed between parallel plates. Structures with optimal parallel-plates spacings have been developed for natural convection [2,3] and forced convection [4]. Spacings have also been optimized for packings of cylinders in crossflow, staggered parallel plates, fin arrays with impinging flow: a collection of such results is reviewed in [1].

In this paper we extend to mixed convection the search for optimal spacings for volumes with maximal heat transfer density. Mixed convection bridges the gap between the structures optimized for natural convection and forced convection. This previously uncharted domain offers us an opportunity to develop compact correlations for optimal spacing and maximal heat transfer density over the entire domain: natural, mixed, and forced convection. We focus the study on the simplest class of flows, where natural convection is aided by forced convection, and fluctuations and reverse flow are absent.

2 Mathematical Formulation

Figure 1(a) shows one of the channels. The flow length L is fixed by the global dimension of the package volume. The spacing D is free to vary, and must be selected such that the total heat transfer density is maximized. The plates are modeled as isothermal at the highest allowable temperature T_w. The lowest temperature is the coolant inlet temperature T_∞. The fluid is newtonian. The temperature variations in the $D\times L$ space are sufficiently small relative to the absolute temperature so that Boussinesq approximation is valid.

The two-dimensional computational domain is shown in Fig. 1(b). The $D\times L$ elemental channel is fitted with an upstream section ($D\times L_u$) and a downstream section ($D\times L_d$). The lengths L_u and L_d were selected based on accuracy tests described later in this section. The conservation equations for mass, momentum and energy in the steady state require

$$\frac{\partial u}{\partial x}+\frac{\partial v}{\partial y}=0 \tag{1}$$

$$u\frac{\partial u}{\partial x}+v\frac{\partial u}{\partial y}=-\frac{1}{\rho}\frac{\partial P}{\partial x}+\nu\nabla^2 u \tag{2}$$

$$u\frac{\partial v}{\partial x}+v\frac{\partial v}{\partial y}=-\frac{1}{\rho}\frac{\partial P}{\partial y}+\nu\nabla^2 v+g\beta(T-T_\infty) \tag{3}$$

$$u\frac{\partial T}{\partial x}+v\frac{\partial T}{\partial y}=\alpha\nabla^2 T \tag{4}$$

where $\nabla^2=\partial^2/\partial x^2+\partial^2/\partial y^2$. The system of coordinates (x,y) and the velocity components (u,v) are defined in Fig. 1. The variables are defined in Nomenclature. The numerical work of solvingf Eqs. (1)–(4) is based on a dimensionless formulation using the variables

$$(\tilde{x},\tilde{y})=\frac{(x,y)}{L}\quad(\tilde{u},\tilde{v})=\frac{(u,v)}{(\mathrm{BeRa}\Delta P/\mathrm{Pr}\rho)^{1/2}} \tag{5}$$

$$\theta=\frac{T-T_\infty}{T_w-T_\infty}\quad\tilde{P}=\frac{PL}{\mu(\mathrm{BeRa}\Delta P/\mathrm{Pr}\rho)^{1/2}} \tag{6}$$

where Ra is the Rayleigh number,

$$\mathrm{Ra}=\frac{g\beta L^3(T_w-T_\infty)}{\alpha\nu} \tag{7}$$

and Be is the pressure drop number [5–7]

$$\mathrm{Be}=\frac{\Delta P L^2}{\alpha\mu} \tag{8}$$

The Prandtl number is $\mathrm{Pr}=\nu/\alpha$. The dimensionless version of Eqs. (1)–(4) is

Contributed by the Heat Transfer Division for publication in the JOURNAL OF HEAT TRANSFER. Manuscript received by the Heat Transfer Division September 10, 2003; revision received February 26, 2004. Associate Editor: K. S. Ball.

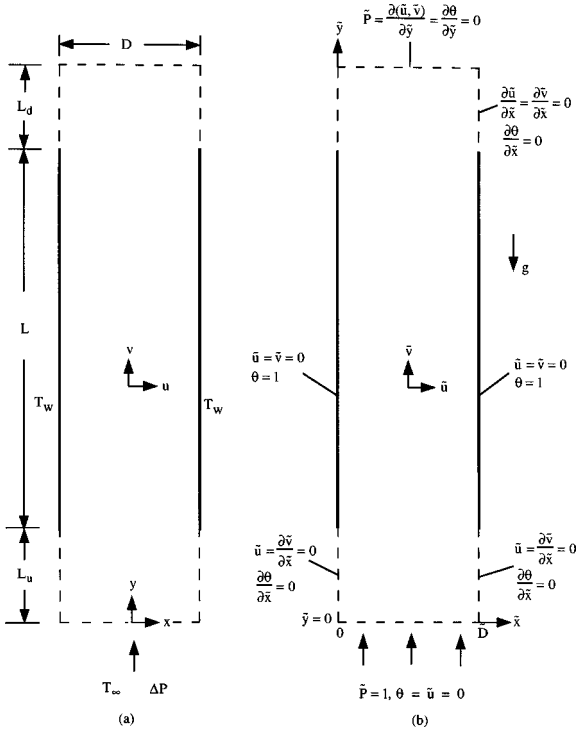

Fig. 1 Computational domain and boundary conditions for parallel plates channel

$$\frac{\partial \tilde{u}}{\partial \tilde{x}} + \frac{\partial \tilde{v}}{\partial \tilde{y}} = 0 \tag{9}$$

$$\mathrm{Be}\frac{\mathrm{Ra}^{1/2}}{\mathrm{Pr}}\left(\tilde{u}\frac{\partial \tilde{u}}{\partial \tilde{x}} + \tilde{v}\frac{\partial \tilde{u}}{\partial \tilde{y}}\right) = -\frac{\partial \tilde{P}}{\partial \tilde{x}} + \nabla^2 \tilde{u} \tag{10}$$

$$\mathrm{Be}\frac{\mathrm{Ra}^{1/2}}{\mathrm{Pr}}\left(\tilde{u}\frac{\partial \tilde{v}}{\partial \tilde{x}} + \tilde{v}\frac{\partial \tilde{v}}{\partial \tilde{y}}\right) = -\frac{\partial \tilde{P}}{\partial \tilde{y}} + \nabla^2 \tilde{v} + \theta\frac{\mathrm{Ra}^{1/2}}{\mathrm{Be}} \tag{11}$$

$$\mathrm{BeRa}^{1/2}\left(\tilde{u}\frac{\partial \theta}{\partial \tilde{x}} + \tilde{v}\frac{\partial \theta}{\partial \tilde{y}}\right) = \nabla^2 \theta \tag{12}$$

The flow boundary conditions are indicated in Fig. 1(b): no slip and no penetration on the plate surfaces; $\tilde{P}=1$, $\tilde{u}=\partial\tilde{v})/\partial\tilde{y}=0$ at the inlet of the computational plane; $\tilde{P}=0$ and $\partial(\tilde{u},\tilde{v}/\partial\tilde{y}=0$ at the exit of the computational domain; and free slip and no penetration $(\tilde{u}=\partial\tilde{v}/\partial\tilde{y}=0)$ at the upstream section of the computational domain $(0\leqslant\tilde{y}\leqslant\tilde{L}_u)$. For the downstream section $(\tilde{L}_u+1\leqslant\tilde{y}\leqslant\tilde{L}_u+1+\tilde{L}_d)$ domain we specified two flow boundary conditions: free slip and no penetration $(\tilde{u}=\partial\tilde{v}/\partial\tilde{y}=0)$ on the left side of the downstream section of the computational domain, and zero stress $[\partial(\tilde{u},\tilde{v})/\partial\tilde{x}=0]$ on the right side of the downstream section of the domain. By specifying $\partial\tilde{u}/\partial\tilde{x}=0$ on this side we allow fluid to flow horizontally into the computational domain. This entrainment effect nullifies the unrealistic vertical acceleration (chimney effect) that would have been generated had we imposed no-slip on that side.

The thermal boundary conditions are $\theta=1$ on the plate surfaces, and $\theta=0$ on the inlet plane of the computational domain. The remaining portions of the computational domain were modeled as adiabatic.

We are interested in the geometric arrangement that maximize the heat transfer density rate density, $q'''=q'/DL$, where q' is the total heat transfer rate integrated over the two plate surfaces. The dimensionless form of the heat transfer density is

Table 1 Grid refinement test for the forced convection limit, natural convection limit, and mixed convection (Pr=1, $\tilde{L}_u=\tilde{L}_d=0.5$)

Number of nodes per L in $\tilde{x}$ and $\tilde{y}$ directions	$\tilde{q}$ Ra=1, Be=10^6 D=0.1	$\tilde{q}$ Ra=10^6, Be=1 D=0.1	$\tilde{q}$ Ra=Be=10^5 D=0.04
50	531.35	412.05	
100	486.53	372.17	3059.4
200	486.32	372.24	2779.7
400	486.46	372.34	2756.5
800			2756.1

$$\tilde{q} = \frac{q'}{k(T_w - T_\infty)DL} \tag{13}$$

3 Numerical Method

Equations (9)–(12) were solved using a finite element code [8] with quadrilateral elements and biquadratic interpolation functions. The explicit appearance of the pressure in the momentum equations was eliminated by using the penalty function method. In all the simulations the compressibility parameter was between 10^{-6} and 10^{-9}, and depended on the values of Be and Ra. The nonlinear equations resulting from the Galerkin finite-element discretization of Eqs. (9)–(12) were solved using successive substitution followed by a quasi-Newton method. As convergence criteria, we used

$$\frac{\|u^{(k)}-u^{(k-1)}\|}{\|u^k\|}\leqslant 10^{-4} \quad \frac{\|R(u^{(k)})\|}{\|R_0\|}\leqslant 10^{-4} \tag{14}$$

where $\mathbf{R(u)}$ is the residual vector, $\mathbf{u}$ is the complete solution vector, k is the iteration counter, and $\|\cdot\|$ is the Euclidian norm. The grid was nonuniform in both $\tilde{x}$ and $\tilde{y}$-directions. The grid was double graded in the $\tilde{x}$-direction in order to put more nodes near the plates surfaces, to capture more accurately the boundary layers. The grid varied from one geometric configuration to the next.

Grid refinement tests were performed in two ranges: $(10^5\leqslant\mathrm{Be}\leqslant10^7,\ 10^{-3}\leqslant\mathrm{Pr}\leqslant10^2,\ \mathrm{Ra}=1)$ and $(10^5\leqslant\mathrm{Ra}\leqslant10^7,\ 10^{-3}\leqslant\mathrm{Pr}\leqslant10^2,\ \mathrm{Be}=1)$. These tests indicated that the solutions are insensitive to further grid doubling in $\tilde{x}$ and $\tilde{y}$ when 200 nodes per L are used in both $\tilde{x}$ and $\tilde{y}$-directions. Table 1 shows how grid independence was achieved. Insensitivity to further grid doubling means that the change in the total heat transfer rate was less than 1%. Finer grids were necessary at larger Ra and Be values. For example, in the range $10^5\leqslant(\mathrm{Ra,Be})\leqslant10^7$ we had to use 400 nodes per L in both $\tilde{x}$ and $\tilde{y}$-directions.

Another set of accuracy tests showed that when $L_u/L=0.5$ and $L_d/L=0.5$, the channel heat transfer rate varied less than 0.5% after the doubling of the upstream and downstream lengths (L_u, L_d).

4 Numerical Results

Numerical simulations were performed for a very large number of configurations, in order to identify accurately the optimal spacings for maximal heat transfer per unit of channel volume. This work was pursued systematically in three parts: the forced convection limit, the natural convection limit, and the intersection of the two limits; mixed convection; or a balance between forced and natural convection. We followed this approach for two reasons. First, the focus on the two limits allow us to validate our numerical results against results that are well documented for natural and forced convection [1,8–12]. Second, the work of correlating the more complicated results of mixed convection benefits greatly from an understanding of what the proper correlations should be in the simpler limits.

Forced Convection. To place the flow in forced convection limits we set Ra to a very low level, Ra=1, and Be in the high range of $10^5 \leqslant \mathrm{Be} \leqslant 10^7$. We simulated the flow and temperature fields for many spacings $\tilde{D}$, and monitored the dimensionless heat transfer density, Eq. (13). We then located the maximum of this function with respect to $\tilde{D}$. The optimal spacing $\tilde{D}_{\mathrm{opt}}$ and maximum heat transfer rate density $\tilde{q}_m$ are shown in Figs. 2(a) and 3(a).

We repeated this work for several Pr values, and found that two patterns of behavior emerge. In the range $0.001 \leqslant \mathrm{Pr} \leqslant 1$, the dimensionless optimal spacing decreases slightly as Pr increases, while in the range $1 \leqslant \mathrm{Pr} \leqslant 100$, $\tilde{D}_{\mathrm{opt}}$ is fairly constant. Figure 3(a) shows the behavior of heat transfer rate versus Be and Pr. In the range $0.001 \leqslant \mathrm{Pr} \leqslant 1$, the maximal heat transfer rate density increases slightly with Pr, and becomes constant when $\mathrm{Pr} \geqslant 1$.

This first set of results was used to develop a correlation for optimal spacings. In the limit of forced convection and $\mathrm{Pr} \geqslant 0.5$, the theoretical spacing $\tilde{\mathrm{D}}_{\mathrm{opt}}$ and maximal $\tilde{q}_m$ are [4]

$$\tilde{D}_{\mathrm{opt}} \cong 2.73 \ \mathrm{Be}^{-1/4} \tag{15}$$

$$\tilde{\mathrm{q}}_{\mathrm{m}} \leqq 0.62 \ \mathrm{Be}^{1/2} \tag{16}$$

These formulas suggest that we may replot Figs. 2(a) and 3(a) as shown in Figs. 2(b) and 3(b). These figures show that in the limit of $\mathrm{Pr} \geqslant 0.5$ the present work agrees with the earlier results published for pure forced convection. In the present work we extended the Prandtl number range to $\mathrm{Pr} < 0.5$. It is worth mentioning that the theoretical optimal spacings of Bejan and Sciubba [4] Eq. (15), were verified later based on numerical experiments [11,12].

Natural Convection. In this limit we set Be=1, and varied Ra and Pr in the range $10^5 \leqslant \mathrm{Ra} \leqslant 10^7$ and $10^{-3} \leqslant \mathrm{Pr} \leqslant 10^2$. The results are shown in Figs. 4(a) and 5(a). The theoretical solution for this limit predicts [2,3]

$$\tilde{D}_{\mathrm{opt}} \cong 2.3 \ \mathrm{Ra}^{-1/4} \tag{17}$$

$$\tilde{q}_m \leqq 0.45 \ \mathrm{Ra}^{1/2} \tag{18}$$

Equations (17) and (18) are the basis for the more compact representation shown in Figs. 4(b) and 5(b). The Prandtl number has an effect on this correlation. Regarding [2] and [3], one reviewer of the original version of this paper argued that [3] should be deleted because "it is unacceptable for an archival journal article to refer to an end-of-chapter textbook exercise". We disagree, because we do not believe that the originality of an idea is indicated by the reputation of the publication or publisher, e.g., the ASME versus Wiley. The originality of an idea is indicated by the moment when it was communicated to the public. This is why every publication has a date. Reference [2] appeared in the August 1984 issue of this journal. Bejan's convection book [3] appeared the same month, in fact, [2] and [3] were both on display at the August 1984 National Heat Transfer Conference in Niagara Falls, NY. We see nothing wrong or unusual about this: good ideas may occur to more than one individual at the same time. More interesting is that what this journal rightly published as a full length paper [2] can also be anticipated with pencil and paper as a book exercise [3] based on an original method: the intersection of asymptotes [13].

The Pr Effect. The correlation of the Pr effect is based on the technique of Churchill and Usagi [14,15]. We assumed the function

$$A(\mathrm{Pr}) = [(c_1)^n + (c_2 \mathrm{Pr}^{c_3})^n]^{1/n} \tag{19}$$

and determined the best set (c_1, c_2, c_3, n) that minimizes the scatter due to Pr when presenting the data as $\tilde{D}_{\mathrm{opt}}\mathrm{Be}^{1/4}/\mathrm{A(Pr)}$ and $\tilde{D}_{\mathrm{opt}}\mathrm{Ra}^{1/4}/A(\mathrm{Pr})$. The objective is to line up the data horizontally, as shown in Figs. 2(c) and 4(c). The constants $c_1=263$, $c_2=2.83$, $c_3=0.667$, and $n=0.52$ correlate $\mathrm{Be}^{1/4}/A(\mathrm{Pr}) \cong 0.0114$ with standard deviation of ± 0.0006, as shown in Fig. 2(c). The same constants correlate $\tilde{D}_{\mathrm{opt}}\mathrm{Ra}^{1/4}/A(\mathrm{Pr}) \cong 0.0104$ with a standard deviation of ± 0.00033.

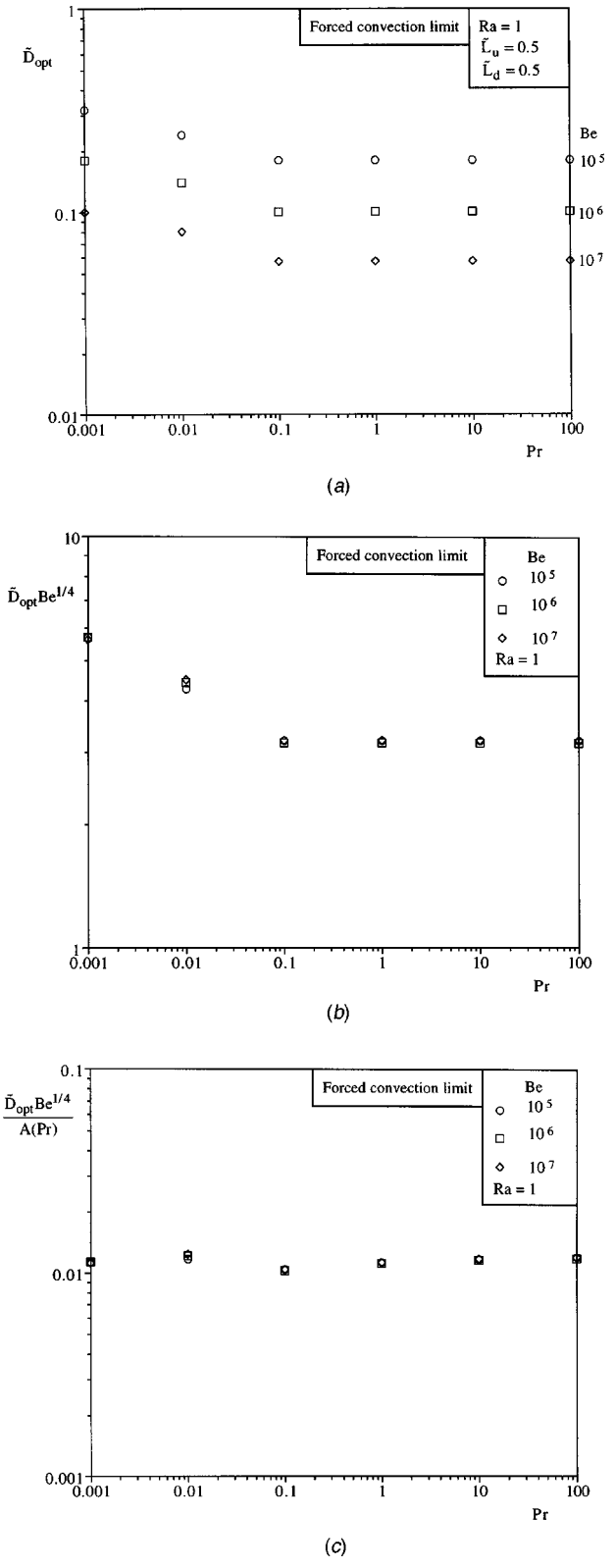

Fig. 2 The effect of Prandtl number and pressure drop number on the optimal spacing in the forced convection limit

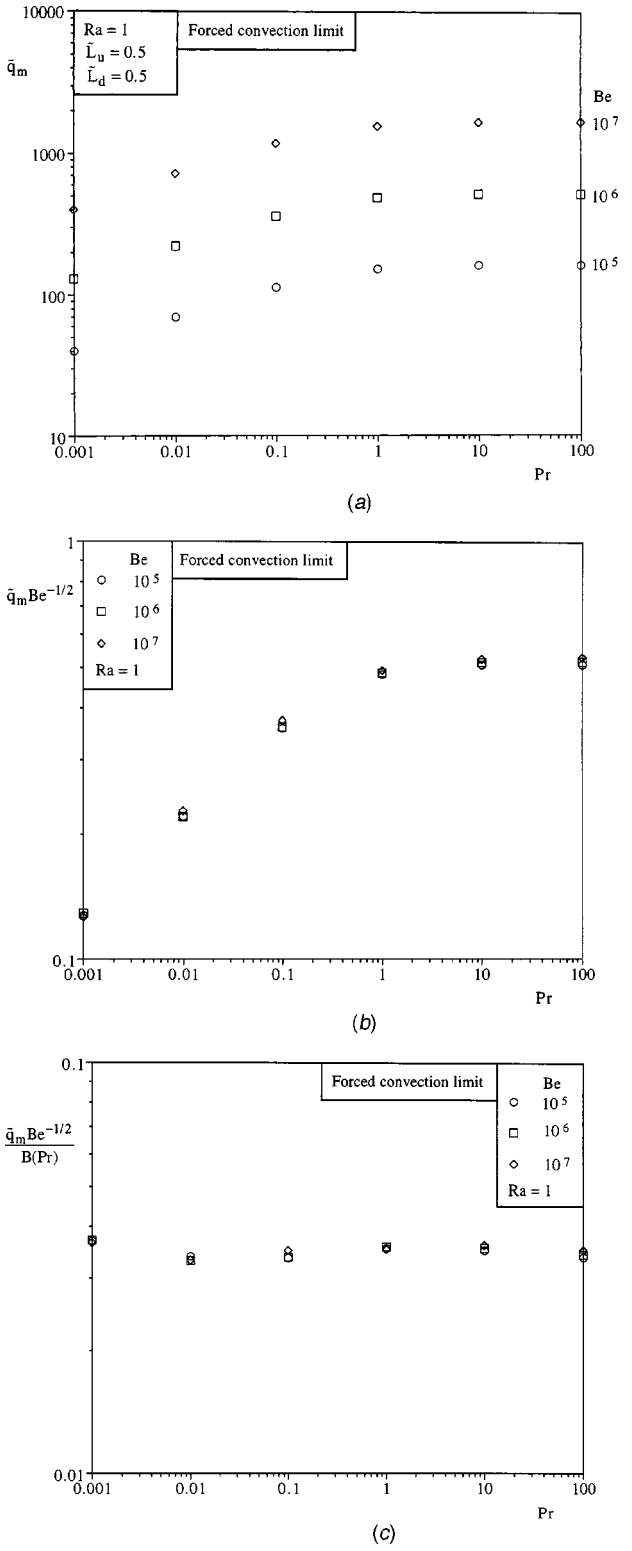

Fig. 3 The effect of Prandtl number and pressure drop number on the maximal heat transfer rate density in the forced convection limit

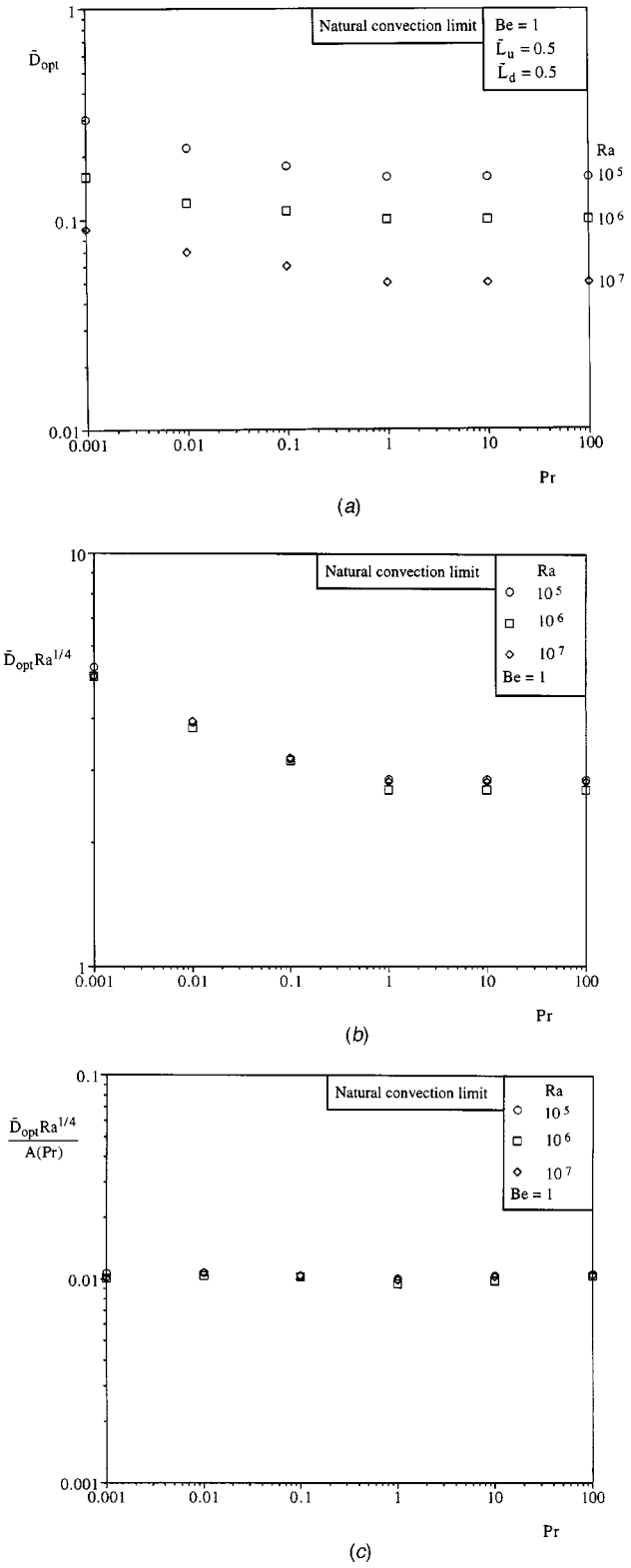

Fig. 4 The effect of Prandtl number and Rayleigh number on the optimal spacing in the natural convection limit

For the maximum heat transfer density, we constructed the Pr function

$$B(\mathrm{Pr}) = [(c_4)^{-m} + (c_5 \mathrm{Pr}^{c_6})^{-m}]^{-1/m} \tag{20}$$

and determined the set (c_4, c_5, c_6, m) that minimizes the scatter due to Pr. The correlations for $\tilde{q}_m \mathrm{Be}^{-1/2}/\mathrm{B(Pr)}$ and $\tilde{q}_m \mathrm{Ra}^{-1/2}/\mathrm{B(Pr)}$ are shown in Figs. 3(c) and 5(c). The correlation shown in Fig. 3(c) is $\tilde{q}_m \mathrm{Be}^{-1/2}/B(\mathrm{Pr}) \cong 0.035$, with a standard deviation of ± 0.00125, for which $c_4 = 15.5$, $c_5 = 181$, $c_6 = 0.81$, and $m = 0.51$. The same constants were used in Fig. 5(c), where

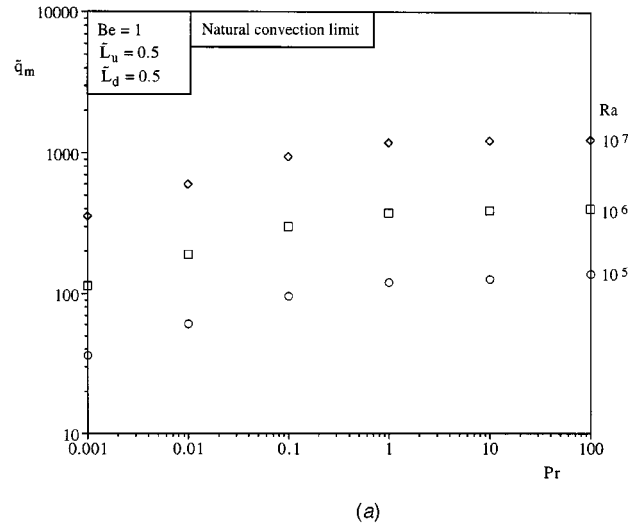

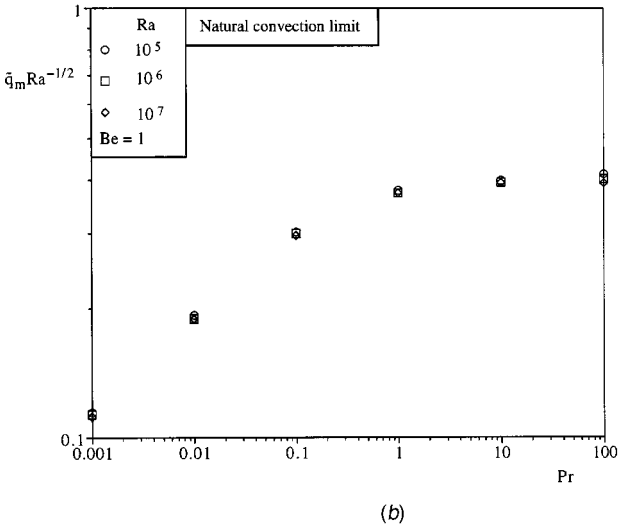

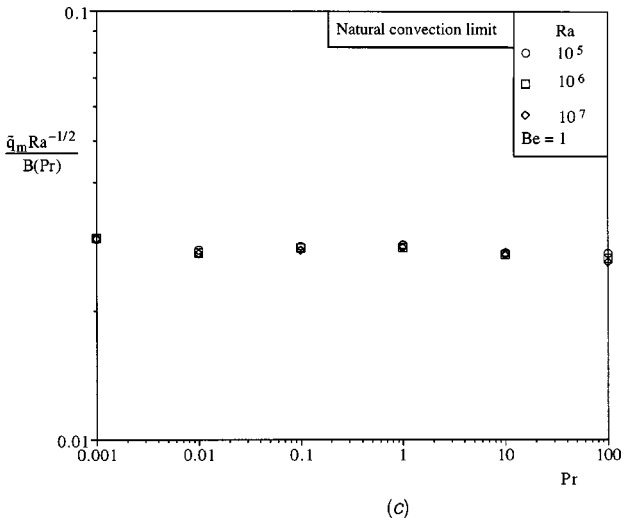

Fig. 5 The effect of Prandtl number and Rayleigh number on the maximal heat transfer rate density in the natural convection limit

$\tilde{q}_m Ra^{-1/2}/B(Pr) \cong 0.028$, with a standard deviation of ± 0.001. Although the Prandtl number effect on the correlation is weak, it is difficult to correlate especially at low Pr. The reason is that the viscous boundary layers are thin and more difficult to capture numerically.

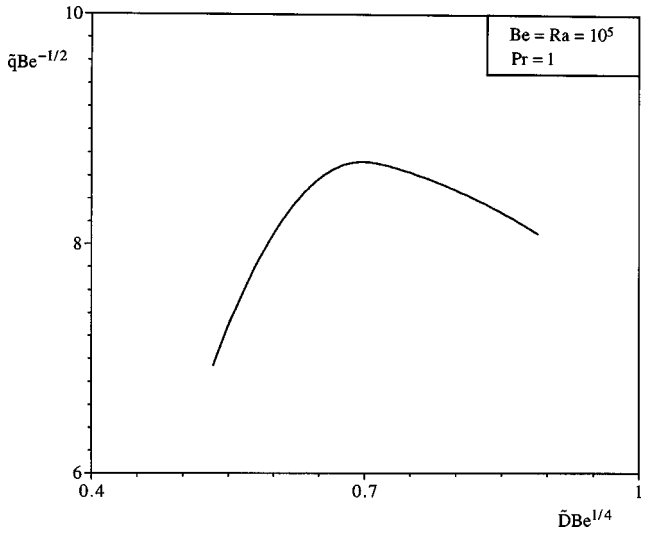

Fig. 6 The effect of channel spacing on the heat transfer density in mixed convection

Mixed Convection. Consider now the range where natural convection and forced convection have comparable strengths. First, we fixed Pr=1, and started with a case of strong natural convection combined with strong forced convection: Ra=Be $=10^5$. In this way we confirmed that $\tilde{q}$ has a maximum with respect to $\tilde{D}$, as shown in Fig. 6.

In the second phase, we fixed the natural convection strength at Ra$=10^5$ and varied the forced convection strength in the range $10^5 \leqslant Be \leqslant 10^7$. The optimization results are reported as the leftmost branches of $\tilde{D}_{opt}Be^{1/4}$ and $\tilde{q}_m Be^{-1/2}$ in Figs. 7(a) and 8(a). The abscissa parameter is $(Ra/Be)^{1/4}$. We will see that this choice of abscissa leads to a compact reporting of all the optimal mixed-convection results generated by this work.

In the third phase we fixed Be$=10^5$, and varied the natural convection strength in the range $10^5 \leqslant Ra \leqslant 10^7$. The results for optimal spacing and maximal heat transfer density have been added to Figs. 7(a) and 8(a). This new phase of the work extended the curves of Figs. 7 and 8 to the right of $(Ra/Be)^{1/4} \sim 1$.

In the fourth phase, we investigated the effect of the Prandtl number on $\tilde{D}_{opt}$ and $\tilde{q}_m$. We accomplished this by repeating the second and third phases for several different Pr values in the range $10^{-3} \leqslant Pr \leqslant 10^2$. These results are shown in Figs. 7(a) and 8(a). The Pr effect is similar to what we found for pure natural convection and pure forced convection in Figs. 2(a), 3(a), 4(a), and 5(a).

Global Correlation for Mixed Convection. Our ultimate objective was to develop a single correlation for optimal spacings for the entire domain covered by this study. First, we correlated the mixed convection data of Fig. 7(a) by using the composite relation $A(Pr)$ from Figs. 2(c) and 4(c), and then we replotted these data as Fig. 7(b). Next, we constructed a new composite relation,

$$C(\eta) = \left[r_1^n + \left(\frac{r_2}{\eta} \right)^n \right]^{1/n} \tag{21}$$

which accounts for the mixed convection effect $\eta = (Ra/Be)^{1/4}$. The constants that minimize the scatter due to $(Ra/Be)^{1/4}$ are $r_1 = 17.69$, $r_2 = 28.27$ and $n = -2.08$. As shown in Fig. 7(c), the correlation is

$$\tilde{D}_{opt}Be^{1/4}/AC \cong 1.76 \times 10^{-4} \tag{22}$$

for which the standard deviation is $\pm 6.4 \times 10^{-6}$.

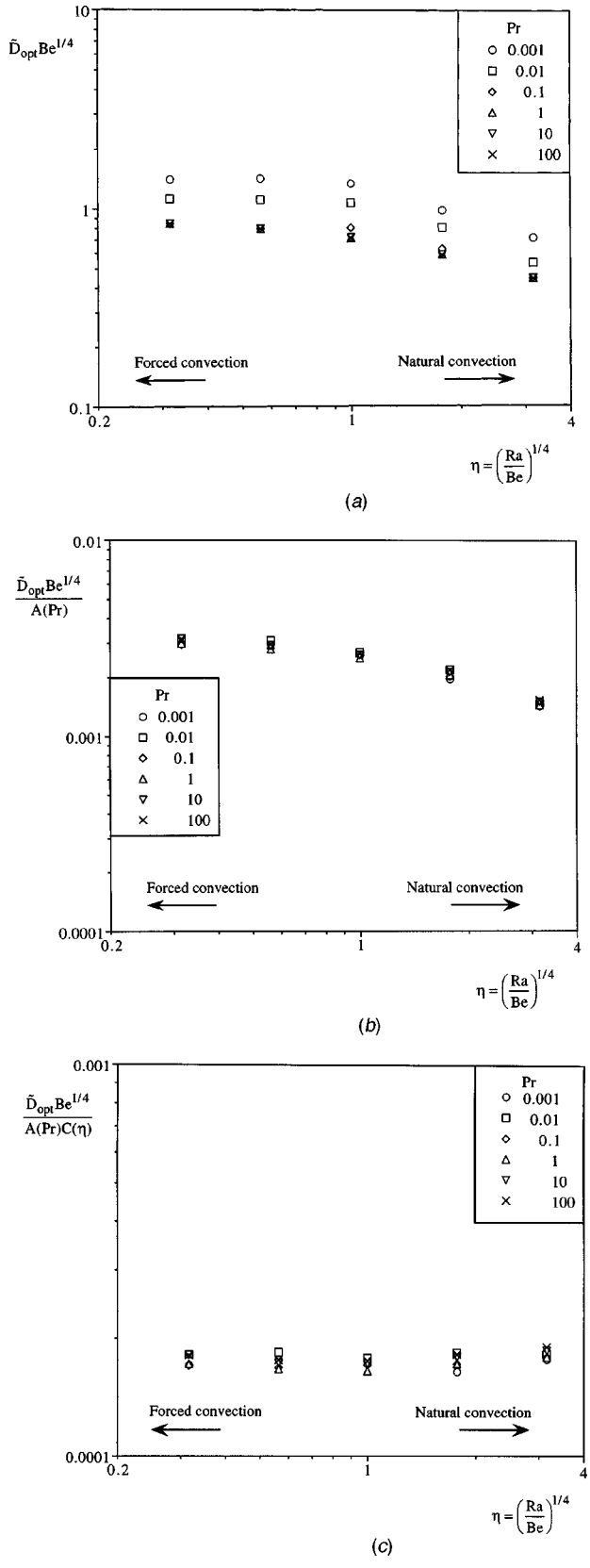

Fig. 7 The effect of the mixed convection parameter $(Ra/Be)^{1/4}$ and Prandtl number on the optimal spacing

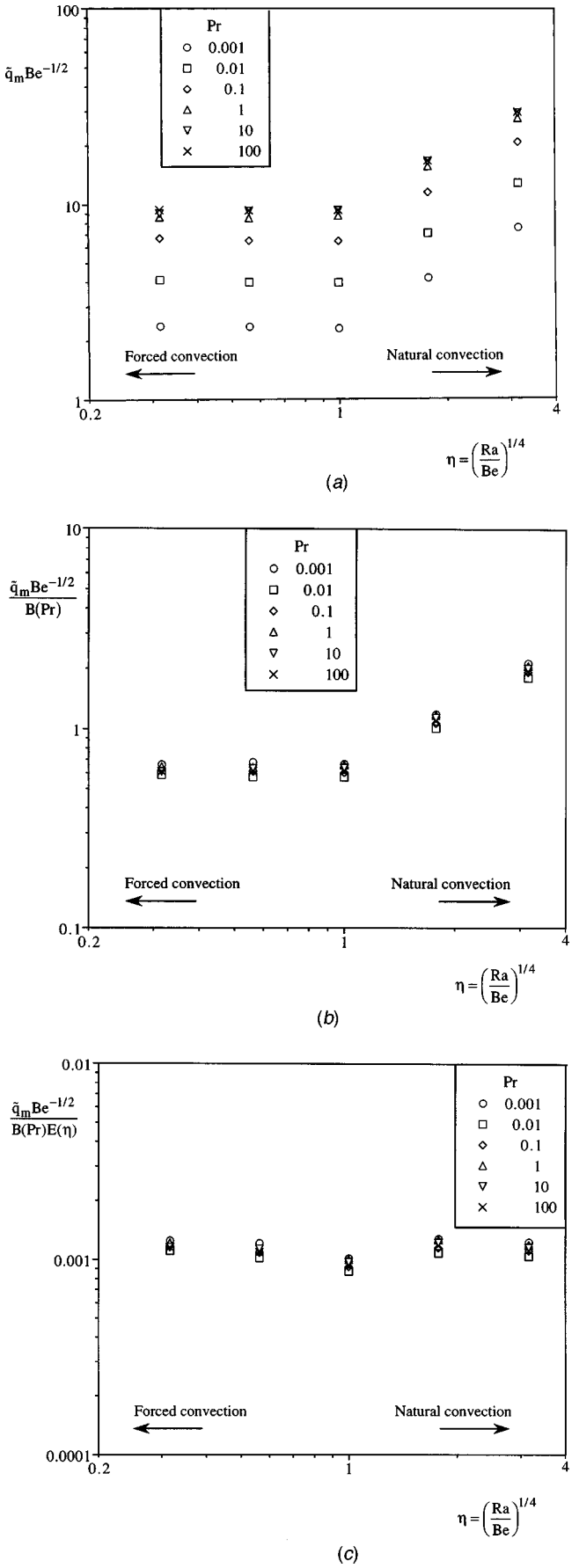

Fig. 8 The effect of the mixed convection parameter $(Ra/Be)^{1/4}$ and Prandtl number on the maximal heat transfer rate density

We devised a similar procedure for the maximal heat transfer rate density, Fig. 8(a). The Pr effect was correlated by using the composite relation B(Pr), as shown in Figs. 3(c) and 5(c). This relation was used to plot Fig. 8(b). A new composite relation was then constructed to account for the mixed convection effect

$$E(\eta)=[r_3^m+(r_4\eta^2)^m]^{1/m} \tag{23}$$

where, again, $\eta=(\mathrm{Ra/Be})^{1/4}$. The constants (r_3, r_4, m) were optimized in order to replot Fig. 8(b) such that the scatter due to η is minimized, and the data for $\tilde{q}_m \mathrm{Be}^{-1/2}/BE$ line up as a straight line as shown in Fig. 8(c). The optimized constants are $r_3=511$, $r_4=110.5$, and $m=0.9$. The correlation is

$$\tilde{q}_m \mathrm{Be}^{-1/2}/BE \cong 0.0011 \tag{24}$$

with a standard deviation of $\pm 1.06\times 10^{-4}$.

5 Conclusions

This paper covered the mixed convection gap between the optimal spacings known to exist in the limits of pure natural convection and pure forced convection. It showed that optimal spacings also exist in channels with mixed convection, and that they can be correlated smoothly with the optimal spacings for natural and forced convection.

The success of the universal correlation (Eq. (22), (24)) is due to the systematic manner in which it was developed. First, the accuracy of the numerical simulation and optimization was tested against the known natural and forced convection limits. This "pinned" the ends of the correlation on firm ground. The middle of the correlation was then developed in a sequence of two steps, each step isolating the effect of one of the dimensionless groups that govern the optimized flow structure: the Prandtl number, and the mixed convection ratio Ra/Be.

The construction of the universal correlation shows once more that Ra and Be play equivalent roles in the limits: Ra is the dimensionless temperature difference that drives natural convection, and Be is the dimensionless pressure drop that drives forced convection. Another basic message is that optimal spacings represent flow structures with maximal heat transfer density, and that maximal density can be achieved through the generation (construction) of flow architecture under constraints [1].

One reviewer commented on the fact that in the current literature mixed convection is described in terms of Ra and the Reynolds number Re, and that the transition between natural and forced convection is governed by the ratio $\mathrm{Gr/Re}^2$ (incidentally, this is incorrect; the correct ratio for $\mathrm{Pr}\gtrsim 1$ fluids is $\mathrm{Ra/Re}^2\,\mathrm{Pr}^{4/3}$, or $\mathrm{Gr/Re}^2\,\mathrm{Pr}^{1/3}$, cf. Fig. 4.13 in [16]). The reviewer's observation applies to cases where the forced convection is 'assumed' to have a fixed (known) inlet velocity. In such cases, optimal spacings do not exist in forced convection. On the contrary, in this paper forced convection is driven by the imposed pressure difference, which is consistent with the fact that natural convection is driven by the imposed temperature difference. This is why in the present case the relevant dimensionless groups for mixed convection are Be and Ra, and why the transition between forced and natural convection is governed by the ratio Ra/Be, cf. Figs. 7 and 8.

Acknowledgment

This study was conducted with support from the grant received from the National Science Foundation.

Nomenclature

A = function, Eq. (19)
B = function, Eq. (20)
Be = pressure drop number, Eq. (8)
$c_1, \ldots, c_6$ = constants
C = function, Eq. (21)
D = spacing between parallel plates, m
E = function, Eq. (23)
k = thermal conductivity, W/m K
L = flow length, m
L_d = downstream length, m
L_u = upstream length, m
m = exponent
n = exponent
P = pressure, Pa
Pr = Prandtl number
$r_1, \ldots, r_4$ = constants
Ra = Rayleigh number, Eq. (7)
q = total heat transfer rate, W
$\tilde{q}$ = dimensionless heat transfer density, Eq. (13)
q' = heat transfer rate per unit length, W/m
q''' = heat transfer rate density, $\mathrm{W/m^3}$
T = temperature, K
T_w = wall temperature, K
T_∞ = inlet temperature, K
u, v = velocity components, m/s
x, y = cartesian coordinates, m

Greek Symbols

α = thermal diffusivity, $\mathrm{m^2/s}$
ΔP = pressure difference, Pa
η = mixed convection group, $(\mathrm{Ra/Be})^{1/4}$
θ = dimensionless temperature
μ = viscosity, kg/sm
ν = kinematic viscosity, $\mathrm{m^2/s}$
ρ = density, $\mathrm{kg/m^3}$

Subscripts

m = maximum
opt = optimum
w = wall

Superscripts

$(\sim)$ = dimensionless variables, Eq. (5)

References

[1] Bejan, A., 2000, *Shape and Structure: From Engineering to Nature*, Cambridge University Press, Cambridge, UK.
[2] Bar-Cohen, A., and Rohsenow, W. M., 1984, "Thermally Optimum Spacing of Vertical, Natural Convection Cooled, Parallel Plates," ASME J. Heat Transfer, **106**, pp. 116–123.
[3] Bejan, A., 1984, *Convection Heat Transfer*, Wiley, New York, Problem 11, p. 157, Chpt. 4.
[4] Bejan, A., and Sciubba, E., 1992, "The Optimal Spacing for Parallel Plates Cooled by Forced Convection," Int. J. Heat Mass Transfer, **35**, pp. 3259–3264.
[5] Bhattacharjee, S., and Grosshandler, W. L., 1988, "The Formation of Wall Jet Near A High Temperature Wall Under Microgravity Environment," *ASME HTD 96*, ASME, New York, pp. 711–716.
[6] Petrescu, S., 1994, "Comments on the Optimal Spacing of Parallel Plates Cooled by Forced Convection," Int. J. Heat Mass Transfer, **37**, p. 1283.
[7] Furukawa, T., and Yang, W.-J., 2003, "Thermal Optimization of Channel Flows With Discrete Heating Sections," J. Non-Equilib. Thermodyn., **28**, pp. 299–310.
[8] *FIDAP Theory Manual*, 1998, Fluid Dynamics International, Evanston, IL, Revision 8.6.
[9] Anand, N. K., Kim, S. H., and Fletcher, L. S., 1992, "The Effects of Plate Spacing on Free Convection Between Heated Parallel Plates," ASME J. Heat Transfer, **114**, pp. 515–518.
[10] Kim, S. J., and Lee, S. W., eds., 1996, *Air Cooling Technology for Electronic Equipment*, CRC Press, Boca Raton, FL, Chap. 1.
[11] Mereu, S., Sciubba, E., and Bejan, A., 1993, "The Optimal Cooling of a Stack of Heat Generating Boards With Fixed Pressure Drop, Flow Rate or Pumping Power," Int. J. Heat Mass Transfer, **36**, pp. 3677–3686.
[12] Fowler, A. J., Ledezma, G. A., and Bejan, A., 1997, "Optimal Geometric Arrangement of Staggered Plates in Forced Convection," Int. J. Heat Mass Transfer, **40**, pp. 1795–1805.
[13] Lewins, J., 2003, "Bejan's Constructal Theory of Equal Potential Distribution," Int. J. Heat Mass Transfer, **46**, pp. 1541–1543.
[14] Churchill, S. W., and Usagi, R., 1972, "A General Expression for Correlation of Rates of Transfer and Other Phenomena," AIChE J., **18**, pp. 1121–1128.
[15] Churchill, S. W., and Chu, H. H. S., 1975, "Correlating Equations for Laminar and Turbulent Free Convection From Vertical Plates," Int. J. Heat Mass Transfer, **18**, pp. 1323–1329.
[16] Bejan, A., 2004, *Convection Heat Transfer*, third edition, Wiley, New York.

The Dynamics of Two-Dimensional Buoyancy Driven Convection in a Horizontal Rotating Cylinder

Nadeem Hasan
Research Scholar,
Dept. of Applied Mechanics,
IIT Delhi,
New Delhi, India-110016

Sanjeev Sanghi
Assoc. Prof.,
Dept. of Applied Mechanics, IIT Delhi,
New Delhi, India-110016

The present study involves a numerical investigation of buoyancy induced two-dimensional fluid motion in a horizontal, circular, steadily rotating cylinder whose wall is subjected to a periodic distribution of temperature. The axis of rotation is perpendicular to gravity. The governing equations of mass, momentum and energy, for a frame rotating with the enclosure, subject to Boussinesq approximation, have been solved using the Finite Difference Method on a Cartesian colocated grid utilizing a semi-implicit pressure correction approach. The problem is characterized by four dimensionless parameters: (1) Gravitational Rayleigh number Ra_g; (2) Rotational Rayleigh number Ra_Ω; (3) Taylor number Ta; and (4) Prandtl number Pr. The investigations have been carried out for a fixed $Pr=0.71$ and a fixed $Ra_g=10^5$ while Ra_Ω is varied from 10^2 to 10^7. From the practical point of view, Ra_Ω and Ta are not independent for a given fluid and size of the enclosure. Thus they are varied simultaneously. Further, an observer attached to the rotating cylinder, is stationary while the "g" vector rotates resulting in profound changes in the flow structure and even the flow direction at low enough flow rates ($Ra_\Omega < 10^5$) with phase "ϕ_g" of the "g" vector. For $Ra_\Omega \geqslant 10^5$, the global spatial structure of the flow is characterized by two counter-rotating rolls in the rotating frame while the flow structure does not alter significantly with the phase of the rotating "g" vector. The frequency of oscillation of Nusselt number over the heated portion of the cylinder wall is found to be very close to the rotation frequency of the cylinder for $Ra_\Omega \leqslant 10^5$ whereas multiple frequencies are found to exist for $Ra_\Omega > 10^5$. The time mean Nusselt number for the heated portion of the wall undergoes a nonmonotonic variation with Ra_Ω, depending upon the relative magnitudes of the different body forces involved.
[DOI: 10.1115/1.1833370]

Keywords: Cylinder, Enclosure Flows, Heat Transfer, Natural Convection, Rotating

1 Introduction

The problem of natural convection in a nonuniformly heated horizontal cylinder is of relevance in areas like thermal energy storage, crystal growth, metallurgy and process equipment. In this connection two basic heating configurations have been studied: one in which the temperature maximum is at the bottom and the other where the temperature maximum is along the side of the cylinder wall. For the side heating case a number of studies have been performed. Ostrach [1] considered the steady laminar flow generated in a horizontal cylinder by an imposed cosine temperature distribution on the cylinder wall. The temperature extremas were along the horizontal diameter. Experiments on a similar configuration were performed by Martini [2]. Brooks and Ostrach [3] experimentally investigated natural convection in a horizontal cylinder by varying the location of temperature extremas on the periphery of the cylinder. Weinbaum [4] investigated the convection phenomenon in a horizontal cylinder for different locations of temperature extremas on the wall of the cylinder. He also carried out a linear stability analysis for the bottom heating case. Surprisingly though, there have been few numerical studies for natural convection in a horizontal cylinder. Hellums and Churchill [5], Heinrich and Yu [6] and more recently Xin et al. [7] have investigated the problem numerically. Xin et al. have provided detailed information regarding flow structure and heat transfer for a range of Rayleigh and Prandtl numbers for the case of temperature extremas along the horizontal diameter. Their investigation revealed that the flow is essentially of the boundary layer type with motion confined to a thin layer close to the cylinder wall and the core being nearly isothermal and stagnant. They have also carried out a linear stability analysis to determine the critical Ra_g for the loss of stability of steady convection.

The current study is motivated by the fact that rotation can significantly influence the convective motion due to nonuniform heating when the Coriolis and Centrifugal forces are in comparable magnitudes with the thermal buoyancy. There have been a number of numerical as well as experimental studies involving thermal convection in horizontal layers rotating about a vertical axis parallel to gravity [8–10]. Invariably all of these studies neglect Centrifugal buoyancy forces so that the results apply only for low rotation rates governed by the condition centrifugal accn/gravitational accn$\ll$1. In the numerical works both rigid as well as stress free boundaries were treated. It was found that rotation has a stabilizing effect with critical Ra increasing with an increase in the rotation rate or the Taylor number. A numerical study by Veronis [8] revealed that the Prandtl number affects the flow and thermal structures significantly. For the limit of an infinite Prandtl number Kupper and Lortz [9] showed that no stable steady state convective flow exists beyond a certain critical value of Taylor number. Rossby [10] experimentally found that for water at$Ra_g > 10^4$, the Nusselt number was found to increase with Taylor number. The opposite trend is observed for air. More recently,researchers have started focussing on convection in differentially

Contributed by the Heat Transfer Division for publication in the JOURNAL OF HEAT TRANSFER. Manuscript received by the Heat Transfer Division January 14, 2004; revision received September 16, 2004. Associate Editor: C. H. Oh.

heated, rotating cubical enclosures. Lee and Lin [11] numerically investigated the three-dimensional flow in a rotating, differentially heated, cubical cavity.

While most of the studies involving rotation consider rotation about an axis parallel to gravity vector, there have been very few studies with rotation axis perpendicular to gravity or any component of gravity. This scenario introduces an explicit time dependency of the gravitational buoyancy force in the rotating frame of reference. Hamady et al. [12] investigated, both numerically and experimentally, 2D natural convection in an air filled differentially heated square enclosure rotating about an axis perpendicular to the plane of motion. Their investigation was carried out at low enough rotation rates so that the centrifugal or rotational buoyancy was insignificant. To the authors' knowledge, the work of Ker and Lin [13] which focused on 3D flow in a tilted, rotating, differentially heated cubical enclosure is perhaps the only detailed numerical and experimental study for the case of the rotation axis perpendicular to the component of gravity. They found that the oscillation levels of the flow field and the heat transfer rates could be effectively controlled using rotation. Ker and Lin, however, carried out a dimensional study and have not correlated the flow structure to the different body forces involved. Further, they have not investigated the effect of rotation of the "*g*" vector on the flow structure. To the best of this author's knowledge, the case of a differentially heated horizontal cylinder, rotating about its axis, has not been numerically investigated by any worker. Since the rotation axis is perpendicular to the gravity vector, the Centrifugal or Rotational Buoyancy and the Coriolis Forces lie within the cross sectional plane of the cylinder. Thus, excluding the end effects, the flow generated relative to solid body rotation, essentially has a two-dimensional structure. Three dimensionality can only be generated through inherent instabilities of the flow to three-dimensional perturbations. It is felt that two-dimensional calculations for the case of a horizontal rotating cylinder provide a good platform for understanding the basic flow dynamics and the roles played by the time varying Gravitational Buoyancy, the Rotational Buoyancy and the Coriolis forces in affecting the flow structure.

In Section 2 we present the formulation of the problem comprising of the governing equations and the numerical scheme employed. In Section 3, validation of the code is presented. In Sections 4 and 5, the results and conclusions are presented.

2 Formulation

2.1 Governing Equations. The formulation of the problem of buoyancy (gravitational and rotational) induced motion of a fluid in a two-dimensional circular enclosure is done by utilizing the conventional Boussinesq approximation to the governing equations of mass, momentum and energy, in a frame rotating with the enclosure. Figure 1 shows the geometry of the problem together with the Cartesian rotating frame. It is assumed that the temperature perturbation is applied impulsively to the wall of a steadily rotating cylinder with the fluid in a state of solid body rotation at time $t=0$. The problem is formulated using a Cartesian frame in order to avoid the numerical difficulties at the origin in the cylindrical polar frame. The governing equations in nondimensional form are:

Mass:

$$\frac{\partial u}{\partial x}+\frac{\partial v}{\partial y}=0 \tag{1}$$

x-momentum:

$$\frac{\partial u}{\partial \tau}=-\frac{\partial p_m}{\partial x}+\mathrm{Ra}_g\,\mathrm{Pr}\,\theta\sin(\mathrm{Ta}^{0.5}\,\mathrm{Pr}\,\tau)-\mathrm{Ra}_\Omega\,\mathrm{Pr}\,\theta x+2\,\mathrm{Ta}^{0.5}\,\mathrm{Pr}\,v$$
$$-u\frac{\partial u}{\partial x}-v\frac{\partial u}{\partial y}+\mathrm{Pr}\,\nabla^2 u \tag{2}$$

y-momentum:

$$\frac{\partial v}{\partial \tau}=-\frac{\partial p_m}{\partial y}+\mathrm{Ra}_g\,\mathrm{Pr}\,\theta\cos(\mathrm{Ta}^{0.5}\,\mathrm{Pr}\,\tau)-\mathrm{Ra}_\Omega\,\mathrm{Pr}\,\theta y-2\,\mathrm{Ta}^{0.5}\,\mathrm{Pr}\,u$$
$$-u\frac{\partial v}{\partial x}-v\frac{\partial v}{\partial y}+\mathrm{Pr}\,\nabla^2 v \tag{3}$$

Energy Equation:

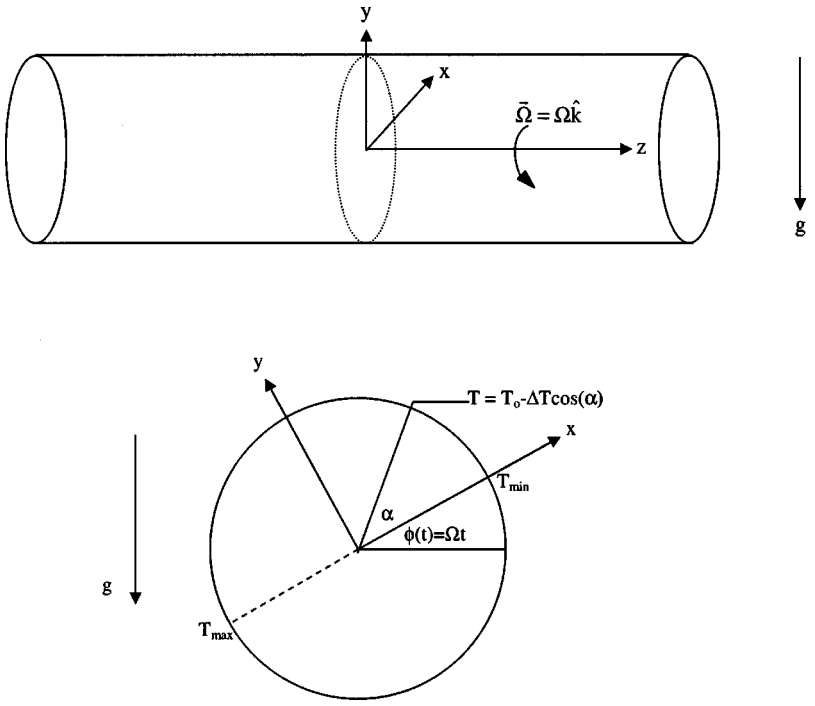

Fig. 1 Geometry of the problem

$$\frac{\partial \theta}{\partial \tau} = -u\frac{\partial \theta}{\partial x} - v\frac{\partial \theta}{\partial y} + \nabla^2 \theta \tag{4}$$

The length, time and velocity scales employed in the nondimensionalization are R, R^2/κ, κ/R. The pressure p_m in (2) and (3) is the dimensionless motion pressure over and above the dimensionless pressure in the solid body rotation state with respect to a fixed frame or a hydrostatic state with respect to an observer rotating with the cylinder, at a uniform temperature T_0 and density ρ_0. This is the rotational analogue of piezometric pressure.

As pointed out by Ker and Lin [13], the ratio of Taylor Number to Rotational Rayleigh Number is given as $1/(\beta\,\Delta T\,\mathrm{Pr})$. Since the product $(\beta\,\mathrm{Pr})$ is nearly the same for commonly occurring liquids and gases and is $O(10^{-3}{}^{\circ}\mathrm{C}^{-1})$, this ratio essentially depends on the amplitude of the imposed temperature perturbation. For the validity of linear variation of density with temperature in the Boussinesq approximation, ΔT is generally taken to be $O(10^{\circ}\mathrm{C})$. This provides an approximate order of the ratio of the two numbers viz. Ta and Ra_{Ω} to be $O(10^2)$ for commonly occuring fluids like air and water. In the current investigation we take this ratio to be fixed and equal to 100.

Boundary conditions used are:

$$u=0,\ v=0,\ \theta=-\cos(\alpha)\ \text{ on }\ x^2+y^2=1.0 \tag{5}$$

The initial conditions are as follows:

$$u=0,\ v=0,\ \theta=0,\ p_m=0 \quad \text{for } x^2+y^2<1.0 \tag{6}$$

2.2 Numerical Scheme

2.2.1 Discretization. For the purpose of capturing the unsteady physics of the flow we employ a semi-implicit, pressure correction type scheme, on a nonstaggered mesh and utilize the concept of momentum interpolation of Rhie and Chow [14] in order to avoid grid scale pressure oscillations that can result, owing to decoupling between the velocity and pressure at a grid point. The scheme is described by Hirsch [15] and is conceptually similar to the SMAC algorithm given by Amsden and Harlow [16]. Guided by the works of Kim and Benson [17] and Cheng and Armfield [18] who have demonstrated the computational efficiency of SMAC scheme over the SIMPLE, SIMPLEC, and PISO methods for computing of unsteady, incompressible flows, the present work also utilizes a scheme that is essentially similar to SMAC.

The time integration of momentum and energy equations is performed using a first-order Euler method to obtain the guessed velocity field at the new time step. Formally the scheme is given as follows:

$$\overline{u}_{i,j}^{n+1} = u_{i,j}^n + \delta\tau\left\{H_{i,j}^n - \left(\frac{\partial p}{\partial x}\right)_{i,j}^n\right\} \tag{7a}$$

$$\overline{v}_{i,j}^{n+1} = v_{i,j}^n + \delta\tau\left\{G_{i,j}^n - \left(\frac{\partial p}{\partial y}\right)_{i,j}^n\right\} \tag{7b}$$

$$\theta_{i,j}^{n+1} = \theta_{i,j}^n + \delta\tau\{F_{i,j}^n\} \tag{7c}$$

Also,

$$u_{i,j}^{n+1} = u_{i,j}^n + \delta\tau\left\{H_{i,j}^n - \left(\frac{\partial p}{\partial x}\right)_{i,j}^{n+1}\right\} \tag{8a}$$

$$v_{i,j}^{n+1} = v_{i,j}^n + \delta\tau\left\{G_{i,j}^n - \left(\frac{\partial p}{\partial y}\right)_{i,j}^{n+1}\right\} \tag{8b}$$

where superscript n indicates the flow field at time level n, while the superscript $n+1$ represents the flow field at time level $n+1$. The overbar is used to represent the guessed velocity components at time level $n+1$ which do not satisfy continuity. The velocity and pressure corrections ($u'_{i,j}$, $v'_{i,j}$ and $p'_{i,j}$) are defined as:

$$u'_{i,j} = u_{i,j}^{n+1} - \overline{u}_{i,j}^{n+1}$$

$$v'_{i,j} = v_{i,j}^{n+1} - \overline{v}_{i,j}^{n+1}$$

$$p'_{i,j} = p_{i,j}^{n+1} - p_{i,j}^n \tag{9}$$

The relationship between velocity corrections and pressure corrections can be obtained by subtracting Eq. (7*a*) from Eq. (8*a*) and Eq. (7*b*) from Eq. (8*b*), respectively. This yields the following relations:

$$u'_{i,j} = -\delta\tau\left(\frac{\partial p'}{\partial x}\right)_{i,j}$$

$$v'_{i,j} = -\delta\tau\left(\frac{\partial p'}{\partial y}\right)_{i,j} \tag{10}$$

The pressure correction must be such that it enforces continuity at the new time level. This is achieved as follows:

$$\left(\frac{\delta u}{\delta x}\right)_{i,j}^{n+1} + \left(\frac{\delta v}{\delta y}\right)_{i,j}^{n+1} = 0 \tag{11}$$

$$\left(\frac{\delta \overline{u}}{\delta x}\right)_{i,j}^{n+1} + \left(\frac{\delta \overline{v}}{\delta y}\right)_{i,j}^{n+1} + \left(\frac{\delta u'}{\delta x}\right)_{i,j} + \left(\frac{\delta v'}{\delta y}\right)_{i,j} = 0 \tag{12}$$

Using Eq. (10) we get

$$\frac{\delta}{\delta x}\left(\frac{\partial p'}{\partial x}\right)_{i,j} + \frac{\delta}{\delta y}\left(\frac{\partial p'}{\partial y}\right)_{i,j} = \left(\frac{1.0}{\delta\tau}\right)\left[\left(\frac{\delta \overline{u}}{\delta x}\right)_{i,j}^{n+1} + \left(\frac{\delta \overline{v}}{\delta y}\right)_{i,j}^{n+1}\right] \tag{13}$$

The pressure correction is thus obtained by solving the above Poisson equation.

The pressure correction is obtained in the interior from Eq. (13) subject to the condition:

$$\frac{\partial p'}{\partial n} = 0 \tag{14}$$

where n is the local normal direction to the boundary of the domain.

This condition stems from the fact that the fluid cannot penetrate into the wall. Hence, its normal component at the solid wall must vanish. The current method is thus similar to the SMAC method where the guessed velocity field obtained from the momentum equations is corrected by adding irrotational velocity corrections to enforce continuity at the new time level.

The discretization of (13) needs to be handled carefully as a central discretization of terms on both sides of (13) leads to an effective discrete equation for (13) on a mesh twice as coarse as the actual grid. Further, central discretization of the divergence term on the right hand side of (13) results in pressure–velocity decoupling. These effects generally lead to spurious grid scale pressure oscillations [18,19]. In order that the scheme does not permit such nonphysical solutions specifically due to the above mentioned reasons, the discretization of (13) is carried out as follows:

In Eq. (13) the divergence operator $\delta/\delta x$ is discretized as

$$\frac{\delta}{\delta x}\left(\frac{\partial p'}{\partial x}\right)_{i,j} \cong \left(\frac{2.0}{dx1+dx2}\right)\left[\left(\frac{\partial p'}{\partial x}\right)_{i+1/2,j} - \left(\frac{\partial p'}{\partial x}\right)_{i-1/2,j}\right]$$

$$\left(\frac{\delta \overline{u}}{\delta x}\right)^{n+1} \cong \left(\frac{2.0}{dx1+dx2}\right)[\overline{u}^{n+1}_{i+1/2,j} - \overline{u}^{n+1}_{i-1/2,j}] \tag{15}$$

where $dx1 = x_{i+1} - x_i$ and $dx2 = x_i - x_{i-1}$.

The pressure gradients are discretized as:

$$\left(\frac{\partial p'}{\partial x}\right)_{i+1/2,j} = \frac{p'_{i+1,j} - p'_{i,j}}{dx1}$$

$$\left(\frac{\partial p'}{\partial x}\right)_{i-1/2,j} = \frac{p'_{i,j} - p'_{i-1,j}}{dx2} \tag{16}$$

The velocities $\overline{u}^{n+1}_{i+1/2,j}$ and $\overline{u}^{n+1}_{i-1/2,j}$ are obtained using a special interpolation procedure of Rhie and Chow [14]. This is given as follows:

$$\overline{u}^{n+1}_{i+1/2,j} = 0.5(up^{n+1}_{i+1,j} + up^{n+1}_{i,j}) - \delta\tau\left(\frac{p^n_{i+1,j} - p^n_{i,j}}{dx1}\right)$$

$$\overline{u}^{n+1}_{i-1/2,j} = 0.5(up^{n+1}_{i,j} + up^{n+1}_{i-1,j}) - \delta\tau\left(\frac{p^n_{i,j} - p^n_{i-1,j}}{dx2}\right) \tag{17}$$

The velocity $up^{n+1}_{i,j}$ is obtained from Eq. (7*a*) without the pressure gradient term. The compact discretization in (15) and (16) together with Rhie and Chow interpolation, to obtain the guessed velocities midway between adjacent grid points, helps to maintain the coupling between the velocity and pressure fields. It is worth mentioning here that the above discretization should not be regarded as an attempt to a priori suppress the ''wiggles'' as they can still appear due to several factors like improper grid spacing in regions of high gradients, improper specification of boundary and initial conditions as discussed by Gresho and Sani [20]. In fact, during the validation exercise involving thermally driven convection in a stationary cylinder, wiggles were observed in the flow field for some improperly spaced grids. These spatial oscillations were removed using properly spaced grids as suggested in [20], and grid independence was established. The discrete Poisson equation is solved numerically using Stone's SIP procedure [19].

Equations (10) and (13) are used only in the interior to obtain the corrections and hence the flow field at the new time step. At the walls the no-slip condition is explicitly specified for the velocities. The pressure at the boundary is updated through the normal momentum equation. These conditions are the same as employed in [18].

Owing to explicit first-order Euler integration to obtain the temperature and guessed velocities at the new time level, Eqs. 7(*a*)–7(*c*) together with initial conditions given in (6) constitute an intial value problem. In this regard the Cauchy–Kovalevskaya theorem can be utilized to assess whether the intial value problem is well posed or not. According to the theorem, for an intial value problem, specified through a set of quasi-linear pdes involving several unknowns or dependent variables, the problem is well posed if the coefficients of the set of equations are analytic over the intial data or conditions [21]. Thus it can be judged that the problem considered is well posed.

2.2.2 Consistency, Stability and Accuracy. The consistency of the numerical scheme in 2.2.1 has been checked and it has been found that the scheme is fully consistent and the original pde's are recovered as $\delta t \to 0$, $(\Delta x, \Delta y) \to 0$. Since the scheme employs an explicit time integration (Eqs. 7(*a*)–7(*c*)), the maximum time step needed for stable computations on a given grid is governed by some stability criterion. For the current investigation, the proper time step leading to stable computations was determined through experimentation or trials. The linear stability procedures like the Von Neumann Method or the Matrix Method are strictly applicable only to linear difference equations. For difference equations involving two or more dependent variables, the Von Neumann conditions are necessary but not sufficient conditions for the stability of the scheme [22]. In the absence of any universally applicable method for a complex, coupled, and nonlinear problem like the one under consideration, it was considered appropriate to determine the time step through experimentation or trials. However, the trials are guided by the physical criteria that for an explicit treatment of convection and viscous terms the time step should be such that the disturbance at any point is not allowed to propagate by a distance more than a grid spacing under the combined influence of diffusion and convection [19]. Heinrich and Yu [6] have treated the nonlinear convection terms explicitly, and have based their time step estimation on the above criteria.

For the interior nodes, the convection terms are discretized using a hybrid scheme of a fourth-order, symmetric four point central differencing and a third-order Taylor series based upwinding scheme employing two points on the upstream side and one point on the downstream side of the grid point under consideration. The choice between upwinding and central differencing is made on the basis of the local cell Peclet number. If $|\mathrm{Pe}| < 2$ then central differencing is preferred, otherwise upwinding is utilized. For near boundary nodes, the convective terms are discretized using a second-order central differencing. The viscous terms are discretized using a fourth-order five point, symmetric, central differencing in the interior while a second-order three point, symmetric, central differencing scheme is utilized for near boundary nodes. The local orders of accuracy of the various discretizations are for a uniformly spaced grid.

3 Validation

Xin et al. [7] have provided detailed numerical solutions for the nonrotating situation with temperature extremas located across the horizontal diameter. A structured Cartesian grid has been generated such that the intersection of grid lines lies on the boundary of the circular domain, thereby ensuring that a grid point lies on the domain boundary for the specification of boundary conditions. This limits the choice of grid spacing to one of the spatial directions only. A typical 91×91 grid has been spaced in the x direction with a minimum spacing of 5×10^{-4} at $x = -1.0$ and a maximum spacing of 0.038 near $x = 0$ or the center of the enclosure. The grid spacing has been adjusted so that the angular spacing of grid points on the boundary does not exceed 1.5 deg. The grid spacing is kept symmetric about $x = 0$. Since the geometry is symmetric about both $x = 0$ and $y = 0$ the grid is also symmetric about $y = 0$. The circumferential variations in the flow variables are found to be extremely sensitive to the angular spacing of the grid points on the boundary and therefore through different trials the grid spacing had to be adjusted to yield smooth and grid independent solutions for the fixed cylinder problem. This sensivity is due to the fact that, since the grid points are forced to lie on the circular boundary, the angular spacing of grid points on the boundary essentially govern the grid spacings both in the x and y directions for the entire mesh. Further, for the nonrotating case, the flow is of a boundary layer type with motion essentially confined to a thin layer close to the wall. Hence as discussed by Gresho and Sani [20], if the grid spacing in the wall normal direction is not

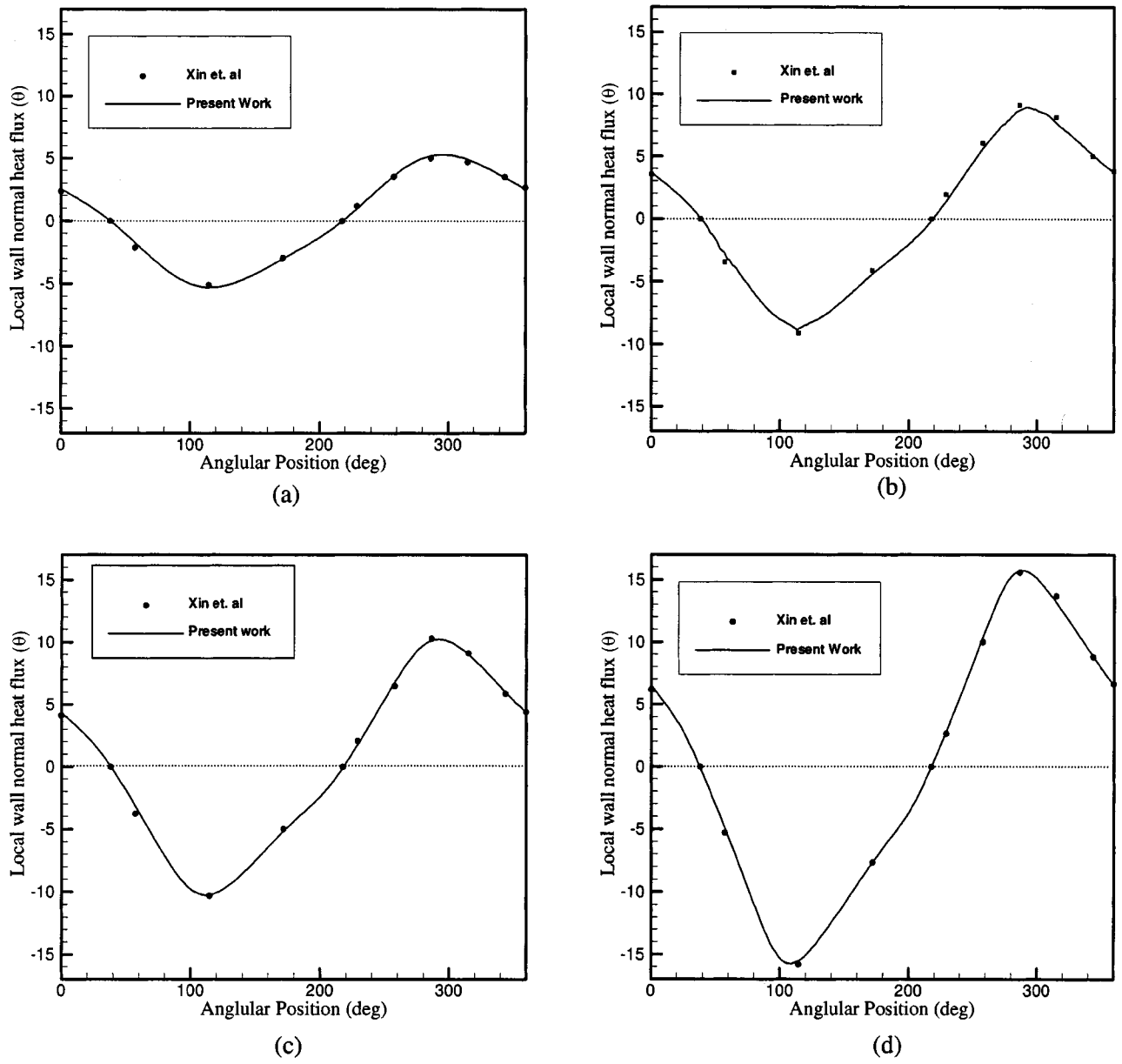

Fig. 2 A comparison of circumferential distribution of local wall normal heat flux with that of Xin et al. [7] for (*a*) $Ra_g=1\times10^4$; (*b*) $Ra_g=5\times10^4$; (*c*) $Ra_g=1\times10^5$; (*d*) $Ra_g=5\times10^5$

appropriate to generate strong enough diffusion to balance the strong advection, oscillations or "wiggles" tend to show up in the numerical solution. Thus suitably spaced grid points, which are in turn governed by their angular spacing on the boundary, are needed to yield nonoscillatory and grid independent solutions. Figures 2(*a*)–2(*d*) compare the local wall normal heat flux variation over the entire wall of the cylinder with the numerical data of Xin et al. [7] for four different Ra_g and Pr=0.71. The angular location on the wall is measured from the bottom most point in the counter clockwise direction as in [7]. The agreement for all the four cases is quite good. The space patterns for $Ra_g=10^5$ and Pr=0.71 shown in Fig. 3(*a*) depict the strong boundary layer type of flow with the inner core being stably stratified and nearly stagnant. These space patterns are in good agreement with Xin's results. For different Ra_g and Pr=0.71, the Nusselt number over the heated portion of the cylinder wall, as shown in Table 1, agrees very well with the data reported in [7] with a maximum deviation of 1.5 percent. Figures 3(*b*) and 3(*c*) depict the similar character of the variations of θ and the circumferential velocity v_θ, along the horizontal diameter for $x<0$, as functions of the product of the distance from the hot end and $Ra_g^{0.25}$. The profiles for different Ra_g all collapse into a single universal profile for these choice of coordinates. This indicates an excellent agreement with the classical result of boundary layer theory that the thickness of the boundary layer (hydrodynamic and thermal), δ, varies as $-1/4$ power of Ra_g. The similar profiles also match very well with those in [7]. The values of v_θ over the left half of the horizontal diameter have been calculated using the fact that it is simply equal to $-v$ using the convention that anticlockwise circumferential velocity is positive. It is also pointed out that since the velocity scale employed in [5] is different from the one currently utilized, the v velocity has been rescaled for comparison purposes. All the validation runs were carried out for a 73×73 symmetric grid having a minimum spacing of 8×10^{-4} near $x=-1.0$ and a maximum spacing of 0.046 near $x=0$ in the x direction, except for the case of $Ra_g=5\times10^5$ for which a 91×91 grid was employed to resolve the thin boundary layer.

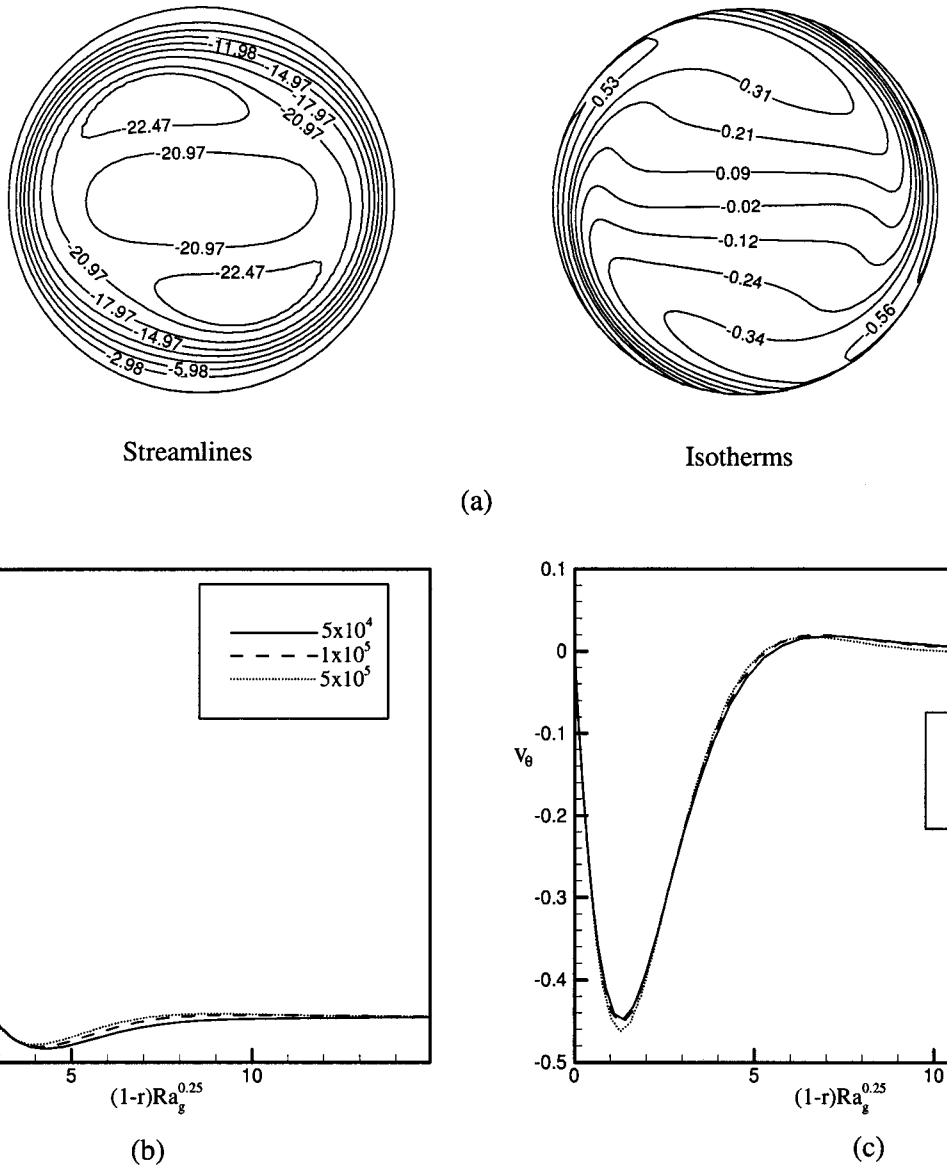

Fig. 3 (*a*) **Streamline (left) and isotherm (right) patterns at $Ra_g=10^5$, $Ra_\Omega=0$.** (*b*) **Similar variation of nondimensional temperature θ along the horizontal diameter for $x<0$ for different Ra_g;** (*c*) **similar variation of nondimensional circumferential velocity v_θ along the horizontal diameter for $x<0$ for different Ra_g.**

Table 1 Comparison of Nusselt number for the hot portion of the cylinder wall with numerical data of Xin et al [7] for different Ra_g in steady state convection.

Ra_g	Present	Xin et .al
$1x10^4$	2.61	2.61
$5x10^4$	4.04	4.03
$1x10^5$	4.86	4.91
$5x10^5$	7.41	7.51

4 Results

To check the grid independence of the results for the rotating cases, three symmetric grids of 73×73, 91×91, and 105×105 nodes were employed. The time histories of Nusselt number over the hot wall as well as v velocity at $(-0.72,0)$ showed a maximum difference of about 4 percent between the 73×73 grid and the 91×91 grid, and about 1 percent between 91×91 and 105×105 grids throughout the entire transients. Hence for all computations a 91×91 grid is employed in order to save the computational time. The time step employed varied from 1×10^{-6} to 1×10^{-7}.

The effects of rotation on the flow structure are investigated by generating instantaneous snapshots of the flow field. Since the cylinder rotates in the counter-clockwise sense, the "g" vector rotates in a clockwise sense in the rotating frame, with the phase "ϕ_g" changing from $3\pi/2$ to π, and then to $\pi/2$ and 0 radians. The changes in the flow structure as the "g" vector rotates are observed by generating snapshots of the flow field, represented by streamfunction contour and isotherm contour plots as well as ve-

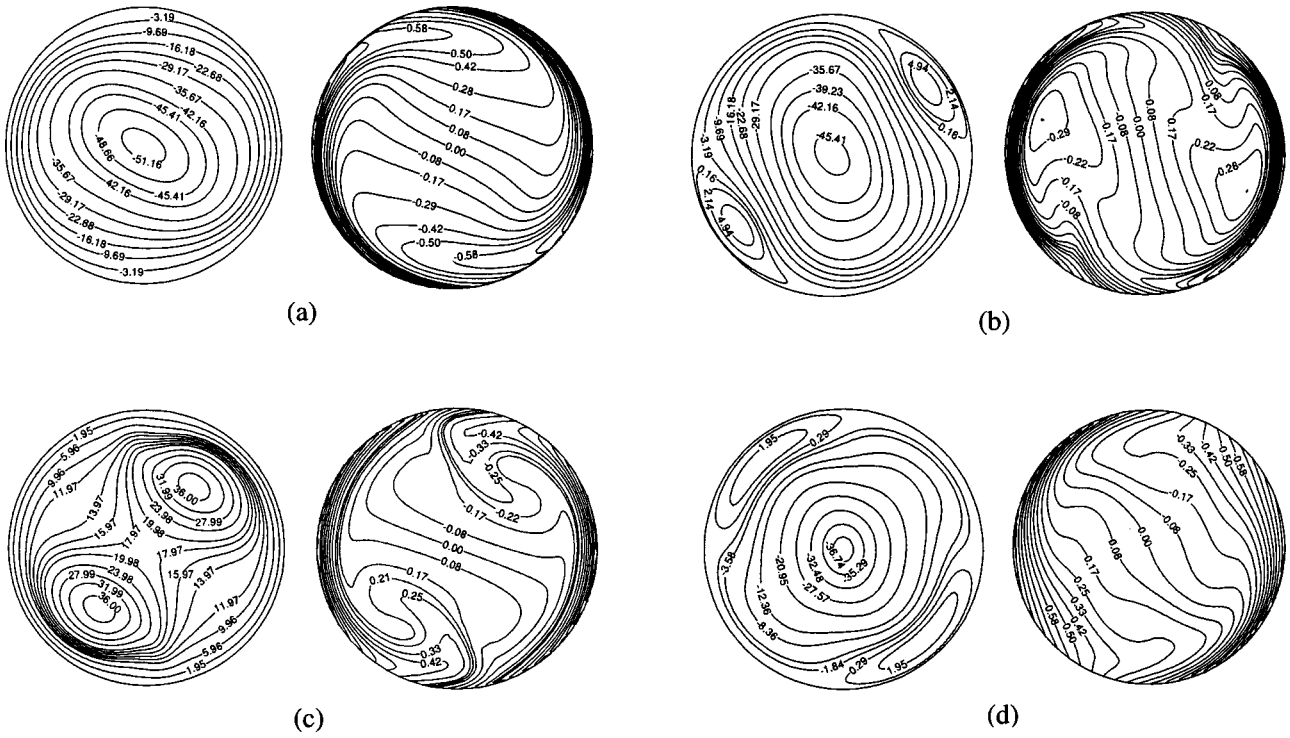

Fig. 4 Streamline and Isotherm patterns for $Ra_\Omega = 10^2$, $Ta = 10^4$ at (*a*) $\phi_g = 3\pi/2$, (*b*) $\phi_g = \pi$, (*c*) $\phi_g = \pi/2$, (*d*) $\phi_g = 0$

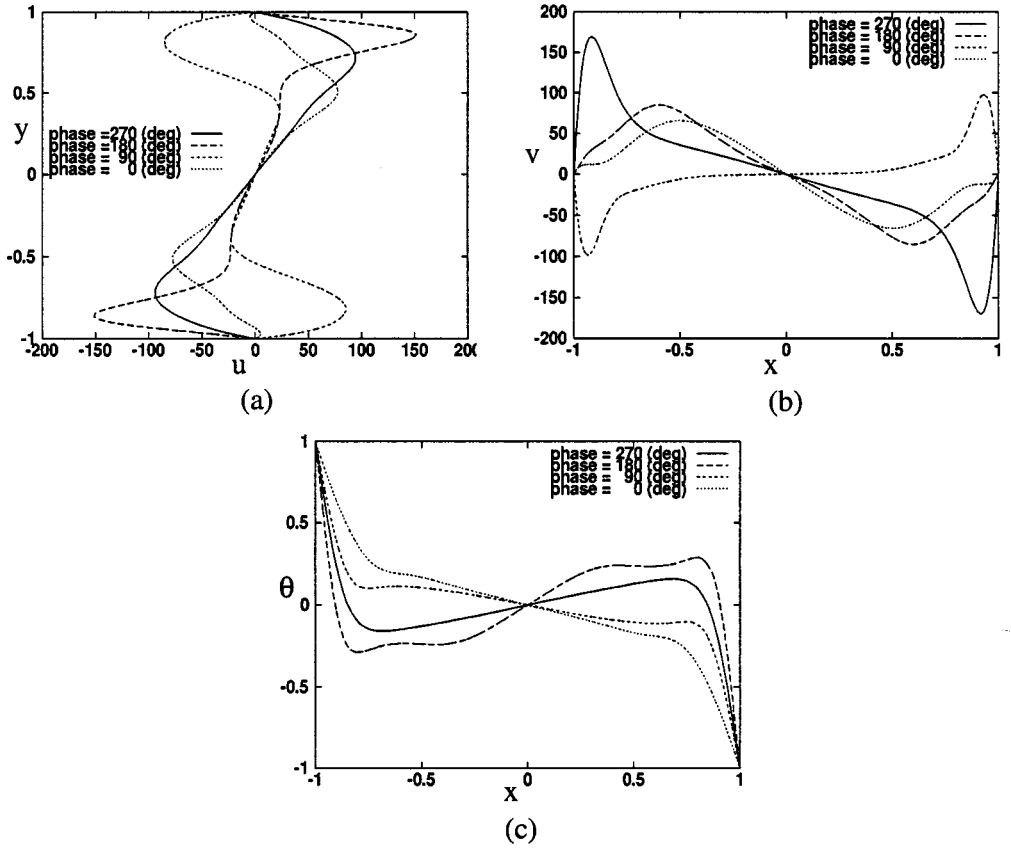

Fig. 5 Profiles of (*a*) *u* velocity across the vertical diameter; (*b*) *v* velocity across the horizontal diameter; and (*c*) θ across the horizontal diameter for different ϕ_g at $Ra_\Omega = 10^2$, $Ta = 10^4$

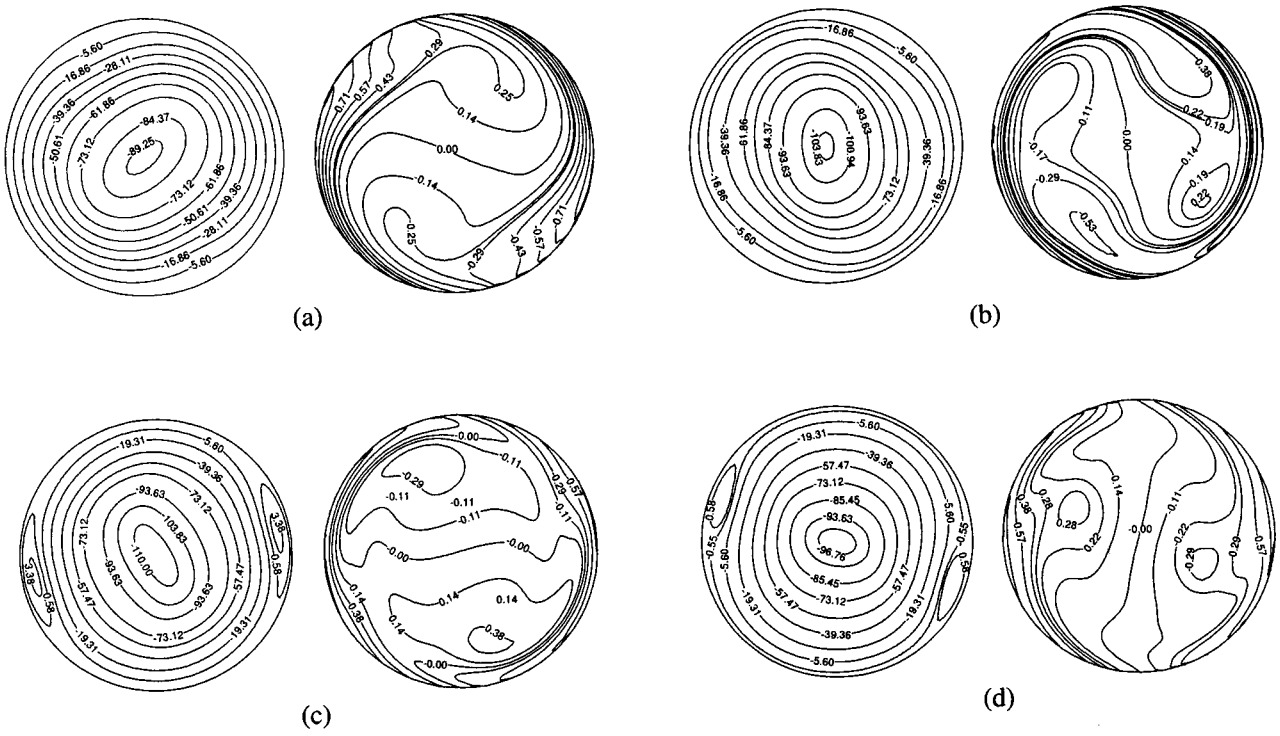

Fig. 6 Streamline and isotherm patterns for $Ra_\Omega = 10^3$, $Ta = 10^5$ at (*a*) $\phi_g = 3\pi/2$, (*b*) $\phi_g = \pi$, (*c*) $\phi_g = \pi/2$, (*d*) $\phi_g = 0$

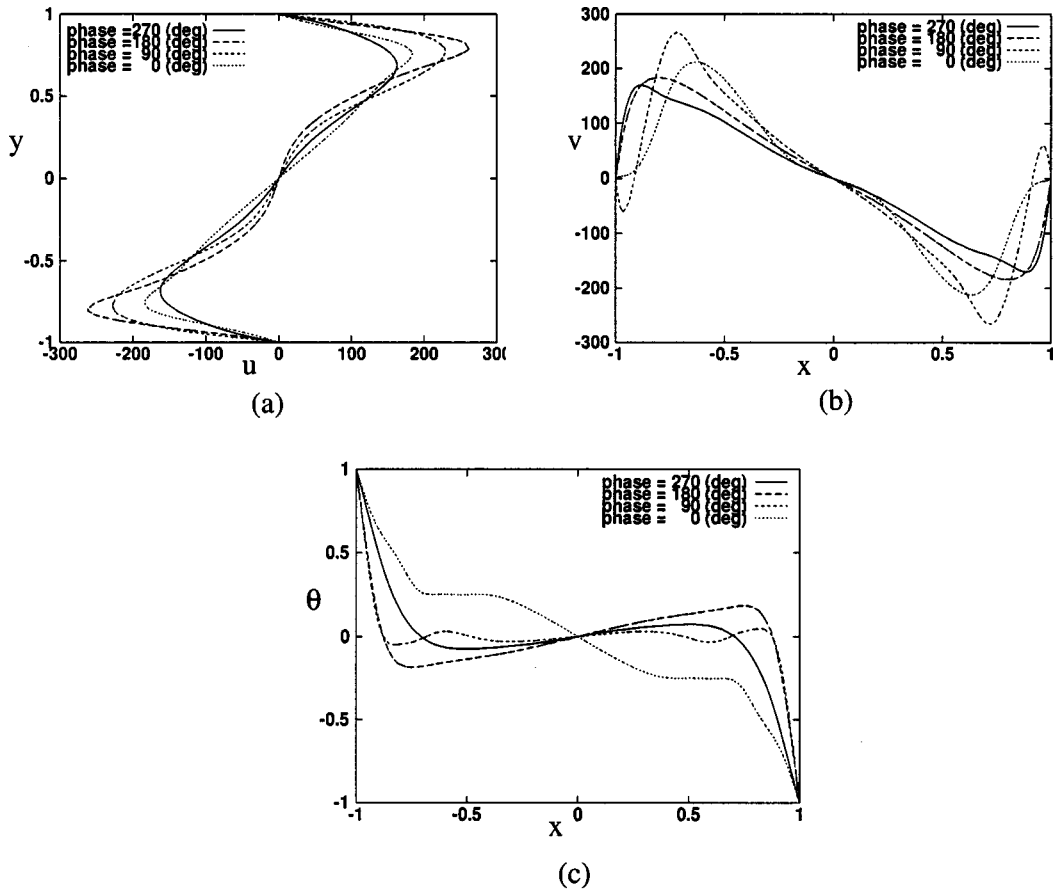

Fig. 7 Profiles of (*a*) *u* velocity across the vertical diameter, (*b*) *v* velocity across the horizontal diameter, and (*c*) θ across the horizontal diameter for different ϕ_g at $Ra_\Omega = 10^3$, $Ta = 10^5$

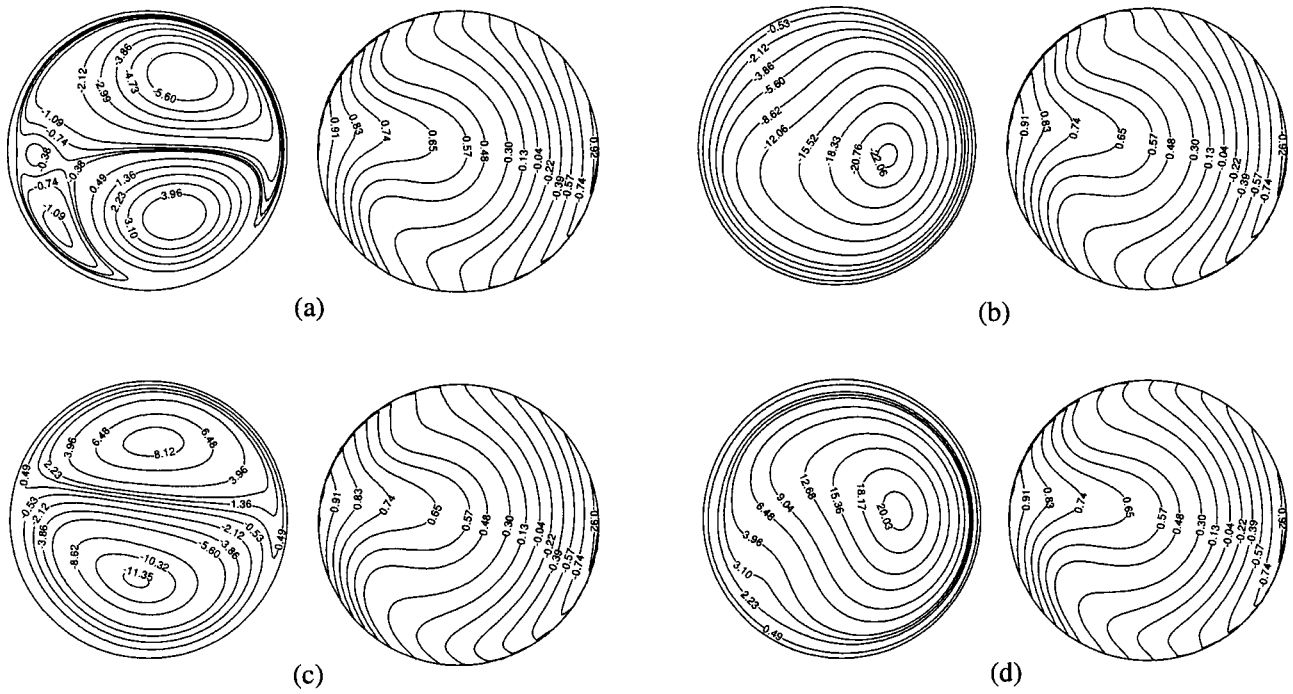

Fig. 8 Streamline and isotherm patterns for $Ra_\Omega = 10^4$, $Ta = 10^6$ at (*a*) $\phi_g = 3\pi/2$, (*b*) $\phi_g = \pi$, (*c*) $\phi_g = \pi/2$, (*d*) $\phi_g = 0$

locity and temperature profiles across horizontal and vertical diameters of the enclosure, at four different phases of the "*g*" vector given by $\phi_g = 3\pi/2$, π, $\pi/2$, 0. The results are organized in four subsections. Subsection 4.1 discusses the spatial and temporal flow structure and the changes that take place in it as Ra_Ω is increased. In subsections 4.2 and 4.3, the structure of vorticity and kinetic energy is examined, respectively. Finally in subsection 4.4, the heat transfer characteristics, represented by a Nusselt number over the hot portion of the wall, are presented.

4.1 Flow Structure. Figures 4(*a*)–4(*d*) show the instantaneous streamline and isotherm patterns for different phase ϕ_g of the rotating "*g*" vector at ($Ra_\Omega = 10^2$, $Ta = 10^4$). The phase of the "*g*" vector is measured from the positive direction of the *x* axis of the rotating frame. At this low value of Ra_Ω and Ta, it can be seen from a rough order of magnitude analysis that the dynamics is essentially controlled only by the Gravitational Buoyancy force, hereinafter referred to as GB, while the Rotational Buoyancy and Coriolis forces, referred to as RB and CF from this point onward, are too weak to exert any significant influence. It should be noted that the motion relative to the rotating frame can only be initiated by GB or by RB and CF only becomes significant in regions of significant velocity. For $\phi_g = 3\pi/2$, the flow takes place in a single clockwise circulatory loop but the motion is not confined in a thin layer close to the cylinder walls as is the case with a nonrotating cylinder. Further, as the direction of GB changes with time, for $\phi_g = \pi$, in the first and the third quadrants the separated recirculation zones appear. These appear because due to clockwise circulation in the previous state some hot fluid is convected into the I quadrant in the vicinity of a cold solid wall while some cold fluid is convected into the III quadrant in the vicinity of a hot solid wall. Hence localized convective loops driven by GB are formed in these regions. For $\phi_g = \pi/2$ the direction of GB again changes acting in the $-y$ direction in hot regions and $+y$ in cold regions with respect to the undisturbed fluid temperature near the cylinder walls. Since GB is proportional to the nondimensional temperature θ, it is stronger near the cylinder walls, thus inducing a counterclockwise circulation near the cylinder walls. Further, two rolls are seen in the I and III quadrants. These are developed because of the fact that due to strong clockwise circulation in the previous states, fluid in some portion of the I quadrant and the III quadrant near the vertical diameter, becomes hotter and colder, respectively, due to convection. Thus, due to the action of GB, hotter fluid particles are accelerated in the $-y$ direction while colder ones are accelerated in the $+y$ direction in these quadrants generating the rolls. Finally for $\phi_g = 0$, GB is in the $-x$ direction in regions where $\theta > 0$ and in the $+x$ direction in space where $\theta < 0$. This again reverses the circulation to a clockwise direction with the appearance of separated recirculating zones in the II and IV quadrants. The recirculating zones are again due to the formation of localized convective loops driven by GB from the cold fluid toward a hot wall in the II quadrant while it is from the cold wall toward the hot fluid in the IV quadrant. These changes in the flow structure are easily seen in the profiles of *u* across vertical and *v* and θ across horizontal diameters, respectively, in Fig. 5. Figures 6(*a*)–6(*d*) show the spatial flow patterns at ($Ra_\Omega = 10^3$, $Ta = 10^5$). The profiles of *u*, *v*, and θ are shown in Fig. 7. At this Ra_Ω, RB is still very weak to exert any influence on the flow field. However, CF is significant and its effect is to assist GB in inducing a clockwise circulation and to oppose it in inducing a counterclockwise circulation. This is readily seen if one compares the velocity profiles in Fig. 5 and Fig. 7. The maximum *u* velocity for $\phi_g = 3\pi/2$ and $\phi_g = \pi$ is greater than for $Ra_\Omega = 10^2$. This is because CF assists the clockwise circulation generated by GB. Further, it is observed that in the case of $Ra_\Omega = 10^3$ there is no reversal of circulation for $\phi_g = \pi/2$, though the velocity is reduced. This is due to the presence of CF that opposes GB in generating a counterclockwise circulation. Since the velocities in the previous state (i.e., $\phi_g = \pi$) are large, the associated CF is large and comparable to GB and is able to nullify it to a large extent. Also in Fig. 6(*c*), we see small separated recirculating zones at the ends of the horizontal diameter. These are generated by GB as close to the wall CF decreases in magnitude. Finally, for $\phi_g = 0$, the recirculating zones appear in the II and IV quadrants due to forcing by GB in the $-x$ direction near the hot wall of the II quadrant and the $+x$ direction near the cold wall of the IV quadrant. Figures 8(*a*)–8(*d*) show the flow structure at $Ra_\Omega = 10^4$ and $Ta = 10^6$. From Fig. 9 it can be readily discerned that

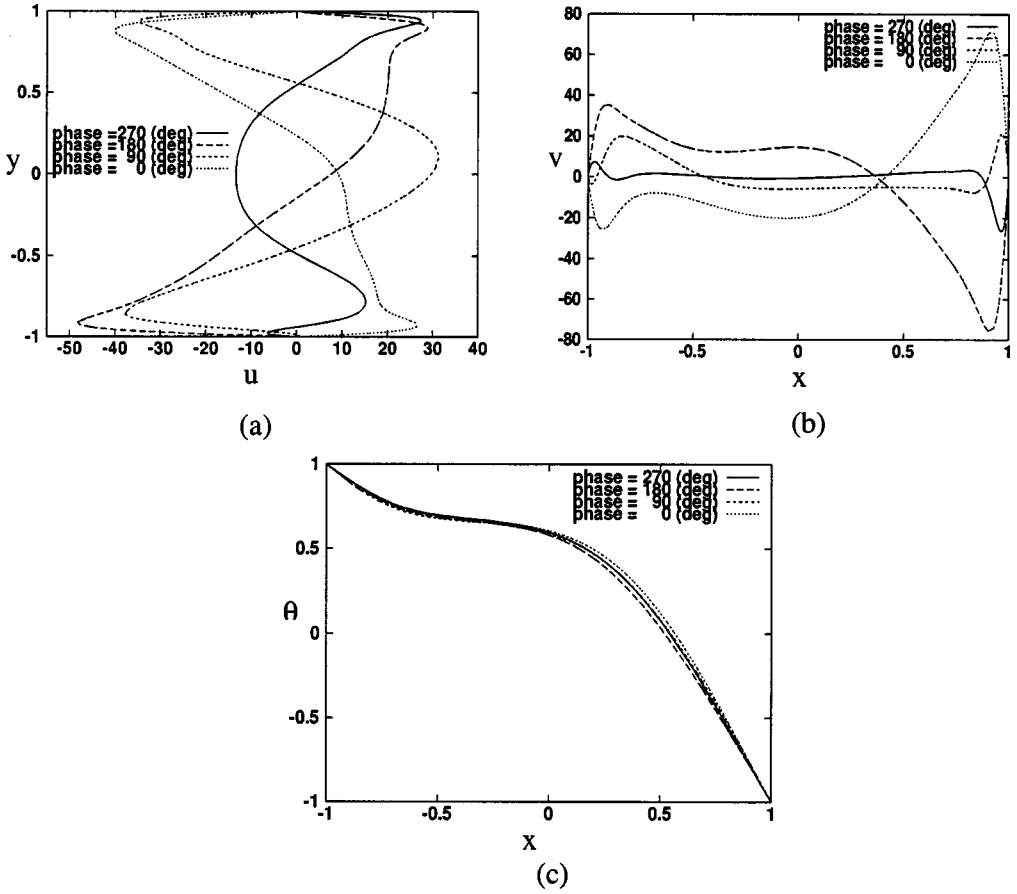

Fig. 9 Profiles of (*a*) *u* velocity across the vertical diameter, (*b*) *v* velocity across the horizontal diameter, and (*c*) θ across the horizontal diameter for different ϕ_g at $Ra_\Omega = 10^4$, $Ta = 10^6$

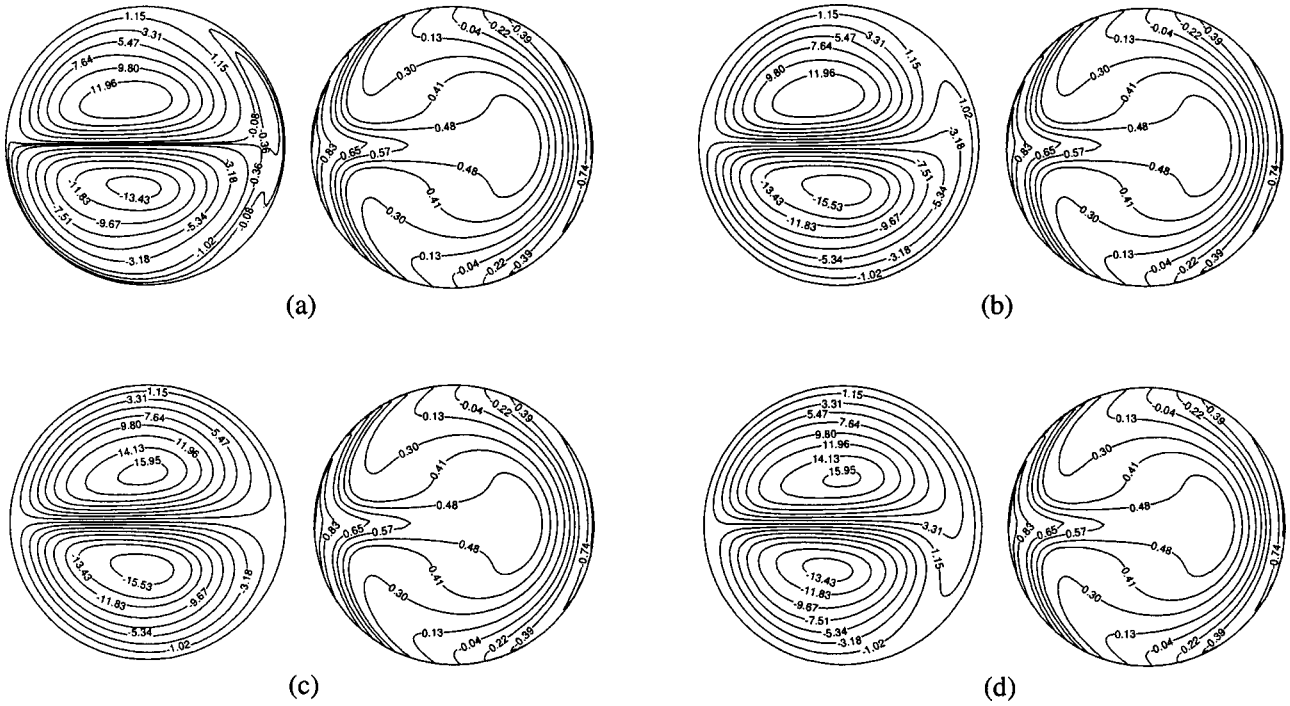

Fig. 10 Streamline and isotherm patterns for $Ra_\Omega = 10^5$, $Ta = 10^7$ at (*a*) $\phi_g = 3\pi/2$ (*b*) $\phi_g = \pi$, (*c*) $\phi_g = \pi/2$, (*d*) $\phi_g = 0$

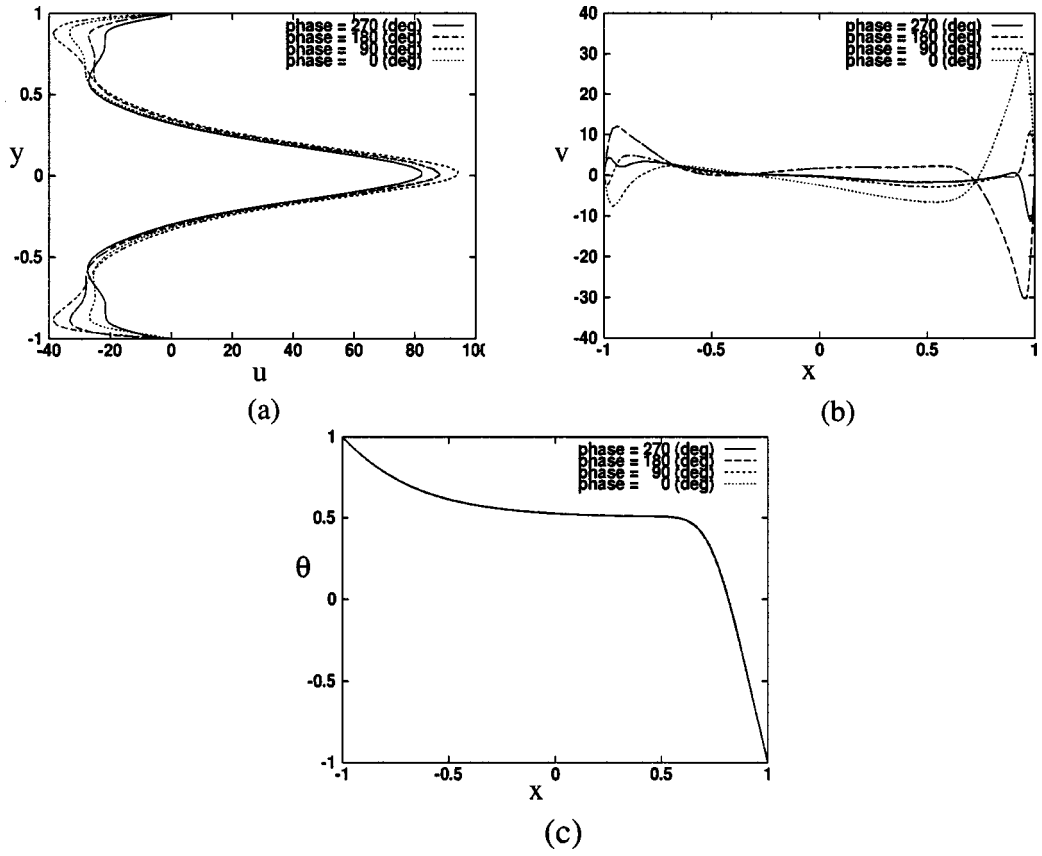

Fig. 11 Profiles of (*a*) *u* velocity across the vertical diameter, (*b*) *v* velocity across the horizontal diameter, and (*c*) θ across the horizontal diameter for different ϕ_g at $Ra_\Omega = 10^5$, $Ta = 10^7$

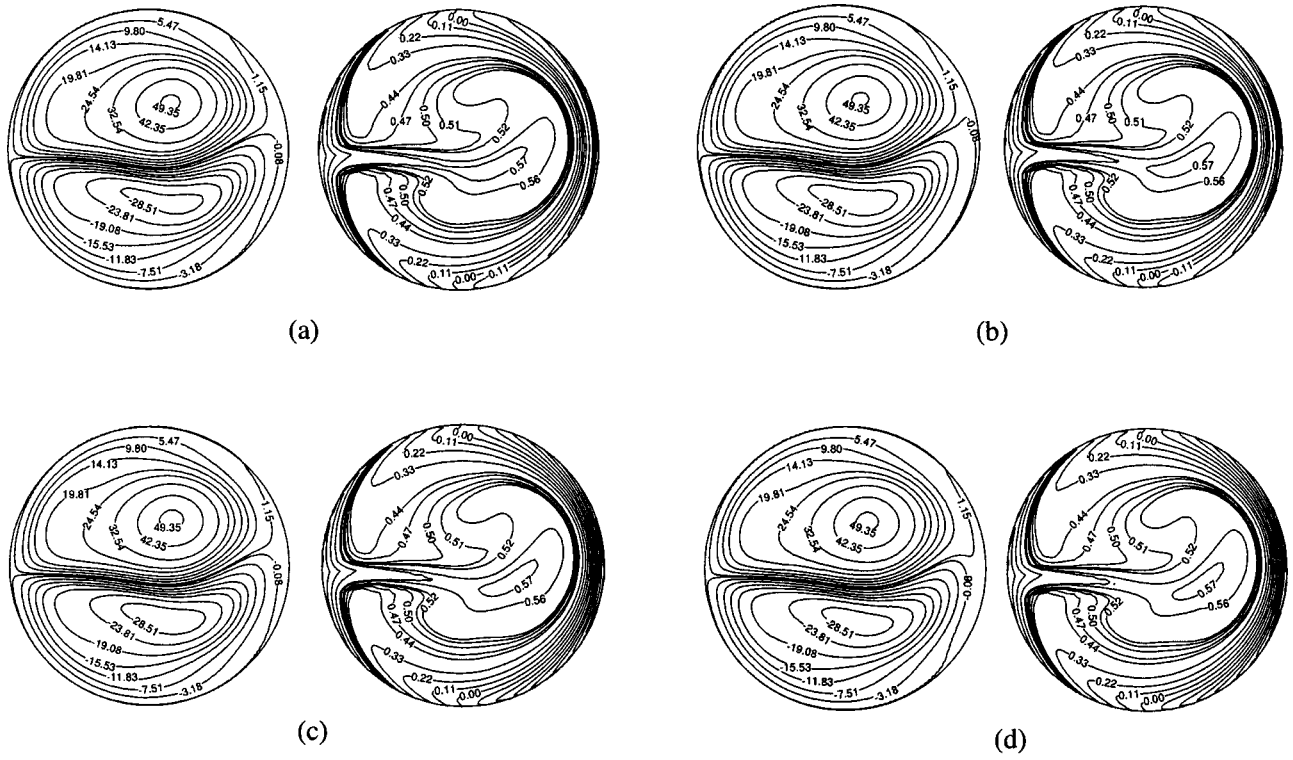

Fig. 12 Streamline and isotherm patterns for $Ra_\Omega = 10^6$, $Ta = 10^8$ at (*a*) $\phi_g = 3\pi/2$, (*b*) $\phi_g = \pi$, (*c*) $\phi_g = \pi/2$, (*d*) $\phi_g = 0$

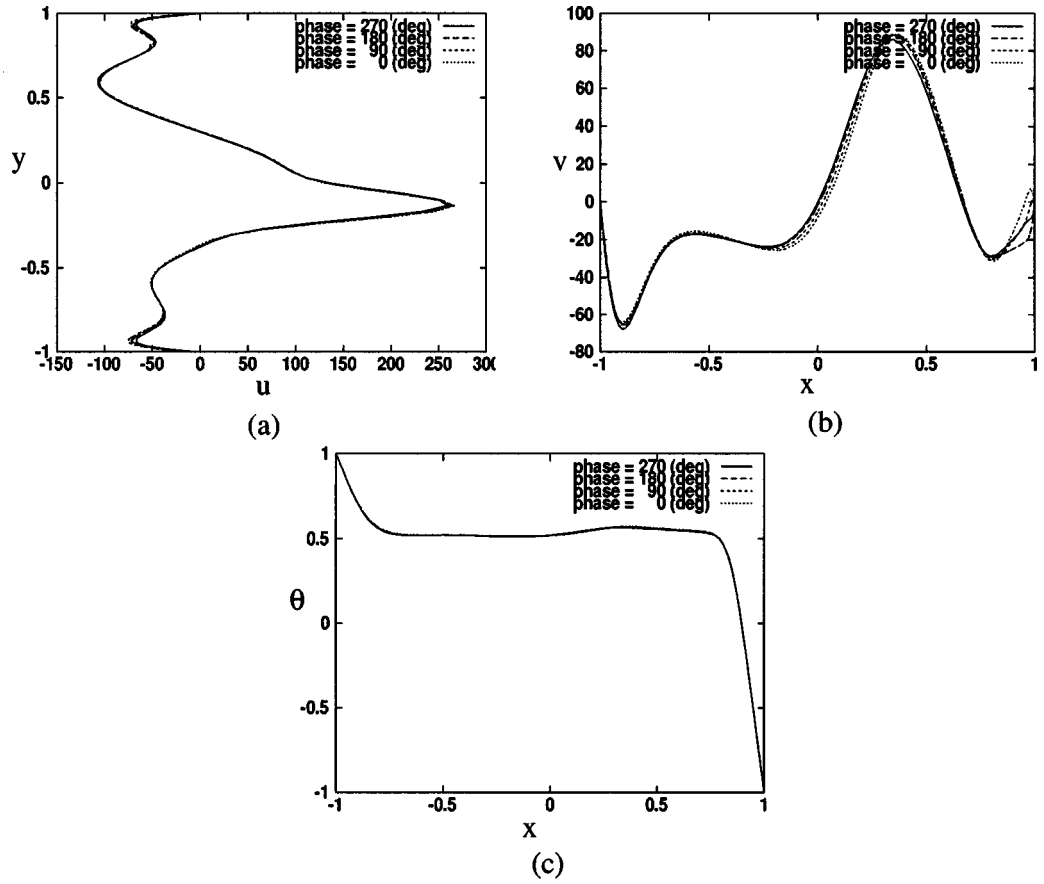

Fig. 13 Profiles of (*a*) *u* velocity across the vertical diameter, (*b*) *v* velocity across the horizontal diameter, and (*c*) θ across the horizontal diameter for different ϕ_g at $Ra_\Omega = 10^6$, $Ta = 10^8$

convection is severely reduced with maximum velocities being reduced by about 5 times. For $\phi_g = 3\pi/2$ two low velocity rolls are seen (Fig. 8(*a*)). These change into a single clockwise roll for $\phi_g = \pi$. For $\phi_g = \pi/2$ again two rolls appear but in the opposite sense as compared to the $\phi_g = 3\pi/2$ case. Finally for $\phi_g = 0$ a single counterclockwise roll appears. An interesting feature in Fig. 8 is that the isotherm pattern does not vary significantly with the rotation of the "*g*" vector. This can be attributed to the fact that the velocities, at this Ra_Ω, are relatively small. Consequently, the temperature field does not experience significant convection. Also, a formation of a bulb-like structure in the isotherm pattern, emanating from the hot point and aligned horizontally, is seen. This bulb-like structure is formed due to the strong convective transport along the interface of the rolls at $\phi_g = \pi/2$. It can also be reasoned that the two cell convection seen for $\phi_g = 3\pi/2$ and $\phi_g = \pi/2$ is primarily generated due to combined effect of CF and GB. At $\phi_g = 3\pi/2$, GB acts in the $+y$ direction in II and III and also in some portions of I and IV quadrants while it acts in the $-y$ direction in some portions in the I and IV quadrants near the cold wall. In order to explain the velocity structure at this instant, one needs to observe the velocity structure and its associated CF in the preceding states. Observing the velocity structure at $\phi_g = 0$, one can say that the x component of CF acts in the $-x$ direction in the II and III quadrants and also in some portions of the I and IV quadrants near the vertical diameter. As the phase of the "*g*" vector starts to change from 0 to $3\pi/2$, the coriolis force causes a flow in the $-x$ direction near the center. This, in combination with GB, generates the two vertically aligned rolls (Fig. 8(*a*)), the top

Fig. 14 Streamline and isotherm pattern for $Ra_\Omega = 10^7$, $Ta = 10^9$ at $\phi_g = 3\pi/2$

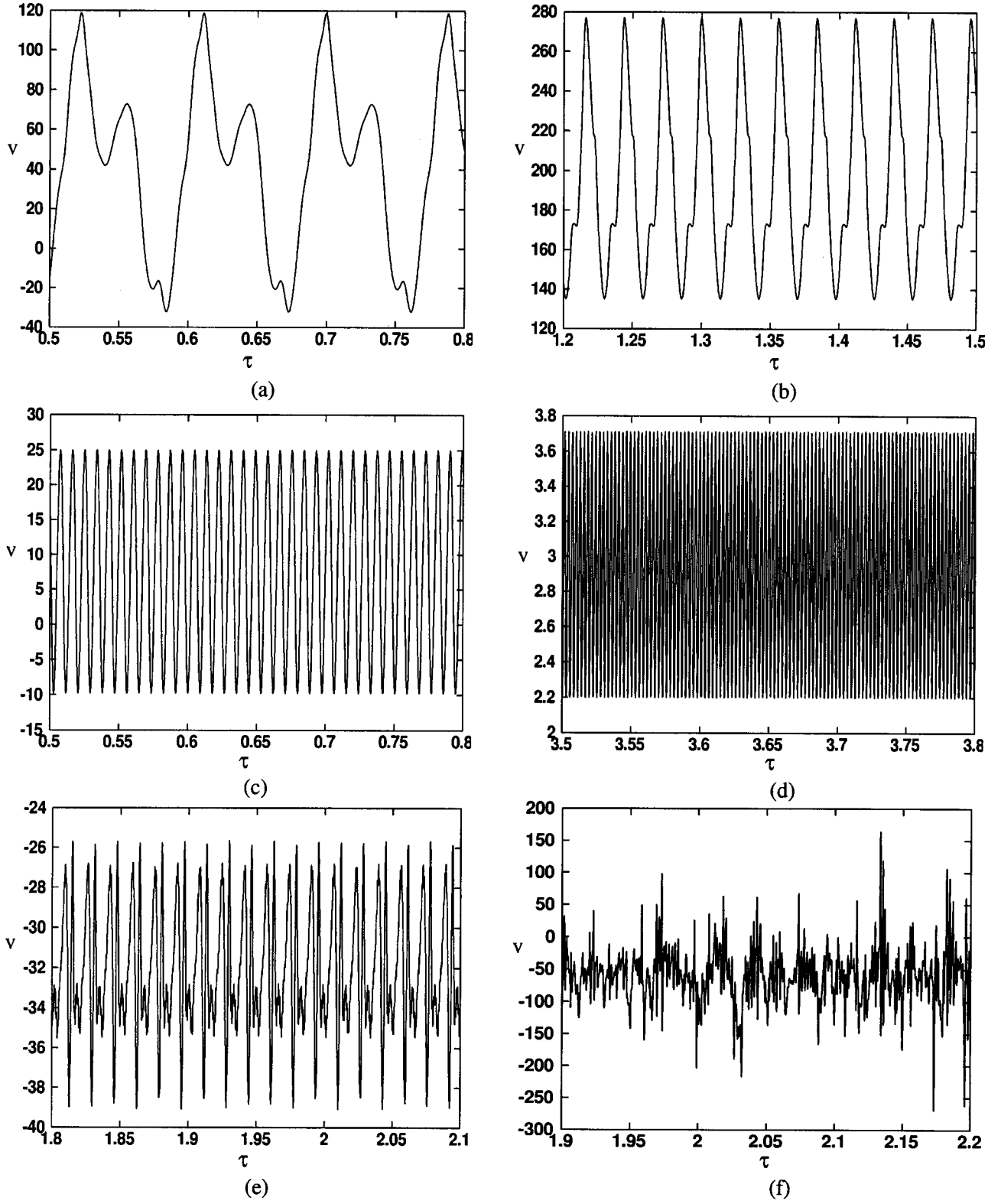

Fig. 15 Time histories of *v* velocity at point (−0.72,0) for (*a*) $Ra_\Omega = 10^2$, (*b*) $Ra_\Omega = 10^3$, (*c*) $Ra_\Omega = 10^4$, (*d*) $Ra_\Omega = 10^5$, (*e*) $Ra_\Omega = 10^6$, (*f*) $Ra_\Omega = 10^7$

one rotating in the clockwise direction and the lower one in the counterclockwise direction. At $\phi_g = \pi/2$ (Fig. 8(*c*)), the slightly nonsymmetric rolls are again due to the Coriolis force, which forces the fluid to separate from the wall in the second quadrant.

For $Ra_\Omega = 10^5$ and $Ta = 10^7$, Figs. 10(*a*)–10(*d*) show that the streamline pattern is totally different from the previous cases. Here it is observed that the overall structure of the velocity and temperature field does not change significantly with rotation of the "*g*" vector. The temperature field, due to strong horizontal convection from the hot point on the wall toward the diametrically

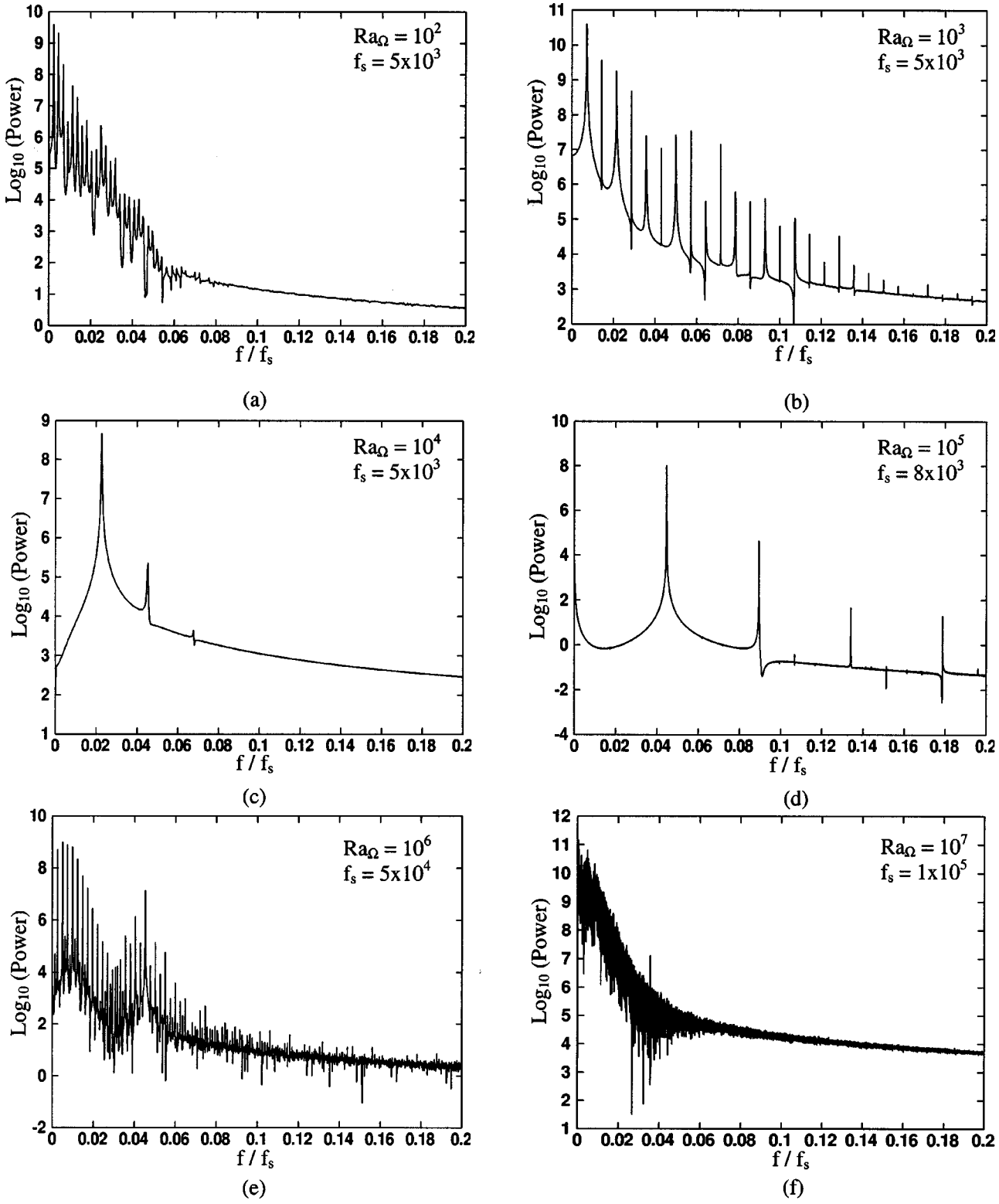

Fig. 16 Power spectral density curves for time series of *v* velocity at (−0.72,0) for (*a*) $Ra_\Omega=10^2$, (*b*) $Ra_\Omega=10^3$, (*c*) $Ra_\Omega=10^4$, (*d*) $Ra_\Omega=10^5$, (*e*) $Ra_\Omega=10^6$, (*f*) $Ra_\Omega=10^7$

opposite cold point on the wall, exhibits a very pronounced bulb-like structure projecting from the hot point. The isotherms suggest that the core is becoming increasingly isothermal at a hotter temperature (around +0.5) in comparison with the undisturbed fluid temperature. This is clearly seen in the temperature profile across the horizontal diameter in Fig. 11(*c*). Since the structure of temperature field and the velocity field is almost same for different phase of the "*g*" vector, the RB has an invariant structure in time while CF has an almost invariant orientation except in small regions near the hot point and the cold point on the extremes of the horizontal diameter. At this Ra_Ω the motion is initiated by both RB and GB, as they are comparable in magnitude. This results in

the formation of two rolls near the hot point in the initial phase of motion. These rolls then grow in time to fill the entire enclosure. The effect of rotation of the "g" vector is only seen in portions near the ends of the vertical and the horizontal diameters, as shown in Figs. 11(a) and 11(b). This is because the x component of RB and CF near the ends of the vertical diameter and the y components of RB and CF near the ends of the horizontal diameter are extremely small. Hence, the effect of GB is easily seen in the u velocity and v velocity profiles, especially near the ends. In the u velocity profile, as shown in Fig. 11(a), it is seen that as ϕ_g changes from $3\pi/2$ to π, GB enhances the u velocity near the center of the cavity. Since the circulation is enhanced near the horizontal diameter, there is a corresponding increase in the u velocity in the opposite direction near the ends of the vertical diameter. The increase in the u velocity near the horizontal diameter continues until $\phi_g=\pi/2$. Finally, for $\phi_g=0$ the u velocity decreases near the center. For the v velocity the effect of GB is seen at the ends of the horizontal diameter (see Fig. 11(b)). As ϕ_g changes from $3\pi/2$ to π the v velocity rises in the positive direction and falls and changes direction as ϕ_g changes from π to 0. Near the cold end the v velocity follows the same trend but in the opposite direction with a larger magnitude. Also over the central portion on the horizontal diameter where $\theta>0$ (Fig. 11(c)), the v velocity increases during the change of ϕ_g from 0 to $3\pi/2$ and then to π and then decreases for the remaining portion of the "g" cycle.

When Ra_Ω is increased to 10^6 and Ta to 10^8, Figs. 12(a)–12(d) show that the flow structure in the entire domain nearly becomes invariant over the entire "g" cycle. This is simply because of the dominance of RB and CF over GB. The flow structure shows that the symmetry of the two rolls is destroyed and that a large portion in the interior of the cavity becomes nearly isothermal at a higher temperature than the undisturbed fluid temperature. The temperature profile in Fig. 13(c) clearly depicts this fact. The fluid particles are transported horizontally from the hot end of the cavity toward the cold end at a high velocity. Owing to the high positive u velocity, CF generates a strong downward force pushing the particle downward as is indicated by the downward slope of the interface of the two rolls. Finally for $\mathrm{Ra}_\Omega=10^7$ and $\mathrm{Ta}=10^9$ the patterns are similar to the previous case with the difference that the temperature field becomes isothermal over a larger portion of the flow domain as shown in Fig. 14. The interface of the convective rolls is pushed downward due to the very strong CF acting along the horizontal diameter in the interior.

To observe the changes in the flow structure in the time domain, the time histories of v velocity are plotted at a fixed point $(-0.72,0)$, as shown in Figs. 15(a)–15(f). The transients have been removed from these histories and only the long term temporal behavior that is found to exist for large times has been plotted. For each Ra_Ω, the integrations are started from the same initial conditions, i.e., the state of rest with respect to the rotating frame. The typical nondimensional times needed for transients to die out were 0.18, 0.2, 0.5, 0.9, 1.0, and 1.1 at $\mathrm{Ra}_\Omega=10^2$, 10^3, 10^4, 10^5, 10^6, and 10^7, respectively. In terms of number of "g" cycles this corresponds to 2, 7, 57, 322, 1695, and 3574 cycles. It is observed that the flow is periodic for $\mathrm{Ra}_\Omega\leqslant 10^5$ while for $\mathrm{Ra}_\Omega=10^6$ it is quasiperiodic, and finally for $\mathrm{Ra}_\Omega=10^7$ the time history appears to be having random fluctuations. To examine the frequency content of these time series, the PSD (Power Spectral Density) curves are generated as shown in Figs. 16(a)–16(f). Each time history has been recorded for a sufficiently long time with 2^{10}–2^{15} sample points after the initial transients have died out. A FFT is applied to the discrete time history after removing the steady or the mean part from the discrete series. The Power is then computed as the square of the FFT amplitudes. The dimensionless frequencies associated with the first n peaks in the spectrum are denoted as f_i, $i=1,\ldots,n$. At $\mathrm{Ra}_\Omega=10^2$, from the PSD data we have $f_1=11.34$, $f_2=22.67$, and $f_3=34.02$. Since $f_2=2f_1$ and $f_3=3f_1$, one can regard f_1 as the fundamental frequency while f_2 and f_3 are the 2nd and 3rd harmonics. In fact, other peaks in the spectrum are higher harmonics of f_1. For $\mathrm{Ra}_\Omega=10^3$, $f_1=35.495$, $f_2=71.47$ and $f_3=106.97$. Here again f_1 is the fundamental frequency while f_2 and f_3 are the 2nd and 3rd harmonics. Further, a series of higher harmonics with a decreasing power content are observed. At $\mathrm{Ra}_\Omega=10^4$, $f_1=113.38$ and $f_2=226.755$. Here f_1 is the fundamental frequency while f_2 is the 2nd harmonic. It is also observed that a large number of higher harmonics are completely absent. At $\mathrm{Ra}_\Omega=10^5$, $f_1=357.35$ and $f_2=714.712$. Thus f_1 is the fundamental frequency while f_2 is the 2nd harmonic. The other peaks are higher harmonics of f_1. At $\mathrm{Ra}_\Omega=10^6$, a somewhat different spectrum than the previous cases is observed. Here, $f_1=121.75$, $f_2=243.5$, $f_3=365.25$, $f_4=487.05$, $f_5=608.8$, $f_6=730.55$. One can conclude that f_1 is the fundamental frequency while f_2-f_6 are the harmonics of f_1. However, peaks with significant power are also observed for $f_{\mathrm{II}}=2015.95$ and $f_{\mathrm{III}}=2259.5$. These frequencies are not harmonics of f_1. Hence it is concluded that the flow is quasiperiodic. Finally, for $\mathrm{Ra}_\Omega=10^7$, the spectrum has a broadband type of structure having a very large number of frequencies. For $\mathrm{Ra}_\Omega=10^2$, 10^3, 10^4, and 10^5 the corresponding values of dimensionless frequency "f_g" of the rotating "g" vector are 11.3, 35.73, 113 and 357.3, respectively. Thus, it is observed that for $\mathrm{Ra}_\Omega\leqslant 10^5$, the fundamental frequencies of the periodic flow are extremely close to the corresponding dimensionless frequency "f_g" of the rotating "g" vector. This leads one to conclude that the temporal variations for $\mathrm{Ra}_\Omega\leqslant 10^5$ are caused by the harmonic gravitational buoyancy force.

The above study of flow patterns reveals the structural changes in the flow and temperature fields with increasing rotation rates. However, owing to the complex nature of the interactions of the three body forces that affect the overall velocity and temperature fields, it is difficult to clearly separate out the various regimes where different body forces dominate and to determine approximately the point where one regime gives way to another. It is with this motivation that in the following section we discuss the dynamics of vorticity in the flow to gain a deeper insight into the problem.

4.2 Vorticity Dynamics. The vorticity transport equation for the current problem can be readily obtained by taking the curl of the momentum equations. It is given as:

$$\frac{\partial \omega_z}{\partial \tau}=-u\frac{\partial \omega_z}{\partial x}-v\frac{\partial \omega_z}{\partial y}+\mathrm{Pr}\,\nabla^2\omega_z+P \tag{18}$$

where P is the production term given as:

$$P=\mathrm{Ra}_g\,\mathrm{Pr}\left(\frac{\partial \theta}{\partial x}\cos\left(\frac{3\pi}{2}-\phi_g\right)-\frac{\partial \theta}{\partial y}\sin\left(\frac{3\pi}{2}-\phi_g\right)\right)$$
$$-\mathrm{Ra}_\Omega\,\mathrm{Pr}\left(y\frac{\partial \theta}{\partial x}-x\frac{\partial \theta}{\partial y}\right) \tag{19}$$

where $\phi_g=3\pi/2-\mathrm{Ta}^{0.5}\,\mathrm{Pr}\,\tau$.

While the production term serves to generate vorticity, the other two terms are responsible for a distribution of vorticity through molecular diffusion and macroscopic fluid motion. It is observed that in the current scenario only the GB and RB contribute to vorticity production. The Coriolis forces, being irrotational in the context of the problem being investigated, indirectly affect the distribution of vorticity through the velocity field. Next we look at the structure of vorticity across the horizontal diameter.

Figures 17(a)–17(f) show the variation of vorticity along the horizontal diameter for different Ra_Ω and at each Ra_Ω for different ϕ_g. At $\mathrm{Ra}_\Omega=10^2$, Fig. 17(a) shows that the vorticity structure is symmetric about the center with strong positive values near the wall for $\phi_g=3\pi/2$, associated with clockwise circulation, and strong negative values for $\phi_g=\pi/2$, associated with counterclockwise circulation near the walls. This is essentially the viscous

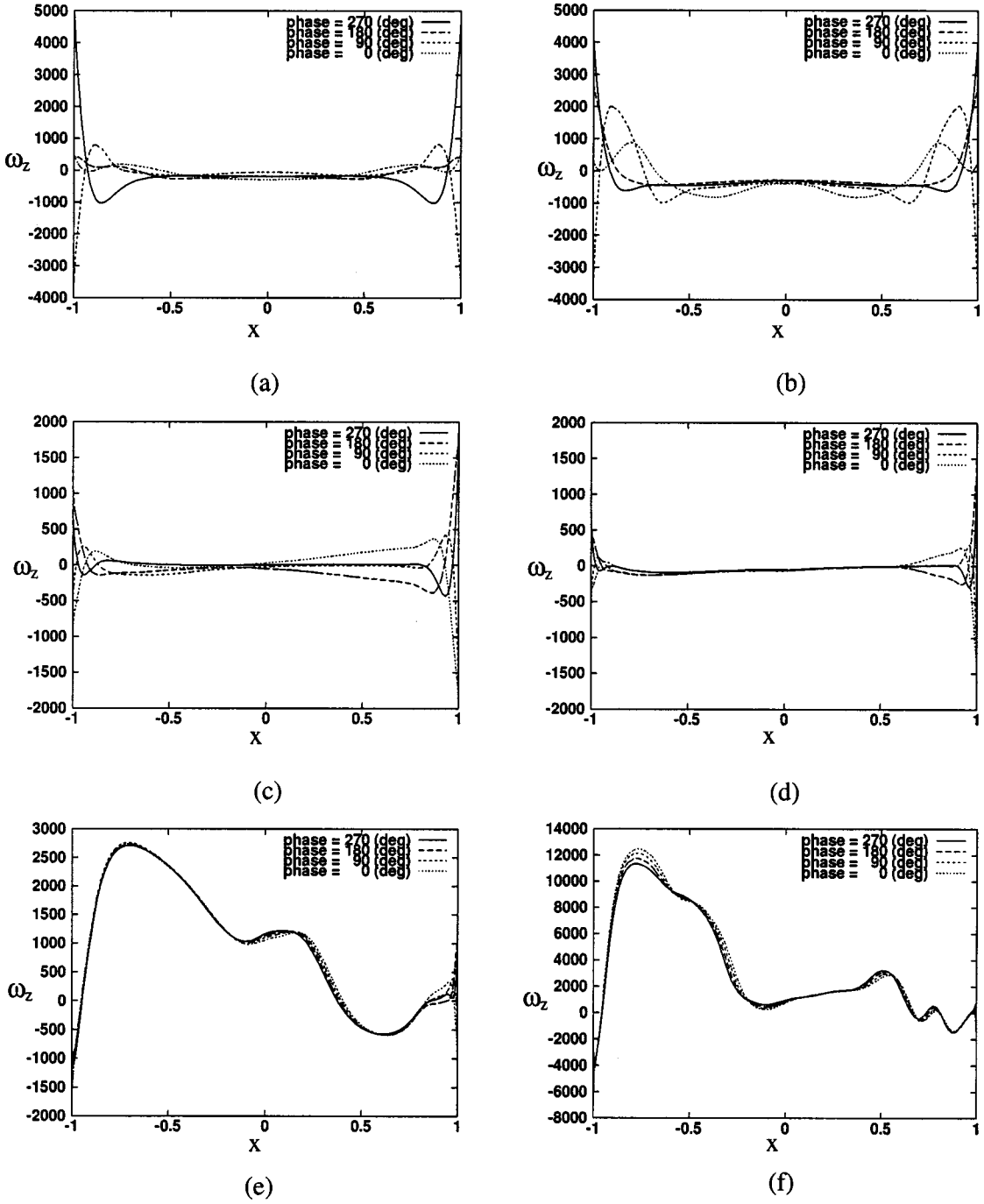

Fig. 17 Profiles of vorticity across the horizontal diameter for different ϕ_g at (*a*) $Ra_\Omega = 10^2$, (*b*) $Ra_\Omega = 10^3$, (*c*) $Ra_\Omega = 10^4$, (*d*) $Ra_\Omega = 10^5$, (*e*) $Ra_\Omega = 10^6$, (*f*) $Ra_\Omega = 10^7$

generation of vorticity at the wall. From the profiles of θ across the horizontal diameter, as shown in Fig. 5(*c*), it is observed that near the ends of the diameter $\partial\theta/\partial x$ is strongly negative for all ϕ_g while in the interior it is weakly positive for $\phi_g = 3\pi/2$ and $\phi_g = \pi$ and weakly negative for $\phi_g = \pi/2$ and $\phi_g = 0$. Neglecting the production of vorticity due to RB as $Ra_\Omega \ll Ra_g$, there is a production of negative vorticity by GB at $\phi_g = 3\pi/2$ whereas it is positive for $\phi_g = \pi/2$. In the interior, the production term due to GB is positive for $\phi_g = 3\pi/2$ whereas it is also positive for $\phi_g = \pi/2$. Hence, near the ends, the vorticity structure exhibits negative undershoots for $\phi_g = 3\pi/2$ and positive overshoots for $\phi_g = \pi/2$. At $\phi_g = \pi$ and $\phi_g = 0$, the viscous production at the walls is small as can be seen from v velocity structure in Fig. 5(*b*). The production term due to GB at $\phi_g = \pi$ and $\phi_g = 0$ is proportional to $\partial\theta/\partial y$ which is much smaller than $\partial\theta/\partial x$ near the ends of the horizontal diameter. Thus the wall vorticity is much smaller at $\phi_g = \pi$ and $\phi_g = 0$. It is interesting to observe that the vorticity in the interior is roughly same for all phases of the rotating "g" vector. The most important feature is the symmetry of the vorticity structure for all phases of the "g" vector. This is indicative of the fact that the convection of vorticity along the horizontal diameter and the production contribution by centrifugal buoyancy forces are negligible.

For $Ra_\Omega = 10^3$, the CF maintains a clockwise circulation in the interior or core of the flow field. This circulation is very much like

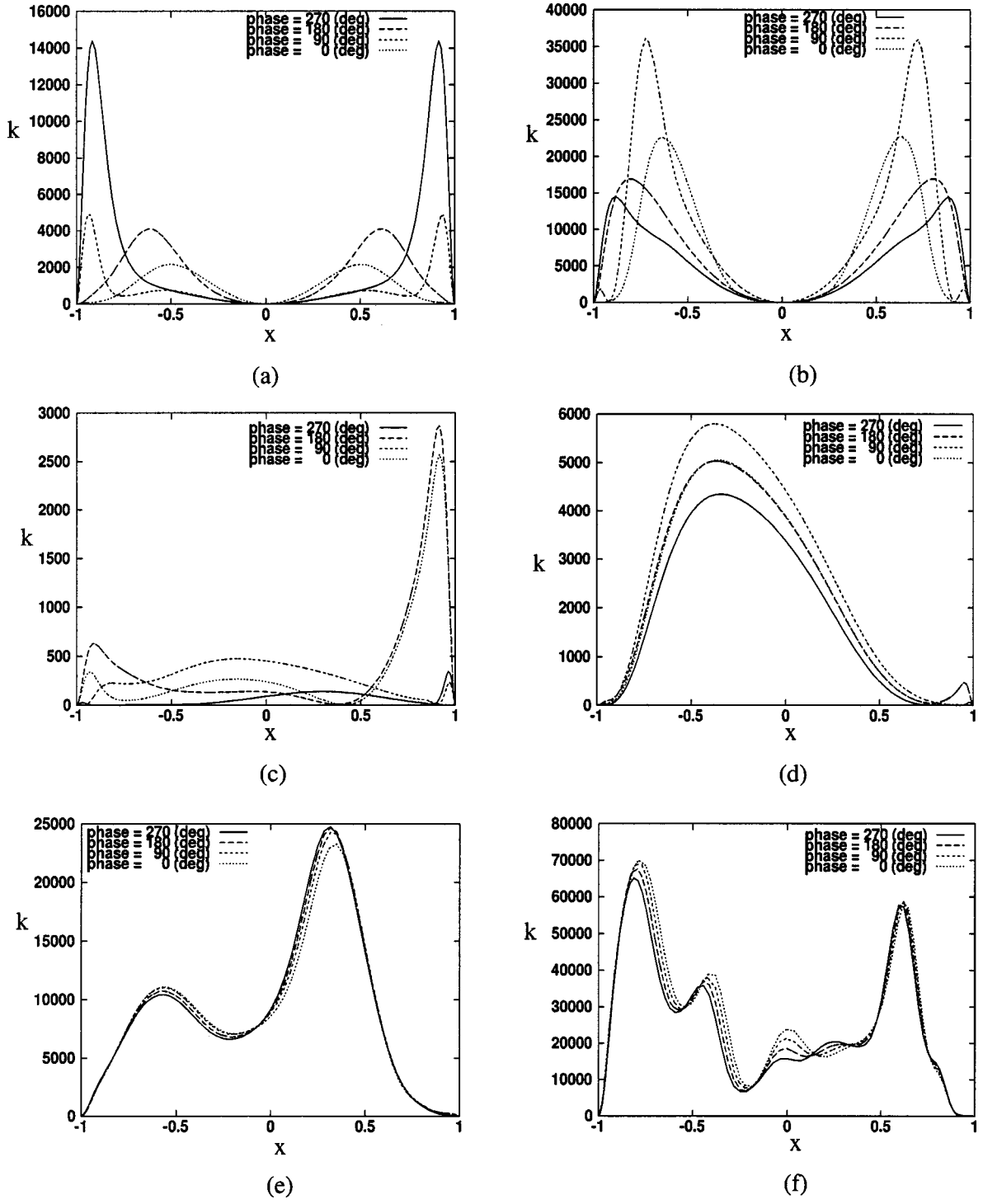

Fig. 18 Profiles of kinetic energy across the horizontal diameter for different ϕ_g at (*a*) $Ra_\Omega = 10^2$, (*b*) $Ra_\Omega = 10^3$, (*c*) $Ra_\Omega = 10^4$, (*d*) $Ra_\Omega = 10^5$, (*e*) $Ra_\Omega = 10^6$, (*f*) $Ra_\Omega = 10^7$

a rigid body clockwise rotation with a nearly constant negative vorticity in the core. As seen in Fig. 17(*b*), the value of the negative vorticity in the core is much larger than at $Ra_\Omega = 10^2$. The vorticity structure is still symmetric, which indicates that at $Ra_\Omega = 10^3$, the rotational buoyancy effects are still not significant. For $\phi_g = 3\pi/2$, from the profile of θ (Fig. 7(*c*)), one can readily observe that near the walls the gradient of nondimensional temperature in the x direction is less negative, leading to a lower negative production by GB. Hence the undershoots are much smaller for $\phi_g = 3\pi/2$. For $\phi_g = \pi$ one observes a large change in the wall values. This is because clockwise circulation maintained in the interior by CF also increases the velocity near the wall through the diffusion of momentum. For $\phi_g = \pi/2$, because of the formation of separated zones at the ends of the horizontal diameter having counter-clockwise circulation, the negative wall vorticity has a large positive overshoot. Finally, for $\phi_g = 0$, no significant production takes place and the diffusion of vorticity tends to flatten out the profile by reducing the peaks and elevating the valleys.

For $Ra_\Omega = 10^4$, Fig. 17(*c*) shows that the vorticity structure is asymmetric about the center for each ϕ_g. Further, the wall values

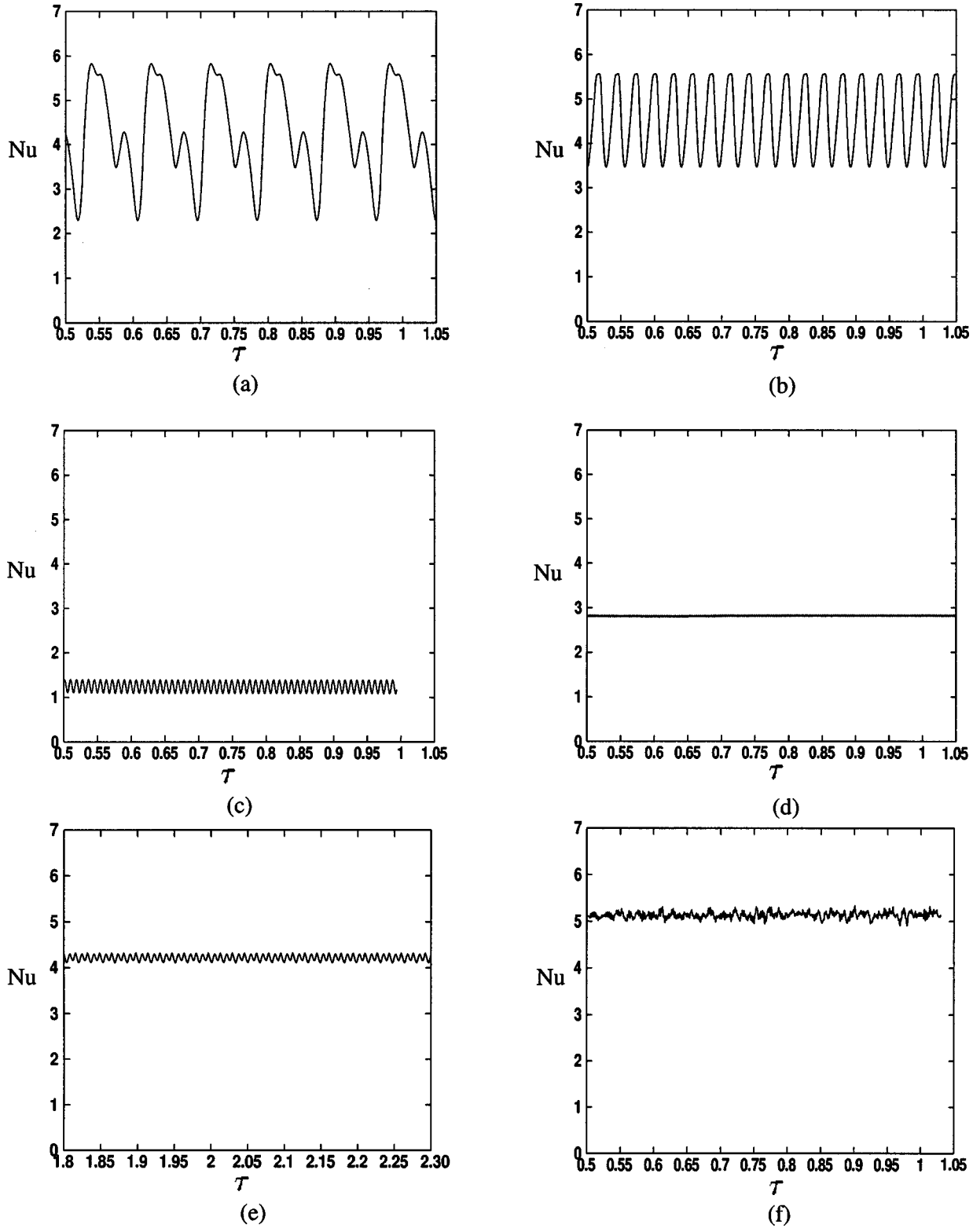

Fig. 19 The time history of Nu over the hot portion of the cylinder wall at (*a*) $Ra_\Omega = 10^2$, (*b*) $Ra_\Omega = 10^3$, (*c*) $Ra_\Omega = 10^4$, (*d*) $Ra_\Omega = 10^5$, (*e*) $Ra_\Omega = 10^6$, (*f*) $Ra_\Omega = 10^7$

are much smaller than for $Ra_\Omega = 10^3$ indicating that the velocities, developed under the action of competing forces of GB, RB, and CF, are quite low in comparison with the previous cases. Another difference from the previous cases is that the end values are higher for $\phi_g = \pi$ and $\phi_g = 0$ than for $\phi_g = 3\pi/2$ and $\phi_g = \pi/2$. This is because higher velocities near the ends are found to occur for $\phi_g = \pi$ and $\phi_g = 0$ than for $\phi_g = 3\pi/2$ and $\phi_g = \pi/2$. It is interesting to observe that for $\phi_g = 3\pi/2$ and $\phi_g = \pi/2$, the vorticity along the horizontal diameter in the interior or core is nearly zero. This lends further support to the earlier proposed explanation that the convection along the horizontal diameter found at these phases (Fig. 8(*a*) and Fig. 8(*c*)) is primarily driven by CF which are

Table 2 Comparison of the observed frequency of cyclic variations in Nu with time and the rotation frequency 'f_g' of the 'g' vector for different Ra_Ω

Ra_Ω	Ta	f	$f_g = (Ta^{0.5}Pr) / (2\pi)$
10^2	10^4	11.5	11.3
10^3	10^5	33.3	35.73
10^4	10^6	111	113
10^5	10^7	352	357.3

conservative in the current scenario. The asymmetry in the structure of vorticity with higher values near the cold end suggests that the effects of RB are significant for this Ra_Ω. The flow patterns in Fig. 8(*b*) and Fig. 8(*d*) clearly show that, for $\phi_g = \pi$ and $\phi_g = 0$, the single roll convective structure is shifted towards the cold end under the action of RB resulting in higher gradients in v velocities near the cold end than at the hot end.

For $Ra_\Omega = 10^5$, it is observed from Fig. 17(*d*) that the vorticity is nearly absent over a large interior portion of the horizontal diameter for all phases except near the ends. This is because, at this Ra_Ω, the flow takes place in the form of two nearly symmetric rolls with their interface aligned with the horizontal diameter. Hence, the horizontal diametral plane behaves as a plane of symmetry with $v \approx 0$ and $\partial u/\partial y \approx 0$. For $Ra_\Omega = 10^6$, as seen in Fig. 17(*e*), a completely different vorticity structure is encountered. The structure is totally asymmetric and the influence of GB is negligible, except near the cold end, as pointed out earlier. The vorticity production term is very small in the interior as the thermal gradients are very low in the core region.

Finally, for $Ra_\Omega = 10^7$ (Fig. 17(*f*)), the vorticity structure is highly asymmetric due to very strong convection along the horizontal diameter. The wall values at the hot end are also higher as compared to the previous case, indicating that the velocities in the vicinity of the wall have increased. The peak value of vorticity has increased quite significantly in comparison to the previous case ($Ra_\Omega = 10^6$).

4.3 Kinetic Energy. Figures 18(*a*)–18(*f*) depict the variation of kinetic energy over the horizontal diameter. The kinetic energy "*k*" is defined as $0.5(u^2+v^2)$. At $Ra_\Omega = 10^2$, the structure is symmetric about the center for each "ϕ_g". The kinetic energy is large for $\phi_g = 3\pi/2$ and is comparatively quite less for other phases. The structure also shows that more kinetic energy is concentrated near the wall for $\phi_g = 3\pi/2$ and $\phi_g = \pi/2$ than for $\phi_g = \pi$ and $\phi_g = 0$, where the maxima in the kinetic energy profile is shifted toward the interior. At $Ra_\Omega = 10^3$ (Fig. 18(*b*)) the symmetry in the structure is still preserved, which is an indicator that the centrifugal effects are not significant at this Ra_Ω. The kinetic energy continues to rise for the first π rotation of the "*g*" vector, starting from $\phi_g = 3\pi/2$. This is due to the Coriolis forces assisting GB in enhancing the clockwise circulation. Also, the peak kinetic energy for $\phi_g = \pi/2$ is much higher (nearly 2.5 times) than for $Ra_\Omega = 10^2$.

At $Ra_\Omega = 10^4$, the kinetic energy structure is asymmetric with more energy accumulated at the cold end than at the hot end of the horizontal diameter under the influence of RB. Further, the kinetic energy is much less than that for the previous cases. For $Ra_\Omega = 10^5$, the flow structure consists of two nearly symmetric aligned along the horizontal diameter. It is also observed that the kinetic energy increases near the center and falls off near the wall. Further, energy increases for the first π rotation of the "*g*" vector, starting from $\phi_g = 3\pi/2$ and ending at $\phi_g = \pi/2$. Under the action of RB, the kinetic energy again picks up as higher values are observed, in comparison to the previous case of $Ra_\Omega = 10^4$. For $Ra_\Omega = 10^6$ and $Ra_\Omega = 10^7$, the kinetic energy profiles depict a complex structure that does not undergo significant variation with ϕ_g. As mentioned earlier, this is due to the diminishing influence of GB over RB and CF.

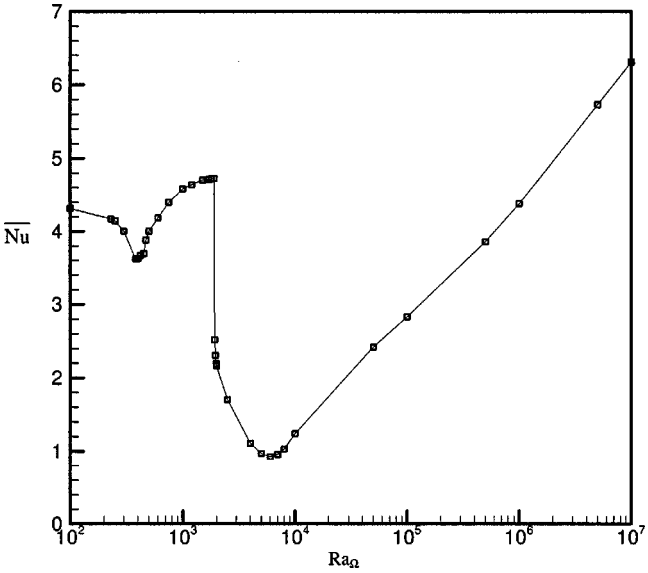

Fig. 20 Variation of $\overline{Nu}$ with Ra_Ω

Thus, the vorticity and kinetic energy structure helps in detecting the changes in the dynamics of the problem, particularly as affected by the different body forces involved.

4.4 Heat Transfer. The effect of rotation on heat transfer characteristics is observed by computing the Nusselt number over the hot wall of the cylinder. This is identified by $\alpha \in [\pi/2, 3\pi/2]$ (Fig. 1). The local dimensional heat flux on the cylinder wall is defined as:

$$q_w = -k(\nabla T)_w \tag{20}$$

where k is the thermal conductivity.

The heat transfer rate per unit length of cylinder across the hot wall is given as:

$$Q = \int_{\pi/2}^{3\pi/2} q_w \cdot \hat{n} R \, d\alpha \tag{21}$$

where $\hat{n}$: local, inward directed, unit normal vector to the cylinder surface.

The Nusselt number for the hot wall is defined as:

$$\mathrm{Nu} = \frac{QL}{Ak\,\Delta T} \tag{22}$$

Here A is the area of the heat transfer surface under consideration and L is the length scale of the problem. Using Eq. (20) and Eq. (21) and the definition of nondimensional temperature, we have:

$$\mathrm{Nu} = -\frac{1}{\pi}\int_{\pi/2}^{3\pi/2}\left(\frac{\partial\theta}{\partial n}\right)_w d\alpha \tag{23}$$

Here n is the normal, positive inward coordinate.

It may be pointed out that the actual heating region is different from the one considered, since it is the region over which $-(\partial\theta/\partial n)_w$ is positive. However, we follow the convention of Xin et al. [7], and define the instantaneous Nusselt number as in Eq. (23).

Figures 19(*a*)–19(*f*) shows the time variation of Nu for different cases involving rotation. The value for zero rotation is found to be 4.86, which is in good agreement with the value reported by Xin et al. [7]. For $Ra_\Omega \leq 10^5$ ($= Ra_g$), Nu varies periodically with time as the flow patterns exhibit cyclic changes with the rotation

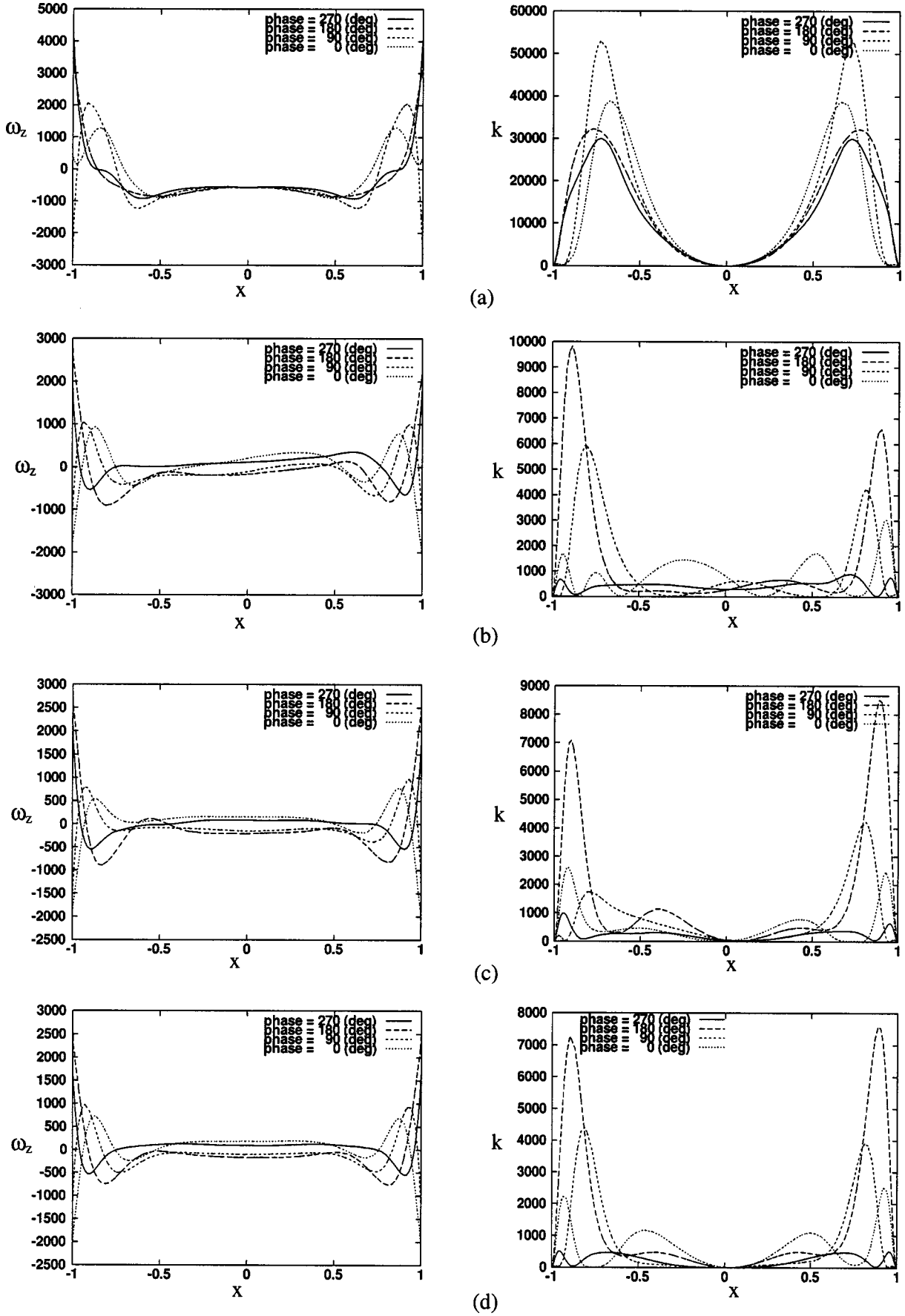

Fig. 21 Profiles of vorticity (left) kinetic energy (right) across the horizontal diameter for different ϕ_g at (*a*) $Ra_\Omega = 1.9\times10^3$, (*b*) $Ra_\Omega = 1.92\times10^3$, (*c*) $Ra_\Omega = 1.95\times10^3$, (*d*) $Ra_\Omega = 2\times10^3$

of the "g" vector. The close agreement between the frequency "f" of periodic variation in Nu with time and the rotation frequency "f_g" of the "g" vector, as shown in Table 2, lends further support to the argument that for $Ra_\Omega \leq 10^5$ $(=Ra_g)$ the temporal variations in the flow are essentially caused by harmonic nature of GB. The slight discrepancy in the frequencies is due to the fact that the frequencies for the Nusselt number have been determined from the time periods obtained graphically. Further, as Ra_Ω is increased, the influence of GB on the overall spatial structure of flow diminishes resulting in decrease in amplitude of fluctuations in Nu. In fact, the flow at $Ra_\Omega = 10^5$ $(=Ra_g)$ is almost steady. For $Ra_\Omega > 10^5$, the time history exhibits small amplitude multiple frequencies.

Figure 20 shows the variation of the time mean Nusselt number over the hot wall, $\overline{Nu}$ with Ra_Ω. To resolve the variation more accurately, more runs were taken at different values of Ra_Ω in addition to the six cases discussed so far. The six cases represent typically the changes in the flow structure as the rotation rate is increased, and serve as representatives of different flow regimes encountered. Starting from a very low value, as Ra_Ω is increased, it is interesting to observe that the time mean value of Nu first decreases until Ra_Ω reaches a value of 3.86×10^2 and then again increases until $Ra_\Omega = 1.9\times10^3$ or $Ta = 1.9\times10^5$ beyond which there is a sharp decline in the heat transfer. The sharp decline continues until $Ra_\Omega = 2.0\times10^3$. At this point the rate of decrease of heat transfer starts to decrease, attains a minimum at about $Ra_\Omega = 6.0\times10^3$, beyond which it again starts to increase. This variation is very much indicative of the different flow regimes dominated by different body forces. It can be concluded that for $Ra_\Omega \leq 3.86\times10^2$, the dynamics is essentially controlled by GB only. The increase in Ra_Ω, in this regime, brings about a decrease of the mean heat transfer, as the changing orientation of the "g" vector does not allow sufficient time for convection to develop. However, as Ra_Ω is increased CF becomes significant, and for $Ra_\Omega > 3.86\times10^2$, the heat transfer starts to increase due to the assistance provided by CF to GB during the first π rotation phase of the "g" vector (from $\phi_g = 3\pi/2$ to $\phi_g = \pi/2$), leading to an increase in the clockwise circulation in the cylinder, as explained earlier in Section 4.1. This effect is only observed until about $Ra_\Omega = 1.9\times10^3$ or $Ta = 1.9\times10^5$, beyond which CF becomes the dominant force right from the early phase of motion and largely negates the destabilizing effect of GB, thus suppressing convection and leading to a sharp decline in heat transfer. The rate of decline in heat transfer starts to change at about $Ra_\Omega = 2.0\times10^3$. This indicates the point from which RB starts to become significant. This is better understood if one considers the changes in the vorticity and kinetic energy structure as Ra_Ω increases from 1.9×10^3 to 2.0×10^3, as shown in Figs. 21(*a*)–21(*d*). At $Ra_\Omega = 1.9\times10^3$, as shown in Fig. 21(*a*), the structures of vorticity and kinetic energy are similar to those at $Ra_\Omega = 1.0\times10^3$ (Fig. 17(*b*) and Fig. 18(*b*)) except that the kinetic energy of the clockwise circulation is significantly higher, leading to an increase in the heat transfer rate. At $Ra_\Omega = 1.92\times10^3$, it is observed from Fig. 21(*b*) that while the vorticity is nearly symmetric near the ends of the diameter, it is asymmetric in the core $(-0.5 \leq x \leq +0.5)$. This asymmetry can be attributed to the convection of vorticity along the diameter under the action of CF. The kinetic energy profile indicates a sharp decline in convective motion, as explained earlier. More significantly, it exhibits a pronounced asymmetry at about $x = 0$, with more energy toward the hot end for $\phi_g = \pi$ and $\phi_g = \pi/2$. These structures indicate that RB is not significant, even at $Ra_\Omega = 1.92\times10^3$. A further increase in Ra_Ω to 1.95×10^3 and 2×10^3 progressively reduces the asymmetries in vorticity and kinetic energy profiles, as observed in Fig. 21(*c*) and Fig. 21(*d*). This is due to the fact that the cause of asymmetry at these Ra_Ω i.e., CF is partly negated by RB, which starts to become significant at about $Ra_\Omega = 2\times10^3$. The heat transfer rate continues to decrease under the dominating influence of CF until RB becomes strong enough to reverse the decreasing trend at about $Ra_\Omega = 6.0\times10^3$. Beyond this Ra_Ω, the heat transfer again picks up under the combined effect of GB and RB. As Ra_Ω is increased further, the effects of GB progressively diminish and the heat transfer continues to rise under the influence of RB and CF. The nonmonotonic character of variation of heat transfer with Ra_Ω has been reported earlier in the experimental work of Tang and Hudson [23] for a bottom heated, rotating, vertical cylinder. Also, from the two-dimensional study of Hamady et al. [12] on a square cylinder, it can be inferred that at low rotation rates (negligible RB) the mean heat transfer from the hot wall first increases and then decreases. Thus it is inferred that the heat transfer characteristic stems from the basic equations and is not specific to any particular geometry or boundary conditions. Ker and Lin [13], working with an inclined, cubic, rotating, air filled enclosure, reported that the amplitude of fluctuations in the flow can be minimized at a certain rotation rate. This phenomenon is also found for the present configuration, where the flow becomes nearly steady for $Ra_\Omega = 10^5$ $(=Ra_g)$, and the fluctuation amplitude again starts to increase for $Ra_\Omega > 10^5$.

5 Conclusions

The dynamics of two-dimensional buoyancy driven convection in a horizontal, rotating cylinder has been studied at a fixed $Ra_g = 10^5$ and $Pr = 0.71$. The detailed study of flow structure and heat transfer characteristics, as Ra_Ω is varied, reveals different regimes of flow in which different body forces dominate. The range of Ra_Ω considered is wide enough to capture a variety of physical behavior ranging from the dynamics of flow driven solely by gravity to the dynamics at high enough rotation rate so that the effects of gravity are insignificant in comparison to centrifugal and Coriolis effects. This is the main feature of the study, as all the previous studies have invariably explored the physics of such a class of flows in a limited manner, either restricting themselves to low rotation rates where centrifugal effects are negligible or high rotation rates where effects of gravity are negligible.

The space and time patterns of flow have been correlated to the different body forces. In the flow regime controlled by gravitational buoyancy and Coriolis forces, the Coriolis forces play a dual role of enhancing the convection as well as suppressing it depending upon whether they start to dominate over gravitational buoyancy right from the start of the fluid motion. The centrifugal effects generate a strong convective current directed from the hot end of the horizontal diameter towards the cold end resulting in the formation of two rolls. For $Ra_\Omega \leq 10^5$, the flow exhibits periodicity with the frequency locked on to the forcing frequency of the harmonic gravitational buoyancy force. The amplitude of the fluctuations go on decreasing and the flow becomes almost steady for $Ra_\Omega = 10^5$. For $Ra_\Omega > 10^5$, bifurcations to quasiperiodic flow take place.

The existence of different flow regimes dominated by different body forces complicates the time mean heat transfer characteristics with a different behavior in each of the regimes. This is of particular importance from the point of view of development of correlations for mean heat transfer with relevant parameters of the problem. The time mean heat transfer characteristic also serves as a guide for the selection of system parameters with the objective of either suppression or enhancement of convection.

It is felt that to widen the scope of the current investigation and to generalize the dynamics, the effect of Ra_g and Pr also need to be considered. This will be taken up in further studies.

Nomenclature

- k = thermal conductivity of the fluid (W/(m-K))
- Nu = instantaneous Nusselt number associated with heat transfer through the hot portion of cylinder wall
- Pr = Prandtl Number $= \nu/\kappa$
- Q = heat transfer rate per unit length through the hot portion of the cylinder wall (W/m)

R = radius of the cylinder (m)
Ra_g = gravitational Rayleigh Number$=g\beta\,\Delta T\,R^3/\nu\kappa$
Ra_Ω = rotational Rayleigh Number$=\beta\,\Delta T\,\Omega^2R^4/\nu\kappa$
Ta = Taylor number$=\Omega^2R^4/\nu^2$
(u,v) = nondimensional Cartesian velocity components with respect to the rotating frame
(x,y) = nondimensional Cartesian coordinates
p = dimensional pressure ($\mathrm{N/m^2}$)
p_m = dimensionless motion pressure$=(p-p_0)R^2/\rho_0\kappa^2$
p_0 = dimensional pressure in the state of solid body rotation at uniform temperature T_0 ($\mathrm{N/m^2}$)
q_w = local heat flux at the wall of the cylinder ($\mathrm{W/m^2}$)
t = dimensional time (s)
$T_{\max}$ = maximum temperature on the periphery of the rotating enclosure wall$=T_0+\Delta T$ (K)
$T_{\min}$ = minimum temperature on the periphery of the rotating enclosure wall$=T_0-\Delta T$ (K)
T_0 = temperature of the undisturbed fluid at time $t=0$ (K)
ΔT = amplitude of the imposed periodic temperature perturbation (K)
Ω = uniform rotation rate of the enclosure (rad/s)
β = coefficient of volume expansion of the fluid ($\mathrm{K^{-1}}$)
κ = thermal diffusivity of fluid ($\mathrm{m^2/s}$)
ν = kinematic viscosity of fluid ($\mathrm{m^2/s}$)
θ = nondimensional temperature$=(T-T_0)/\Delta T$
ϕ_g = phase of the rotating "g" vector measured from the positive x direction in the rotating frame
ρ_0 = density of fluid at T_0 ($\mathrm{Kg/m^3}$)
τ = nondimensional time$=tR^2/\kappa$
ω_z = z component of dimensionless vorticity

Subscripts

i, j = grid indices of a node in the Cartesian structured grid

Superscripts

n = values of the flow variables at the current time level
$n+1$ = values of the flow variables at the next time level

References

[1] Ostrach, S., 1950, "A Boundary Layer Problem in the Theory of Free Convection," Ph.D thesis, Graduate Division of Applied Mathematics, Brown Univ., Providence, RI.
[2] Martini, W. R., and Churchill, S. W., 1960, "Natural Convection Inside a Horizontal Cylinder," AIChE J., **6**, pp. 251–257.
[3] Brooks, I. H., and Ostrach, S., 1970, "An Experimental Investigation of Natural Convection in a Horizontal Cylinder," J. Fluid Mech., **44**, pp. 545–561.
[4] Weinbaum, S., 1964, "Natural Convection in a Horizontal Cylinder," J. Fluid Mech., **18**, pp. 409–437.
[5] Hellums, J. D., and Churchill, S. W., 1962, "Transient and Steady State, Free and Natural Convection, Numerical Solutions: Part II—The Region Inside a Horizontal Cylinder," AIChE J., **8**, pp. 692–695.
[6] Heinrich, J. C., and Yu, C. C., 1988, "Finite Element Simulation of Buoyancy Driven Flows With Emphasis on Natural Convection in a Horizontal Circular Cylinder," Comput. Methods Appl. Mech. Eng., **69**, pp. 1–27.
[7] Xin, S., Le Quere, P., and Daube, O., 1997, "Natural Convection in a Differentially Heated Horizontal Cylinder: Effects of Prandtl Number on Flow Structure and Instability," Phys. Fluids, **4**, pp. 1014–1033.
[8] Veronis, G., 1968, "Large Amplitude Benard Convection in a Rotating Fluid," J. Fluid Mech., **31**, pp. 113–139.
[9] Kuppers, G., and Lortz, D., 1969, "Transition From Laminar Convection to Thermal Turbulence in a Rotating Fluid Layer," J. Fluid Mech., **35**, pp. 609–620.
[10] Rossby, H. T., 1969, "A Study of Benard Convection With and Without Rotation," J. Fluid Mech., **36**, pp. 309–335.
[11] Lee, T. L., and Lin, T. F., 1996, "Transient Three-Dimensional Convection of Air in a Differentially Heated Rotating Cubic Cavity," Int. J. Heat Mass Transfer, **39**, pp. 1243–1255.
[12] Hamady, F. J., Lloyd, J. R., Yang, K. T., and Yang, H. Q., 1994, "A Study of Natural Convection in a Rotating Enclosure," ASME J. Heat Transfer, **116**, pp. 136–143.
[13] Ker, Y. T., and Lin, T. F., 1996, "A Combined Numerical and Experimental Study of Air Convection in a Differentially Heated Rotating Cubic Cavity," Int. J. Heat Mass Transfer, **39**, pp. 3193–3210.
[14] Rhie, C. M., and Chow, W. L., 1983, "Numerical Study of the Turbulent Flow Past an Airfoil With Trailing Edge Separation," AIAA J., **21**, pp. 1525–1532.
[15] Hirsch, C., 1990, *Numerical Computation of Internal and External Flows*, Wiley Interscience Publication, John Wiley and Sons Ltd., Chap 23, page no. 661.
[16] Amsden, A. A., and Harlow, F. H., 1970, "The SMAC Method: A Numerical Technique for Calculating Incompressible Fluid Flows," Los Alamos Scientific Report, LA 4370.
[17] Kim, S. W., and Benson, T. J., 1992, "Comparison of the SMAC, PISO and Iterative Time Advancing Schemes For Unsteady Flows," Comput. Fluids, **21**, pp. 435–454.
[18] Cheng, L., and Armfield, S., 1995, "A Simplified Marker and Cell Method for Unsteady Flows on Non-Staggered Grids," Int. J. Numer. Methods Fluids, **21**, pp. 15–34.
[19] Ferziger, J. H., and Peric, M., 1996, *Computational Methods for Fluid Dynamics*, Springer-Verlag, Berlin, Chap. 5, pp. 95–98.
[20] Gresho, P. M., and Sani, R. L., 1998, *Incompressible Flow and the Finite Element Method*, John Wiley and Sons, New York, Chap. 2, pp. 125–129.
[21] Gustafson, K. E., 1980, *Introduction to Partial Differential Equations and Hilbert Space Methods*, John Wiley and Sons, New York, Chap. 1, pp. 89–90.
[22] Smith, G. D., 1985, *Numerical Solution of Partial Differential Equations: Finite Difference Methods*, Clarendon Press, Oxford Applied Mathematics and Computing Science Series, Chap. 2, pp. 47–72.
[23] Tang, D., and Hudson, J. L., 1983, "Experiments on a Rotating Fluid Heated From Below," Int. J. Heat Mass Transfer, **26**, pp. 943–949.

Anisotropic Slope Distribution and Bidirectional Reflectance of a Rough Silicon Surface

Q. Z. Zhu

Z. M. Zhang*
e-mail: zzhang@mail.me.gatech.edu

The George W. Woodruff School of Mechanical Engineering,
Georgia Institute of Technology,
Atlanta, GA 30332

Both one-dimensional (1D) and two-dimensional (2D) slope distributions were obtained from the surface topographic data, measured using an atomic force microscope for a rough silicon surface. The resulted slope distributions deviate significantly from the Gaussian distribution, with noticeable side peaks. The bidirectional reflectance distribution function (BRDF) of the same surface, measured with a laser scatterometer at 635 nm and 785 nm, exhibits subsidiary peaks. The measured slope distributions are implanted into a geometric optics model to predict the in-plane BRDF for different azimuthal angles. The 1D slope distribution has some success in predicting the BRDF at limited azimuthal angles, but is not applicable to other cases. On the other hand, the BRDF predicted using the 2D slope distribution matches well with the experimental results for any azimuthal angles. The method developed here may also help predict the BRDF for other rough surfaces with microstructures. [DOI: 10.1115/1.1795244]

Keywords: Properties, Radiation, Roughness, Scattering, Surface

1 Introduction

The temperature of the silicon wafer during microelectronics fabrication is usually monitored by a radiation thermometer, whose uncertainty depends on how accurate the effective emissivity of the silicon wafer can be determined [1,2]. The bidirectional reflectance distribution function (BRDF) is a fundamental property of rough surfaces and knowledge of the BRDF is crucial to the emissivity modeling and heat transfer analysis [3–6]. The BRDF of a surface can be predicted by solving the Maxwell equations if the surface roughness is fully characterized. Since the rigorous electromagnetic-wave solution generally requires a huge memory with a high-speed CPU, this approach is practically applicable to one-dimensional (1D) rough surfaces only [7,8], though in some cases, solutions for two-dimensional (2D) rough surfaces have been obtained [9]. It is common to use approximation methods, such as the Rayleigh-Rice perturbation theory, the Kirchhoff approximation, and the geometric optics approximation [8,10]. These approximations are only appropriate within certain ranges of roughness and wavelength.

The Rayleigh-Rice perturbation theory can be used for relatively smooth surfaces. The Kirchhoff approximation, also known as the tangent-plane approximation, is applicable when the surface profile is slightly undulating (i.e., without sharp crests and deep valleys). In the Kirchhoff approximation, the effects of shadowing and multiple scattering, which may be significant at large angles of incidence, are usually neglected. Furthermore, it is difficult to consider the depolarization when the Kirchhoff approximation is applied to 2D rough surfaces. The geometric optics approximation is applicable to surfaces whose root-mean-square (rms) roughness and autocorrelation length are greater than the wavelength of the incident radiation [8,11]. This approach can be easily incorporated into a statistical and Monte Carlo method [12,13]. The shadowing and multiple scattering can be taken into account through the ray-tracing scheme. There exists good agreement between the simulation results employing the geometric optics approximation and the rigorous electromagnetic-wave solution [8]. However, the simulation based on geometric optics requires much less computational resources and takes much less time than that based on the rigorous solution.

Since BRDF is intrinsically dependent on the surface characteristics, several analytical expressions are available to approximately correlate the surface statistics to the BRDF [13–15]. Therefore, the roughness parameters may be estimated from the measured BRDF using an inverse method. Some common roughness parameters and functions include the rms roughness, the power spectral density (PSD), the rms slope, and the slope distribution. If the surface is relatively rough, the geometric optics approximation is preferred and the resultant BRDF model is linked to the slope distribution. The study of slope distribution is also important in object rendering [16,17] and surface characterization [18,19]. Before the invention of the atomic force microscope (AFM), the surface profile was usually measured with a mechanical profiler that scans the surface line by line. Some mechanical stylus profilers can measure rough surfaces with a vertical resolution of a few nanometers. However, the lateral resolution is usually on the order of a micrometer due to the large radius of the stylus probe [20,21]. On the other hand, the radius of curvature of an AFM probe tip is in the range from 20–60 nm; thus, AFM can provide detailed information of the topography of a small area on the microrough surfaces with a vertical resolution of subnanometers and a lateral resolution around 10 nm [22]. Attention has been paid to compare the surface roughness statistics determined from the topographic measurements to that obtained from the light scattering experiments [23–26].

In most studies, surface roughness is assumed to satisfy the Gaussian statistics in the derivation of the BRDF model and for the surface generation in the Monte Carlo simulation [8,10]. Furthermore, the roughness statistics of 2D rough surfaces is mostly assumed to be isotropic so that the autocorrelation function is independent of the direction. As pointed out by Guérin [27], however, the Gaussian distribution may miss important features of natural surfaces because this symmetric and monotonic function does not allow any abrupt event in the rapidly decreasing tails. Very few papers have been devoted to the BRDF of non-Gaussian and anisotropic 2D rough surfaces. Ward [28] assumed that the 2D slope function of anisotropic surfaces was elliptical and fitted the rms slopes of two uncorrelated 1D Gaussian distributions from the

*To whom all correspondences should be sent.

Contributed by the Heat Transfer Division for publication in the JOURNAL OF HEAT TRANSFER. Manuscript received by the Heat Transfer Division January 27, 2004; revision received May 4, 2004. Associate Editor: S. Thynell.

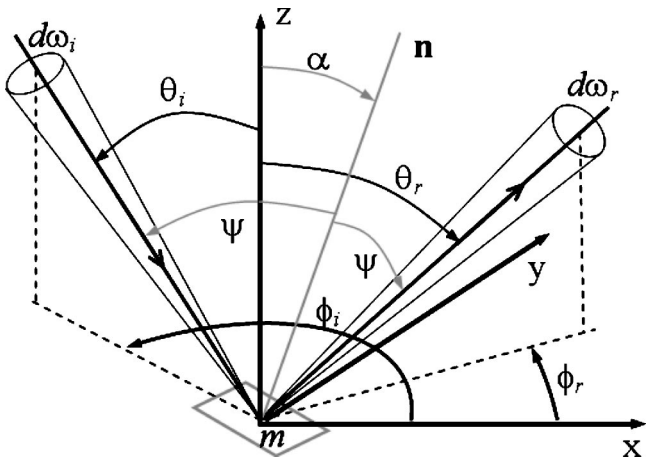

Fig. 1 Illustration of the BRDF definition and the specular reflection from a microfacet. The *z*-axis is normal to the mean surface, n is the normal of the microfacet *m*, α is the angle between the *z*-axis and n, and ψ is local incidence angle. For specular reflection, n bisects the directions of incidence and reflection.

measured BRDF. Little has been done to correlate BRDF, predicted using the measured slope distribution with the BRDF from light scattering measurements.

The present work focuses on the correlation between the actual slope distribution and the measured BRDF for the rough side of a silicon wafer. It is hoped that a better understanding of the relation of the surface microstructure and BRDF will help develop improved heat transfer models for accurate radiometric temperature measurements in semiconductor manufacturing. The objectives are to determine the actual slope distribution function from the AFM topographic data, to predict the BRDF by incorporating the slope distribution into the geometric optics framework, and to compare the predicted BRDF with the measured using a laser scatterometer.

2 BRDF Modeling Based on Geometric Optics

The bidirectional reflectance distribution function (BRDF), also called bidirectional reflectivity, is defined as the ratio of the reflected radiance (or intensity in most heat transfer textbooks) to the incident irradiance [3–5],

$$f_r(\theta_i,\phi_i,\theta_r,\phi_r)=\frac{dL_r(\theta_i,\phi_i,\theta_r,\phi_r)}{L_i(\theta_i,\phi_i)\cos\theta_i d\omega_i}[\mathrm{sr}^{-1}] \tag{1}$$

In the above equation (θ_i, ϕ_i) and (θ_r, ϕ_r) denote the incoming and scattering directions, as shown in Fig. 1, L_i is the incoming radiance, $L_i\cos\theta_i d\omega_i$ represents the incident irradiance (power per unit projected area), and dL_r is the radiance in the scattering direction and is a function of both the incoming and scattering directions. Note that L_i, dL_r, and f_r are spectral properties that depend on the wavelength of the incident radiation.

A rough surface can be imagined as a combination of numerous randomly oriented mirrorlike microfacets on the mean plane [12–15]. In the geometric optics approximation, it is assumed that the dimension of the microfacet is much larger than the wavelength of the incident radiation and that the reflection on the mirrorlike surface obeys Snell's law. Generally speaking, the applicable roughness region of the geometric optics approximation is $\sigma>\lambda$ and $\sigma<\tau$, where σ is the rms roughness, τ is the autocorrelation length, and λ is the wavelength. Nevertheless, this region can be extended to $\sigma\cos(\theta_i)/\lambda>0.2$ and $\sigma/\tau<2$ with reasonable accuracy [11]. The orientation of a given microfacet *m* can be described by an inclination angle α between the *z*-axis and the facet normal **n** and an azimuthal angle, as shown in Fig. 1, or by the slopes in the *x* and *y* directions $\zeta_x=\partial z/\partial x$ and $\zeta_y=\partial z/\partial y$. From the geometrical relation between the incident beam and the reflected beam, slopes of the microfacet are related to the incoming and scattering directions by

$$\zeta_x=-\frac{\sin\theta_i\cos\phi_i+\sin\theta_r\cos\phi_r}{\cos\theta_i+\cos\theta_r} \tag{2a}$$

$$\zeta_y=-\frac{\sin\theta_i\sin\phi_i+\sin\theta_r\sin\phi_r}{\cos\theta_i+\cos\theta_r} \tag{2b}$$

A two-dimensional distribution function can be used to describe the probability of microfacets. The BRDF is proportional to the probability of the microfacet that will reflect the incident radiation to the prescribed scattering direction. Therefore, in the microfacet model, the roughness statistics affects the predicted BRDF via the microfacet slope distribution, which is usually modeled as a 2D Gaussian function [13,15]. The uniqueness of the present work is to replace the Gaussian slope distribution with the actual slope distribution function, obtained directly from the surface topographic data.

With the 2D nature of the microfacet orientation, the scattered radiance is generally comprised of both *p* and *s* polarizations, even if the irradiation is purely *p* or *s* polarized. When the scattering direction lies in the plane of incidence, depolarization will not occur and the reflected radiation will be *p* or *s* polarized if the incidence radiation does. Only in-plane BRDF is concerned in the present study, and for in-plane scattering if ϕ_i is set to 0 deg, then $\phi_r=0$ deg or 180 deg. To satisfy Snell's law, the local incidence angle $\psi=(\theta_i+\theta_r)/2$ and the inclination angle of the microfacet is $\alpha=|\theta_r-\theta_i|/2$; see Fig. 1. The sample is assumed to be opaque without internal scattering, that is, all the radiation entering from air to the medium will be absorbed. Note that silicon is opaque at wavelengths shorter than 1.1 μm at room temperature.

The shadowing and masking effects are essential in dealing with radiation scattering from a rough surface, especially for large angles of incidence or reflection. The shadowing function stands for the probability of the incident beam reaching a microfacet without being shadowed by another (shadowing effect) or of the reflected beam leaving the microfacet to the hemisphere without being blocked by another (masking effect). Based on the Gaussian surface statistics, Smith [29] derived a shadowing function that has been widely used and can be expressed as

$$S(\theta)=\frac{1-0.5\,\mathrm{erfc}(\Gamma)}{1-0.5\,\mathrm{erfc}(\Gamma)+\exp(-\Gamma^2)/(2\sqrt{\pi}\Gamma)},\quad 0\leqslant\theta\leqslant 90\ \mathrm{deg} \tag{3}$$

where θ is the zenith angle of incidence (for shadowing) or reflection (for masking) and $\Gamma=\tan(90\ \mathrm{deg}-\theta)/(\sqrt{2}\zeta_{rms})$ with ζ_{rms} being the rms slope. Equation (3) is conveniently adopted in the present study, although it may not accurately represent the shadowing function when the surface is not Gaussian.

Several geometric optics-based BRDF models have been reported in the literature. Here, a comparison is made to check for consistency and to help develop an appropriate expression for the present study. Torrance and Sparrow [14] assumed that the statistics of the inclination angle is Gaussian and derived the very first microfacet-based BRDF model, which has been widely used [12,16,17]. If the diffuse term is neglected, the semi-empirical model developed by Torrance and Sparrow [14] can be written as

$$f_r(\theta_i,\phi_i,\theta_r,\phi_r)=\frac{b\exp(-c^2\alpha^2)}{4\cos\theta_i\cos\theta_r}\rho(n,\kappa,\psi)G \tag{4}$$

In Eq. (4), $\rho(n,\kappa,\psi)$ is the microfacet reflectivity that depends on the refractive index *n* and the extinction coefficient κ of the medium and the local incidence angle ψ. The reflectivity is wavelength dependent and can be calculated from Fresnel's equations for each polarization [3]. Constants *b* and *c* are related to the

Gaussian distribution of the inclination angle and may be determined by fitting the measurement results [30]. The role of the geometrical attenuation factor G is the same as that of the Smith shadowing function.

Caron et al. [15] derived an analytical expression for the ratio of the reflected radiance to the incident power flux following the geometric optics formulation [31]. The in-plane BRDF based on Refs. [15,31] can be written as follows:

$$f_r(\theta_i,\phi_i,\theta_r,\phi_r)=\frac{p(\zeta_x,\zeta_y)}{4\cos\theta_i\cos\theta_r\cos^4\alpha}\rho(n,\kappa,\psi) \tag{5}$$

where $p(\zeta_x,\zeta_y)$ is the joint probability density function of the slope or the 2D slope distribution. Notice that in writing Eq. (5), it is assumed that $\phi_i=0$ deg and $\phi_r=0$ deg or 180 deg; thus, the y slope ζ_y has to be zero for in-plane scattering. When ϕ_i is not zero, Eq. (5) can be used after rotating the x-y coordinates with respect to the z-axis.

Tang and Buckius [13] developed a comprehensive statistical model that deals separately with the first-order and higher-order scattering terms. They showed that multiple scattering is important for very rough surfaces and insignificant for a shallow rough surface with $\sigma<0.2\tau$ [8,13]. The first-order in-plane BRDF, derived by Tang and Buckius [13], is

$$f_r(\theta_i,\phi_i,\theta_r,\phi_r)=\frac{p(\zeta_x,\zeta_y)(1+\zeta_x\tan\theta_i)d\zeta_x d\zeta_y}{\cos\theta_r\sin\theta_r d\theta_r d\phi_r}\rho(n,\kappa,\psi)S(\theta_i)S(\theta_r) \tag{6}$$

where $S(\theta_i)$ and $S(\theta_r)$ are the shadowing functions for the incoming radiation and outgoing radiation, respectively. In Eq. (6), the term $d\zeta_x d\zeta_y/d\theta_r d\phi_r$ cancels out for in-plane scattering when the derivatives of Eq. (2) with respect to θ_r and ϕ_r are inserted. It can be shown that, after some cumbersome derivations, Eq. (6) reduces to Eq. (5) if $S(\theta_i)$ and $S(\theta_r)$ are both set to one.

The differences between Eq. (4) and the others lie in that Eq. (4) uses the distribution of the inclination angle, while Eqs. (5) and (6) use the distribution of the surface slope (ζ_x and ζ_y); further, Eq. (4) uses geometrical attenuation factor G, while Eq. (6) uses the shadowing function $S(\theta)$. The constants in Eq. (4) can be derived for a Gaussian isotropic rough surface with b being $1/(2\pi\zeta_{rms}^2\cos^4\alpha)$ and c being $1/(\sqrt{2}\zeta_{rms})$, and the distribution of the inclination angle replaced by the distribution of the tangent of the inclination angle ($\zeta=\tan\alpha$) [32]. Thus, it can be shown that Eq. (4) is equivalent to Eq. (5) if $G=1$, since $\zeta_x=\tan\alpha$ in the plane of incidence.

It can be concluded that, when multiple scattering is negligible, the expressions obtained by different researchers, Eqs. (4)–(6), are essentially the same for in-plane BRDF. The expression given in Eq. (5) is adopted by adding the shadowing function to address the shadowing and masking effects, which are important at grazing angles. The modified BRDF is given as

$$f_r(\theta_i,\phi_i,\theta_r,\phi_r)=\frac{p(\zeta_x,\zeta_y)}{4\cos\theta_i\cos\theta_r\cos^4\alpha}\rho(n,\kappa,\psi)S(\theta_i)S(\theta_r) \tag{7}$$

Equation (7) will be used in the following to predict BRDF from the actual slope distribution $p(\zeta_x,\zeta_y)$, which may be non-Gaussian and anisotropic.

3 Surface Characterization

A Digital Instruments (Dimension 3100 SPM) AFM was used to characterize the surface topography, in the contact mode with a silicon nitride probe, that raster scans the rough surface of a silicon wafer. The result is stored in an array containing the height information, $z(m,n)$, where $m=1,2,\ldots M$; $n=1,2,\ldots,N$ are the points along the x and y directions, respectively. The silicon wafer used in the study is single-side polished, approximately 525 μm thick and 100 mm in diameter. The material was produced by the floating-zone (FZ) process, which yields a high-purity ⟨100⟩ oriented single-crystal n-type silicon. Figure 2(a) shows a three-dimensional image of the rough side of the wafer. In the measurement, both M and N are equal to 256. The AFM scanned area is 40 μm×40 μm, resulting in a sampling interval $d=156$ nm. The average height (mean surface) is at $z=0$. The rms roughness σ is 0.47 μm and the estimated autocorrelation length τ is 2.6 μm. If the autocorrelation length is taken as the average surface wavelength, there are 16 to 17 data points for each surface wavelength; this allows detailed surface features to be revealed [19–24,33]. The height distribution of the rough surface is plotted in Fig. 2(b), together with a Gaussian distribution with a standard deviation of 0.47 μm. The agreement between the measured and calculated histograms suggests that the height distribution is close to the Gaussian.

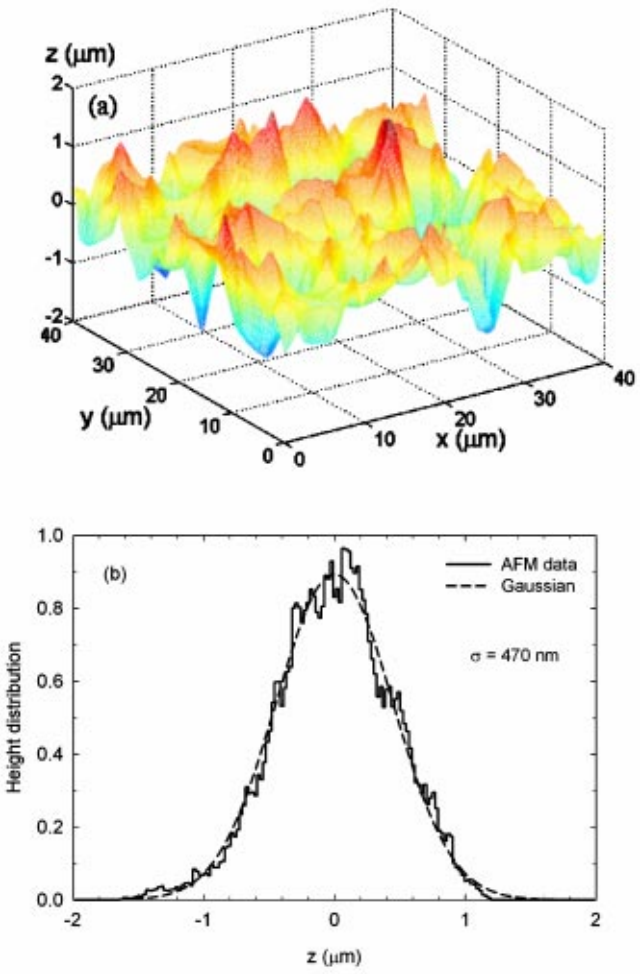

Fig. 2 Topographic characteristics of the rough side of the silicon wafer: (*a*) 3D surface image; (*b*) height distribution

The joint probability density function $p(\zeta_x,\zeta_y)$ in Eq. (7) is a function of both ζ_x and ζ_y. If the events concerning ζ_x and ζ_y are independent, $p(\zeta_x,\zeta_y)=p_1(\zeta_x)\times p_2(\zeta_y)$, where $p_1(\zeta_x)$ and $p_2(\zeta_y)$ are the marginal probability density functions, which are the 1D slope distribution functions along two orthogonal directions, respectively [34]. If the surface is isotropic, $p_1(\zeta_x)$ and $p_2(\zeta_y)$ are of the same functional relationship; thus, the 1D slope distribution commonly used in the literature is sufficient [20]. If the surface is anisotropic, the joint probability density function (2D slope distribution) may become necessary. In the present

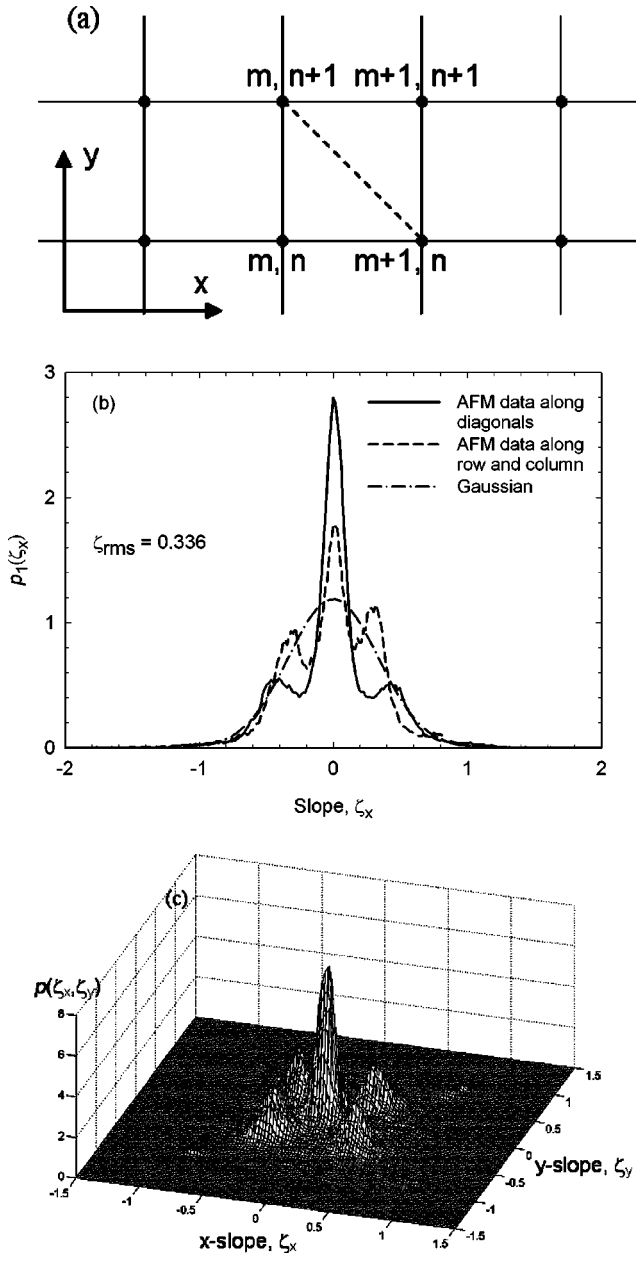

Fig. 3 Nodal network and the slope distributions: (*a*) schematic of the nodal network; (*b*) 1D slope distributions, $p_1(\zeta_x)$; (*c*) 2D slope distribution, $p(\zeta_x,\zeta_y)$

work, both the 1D and 2D slope distributions will be determined from the topographic data array and their applicability in modeling the BRDF will be examined.

The nodal network used to calculate the slope is shown in Fig. 3(*a*). To obtain the 1D slope distribution, one can use $\zeta_x=[z(m+1,n)-z(m,n)]/d$ or $\zeta_y=[z(m,n+1)-z(m,n)]/d$ to compute the slopes along the row or column and $\zeta_{x'}=[z(m+1,n+1)-z(m,n)]/(\sqrt{2}d)$ or $\zeta_{y'}=[z(m,n+1)-z(m+1,n)]/(\sqrt{2}d)$ to compute the slopes along each diagonal, respectively. As an example, the rms slope ζ_{rms} along the x direction can be evaluated by

$$\zeta_{rms,x}=\sqrt{\frac{1}{MN}\sum_{n=1}^{N}\sum_{m=1}^{M}(\zeta_x-\langle\zeta_x\rangle)^2} \tag{8}$$

where $\langle\zeta_x\rangle$ is the slope averaged along all rows. It is found that the mean slope in any direction is approximately zero for the measured silicon surface. The rms slope and slope distribution function are generally dependent on the sampling area and intervals [20]. However, for the surface studied here, the calculated rms slope and slope distribution function vary little when the sampling interval is increased from d to $3d$. This suggests that the chosen sampling interval is appropriate in the present study.

The calculation shows that the slope distributions along the row and column are very close to each other, as are the slope distributions along the two diagonals, i.e., $p_1(\zeta_x)\approx p_2(\zeta_y)$. However, there is significant difference between the former category and the latter category. The slope distributions averaged within each category are plotted in Fig. 3(*b*), where ζ_x is used in a broad sense to indicate the slope along the specified directions. The solid line represents the average slope distribution over the diagonals and the dashed line represents that over the row and column. The slope distributions show some extent of symmetry about $\zeta_x=0$ and the mean slope is almost zero. The rms slope of the rough surface is approximately 0.336 for both categories. A Gaussian distribution with a standard deviation of 0.336 is shown as the dash-dot line. Although the height distribution of this rough surface is very close to the Gaussian, the measured slope distributions deviate significantly from the Gaussian distribution. The peak at $\zeta_x=0$ in the diagonal slope distribution (solid line) is much higher than that in the Gaussian. Furthermore, instead of decreasing monotonically, there are two side peaks at $\zeta_x\approx\pm0.47$ in the solid line and the magnitude of these peaks is about one-fourth of that at $\zeta_x=0$. The slope distribution calculated along the row and column (dashed line) has a lower central peak than that calculated along the diagonals and the side peaks appear at $\zeta_x\approx\pm0.33$, closer to the center than those in the solid line. It is well understood that the peak at $\zeta_x=0$ in the slope distribution results in a specular peak in the BRDF. The impact of the side peaks on the BRDF will be discussed in Section 5, along different directions.

To evaluate the 2D slope distribution $p(\zeta_x,\zeta_y)$, each surface element is determined by the four closest nodes in the data array. The four-node element may be thought of as two triangular surfaces with a common side [shown as a dashed line in Fig. 3(*a*)]. The surface normals for the two triangles can be averaged to give the mean slope of the surface element such that

$$\zeta_x=\frac{z_{m+1,n}-z_{m,n}}{2d}+\frac{z_{m+1,n+1}-z_{m,n+1}}{2d} \tag{9a}$$

$$\zeta_y=\frac{z_{m,n+1}-z_{m,n}}{2d}+\frac{z_{m+1,n+1}-z_{m+1,n}}{2d} \tag{9b}$$

Figure 3(*c*) presents the 2D slope distribution function, based on the average of AFM measurements at two different locations. The main peak is located at the origin ($\zeta_x=\zeta_y=0$) and is shaped like a cone, suggesting that the slope distribution is nearly isotropic within a small inclination angle. About one-third of all the slopes fall within $\zeta=\sqrt{\zeta_x^2+\zeta_y^2}\leqslant0.2$, corresponding to an inclination angle $\alpha=11$ deg. A striking feature in the 2D slope distribution is the four side peaks, located symmetrically around the main peak, on the diagonal lines ($\zeta_x\pm\zeta_y=0$). The distance between the centers of the side peaks and the origin is approximately $\zeta=\sqrt{\zeta_x^2+\zeta_y^2}=0.33\sqrt{2}=0.47$. This number is in good agreement with that corresponding to the position of the side peaks in the 1D slope distribution along the diagonals. All side peaks have a similar magnitude, which is about one-fourth of that of the main peak. It can be inferred that there are many microfacets with an inclination angle near 25 deg in the measured surface.

4 BRDF Measurements Using a Laser Scatterometer

Different designs and instruments have been used to measure the BRDFs of metal, semiconductor, and dielectric surfaces at various wavelengths and temperatures [5,6,35–38]. In the present study, the BRDF of the wafer surface was measured at room tem-

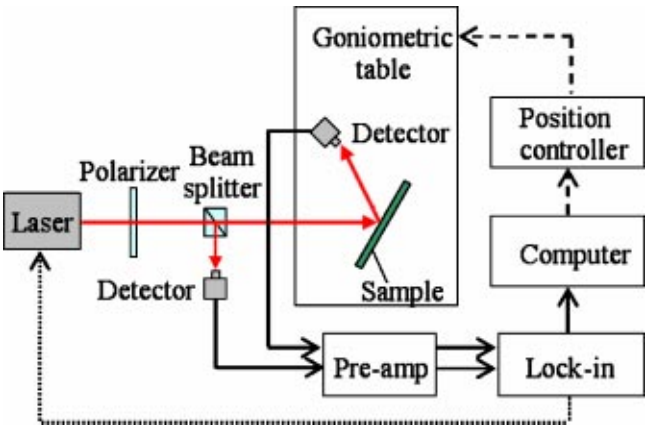

Fig. 4 The experimental setup of the TAAS

perature using the Three-Axis Automated Scatterometer (TAAS) [39]. As shown in Fig. 4, TAAS has three major components: a laser source, goniometric table, and detection assembly with a data acquisition unit. A thermoelectric-cooled fiber-coupled photodiode laser system provides a narrow band source at 635 nm or 785 nm (by interchange the laser diodes). The compact laser system has excellent wavelength and power stability. The maximum power coming out of the fiber is approximately 5 mW. The light source is stationary, and the laser beam is parallel to the optical table. Three automated rotary stages, actuated by the step motors, allow the incidence direction and the reflection direction to be changed. A sample holder is mounted to one of the rotary stages, and the wafer to be measured is attached to the sample holder. The surface of the sample is then set perpendicular to the optical table. When the rotary stage moves, the sample rotates along a vertical axis; thus, the incidence zenith angle θ_i is changed automatically. A dial on the sample holder is used to rotate the sample around its surface normal, manually changing the incidence azimuthal angle ϕ_i. The other two automated rotary stages move a silicon photodiode detector, which is positioned in a light tight tube fastened to the end of a rigid rotary arm, to measure the reflected radiation. A reference detector monitors the power of the incident radiation by using a beam splitter. Two transimpedance amplifiers maintain a near zero bias across the photodiodes and have a large dynamic range. A lock-in amplifier supplies a modulated current to the laser diode controller so that the outputs of two detectors are phase-locked to the internal reference of the lock-in amplifier. Therefore, the influence of the background radiation is eliminated without using a mechanical chopper. A computer controls the position of the goniometric table and records the data. A linear polarizer is used and the BRDF measurements are performed separately for *s*- and *p*-polarized incidence.

Since the output of the detector is proportional to its collected power, BRDF can be calculated from outputs of the movable detector and the reference detector. The measurement equation is [5,39]

$$f_r(\theta_i,\phi_i,\theta_r,\phi_r)=\frac{V_A}{V_B C_I \cos\theta_r \Delta\omega_r} \tag{10}$$

where V_A and V_B are the output signals from the movable detector and the reference detector, respectively, $\Delta\omega_r$ is the reflection solid angle (which is 1.84×10^{-4} sr for the TAAS), and the instrument constant C_I is included to address the ratio of the beam splitter and the different responsivities of the two detectors. Measurements can be performed with a scattering angle up to 88 deg. The instrument cannot measure retroreflection within a narrow angular region of about ±3 deg around the incidence direction because the detector tube will block the laser beam. The estimated uncertainty of the measurement is 0.5% at $\theta_r=45$ deg and 2% at $\theta_r=80$ deg, without considering stray light or misalignment. To calibrate the TAAS, several different samples were also measured with a reference instrument at the National Institute of Standards and Technology (NIST) [5]. Comparison results have shown that, at $\lambda=635$ nm and 785 nm, the relative difference is within 5% between the two instruments [39].

5 Comparison of Predicted and Measured BRDFs

The silicon wafer is opaque at wavelengths less than 1100 nm, corresponding to the band gap energy at room temperature [35]. The optical constants of silicon are taken from the handbook [40]. Since σ/λ is from 0.60 to 0.74 and $\sigma/\tau=0.18$ for the studied surface, geometric optics approximation is appropriate for θ_i and θ_r up to 70 deg [11]. The model given in Eq. (7) did not include multiple scattering. For a perfect conducting surface with $\sigma/\tau=0.2$ at $\theta_i=30$ deg, it has been shown that the reflected energy due to the multiple scattering is only 2% [13]. Therefore, neglecting the multiple scattering will not cause significant error for the studied surface at most angles. The predict BRDF from Eq. (7) using the 1D and 2D slope distribution functions are to be compared with the measurement results. For convenience, an observation angle θ_{obs} is defined as $\theta_{obs}=\theta_r$ when $\phi_r=\phi_i+180$ deg, and $\theta_{obs}=-\theta_r$ when $\phi_r=\phi_i$. Because the term $\cos\theta_r$ in Eq. (10) is very small when θ_r gets close to 90 deg, $f_r\cos\theta_r$ is used as the y-axis in the following.

5.1 Using 1D Slope Distribution. To use the 1D slope distribution, it is assumed that the two functions $p_1(\zeta_x)$ and $p_2(\zeta_y)$ are the same. Since ζ_y has to be zero for in-plane scattering, the joint probability density function $p(\zeta_x,\zeta_y)$ can be written as $p_1(\zeta_x)\times p_1(0)$. The x-y coordinates are rotated 45 deg for the diagonal directions. Figure 5 compares the predicted BRDFs using the slope distribution along the diagonals with the BRDFs measured at $\lambda=635$ nm with $\phi_i=45$ deg, for $\theta_i=15$ and 45 deg. No data could be taken within ±3 deg about the retroreflection direction because the detector tube would block the incident beam. The peak in $f_r\cos\theta_r$ is located at the specular reflection direction. The predicted and measured BRDFs at $\theta_i=15$ deg agree well for both *p* and *s* polarizations, except for the region around the specular direction, at which the predicted value is 28% lower. At $\theta_i=45$ deg, however, the predicted BRDF in the specular direction ($\theta_r=45$ deg) is 7% higher than the measured. The discrepancy at the specular direction might be due to the diffraction effect, not included in the geometric optics framework. The magnitude of the specular peak is given by $f_r\cos\theta_r=p_1^2(0)\rho(n,\kappa,\psi)/\cos\theta_i$, which is only a function of the reflectivity that is dependent on polarization and angle of incidence. This explains the high specular peaks at $\theta_i=45$ deg for *s* polarization as seen in Fig. 5(*b*).

In the BRDF curve at $\theta_i=15$ deg, subsidiary peaks can be seen on both sides of the specular direction at $\theta_{obs}\approx-35$ and 62 deg. These peaks are not sharp, but with a plateau region. The excellent agreement between the measured and predicted BRDFs at the subsidiary peaks suggests that the occurrence of the subsidiary peak in the BRDF is related to the distribution of the microfacet orientation. The side peaks in the slope distribution is at $\zeta\approx0.47$, which corresponds to $\alpha\approx25$ deg. When the incident beam hits a microfacet with an inclination angle $\alpha=25$ deg (in the plane of incidence), the scattering angle will be at $\theta_{obs}=\theta_i\pm2\alpha$. For $\theta_i=15$ deg, the corresponding reflection angles are $\theta_{obs}=-35$ and 65 deg, which is close to -35 and 62 deg, from the BRDF measurements. For $\theta_i=45$ deg, the predicted subsidiary peak at $\theta_{obs}=-5$ deg is observed in Fig. 5, whereas the other at $\theta_{obs}=95$ deg is not physical. It might be expected that $f_r\cos\theta_r$ would increase toward 90 deg due to the side peak. However, the situation is more complicated when θ_{obs} is close to 90 deg since $f_r\cos\theta_r$ is also dependent on the reflectivity of the microfacet. For *p* polarization, the reflectivity ρ decreases to almost zero at the Brewster angle [3], which is approximately 75 deg for silicon

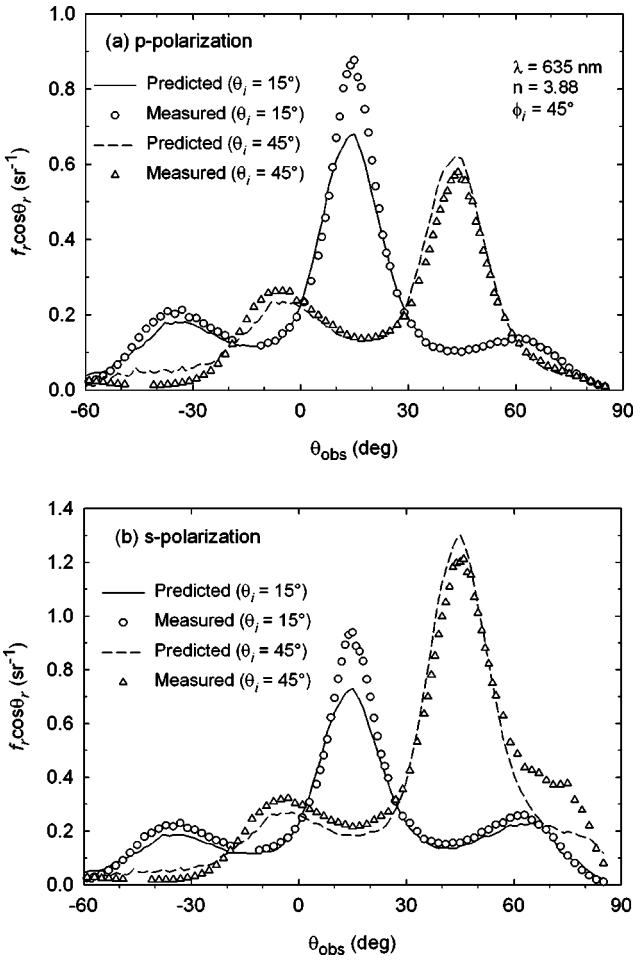

Fig. 5 Comparisons of the predicted and measured BRDFs at λ = 635 nm: (*a*) *p* polarization; (*b*) *s* polarization

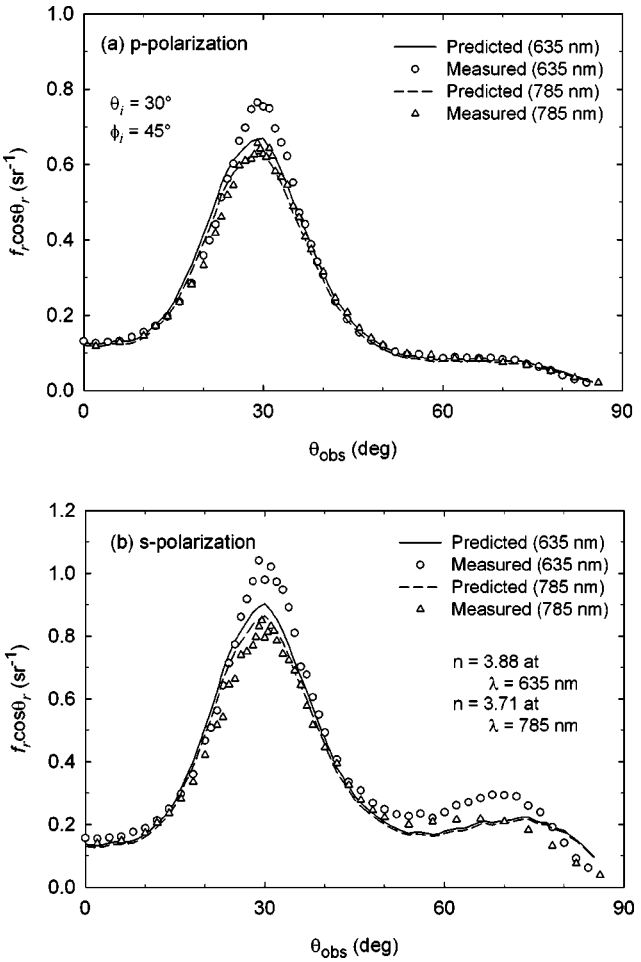

Fig. 6 Effect of wavelength on BRDF: (*a*) *p* polarization, (*b*) *s* polarization

at $\lambda = 635$ nm. The local incidence angle ψ is close to 70 deg when $\theta_{obs} = 90$ deg. Therefore, both the predicted and measured values of $f_r \cos\theta_r$ decrease monotonically from the specular direction towards 90 deg as shown in Fig. 5(*a*).

On the other hand, the reflectivity for *s* polarization increases with the angle of incidence. However, the masking effect will reduce the scattered radiation towards 90 deg. Both the predicted and measured values of $f_r \cos\theta_r$ exhibit a shoulder between $\theta_{obs} = 60$ and 90 deg. Their magnitudes, however, are quite different. The measured values are much higher than the predicted. Repeated measurements gave the same BRDF when a significant stray light was intentionally introduced or carefully removed during the experiment. Hence, the observed feature is the actual behavior of the sample surface rather than an instrument artifact. The discrepancy for *s* polarization may be attributed to multiple scattering, which can be significant at large reflection angles, and the breakdown of Smith's shadowing function at large reflection angles, when the surface statistics is not Gaussian. The influence of multiple scattering and masking is not as significant for *p* polarization due to the small reflectivity around the Brewster angle.

To study the effect of wavelength, the BRDFs with $\theta_i = 30$ deg and $\phi_i = 45$ deg are shown in Fig. 6 at $\lambda = 635$ nm and 785 nm, for positive observation angles only. At $\lambda = 635$ nm, the predicted BRDF peak is 14% lower than the measured, whereas at $\lambda = 785$ nm, the predicted and measure BRDF peaks are close to each other. For this incidence angle, subsidiary peaks corresponding to the slope $\alpha = 25$ deg are at $\theta_{obs} = -20$ and 80 deg. Subsidiary peaks were observed at $\theta_{obs} = -20$ deg in the measured BRDF (not shown in Fig. 6). However, no peaks were observed around 80 deg due to the low reflectivity for *p* polarization. For *s* polarization, the subsidiary peak tends to shift to a smaller reflection angle since the shadowing function $S(\theta_r)$ decreases very fast with increasing reflection angle. Similar to the argument for $\theta_i = 45$ deg, multiple scattering and the breakdown of Smith's shadowing function may be the reason why the measured and predicted BRDF does not agree well for *s* polarization at lager observation angles. According to the geometric optics model, the effect of wavelength is introduced through the reflectivity that depends on the optical constants. The refractive index of silicon at room temperature is 3.88 at $\lambda = 635$ nm and 3.71 at $\lambda = 785$ nm [40]. Therefore, the reflectivity $\rho(n, \kappa, \psi)$ for a smooth surface is slightly higher at the shorter wavelength at $\psi < 70$ deg. According to Eq. (7), the BRDF in the specular direction should be about 5% higher at $\lambda = 635$ nm than at $\lambda = 785$ nm due to the difference in the refractive index at the two wavelengths. However, for both polarizations the measured BRDF at $\lambda = 635$ nm around the specular direction is more than 15% higher than that at 785 nm. This suggests that the effect of wavelength requires further investigation and wave-optics-based models may be required to take into account the diffraction effect.

Although the predicted BRDF using the slope distribution along the diagonals is in good agreement with the measurement at $\phi_i = 45$ deg, the same cannot be said when the predicted BRDF using the slope distribution along the row and column is compared with the measurement result at $\phi_i = 0$ deg. This is clearly demonstrated in Fig. 7, in which the predicted and measured BRDFs at $\phi_i = 0$ deg are plotted with $\lambda = 635$ nm and $\theta_i = 0$ deg. The solid line represents the predicted BRDF using the 1D slope distribu-

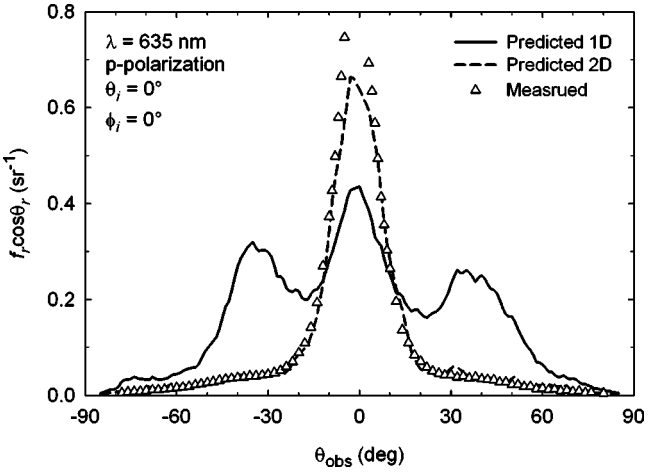

Fig. 7 Comparison of BRDFs at azimuthal angle $\phi_i=0$ deg

tion and has three prominent peaks. On the contrary, the measurement data, represented by the triangular marks, showed only one, but a much higher specular peak. In this case, the BRDF at the specular direction cannot be measured due to beam blocking. The measured BRDF at $\phi_i=90$ deg is very similar to that measured at $\phi_i=0$ deg. It is clear that the 1D slope distribution along the row and column does not correlate with the measured BRDF along the same directions. Nevertheless, the 2D slope distribution can be used to obtain a much better matching with the experiments, as shown by the dashed line in Fig. 7.

5.2 Using 2D Slope Distribution. For the in-plane scattering, one component of the slope must be equal to zero. Therefore, the cross-sections of the 2D slope distribution are related to the in-plane BRDFs at different azimuthal angles. For example, at $\phi_i=0$ deg the plane of incidence is the x-z plane and the probability of microfacets that contribute to the in-plane scattering is $p(\zeta_x,0)$, which is the cross-section of $\zeta_y=0$ in the 2D slope distribution. The cross-section $p(\zeta_x,0)$ is substituted into Eq. (7) to predict the in-plane BRDF at $\phi_i=0$ deg, and this result is represented by the dashed line in Fig. 7. The prediction agrees well with the measured result except near the specular region. There is no subsidiary peak in the predicted BRDF using the cross-section and the measured BRDF. Hence, the side peaks presented in the slope distribution along the row and column do not correlate with the in-plane BRDF. This can be understood by examining the cross-section of the two dimensional slope distribution $p(\zeta_x,0)$, where there are no side peaks in the x-z plane with an $\alpha=18$ deg ($\zeta_x=0.33$, $\zeta_y=0$). These side peaks in the 1D slope distribution along the row (or column) are the artifact resulting from the microfacets, whose normal is in the $\zeta_x\pm\zeta_y=0$ plane with $\alpha=25$ deg, as they are projected to the x-z plane. Furthermore, the predicted BRDF using the cross-section of $\zeta_x\pm\zeta_y=0$ is very close to that using the 1D slope distribution along the diagonals. The reason is that the way in which the 1D slope is calculated happens to result in the correct distribution, since the normal of most microfacets that contribute to the side peaks is close to the plane $x\pm y=0$. Therefore, care must be taken when using the 1D slope distribution to predict the BRDF for anisotropic surfaces.

Further measurements are performed at several azimuthal angles, and the results are compared to the predicted BRDF using the corresponding cross-sections of the 2D slope distribution. The comparisons are shown in Figs. 8 and 9. The solid line is the averaged result at $\phi_i=0$ deg and $\phi_i=90$ deg. The dashed line is the averaged result at $\phi_i=45$ deg and $\phi_i=135$ deg. The dash-dot line is the result at $\phi_i=30$ deg. The variation of the predicted BRDF with the azimuthal angle agrees well with that in the measured BRDF. It should be noted that the sampling area to calculate

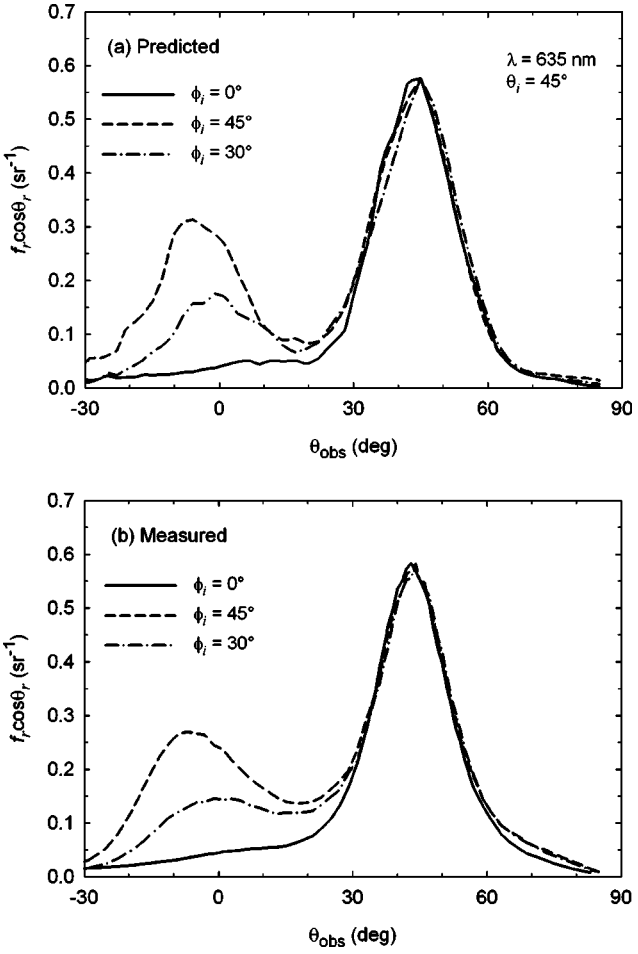

Fig. 8 BRDFs at different azimuthal angles for *p* polarization: (*a*) predicted; (*b*) measured

the slope distribution is only 40 μm$\times$40 μm, whereas in the light scattering measurement the beam spot on the sample is near 5 mm in diameter, which might better represent the average behavior of the surface. The discrepancy in Fig. 9(b) at large positive observation angles is due to the same reason as given in the discussion of Fig. 5(b). The variation of the BRDFs with the azimuthal angles is attributed to the anisotropic slope distribution. When the azimuthal angle is at 0 deg (or 90 deg), there are no subsidiary peaks in the BRDF because the cross-section is cut at $\zeta_y=0$ (or $\zeta_x=0$). When the azimuthal angle is at 45 and 135 deg, the cross-sections with $\zeta_x\pm\zeta_y=0$ have to be chosen, which exhibit side peaks. Consequently, there are prominent subsidiary peaks in BRDF. When the azimuthal angle is at 30 deg, the subsidiary peaks in the BRDF are noticeable but less significant.

As an inverse scattering problem, the BRDF may be used to determine the slope distribution [26]. The cross-section of the 2D slope distribution can be calculated from the measured in-plane BRDF. Iterations are necessary because the rms slope is an input of the shadowing function and it is not known until the slope distribution is evaluated. To obtain the 2D slope distribution from the angular-resolved scattering data, one needs to measure the BRDF for additional azimuthal angles. This approach to determine the 2D slope distribution would not be as effective as the one using the AFM topographic data.

Subsidiary peaks were also observed by Shen et al. [30] for a different silicon wafer with σ of 0.94 μm and at $\lambda=0.95$ μm. The difference between the specular direction and the direction where the subsidiary peak occurs is about 50 deg, which corresponds to an inclination angle $\alpha=25$ deg. This angle is also the angle observed for the studied surface in the present work, indicating that

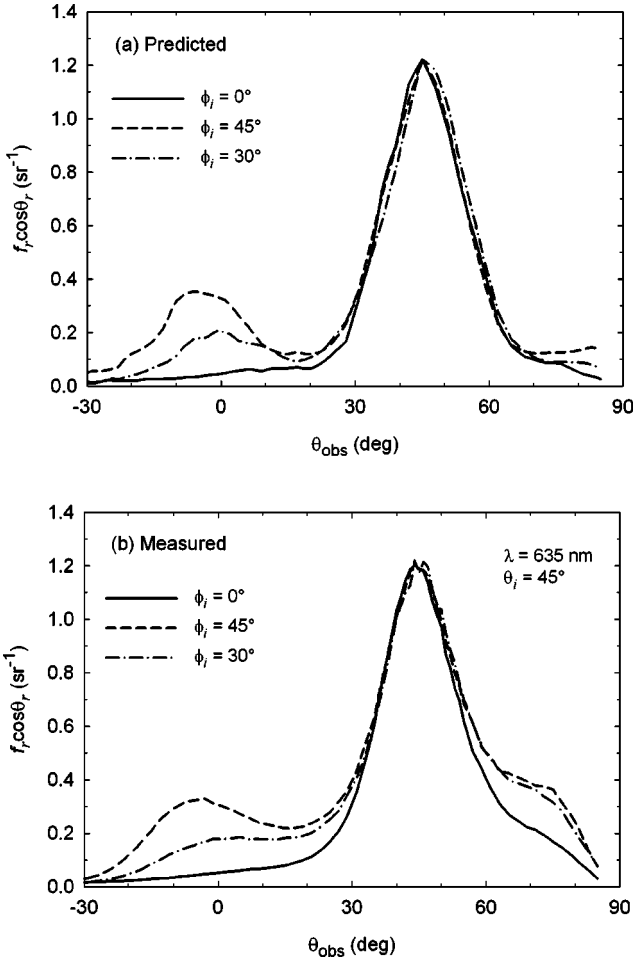

Fig. 9 BRDFs at different azimuthal angles for *s* polarization: (*a*) predicted; (*b*) measured

the peaks in the slope distribution may be related to the microstructure of the ''random'' rough silicon surface resulted from the wafer manufacturing process. In fact, the side peaks may be attributed to the resurfacing of the randomly oriented microfacets by the chemical etching process. The wafer has $\langle 100 \rangle$ crystalline orientation. The angle between the (100) plane and the (311) plane is $\cos^{-1}(3/\sqrt{11}) = 25.2$ deg, which is in excellent agreement with the angle observed in the measured slope distribution and BRDF. The {311} planes are stable because the etch rate for the {311} planes is much slower than that of the {100} plane [41]. Furthermore, there are four planes in the crystallographic plane family {311}, and the projection of the directions $\langle 311 \rangle$ in the (100) plane is separated by every 90 deg. The non-Gaussian and anisotropic features in the studied surface may also exist in other semiconductor wafers because the chemical etching is a standard process to treat the rough side of wafers. However, when measured with AFM and the scatterometer, many wafers do not exhibit side peaks at all. Further study is needed to identify the exact cause of the structure seen in the slope distribution and BRDF.

6 Conclusions

The rough side of a silicon wafer was characterized using an atomic force microscope. The 1D and 2D slope distribution functions were obtained from the AFM surface topographic data and found to deviate from the Gaussian distribution significantly with remarkable side peaks. The 1D slope distributions and the cross-sections of the 2D slope distribution are incorporated into a geometric optics model to predict the in-plane BRDF, which are then compared with the BRDF measured with a laser scatterometer. The predicted BRDF using the 1D slope distribution along the diagonals agrees reasonably well with the BRDF measured at $\phi_i = 45$ deg. The discrepancy in the specular direction may be attributed to the limitation of the geometric optics approximation. However, the predicted BRDF using the 1D slope distribution along the row and column fails to describe the BRDF measured at $\phi_i = 0$ deg. Nevertheless, the prediction using the cross-section of the 2D slope distribution are in good agreement with the measured result at $\phi_i = 0$ deg as well as at other azimuthal angles. The occurrence of the subsidiary peaks in the BRDF can be correlated quantitatively with the side peaks in the 2D slope distribution. The deviations at large positive observation angles for *s* polarization may be attributed to multiple scattering, and the breakdown of the shadowing function for the non-Gaussian surface at large reflection angles.

The method used in this work may be applied to predict the BRDF of other anisotropic or non-Gaussian rough surfaces and the present study may help characterize the microstructure of the particular surface. The BRDF obtained in this study may be applied to model the effective emissivity of silicon wafers to improve the temperature measurement accuracy in semiconductor manufacturing processes. Further studies are needed to relate the occurrence of side peaks and the key parameters in the wafer manufacturing process so that the slope distribution might provide useful information for the manufacturing process.

Acknowledgments

This work was supported by the National Science Foundation (CTS-0236831). The authors thank Dr. Kakuen Tang and Hyunjin Lee for valuable discussions, and Vinh Khuu and Daniel McCormick for carefully reviewing the manuscript.

Nomenclature

C_I = instrument constant
d = sampling interval
f_r = bidirectional reflectance distribution function (BRDF)
L = radiance
$\mathbf{n}$ = microfacet normal
n = refractive index
p = probability density function
S = shadowing function
V = output of detector

Greek symbols

α = inclination angle
ζ = slope
θ = polar angle
θ_{obs} = observation angle
κ = extinction coefficient
λ = wavelength
ρ = reflectivity of smooth surface
σ = root-mean-square roughness
τ = autocorrelation length
ϕ = azimuthal angle
ψ = local incidence angle
ω = solid angle

Subscripts

i = incoming
r = reflected

References

[1] Zhang, Z. M., 2000, ''Surface Temperature Measurement Using Optical Techniques,'' Annu. Rev. Heat Transfer, **11**, pp. 351–411.
[2] Zhou, Y. H., Shen, Y. J., Zhang, Z. M., Tsai, B. K., and DeWitt, D. P., 2002, ''A Monte Carlo Model for Predicting the Effective Emissivity of the Silicon Wafer in Rapid Thermal Processing Furnaces,'' Int. J. Heat Mass Transfer, **45**, pp. 1945–1949.
[3] Modest, M. F., 1993, *Radiative Heat Transfer*, McGraw-Hill, New York.

[4] Siegel, R., and Howell, J. R., 2002, *Thermal Radiation Heat Transfer*, Fourth Edition, Taylor & Francis, New York.
[5] Barnes, P. Y., Early, E. A., and Parr, A. C., 1998, *Spectral Reflectance*, NIST Special Publication 250-48.
[6] Zaworski, J. R., Welty, J. R., Palmer, B. J., and Drost, J. R., 1996, ''Comparison of Experiment With Monte Carlo Simulations on a Reflective Gap Using a Detailed Surface Properties Model,'' ASME J. Heat Transfer, **118**, pp. 388–393.
[7] Maradudin, A. A., Michel, T., McGurn, A. R., and Méndez, E. R., 1990, ''Enhanced Backscattering of Light from a Random Grating,'' Ann. Phys. (San Diego), **203**, pp. 255–307.
[8] Tang, K., Yang, Y., and Buckius, R. O., 1999, ''Theory and Experiments on Scattering from Rough Interfaces,'' Annu. Rev. Heat Transfer, **10**, pp. 100–140.
[9] Saillard, M., and Sentenac, A., 2001, ''Rigorous Solutions for Electromagnetic Scattering from Rough Surfaces,'' Waves Random Media, **11**, pp. R103–R137.
[10] Beckmann, P., and Spizzichino, A., 1987, *The Scattering of Electromagnetic Waves From Rough Surfaces*, Artech House, Norwood, MA.
[11] Tang, K., Dimenna, R. A., and Buckius, R. O., 1997, ''Regions of Validity of the Geometric Optics Approximation for Angular Scattering From Very Rough Surfaces,'' Int. J. Heat Mass Transfer, **40**, pp. 49–59.
[12] Zhou, Y. H., and Zhang, Z. M., 2003, ''Radiative Properties of Semitransparent Silicon Wafers With Rough Surfaces,'' ASME J. Heat Transfer, **125**, pp. 462–470.
[13] Tang, K., and Buckius, R. O., 2001, ''A Statistical Model of Wave Scattering From Random Rough Surfaces,'' Int. J. Heat Mass Transfer, **44**, pp. 4059–4073.
[14] Torrance, K., and Sparrow, E., 1967, ''Theory for Off-Specular Reflection From Roughed Surfaces,'' J. Opt. Soc. Am., **57**, pp. 1105–1114.
[15] Caron, J., Lafait, J., and Andraud, C., 2003, ''Catastrophe Theory Interpretation of Multiple Peaks Produced by Light Scattering From Very Rough Dielectric Surfaces,'' Physica B, **325**, pp. 76–85.
[16] Phong, B. T., 1975, ''Illumination for Computer Generated Images,'' Commun. ACM, **18**, pp. 311–317.
[17] Blinn, J. F., 1977, ''Models of Light Reflection for Computer Synthesized Pictures,'' Comput. Graph., **11**, pp. 192–198.
[18] Schleef, D., Schaefer, D. M., Andres, R. P., and Reifenberger, R., 1997, ''Radial-Histogram Transform of Scanning-Probe-Microscope Images,'' Phys. Rev. B, **55**, pp. 2535–2542.
[19] Hegeman, J. B. J. W., Kooi, B. J., Groen, H. B., and de Hosson, J. Th. M., 1999, ''Analyses of Small Facets Imaged With Scanning-Probe Microscopy,'' J. Appl. Phys., **86**, pp. 3661–3669.
[20] Bennett, J. M., and Mattsson, L., 1999, *Introduction to Surface Roughness and Scattering*, Second Edition, Optical Society of America, Washington, DC.
[21] Thomas, T. R., 1999, *Rough Surface*, Second Edition, Imperial College Press, London.
[22] Wiesendanger, R., 1994, *Scanning Probe Microscopy and Spectroscopy: Methods and Applications*, Cambridge University Press, Cambridge, England.
[23] Stover, J. C., Ivakhnenko, V. I., and Scheer, C. A., 1998, ''Comparison of Surface PSD's Calculated From Both AFM Profiles and Scatter Data,'' *Proc. of SPIE*, **3275**, pp. 37–46.
[24] Bawolek, E. J., Mohr, J. B., Hirleman, E. D., and Majumda, A., 1993, ''Light Scattering From Polysilicon and Aluminum Surfaces and Comparison With Surface-Roughness Statistics by Atomic Force Microscopy,'' Appl. Opt., **32**, pp. 3377–3400.
[25] Cao, L. X., Vorburger, T. V., Lieberman, A. G., and Lettieri, T. R., 1991, ''Light-Scattering Measurement of the RMS Slopes of Rough Surfaces,'' Appl. Opt., **30**, pp. 3221–3226.
[26] Nee, S.-M. F., Dewees, R. V., Nee, T.-W., Johnson, L. F., and Moran, M. B., 2000, ''Slope Distribution of a Rough Surface Measured by Transmission Scattering and Polarization,'' Appl. Opt., **39**, pp. 1561–1569.
[27] Guérin, C.-A., 2002, ''Scattering on Rough Surfaces With Alpha-Stable Non-Gaussian Height Distributions,'' Waves Random Media, **12**, pp. 293–306.
[28] Ward, G. J., 1992, ''Measuring and Modeling Anisotropic Reflection,'' Comput. Graph., **26**, pp. 265–272.
[29] Smith, B., 1967, ''Geometrical Shadowing of a Random Rough Surface,'' IEEE Trans. Antennas Propag., **15**, pp. 668–671.
[30] Shen, Y. J., Zhang, Z. M., Tsai, B. K., and DeWitt, D. P., 2001, ''Bidirectional Reflectance Distribution Function of Rough Silicon Wafers,'' Int. J. Thermophys., **22**, pp. 1311–1326.
[31] Tsang, L., and Kong, J. A., 1980, ''Energy Conservation for Reflectivity and Transmissivity at a Very Rough Surface,'' J. Appl. Phys., **51**, pp. 673–380.
[32] Priest, R. G., and Germer, T. A., 2000, ''Polarimetric BRDF in the Micro-Facet Model: Theory and Measurements,'' *Proc. of 2000 Meeting of the Military Sensing Symposia Specialty Group on Passive Sensors*, Infrared Information Analysis Center, Ann Arbor, MI, Vol. 1, pp. 169–181.
[33] Zhu, Q. Z., Sin, S., and Zhang, Z. M., 2002, ''Surface Characterization of the Rough Side of Silicon Wafers,'' *Developments in Theoretical and Applied Mechanics*, A. J. Kassab et al., eds., Rivercross Publishing, Orlando, pp. 49–55.
[34] Flury, B., 1997, *A First Course in Multivariate Statistics*, Springer, New York.
[35] Zhang, Z. M., Fu, C. J., and Zhu, Q. Z., 2003, ''Optical and Thermal Radiative Properties of Semiconductors Related to Micro/Nanotechnology,'' Adv. Heat Transfer, **37**, pp. 179–296.
[36] Drolen, B. L., 1992, ''Bidirectional Reflectance and Specularity of Twelve Control Materials,'' J. Thermophys. Heat Transfer, **6**, pp. 672–679.
[37] Ford, J. N., Tang, K., and Buckius, R. O., 1995, ''Fourier Transform Infrared System Measurement of the Bidirectional Reflectivity of Diffuse and Grooved Surfaces,'' ASME J. Heat Transfer, **117**, pp. 955–962.
[38] Roy, S., Bang, S. Y., Modest, M. F., and Stubican, V. S., 1993, ''Measurement of Spectral Directional Reflectivities of Solids at High Temperatures Between 9 and 11 μm,'' Appl. Opt., **32**, pp. 3550–3558.
[39] Shen, Y. J., Zhu, Q. Z., and Zhang, Z. M., 2003, ''A Scatterometer for Measuring the Bidirectional Reflectance and Transmittance of Semiconductor Wafers With Rough Surfaces,'' Rev. Sci. Instrum., **74**, pp. 4885–4892.
[40] Edwards, D. F., 1985, ''Silicon(Si),'' *Handbook of Optical Constants of Solids*, E. D. Palik, ed., Academic Press, Orlando, FL, pp. 547–569.
[41] Resnik, D., Vrtacnik, D., and Amon, S., 2000, ''Morphological Study of {311} Crystal Planes Anisotropically Etched in (100) Silicon: Role of Etchants and Etching Parameters,'' J. Micromech. Microeng., **10**, pp. 430–439.

Entropy Generation Extrema and Their Relationship With Heat Exchanger Effectiveness—Number of Transfer Unit Behavior for Complex Flow Arrangements

Ramesh K. Shah
e-mail: rkseme@rit.edu
Rochester Institute of Technology,
Department of Mechanical Engineering,
Rochester, NY 14623-5604, USA

Teodor Skiepko
e-mail: tskiepko@pb.bialystok.pl
Bialystok Technical University,
Department of Mechanical Engineering,
Wiejska 45C, 15-351 Bialystok,
Poland

While the concept of minimum irreversibility is associated with the maximum energy efficiency for energy conversion processes in thermal systems, we have found that it is not quite applicable to the heat exchanger analysis. We have shown that the heat exchanger effectiveness can be maximum, having an intermediate value or minimum at the maximum irreversibility operating point depending on the flow arrangement of the two fluids. Similarly, the heat exchanger effectiveness can be minimum or maximum at the minimum irreversibility operating point. The objective of this paper is to illustrate and discuss such heat exchanger performance and irreversibility trends by combining the temperature difference irreversibility with the P-NTU results for complex flow arrangements.
[DOI: 10.1115/1.1846694]

Keywords: Heat Transfer, Heat Exchangers, Second Law, Thermodynamics

Introduction

Dimensionless closed-form algebraic P-NTU-R or ε-NTU-C^* relationships[1] are presented in the literature (Kays and London [1], Pignotti and Shah [2], Shah and Sekulic [3], Kandlikar and Shah [4]) for over 100 different flow arrangements for two-fluid heat exchangers design and analysis. When one reviews such P-NTU or ε-NTU results for a variety of two-fluid exchanger flow arrangements, the following observations can be made:

- The P-NTU or ε-NTU results for any R or C^* value (except for R or $C^*=0$) are different and dependent upon the flow arrangement of the two fluids.
- For some flow arrangements (such as counterflow, parallelflow, unmixed-unmixed crossflow), P or ε increases monotonically with increasing NTU and reaches an asymptotic maximum value that may be dependent upon the R or C^* value. This asymptotic value can be unity or less than unity.
- For some flow arrangements (such as mixed-mixed crossflow, 1-2 TEMA G and H having overall parallelflow, and 1-2 TEMA J exchangers), P increases with NTU, reaches a maximum value, and then decreases with a further increase in NTU and reaches an asymptotic minimum value lower than unity for any given R value ($0<R_1<\infty$).
- For other flow arrangements (such as a 3 pass $-$3 pass plate heat exchanger with overall parallelflow and individual passes in counterflow), P first increases with NTU, reaches an almost flat value at some NTU and then the rate of increase in P decreases up to some another value of NTU beyond which the rate of increase of P with NTU continues to increase with further increase in NTU to reach finally an asymptotic value at $NTU=\infty$.

In order to explain the aforementioned P-NTU or ε-NTU performance behavior for complex flow arrangements, limited attempts have been made in the literature to evaluate the entropy generation rate and conduct an irreversibility analysis, based on the Second Law. Our initial objective was to explain why for the same surface area and identical surfaces, inlet temperatures and flow rates, different exchanger flow arrangements have different heat transfer rates. For some flow arrangements, we are successful to explain the reasoning using analysis of total irreversibility associated with a heat exchanger. For example, we can explain why a parallelflow heat exchanger will transfer 50 percent of the heat compared to that for a counterflow heat exchanger for $R_1=1$ and $NTU_1\rightarrow\infty$. However, such reasoning is not possible to explain the phenomena for many complex flow arrangements. This is what we will address in the paper. In order to cover a broad spectrum of the flow arrangements, we have considered a total of 18 flow arrangements: conventional single pass flow arrangements, commonly used shell-and-tube heat exchanger flow arrangements, and some key multipass plate heat exchanger flow arrangements. The results presented then should cover the trends for many other flow arrangements that are also not covered in the analysis of this paper. From the thermodynamics point of view, the temperature cross and fluid mixing analogy, the definition of heat exchanger effectiveness, thermodynamics figure of merit, etc. are important points for heat exchanger analysis and interpretation, but are beyond the scope of this paper.

We will first briefly explain the concept of the temperature cross, and then relate the temperature cross phenomena with irreversibility analysis.

Temperature Cross, Irreversibility and Effectiveness

Since some of the peculiar behavior of the P-NTU or ε-NTU results is related to the temperature cross, let us first define it. The temperature cross derives its name from fictitious or actual crossing of the temperature distributions of the hot and cold fluids in an

This paper was presented at the Fifth ISHMT/ASME Heat and Mass Transfer Conference in Calcutta, India, and published in Heat and Mass Transfer 2002, Proc. 5th ISHMT-ASME Heat Mass Transfer Conf., Tata McGraw-Hill Pub. Co. Ltd., New Delhi, India, pp. 910–919, 2002. Reprinted with permission. Manuscript received by the Heat Transfer Division November 27, 2002; revision received August 28, 2003. Associate Editor: M. K. Jensen.

[1]The P-NTU-R method is preferred over the ε-NTU-C^* method for a stream asymmetric exchanger since only one formula covers the complete range of R from 0 to ∞. One needs two different ε-NTU-C^* formulas to cover the complete range of the heat capacity rate ratio.

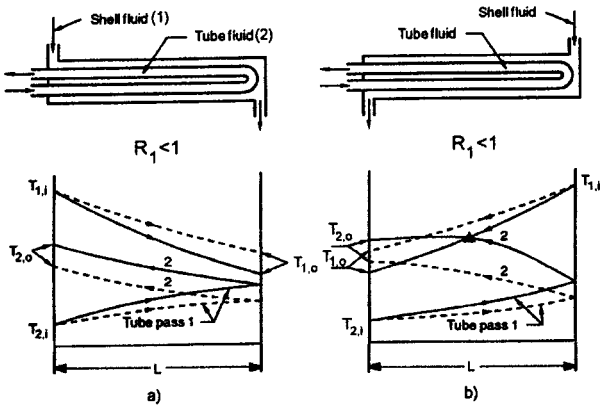

Fig. 1 Idealized temperature distributions in a 1-2 TEMA E exchangers (different by the shell fluid nozzle orientation) with shell fluid mixed for low *NTU* (with dashed lines)—case of no TC, and high *NTU* (with solid lines): (*a*) case of *external* TC, and (*b*) *external* and *internal* (▲) TC.

exchanger. If there is no actual crossing of hot and cold fluid temperature distributions as a function of the axial length within an exchanger for any flow arrangement and $T_{c,o} > T_{h,o}$, we will refer to it as an external temperature cross as found in the temperature distributions of a counterflow exchanger and the 1-2 TEMA E shell-and-tube heat exchanger of Fig. 1(*a*) for a high *NTU* case. On the contrary no temperature cross occurs at low *NTU* represented in Fig. 1(*a*) and 1(*b*) by dashed lines. We will call it an internal temperature cross if there is an actual crossing of hot and cold fluid temperature distributions ($T_c > T_h$) locally somewhere within an exchanger; and beyond that point along the flow length $T_c > T_h$, and reverse heat transfer takes place (original cold fluid transferring heat to the original hot fluid). There are two possibilities for the internal temperature cross: (i) $T_c > T_h$, as in the 1-2 TEMA E exchanger of Fig. 1(*b*) at high *NTU*, or (ii) $T_{c,o,\text{local}} > T_{h,o,\text{local}}$ where the subscript local means one of the multiple outlets on one or both fluid sides of an exchanger such as that occurs in a 1-2 TEMA J exchanger. Note in Fig. 1 that there can be an external temperature cross/meet at the exchanger outlet with or without an internal temperature cross. Similarly, there can be an internal temperature cross with (e.g., 1-2 TEMA J exchanger) or without (e.g., 1-2 TEMA G and H exchanger with overall parallelflow) a temperature cross at the exchanger outlet.

An irreversible process is referred to as a thermodynamic process, which cannot revert to the original state from the final stage without additional energy interaction(s) from surrounding. The factors that cause a process to be irreversible are called irreversibilities. There are several irreversibilities present in a heat exchanger. The most important ones are: (1) heat transfer across a finite temperature difference, (2) mixing of fluid streams, and (3) fluid flow friction phenomena, among many other possible irreversibilities. Our focus in this paper will be to address only the first two irreversibilities because they are the only one responsible for different theoretical heat transfer performance behavior (P_1-NTU_1) of the exchangers of different flow arrangements (i.e., we do not consider flow friction effects while deriving *P-NTU* or ε-*NTU* formulas).[2] The irreversibility can be measured in terms of the entropy generation or energy losses (exergy destruction), and are designated as $\dot{S}_{\text{irr}}$ and $\dot{I}_{\text{irr}}$ respectively here. The measures $\dot{S}_{\text{irr}}$ and $\dot{I}_{\text{irr}}$ are related by $\dot{I}_{\text{irr}} = T_o \cdot \dot{S}_{\text{irr}}$ where T_o is a temperature weighting factor, interpreted as the temperature of the surroundings, which is identified as a thermodynamic reference state for measuring the thermal energy potential of the system at hand. Since our focus is on a heat exchanger as a component in this paper, and we are not going to discuss any system in which a heat exchanger is one of the components, we will consider only the irreversibility measured in terms of the entropy measure.

The heat exchanger analysis just involves heat (thermal energy) as the same form of energy in transfer rejected by one fluid and absorbed by another fluid in equal amounts. Therefore, we measure the efficiency of the heat transfer process by the ''exchanger heat transfer effectiveness'' defined as ratio of actual heat transfer rate and maximum possible heat transfer rate from one fluid to the other, Kays and London [1]. The effectiveness thus ranges from zero to 100 percent, and in fact, some commercial heat exchangers are available today that has effectiveness of 98 percent and higher at some operating points. We can apply the irreversibility analysis to the heat exchangers to understand why the heat exchangers of different flow arrangements differ in performance for the same given design conditions (flow rates, inlet fluid temperatures and heat transfer surface area). However, such analysis does not always explain the reasoning of different performance behavior of various exchanger flow arrangements by the conventional irreversibility analysis. This is because it can be found that the heat exchanger effectiveness can be maximum, having an intermediate value or minimum at the maximum irreversibility operating point depending upon the flow arrangement; similarly, the heat exchanger effectiveness can be minimum or maximum at the minimum irreversibility operating point. Thus while the concept of minimum irreversibility is associated with the maximum efficiency for a power thermal system, it may not quite applicable for the heat exchanger analysis. Sekulic [5] has noted some such inconsistencies between the highest effectiveness and the highest entropy generation level for cases of $C^* = 0$ as well as single-pass counterflow and parallelflow arrangements. Therefore, our purpose will be to juxtapose and discuss such heat exchanger performance trends and the temperature difference irreversibilities associated with transfer processes in complex flow arrangements of shell-and-tube and plate heat exchangers.

Literature Review on Temperature Cross and Irreversibility in Heat Exchangers

The common method of exchanger analysis in the process industry is the mean (or log-mean) temperature difference method. The concept of the temperature cross is well known in the process industry due to Kern [6]. While Kern recommended the limiting value of mean (or log-mean) temperature difference correction factor F as 0.75, the commonly used limiting value of the F factor is 0.8 and higher in the process industry. No reasoning for the selection of this $F_{\min} = 0.8$ was reported in the literature. Shah [7] showed that when the temperature cross (using its definition) occurs at the exchanger outlet, $F \approx 0.8$ for most of the operating range of R_1 (0.1 to 20.0) for the 1-2 TEMA E exchanger (the most commonly used exchanger for single-phase fluids in the process industry), thus providing an analytical basis for the well-thought rule of thumb of $F_{\min} \approx 0.8$.

Bejan [8,9] introduced the concept of irreversibility in heat exchanger design analyzing a counterflow heat exchanger. His analysis included entropy generation due to finite temperature difference as well as fluid friction (pressure drop). To estimate quantitatively the entropy generation, he introduced an entropy generation number N_s defined as the entropy generation rate normalized with respect to the maximum fluid heat capacity rate, i.e., $\dot{S}_{\text{irr}}/C_{\max}$. Assuming nearly ideal behavior attributed by $\varepsilon \approx 1$, he provided the formulation for N_s for a counterflow heat exchanger and discussed the results for $R_1 = C^* = 1$ as well as $R_1 \neq 1$ for various values of the inlet temperature ratio $\vartheta = T_{1,i}/T_{2,i}$. He showed that N_s is zero at $NTU_1 = 0$ and ∞ and has a maximum value at some finite value of NTU_1. He referred to this symmetry behavior as the ''entropy generation paradox.'' Sekulic [10] have provided an explanation of this paradox. Hesselgreaves [11] proposed an approach that eliminates the paradoxical behavior of the

[2]It should be emphasized that the total exchanger irreversibility is the sum of the heat transfer and pressure drop (due to flow friction) and any other irreversibilities present.

temperature difference irreversibilities by nondimensionalizing the entropy generation rate (due to heat exchange at finite temperature difference) by $(q/T_{c,i})$.

Our explanation of the paradox is as follows. Let us consider a heat exchanger at any value of R_1 with inlet temperatures of two fluids specified. At $NTU_1=0$, the surface area of any heat exchanger approaches zero, and results in $dq=0$ and $\dot{S}_{\rm irr}=0$. Thus, increasing NTU_1 above zero whenever there is a finite temperature difference must always increase in $\dot{S}_{\rm irr}$ because accordingly to the 2nd Law, $\dot{S}_{\rm irr}$ cannot be negative. This increase in $\dot{S}_{\rm irr}$ cannot continue to infinity as NTU_1 increases because $\dot{S}_{\rm irr}$ has a finite upper bound attainable for the case of two contiguous systems exchanging heat at spatially constant temperatures equal the inlet temperatures of fluids for a heat exchanger. Such upper limit for $\dot{S}_{\rm irr}$ is not attainable for a real heat exchanger because the fluid temperature difference $(T_h\text{-}T_c)$ throughout the exchanger will be less than $(T_{h,i}\text{-}T_{c,i})$. As NTU_1 approaches infinity, the behavior of $\dot{S}_{\rm irr}$ becomes dependent on how fluid temperatures can differ, and $\dot{S}_{\rm irr}$ can be zero or a minimum value for all exchangers except for a parallelflow exchanger for which the initial increase is asymptotically continued to a maximum value. As an example, for a special case of the pure counterflow exchanger with $R_1=1$, the temperature difference $(T_h\text{-}T_c)$ tends to zero throughout heat exchanger as $NTU_1\rightarrow\infty$ and $\dot{S}_{\rm irr}$ approaches zero. Hence, a nonnegative function $\dot{S}_{\rm irr}$ possessing always a finite upper bound and with two minimum values (at $NTU_1=0$ and ∞) must have at least one maximum in between leading to the so-called entropy generation paradox. In turn, this paradox for the standalone heat exchanger is an intrinsic behavior of the temperature difference irreversibility function and it can never be removed without violating the 2nd Law. Thus in reality, there is no paradox if one considers the temperature difference irreversibility for a standalone heat exchanger.

Sekulic [5] conducted an irreversibility analysis for heat exchangers and presented the results in terms of $Y_s(=1-\dot{S}_{\rm irr}/\dot{S}_{\rm irr,max})$, designated as Heat Exchanger Reversibility Norm (HERN), as a function of NTU for six single-pass exchangers. He also presented the results in terms of $\dot{S}_{\rm irr}/\dot{S}_{\rm irr,max}$ versus NTU for the 1-2 TEMA E shell-and-tube heat exchanger (with the shell fluid mixed or unmixed), and three two-pass and three-pass crossflow exchangers of different flow arrangements. He then compared and discussed these results, and concluded that compared to a base exchanger, those exchangers having higher $\dot{S}_{\rm irr}/\dot{S}_{\rm irr,max}$ after the NTU value for $\dot{S}_{\rm irr,max}$ have poorer heat transfer performance. He showed graphically Y_s as a function of NTU for a mixed-mixed crossflow exchanger, and mentioned that a local maximum occurs after a minimum value of Y_s. However, no explanation of this Y_s-NTU behavior was provided. Note that Sekulic [5] makes $S_{\rm irr}$ nondimensional as $\dot{S}_{\rm irr}/C_{\max}$. Sekulic [10] demonstrated that the temperature cross point occurs at the NTU value that corresponds to the maximum irreversibility for all exchanger flow arrangements except for parallelflow. Exceptions to this fact will be noted later in this paper.

Kmecko [12] conducted an irreversibility analysis of 1-2 TEMA G and H (both overall parallelflow) and J exchangers and provided an explanation on the reasoning and implication of one or two maximums present in $S^*/S^*_{\max}$ versus NTU curves by computing the heat transfer rate in four zones of the exchanger (due to two tube passes and the shell fluid splitting into two streams in the exchanger).

Hesselgreaves [11] conducted an irreversibility analysis for heat exchangers with zero and finite pressure drop. For the zero pressure drop case, he analyzed counterflow $(C^*\leqslant 1)$, parallelflow exchangers and a condenser and an evaporator. He made $\dot{S}_{\rm irr}$ dimensionless in a manner similar to Witte [13] and presented results in terms of a modified entropy generation number N_{s1} based on heat flow rate as a function of ε thus $N_{s1}=N_s/[\varepsilon\cdot(T_{h,i}/T_{c,i}-1)]$ where $N_s=\dot{S}_{\rm irr}/C_{\min}$.

To overcome the Bejan's entropy generation paradox, Ogiso [14] emplyoed the total thermal conductance of heat exchanger UA to define dimensionless entropy generation index as $\dot{S}_{\rm irr}/(UA)$; this results in $(\dot{S}_{\rm irr}/C_{\min})/NTU$. For a balanced counterflow arrangement, Ogiso [14] demonstrated that the Bejan's paradox can be removed by using the entropy generation index $S_{\rm irr}/UA$.

This literature review suggests that the irreversibility analysis has been reported for some flow arrangements and the performance behavior patterns with irreversibility analysis have not been analyzed systematically and in any detail for complex flow arrangements. Our goal is to fill this gap based on the most representative population of 18 flow arrangements of two fluid heat exchangers.

Irreversibility Analysis for Exchangers

We consider heat exchangers within the framework of the control volume approach with inlet/outlet ports allowing for mass flows while the external walls of the exchanger are adiabatic and there is no work interactions with surroundings. The internal wall separating the fluids permits only heat transfer between the fluids. The entropy measure of the irreversibility for such a heat exchanger can be written as follows:

$$\dot{S}_{\rm irr}=\Delta\dot{S}=\dot{m}_1\cdot\Delta s_1+\dot{m}_2\cdot\Delta s_2 \tag{1}$$

where $\dot{m}_1$ and $\dot{m}_2$ are the mass flow rates of Fluids 1 and 2, and Δs_j $(j=1,2)$ are the changes in their specific entropies within the exchanger. Now we will develop a relationship between the exchanger irreversibility and exchanger performance parameters (P_1 and R_1 or NTU_1 and R_1). The exchanger effectiveness formulas are derived based on the assumption that the heating effect due to viscous fluid friction effect is negligible. Hence, we will evaluate $\dot{S}_{\rm irr}$ only due to finite temperature differences considering the fluids as pure simple single-phase compressible substances. Thus Eq. (1) results in

$$\dot{S}_{\rm irr}=\sum_{\rm j=1}^{2}\dot{m}_{\rm j}\cdot\Delta s_{\rm j}=\dot{m}_1\cdot c_{\rm p,1}\cdot\ln\frac{T_{1,\rm o}}{T_{1,\rm i}}+\dot{m}_2\cdot c_{\rm p,2}\cdot\ln\frac{T_{2,\rm o}}{T_{2,\rm i}} \tag{2}$$

Note that $\dot{S}_{\rm irr}>0$ always, and only inlet and outlet temperatures are required in Eq. (2) irrespective of the exchanger flow arrangement. Also note that a formula of Eq. (2) can represent the irreversibility associated with mixing of the same fluids having different temperatures, particularly if one wishes to analyze of segment irreversibilities due to mixing, for example, in an outlet pipe from multiple outlets (e.g., 1-2 TEMA J) and headers/manifolds.

Now we will present the entropy measure of irreversibility of Eq. (2) in terms of the exchanger temperature effectiveness P_1, the heat capacity rate ratio $R_1=C_1/C_2$, and the inlet temperature ratio $\vartheta=T_{1,\rm i}/T_{2,\rm i}$. Using the following definitions,

$$P_1=\frac{T_{1,\rm i}-T_{1,\rm o}}{T_{1,\rm i}-T_{2,\rm i}}\quad R_1=\frac{C_1}{C_2}=\frac{T_{2,\rm o}-T_{2,\rm i}}{T_{1,\rm i}-T_{1,\rm o}}\quad \vartheta=\frac{T_{1,\rm i}}{T_{2,\rm i}} \tag{3}$$

and substituting them in Eq. (2) results in Eq. (4)[3]

$$\frac{\dot{S}_{\rm irr}}{C_1}=S^*=\ln[1+P_1\cdot(\vartheta^{-1}-1)]+\frac{1}{R_1}\cdot\ln[1+R_1\cdot P_1\cdot(\vartheta-1)] \tag{4}$$

where Fluid 1 is the $C_{\min}$ fluid. Here $\dot{S}_{\rm irr}\neq 0$ for $\vartheta\neq 1$ and $\dot{S}_{\rm irr}=0$ for $\vartheta=1$. To demonstrate the intrinsic behavior of $\dot{S}_{\rm irr}$ versus

[3]We have made the dimensionless $S^*=\dot{S}_{\rm irr}/C_1$. An alternative is to define $S^*=\dot{S}_{\rm irr}T_{\rm ref}/q$ which takes into account heat transfer in the exchanger, and $T_{\rm ref}$ can be $T_{h,i}$, $T_{c,i}$ or $T_{\rm ambient}$ depending on the system. Our S^* definition does not involve $T_{\rm ref}$ and is used for the heat exchanger as a component and not for any thermodynamic system analysis.

exchanger performance for complex flow arrangements, $\dot{S}_{irr}$ is made nondimensional as $\dot{S}=\dot{S}_{irr}/C_{min}$. The motivation in favor of such an approach is that nondimensionalization based on heat flow rate $(q/T_{c,i})$, Hesselgreaves [11], and that based on total thermal conductance (UA), Ogiso [14], may be inadequate or fails when used with complex flow arrangements. It will be demonstrated later in this paper. The S^* expression of Eq. (4) is valid for all exchanger flow arrangements and can be evaluated by employing its appropriate P_1-NTU_1 (or ε-NTU after pertinent modifications) formula. If Fluid 1 is the C_{max} fluid, we refer $\dot{S}_{irr}$ to the $C_{min}=C_2$ and modify Eq. (4) accordingly. Note that Sekulic [5] defines S^* differently as $S^*=\dot{S}_{irr}/C_2$ or $S^*=\dot{S}_{irr}/C_{max}$. Equation (4) indicates the following functional relationship:

$$S^*=\phi_1(P_1,R_1,\vartheta,\text{flow arrangement})$$
$$=\phi_2(NTU_1,R_1,\vartheta,\text{flow arrangement}) \tag{5}$$

where the last equality is based on $P_1=\phi_2(NTU_1,R_1,\text{flow arrangement})$. Using that equality, we will evaluate the maximum value of S^*, designated as S^*_{max}, and illustrate some results for S^*/S^*_{max} for specific flow arrangements as a function of NTU_1 and R_1 for $\vartheta=2.0$. In order to find S^*_{max} or S^*_{min}, let us find the first and second derivatives of S^* of Eq. (4):

$$\frac{dS^*}{dNTU_1}=\frac{dS^*}{dP_1}\frac{dP_1}{dNTU_1}$$
$$=\underbrace{\left[\frac{\vartheta^{-1}-1}{1+P_1\cdot(\vartheta^{-1}-1)}+\frac{\vartheta-1}{1+R_1\cdot P_1\cdot(\vartheta-1)}\right]}_{M}\cdot\underbrace{\frac{dP_1}{dNTU_1}}_{N} \tag{6}$$

Based on this equation, S^*_{max} or S^*_{min} will occur at either $M=dS^*/dP_1=0$, $N=dP_1/dNTU_1=0$ or $M=N=0$. Note that M represents the slope or gradient (or intensity of variation) of S^* with P_1, and N represents the slope of P_1 with NTU_1. Now the second derivative of Eq. (6) is given by

$$\frac{d^2S^*}{dNTU_1^2}=-\underbrace{\left[\frac{(\vartheta^{-1}-1)^2}{[1+P_1\cdot(\vartheta^{-1}-1)]^2}+\frac{R_1\cdot(\vartheta-1)^2}{[1+R_1\cdot P_1\cdot(\vartheta-1)]^2}\right]}_{J}\cdot N^2$$
$$+M\cdot\left(\frac{d^2P_1}{dNTU_1^2}\right) \tag{7}$$

where J is defined as the bracketed term; also note a negative sign in the front of this term. The following cases are possible for S^*_{max} or S^*_{min} based on Eqs. (6)-(7).

Case 1. $M=dS^*/dP_1=0$ of Eqs. (6)–(7). We will now discuss the case of extremum in S^* with NTU_1 when M, the gradient of S^* with P_1, is zero. It is clear that if $M=0$, the right-hand side of Eq. (7) is always negative since R_1 and J are positive. This means $M=0$ yields $dS^*/dNTU_1=0$ of Eq. (6) and S^* of Eq. (4) as maximum. For this particular case, simplification of M of Eq. (6) as zero yields

$$P_1=\frac{1}{1+R_1}\quad\text{or}\quad\varepsilon=\frac{1}{1+C^*} \tag{8}$$

regardless of the value of ϑ. Substituting into Eq. (8) the definitions of P_1 and R_1 given by Eq. (3) yields $T_{1,o}=T_{2,o}$. Thus, the condition $M=0$ means the temperature cross exists at the exchanger outlet; this operating point $(T_{1,o}=T_{2,o})$ will be referred to as the TC point now onwards. This was the specific case that was reported by Shah [7] and Sekulic [5] as the temperature cross at the exchanger outlet and was implied that it is valid for all flow arrangements. However, as shown above, it is true only if $M=0$ within range of variability of P_1 or ε for a given flow arrangement.

All exchanger flow arrangements reported in Table 1 have a TC point for some finite value of NTU_1 except (i) it occurs at $NTU_1=\infty$ for a parallelflow exchanger, and (ii) no TC point exists for the 1-2 TEMA G and H exchangers having overall parallelflow. The location of the temperature cross, in terms of the value of NTU_1 designated as NTU_1^*, can be obtained from P_1-NTU_1-R_1 formula for each heat exchanger. This means that the value of NTU_1^* can be calculated from

$$P_1=\frac{1}{1+R_1}=\phi(NTU_1^*,R_1) \tag{9}$$

where the functional relationship $\phi(NTU_1^*,R_1)$ is dependent upon the flow arrangement. For example for $R_1=1$, the TC point occurs at $NTU_1^*=1$ and ∞ for the counterflow and parallelflow exchangers, respectively. For all other flow arrangements at $R_1=1$ where the temperature cross exists at the exchanger outlet, the value of NTU_1^* will be between 1 and ∞. Also note that all flow arrangements reported in Table 1, there is only one root or one value of NTU_1^* of Eq. (9) for a given value of R_1 except for the following exchangers: 1-2 TEMA J and 1-4 TEMA J exchangers have two finite values of NTU_1^* and three additional exchangers have the second value of NTU_1^* at infinity for a given value of R_1, as mentioned in Table 1 and as an example shown in Fig. 3 for a 1-2 TEMA J exchanger. So these exchangers have two TC points for any $0<R_1<\infty$.

Also note from Eq. (7) that if $M=0$, $d^2S^*/dNTU_1^2$ is always negative since J and N^2 are positive. This means that value of S^* of Eq. (4) for all flow arrangements reported in Case 1 of Table 1 and additional ones in Pignotti and Shah [2] have a maximum entropy generation when the external/internal temperature cross exists at the exchanger outlet. Substituting Eq. (8) in Eq. (4) results in

$$S^*_{max}=\ln\left[1+\frac{\vartheta^{-1}-1}{1+R_1}\right]+\frac{1}{R_1}\cdot\ln\left[1+\frac{R_1}{1+R_1}\cdot(\vartheta-1)\right] \tag{10}$$

Thus for a specified values of R_1 and ϑ, $S^*_{max}=[S_{irr}/C_1]_{max}$ value can be evaluated from Eq. (10), and P_1 from Eq. (8) which is designated as P_1^*. From Eqs. (8) and (10), one can see that values of P_1^* and S^*_{max} are identical for all exchanger flow arrangements of Table 1 except for 1-2 TEMA G and H exchangers with overall parallelflow, since for these flow arrangements $M\neq0$, and $T_{c,o}<T_{h,o}$ for all values of NTU_1; there is no TC point. The specific thermal size for the exchanger at S^*_{max}, designated as NTU_1^*, will be flow arrangement dependent (somewhere between 1 and ∞), and can be found knowing the P-NTU-R or ε-NTU-C^* formula for the specific flow arrangement. Note that $(T_{c,o}/T_{h,o})$ will be maximum but less than unity at S^*_{max} for 1-2 TEMA G and H exchangers with overall parallelflow.

Case 2-6. $N=dP_1/dNTU_1=0$ of Eqs. (6)–(7). We discuss here various cases of extremum (maximum or minimum) in S^* when the slope of effectiveness P_1 versus NTU_1 curve for various flow arrangements is zero. Since there are many different P_1-NTU_1 performance behaviors dependent on the flow arrangements, these cases will illustrate accordingly different behaviors in S^*_{max} or S^*_{min}. From Eq. (7), depending on the signs of M (three cases) and $d^2S^*/dNTU_1^2$ (two cases), S^* of Eq. (4) can be maximum or minimum; there are five possible cases as summarized in Table 1. The value of M can be less than, equal to or greater than zero (this translates into $T_{1,o}$ as greater than, equal to or less than $T_{2,o}$) depending on the flow arrangements. In addition,

Table 1 Summary of the existence of maximum or minimum in S^* and P_1 and the TC point (at finite or infinite values of NTU_1) for various exchanger flow arrangements

Cases for $dS^*/dNTU_1=0$	Conditions for the Second Derivative	Results for Conditions of Columns 1 and 2	Applicable to Exchanger Flow Arrangements at			
			NTU_1 = finite		NTU_1 = infinite	
1. M = 0, Fig. 2	$d^2P_1/dNTU_1^2<0$ $\therefore d^2S^*/dNTU_1^2<0$	S^*_{max} and the temperature cross at the exchanger outlet, both occur at the same NTU_1	Counterflow Unmixed-Unmixed Crossflow 1-2 TEMA E 1-2 TEMA G Overall Counterflow 1-2 TEMA H Overall Counterflow Mixed-Mixed Crossflow 1-3 TEMA E 1pf-2cf 1-3 TEMA E 2pf-1cf 1-4 TEMA E 2-2 PHE Overall Parallelflow, i-cf 2-4 PHE Overall Parallelflow, 2pf-2cf 3-3 PHE Overall Parallelflow, i-cf 4-4 PHE Overall Parallelflow, i-cf	One S^*_{max} One TC	Parallelflow Mixed-Mixed Crossflow 1-3 TEMA E 2pf-1cf	S^*_{max} TC
			1-2 TEMA J 1-4 TEMA J	Two S^*_{max} Two TC		
2. N = 0, Fig. 3	$d^2P_1/dNTU_1^2<0$ $M<0$ $\therefore d^2S^*/dNTU_1^2>0$	S^* vs. NTU_1 has a minimum and P_1 vs. NTU_1 has a maximum; both occur at the same NTU_1	Mixed-Mixed Crossflow 1-3 TEMA E 2pf-1cf 1-4 TEMA E 1-2 TEMA J 1-4 TEMA J	One S^*_{min} One $P_{1,max}$	Counterflow Unmixed-Unmixed Crossflow 1-2 TEMA E and 1-3 TEMA E 1pf-2cf 1-2 TEMA G Overall Counterflow 1-2 TEMA H Overall Counterflow 3-3 PHE Overall Parallelflow, i-cf The 3rd segment of the P_1-NTU_1 curve	S^*_{min} $P_{1,max}$
3. N = 0, Fig. 4	$d^2P_1/dNTU_1^2<0$ $M>0$ $\therefore d^2S^*/dNTU_1^2<0$	S^* and P_1 vs. NTU_1, both have a maximum at the same NTU_1	1-2 TEMA G Overall Parallelflow 1-2 TEMA H Overall Parallelflow	One S^*_{max} One $P_{1,max}$	Parallelflow	S^*_{max} $P_{1,max}$
4. N = 0, Fig. 5	$d^2P_1/dNTU_1^2<0$; $M=0$ at S^*_{max} and $P_{1,max}$ $\therefore d^2S^*/dNTU_1^2<0$	S^*_{max}, $P_{1,max}$ and the temperature cross at exchanger outlet all occur at the same NTU_1	2-2 PHE Overall Parallelflow, i-cf 2-4 PHE Overall Parallelflow, 2pf-2cf 4-4 PHE Overall Parallelflow, i-cf	One S^*_{max} One $P_{1,max}$		
			3-3 PHE Overall Parallelflow, i-cf The 1st segment of the P_1-NTU_1 curve			
5. N = 0, Fig. 6	$d^2P_1/dNTU_1^2>0$ $M<0$ $\therefore d^2S^*/dNTU_1^2<0$	S^* vs. NTU_1 has a maximum and P_1 vs. NTU_1 has a minimum, both at the same NTU_1	3-3 PHE Overall Parallelflow, i-cf The 2nd segment of the P_1-NTU_1 curve	One S^*_{max} One $P_{1,min}$	Mixed-Mixed Crossflow 1-3 TEMA E 2pf-1cf 1-4 TEMA E	S^*_{max} $P_{1,min}$
6. N = 0, Fig. 4	$d^2P_1/dNTU_1^2>0$ $M>0$ $\therefore d^2S^*/dNTU_1^2>0$	S^* and P_1 vs. NTU_1 both have a minimum at the same NTU_1			1-2 TEMA G Overall Parallelflow 1-2 TEMA H Overall Parallelflow 1-2 TEMA J and 1-4 TEMA J 2-2 PHE Overall Parallelflow, i-cf 2-4 PHE Overall Parallelflow 2pf-2cf 4-4 PHE Overall Parallelflow, i-cf	S^*_{min} $P_{1,min}$

$d^2P_1/dNTU_1^2$ can be greater or less than zero as follows dependent on the P_1 versus NTU_1 curve for a given R_1 value ($R_1>0$).

(1) If P_1 monotonically increases with NTU_1 and reaches an asymptotic value (e.g., for a counterflow, unmixed-unmixed crossflow or 1-2 TEMA E exchanger), $d^2P_1/dNTU_1^2$ is negative.

(2) If P_1 first increases with NTU_1, reaches maximum and then decreases with a further increase in NTU_1 (the curve looks similar to an inverted parabola, e.g., 1-2 TEMA G and H overall parallelflow), $d^2P_1/dNTU_1^2$ is also negative.

(3) If P_1 first increases with NTU_1, reaches an almost flat value (local maximum) at some intermediate NTU_1 and then the rate of increase in P_1 decreases up to some another value of NTU_1 beyond which the rate of increase of P_1 with NTU_1 continues to increase with further increase in NTU_1. The value of $d^2P_1/dNTU_1^2$ is first negative, then positive and then negative again, as found for the 3 pass $-$3 pass plate heat exchanger with overall parallelflow and individual passes in counterflow.

Results and Discussion

In order to explain the heat transfer performance behavior of various exchangers, we have prepared tabular and graphical results for a range of values of R_1, and the inlet temperature ratio $\vartheta=T_{1,i}/T_{2,i}=2.0$ and 0.5 for all exchanger flow arrangements analyzed. However, due to space limitations, we present only a summary of various cases in Table 1 and some typical graphical results in Figs. 2–6.

Let us first review the results. The possible cases are summarized in Table 1. The following important observations can be made from the results of this table.

- Of the 18 flow arrangements considered here, S^*_{max} and $T_{2,o}/T_{1,o}=1$ (the TC point) occur at the same value of NTU_1, and $P_{1,max}$ or $P_{1,min}$ does not occur at the same value of NTU_1 for 15 flow arrangements; S^*_{max}, $T_{2,o}/T_{1,o}=1$ and $P_{1,max}$ occur for the parallelflow exchanger at $NTU_1=\infty$; and S^*_{max}, $(T_{2,o}/T_{1,o})_{max}$ and $P_{1,max}$ occur at the same finite value of NTU_1 for the two remaining flow arrangements (1-2 TEMA G and H with overall parallelflow).
- Based on the general thermodynamics background as pro-

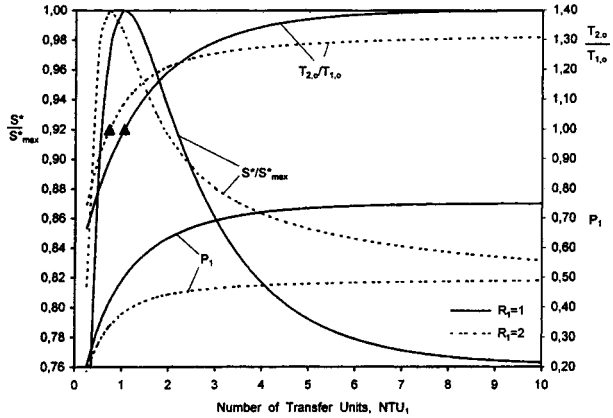

Fig. 2 S^*/S^*_{max}, $T_{2,o}/T_{1,o}$ and P_1 as function of NTU_1 for a 1-2 TEMA G exchanger with overall counterflow for $\vartheta=2.0$, ▲-temperature cross (TC)

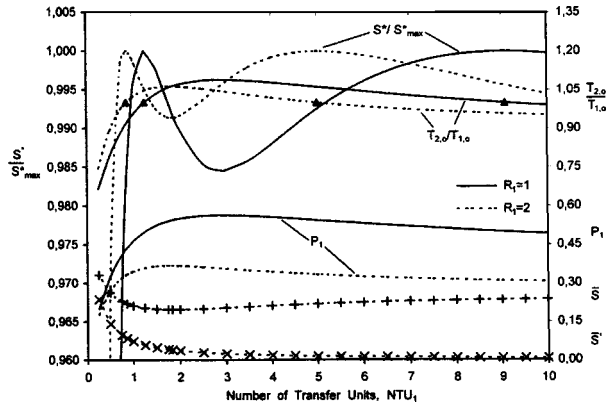

Fig. 3 S^*/S^*_{max}, $\bar{S}$, $\bar{S}'$, $T_{2,o}/T_{1,o}$ and P_1 as a function of NTU_1 for a 1-2 TEMA J exchanger for $\vartheta=2.0$. Note $\bar{S}=S_{irr}/(q/T_{c,i})$ used by Hesselgreaves [11] marked with +, $\bar{S}'=S_{irr}/UA$ used by Ogiso [14] marked with ×

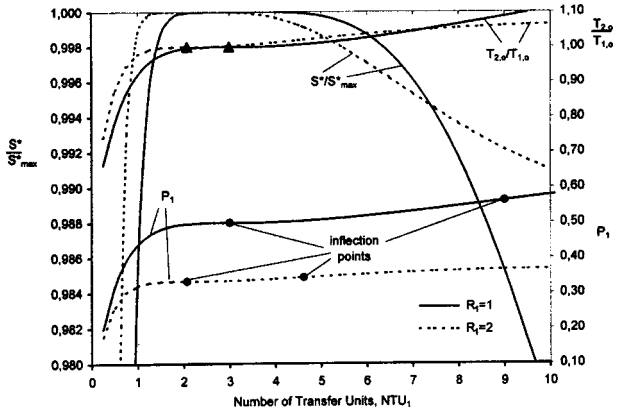

Fig. 6 S^*/S^*_{max}, $T_{2,o}/T_{1,o}$ and P_1 as a function of NTU_1 for a 3 Pass—3 Pass plate heat exchanger with overall parallelflow and individual passes in counterflow for $\vartheta=2.0$

vided in the subsection of Introduction, one would expect the maximum exchanger effectiveness or $P_{1,max}$ when S^*_{min}. Out of 18 flow arrangements analyzed, this occurs at a finite value of NTU_1 for five exchanger flow arrangements and at $NTU_1=\infty$ for seven flow arrangements as summarized in Columns 4 and 6 of Case 2 in Table 1.

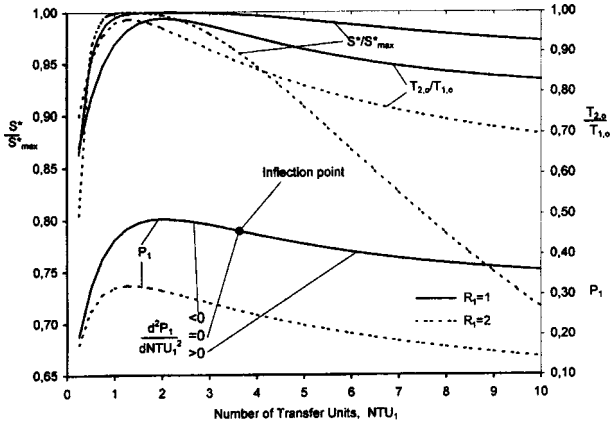

Fig. 4 S^*/S^*_{max}, $T_{2,o}/T_{1,o}$ and P_1 as a function of NTU_1 for a 1-2 TEMA G with overall parallelflow exchanger for $\vartheta=2.0$

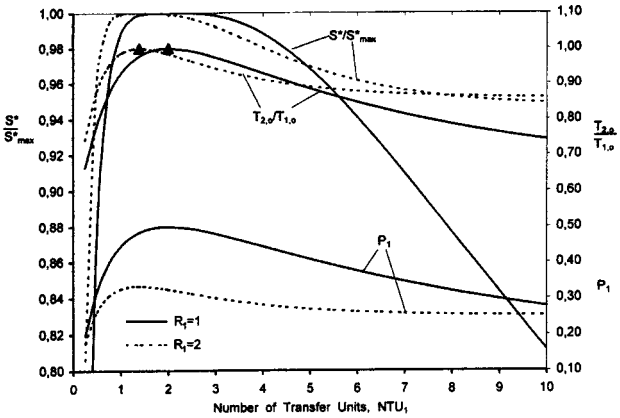

Fig. 5 S^*/S^*_{max}, $T_{2,o}/T_{1,o}$ and P_1 as a function of NTU_1 for a 2 Pass—2 Pass plate heat exchanger with overall parallelflow and individual passes in counterflow for $\vartheta=2.0$

• Similarly, one would expect the minimum exchanger effectiveness or $P_{1,min}$ at S^*_{max}. Out of 18 flow arrangements analyzed, this occurs at $NTU_1=\infty$ at the second maximum in S^* versus NTU_1 curve only for three flow arrangements as summarized in Columns 4 and 6 of Case 5 in Table 1.

• Contrary to the expectations, $P_{1,max}$ occurs when S^*_{max} at some finite value of NTU_1 for four plate heat exchanger flow arrangements as summarized in Column 4 of Case 4. This behavior is due to the combinations of counterflow and parallelflow passes in the plate heat exchanger.

• Similarly, contrary to the expectations, $P_{1,min}$ occurs at S^*_{min} for six flow arrangements at $NTU_1=\infty$ as summarized in Column 5 of Case 6 of Table 1.

Thus we can find that the general thermodynamic relationship between the irreversibility and system efficiency does not necessarily apply to heat exchanger irreversibility and its effectiveness. The interrelationship between the irreversibility and exchanger effectiveness can only be understood in the context of the six Cases specified in Column 1 of Table 1. This interrelationship takes into account the independent nature of the P_1-NTU_1 curve for different heat exchangers, and its impact on the S^*-NTU_1 curve.

While analyzing 18 flow arrangements, we have generated a vast amount of numerical data illustrating not only irreversibilities but also temperature crosses, effectivenesses, extrema, inflection points, etc. Due to space limitations, we have not presented detailed numerical values of P_1, NTU_1, $T_{1,o}/T_{2,o}$ etc. for S^*_{max} and S^*_{min} for a given value of R_1. However, the observations and conclusions derived from those detailed tabular results are summarized below.

• The values of S^*_{max} are dependent only upon R_1 for all flow arrangements for specified values of ϑ [as can be found by substituting Eq. (8) into Eq. (4) as long as the flow arrangements have one or more TC points. As mentioned above, 1-2 TEMA G and H exchangers with overall parallelflow do not have a TC point at any value of NTU_1. Their S^*_{max} values are slightly different (for most cases beyond four significant digits, higher or lower depending upon the value of ϑ) from those found for other 16 flow arrangements; the difference increases with values of R_1 and ϑ significantly away from unity.

• S^*_{max} has a minimum value at $R_1=1$ for all flow arrangements and increases with $R_1\to 0$ or ∞ from $R_1=1$.

• As R_1 is increased from 0 to ∞, the value of NTU_1 for S^*_{max} (i.e., NTU^*_1) decreases from ∞ to 0.

• For a parallelflow exchanger, $NTU^*_1=\infty$ for S^*_{max} for all values of R_1. This means that the value of NTU^*_1 varies from the

lowest value for a counterflow exchanger for any given value of R_1 to the highest value for a parallelflow exchanger. For all exchangers, the value of NTU_1^* is in between these two extremes. This means that the point of maximum irreversibility moves from the lowest value of $NTU_1^*=1$ to ∞ at $R_1=1$ for a counterflow exchanger to a parallelflow exchanger.

Some typical results are presented graphically in Figs. 2-6 in terms of P_1, $T_{2,o}/T_{1,o}$ and S^*/S^*_{max} as a function of NTU_1 with R_1 as a parameter for the following reasons.

- The P_1 versus NTU_1 curve will show how the temperature effectiveness P_1 varies with NTU_1 for the given exchanger—whether (i) it increases monotonically (at a slow or fast rate) with NTU_1 to an asymptotic value, (ii) it increases first, reaches a maximum and then decreases to an asymptotic value with increasing values of NTU_1, or (iii) the curve has inflection points in the P_1 versus NTU_1 graph.
- The ratio of the outlet temperature of Fluid 2 to that of Fluid 1, $T_{2,o}/T_{1,o}$, as a function of NTU_1 will demonstrate the TC point when $T_{2,o}/T_{1,o}=1$. With a further increase in NTU_1, the value of $T_{2,o}/T_{1,o}$ can be larger or smaller than unity depending upon the exchanger flow arrangement. If $T_{2,o}/T_{1,o}$ continues to increase above unity, the temperature cross point will move from the exit to inside within the last pass of the exchanger.
- The S^*/S^*_{max} curve indicates how the normalized irreversibility in the exchanger varies with NTU_1. The S^*_{max} always occurs at the TC point, $T_{2,o}/T_{1,o}=1$ (16 flow arrangements of Table 1), or when $T_{2,o}/T_{1,o}$ is maximum (1-2 TEMA G and H with overall parallelflow). In some exchangers with a further increase in NTU_1, S^*/S^*_{max} will reach to a minimum value corresponding to $P_1=P_{1,max}$ and beyond this point (NTU_1 value), it will increase and reach a second maximum point (corresponding to the second TC point), and then decrease and reach a lower asymptotic value. Note that beyond the NTU_1 value for the second peak in S^*/S^*_{max}, there is no TC point (i.e., $T_{2,o}/T_{1,o}\neq 1$), and beyond $(S^*/S^*_{max})_{min}$ point, the temperature effectiveness P_1 will monotonically decrease with NTU_1 to an asymptotic value for $NTU_1\rightarrow\infty$.

Now let us illustrate and discuss some of the unique performance behaviors of some heat exchangers as identified by various cases in Table 1.

Case 1, $M=0$. As shown in Fig. 2 for the 1-2 TEMA G exchanger with overall counterflow, this case refers to the heat exchangers which attain the temperature cross at the outlet ($T_{2,o}/T_{1,o}=1$) at some finite value of NTU_1 (denoted by a triangle in Fig. 2), and it also has maximum entropy generation S^*_{max} at that operating point. The first five flow arrangements listed in Column 4 of Case 1 in Table 1 has P_1 monotonically increasing with NTU_1 for any value of R_1 and the other performance behavior similar to that shown in Fig. 2 except that the asymptotic value of P_1 and $T_{2,o}/T_{1,o}$ are different at $NTU_1=\infty$. For the rest of the flow arrangements listed in Column 4 of Case 1, for any value of R_1, P_1 increases with NTU_1, reaches a maximum and then decreases with a further increase in NTU_1 and reaches an asymptotic value lower than unity. Heat exchangers having such performance behavior have either one or two TC points and correspondingly one or two S^*_{max} over the complete range of NTU_1 (see Fig. 3). Notice that the exchanger effectiveness or P_1 is not maximum at the TC point or where S^*_{max} occurs either at the finite or infinite value of NTU_1.

Case 2, $N=0$, and $d^2P_1/dNTU_1^2<0$ and $M<0$. When P_1 monotonically increases or has only one maximum with NTU_1, S^*_{min} is achieved at $P_{1,max}$ as noted in Case 2 in Table 1. These $P_{1,max}$ and S^*_{min} can occur at either a finite or infinite value of NTU_1 as summarized in Table 1. Note also that all these flow arrangements have one or two S^*_{max} in the S^* versus NTU_1 curve and at those NTU_1^* points, there is also a TC point (see Case 1). Typical results for two S^*_{max} and two TC points with one S^*_{min} between them are shown in Fig. 3 for the 1-2 TEMA J exchanger.

It is clear that after the first TC point (Fig. 3) with a further increase in NTU_1, the exchanger reaches the S^*_{min} point where $P_{1,max}$ occurs; however, $T_{2,o}/T_{1,o}>1$ (Fig. 3). Further increase in NTU_1 reduces P_1 and the S^*-NTU_1 curve reaches the second S^*_{max} and TC point (Fig. 3); after that point, $T_{2,o}/T_{1,o}<1$. Eventually, S^*_{min} and $P_{1,min}$ values are obtained at $NTU_1=\infty$.

Also notice in Fig. 3 that the variation in S^*/S^*_{max} between S^*_{max} and S^*_{min} from the irreversibility point of view is negligibly small (1 to 0.985). However, the S^*/S^*_{max} behavior as a function of NTU_1 for NTU_1 above about 0.5 is peculiar going through two maximum peaks due to reverse heat transfer region in the exchanger. This phenomenon cannot be readily found using the 1st law analysis, and by other nondimensional entropy generation groups, $\overline{S}=S_{irr}/(q/T_{c,i})$ of Hesselgreaves [11] or $\overline{S'}=S_{irr}/UA$ of Ogiso [14], as compared in Fig. 3. The temperature cross phenomena also cannot be detected using $\overline{S}$ or $\overline{S'}$ versus NTU_1 plot.

Case 3, $N=0$, and $d^2P_1/dNTU_1^2<0$ and $M>0$. In 1-2 TEMA G and H exchangers with overall parallelflow, shell and tube side fluids in two zones out of four zones are in counterflow and the rest two in parallelflow. There is never an external TC point (i.e., $T_{2,o}/T_{1,o}=1$) at any NTU_1 for this exchanger; see a typical behavior in Fig. 4. The S^* value reaches a maximum value at $(T_{2,o}/T_{1,o})_{max}<1$. Also note that beyond the NTU_1 value after reaching $(T_{2,o}/T_{1,o})_{max}$ at any R_1 value, the exchanger effectiveness or P_1 starts decreasing with a further increase in NTU_1. Thus, this flow arrangement has both S^*_{max} and $P_{1,max}$ at $(T_{2,o}/T_{1,o})_{max}$, all at the same NTU_1^*; and S^*_{min} and $P_{1,min}$ occur at $NTU_1=\infty$. Based on the comparison of performance of 1-2 TEMA G overall counterflow and parallelflow exchangers (Figs. 2 and 4), we can find a significant detrimental effect of overall parallelflow on P_1, $T_{2,o}/T_{1,o}$, and a significant increase in S^*/S^*_{max} as NTU_1 is increased.

Case 4, $N=0$, and $d^2P_1/dNTU_1^2<0$ and $M=0$. As noted in Case 3, there are a few flow arrangements that have the characteristics of S^*_{max} and $P_{1,max}$ at $(T_{2,o}/T_{1,o})_{max}$. However, for the flow arrangements reported in Case 4, $(T_{2,o}/T_{1,o})_{max}=1$ exists at the same value of NTU_1 (only one point in the $T_{2,o}/T_{1,o}$ versus NTU_1 curve) for any given R_1 value where S^*_{max} and $P_{1,max}$ occur (as an example see Fig. 5 for the 2 pass—2 pass PHE). For these flow arrangements, like for the Case 3, S^*_{min} and $P_{1,min}$ occur at $NTU_1=\infty$. However, the trends of all similar curves in Figs. 4 and 5 are quite different and can be readily understood based on the previous discussions. As the number of passes is increased, such as a 4 pass—4 pass plate heat exchanger with overall parallelflow and individual passes in counterflow, the performance of the exchanger approaches that of a single-pass parallelflow exchanger.

Case 5, $N=0$, and $d^2P_1/dNTU_1^2>0$ and $M<0$. As shown in Fig. 6, the 3 pass-3 pass plate heat exchanger with overall parallelflow and individual passes in counterflow is a unique flow arrangement; the exchanger behaves as a parallelflow exchanger with $P_1=0.5$ between NTU_1 of 2.5 and 3.5, and with a further increase in NTU_1, P_1 increases and reaches a value of unity at $NTU_1=\infty$ for $R_1=1$ like a counterflow exchanger. Thus, it has two inflection points in the P_1 versus NTU_1 curve. Hence, as the phenomena demonstrated in Figs. 4 and 5, S^*_{max}, local $P_{1,max}$ and TC occur at the at the first inflection point of the P_1 versus NTU_1 curve; S^*_{max} and local $P_{1,min}$ occur at the end of the second inflection point of the P_1 versus NTU_1 curve; and S^*_{min} and $P_{1,max}$ occur at $NTU_1=\infty$. Also note that the variation in S^*/S^*_{max} with NTU_1

is negligible between NTU_1 of 1 and 3 and hence its impact of irreversibility analysis can be ignored in this NTU_1 range for industrial applications.

Case 6, and $d^2P_1/dNTU_1^2>0$ and $M>0$. The exchangers of this case have both $S^*_{\min}$ and $P_{1,\min}$ occur at $NTU_1=\infty$. There may be some multipass flow arrangements that may behave similarly at some finite value of NTU_1 that are not analyzed in this paper.

Practical Usefulness

A practical methodology to account for the cost of irreversibilities in a heat exchanger as a standalone unit has been developed with an example by London [15] and London and Shah [16]. In this methodology, first the costs of individual irreversibilities incurred during heat exchanger operation are identified that includes both the capital (initial design) and operating costs. This is because some small irreversibilities may be very expensive (such as airflow friction irreversibility for an automotive radiator) and some large irreversibilities may be less expensive (such as liquid side friction in a gas-liquid heat exchanger). This approach uses the energy measure of the irreversibilities (i.e., exergy destruction rates) rather than the exergy rates as used in modern thermodynamics books. Individual energy measures of irreversibility are determined by multiplying individual entropy generation rates with a temperature-weighting factor, T_{ref}. These irreversibilities have an energy monetary value. Once the monetary values or costs of various irreversibilities are determined, the analyst is in a position of deciding which particular irreversibilities are the most costly and should be first reduced for a cost effective heat exchanger. Hence, the industrial approach to the design of a heat exchanger is to reduce the most costly irreversibilities rather than reducing all irreversibilities in a heat exchanger. Note that reducing one irreversibility may increase or require an addition of another, or involve an increase in capital investment. These considerations lead to development of trade-off factors, useful criteria for arriving at an optimum heat exchanger design as a component. In order to understand this process, a detailed example of a condenser in a thermal power plant is provided in [15,16] with a clear demonstration of the above accounting procedure including how to develop the trade-off factors.

One of the major irreversibilities in a heat exchanger is the temperature difference irreversibility, and this is the subject of this paper covering many flow arrangements. We have provided the expressions this irreversibility evaluation, how does it measure at different operating points (NTU) for different flow arrangements, explain its behavior at different operating points and its interrelation with effectiveness extremum. The results provide an analytical tool to a designer to determine appropriateness of his/her design from the viewpoint of irreversibility and effectiveness. We have also provided an indication of existence (or not) of the temperature cross phenomenon for complex flow arrangements, which can indicate the possibility of reverse heat transfer in a heat exchanger.

In the foregoing analysis, one needs to consider all irreversibilities present in the exchanger. These irreversibilities are simple additive if one considers the ''heating effect'' due to various irreversibilities can be ignored. The other important irreversibility in the exchanger may be flow friction irreversibility. It is independent on the exchanger flow arrangements and depends on the individual fluid side surface geometry, flow length, free flow area, etc. Hence, one needs to add this irreversibility evaluated for both fluid sides in a heat exchanger to the temperature difference irreversibility presented in this paper for a given exchanger.

Conclusions

Based on the First and Second Law analyses, heat exchanger performance behavior is discussed in the text for 18 exchanger flow arrangements with the emphasis on investigating the existence of entropy generation extrema and a relationship between the extrema and the heat exchanger effectiveness. This analysis is based on various combinations of values of the slope of the entropy generation rate with exchanger effectiveness or P_1 (i.e., $M=dS^*/dP_1$) and the slope of P_1 with NTU_1 (i.e., $N=dP_1/dNTU_1$) at entropy generation extrema. Depending upon how complex is the exchanger flow arrangement and resultant slope of the P_1-NTU_1 curve, the exchanger effectiveness or P_1 can be maximum, minimum or in between when the irreversibility is maximum or minimum. All these cases are systematically categorized in Table 1 so that the conditions outlined in Columns 1 and 2 of this table clearly explains various combinations of $S^*_{\max}$ or $S^*_{\min}$ with $P_{1,\max}$, $P_{1,\min}$ or in between. For each of the cases in Table 1, some results for specific flow arrangements are presented in figures in the text.

For all flow arrangements except for two (1-2 TEMA G and H exchangers with overall parallelflow), a temperature cross (TC) point at the exchanger outlet (i.e., $T_{1,o}=T_{2,o}$) exists when $S^*=S^*_{\max}$ for finite or infinite values of NTU_1. The variation in S^* with NTU_1 is small for a number of flow arrangements (see Figs. 3 and 6) for $1\leqslant NTU_1\leqslant 3$ but its significance cannot be ignored from the practical point of view since $S^*=S^*_{\max}$ point identifies the phenomenon of the temperature cross and potential reverse heat transfer taking place for NTU_1 higher than that for $S^*_{\max}$ for those exchangers having an internal temperature cross. Thus, the results of the second law analysis supplements the first law analysis to advantage in heat exchanger design.

With the clear demonstration of the complex results from the First and Second Law analyses, we pose a challenge to the researchers to arrive at alternate flow arrangements to attain higher effectivenesses, while keeping the same original imposed design and operating condition constraints, for those specific flow arrangements used in industry that have low values of the effectiveness for given NTU and R or C^*.

Nomenclature

- A = heat transfer surface area on which U is referred to, m^2
- C = flow stream heat capacity rate with a subscript c or h, $\dot{m}c_p$ (where c_p is the specific heat), W/°C
- C^* = heat capacity rate ratio, $C_{min}/C_{\max}$, dimensionless
- $\dot{m}$ = fluid mass flow rate, kg/s
- M = slope of S^* with P_1, dS^*/dP_1
- N = slope of P_1 with NTU_1, $dP_1/dNTU_1$
- NTU = number of heat transfer units, $NTU=UA/C_{\min}$, it represents the total number of transfer units in a multipass unit, $NTU_1=UA/C_1$, $NTU_2=UA/C_2$, dimensionless
- P = temperature effectiveness for a fluid, P_1 for Fluid 1, dimensionless
- R = heat capacity rate ratio, $R_1=C_1/C_2$, $R_2=C_2/C_1$, dimensionless
- S^* = Normalized entropy generation rate, defined by Eq. (4), $\dot{S}_{\text{irr}}/C_1$ or $\dot{S}_{\text{irr}}/C_{\min}$, dimensionless
- $\dot{S}_{\text{irr}}$ = entropy generation rate, W/K
- s = specific entropy, J/kgK
- T = fluid static temperature, K
- TC = temperature cross or temperature meet at the exchanger outlet where $T_{2,o}/T_{1,o}=1$
- U = overall heat transfer coefficient, W/m^2K
- ε = heat exchanger effectiveness, it represents an overall exchanger effectiveness for a multipass unit, dimensionless
- ϑ = fluid inlet temperature ratio, $T_{1,i}/T_{2,i}$, dimensionless

Subscripts

- c = cold fluid side
- cf = counterflow

h = hot fluid side
i = inlet to the exchanger
max = maximum
min = minimum
o = outlet to the exchanger when used as a second subscript with the temperature
pf = parallelflow
1 = Fluid 1; one section (inlet or outlet) of the exchanger
2 = Fluid 2; other section (outlet or inlet) of the exchanger

References

[1] Kays, W. M., and London, A. L., 1998, *Compact Heat Exchangers*, Krieger Publishing, Malabar, FL.
[2] Pignotti, A., and Shah, R. K., 1992, ''Effectiveness-Number of Transfer Units Relationships for Heat Exchanger Complex Flow Arrangements,'' Int. J. Heat Mass Transfer, **35**, pp. 1275–1291.
[3] Shah, R. K., and Sekulic, D. P., 1998, ''Heat Exchangers,'' in *Handbook of Heat Transfer*, W. M. Rohsenow, J. P. Hartnett, and Y. I. Cho, eds., McGraw-Hill, New York, Chap. 17.
[4] Kandlikar, S. G., and Shah, R. K., 1989, ''Asymptotic Effectiveness-NTU Formulas for Multipass Plate Heat Exchangers,'' ASME J. Heat Transfer, **111**, pp. 314–321.
[5] Sekulic, D. P., 1990, ''The Second Law Quality of Energy Transformation in a Heat Exchanger,'' ASME J. Heat Transfer, **112**, pp. 295–300.
[6] Kern D. Q., 1950, *Process Heat Transfer*, McGraw-Hill, New York.
[7] Shah R. K., 1983, ''Heat Exchanger Basic Design Methods,'' in *Low Reynolds Number Flow Heat Exchangers*, S. Kakaç, R. K. Shah, and A. E. Bergles, eds., Hemisphere Publishing Corp. Washington, DC, pp. 21–72.
[8] Bejan, A., 1977, ''The Concept of Irreversibility in Heat Exchanger Design: Counterflow Heat Exchangers for Gas-to-Gas Applications,'' ASME J. Heat Transfer, **99**, pp. 374–380.
[9] Bejan A., 1982, ''Second-Law Analysis in Heat Transfer and Thermal Design,'' *Advances in Heat Transfer*, T. F. Irvine and J. P. Hartnett, eds., 15, pp. 1–58.
[10] Sekulic, D. P., 1986, ''Entropy Generation in a Heat Exchanger,'' Heat Transfer Eng., **7**(1-2), pp. 83–88.
[11] Hesselgreaves, J. E., 2000, ''Rationalization of Second Law Analysis of Heat Exchangers,'' Int. J. Heat Mass Transfer, **43**, pp. 4189–4204.
[12] Kmecko I., 1998, ''Paradoxical Irreversibility of Enthalpy Exchange in Some Heat Exchangers,'' M.S. thesis, University of Novi Sad, Novi Sad, Yugoslavia.
[13] Witte, L. C., 1988, ''The Influence of Availability Costs on Optimal Heat Exchanger Design,'' ASME J. Heat Transfer, **110**, pp. 830–835.
[14] Ogiso K., 2002, ''Duality of Heat Exchanger Performance in Balanced Counter-Flow Systems,'' *Proc. of the International Symposium on Compact Heat Exchangers*, G. P. Celata et al., eds., Edizioni ETS, Pisa, pp. 203–205.
[15] London, A. L., 1982, ''Economics and the Second Law: An Engineering View and Methodology,'' Int. J. Heat Mass Transfer, **25**, pp. 743–751.
[16] London, A. L., and Shah, R. K., 1983, ''Costs of Irreversibilities in Heat Exchanger Design,'' *Heat Transfer Engineering*, 4(2), pp. 59–73; Discussion by W. Roetzel, in 5(3-4), 1984, pp. 15, 17, and 6(2), 1985, p. 73.

Simulation of Pendant Droplets and Falling Films in Horizontal Tube Absorbers

Jesse D. Killion

Srinivas Garimella[1]
e-mail: srinivas.garimella@me.gatech.edu

George W. Woodruff School of Mechanical Engineering,
Georgia Institute of Technology,
Atlanta, GA 30332-0405

Recent literature suggests that the droplets that form in horizontal-tube, falling-film absorbers play a major role in the absorption process. The performance of such absorbers is critical to the performance of many absorption heat pump systems. The simulation of droplets of aqueous Lithium Bromide pendant from horizontal tubes was performed by numerically solving the equations of motion on a fixed three-dimensional (3D) grid. The so-called volume of fluid method was used to handle the interface between the liquid and vapor phase. Results are compared with simplified axisymmetric models and with high speed video taken during flow visualization experiments. The results show that simplified axisymmetric models do not satisfactorily represent the evolution of the droplets under horizontal tubes, and that the 3D numerical model appears to accurately match the important characteristics of droplet formation, detachment, and impact observed in the experiments. [DOI: 10.1115/1.1833364]

Keywords: Absorption, Computational, Droplet, Film, Heat transfer, Two-phase, Visualization

Introduction

Commercial absorption chillers frequently utilize horizontal tube banks for the heat/mass exchangers that comprise the main components of the system (see the ASHRAE Fundamentals Handbook [1] for a system description). In a horizontal-tube absorber, absorbent-rich liquid solution is dispensed on the outside of the top row of tubes and falls as films around the tubes and as droplets between the tubes by the force of gravity (see Fig. 1) while absorbing surrounding refrigerant vapor that enters from the evaporator; the heat of absorption is transferred to coolant flowing through the tubes. The role of droplets in horizontal tube absorbers, in particular those employing the working fluid pair water/Lithium Bromide, has recently been highlighted in the literature [2–5]. This paper presents a numerical simulation of the behavior of the falling film and droplets in horizontal tube banks. The model developed here accounts for the details of the droplet formation and impact process for absorption on horizontal tubes, which has largely been ignored in previous studies. The results from this three-dimensional (3D) model are compared with two-dimensional (2D), axisymmetric models, such as those more frequently studied in the literature, and with experimental observations taken with a high-speed digital video camera. What follows is a brief review of the pertinent literature. This review is divided into three sections: i) investigations of the role of droplets in falling-film absorption, ii) techniques for modeling droplet formation and impact, and iii) methods for handling two-phase flow with a free interface in computational fluid dynamics (CFD).

The Role of Droplets in Falling-Film Absorption. Nomura et al. [2] measured the temperature of the falling liquid absorbent in a horizontal tube absorber both on and between the tubes. Their results show that the liquid temperature is higher between the tubes than on them. While the liquid flows as a film around the tube, the heat transfer outpaces the mass transfer, and consequently the film is subcooled as it flows to the bottom of the tube. While the liquid collects in the pendant droplets under the tube, absorption continues with very little heat removal, thus raising the temperature of the droplets. This suggests that direct absorption onto the hanging droplets is a significant part of the total absorption process. Kirby and Perez-Blanco [3] developed a model of a horizontal falling-film absorber using transfer coefficients from the literature for three separate flow mechanisms: the film, the forming droplet, and the falling droplet. Their model predicted similar trends in the temperature of the film and droplets as were measured by Nomura et al. [2]. Their model compared favorably with experimental measurements of overall heat rejection rates in a single-column absorber with a variety of tube arrangements and operating conditions [6]. Jeong and Garimella [4] developed a model that also accounts for absorption on the film, forming droplets, and falling droplets separately. In addition, incomplete tube surface wetting was included. Their model is able to predict the temperature measurements of Nomura et al. [2]. They quantify the relative amount of absorption in the droplets and film for a variety of operating conditions. Their results predict that direct absorption on the forming droplets may account for up to 50% or more of the total absorption and that the role of droplets becomes more important at higher flow rates and lower surface wetting ratios. Several other noteworthy models of falling-film absorption on horizontal tube absorbers can also be found in the literature [7–10]; however, all of these models share several simplifying assumptions that limit their usefulness: the film is assumed to be smooth and evenly distributed along the tubes, and it is assumed that no absorption occurs between the tubes. The droplet mode of flow between successive tubes is completely ignored. The degree of agreement of these models with experimental results is very limited [11]. Killion and Garimella [5] utilized high-speed digital video to investigate the details of the flow of droplets and films on horizontal tube banks. Their results reveal many of the characteristics of the evolution of the droplet: a primary droplet that initially is nonaxisymmetric and elongated along the tube axis, a trailing liquid thread that is formed as the primary droplet volume increases and it pulls away from the tube, the eventual thinning and breakup of the thread into a number of satellite droplets, the impact of the droplet accompanied by impulses that propagate back up through the droplet, the saddle-shaped wave formed by the spreading liquid lamella of the impacting droplet, the axial and circumferential velocity components of the spreading lamella, and the nonuniform distribution of liquid along the tube. It should be

[1]To whom correspondence should be addressed.

Contributed by the Heat Transfer Division for publication in the JOURNAL OF HEAT TRANSFER. Manuscript received by the Heat Transfer Division October 31, 2003; revision received June 8, 2004. Associate Editor: S. P. Vanka.

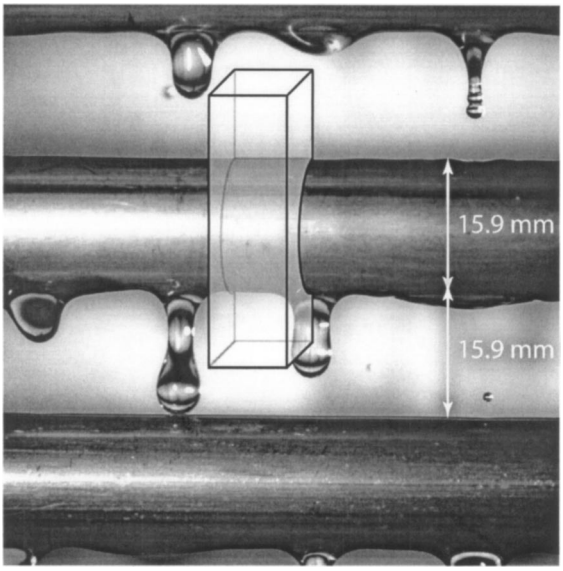

Fig. 1 Photograph of droplet formation in a falling film of aqueous LiBr over 15.9 mm outer diameter horizontal tubes [12] (box illustrates typical domain of CFD model)

noted that during this entire droplet formation process, the droplet rarely resembles a sphere. Subsequently, Killion and Garimella [12] developed an image analysis process to quantify the surface area and volume of droplets during their evolution in the region between the tubes where the droplets are basically axisymmetric. Their analysis of aqueous LiBr (53.4%-wt) droplets formed under 15.9 mm tubes showed that droplet volume and surface area steadily increase until the moment that the primary droplet impacts the tube underneath. As the primary droplet spreads onto the tube, the surface area and volume of the liquid between the tubes decrease sharply until the primary droplet has completely coalesced with the film on the tube. The remaining thinning liquid thread shows a more gradual decrease in surface area and volume and an increase in surface-area-to-volume ratio. This ratio reaches a maximum after the thread breaks into satellite droplets. This suggests that, although the satellite droplets may have a small total volume and surface area, they may still account for a significant fraction of the overall absorption.

Several experimental investigations have illustrated the transition between droplet, column and sheet flow in liquid films falling over a bank of horizontal tubes. Tang et al. [13] utilized a linear stability analysis to investigate the effect of several nondimensional parameters on the droplet spacing underneath horizontal tubes. They noted that with aqueous LiBr in the range of most practical operating conditions, the nondimensional spacing is nearly constant. They also noted that the transition from droplet-mode to column-mode flow occurs around a flow rate, $\Gamma = 200$–225 kg/h m for aqueous LiBr, which corresponds to a film Reynolds number ($4\Gamma/\mu$) of about 51. Limat et al. [14] and Giorgiutti et al. [15] investigated the transitions and spacing between departure sites underneath a single tube using a silicone oil. Noting that the spacing could be influenced by a controlled perturbation, they investigated the coalescence, creation and oscillation of departure sites versus the external perturbation. de Bruyn [16] investigated the transition from Rayleigh (surface tension) instability to Rayleigh-Taylor (gravity) instabilities for initially uniform films surrounding cylinders with diameters ranging from 0.02 to 25.4 mm using a variety of fluids. He finds that as the diameter increases, the Rayleigh-Taylor instability becomes dominant; the transition between the two mechanisms occurs around $r/l_c = 0.5$, where r is the tube radius and $l_c = (\sigma/\rho g)^{1/2}$ is the capillary length. This would correspond to a tube diameter of about 5 mm in the present study. Hu and Jacobi [17,18] considered several different fluids and developed correlations that predict the film Reynolds number at which these transitions occur as a function of a modified Gallileo number, $(\rho\sigma^3/\mu^4 g)$, and noted a hysteresis effect depending on if the flow rate is increasing or decreasing. Their correlations suggest that the transition between droplet and column modes would occur around a film Reynolds number of 30 ($\Gamma = 123$ kg/h m) in the present study. Using an innovative array of thermocouples embedded in the tube surface, they also studied the local enhancement of sensible heat transfer coefficient near the impact locations [19]. Cavallini et al. [20] also investigated the flow-mode transitions for aqueous LiBr and pure water on a bank of relatively closely spaced tubes. They noted that the transitions occurred at slightly lower Reynolds numbers due to the small space between tubes. Recently, Roques et al. [21] and Roques and Thome [22] investigated these flow transitions on tubes with enhanced external surfaces, such as low-fins and spines. They develop modified correlations for each tube surface, including smooth, similar to those of Hu and Jacobi [17] that more systematically account for tube spacing.

Techniques for Modeling Droplet Formation and Impact. The phenomenon of droplet formation has been studied for hundreds of years. According to the review by Eggers [23], droplet formation was first mentioned in scientific literature in 1686 by Mariotte [24]. Investigating the formation of droplets from fluid jets, Savart [25], Plateau [26], and the famous works of Lord Rayleigh [27,28] laid much of the foundation for the modern understanding of the formation of droplets. In 1908, Worthington published ''A Study of Splashes'' which contains 197 remarkable photographs of the coronet splashes that occur when droplets or solids fall onto films or into pools [29]. Work in this field continues today aided by the advent of high performance computers and high-speed, high-resolution video cameras. Many empirical/modeling techniques have been developed as a result of experimental investigations into the problem of droplet formation. Some of these are summarized by Kumar and Kuloor [30], Clift et al. [31] and Frohn and Roth [32]. Many early investigations of droplet formation were concerned primarily with predicting droplet size and/or the jet length before droplets formed, e.g., Refs. [30,33,34]. In the 1970s, the study of so-called ''drop-on-demand'' droplet generation (drops generated by accelerating an initially quiescent fluid in a nozzle by the sudden imposition of a pressure pulse of very short duration) received significant attention due to the development of ink-jet printers. However, many of these models neglect the influence of viscosity [23] and the droplets formed in this case are generally on the order of 25 μm [35], almost 250 times smaller than those of interest in the current case. A recent review by Eggers [23] provides an excellent summary of many modern mathematical, experimental, and computation methods utilized to better understand the details of the droplet behavior; Eggers gives special attention to the case of droplets forming from jets or capillary tubes and the dynamics of the bifurcation (droplet detachment, bridge breakup, etc.) events. Other reviews covering similar topics can be found in Refs. [35–37].

At a low flow rate, a forming pendant drop essentially assumes a series of equilibrium shapes until the surface tension can no longer support the weight of the drop; equilibrium droplet shape and stability have been considered in the literature [23,35,38,39]. Even at exceedingly low flow rate, the events occurring near the final pinch point or bifurcation proceed at very short time and length scales that depend almost entirely on fluid properties. It has been shown that the only scales governing the motion at the break are: $t_0 = (r^3\rho/\sigma)^{1/2}$ which is on the order of 4 ms for a 2 mm diameter droplet of water [23] or aqueous LiBr (ρ is the fluid density, σ is surface tension, and r is a characteristic length of the droplet such as the radius), and the viscous length scale, $l_v = \rho\nu^2/\sigma$ [40] which is only around 140 Å for water and 200 Å for aqueous LiBr (ν is the kinematic viscosity).

It is important to note that the impact of droplets in the case of horizontal tubes and falling films has not received a great deal of attention. However, droplet impact in general is a field that is widely studied. The bulk of the studies can be divided into two groups: impact of droplets onto dry surfaces and impact of droplets into liquid pools. The case of impact onto thin films has received considerably less attention and when studied, the film thicknesses used are generally of the order of the drop size; much thicker than the films considered here. Rein [41] has provided a good review of impacts on dry walls and liquid pools. Tropea and Marengo [42] have also reviewed the impact of droplets on walls and films. In an informative and entertaining review, Prosperetti and O͂guz [43] have summarized the impact of liquid drops into liquid pools with the objective of understanding the characteristics of sound generated underwater by rain; the results are useful for determining rainfall amounts over large bodies of water. Splashing can be defined as any case where the droplet impact leads to the generation of satellite drops. Rein [41] and Mundo et al. [44] review several methods for estimating the conditions required for the onset of splashing. Although the exact predicted thresholds for these correlations do not agree, for the case considered here, they do all predict that splashing would be suppressed, as is indeed observed [45]. On horizontal tubes, the resulting spreading lamellae expand in the axial direction until they interact with other waves or are no longer distinguishable features; in the circumferential direction expansion is limited at the bottom of the tube where it often leads to the formation of another droplet.

The vast majority of the attention to droplet formation in the literature has been paid to axisymmetric cases such as formation from a jet or capillary tube and impact onto flat plates or liquid pools. The case of formation under and impact onto horizontal tubes, however, leads to differences from most of the literature in terms of the overall shape, size, and internal velocity fields of the droplets and spreading lamellae. Especially in the early stages of droplet formation, the extent of the drop in the lengthwise direction of the tube may be several times its extent in the circumferential direction. During impact, the spreading lamella is saddle-shaped and not axisymmetric; furthermore, it may interact with itself at the bottom of the tube and other lamellae from neighboring droplets. The likelihood of droplet impact influencing or interacting with nearby droplets is high in the case of tube banks (see Fig. 1), especially as the flow rate is increased. The possibility of this type of interaction does not exist in droplet formation from capillary tubes or liquid jets. The predicted results presented here exhibit all of these 3D and interacting effects.

Methods for Handling Two-Phase Flow With a Free Interface in CFD. Due to the complexity of the problem and the ever increasing computation speed of computers, most recent attempts to mathematically analyze droplet formation have relied heavily on numerical techniques. There are, however, still simplifications and innovative techniques that must be employed to make the problems tractable. One major challenge is to efficiently handle/track/capture the free interface between the two phases. The many methods developed for this generally fall into two categories (although hybrid approaches have also been proposed): tracking/capturing the interface on a *fixed grid*, or using a *conformal grid* that is updated to adhere to the shape of the interface at every step. Some time ago, Hyman [46] provided a review of several of these techniques which include the so-called marker-and-cell and volume-of-fluid (VOF) methods. Other techniques found in the literature include the level-set method [47,48], various front-tracking schemes, e.g., Refs. [49–52], free surface capturing techniques [53], finite element techniques [54,55], boundary element/integral techniques [56–58], and one-dimensional slender jet Navier-Stokes approximations [59–64]. Many of these techniques, however, have limitations that make them inappropriate for application to the case studied here. For instance, the 1D approximations do not predict the size of the droplets or handle internal circulation within the drop well [54] and would be impossible to generalize to the nonaxisymmetric geometry presently considered, most boundary element/integral techniques neglect viscosity [56,58] or assume Stokes flow [57] and cannot arbitrarily handle the rupture and rejoining of interfaces [56], similarly, finite element techniques, though accurate, are also difficult to extend beyond the point of bifurcation [54], free-surface capturing techniques have not been thoroughly developed to include surface tension forces [53], and so on. The VOF technique, originally proposed in the mid 1970s by several different investigators (see Ref. [65]), has proven to be one of the most effective, generally applicable techniques. The VOF method has been advanced by many contributors including [66–71]; it has been successfully extended to three dimensions [70,71], can appropriately handle surface-tension-driven flow [67,68], and moving boundaries [69]. Recent summaries of the historical development of the VOF method and several other methods of handling free-surface problems are given by Rudman [72,73] and by Rider and Kothe [65]. The number of investigations that have, with varied degrees of success, utilized some implementation of the VOF method is significant and growing rapidly. The principle of the VOF method is that a single, scalar value in each computational cell is used to represent the fraction of that cell occupied by a particular phase. In cells containing only a single phase, the value will be either 1 or 0. In cells through which the phase-interface passes, the value will be between 1 and 0 representing the volume fraction of the primary phase in that cell. The two main challenges in this method are: (1) to reconstruct the shape of the interface based on the volume of fluid in neighboring cells, and (2) to advect fluid near the interface in such a way that the interface remains sharp (does not diffuse) while rigorously satisfying mass conservation. Methods for handling these challenges are still areas of current research, e.g., Refs. [65,70–73]. Nevertheless, the method has proven to provide reasonable accuracy, is quite economical in terms of memory usage (requiring only one scalar value to be stored for each cell in the solution domain), and has no inherent difficulties when interfaces rupture or coalesce, unlike other methods such as the marker-and-cell or conformal grids, which can exhibit gaps or highly distorted cells when the interface shape becomes complex. It also provides one of the more straightforward ways to add interface tracking to an existing single-phase CFD solver, it works for three-dimensional nonaxisymmetric problems, and it is computationally economical. Some of its disadvantages are that, until recently [71], the advection methods could lead to ''flotsam'' or numerical debris, the interface reconstruction and advection methods could produce slightly jagged interface profiles when the velocity of the interface was not normal to the grid faces, and for an interface reversibly sheared forward and backward the same amount (typical of advection tests for different VOF implementations) the final interface location will show some disagreement or noise when compared with the initial position (see Refs. [65,71–73]). Even with these potential pitfalls, the VOF method has seen widespread implementation in commercial CFD packages. Applications in the literature include the prediction of droplet formation of a viscous fluid in air from the end of a capillary tube [70,74], jet breakup in liquid-liquid flows [75,76], bubble formation and oscillation during the impact of raindrops into deep pools of liquid [43], the formation and breakup of crown splashes in droplet impacts on thin liquid layers [77,78], the formation of droplets from a capillary tube surrounded by a viscous medium [79], the formation [58], rise [70] and burst-through [80–82] of a bubble in a liquid medium. However, no literature has been found that has attempted to apply VOF techniques to the three dimensional case of modeling the formation of droplets and waves in horizontal-tube, falling-film flow.

Computational Method

The objective stated earlier for the computational work is part of a larger objective to improve the prediction of fluid flow and heat and mass transfer of falling-film, horizontal-tube absorbers,

Table 1 Summary of thermophysical properties used in computational analysis

	Air	Water	55%-wt LiBr
Density, ρ (kg/m^3)	1.185	997	1592
Viscosity, μ (kg/m s)	1.85×10^{-5}	8.905×10^{-4}	4.635×10^{-3}
Surface tension, σ (N/m)		7.255×10^{-2}	9.152×10^{-2}

thus enabling more efficient design. Therefore the future utility of this model requires that it be adaptable to include coupled heat and mass transfer as well as potentially complex models for surface tension required to capture the effect of surfactants. Therefore, a commercially available CFD package [83] that has these capabilities *and* grants the user access to primitive variables and a large amount of control over the details of the solution procedure, including implementation of user-defined algorithms and functions, was selected as the environment in which to develop this model.

Assumptions and Fluid Properties. The flow was assumed to be laminar throughout the solution domain in all cases considered here. This is a justifiable assumption given the low film Reynolds numbers under consideration (less than 100). Even though bifurcation and impact events can lead to locally high velocities, it is assumed that they do not generate turbulence in a way that would require any special modeling.

The thermophysical properties of the surrounding vapor (taken to be air at room conditions) and the fluid phase (aqueous LiBr for comparison with experiments) were assumed to be constant within each phase. These were evaluated at 25°C and 101.325 kPa based on the data in Ref. [84] for air. For 55%-wt LiBr, the data of Ref. [85] was used to evaluate the viscosity and a correlation developed by Herold [86] was used to evaluate the density (correlations in Ref. [87] were used to evaluate properties of water for comparison). The surface tension between air and aqueous LiBr was estimated by interpolating the data in Ref. [88] which includes a survey of values in the literature and new experimental data at room temperature and atmospheric pressure. All of these correlations were implemented in the commercially available software program EES [86]. Table 1 summarizes the properties, with water properties shown for comparison. Implicit in the assumption of the constant properties stated earlier is the assumption that the flow is incompressible and Newtonian. This allows a standard form of the Navier-Stokes equations to be used as discussed in the next section.

Governing Equations and the VOF Method. Conservation of mass, the so-called continuity equation, can be derived by applying Reynolds' Transport Theorem (RTT) to any material volume. Noting that the mass, *m*, within a material volume is, by definition, constant, the derivative of the mass with respect to time, *t*, must be zero

$$\frac{dm}{dt}=0 \tag{1}$$

Applying RTT leads to the general continuity equation which can be written in many ways, for instance

$$\frac{\partial\rho}{\partial t}+\nabla\cdot(\rho\vec{\mathrm{v}})=0 \tag{2}$$

where ρ is the density, $\vec{\mathrm{v}}$ is the velocity vector, and ∂ denotes the partial derivative operator. For the case of constant density, (2) simplifies to the statement

$$\nabla\cdot\vec{\mathrm{v}}=0 \tag{3}$$

The divergence operator, $\nabla\cdot$, must be appropriately defined for the coordinate system. In the present work, the coordinates were either cylindrical (2D case) or Cartesian (3D model of horizontal tubes). In the cylindrical case, axial symmetry was assumed (no swirl velocity permitted), thus reducing the problem to two spatial dimensions. Thus the continuity equation becomes:

Cartesian 3D

$$\nabla\cdot\vec{\mathrm{v}}=\frac{\partial v_x}{\partial x}+\frac{\partial v_y}{\partial y}+\frac{\partial v_z}{\partial z}=0 \tag{4}$$

Axisymmetric cylindrical coordinates with no swirl velocity

$$\nabla\cdot\vec{\mathrm{v}}=\frac{1}{r}\frac{\partial}{\partial r}(rv_r)+\frac{\partial \mathrm{v_z}}{\partial z}=0 \tag{5}$$

where the subscripted v's denote the components of the vector $\vec{\mathrm{v}}$.

From a statement of Newton's Second Law of Motion, $\vec{\mathrm{F}}=m\vec{\mathrm{a}}$ where the force, $\vec{F}$, and acceleration, $\vec{\mathrm{a}}$, are both vectors, Cauchy derived the general equation of motion for any continuum irrespective of the relationship between applied stress and exhibited rate of strain [89] (p. 102). For the case of a Newtonian fluid, where the stress tensor is at most a linear function of the rate of strain tensor, the standard incompressible Navier-Stokes equations can be derived [89–91] resulting in one equation for each spatial dimension

Cartesian 3D

$$\left(\frac{\partial v_x}{\partial t}+v_x\frac{\partial v_x}{\partial x}+v_y\frac{\partial v_x}{\partial y}+\mathrm{v_z}\frac{\partial v_x}{\partial z}\right)=-\frac{1}{\rho}\frac{\partial \mathrm{p}}{\partial x}+\frac{\mu}{\rho}\left(\frac{\partial^2 v_x}{\partial x^2}+\frac{\partial^2 v_x}{\partial y^2}+\frac{\partial^2 v_x}{\partial z^2}\right)+g_x \tag{6}$$

$$\left(\frac{\partial v_y}{\partial t}+\mathrm{v_x}\frac{\partial v_y}{\partial x}+\mathrm{v_y}\frac{\partial v_y}{\partial y}+v_z\frac{\partial v_y}{\partial z}\right)=-\frac{1}{\rho}\frac{\partial \mathrm{p}}{\partial y}+\frac{\mu}{\rho}\left(\frac{\partial^2 v_y}{\partial x^2}+\frac{\partial^2 v_y}{\partial y^2}+\frac{\partial^2 v_y}{\partial z^2}\right)+g_y \tag{7}$$

$$\left(\frac{\partial v_z}{\partial t}+\mathrm{v_x}\frac{\partial v_z}{\partial x}+v_y\frac{\partial v_z}{\partial y}+\mathrm{v_z}\frac{\partial v_z}{\partial z}\right)=-\frac{1}{\rho}\frac{\partial \mathrm{p}}{\partial z}+\frac{\mu}{\rho}\left(\frac{\partial^2 v_z}{\partial x^2}+\frac{\partial^2 v_z}{\partial y^2}+\frac{\partial^2 v_z}{\partial z^2}\right)+g_z \tag{8}$$

Axisymmetric cylindrical

$$\left(\frac{\partial v_z}{\partial t}+v_r\frac{\partial v_z}{\partial r}+v_z\frac{\partial v_z}{\partial z}\right)=-\frac{1}{\rho}\frac{\partial \mathrm{p}}{\partial z}+\frac{\mu}{\rho}\left[\frac{1}{r}\frac{\partial}{\partial r}\left(r\frac{\partial v_z}{\partial r}\right)+\frac{\partial^2 v_z}{\partial z^2}\right]+g_z \tag{9}$$

$$\left(\frac{\partial v_r}{\partial t}+\mathrm{v_r}\frac{\partial v_r}{\partial r}+v_z\frac{\partial v_r}{\partial z}\right)=-\frac{1}{\rho}\frac{\partial \mathrm{p}}{\partial r}+\frac{\mu}{\rho}\left[\frac{\partial}{\partial r}\left(\frac{1}{r}\frac{\partial}{\partial r}(rv_r)\right)+\frac{\partial^2 v_r}{\partial z^2}\right]+g_r \tag{10}$$

where μ is the viscosity, p is the pressure, and subscripted g is the component of the acceleration of gravity (or any other body force) in the direction of the subscript.

A finite-volume method was employed to translate these coupled, partial differential equations into algebraic expressions that can be solved with a computer. In this process, the equations of motion and continuity are integrated over each computational cell and then discretized. The advantages of this method are that application to irregular meshes is reasonably straightforward, and that the resulting discretization automatically satisfies the conservative property for mass and momentum [92]. There are several options for performing the discretization of the equations, but for the current work, a second-order upwind scheme was used. The discretized equations are linearized and solved in a segregated, first-order implicit manner. For a given unknown (velocity in one

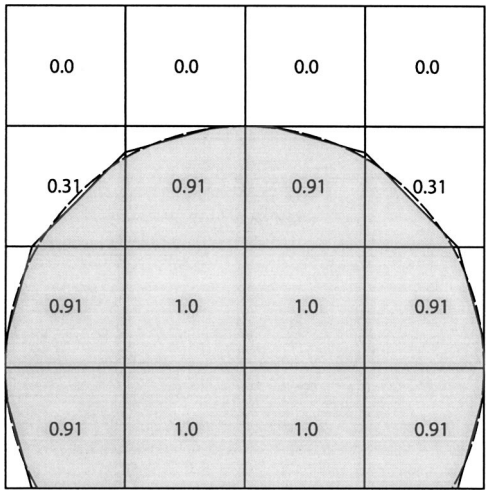

Fig. 2 Illustration of piecewise linear reconstruction of interface, adapted from Ref. [65] (reproduced with permission from Elsevier). Smooth line shows actual interface (circle), numbers represent volume fractions.

direction, for example) each governing equation is linearized implicitly with respect to that unknown at a future time. The resulting linear system of simultaneous equations (one for each cell in the domain) is then solved using a Gauss-Siedel equation solver in combination with an algebraic multigrid method (which generates coarse level equations using a Galerkin method without actually performing any rediscretization). This is done for each of the unknowns in the system separately, viz. ''segregated.'' The resulting solution may not satisfy the continuity equation within the convergence tolerance. If this is the case, a pressure correction is calculated and the segregated solver iterates through the solution for each of the unknowns again, and so on until the solution is converged within the specified tolerance. The solution variables are stored at the cell centers. Since cell face values for pressure are required in the discretized form of the momentum equations, an interpolation technique must be used. The so called ''body-force-weighted'' scheme was used because it is the most appropriate for buoyancy driven flows as in this work. Face fluxes are related to the velocity at the cell centers using a momentum-weighted averaging technique to avoid the ''checkerboarding'' that can occur with a linear averaging technique [83]. To relate the solution of the continuity equation to the pressure correction, the pressure-implicit with splitting of operators (PISO) method [93], a part of the SIMPLE family of algorithms, was used. Since the flow in this application is driven more by body forces than pressure gradients, an ''implicit body force'' treatment in the PISO algorithm was used. This utilizes the body forces in the flow in the pressure correction step, resulting in a more realistic pressure field at each iteration. The Fluent solver has sophisticated controls for determining the multigrid cycles (*W*, *V*, combined, etc.) for obtaining more rapid convergence. Within the scope of this project, the parameters governing the controls of the multigrid cycles were not modified from their default settings.

The basic concept of the VOF method was described in the introduction. As was mentioned, there are several options for interface reconstruction and cell advection algorithms (sometimes called donor-acceptor schemes) near the interface. In cells that do not contain an interface (i.e., the volume fraction is either 1 or 0) the standard solution method outlined earlier is used. Many of the various techniques used throughout the literature are summarized by Ref. [65]. The interface reconstruction used in the present work is a piecewise linear scheme adapted for unstructured grids from Ref. [94]. Figure 2 illustrates what is meant by a piece-wise linear reconstruction. In some recent papers [71–73], Youngs method has proven to be one of the most accurate at maintaining the interface across arbitrary grid structure even compared with recently developed methods, although it does not necessarily eliminate the problem of fluid ''flotsam and jetsam'' that may sometimes remain after a thin film or thread ruptures in the simulation [71]. In this application, flotsam and jetsam refer to ''isolated, submesh-size material bodies that separate from the main material body because of errors induced by the volume tracking algorithm'' [65]. The isolated satellites that can be created do not violate conservation of mass, but represent features that are below the resolution of the grid. These were occasionally observed during the simulations; sometimes reducing the time step would ameliorate the problem, but not always. However, the net result on the overall predictions was small since the size of these aberrations is much less than the size of a mesh element, so the occasional flotsam/jetsam in the simulation was deemed acceptable.

Surface tension is handled using the so-called ''continuum surface force'' method of Brackbill et al. [67,68]. In this, the pressure rise across the interface due to surface tension is converted to a source term in the momentum equations. This source term is a body force similar to the way gravity appears in the equations. To compute the magnitude of this force, the local curvature (sum of the inverse of the two principal radii of curvature) is computed. The normal vector at the interface is defined by the gradient of the volume fraction. The divergence of the unit normal is, from differential geometry, the curvature. With the curvature known, the surface tension force can be described in terms of the jump in pressure across the interface which, in turn, can be expressed as a volume force using the divergence (also referred to as Green's, Gauss's Divergence, LaGrange's, and Ostrogradsky's) theorem [89]. In addition, a wall contact angle can be specified which is used to adjust the surface normal in the cells near the wall. In most cases, walls were specified to have a 0° contact angle to ensure complete wetting in the simulation.

In the VOF formulation, the momentum equations are identical and solved in the same manner as described earlier (i.e., a single equation spans the entire solution domain, irrespective of the location of the phases). The continuity equation is slightly modified to be solved for one phase

$$\frac{\partial \alpha_2}{\partial t} + \overline{\mathrm{v}} \cdot \nabla \alpha_2 = 0 \tag{11}$$

where α_2 is the volume fraction of phase 2. The solution for the volume fraction for phase 1 is simply

$$\alpha_1 = (1 - \alpha_2) \tag{12}$$

The dependence upon the volume fraction in the other equations enters simply through the evaluation of the fluid properties. For instance, the density in any cell can be expressed by

$$\rho = \alpha_2 \rho_2 + (1 - \alpha_2)\rho_1 \tag{13}$$

where ρ is the evaluated density within the cell, ρ_1 and ρ_2 are the densities of phase 1 and phase 2, respectively. This leads to one limitation of the VOF method: large gradients in velocity across the interface are not accurately recreated (of course, as is almost always the case in computational work, the more refined the grid, the easier it is to accurately capture steep gradients). Fortunately, in the present work, this situation rarely arises.

A final important capability provided by the solver environment used here is the ability to run on parallel processor machines with shared or distributed memory. Several methods are available for grid partitioning. The computer used for most of the analyses was a SUN FIRE V480 with four 900 MHz cu SPARC CPUs (and 16 GB of RAM). When the fully three-dimensional simulation was

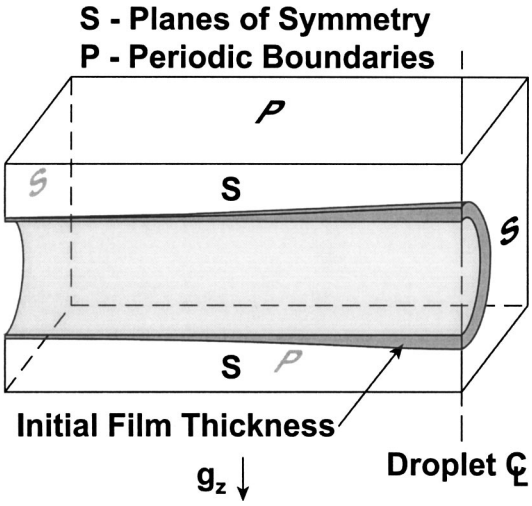

Fig. 3 Domain of droplet and tube model showing boundary and initial conditions (not to scale, film thickness greatly exaggerated)

run in parallel on four processors, the speed-up was nearly fourfold, indicating that the overhead of parallel communication was quite low.

The fixed grids used in the present work were made up of quadrilateral (2D) or hexahedral (3D) volumes. Quadrilateral and hexahedral cells are known to be slightly more accurate when surface tension is an important force (Ref. [83] see Section 22.2.8), as is the case here, than triangles/tetrahedrals. The grids were generated using the program GAMBIT [83].

Geometry and Model Initialization. Simulating a droplet forming from the underside of a horizontal tube requires a fully 3D model; however, examination of the droplets (see Fig. 1, for example) reveals that there are two vertical planes of symmetry that allow the model to be reduced to 1/4 of a full droplet model. It was assumed that the vertical plane intersecting the axis of the tube that cuts the tube in half along its length and the vertical plane perpendicular to this intersecting the center of the droplet (vertical lines in box shown on Fig. 1) were both planes of mirror symmetry. Moreover, the model included one tube and half of the tube-to-tube spacing above and beneath the tube; the top and bottom boundaries (horizontal lines in box shown on Fig. 1) were assumed to be periodic. Thus the droplet that fell from the tube would exit the bottom of the solution domain and reenter at the top to impact on the top of the tube making a continuous bank of tubes out of the solution domain. Finally, the tube length was taken to be half of the distance between droplet formation sites (as observed in the experimental work described in Ref. [12], approximately 11 mm) and the boundary opposite of the center of the droplet was also assumed to be a plane of symmetry. This is equivalent to assuming that droplets form and fall equally spaced at 22 mm on center and in perfect unison. According to linear stability analysis for a thin film suspended over a less dense phase [16], the fastest growing wavelength should be $\lambda = l_c 2\pi\sqrt{2}$, where l_c is the capillary wavelength. For the properties shown in Table 1, this gives: $\lambda = 21.5$ mm, which is very close to the observed value. This is an oversimplification compared to a real system where droplet spacing and sequencing are observed to be variable (although spacing is usually close to the characteristic dimension used). However, this assumption does lead to realistic interaction between the spreading lamellae of droplets impacting adjacent to one another. In the case where neighboring droplets are more out-of-phase, the spreading lamellae would continue to expand along the length of the tube until they become indistinguishable or interact with other out-of-phase droplet impacts creating more complicated wave patterns. Modeling the various possible phase relationships would require extending the current model to include more than one droplet and/or incorporating more sophisticated boundary conditions. The complications of this stochastic behavior of the droplet interactions was previously observed [5] and will be studied computationally in future work. The initial conditions were taken to be quiescent with a smooth film surrounding the tube. The thickness of this film was made to vary in a sinusoidal fashion from 0.20 mm at one end to 0.53 mm at the other end; this ensured that the droplet formed at one of the planes of symmetry. Figure 3 shows the solution domain with an exaggerated initial film thickness profile. The solution domain was divided into quadrilateral elements that were finer near the tube walls and in regions where the two-phase interface was expected to pass, and coarser in regions where only the gas-phase was expected. The edge length varied from a minimum of 1×10^{-4} m near the tube surface to a maximum of 2.5×10^{-4} m. The face mesh, shown in Fig. 4, contained 16,941 quadrilaterals; this pattern was repeated along the length of the tube to form 1,185,870 hexahedral elements. The shading in Fig. 4 corresponds to the partitioning of the grid to the four processors used for the parallel computing (each processor has two neighbors due to the periodic boundary condition at the top and bottom).

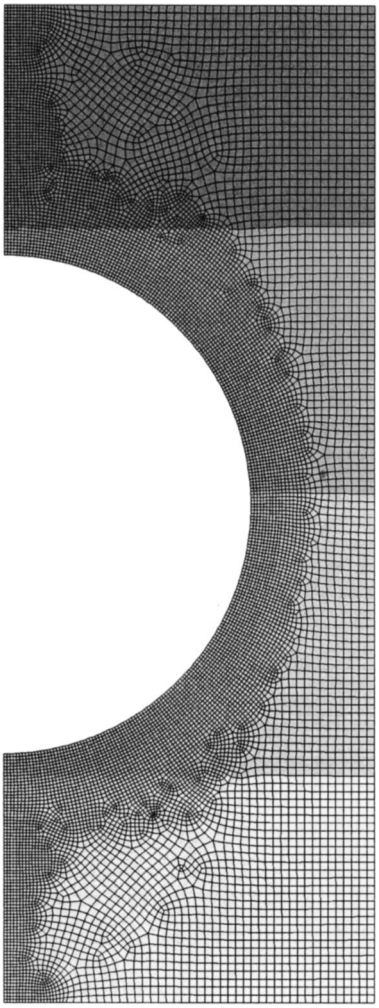

Fig. 4 Mesh used for three-dimensional model of tubes, shades of gray indicate partitioning for parallel computing

Results

The model was solved using time steps of 0.2 ms. Taking much larger time steps would lead to numerical instabilities at the liquid vapor interface; smaller time steps had no effect on the results. A typical droplet formation cycle required around 2000 time steps when beginning with a stagnant film. The interface was taken to be the surface where the volume of fluid was 0.5 (interpolated from the VOF values at each grid location). Defining this surface allowed rendered images of the droplet and film to be generated at regular time intervals. To aid visualization, the images were reflected about the planes of symmetry (to show a complete droplet) and duplicated about the periodic boundaries (to show multiple tubes and droplets). The results are shown in Fig. 5. Because of the reflections, four identical droplets are shown, which aids in the visual interpretation of the interference patterns of the interacting lamellae. To validate these results, they are compared with the flow visualization results presented in Killion and Garimella [5,12]. Using the moment of impact to synchronize the sequences, Fig. 6 shows several selected frames of the simulation from the present study and high-speed video from Ref. [12]. The agreement is quite good. No special selection criteria was used to choose the particular droplet video used for comparison; however, visual inspection of numerous video recordings of the corresponding flow at these conditions showed that the droplet behavior was quite regular and repeatable. In addition, no model parameters, save the tube geometry, were obtained from the experimental results. The simulation exhibits all of the characteristics observed in the experiments including the stretching of the drop along the tube early in the formation process, the formation of a primary droplet and trailing liquid thread, the saddle-shaped spreading lamella, and the thinning and breakup of the liquid bridge into a number of satellite droplets. There are some differences that can be seen as well. For instance the droplet and thread volume in the simulation appear to be slightly smaller than in the experiment which leads to an earlier breakup of the liquid thread into satellites. In addition, the early droplet formation process took longer in the simulation than was observed experimentally. This is most likely due to the quiescent initial conditions used in the simulation. It has been observed that the early formation of the droplets is often accelerated by the arrival of a quantity of liquid from a previous droplet impact [5,12,45]. Potentially this effect would be captured if the simulation were continued for several more droplet cycles. The sensitivity of these results to thermophysical properties is ostensibly low based on the similarity previous experimental observations made using both pure water and aqueous LiBr, which have significantly different thermophysical properties (see Table 1) [5,12,45]. The digital image analysis routine presented in Killion and Garimella [12] was also applied to the rendered images produced from the CFD results. This analysis uses guided edge detection techniques to estimate droplet surface area and volume in the intertube region where the droplet is nearly axisymmetric over a sequence of images. A comparison is shown in Fig. 7. The solid line shows the analysis of experimental results and the dashed line the simulation. Also shown on this plot is an axisymmetric model (dotted line) that will be discussed later. The largest discrepancy between the model and experimental results appears early in the droplet formation. As mentioned earlier, the simulation begins slowly because of the assumed initial conditions, whereas the experimental results are typically accelerated early by the arrival of liquid from droplet impacts above. It is clear though, that after the droplet volume reaches about 75 mm^3 the results track very well, although the ultimate volume of the droplet is slightly smaller in the simulation, which results in the deviation seen near the point of impact (the peak in the curves at time 0). This slight difference is also somewhat apparent in frames *g* and *h* of Fig. 6, especially in the liquid thread. As the droplet spreads onto the tube and the thread breaks up, the volume and surface area between the tubes drop sharply in both the simulation and experiments. The difference between the two at impact appears to be maintained throughout this process. The liquid thread breaks up slightly earlier in the simulation (frames *j*–*m* of Fig. 6). And so the increase in surface-area-to-volume ratio associated with the creation of satellite droplets also occurs somewhat earlier in the simulation, although throughout the evolution the agreement in this parameter is also quite good. The agreement between the simulation and experiment suggests that the model provides a sound basis for investigating the details of heat and mass transfer of absorption on falling films on horizontal tubes. As mentioned in the introduction, previous attempts have had to rely on gross assumptions about the shape (therefore surface area) and transport within the forming droplet and falling film. Since the transport processes depend extensively on the size and location of the interface as well as the flow pat-

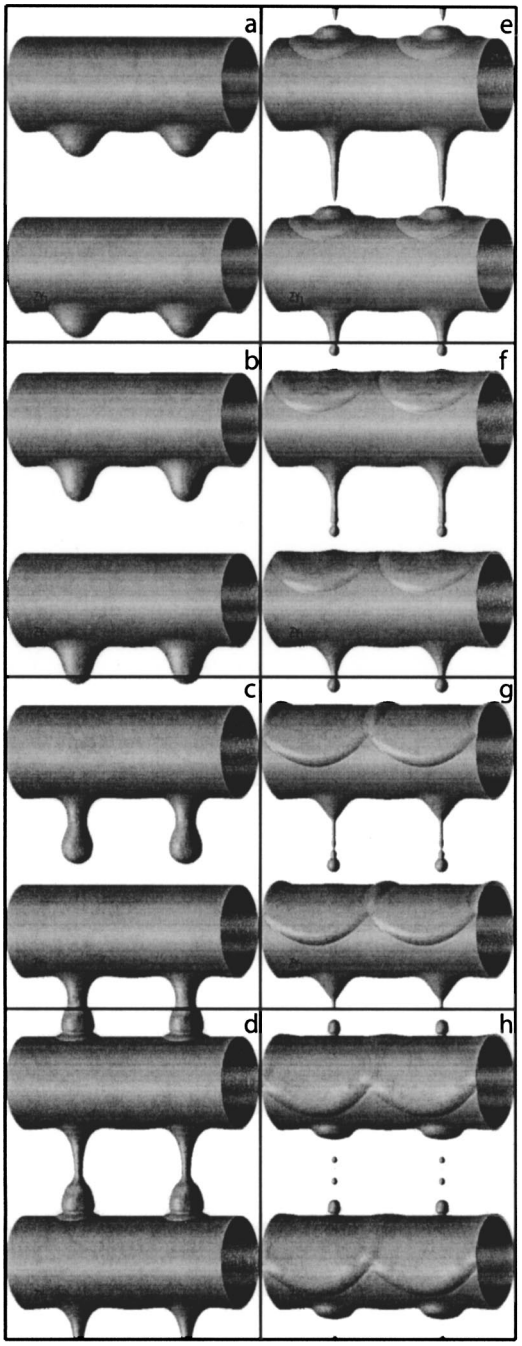

Fig. 5 Results of simulation of falling film on horizontal tubes [(*a*)–(*c*) 50 ms between frames, (*c*)–(*d*) 20 ms between frames, (*d*)–(*h*) 10 ms between frames]

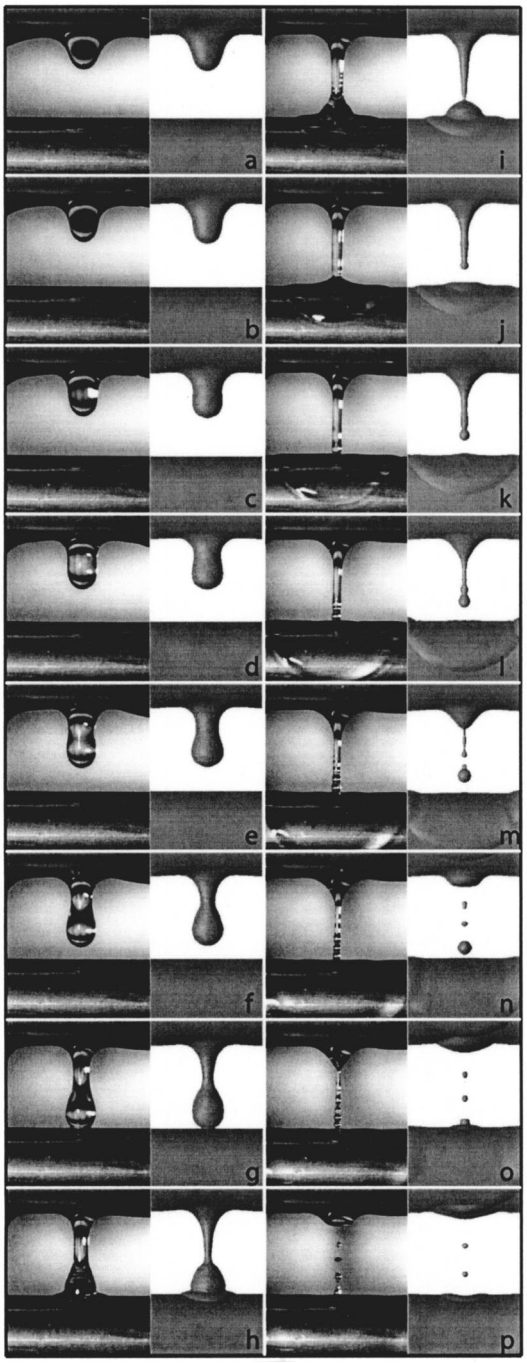

Fig. 6 Visual comparison of experiment (left) with simulation (right) synchronized at impact [frames (*a*)–(*g*) 10 ms between frames, frames (*g*)–(*p*) 6 ms between frames]

terns within the film and droplets, it is clear that a more accurate and detailed understanding of the shape and velocity of the fluid will allow much more accurate predictions of the absorption process.

Because the computational cost of performing a 3D transient simulation is quite high, an axisymmetric approximation of the tube bank was also considered. An axisymmetric system can be modeled in 2D and thus requires much less computational effort. A column of spheres of the same diameter and spacing as the tubes was modeled. The mesh is similar to that shown in Fig. 4. The same fluid properties listed in Table 1 were used. Because of the greater computational speed, the 2D column-of-spheres model

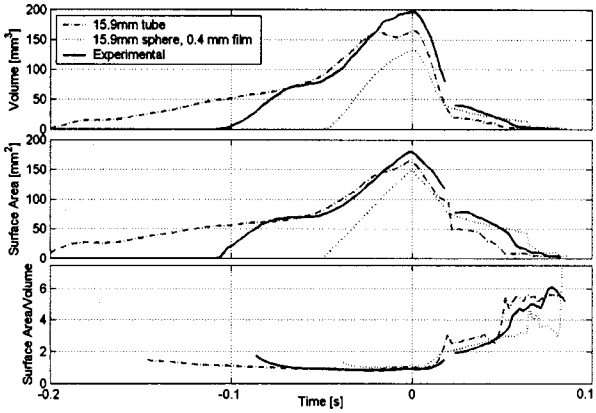

Fig. 7 Comparison of droplet volume and surface area from analysis of video and simulation

was used to investigate grid independence of the calculation. Because the algorithms used in the 3D models are computationally equivalent to the 2D models, the grid sensitivity of the 2D models can be used to deduce the same in the 3D case. Three models were generated with the characteristic mesh lengths of 1×10^{-4} m, 8.0×10^{-5} m, and 6.4×10^{-5} m at the surface of the sphere. This resulted in 2D meshes with 15,425, 19,740, and 24,893 quadrilateral cells, respectively. The coarsest mesh corresponds to the mesh used in the 3D results reported earlier. A uniform initial film thickness of 0.35 mm was used. The results are compared in the three columns of Fig. 8 at various phases of the droplet evolution. The first row corresponds to 62 ms from the start of the simulation. This figure shows that all three models predict the early development of the droplet in a virtually identical manner. The second row shows the predictions 127 ms after the initialization of the model. The third row of this figure shows the predicted shapes at the moment of the rupture of the liquid thread, and the fourth shows some of the predicted satellite droplets. The shape of the thread at rupture is nearly identical in all three models.

It can be seen in Fig. 8 that irrespective of grid size, the models show good overall agreement in the predicted behavior of the primary drop, trailing liquid thread, and satellite droplet formation throughout the course of the entire droplet evolution cycle. The only noticeable dependence on grid density appears in row two, where the coarser meshes result in droplet pulling away from the tube somewhat faster than in the finest mesh. The reason for this effect of grid size is currently being investigated. However, the shapes and sizes of the predicted droplets in all three models are in very good agreement. Also, this slight difference does not significantly affect the latter stages of the evolution of the droplets, as seen in rows three and four. Furthermore, it is no surprise that the details of the satellite droplet formation vary slightly from model to model, since it has been well demonstrated in the literature [5,12,35] that the development of satellite droplets observed in practice is highly variable from droplet to droplet. In addition, recent detailed models of satellite droplet dynamics [45] suggest that, even with simplified initial conditions, they exhibit highly irregular behavior that is difficult to accurately predict in detail. Nevertheless, all three models considered here predict satellite droplet formation of approximately the same size.

The 2D sphere model was also used to investigate the effect of the initial film thickness. Uniform films ranging from 0.20 to 0.50 mm were considered. With the thinnest initial film, liquid collected at the bottom of the sphere, but did not ever drop; with the thickest film, the liquid flowed as a continuous column. Table 2 summarizes the results for several intermediate initial film thicknesses. It can be seen that the predicted droplet diameter (measured at the horizontal equator the moment before impact) was fairly insensitive to initial film thickness, but the diameter of the

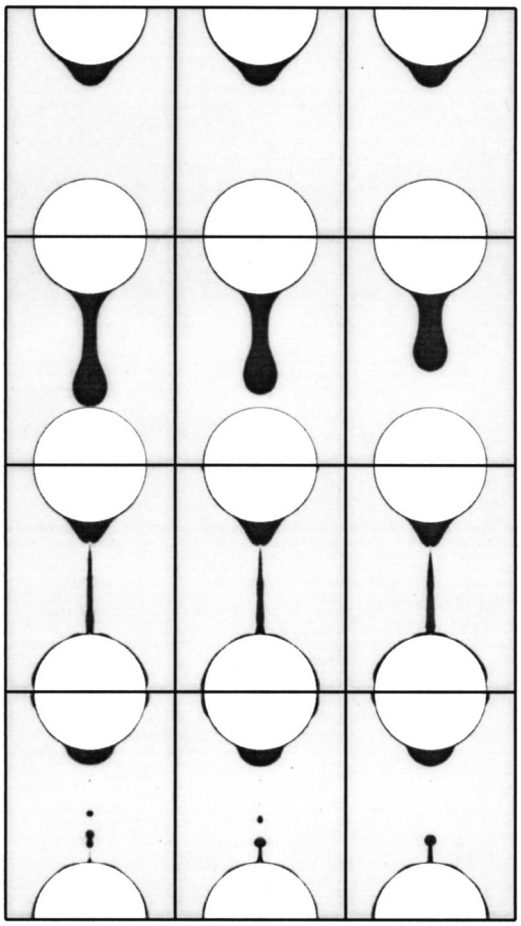

Fig. 8 Investigation of grid independence using column-of-spheres model with 0.35 mm initial film thickness

trailing liquid thread increased with increasing liquid inventory. In addition, the time for enough liquid to collect at the bottom of the sphere and pull away in a droplet was less as the liquid inventory increased. An analysis of these models revealed that they all significantly underpredict the droplet size and the time for droplet evolution; for reference, the equatorial diameter of the droplets observed in Killion and Garimella [12] were closer to 6 mm the moment before impact. Figure 9 illustrates the agreement of these models with the measurements in terms of surface area and volume. Both the initial droplet formation and the thread breakup and formation of satellite droplets also occur much quicker than observed for the horizontal tube case. It is thought that the geometry accounts for these differences. In the case of horizontal tubes, the surface tension in the direction of the axis of the tube tends to elongate the droplet and thus cause it to be larger. In addition, the

Table 2 Summary of effect of film thickness on droplet dynamics in spheres model

Initial film thickness (mm)	Diameter of primary droplet at impact (mm)	Minimum diameter of bridge at impact (mm)	Time to first impact (msec)
0.20	No droplet falls		
0.23	5.09	1.3	611
0.25	5.03	1.6	158
0.30	4.88	1.9	124
0.35	4.89	2.2	112
0.40	5.18	2.7	98
0.50	Fluid flowed as continuous column		

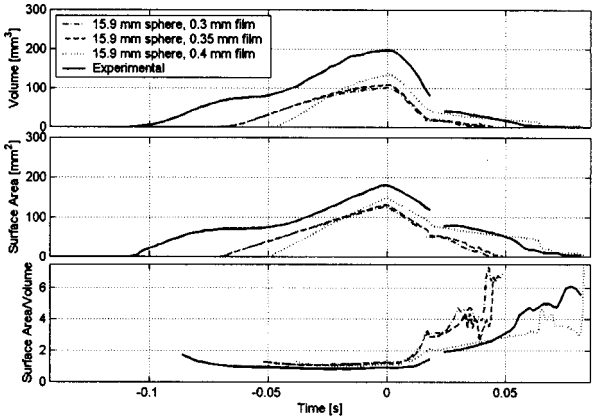

Fig. 9 Comparison of experimental results with axisymmetric "column-of-spheres" models with various liquid inventories

flow of the film toward the droplet is more direct in the case of a sphere; in the horizontal tube case, some of the falling film must move axially along the tube to arrive at the forming droplet. This seems to explain the longer evolution time observed with in the horizontal tube case. These findings suggest that it is best to use a 3D model to accurately capture all the flow phenomena observed in the flow of liquid films and droplets on horizontal tube banks.

Conclusions

Understanding absorption heat and mass transfer on falling films over horizontal tubes presents many challenging problems that depend largely upon understanding the fluid flow pattern; especially for the case of water-Lithium Bromide where mass transfer in the liquid phase tends to be the limiting resistance. Flow visualization experiments previously conducted [5,12] revealed many of the details of this flow pattern and suggested that the idealized flow patterns frequently assumed in the literature were too simple to allow accurate predictions of the absorption rate. A three-dimensional computational model of the two-phase flow of falling films and droplets of aqueous Lithium Bromide around horizontal tubes was presented. One 15.9 mm diameter tube was modeled with periodic boundary conditions (to minimize the size of the computational model) representing a distance of 15.9 mm between the tubes. The results of the model were in good agreement with the observed droplet and film behavior. The results showed virtually all of the phenomena observed in the experiments. In addition, the droplet volume and surface area between the tubes were predicted with a satisfactory degree of quantitative agreement over the entire droplet evolution. There were some differences between the simulation and experiment that are probably due to the oversimplified initial conditions assumed (quiescent film). The initial droplet formation took longer in the simulation than is typically observed in experiment where early droplet formation is frequently accelerated by the arrival of a quantity of liquid from a previous droplet impact. More realistic initial conditions might be obtained by letting the model run for several droplet cycles. After the growing droplet reached about half of its ultimate volume, the experiments and simulation were in very good agreement throughout the remainder of the droplet evolution, although the droplet volume and thread diameter were slightly underpredicted by the model.

Simplified models based on an axisymmetric column of spheres were also considered because they could be modeled in 2D, which requires considerably less computational effort. A column-of-spheres model with spheres of the same diameter and spacing as the horizontal tube case significantly underpredicted droplet size and evolution time irrespective of the initial film thickness used. In addition, it was noted that this approximate model is unable to exhibit the effects of interacting droplets and the saddle waves

formed in the case of horizontal tubes. Thus, it is concluded that a fully 3D model is required to capture the characteristics of droplet and film behavior on horizontal tubes.

The present work provides a sound foundation to investigate the role of droplets in falling film absorption in greater detail than has been done to date. Recent literature has suggested that droplets may contribute significantly to the absorption process both through direct absorption and by driving the mixing and film waviness that is a key advantage of horizontal tube absorbers. Because this model predicts the fluid behavior in the droplets and the waviness they create on the film, it is expected that it will provide realistic conditions for modeling the coupled heat and mass transfer of absorption.

Acknowledgments

The authors gratefully acknowledge the support of the National Science Foundation through grant number 9875010, ASHRAE through a Grant-in-Aid, and John Dickerson, Noah Hughes and Matt Bradshaw of Engineering Computing Support Services at Iowa State University.

Nomenclature

g = Gravitational acceleration (m/s^2)
l_c = Capillary length scale (m)
m = Mass (kg)
p = Pressure (Pa)
r = Radial coordinate, radius (m)
t = Time (s)
v = Velocity (m/s)
x = Axis coordinate
y = Axis coordinate
z = Axis coordinate

Greek Symbols

α = Volume fraction (m^3/m^3)
Γ = Solution flow rate per unit length per side (kg/s m)
λ = Departure site wavelength (m)
μ = Viscosity (kg/m s)
ρ = Density (kg/m^3)
σ = Surface tension (N/m)

Subscripts

1 = Species 1
2 = Species 2
r = Component in radial direction
x = Component in x direction
y = Component in y direction
z = Component in z direction

References

[1] ASHRAE, 1997, *1997 ASHRAE Handbook—Fundamentals*, American Society of Heating, Refrigerating and Air-Conditioning Engineers, Inc.
[2] Nomura, T., Nishimura, N., Wei, S., Yamaguchi, S., and Kawakami, R., 1993, ''Heat and Mass Transfer Mechanism in the Absorber of Water/LiBr Conventional Absorption Refrigerator: Experimental Examination by Visualized Model,'' *International Absorption Heat Pump Conference*, New Orleans, Louisiana, Vol. AES-31, The Advanced Energy Systems Division, ASME, pp. 203–208.
[3] Kirby, M. J., and Perez-Blanco, H., 1994, ''A Design Model for Horizontal Tube Water/Lithium Bromide Absorbers,'' *ASME Heat Pump and Refrigeration Systems Design, Analysis and Applications*, Conference proceedings, **32**, ASME New York, pp. 1–10.
[4] Jeong, S., and Garimella, S., 2002, ''Falling-Film and Droplet Mode Heat and Mass Transfer in a Horizontal Tube LiBr/Water Absorber,'' Int. J. Heat Mass Transfer, **45**(7), pp. 1445–1458.
[5] Killion, J. D., and Garimella, S., 2003, ''Gravity-Driven Flow of Liquid Films and Droplets in Horizontal Tube Banks,'' Int. J. Refrig., **26**(5), pp. 516–526.
[6] Atchley, J. A., Perez-Blanco, H., Kirby, M. J., and Miller, W. A., 1998, ''An Experimental and Analytical Study of Advanced Surfaces for Absorption Chiller Absorbers,'' *Gas Research Institute Report GRI*.
[7] Andberg, J. W., and Vliet, G. C., 1987, ''Absorption of Vapors Into Liquid Films Flowing Over Cooled Horizontal Tubes,'' *Second ASME-JSME Thermal Engineering Joint Conference, Honolulu, Hawaii*, Vol. 2, pp. 533–541.
[8] Choudhury, S. K., Nishiguchi, A., Hisajima, D., Fukushima, T., Ohuchi, T., and Sakaguchi, S., 1993, ''Absorption of Vapors Into Liquid Films Flowing Over Cooled Horizontal Tubes,'' *Proceedings of the 1993 Annual Meeting of the American Society of Heating, Refrigerating and Air-Conditioning Engineers, Inc.*, 27–30 June, 1993, Denver, CO ASHRAE, Atlanta, Vol. 99, pp. 81–89.
[9] Conlisk, A. T., and Mao, J., 1996, ''Nonisothermal Absorption on a Horizontal Cylindrical Tube–1. The Film Flow,'' Chem. Eng. Sci., **51**(8), pp. 1275–1285.
[10] Lu, Z., Li, D., Li, S., and Yu-Chi, B., 1996, ''A Semi-Empirical Model of the Falling Film Absorption Outside Horizontal Tubes,'' *International Ab-Sorption Heat Pump Conference*, Vol. 2, pp. 473–480.
[11] Killion, J. D., and Garimella, S., 2001, ''A Critical Review of Models of Coupled Heat and Mass Transfer in Falling-Film Absorption,'' Int. J. Refrig., **24**(8), pp. 755–797.
[12] Killion, J. D., and Garimella, S., 2003, ''Pendant Droplet Dynamics for Absorption on Horizontal Tube Banks,'' Int. J. Heat Mass Transfer, (submitted).
[13] Tang, J., Lu, Z., Yu-chi, B., and Lin, S., 1991, ''Droplet Spacing of Falling Film Flow on Horizontal Tube Bundles,'' *Proceedings of the XVIIIth International Congress of Refrigeration, Montreal*, Vol. II, pp. 474–478.
[14] Limat, L., Jenffer, P., Dagens, B., Touron, E., Fermigier, M., and Wesfreid, J. E., 1992, ''Gravitational Instabilities of Thin Liquid Layers. Dynamics of Pattern Selection,'' Physica D, **61**(1–4), p. 166.
[15] Giorgiutti, F., Bleton, A., Limat, L., and Wesfreid, J. E., 1995, ''Dynamics of a One-Dimensional Array of Liquid Columns,'' Phys. Rev. Lett., **74**(4), p. 538.
[16] de Bruyn, J. R., 1997, ''Crossover Between Surface Tension and Gravity-Driven Instabilities of a Thin Fluid Layer on a Horizontal Cylinder,'' Phys. Fluids, **9**(6), p. 1599.
[17] Hu, X., and Jacobi, A. M., 1996, ''The Intertube Falling Film: Part 1—Flow Characteristics, Mode Transitions, and Hysteresis,'' J. Heat Transfer, **118**(3), pp. 616–625.
[18] Hu, X., and Jacobi, A. M., 1998, ''Departure-Site Spacing for Liquid Droplets and Jets Falling Between Horizontal Circular Tubes,'' Exp. Therm. Fluid Sci., **16**(4), pp. 322–331.
[19] Hu, X., and Jacobi, A. M., 1996, ''The Intertube Falling Film: Part 2—Mode Effects on Sensible Heat Transfer to a Falling Liquid Film,'' J. Heat Transfer, **118**(3), pp. 626–633.
[20] Cavallini, A., Doretti, L., Fornasieri, E., and Zilio, C., 2001, ''Heat and Mass Transfer and Flow Patterns During Absorption of Steam in LiBr+Water Falling Film,'' *IIF-IIR-Commission B1*, Paderborn, Germany.
[21] Roques, J. F., Dupont, V., and Thome, J. R., 2002, ''Falling Film Transitions on Plain and Enhanced Tubes,'' J. Heat Transfer, **124**(3), pp. 491–499.
[22] Roques, J.-F., and Thome, J. R., 2003, ''Falling Film Transitions Between Droplet, Column, and Sheet Flow Modes on a Vertical Array of Horizontal 19 FPI and 40 FPI Low-Finned Tubes,'' Curr. Opin. Pediatr., **24**(6), pp. 40–45.
[23] Eggers, J., 1997, ''Nonlinear Dynamics and Breakup of Free-Surface Flows,'' Rev. Mod. Phys., **69**(3), pp. 865–929.
[24] Mariotte, E., 1686, *Traite' Du Mouvement Des Eaux Et Des Autres Corps Fluids*, E. Michallet, Paris.
[25] Savart, F., 1833, Ann. Chim. (Paris), **53**, p. 337 (with additional plates in Vol. 54).
[26] Plateau, J. P., 1849, ''Recherches Expérimentales Et Théorique Sur Les Figures D'équilibre D'une Masse Liquide Sans Pesanteur,'' Mémoires de l'Académie Royale des Sciences, des Lettres et des Beaux-Arts de Belgique, **23**, pp. 1–55.
[27] Rayleigh, L., and Rayleigh, J. W. S., 1879, Proc. London Math. Soc., **10**, p. 4.
[28] Rayleigh, L., and Rayleigh, J. W. S., 1879, Proc. R. Soc. London, Ser. A, **29**, p. 94.
[29] Worthington, A. M., 1908, *A Study of Splashes*, Longmans Green and Co., London, pp. xii, 129, 11.
[30] Kumar, R., and Kuloor, N. R., 1970, ''The Formation of Bubbles and Drops,'' Adv. Chem. Eng., **8**, pp. 255–368.
[31] Clift, R., Grace, J. R., and Weber, M. E., 1978, *Bubbles, Drops, and Particles*, Academic Press, New York, p. 380.
[32] Frohn, A., and Roth, N., 2000, *Dynamics of Droplets, in Experimental Fluid Mechanics*, Springer, New York, p. 292.
[33] Scheele, G. F., and Meister, B. J., 1968, ''Drop Formation at Low Velocities in Liquid-Liquid Systems: Part 1. Prediction of Drop Volume,'' AIChE J., **14**(1), pp. 9–19.
[34] Heertjes, P. M., de Nie, L. H., and de Vries, H. J., 1971, ''Drop Formation in Liquid-Liquid Systems-I Prediction of Drop Volumes at Moderate Speed of Formation,'' Chem. Eng. Sci., **26**, pp. 441–449.
[35] Middleman, S., 1995, *Modeling Axisymmetric Flows: Dynamics of Films, Jets, and Drops*, Academic Press, San Diego, p. 299.
[36] Bogy, D. B., 1979, ''Drop Formation in a Circular Liquid Jet,'' Annu. Rev. Fluid Mech., **11**, pp. 207–228.
[37] Yarin, A. L., 1993, *Free Liquid Jets and Films: Hydrodynamics and Rheology*, Longman, Scientific & Technical, New York.
[38] Worthington, A. M., 1881, ''On Pendent Drops,'' Proc. R. Soc. London, **32**, pp. 362–377.
[39] Pitts, E., 1974, ''The Stability of Pendant Liquid Drops. Part 2. Axial Symmetry,'' J. Fluid Mech., **63**, pp. 487–508.
[40] Peregrine, D. H., Shoker, G., and Symon, A., 1990, ''The Bifurcation of Liquid Bridges,'' J. Fluid Mech., **212**, pp. 25–39.
[41] Rein, M., 1993, ''Phenomena of Liquid Drop Impact on Solid and Liquid Surfaces,'' Fluid Dyn. Res., **12**(2), pp. 61–93.
[42] Tropea, C., and Marengo, M., 1999, ''Impact of Drops on Walls and Films,'' Multiphase Sci. Technol., **11**(1), pp. 19–36.

[43] Prosperetti, A., and Oguz, H. N., 1993, ''Impact of Drops on Liquid Surfaces and the Underwater Noise of Rain,'' Annu. Rev. Fluid Mech., **25**, p. 577.
[44] Mundo, C., Sommerfeld, M., and Tropea, C., 1995, ''Droplet-Wall Collisions: Experimental Studies of the Deformation and Breakup Process,'' Int. J. Multiphase Flow, **21**(2), pp. 151–173.
[45] Killion, J. D., 2003, *Masters Thesis: An Investigation of Droplets and Films Falling over Horizontal Tubes*, in *Department of Mechanical Engineering*, Iowa State University, Ames, Iowa, p. 156.
[46] Hyman, J. M., 1983, ''Numerical Methods for Tracking Interfaces,'' Physica D, **12D**(1–3), pp. 396–407; Fronts, Interfaces and Patterns, Proc of the 3rd Annu Int Conf of the Cent for Nonlinear Stud, 2–6 May, 1983.
[47] Sussman, M., Fatemi, E., Smereka, P., and Osher, S., 1998, ''Improved Level Set Method for Incompressible Two-Phase Flows,'' Comput. Fluids, **27**(5–6), pp. 663–680.
[48] Sussman, M., Smereka, P., and Osher, S., 1994, ''A Level Set Approach for Computing Solutions to Incompressible Two-Phase Flow,'' J. Comput. Phys., **114**(1), pp. 146–159.
[49] Unverdi, S. O., and Tryggvason, G., 1992, ''A Front Tracking Method for Viscousm Incompressible Multi-Fluid Flows,'' J. Comput. Phys., **100**, p. 25.
[50] Unverdi, S. O., and Tryggvason, G., 1992, ''Computations of Multi-Fluid Flows,'' *Physica D: Nonlinear Phenomena Proceedings of the 11th Annual International Conference of the Center for Nonlinear Studies*, 20–24 May, 1991, **60**(1–4): p. 70.
[51] Boulton-Stone, J. M., 1993, ''Comparison of Boundary Integral Methods for Studying the Motion of a Two-Dimensional Bubble in an Infinite Fluid,'' Comput. Methods Appl. Mech. Eng., **102**(2), pp. 213–234.
[52] Blake, J. R., Boulton-Stone, J. M., and Tong, R. P., 1995, *Boundary Integral Methods for Rising, Bursting and Collapsing Bubbles*, in *Boundary Element Applications in Fluid Mechanics*, H. Power, ed., Computational Mechanics Publications, WIT Press, Boston, MA, pp. 31/376.
[53] Kelecy, F. J., and Pletcher, R. H., 1997, ''The Development of a Free Surface Capturing Approach for Multidimensional Free Surface Flows in Closed Containers,'' J. Comput. Phys., **138**(2), p. 939.
[54] Wilkes, E. D., Phillips, S. D., and Basaran, O. A., 1999, ''Computational and Experimental Analysis of Drop Formation,'' Phys. Fluids, **11**(12), pp. 3577–3860.
[55] Notz, P. K., Chen, A. U., and Basaran, O. A., 2001, ''Satellite Drops: Unexpected Dynamics and Change of Scaling During Pinch-Off,'' Phys. Fluids, **13**(3), pp. 549–552.
[56] Schulkes, R. M. S. M., 1994, ''The Evolution and Bifurcation of a Pendant Drop,'' J. Fluid Mech., **278**, pp. 83–100.
[57] Zhang, D. F., and Stone, H. A., 1997, ''Drop Formation in Viscous Flows at a Vertical Capillary Tube,'' Phys. Fluids, **9**(8), pp. 2234–2242.
[58] Oguz, H. N., and Prosperetti, A., 1993, ''Dynamics of Bubble Growth and Detachment From a Needle,'' J. Fluid Mech., **257**, pp. 111–145.
[59] Eggers, J., and Dupont, T. F., 1994, ''Drop Formation in a One-Dimensional Approximation for the Navier-Stokes Equation,'' J. Fluid Mech., **262**, pp. 205–221.
[60] Papageorgiou, D. T., 1995, ''On the Breakup of Viscous Liquid Threads,'' Phys. Fluids, **7**(7), p. 1529.
[61] Shi, X. D., Brenner, M. P., and Nagel, S. R., 1994, ''Cascade of Structure in a Drop Falling From a Faucet,'' Science, **265**(5169), p. 219.
[62] Eggers, J., 1993, ''Universal Pinching of 3D Axisymmetric Free-Surface Flow,'' Phys. Rev. Lett., **71**, p. 3458.
[63] Eggers, J., 1995, ''Theory of Drop Formation,'' Phys. Fluids, **7**(5), p. 941.
[64] Brenner, M. P., Eggers, J., Joseph, K., Nagel, S. R., and Shi, X. D., 1997, ''Breakdown of Scaling in Droplet Fission at High Reynolds Number,'' Phys. Fluids, **9**(6), p. 1573.
[65] Rider, W. J., and Kothe, D. B., 1998, ''Reconstructing Volume Tracking,'' J. Comput. Phys., **141**(2), p. 112.
[66] Kothe, D. B., and Mjolsness, R. C., 1992, ''Ripple: A New Model for Incompressible Flows With Free Surfaces,'' AIAA J., **30**(11), pp. 2694–2700.
[67] Brackbill, J. U., Kothe, D. B., and Zemach, C., 1992, ''A Continuum Method for Modeling Surface Tension,'' J. Comput. Phys., **100**(2), pp. 335–354.
[68] Brackbill, J. U., and Kothe, D. B., 1996, ''Dynamical Modeling of Surface Tension,'' *Proceedings of the 1996 3rd Microgravity Fluid Physics Conference*, 13–15 July, 1996, Cleveland, OH, NASA, pp. 693–698.
[69] Kelkar, K. M., and Patankar, S. V., 1994, ''Numerical Method for the Prediction of Two-Fluid Flows in Domains With Moving Boundaries,'' *Proceedings of the 1994 ASME Fluids Engineering Division Summer Meeting. Part 7 (of 18)*, 19–23 June, 1994, Lake Tahoe, NV, Vol. 185, ASME, pp. 169–176.
[70] Gueyffier, D., Li, J., Nadim, A., Scardovelli, R., and Zaleski, S., 1999, ''Volume-of-Fluid Interface Tracking With Smoothed Surface Stress Methods for Three-Dimensional Flows,'' J. Comput. Phys., **152**(2), pp. 423–456.
[71] Harvie, D. J. E., and Fletcher, D. F., 2001, ''A New Volume of Fluid Advection Algorithm: The Defined Donating Region Scheme,'' Int. J. Numer. Methods Fluids, **35**(2), pp. 151–172.
[72] Rudman, M., 1997, ''Volume-Tracking Methods for Interfacial Flow Calculations,'' Int. J. Numer. Methods Fluids, **24**(7), pp. 671–691.
[73] Rudman, M., 1998, ''Volume-Tracking Method for Incompressible Multifluid Flows With Large Density Variations,'' Int. J. Numer. Methods Fluids, **28**(2), pp. 357–378.
[74] Zhang, X., 1999, ''Dynamics of Growth and Breakup of Viscous Pendant Drops Into Air,'' J. Colloid Interface Sci., **212**(1), pp. 107–122.
[75] Richards, J. R., Beris, A. N., and Lenhoff, A. M., 1995, ''Drop Formation in Liquid-Liquid Systems Before and After Jetting,'' Phys. Fluids, **7**(11), pp. 2617–2630.
[76] Richards, J. R., 1994, *Doctoral Thesis: Fluid Mechanics of Liquid-Liquid Systems*, in *Chemical Engineering*, University of Delaware, p. 241.
[77] Rieber, M., and Frohn, A., 1999, ''Numerical Study on the Mechanism of Splashing,'' Int. J. Heat Fluid Flow, **20**(5), pp. 455–461.
[78] Gueyffier, D., 2000, *Doctoral Dissertation: Etude De L'impact De Gouttes Sur Un Film Liquide Mince. Développement De La Corrolle Et Formation De Projections (in French)*, in *Mécanique*, Université Pierre et Marie Curie, Paris 6, p. 177.
[79] Zhang, X., 1999, ''Dynamics of Drop Formation in Viscous Flows,'' Chem. Eng. Sci., **54**, pp. 1759–1774.
[80] Chen, L., Garimella, S. V., Reizes, J. A., and Leonardi, E., 1997, ''Motion of Interacting Gas Bubbles in a Viscous Liquid Including Wall Effects and Evaporation,'' Numer. Heat Transfer, Part A, **31**(6), pp. 629–654.
[81] Yoshikawa, T., Murai, Y., and Yamamoto, F., 1997, ''Numerical and Experimental Investigations of Bursting Bubble on Free Surface,'' *Proceedings of the 1997 ASME Fluids Engineering Division Summer Meeting, FEDSM'97. Part 13 (of 24)*, 22–26 June, 1997, Vancouver, Can, Vol. 13, ASME, New York, NY, p. 6.
[82] Suzuki, T., Mitachi, K., and Fukuda, A., 1998, ''Numerical Analysis of Free Surface Motion Ensuing Burst of Bubble Dome,'' *Proceedings of the 1998 ASME/JSME Joint Pressure Vessels and Piping Conference*, 26–30 July, 1998, San Diego, CA, Vol. 377, ASME, Fairfield, NJ, pp. 235–241.
[83] Fluent Inc., 2003, *Fluent*, Lebanon, NH.
[84] Keenan, J. H., Chao, J., and Kaye, J., 1983, *Gas Tables International Version Thermodynamic Properties of Air Products of Combustion and Component Gases Compressible Flow Functions, Including Those of Ascher H. Shapiro and Gilbert M. Edelman*, Wiley, New York, pp. xvi, 211.
[85] Lee, R. J., DiGuilio, R. M., Jeter, S. M., and Teja, A. S., 1990, ''Properties of Lithium Bromide-Water Solutions at High Temperatures and Concentrations—Part II: Density and Viscosity,'' ASHRAE Trans., **86**, pp. 220–226.
[86] Klein, S. A., and Alvarado, F. L., 2000, *EES-Engineering Equation Solver*, F-Chart Software, www.fchart.com.
[87] Haar, L., Gallagher, J. S., Kell, G. S., and National Standard Reference Data System (U.S.), 1984, *Nbs/Nrc Steam Tables: Thermodynamic and Transport Properties and Computer Programs for Vapor and Liquid States of Water in SI Units*, Hemisphere Washington, D.C., pp. xii, 320.
[88] Kulankara, S., and Herold, K. E., 2002, ''Surface Tension of Aqueous Lithium Bromide With Heat/Mass Transfer Enhancement Additives: The Effect of Additive Vapor Transport,'' Int. J. Refrig., **25**(3), pp. 383–389.
[89] Aris, R., 1962, *Vectors, Tensors, and the Basic Equations of Fluid Mechanics*, Prentice-Hall International Series in the Physical and Chemical Engineering Sciences, Dover 1989 (Prentice-Hall), Englewood Cliffs, N.J., p. 286.
[90] Bird, R. B., Stewart, W. E., and Lightfoot, E. N., 1960, *Transport Phenomena*, Wiley, New York.
[91] Bird, R. B., Stewart, W. E., and Lightfoot, E. N., 2002, *Transport Phenomena*, Wiley, New York, pp. xii, 895.
[92] Tannehill, J. C., Anderson, D. A., and Pletcher, R. H., 1997, *Computational Fluid Mechanics and Heat Transfer*, Series in Computational and Physical Processes in Mechanics and Thermal Sciences, Taylor & Francis, Washington, D.C., p. 792.
[93] Issa, R. I., 1986, ''Solution of the Implicitly Discretised Fluid Flow Equations by Operator-Splitting,'' J. Comput. Phys., **62**(1), pp. 40–65.
[94] Youngs, D. L., 1982, ''Time-Dependent Multi-Material Flow With Large Fluid Distortion,'' in *Numerical Methods for Fluid Dynamics*, K. W. Morton and M. J. Baines, eds., Academic Press, New York.

Numerical Analysis on the Impact Behavior of Molten Metal Droplets Using a Modified Splat-Quench Solidification Model

D. Sivakumar[1]
JSPS Research Fellow
e-mail: siva@paris.ifs.tohoku.ac.jp

H. Nishiyama
Professor,
e-mail: nishiyama@ifs.tohoku.ac.jp

Electromagnetic Intelligent Fluids Laboratory,
Institute of Fluid Science,
Tohoku University,
2-1-1 Katahira, Aoba-ku,
Sendai 980-8577, Japan

A simple model is formulated for the analysis of the spreading and solidification processes of a molten metal droplet impinging on a solid substrate. At the first stage, the model evaluates the diameter and the radial velocity of the spreading molten metal layer at the instant $t_0 = D/W$ from the start of impact using analytical relations. Here D and W are, respectively, the diameter and the velocity of the impinging droplet. Numerical predictions on the evolution of the spreading metal layer are obtained by using a modified splat-quench solidification model with initial conditions described at the instant $t_0 = D/W$. The model predictions are compared with the experimental data available from the literature. A systematic parametric study is carried out to illustrate the model predictions at different impinging conditions. [DOI: 10.1115/1.1833365]

Keywords: Droplet, Heat Transfer, Impingement, Solidification

Introduction

The impact process of a molten metal droplet impinging on a solid substrate surface is encountered in several technological applications such as thermal spray coating [1,2], spray deposition of metal alloys [3], microfabrication [4], and droplet based manufacturing [5,6]. During the impact process, the molten metal spreads out radially over the substrate surface depending on the fluid inertia and simultaneously solidifies due to the contact heat transfer between the metal layer and the substrate surface. For the earlier applications, it is of specific interest to understand the characteristics of metal splats formed from the spreading and solidification of the impinging molten metal droplets. Several experimental and theoretical studies have been carried out in this context, mainly to understand the various physical processes involved in the spreading and solidification of the molten metal droplets [7–20].

Madejski [7] proposed a simple theoretical model to predict the evolution of the droplet spreading and solidification after the impact. The study was aimed at understanding the characteristics of metal oxide splats formed during plasma spray coating. The governing fluid dynamic equation for the droplet spreading was formulated from the principle of energy conservation by treating the solidification process as one-dimensional Stefan solidification problem. In general, the model [7] is versatile from the view of the complex physical processes involved in the deposition process occurring over a short interval of time. Delplanque and Rangel [12] proposed an improved version of the original Madejski model [7] by better predicting the viscous dissipation losses using the flow field suggested by Markworth and Saunders [21]. The evolution of the spreading droplet radius, R was obtained by solving the governing equation numerically, and a systematic parametric study was carried out to illustrate the effect of various physical parameters on the droplet spreading and solidification processes [12]. In the last decade, several detailed models for the impact of molten metal droplets were reported by solving the full Navier–Stokes equations coupled with the energy equation [9,13,14,19]. The numerical predictions for almost all of these models were obtained by employing complex computational fluid dynamics concepts and essentially require a significant amount of computational power to carry out the calculations.

The simplicity of the Madejski model [7] and its improved version proposed by Delplanque and Rangel [12] is mainly attributed to the basic assumptions made in the models. For the estimation of the initial conditions required to solve the governing differential equation, the models assumed that the impinging spherical droplet takes the shape of cylinder immediately after the instant $t = 0$ at which the droplet touches the substrate surface. The initial radius, R_0 was expressed as a fraction of the initial droplet diameter, D, i.e., $R_0 = \epsilon D$, where ϵ is an assumed positive quantity. It must be emphasized that in these models, the initial conditions for the droplet radius and velocity were expressed in terms of ϵ. Madejski [7] assumed $\epsilon = 0.5$ for the derivation of the maximum spreading droplet radius, R_{max} and later, it was shown by Delplanque and Rangel [12] that $\epsilon = 0.74$ is the only physically possible value. However, the comparison of the model predictions with the experimental data was not quite satisfactory and a better agreement was observed for $\epsilon = 0.39$ during the early stages of impact [13]. Note that the parameter ϵ was treated like an arbitrary parameter in these models and any improper selection of ϵ may be affecting the model predictions significantly. Recently, in a technical note [22], the present authors eliminated the assumed parameter ϵ by modeling the initial conditions at the instant, $t_0 = D/W$ from the start of impact, $t = 0$, where D is the diameter and W, the velocity of the impinging metal droplet. An improvement in the numerical results of the modified model was observed when the modified model predictions were compared with those obtained from the earlier model [12].

In the present work, we made substantial modifications in the initial conditions, proposed in our modified model reported earlier [22], by taking into consideration the effects of wettability, solidification, and heat transfer from the molten metal to the substrate surface. We obtained the numerical predictions on the evolution of the spreading droplet radius and compared with the experimental

[1]To whom correspondence should be addressed.

Contributed by the Heat Transfer Division for publication in the JOURNAL OF HEAT TRANSFER. Manuscript received by the Heat Transfer Division December 10, 2003; revision received July 23, 2004. Associate Editor: C. Amon.

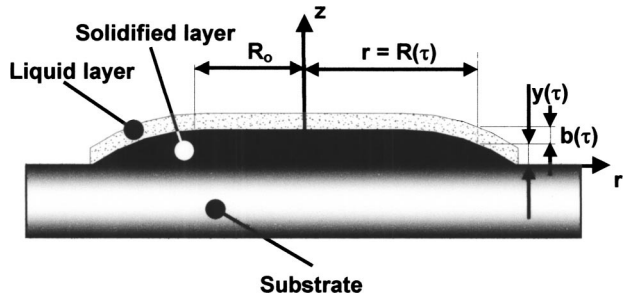

Fig. 1 Schematic sketch of the spreading droplet during the impact process

data reported in the literature. In order to show the features of the modified model, we carried out a parametric study and emphasized the model limitations.

Mathematical Model

Droplet Spreading and Solidification. Consider a molten metal droplet of diameter, D impinging on a substrate surface with velocity, W along the normal to the surface. Figure 1 shows the schematic sketch of the metal droplet spreading over the substrate surface. The governing differential equation for the droplet spreading based on the conservation of mechanical energy is expressed as [12,22]

$$\frac{d}{dt}\left\{\frac{3}{10}\rho_l\left(\frac{dR}{dt}\right)^2\left(R^2 b+\frac{11}{7}b^3\right)+\sigma[R^2(1-\cos\theta)+2Rb]\right\}+\frac{\mu R^2}{b}\left(\frac{dR}{dt}\right)^2\left[\frac{3}{2}+\frac{72}{5}\frac{b^2}{R^2}\right]=0, \quad (1)$$

where R is the radius, b is the liquid layer thickness, and θ is the dynamic contact angle of the spreading molten metal layer at any time t. Here ρ_1 is the density, σ is the surface tension, and μ is the viscosity of the droplet material. Note that the effect of capillary forces on the droplet spreading was not considered in the earlier formulation shown by Delplanque and Rangel [12]. However, the role of capillary forces is dominant in the spreading process for the droplet impact with low Weber number (Weber number, We, is defined as the ratio of inertial to surface tension forces of the impinging droplet). Even for the impact of high We droplets, the capillary forces at the contact line become important during the end of the spreading process where the inertial forces are comparable to the capillary forces.

The energy conservation equation [Eq. (1)] is nondimensionalized by using the variables $\xi=R/R_0$, $\phi=b/R_0$, and $\tilde{t}=Wt/R_0$, where R_0 is the radius of the spreading metal liquid layer at the instant $t_0=D/W$. Figure 2 shows the shape of the spreading droplet assumed in the present model at the instant $t_0=D/W$. As illustrated in the figure, it is assumed in the present study that the impinging droplet takes the shape of cylinder after the time $t_0=D/W$. This assumption may be justified from the experimental observations reported in the literature for the impact of droplets with We$\gg$1 [10,23–27]. The spreading droplet radius, R_0 can be estimated from the conservation of mass as

$$R\left(t=\frac{D}{W}\right)=R_0=\left[\frac{D^3}{6(b_0+y_0)}\right]^{1/2} \quad (2)$$

where b_0 is the thickness of the molten metal layer and y_0 is the thickness of the solidified metal layer at the instant $t_0=D/W$. Note that the variation in density between the liquid layer and the solidified metal layer is ignored in Eq. (2). After nondimensionalization, Eq. (1) becomes

$$\frac{d}{d\tilde{t}}\left[\frac{3}{10}\left(\frac{d\xi}{d\tilde{t}}\right)^2\phi\left(\xi^2+\frac{11}{7}\phi^2\right)+\frac{\sqrt{6\bar{b}_0}}{\mathrm{We}}\xi(\xi(1-\cos\theta)+2\phi)\right]+\frac{\sqrt{\bar{b}_0}}{\mathrm{Re}}\frac{\xi^2}{\phi}\left(\frac{d\xi}{d\tilde{t}}\right)^2\left(\sqrt{\frac{27}{2}}+\frac{72\sqrt{6}}{5}\frac{\phi^2}{\xi^2}\right)=0 \quad (3)$$

where

$$\phi=\frac{\sqrt{6}(\bar{b}_0)^{3/2}}{\xi^2}\left\{1-K\left[\sqrt{\tilde{t}}+2\int_0^{\tilde{t}}\xi(t)\frac{d\xi(t)}{dt}\sqrt{(\tilde{t}-t)}dt\right]\right\}, \quad (4)$$

$$K=\frac{\rho}{\rho_1}U\sqrt{\frac{1}{6^{1/2}\,\mathrm{Pe}(\bar{b}_0)^{5/2}}}, \quad (5)$$

and

$$\bar{b}_0=\frac{b_0+y_0}{D} \quad (6)$$

Here K is the solidification parameter, U, the solidification constant, ρ, the density of the solidified metal layer, and Pe $=WD/\alpha$, the Peclet number with α as the thermal diffusivity of the droplet material.

Initial Conditions. The numerical predictions on the evolution of the spreading droplet radius (R) can be obtained by solving Eqs. (3)–(6) with appropriate initial conditions. In the present work, the initial conditions are modeled at the instant $t_0=D/W$ from the start of impact $t=0$. Therefore the initial radius is taken as R_0 and expressed by using Eqs. (2) and (6) as

$$R(t_0)=R_0=\left(\frac{D^2}{6\bar{b}_0}\right)^{1/2} \quad (7)$$

The term $\bar{b}_0$ is estimated by solving the equation for the axial momentum conservation of an impinging droplet proposed recently by Roisman et al. [28]. In their work, for a given droplet Reynolds number, Re$=\rho_1 WD/\mu$ and We$=\rho_1 W^2 D/\sigma$, the equation for the axial momentum conservation was expressed as

$$3\mathrm{We}+5(1-\cos\bar{\theta})\mathrm{Re}\,\bar{b}_0=10\,\mathrm{Re}\,\mathrm{We}\,\bar{b}_0^3 \quad (8)$$

where $\bar{\theta}$ is an average estimation of the dynamic contact angle of the spreading metal layer in the time interval $[0,D/W]$. Note that Eq. (8) was derived from the pressure distribution developed by the spreading liquid during the impact of liquid droplets, which are free from any solidification process. In the context of molten metal droplets studied in the present work, it is assumed that the solidification process occurring within the short interval of time $[0,D/W]$ during the beginning of impact process may not be altering the flow characteristics within the molten liquid layer significantly. In other words, the droplet spreading process is assumed to be faster than the solidification process and such an assumption may be justifiable if $y_0\ll b_0$. Based on this fact, the

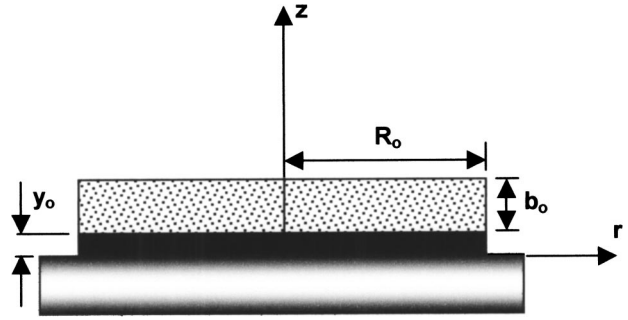

Fig. 2 The shape of the spreading droplet at the instant $t_0=D/W$ from the start of impact $t=0$

effect of solidification on Eq. (8) is ignored in the present study, and therefore the present model may be appropriate for the slow solidification problems.

The thickness of the solidified metal layer, y is estimated from the Neumann solution of the one-dimensional Stefan problem as

$$y = U\sqrt{\alpha t} \tag{9}$$

The thickness of the solidified metal layer at the instant $t_0 = D/W$ is estimated by using Eq. (9) as

$$y\left(t=\frac{D}{W}\right)=y(t_0)=y_0=U\sqrt{\alpha\frac{D}{W}}=\left(\frac{U}{\sqrt{\mathrm{Pe}}}\right)D \tag{10}$$

The initial thickness of the liquid metal layer at $t_0 = D/W$ is expressed by including the solidification process as

$$b\left(t=\frac{D}{W}\right)=b(t_0)=b_0=D\left(\overline{b_0}-\frac{U}{\sqrt{\mathrm{Pe}}}\right) \tag{11}$$

In the absence of solidification process, the value of U is taken as zero and b_0 is expressed only as a function of $\overline{b_0}$.

The initial radial velocity $(dR/dt)_{t=t_0}$ is derived by equating the kinetic energy equation for the spreading droplet at any time to the kinetic energy of the spreading liquid layer estimated at the instant $t_0 = D/W$. The kinetic energy, E_k for the spreading droplet shown in Fig. 1 is expressed as [12,22]

$$E_k=\frac{3}{10}\pi\rho_1\left(\frac{dR}{dt}\right)^2\left(R^2b+\frac{11}{7}b^3\right) \tag{12}$$

The principle of energy conservation at the instant $t_0 = D/W$ can be written as

$$\{[\mathrm{KE}+\mathrm{PE}]_{\mathrm{liquid}}+[\text{Energy due to wetting}]+[\mathrm{KE}+\text{Viscous dissipation}]_{\mathrm{losses}}\}_{t_0=D/W}=\{[\mathrm{KE}+\mathrm{PE}]_{\mathrm{liquid}}\}_{t=0} \tag{13}$$

The initial kinetic and potential energies of the impinging droplet are estimated as

$$\{(\mathrm{KE})_{\mathrm{liquid}}\}_{t=0}=\left(\frac{\pi D^3}{6}\right)\left(\frac{1}{2}\rho_1W^2\right) \tag{14}$$

and

$$\{(\mathrm{PE})_{\mathrm{liquid}}\}_{t=0}=\sigma(\pi D^2) \tag{15}$$

At the instant $t_0 = D/W$,

$$\{[\mathrm{KE}]_{\mathrm{liquid}}\}_{t_0=D/W}=E_k\left(t=\frac{D}{W}\right)=\frac{3}{10}\left(\frac{dR}{dt}\right)^2_{t=t_0}\left(R_0^2b_0+\frac{11}{7}b_0^3\right), \tag{16}$$

$$\{[\mathrm{PE}]_{\mathrm{liquid}}\}_{t_0=D/W}=\sigma(\pi R_0^2+2\pi R_0b_0), \tag{17}$$

and

$$\{[\mathrm{KE}]_{\mathrm{losses}}\}_{t_0=D/W}=(\pi R_0^2y_0)\left(\frac{1}{2}\rho_1W^2\right)=\pi\rho_1W^2D^3\left(\frac{U}{12\overline{b_0}\sqrt{\mathrm{Pe}}}\right) \tag{18}$$

The total viscous dissipation encountered by the spreading droplet liquid during the time interval $[0,D/W]$ can be calculated from

$$\{[\text{Viscous dissipation}]_{\mathrm{losses}}\}_{t_0=D/W}=\int_0^{D/W}\int_0^{R_0}\int_0^{b_0}2\pi r\Phi\,dr \tag{19}$$

where Φ is the dissipation function described by the flow field [12]. By following the procedure adopted by Roisman et al. [28], the viscous dissipation losses is expressed as

$$\{[\text{Viscous dissipation}]_{\mathrm{losses}}\}_{t_0=D/W}=\pi\rho_1D^3W^2\frac{1}{\mathrm{Re}}\left(\frac{1}{20\overline{b_0^3}}+\frac{3}{5\overline{b_0}}\right) \tag{20}$$

As the present work considers that the effect of solidification on the flow field of the spreading metal layer is negligible in the time interval $[0,D/W]$, no attempt is made here to modify the viscous dissipation losses for the solidification process. The energy due to wetting can be written based on the contact angle of the moving contact line of the spreading metal layer as

$$[\text{Energy due to wetting}]_{t_0=D/W}=\sigma(\pi R_0^2\cos\theta) \tag{21}$$

By substituting Eqs. (14)–(21) in Eq. (13), the kinetic energy of the spreading droplet at the instant $t_0 = D/W$ is expressed as

$$E_k\left(t=\frac{D}{W}\right)=E_{k0}=\Lambda(\overline{b_0},\mathrm{Re},\mathrm{We},\mathrm{Pe},U,\theta)\left(\frac{\pi\rho_1D^3W^2}{12}\right) \tag{22}$$

where

$$\Lambda=1+\frac{12}{\mathrm{We}}-\frac{3}{5\,\mathrm{Re}}\left(\frac{1}{\overline{b_0^3}}+\frac{12}{\overline{b_0}}\right)-\frac{2(1-\cos\theta)}{\mathrm{We}\overline{b_0}}-\frac{1}{\mathrm{We}}\sqrt{\frac{96\overline{b_0}}{D}}-\frac{U}{\overline{b_0}\sqrt{\mathrm{Pe}}}. \tag{23}$$

By comparing Eq. (22) with Eq. (16), the initial average spreading velocity is expressed as

$$\frac{dR}{dt}\left(t=\frac{D}{W}\right)=\left(\frac{dR}{dt}\right)_0=W\left\{\frac{\frac{5}{3}\Lambda}{\left[1-\frac{U}{\overline{b_0}\sqrt{\mathrm{Pe}}}\right]\left[1+\frac{66}{7}\overline{b_0^3}\left(1-\frac{U}{\overline{b_0}\sqrt{\mathrm{Pe}}}\right)^2\right]}\right\}^{1/2} \tag{24}$$

The nondimensionalized initial conditions are expressed as

$$\tilde{t}\left[t=\frac{D}{W}\right]=\tilde{t}_0=\sqrt{6\overline{b_0}}, \tag{25}$$

$$\xi(\tilde{t}_0)=\xi_0=1.0, \tag{26}$$

$$\phi(\tilde{t}_0)=\phi_0=\sqrt{6\overline{b_0}}\left(\overline{b_0}-\frac{U}{\sqrt{\mathrm{Pe}}}\right), \tag{27}$$

and

$$\frac{d\xi}{d\tilde{t}}(\tilde{t}_0)=\left(\frac{d\xi}{d\tilde{t}}\right)_0=\left\{\frac{\frac{5}{3}\Lambda}{\left[1-\frac{U}{\overline{b_0}\sqrt{\mathrm{Pe}}}\right]\left[1+\frac{66}{7}\overline{b_0^3}\left(1-\frac{U}{\overline{b_0}\sqrt{\mathrm{Pe}}}\right)^2\right]}\right\}^{1/2} \tag{28}$$

The nondimensional governing differential equation, Eq. (3) can be solved numerically by using the initial conditions given in Eqs. (25)–(28) to obtain the evolution of R during the impact process.

Estimation of Solidification Constant. This section provides the details about the procedure adopted in the present work for the estimation of the solidification constant, U used in the Neumann solution given in Eq. (9). A realistic model for the impact of a molten metal droplet on a cold substrate must include the heat transfer process at the interface between the spreading metal layer and the substrate surface. The heat transfer influences the instantaneous movement of the solidification front of the spreading

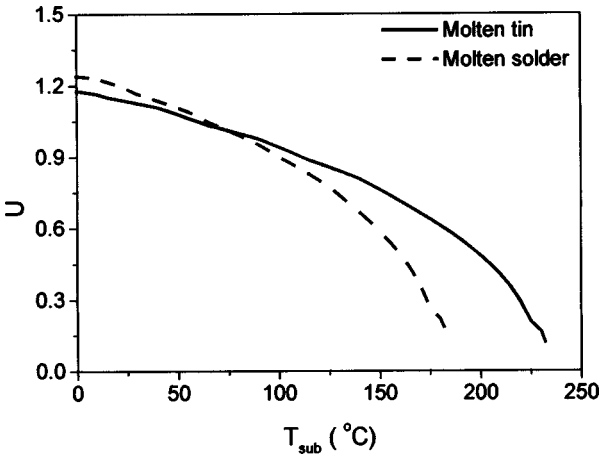

Fig. 3 The variation of solidification constant (*U*) with the substrate surface temperature for different molten metals

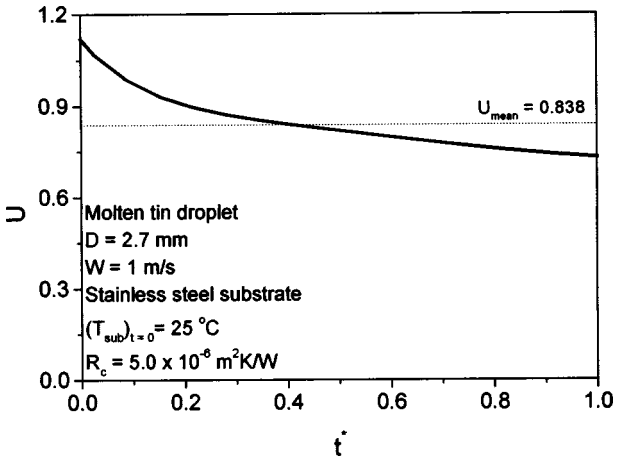

Fig. 4 The instantaneous variation of the solidification constant (*U*) during the droplet impact process for a molten tin droplet impinging on a stainless steel substrate

droplet depending on the contact between the droplet material and the substrate surface. A limited number of experimental investigations have been reported in the literature to show the variation of the droplet and the substrate temperature during the impact process [25,29,30]. Among them, Aziz and Chandra [25] provided the experimental data on the variation of the thermal contact resistance during the droplet spreading process for the molten tin droplets impinging on a stainless steel substrate with W in the range of 1–4 m/s. Their experimental results clearly show a strong correlation between the heat transfer process and the impinging droplet velocity, W.

In the present work, the instantaneous variation of the substrate surface temperature, T_{sub} during the impact process is evaluated by using the expression [31]

$$T_{\text{sub}}=(T_{\text{sub}})_{t=0}+[T_d-(T_{\text{sub}})_{t=0}] \times\left[1-\exp\left(\frac{\alpha_{\text{sub}}t}{R_c^2\lambda_{\text{sub}}^2}\right)\text{erfc}\left(\frac{\sqrt{\alpha_{\text{sub}}t}}{R_c\lambda_{\text{sub}}}\right)\right] \tag{29}$$

where T_d is the temperature of the droplet material, α_{sub} and λ_{sub}, respectively, are the thermal diffusivity and thermal conductivity of the substrate material and R_c is the thermal contact resistance between the droplet material and the substrate surface. Aziz and Chandra [25] showed that the experimental data on the instantaneous variation of T_{sub} obtained during the impact process agree with the predictions of Eq. (29). The solidification constant, U is calculated by solving the equation

$$\text{St}=\sqrt{\pi}\left(\frac{U}{2}\right)\text{erf}\left(\frac{U}{2}\right)\exp\left(\frac{U^2}{4}\right) \tag{30}$$

where $\text{St}=[C_p(T_m-T_{\text{sub}})]/h_{\text{f}}$ is the Stefan number. C_p, h_f, and T_m are, respectively, the specific heat, the latent heat of fusion, and the melting temperature of the droplet material. Equation (30) is the simplified expression, obtained by taking the droplet temperature as same as the melting temperature of the droplet material, of the original relation present in the Neumann solution of the classical Stefan solidification problem. Figure 3 shows the variation of U with T_{sub} for different droplet materials. Note also that Eq. (30) is based on the assumption that the liquid phase is stagnant and, hence, the convection effect of the liquid phase on the solidification process is ignored from the analysis. Apart from the variation of U with of T_{sub}, it is also seen from Fig. 3 that the droplet material influences the variation of U. For the current calculations, the instantaneous value of T_{sub}, calculated from Eq. (29), is used to evaluate the instantaneous variation of U from Eq. (30). Figure 4 shows the typical variation of U, resulting from the variation of T_{sub}, with $t^*(=tW/D)$ during the impact process of a molten tin droplet with $D=2.7$ mm and $W=1$ m/s on a stainless steel substrate with $(T_{\text{sub}})_{t=0}=25°\text{C}$. The value of R_c for this specific case is taken as 5.0×10^{-6} m^2 K/W from the experimental measurements reported by Aziz and Chandra [25]. An average value of U is calculated within the time interval $[0,D/W]$ for the estimation of initial conditions. The value of U estimated at the instant $t_0=D/W$ is considered as the solidification constant for the calculation of R starting from the instant $t_0=D/W$. This procedure is used for all the droplet impact calculations reported in this work. Note that the original Madejski model [7] and its improved version proposed by Delplanque and Rangel [12] had not considered the instantaneous variation of U in their calculations.

Results and Discussion

The governing differential equation and the initial conditions are solved numerically by using Euler predictor-corrector numerical scheme. The relevant nondimensional numbers, required for the computation, are obtained from the impinging droplet conditions (D and W) and the material properties. Tables 1 and 2 show the material properties for the droplet and the substrates used in the calculation. The dynamic contact angle, θ, is taken from the experimental data reported in the literature. The value of U is estimated via the procedure described in the previous section. The predictions are made until the radial velocity of the spreading

Table 1 Thermophysical properties of the droplet material used in the calculations

Reference publications (Droplet—molten tin)	ρ (kg/m^3)	ρ_1 (kg/m^3)	σ (N/m)	μ (kg/ms)	α (m^2/s)
Pasandideh-Fard et al. [14] Aziz and Chandra [25] Trapaga et al. [32] Amada et al. [33]	7310	7000	0.544	0.00184	1.714×10^{-5}
	7310	6957	0.566	0.00197	1.714×10^{-5}

Table 2 Thermophysical properties of the substrates used in the calculations

Reference publications	ρ (kg/m^3)	λ (W/mK)	α (m^2/s)
Pasandideh-Fard et al. [14] (Stainless steel)	7900	15	3.98×10^{-6}
Aziz and Chandra [25] (Stainless steel)			
Amada et al. [33] (Stainless steel)			
Trapaga et al. [32] (Aluminum)	2702	237	9.71×10^{-5}

droplet approaches to zero, and for all the calculations, it is ensured that the radial velocity of the spreading droplet is converging to zero.

Comparison of the Model Predictions With the Experimental Measurements. The model predictions on the time evolution of the spreading droplet radius (R) for the impact of molten tin droplets on a stainless steel substrate, kept at different $(T_{sub})_{t=0}$, are shown in Fig. 5. The experimental measurements on the instantaneous variation of R are taken from Ref. [14]. The plots also included the reported numerical results of R calculated from the detailed model proposed by Pasandideh-Fard et al. [14]. The experimental values of thermal contact resistance (R_c) for the present calculation are taken from the experimental study reported by Aziz and Chandra [25]. As seen in the figure, the present numerical predictions are in agreement with the experimental data and slightly over predicting the values of R. It must be emphasized that the present model calculations are simple, and an extensive calculation procedure may be involved in the detailed model proposed by Pasandideh-Fard et al. [14] which takes a CPU time of the order 2–5 h in a workstation for a typical droplet impact case. The numerical predictions of R obtained from Delplanque and Rangel model [12], an improved version of the original Madejski model [7], are far deviated from the experimental data as shown in Fig. 5(*b*).

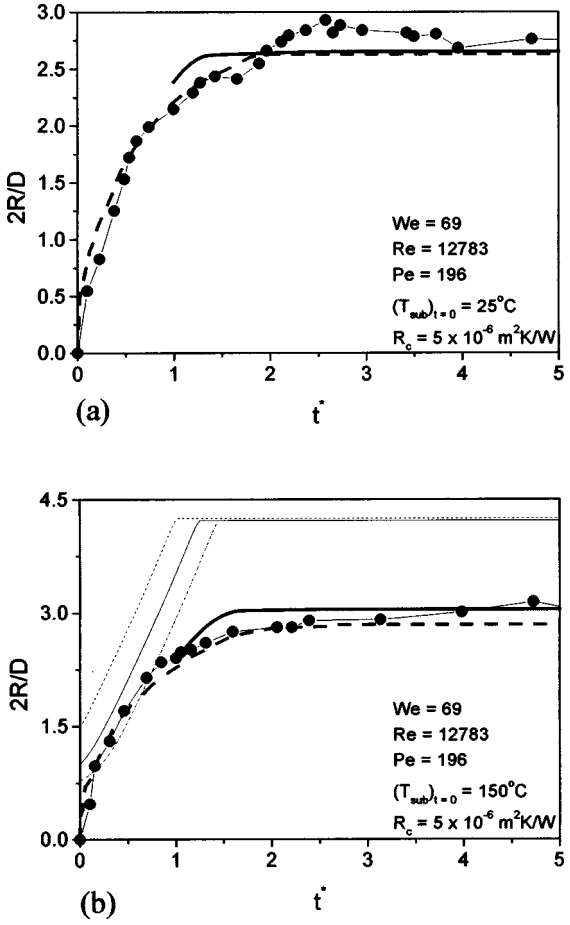

Fig. 5 Comparison of the present model results with the experimental measurements for the evolution of the spreading droplet radius for the impact of molten tin droplets impinging on stainless steel substrates kept at different temperature. The experimental measurements, shown with filled circles (●), are taken from Ref. [14]. The numerical predictions of Pasandideh-Fard et al. model, shown with thick dashed lines (– – –), are taken from Ref. [14], and the predictions obtained from the present model are shown with thick continuous lines (—). The predictions of Delplanque and Rangel model [12] for different values of ϵ are shown with thin lines. ϵ=0.39 (–·–·), ϵ=0.5 (——), and ϵ=0.74 (— — —).

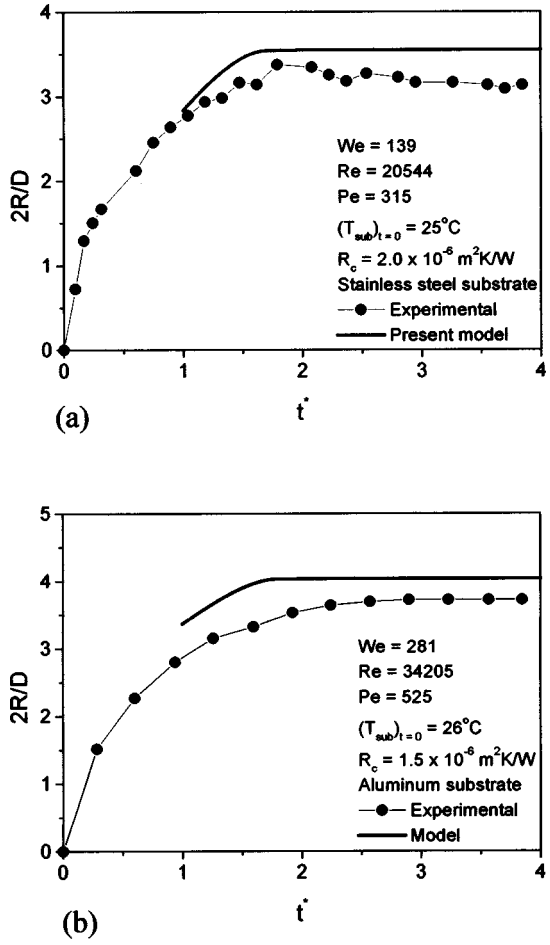

Fig. 6 Comparison of the present model results with the experimental measurements on the evolution of the spreading droplet radius for the impact of molten tin droplets on different substrate materials. The experimental measurements are taken from the literature. (*a*) Aziz and Chandra [25], and (*b*) Tarpaga et al. [32].

Additional calculations are made for the impact of molten tin droplets studied experimentally by different researchers [25,32,33]. The relevant material properties of molten tin are taken from the corresponding references and summarized in Table 1. The value of dynamic contact angle is kept constant during the present calculations and taken as 150° based on the experimental results [14,25,34]. Figure 6 shows the present model predictions on the instantaneous variation of R for the molten tin droplets impinging on metal substrates with different impact conditions. In

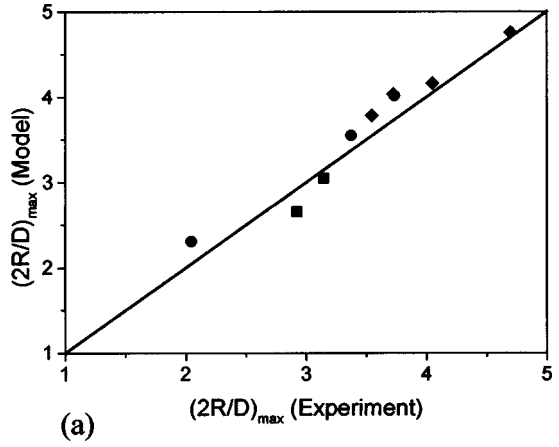

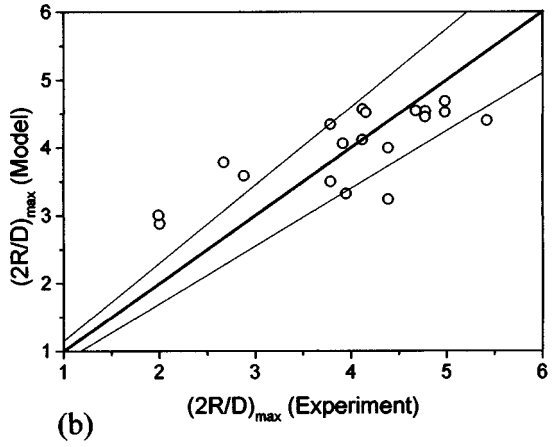

Fig. 7 The present model predictions on R_{max} for the impact of molten tin droplets on stainless substrate surfaces. (*a*) ■ Pasandideh-Fard et al. [14], ● Aziz and Chandra [25], and ♦ Trapaga et al. [32]. (*b*) ○ Amada et al. [33].

general, the model predictions of R are in agreement with the experimental data, both qualitatively and quantitatively. Further results obtained from the calculations are summarized in Fig. 7 by comparing the model predictions of R_{max} with the experimentally measured values. A total of 29 experiments carried out by different investigators [14,25,32,33] are shown in Fig. 7. By following the experimental results reported by Aziz and Chandra [25], the value of R_c is kept in the range 1.0×10^{-6} to 5.0×10^{-6} m^2 K/W for these calculations. Note that the data points shown in Fig. 7(*b*) are taken from the work reported by Amada et al. [33]. Their work had concentrated only on the final metal splat characteristics and no measurements on the instantaneous variation of R were reported. For their experiments, the model predictions of R_{max} are dispersed within $\pm15\%$ variation as shown by the thin lines in Fig. 7(*b*).

Discussion on the Model Features. In literature, four major regimes of the droplet impact are identified based on the droplet Ohnesorge number, Oh$=\mu/\sqrt{\rho_1\sigma D}$ and We: (1) inviscid and impact driven, (2) inviscid and capillarity driven, (3) highly viscous and capillarity driven, and (4) highly viscous and impact driven [11]. The fluid dynamics and heat transfer analysis of the spreading droplet liquid are different for each of these regimes. The values of Oh and We for the droplet impact cases shown in Fig. 7 are plotted in Fig. 8 by following the Oh-We diagram discussed earlier by Schiaffino and Sonin [11]. It may be stated from the

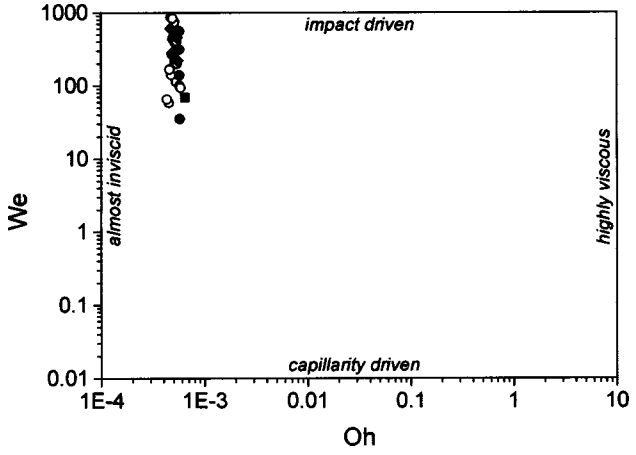

Fig. 8 Oh-We diagram showing the droplet impact cases analyzed in the present study

results shown in Figs. 5–8 that the present model can be successfully used for the impact of metal droplets confined to the inviscid impact driven regime.

The major limitation of the present model is that the initial conditions are modeled at the instant $t_0=D/W$ from the start of

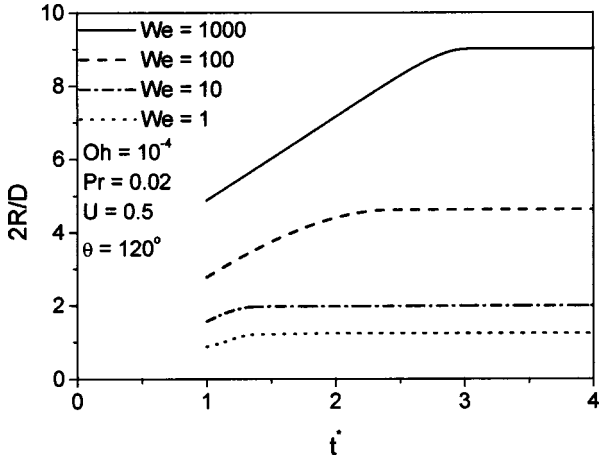

Fig. 9 Numerical predictions on the instantaneous variation of *R* for the impact of molten metal droplets with varying We

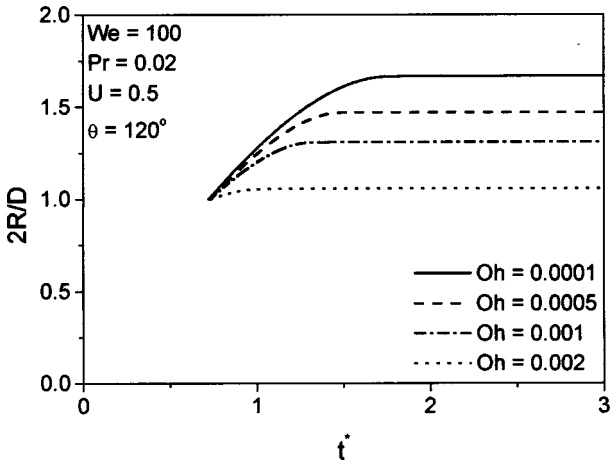

Fig. 10 Numerical predictions on the instantaneous variation of *R* for the impact of molten metal droplets with varying Oh

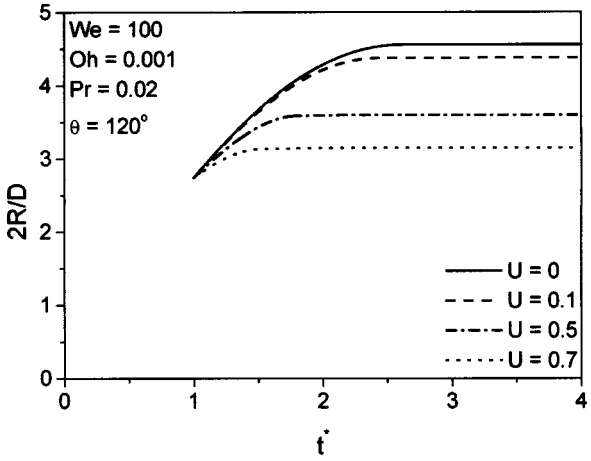

Fig. 11 Numerical predictions on the instantaneous variation of *R* for the impact of molten metal droplets with varying *U*

impact. The model fails if the nondimensional term, Λ, present in the initial radial velocity relation given in Eq. (24), becomes negative. The negative value of Λ basically indicates that the spreading metal layer reaches R_{max} before the instant $t_0 = D/W$. This feature of the present model restricts the model application for the droplet impact with low We as illustrated in Fig. 9. For these calculations, the value of Prandtl number, Pr is taken as 0.02, a typical value for

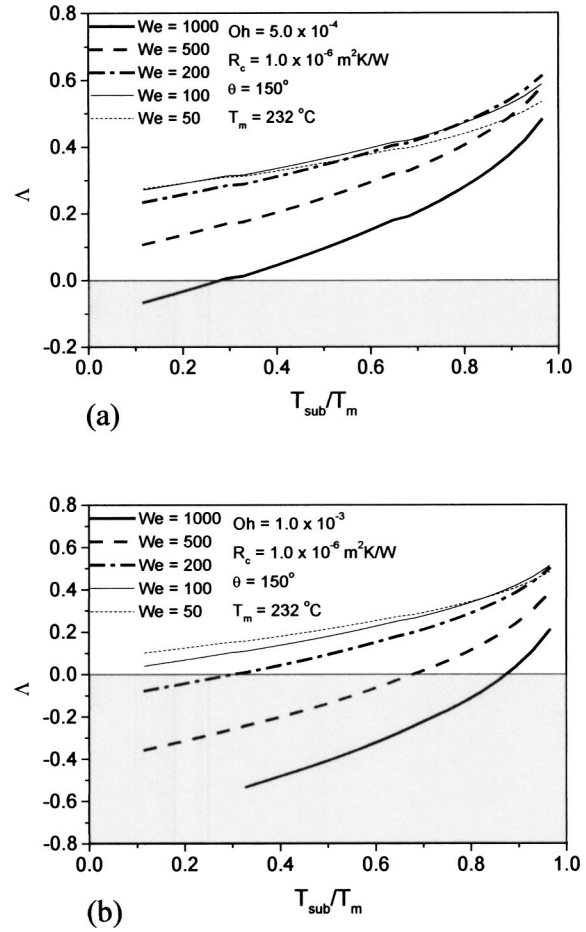

Fig. 12 Plots illustrating the limitations of the present model for the impact of molten tin droplets with different impinging conditions

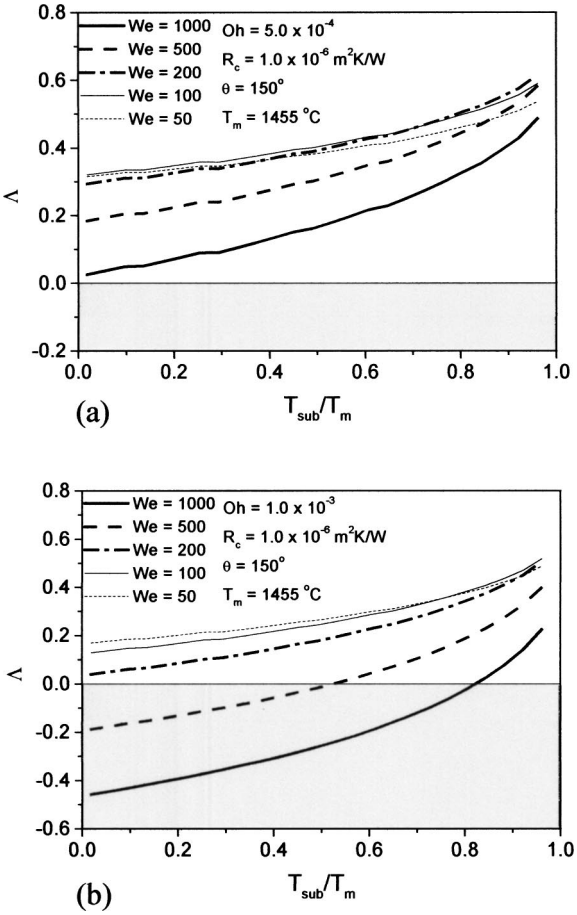

Fig. 13 Plots illustrating the limitations of the present model for the impact of molten nickel droplets with different impinging conditions

liquid metals. Note that the choice of $U = 0.5$ for the calculations shown in Fig. 9 indicates that the effect of solidification may be significant. For the droplet impact with We<1, the complete kinetic energy may be transformed into the surface energy of the spreading liquid layer before reaching the instant $t_0 = D/W$. Similar results are shown in Fig. 10 for the droplet impact with varying Oh. As Oh increases, the contribution of viscous dissipation dominates the energy losses of the spreading metal layer. Figure 11 shows the model predictions for the droplet impact with varying *U*. In this case, the energy loss may be influenced by the amount of liquid mass solidified before reaching the instant $t_0 = D/W$, whose contribution to Λ increases with increasing *U*.

It is evident from Eqs. (29) and (30) that the thermophysical properties of the droplet material and the substrate play a dominant role in determining the solidification constant, *U*. A parametric study is carried out to investigate the model application for different droplet materials. Figure 12 shows the applicability of the present model at different impinging droplet conditions for the molten tin droplets impinging on a stainless steel substrate. For each impinging droplet case (each data point) shown in Fig. 12, the value of *U* is estimated as described before by assuming a typical value for R_c. The shaded portion (negative Λ) shown in the plots corresponds to the droplet impinging conditions at which the present model is not applicable. As seen in the figure, with molten tin as the droplet material, the model can be fairly used for a wide range of impinging conditions. As Oh increases, the applicability of the present model shrinks as shown in Fig. 12(*b*). Similar results are shown in Fig. 13 for molten nickel, a high melting point material. Additional calculations are made for other metals

and the observed trend is similar to the variation shown in Figs. 12 and 13, however, with a shift in the shaded regions.

It can be observed from Figs. 7–13 that the present model can be successfully used for the droplet impact falls under the inviscid impact-driven regime with moderate solidification constant values. Any extension of the present model to other regimes shown in Fig. 8 may require necessary modifications in Λ given in Eq. (23). It must be emphasized that the present modified model has ignored the detailed physical processes involved in the impact process. These processes may include the effect of compressibility developed during the impact of a high speed droplet [35] and freezing of the contact line observed during the impact of molten metal droplets with low We [36].

Conclusions

A numerical analysis is carried out on the evolution of the spreading molten metal layer developed from the impact of a molten metal droplet on a solid substrate by formulating a simple theoretical model. The salient feature of this model is the initial conditions proposed to solve the governing differential equation describing the spreading and solidification processes of the molten metal layer. The initial conditions are modeled at the instant $t_0 = D/W$ from the start of impact. The contact heat transfer process between the droplet and the substrate surface is included in the estimation of the initial conditions by using the experimental measurements of the thermal contact resistance.

Numerical results are presented for the impact of molten tin droplets with varying impact conditions. The experimental data available from the literature are used to compare the model predictions. The predictions on the instantaneous variation of the spreading droplet radius are in agreement with the experimental measurements. The numerical values of the maximum spreading radius for different droplet impact experiments are dispersed over the experimental line within $\pm 15\%$ variation. It is shown that the present model may be more suitable for the metal droplet impact confining to the impact-driven regime with low Oh number.

Acknowledgment

This research has been supported by Japan Society for the Promotion of Science (JSPS) during the academic year 2003–2004.

Nomenclature

b = liquid layer thickness of the spreading droplet (m)
C_p = specific heat (J/kg K)
D = diameter of droplet before impact (m)
E_k = kinetic energy of spreading droplet (J)
h_f = latent heat of fusion (J/kg)
K = solidification parameter
Oh = Ohnesorge number
Pe = Peclet number
Pr = Prandtl number
R = radius of spreading droplet (m)
R_c = thermal contact resistance (m^2 K/W)
Re = Reynolds number
r = radial coordinate
St = Stefan number
T_{sub} = substrate temperature (K)
T_m = melting temperature of droplet material (K)
t = time (s)
$\tilde{t}$ = nondimensionalized time
t^* = nondimensionalized time based on impinging droplet parameters
U = solidification constant
W = droplet impact velocity (m/s)
We = Weber number
y = thickness of solidified metal layer (m)
z = normal coordinate

Greek Letters

α = thermal diffusivity (m^2/s)
Λ = nondimensionalized term used in the kinetic energy equation
ϵ = nondimensional quantity used in the estimation of initial radius
σ = surface tension (N/m)
μ = viscosity (kg/ms)
ρ_1 = density of liquid (kg/m^3)
θ = dynamic contact angle (deg)
θ_s = static contact angle (deg)
ϕ = nondimensionalized liquid layer thickness
τ = time at which freezing begins at any radial location
ξ = nondimensionalized radius of spreading droplet

Subscripts

max = maximum spread condition
sub = substrate
0 = initial condition

References

[1] Pawlowski, L., 1995, *The Science and Engineering of Thermal Spray Coatings*, Wiley, New York.
[2] Cheng, D., Trapaga, G., McKelliget, J. W., and Lavernia, E. J., 2003, "Mathematical Modeling of High Velocity Oxygen Fuel Thermal Spraying of Nanocrystalline Materials: An Overview," Modell. Simul. Mater. Sci. Eng., **11**, pp. R1–R31.
[3] Lavernia, E. J., and Wu, Y., 1996, *Spray Atomization and Deposition*, Wiley, United Kingdom.
[4] Gao, F., and Sonin, A. A., 1994, "Precise Deposition of Molten Micro-Drops: The Physics of Digital Microfabrication," Proc. R. Soc. London, Ser. A, **444**, pp. 533–554.
[5] Amon, C. H., Schmaltz, K. S., Merz, R., and Prinz, F. B., 1996, "Numerical and Experimental Investigation of Interface Bonding Via Substrate Remelting of an Impinging Molten Metal Droplet," ASME J. Heat Transfer, **118**, pp. 164–172.
[6] Orme, M. F., and Smith, R. F., 2000, "Enhanced Aluminum Properties by Means of Precise Droplet Deposition," ASME J. Manuf. Sci. Eng., **122**, pp. 484–493.
[7] Madejski, J., 1976, "Solidification of Droplets on a Cold Surface," Int. J. Heat Mass Transfer, **19**, pp. 1009–1013.
[8] Bennet, T., and Poulikakos, D., 1993, "Splat-Quench Solidification: Estimating the Maximum Spreading of a Droplet Impacting on a Solid Surface," J. Mater. Sci., **28**, pp. 963–970.
[9] Zhao, Z., Poulikakos, D., and Fukai, J., 1996, "Heat Transfer and Fluid Dynamics During the Collision of a Liquid Droplet on a Substrate—I. Modeling," Int. J. Heat Mass Transfer, **39**, pp. 2771–2789.
[10] Zhao, Z., Poulikakos, D., and Fukai, J., 1996, "Heat Transfer and Fluid Dynamics During the Collision of a Droplet on a Substrate—II. Experiments," Int. J. Heat Mass Transfer, **39**, pp. 2791–2802.
[11] Schiaffino, S., and Sonin, A. A., 1997, "Molten Metal Deposition and Solidification at Low Weber Numbers," Phys. Fluids, **9**, pp. 3172–3187.
[12] Delplanque, J. P., and Rangel, R. H., 1997, "An Improved Model for Droplet Solidification on a Flat Surface," J. Mater. Sci., **32**, pp. 1519–1530.
[13] Delplanque, J. P., and Rangel, R. H., 1998, "A Comparison of Models, Numerical Simulation, and Experimental Results in Droplet Deposition Processes," Acta Mater., **46**, pp. 4925–4933.
[14] Pasandideh-Fard, M., Chandra, S., Bhola, R., and Mostaghimi, J., 1998, "Deposition of Tin Droplets on a Steel Plate: Simulations and Experiments," Int. J. Heat Mass Transfer, **41**, pp. 2929–2945.
[15] Zarzalejo, L. J., Schmaltz, K. S., and Amon, C. H., 1999, "Molten Droplet Solidification and Substrate Remelting in Microcasting Part I: Numerical Modeling and Experimental Verification," Heat Mass Transfer, **34**, pp. 477–485.
[16] Schmaltz, K. S., Zarzalejo, L. J., and Amon, C. H., 1999, "Molten Droplet Solidification and Substrate Remelting in Microcasting Part II: Parametric Study and Effect of Dissimilar Materials," Heat Mass Transfer, **35**, pp. 17–23.
[17] Attinger, D., Zhao, Z., and Poulikakos, D., 2000, "An Experimental Study of Molten Microdroplet Surface Deposition and Solidification: Transient Behavior and Wetting Angle Dynamics," ASME J. Heat Transfer, **122**, pp. 544–556.
[18] Wan, Y. P., Zhang, H., Jiang, X. Y., Sampath, S., and Prasad, V., 2001, "Role of Solidification, Substrate Temperature and Reynolds Number on Droplet Spreading in Thermal Spray Deposition: Measurements and Modeling," ASME J. Heat Transfer, **123**, pp. 382–389.
[19] Pasandideh-Fard, M., Chandra, S., and Mostaghimi, J., 2002, "A Three-Dimensional Model of Droplet Impact and Solidification," Int. J. Heat Mass Transfer, **45**, pp. 2229–2242.
[20] Yang, Y.-S., Kim, H.-Y., and Chun, J.-H., 2003, "Spreading and Solidification of a Molten Microdrop in the Solder Jet Pumping Process," IEEE Trans. Compon., Packag. Manuf. Technol., **26**, pp. 215–221.
[21] Markworth, A. J., and Saunders, J. H., 1992, "An Improved Velocity Field for

the Madejski Splat-Quench Solidification Model,'' Int. J. Heat Mass Transfer, **35**, pp. 1836–1837.
[22] Sivakumar, D., and Nishiyama, H., 2004, ''Analysis of Madejski Splat-Quench Solidification Model With Modified Initial Conditions,'' ASME J. Heat Transfer, **126**, pp. 485–489.
[23] Fukai, J., Shiiba, Y., Yamomoto, T., Poulikakos, D., Megaridis, C. M., and Zhao, Z., 1995, ''Wetting Effects on the Spreading of a Liquid Droplet Colliding With a Flat Surface: Experiment and Modeling,'' Phys. Fluids, **7**, pp. 236–247.
[24] Mao, T., Kuhn, D. C. S., and Tran, H., 1997, ''Spread and Rebound of Liquid Droplets Upon Impact on Flat Surfaces,'' AIChE J., **43**, pp. 2169–2179.
[25] Aziz, S. D., and Chandra, S., 2000, ''Impact, Recoil and Splashing of Molten Metal Droplets,'' Int. J. Heat Mass Transfer, **43**, pp. 2841–2857.
[26] Kim, H.-Y., and Chun, J.-H., 2001, ''The Recoiling of Liquid Droplets Upon Collision With Solid Surfaces,'' Phys. Fluids, **13**, pp. 643–659.
[27] Rioboo, R., Marengo, M., and Tropea, C., 2002, ''Time Evolution of Liquid Drop Impact Onto Solid, Dry Surfaces,'' Exp. Fluids, **33**, pp. 112–124.
[28] Roisman, I. V., Rioboo, R., and Tropea, C., 2002, ''Normal Impact of a Liquid Drop on a Dry Surface: Model for Spreading and Receding,'' Proc. R. Soc. London, Ser. A, **458**, pp. 1411–1430.
[29] Liu, W., Wang, G. X., and Matthys, E. F., 1995, ''Thermal Analysis and Measurements for a Molten Metal Drop Impacting on a Substrate: Cooling, Solidification and Heat Transfer Coefficient,'' Int. J. Heat Mass Transfer, **38**, pp. 1387–1395.
[30] Wang, G. X., and Matthys, E. F., 1996, ''Experimental Investigation of Interfacial Conductance for Molten Metal Drop Impinging on a Substrate: Cooling, Solidification and Heat Transfer Coefficient,'' ASME J. Heat Transfer, **118**, pp. 157–163.
[31] Carslaw, H. S., and Jaeger, J. C., 1959, *Conduction of Heat in Solids*, Oxford University Press, London.
[32] Trapaga, G., Matthys, E. F., Valencia, J. J., and Szekely, J., 1992, ''Fluid Flow, Heat Transfer, and Solidification of Molten Metal Droplets Impinging on Substrates: Comparison of Numerical and Experimental Results,'' Metall. Trans. B, **23B**, pp. 701–718.
[33] Amada, S., Tomoyasu, K., and Haruyama, M., 1997, ''Splat Formation of Molten Sn, Cu and Ni Droplets,'' Surf. Coat. Technol., **96**, pp. 176–183.
[34] Amada, S., Haruyama, M., Ohyagi, T., and Tomoyasu, K., 2001, ''Wettability Effect on the Flattening Ratio of Molten Metal Droplets,'' Surf. Coat. Technol., **138**, pp. 211–219.
[35] Haller, K. K., Ventikos, Y., Poulikakos, D., and Monkewitz, P., 2003, ''Shock Wave Formation in Droplet Impact on a Rigid Surface: Lateral Liquid Motion and Multiple Wave Structure in the Contact Line Region,'' J. Fluid Mech., **490**, pp. 1–14.
[36] Schiaffino, S., and Sonin, A. A., 1997, ''Motion and Arrest of a Molten Contact Line on a Cold Surface: An Experimental Study,'' Phys. Fluids, **9**, pp. 2217–2226.

Study of Lateral Merger of Vapor Bubbles During Nucleate Pool Boiling

A. Mukherjee

V. K. Dhir
e-mail: vdhir@seas.ucla.edu

Mechanical and Aerospace Engineering Department,
University of California, Los Angeles, CA 90095
Phone: (310) 825-8507; Fax: (310) 206-4830

In the present work the bubble dynamics and heat transfer associated with lateral bubble merger during transition from partial to fully developed nucleate boiling is studied numerically. Complete Navier–Stokes equation in three dimensions along with the continuity and energy equations are solved using the SIMPLE method. The liquid vapor interface is captured using the Level-Set technique. Calculations are carried out for multiple bubble mergers in a line and also in a plane and the bubble dynamics and wall heat transfer are compared to that for a single bubble. The results show that merger of multiple bubbles significantly increases the overall wall heat transfer. This enhanced wall heat transfer is caused by trapping of liquid layer between the bubble bases during merger and by drawing of cooler liquid towards the wall during contraction after merger. Good agreement with data from experiments is found in bubble growth rate and bubble shapes obtained from numerical simulations. [DOI: 10.1115/1.1834614]

1 Introduction

Boiling heat transfer is one of the most efficient modes of heat transfer. Pool boiling process can be divided into several distinct regimes, such as partial nucleate boiling, fully developed nucleate boiling, transition boiling, and film boiling.

The most widely used regime is perhaps the nucleate boiling. In nucleate boiling, very high wall heat fluxes can be achieved at low superheats. An increase in wall heat flux is observed as the wall superheat is increased and transition takes place from partial to fully developed nucleate boiling. The maximum or critical heat flux sets the upper limit of fully developed nucleate boiling. Most boiling applications avoid this upper limit which can lead to burn out of the heater. Hence the devices are designed to operate in the stable regime of partial-fully developed nucleate boiling.

Gaertner [1] observed in fully developed nucleate boiling, vapor columns and mushroom-type bubbles supported by vapor stems attached to the heater. He proposed that the energy for phase change was supplied by the superheated liquid layer in which the stems were implanted. As the surface temperature or number of active sites increased, vapor mushrooms became more numerous and the latent heat transport mechanism began to predominate.

Mikic and Rohsenow [2] attributed the high heat flux in nucleate boiling, in addition to the natural convection over a part of the heating surface, to the transient conduction to, and subsequent replacement of, the superheated liquid layer in contact with the heating surface. They proposed a model for partial nucleate boiling heat flux, which included the effect of heating surface characteristics.

According to Yu and Mesler [3], at high heat fluxes, a liquid film, which they called the ''macrolayer,'' exists beneath an agglomeration of vapor bubbles attached to the surface, which is paramount in transferring heat. They distinguished the macrolayer from the microlayer and defined microlayer as the liquid film, which was formed between a bubble and the solid surface when an individual bubble grows on a surface during nucleate boiling (Fig. 1). Both evaporation of the microlayer and the macrolayer, resulted in vapor generation at the surface.

Dhir [4] identified four basic mechanisms that contribute to the total boiling heat flux under pool boiling conditions. These are (a) transient conduction at the area of influence of a bubble growing at a nucleation site, (b) evaporation (a fraction of which may be included in the transient conduction) at the vapor liquid interface, (c) enhanced natural convection on the region in the immediate vicinity of a growing bubble, and (d) natural convection over the area that has no active nucleation site and is totally free of the influence of the former three mechanisms. However, according to him, the importance of these mechanisms depends strongly on the magnitude of the wall superheat and other system variables.

Ramanujapu and Dhir [5] experimentally studied the formation of mushroom-type bubbles during nucleate boiling. They observed stems formed under merged bubbles and the entire vapor stem detached from the nucleating cavity at the base, as in the case of a single bubble. They concluded that merger of vapor bubbles leads to premature removal of vapor bubbles from the surface thereby increasing the frequency of vapor removal.

Chen and Chung [6] experimentally studied coalescence of bubbles during nucleate boiling on microheaters. The temperature of each heater was controlled electronically and the wall heat flux variation was obtained during bubble coalescence. They found that bubble departure frequency increased and the wall heat transfer rate was highly enhanced due to coalescence of bubbles.

Chen and Chung [7] also investigated the effects of separation distances between the bubbles and the number of bubbles participating in the process during bubble coalescence on microheaters. They found that the coalescence process is associated with a combination of bubble oscillation, stretching, and sliding on the heaters. They argued that wall heat transfer was enhanced as a result of rewetting of the heater surface by colder liquid and turbulent mixing effects. The results indicated that the heat transfer enhancement rate became higher while the bubbling-cycling duration decreased with increase in the separation distance between the bubbles. The wall heat flux was found to be proportional to the number of bubbles involved in coalescence process. However, no quantitative basis was provided.

Different heat transfer mechanisms at the wall such as transient conduction and convection are strongly influenced by the bubble merger process. The merger leads to a change in their relative contribution to the overall wall heat transfer rate. It is important to understand the underlying mechanisms associated with lateral bubble merger and their effect on the overall heat transfer from the surface. The objective of this study is to numerically investigate bubble dynamics and associated wall heat transfer during lateral bubble merger.

Contributed by the Heat Transfer Division for publication in the JOURNAL OF HEAT TRANSFER. Manuscript received by the Heat Transfer Division November 4, 2003; revision received August 9, 2004. Associate Editor: J. Chung.

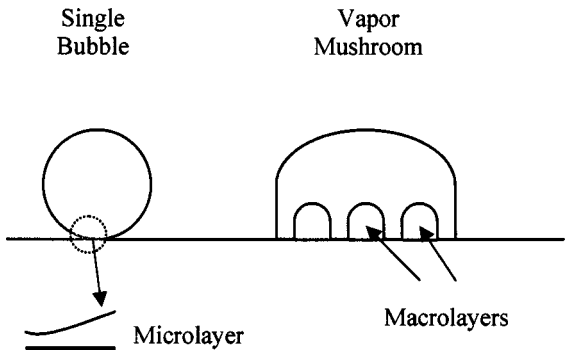

Fig. 1 Microlayer and macrolayer

Numerical calculations are performed for the cases shown in Fig. 2 involving a number of different bubble orientations. Taking advantage of symmetry numerical calculations are carried only for the shaded regions. The distance between the cavities in the last three cases is 1.25 mm. The liquid is saturated water and all properties are taken at 100°C. The wall superheat in all cases is chosen as 10°C. This superheat was chosen since for water boiling on a flat plate at one atmosphere, transition typically takes place from partial to fully-developed nucleate boiling at this superheat and bubbles start to merge with each other. The contact angle between the bubble and the bottom wall is maintained at 54 deg. The contact angle is chosen based on experimentally observed static contact angles. It was measured by placing liquid drops on the silicon wafer and was found to be 54 deg on an average before and after the experiment. The results are sensitive to contact angle and the effect of different contact angles on growth of a single bubble has been previously demonstrated by Son et al. [8]. Additional computations are performed for the cases of two-bubble merger at 5°C superheat and three-bubble merger at 6°C superheat in order to make comparisons with experimental data.

2 Numerical Model

The numerical analysis is carried out by solving the complete incompressible Navier–Stokes equation, using the SIMPLE method [9], which stands for Semi-Implicit Method for Pressure-Linked Equations. This method is chosen because the algorithm is well established and easy to implement. The continuity equation is turned into an equation for the pressure correction. At each iteration the velocities are corrected using velocity-correction formulas. The ''consistent'' approximation [10] is used for the velocity correction. The resulting velocity field exactly satisfies the discretized continuity equation, irrespective of the fact that the underlying pressure corrections are only approximate. The computations proceed to convergence via a series of continuity satisfying velocity fields. The governing equations in three dimensions are discretized as described in [9]. The power-law scheme is used for the convection-diffusion formulation. The algebraic equations are solved using the line-by-line technique, which uses TDMA (tridiagonal matrix algorithm) as the basic unit. The speed of convergence of the line-by-line technique is further increased by supplementing it with the block-correction procedure [11].

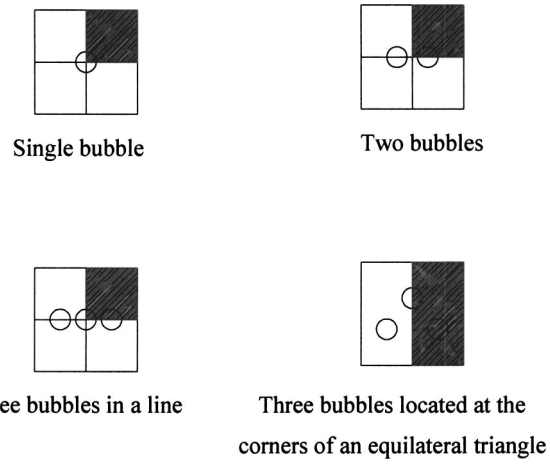

Fig. 2 Bubble orientations

The liquid–vapor interface is identified as the zero level set of a smooth distance function, ϕ [12]. The level set function ϕ, is negative inside the bubble and positive outside the bubble. The interface is located by solving the level set equation. Numerical quantities are smeared out across the interface producing a continuous profile for the density, viscosity, and pressure. This smeared interface approach requires an additional source term in the momentum equation to numerically model the surface tension forces. A fifth order WENO (weighted, essentially nonoscillatory) scheme is used for left sided and right sided discretization of ϕ [13]. While ϕ is initially a distance function, it will not remain so after the level set equation is solved. The solutions of ϕ can develop a jump at the interface when interfaces merge. Maintaining ϕ as a distance function is essential for providing the interface with a width fixed in time. This is achieved by reinitialization of ϕ. A modification of Godunov's method is used to determine the upwind directions. The reinitialization equation is solved in fictitious time after each fully complete time step. With $\Delta t = d/2u_0$, ten t steps are taken with a third order TVD (total variation diminishing) Runge–Kutta method.

One of the main advantages of the level-set method is that it handles topological changes and complex interfacial shapes in a natural way. The solution of complete Navier–Stokes equations ensures that all the relevant physics of the merger process is incorporated in the solution. The smeared interfaces span three grids and the interfaces are assumed to have merged if the distance between them becomes less than one grid spacing. However, the effect of smeared interfaces on the overall results is believed to be only of the second order. The level-set method has been successfully applied to model growth of single bubbles [8] and vertical bubble merger at a single nucleation site [14].

The effect of microlayer evaporation was incorporated using the model developed by Son, Dhir, and Ramanujapu [8]. The model is based on the lubrication theory. The shape of the microlayer interface is governed by balance of forces due to capillary pressure, disjoining pressure, and vapor recoil pressure. Heat is conducted from the solid surface into the liquid microlayer and is utilized for evaporation at the interface. The evaporative heat flux across the liquid–vapor interface is calculated using the modified Clausis–Clayperon equation. The combination of mass, momentum, and energy equations yields a fourth-order nonlinear ordinary differential equation which is solved using specified boundary conditions as described in [8]. The microlayer solution, which is assumed to be two-dimensional with the azimuthal variation being neglected, is applied to each grid point in the macro region at the bubble base and is matched asymptotically for the given contact angle at $y = d/2$. The rate of vapor volume production obtained from solution of the microlayer equations is applied to three cells in the vapor side control volume normal to the bubble interface at the wall.

2.1 Scaling Factors. The governing equations and boundary conditions are made nondimensional using a length scale (l_0) and a time scale (t_0) defined by,

$$l_0 = \sqrt{\frac{\sigma}{g(\rho_l - \rho_v)}} \tag{1}$$

$$t_0 = \sqrt{\frac{l_0}{g}} \tag{2}$$

The characteristic velocity is thus given by,

$$u_0 = \frac{l_0}{t_0} \tag{3}$$

The nondimensional temperature is defined as,

$$T^* = \frac{T - T_{\text{sat}}}{T_w - T_{\text{sat}}} \tag{4}$$

with $T^* = 0$ when $T = T_{\text{sat}}$ and $T^* = 1$ at the wall when $T = T_w$.

For saturated water at 1 atm pressure and earth normal gravity, the length scale is 2.5 mm, the time scale is 16 ms, and the characteristic velocity is 0.157 m/s.

2.2 Governing Equations. The mass, momentum, and energy equations in the three dimensional Cartesian coordinates are given as:

Momentum equation:

$$\rho\left(\frac{\partial \mathbf{u}}{\partial t} + \mathbf{u}\cdot\nabla\mathbf{u}\right) = -\nabla p + \rho\mathbf{g} - \rho\beta_T(T - T_{\text{sat}})\mathbf{g} - \sigma\kappa\nabla H + \nabla\cdot\mu\nabla\mathbf{u} + \nabla\cdot\mu\nabla\mathbf{u}^T \tag{5}$$

Energy Equation:

$$\rho C_p\left(\frac{\partial T}{\partial t} + \mathbf{u}\cdot\nabla T\right) = \nabla\cdot k\nabla T \quad \text{for } \phi > 0$$
$$T = T_{\text{sat}} \quad \text{for } \phi \leqslant 0 \tag{6}$$

Continuity equation:

$$\nabla\cdot\mathbf{u} = \frac{\mathbf{m}}{\rho^2}\cdot\nabla\rho + \dot{V}_{\text{micro}} \tag{7}$$

where $\dot{V}_{\text{micro}}$ is obtained from the microlayer solution as described in [8].

The curvature of the interface in Eq. (5) is defined as,

$$\kappa(\phi) = \nabla\cdot\left(\frac{\nabla\phi}{|\nabla\phi|}\right) \tag{8}$$

The mass of liquid evaporating at the interface is given by,

$$\mathbf{m} = \frac{k_l\nabla T}{h_{fg}} \tag{9}$$

From Eq. (9), the vapor velocity at the interface due to evaporation can be written as,

$$\mathbf{u}_{\text{evp}} = \frac{\mathbf{m}}{\rho_v} = \frac{k_l\nabla T}{\rho_v h_{fg}} \tag{10}$$

To prevent instabilities at the interface the density and viscosity are defined as,

$$\rho = \rho_v + (\rho_l - \rho_v)H \tag{11}$$

and

$$\mu = \mu_v + (\mu_l - \mu_v)H \tag{12}$$

where H is the Heaviside function defined as,

$$H = 1 \quad \text{if } \phi \geqslant +1.5d$$
$$H = 0 \quad \text{if } \phi \leqslant -1.5d$$
$$H = 0.5 + \phi/(3d) + \sin[2\pi\phi/(3d)]/(2\pi) \quad \text{if } |\phi| \leqslant 1.5d \tag{13}$$

Since the vapor is assumed to remain at the saturation temperature, the thermal conductivity is given by,

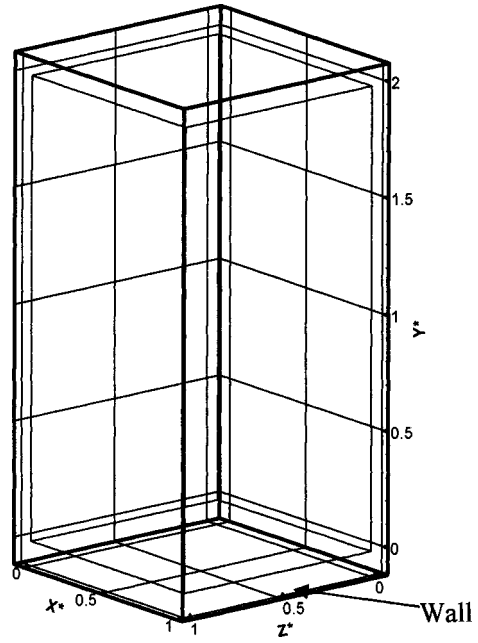

Fig. 3 Typical computational domain

$$k = k_1 H^{-1} \tag{14}$$

To capture the liquid–vapor interface, the level set equation is solved as,

$$\frac{\partial\phi}{\partial t} + (\mathbf{u} + \mathbf{u}_{\text{evp}})\cdot\nabla\phi = 0 \tag{15}$$

After every time step, ϕ is reinitialized by solving the following equation to steady state ($\partial\phi/\partial t$ becoming zero):

$$\frac{\partial\phi}{\partial t} = S(\phi_0)(1 - |\nabla\phi|)u_0 \tag{16}$$

where $\phi(x,0) = \phi_0(x)$ and S is the sign function given as

$$S(\phi_0) = \frac{\phi_0}{\sqrt{\phi_0^2 + d^2}} \tag{17}$$

2.3 Computational Domain. Figure 3 show a typical three-dimensional domain defined to model the bubble merger process. The domain is rectangular in shape. The calculations are carried out in Cartesian coordinates. The bottom of the domain is defined as the wall.

2.4 Initial Conditions. A spherical bubble of $0.1l_0$ radius is placed in the domain on the wall, with a contact angle of 54 deg. This minimum initial bubble size is necessary to resolve it effectively at the start of the calculations. The initial coordinates of the bubble center for a single bubble would be $(0, r\cos\varphi, 0)$. All initial velocities are set to zero. The initial thermal boundary layer thickness is calculated from the correlation for the turbulent natural convection heat transfer [15]. The initial thickness is given by

$$\delta_T = 7.14(\nu_l\alpha_l/g\beta_T\Delta T)^{1/3} \tag{18}$$

2.5 Boundary Conditions. The boundary conditions are as follows:

At the wall ($y = 0$):

$$u = v = w = 0; \quad T = T_w, \quad \frac{d\phi}{dy} = -\cos\varphi \tag{19}$$

where φ is the contact angle.

At the planes of symmetry ($x = 0, x = l_0$):

$$u = v_x = w_x = T_x = \phi_x = 0 \tag{20}$$

At the planes of symmetry ($z = 0, z = l_0$):

$$u_z = v_z = w = T_z = \phi_z = 0 \tag{21}$$

At the top of the domain ($y = 2l_0$):

$$u_y = v_y = w_y = \phi_y = 0, \quad T = T_{\text{sat}} \tag{22}$$

3 Experimental Setup

The experimental setup used is similar to the one used by Son et al. [8]. It consists of a cubic boiling chamber formed by Pyrex glass walls on the four sides, an aluminum cover plate on the top, and a G-10 support plate at the bottom. A 10 cm diameter silicon wafer, with strain gauge heaters and thermocouples attached to the bottom surface, is glued to a G-10 base using high temperature Silicone RTV. The backside of the wafer is heated with strain gauge heaters that are powered using a dc power supply. The strain gauge heaters are typically 7 mm×12 mm in size. The area surrounding the cavity is uniformly heated and high heat flux heaters are placed directly below the cavities to promote nucleation. Micromachined cavities are etched on top of the wafer for bubble nucleation. The cavities are 10 microns in diameter and 20 micron deep and are effective for bubble nucleation at the specified location and superheat. The distance between the cavities is 1.25 mm. The wafer assembly sits inside the boiling chamber and the whole wafer acts as the boiling surface. The pool of water inside the boiling chamber is maintained at the desired temperature using two cartridge heaters provided on either sides of the wafer assembly. The pool heaters are switched off after reaching saturated conditions for water. Data is obtained when both wall and pool temperatures became steady. The time period available for obtaining data is typically less than 1 min after switching off the heaters before pool temperature starts to drop because of heat loss.

A high speed, digital camera is used for capturing visual observations of bubbles. High intensity light is used to illuminate the nucleating cavities and suitable zoom lenses are used to focus on them. High speed photographs of the bubbles are taken from one side only to record merger in the longitudinal direction. They are taken at a rate of 1250 frames per second for a period of approximately 1 s. Each frame is 0.8 ms apart. The pool and the surface temperatures are recorded during the period when photographs are taken. All thermocouples are calibrated prior to the experiments using three-point calibration. Picture of an object of known dimensions is also taken near the nucleating cavities to be used as reference for calculating bubble dimensions. The object is typically the sheath thermocouple used for measuring pool temperature.

The bubble equivalent diameter is the diameter of a sphere having the same volume as the volume of the actual bubble/s. The volume of the actual bubble is calculated by assuming it to be an ellipsoid with major and minor axis. During merger, major uncertainty exists in obtaining bubble shape because of changes taking place in the two orthogonal directions. As such no equivalent diameter is calculated during this phase. However, after merger as the vapor mass becomes axis-symmetric calculations are resumed for the equivalent diameter.

4 Results and Discussion

Figure 4 shows the computed growth and departure of single bubble for a wall superheat of 10°C. Contours of the zero level-set function are plotted in the domain, which depict the shape of the three-dimensional bubble. The time is indicated on each frame. The first frame at 0.0 ms shows the initial bubble placed in the domain. The bubble grows with time due to evaporation, as liquid is converted to vapor at the interface. As the bubble grows, the bubble base also expands. The wall region inward of the inner edge of the microlayer is the dry region. The bubble base diameter reaches maximum at 25 ms. Thereafter, the bubble base shrinks and bubble finally detaches at 47 ms.

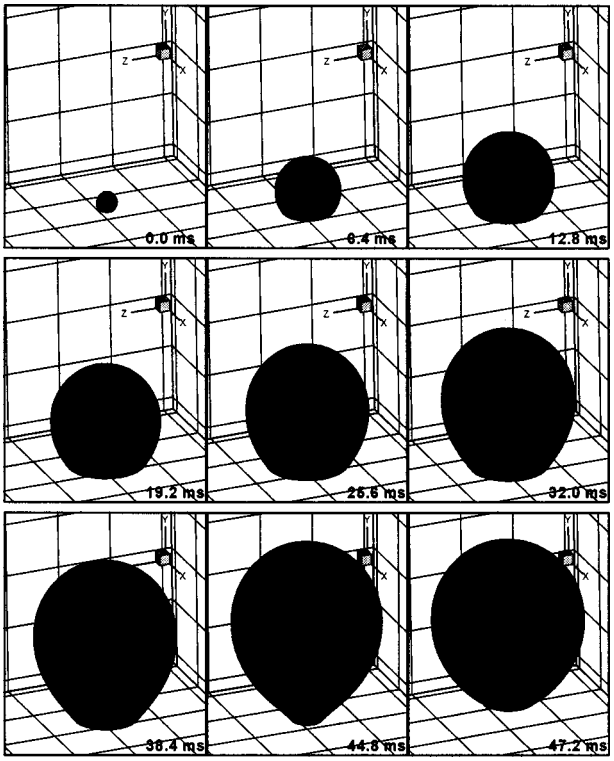

Fig. 4 Growth and departure of single bubble for a wall superheat of 10°C

Calculations are performed for the single bubble case with different mesh sizes to check for convergence. Figure 5(a) shows the equivalent bubble diameter as a function of time for 60, 72, 80 and 90 grids per 0.99 units of nondimensional length. The diameter of the bubble plotted is its equivalent diameter, assuming a sphere of equal volume. The bubble diameter increases rapidly initially and then slows down before growing to about 3.5 mm in diameter at departure. The base diameter first increases and then stays almost constant between 20 ms and 30 ms. Thereafter the base rapidly shrinks and becomes zero at departure. Figure 5(b) shows the bubble departure diameter and time obtained from Fig. 5(a) for the different grids. It is found that as the grid is refined the changes in the above quantities become negligible. The difference in departure diameter and departure time, between 72 and 80 grids is around 2%. Hence to optimize the computation time and memory requirements all our subsequent calculations were performed with 72 grids per 0.99 units of length.

Figure 6(a) shows the effect of time step change on the results for the case with 72 grids. The nondimensional time step used in the calculations shown in Fig. 5 was 0.001. Calculations are carried out by halving the previous time step to 0.0005. The comparison of the results indicates little effect of the change in time step.

Figure 6(b) shows the comparison with the results obtained by Son et al. [8] for a wall superheat of 8.5°C and contact angle of 50 deg. The domain used by Son et al. was cylindrical in shape with a height $3l_0$, whereas the present study uses a rectangular domain of height $2l_0$. Knowing these differences in calculation domain, we find present results to be in good agreement with that of Son et al. [8].

Figure 7 shows merger of two bubbles. When two or more bubbles are connected with each other through a common vapor space, we define that as a merged bubble. The bubbles are as-

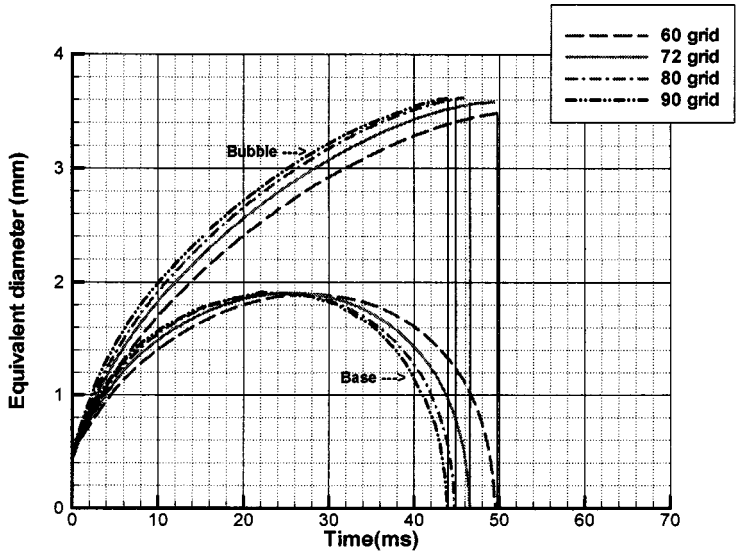

(a)

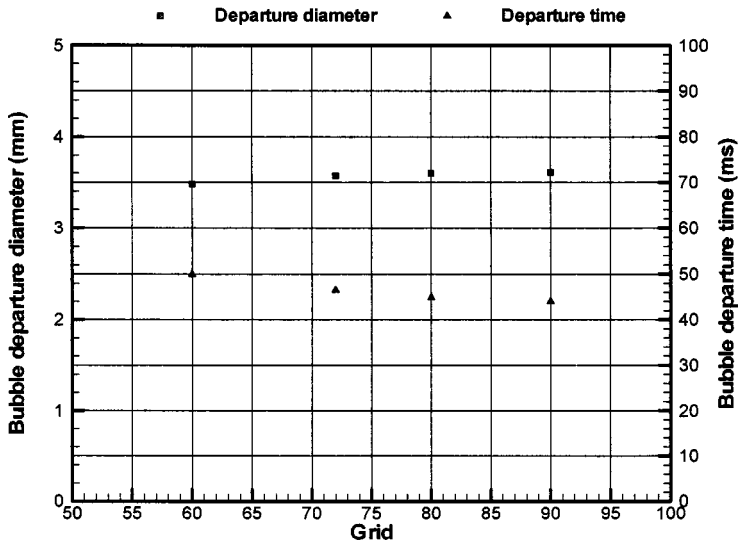

(b)

Fig. 5 Bubble growth rate and convergence check

sumed to have merged when the spacing between adjacent interfaces falls below the grid spacing. The bubbles merge laterally at around 6 ms and a vapor bridge is formed between the bubbles. This can be seen in the second frame at 6.7 ms. A thin layer of liquid is seen trapped between the bubble bases. The vapor bridge gradually expands and the trapped layer of liquid becomes narrower at 7.3 ms. Soon the two bubble bases completely merge and at 8.6 ms the trapped liquid is pushed out. At 12.8 ms, the merged bubble starts to shrink in the *x*-direction under surface tension forces and at the same time expands in the *z*-direction, as the surface tension tends to make the bubble spherical. After sometime, the effect of merger on the bubble shape diminishes and the merged bubble continues to grow like a single bubble. The bubble finally departs at 45.5 ms in the same manner as a single bubble with a departure diameter of around 3.4 mm.

A comparison of results of the numerical simulations of two-bubble merger with the data from experiments was made. Comparison was made for a wall superheat of 5°C since clean experimental data could not be obtained at 10°C superheat. For 5°C wall superheat the merged bubble from numerical simulation departed at 63 ms with a departure diameter of 3.2 mm.

In Fig. 8 the bubble growth rates prior to and after merger are compared. Before merger the figure shows the equivalent diameter of the individual bubbles, whereas after merger it shows the equivalent diameter of the merged bubble. The equivalent diameter in the experiments after merger was obtained when the merged bubble had acquired a shape similar to a single bubble. The merged bubble goes through several cycles of expansion and contraction in the plane of the paper and normal to it. These expansions and contractions are caused by surface tension as it tries to make the merged vapor mass spherical. Since pictures are taken in only one plane, the diameter is calculated in the mean time during each cycle of expansion and contraction. The results agree well, though the predicted departure diameter and time are slightly higher, than that observed in the experiments.

Figure 9 shows a comparison of bubble shapes obtained from

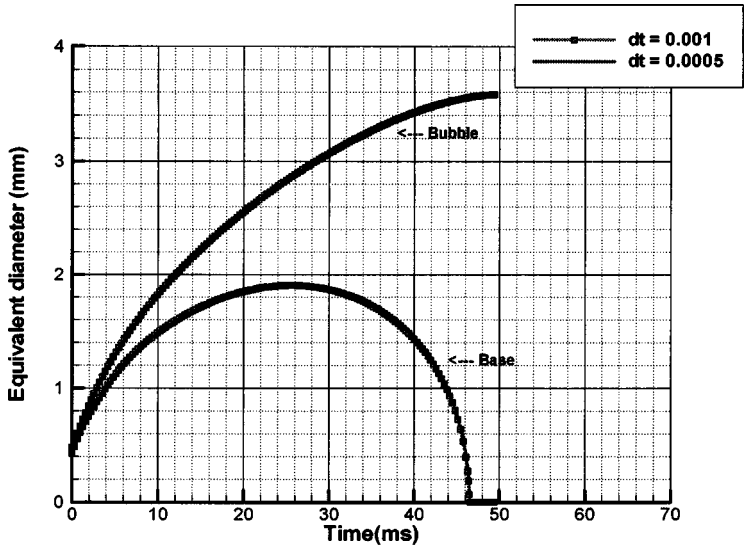

(a)

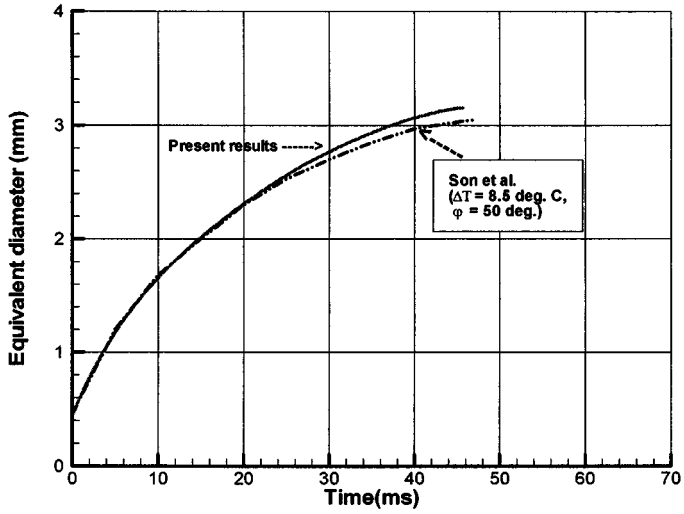

(b)

Fig. 6 Effect of time step change and comparison with Son et al.

numerical simulations with those observed in experiments. The two bubbles are almost of the same size in the experiments and are seen to touch each other around 14 ms. Good agreement is observed between the numerical results and experiments during the entire process of bubble merger until departure. The shapes seen in both cases are very similar though not necessarily at the exact same time. Both experiments and numerical simulations show formation of vapor bridges between the bubbles during merger and formation of vapor tails (16.8 ms in the experiments) during contraction. However the trapped liquid layer between the bubble bases is observed to stay longer in the experiments compared to the numerical calculations. This may be due to small subcooling present in the liquid during experiments.

In Fig. 10 we superimpose the numerically calculated shapes on the experimentally observed bubble shapes at selected times. For the numerical results, the bubble outline at the central $x-y$ plane has been shown. The time indicated on each frame corresponds to the experiment. Good agreement between the bubble shapes can be seen at all times.

Figure 11(a) shows an isometric view of merger of three bubbles in a line at 10°C wall superheat. The bubbles merge at around 5 ms and two layers of liquid get trapped between the bubble bases under the vapor bridges. The bubble bases merge completely thereafter, which can be seen at 6.3 ms. The merged bubble contracts rapidly in the x-direction and simultaneously expands in the z-direction. The oscillations continue for some time. This is evident from comparison of the bubble shapes at 8.8 ms and 12.0 ms. In Fig. 11(b), which shows the merged bubble in the $x-y$ plane, the bubble is wider at 8.8 ms. However in Fig. 11(c), which shows the bubble shape in the $z-y$ plane, the opposite is true. The merged bubble finally departs around 27.4 ms with departure diameter of about 3.2 mm.

Figure 12 shows merger of three bubbles in a plane, with three nucleation sites placed at the corners of an equilateral triangle with sides of length 1.25 mm, for a wall superheat of 10°C. The three bubbles touch each other around 8 ms, trapping a layer of liquid between the bubble bases. Since the bubbles are placed in a plane, they contract more uniformly from all directions compared

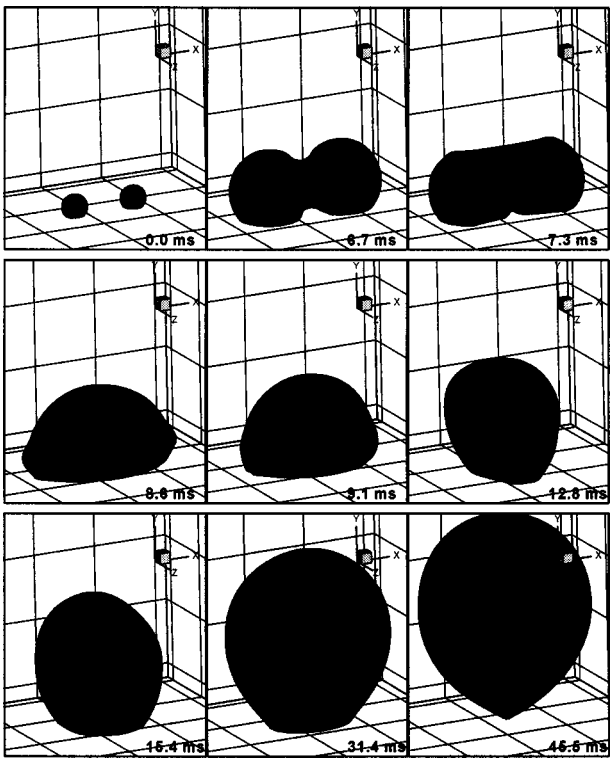

Fig. 7 Merger and departure of two bubbles for a wall superheat of 10°C

to the case of merger in a line. The merged bubble looks very similar to a single bubble at 22.7 ms. The bubble finally departs at 26.1 ms.

Figure 13 shows experimental results of merger of three bubbles in a plane at 6°C wall superheat. Two of the bubbles nucleate almost at the same time but the third bubble nucleates 7.2 ms later, thus leading to a phase difference in the growth of three bubbles in a plane. Hence they are of different sizes as they grow. The first two bubbles start to merge around 11.2 ms and subsequently merge with the third bubble at 12.8 ms. As the merged bubble contracts, vapor tails form at the ends at 13.6 ms. When the smaller third bubble gets sucked into the larger vapor mass a new bubble nucleates at its place at 14.4 ms. This secondary bubble gets sucked into the nearby bigger bubble at 19.2 ms. Another secondary bubble nucleates again at its place at 20.8 ms. This new bubble keeps growing as the bigger merged bubble departs at 27.2 ms.

Figure 14 shows numerical simulation of three-bubble merger in plane for the experimental conditions of Fig. 13. Here we have initially two bubbles nucleating at the same time with a third bubble nucleating at 7.2 ms. The first two bubbles start to merge around 10 ms and contract in the plane of the paper after merger. As the vapor mass contracts, it also expands in the perpendicular direction and merges with the smaller third bubble at 12.0 ms. The smaller bubble gets completely sucked into the bigger bubble at 14.9 ms. This is equivalent to the situation in the experiments at 14.4 ms. However in the experiments, a new bubble nucleates at its place, which we did not simulate in our numerical calculations. This is because in our simulation, we start with a bubble of finite size ($0.1l_0$ radius) that could not be accommodated in that location. Thereafter, the merged bubble in our calculations continues to grow in a manner similar to a single bubble and departs at 59 ms. In the experiments however, secondary bubbles keep nucleating at the exposed cavity as mentioned earlier. The secondary bubble merges with the large vapor mass, thereby increasing the total vapor volume. The next secondary bubble does not merge but keeps growing very close to the merged bubble. This effect of additional nucleating bubbles nearby may have caused the merged bubble in the experiment to depart much earlier compared to our simulation. However, for times prior to the appearance of these additional nucleating bubbles we find calculated bubble shapes to be in reasonable agreement with those observed in the experiments.

Figure 15 compares the bubble equivalent diameter for the above case, found in the numerical simulations and in the experiments. Here individual bubble diameters are plotted before merger and the equivalent bubble diameter corresponding to the total vapor mass in the domain is plotted after merger. At 7.2 ms the third

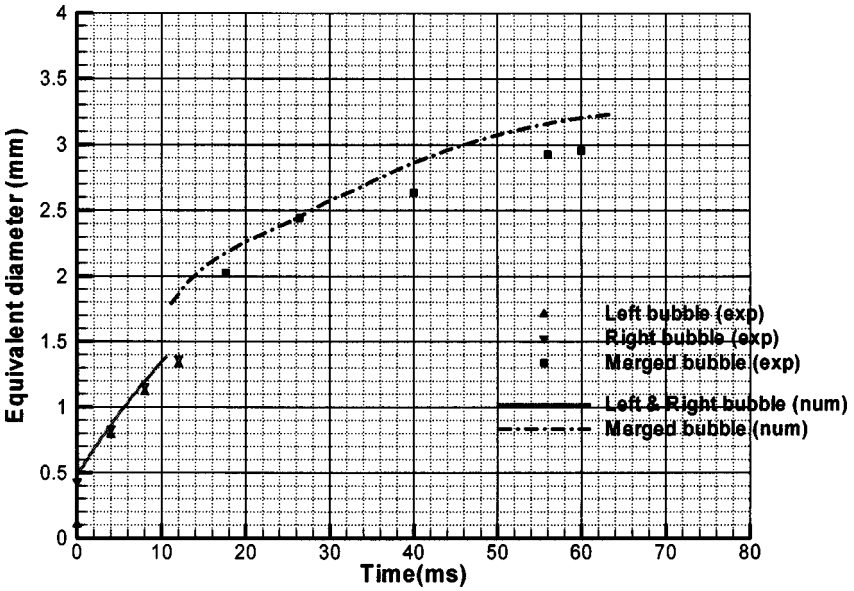

Fig. 8 Comparison of growth rate for two-bubble merger at 5°C wall superheat with experimental data

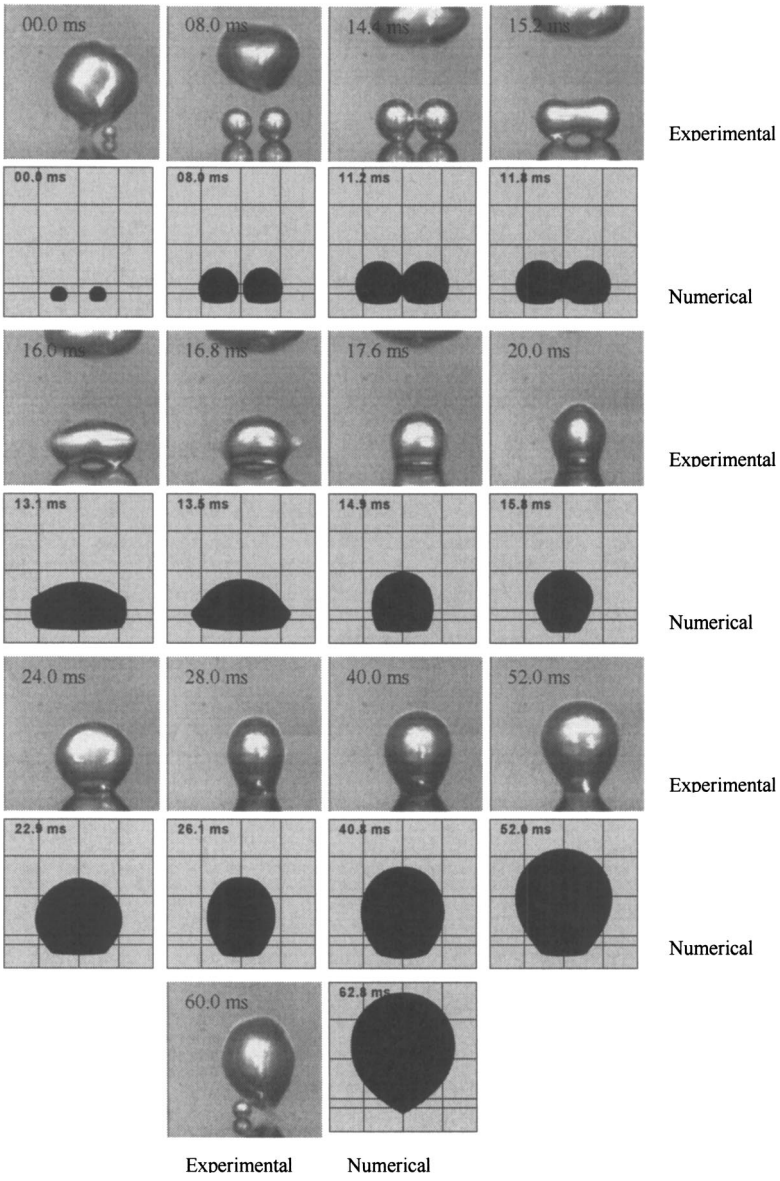

Fig. 9 Numerical results and experimental observations of two-bubble merger at 5°C wall superheat

bubble nucleates both in the experiments and in the simulation. Before merger, the growth rates of individual bubbles are found to be slightly higher in the experiments. Hence the merged bubble diameter just after merger is also comparatively higher in the experiment. There is also a jump in the merged bubble diameter in the experiment between 20 and 22 ms due to absorption of a secondary bubble. The merged bubble departs with a diameter of 3.2 mm at 27 ms in the experiment, whereas in the numerical simulation the bubble departs at 59 ms with a diameter of 3.3 mm.

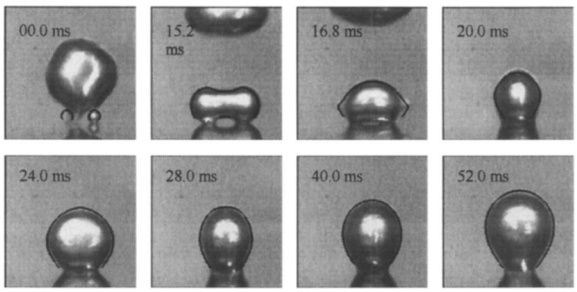

Fig. 10 Comparison of bubble shapes during two-bubble merger at 5°C wall superheat

In Fig. 16(*a*), the equivalent bubble diameter as a function of time is compared for the cases of single bubble, two bubbles, three bubbles in line and three bubbles in plane at 10°C superheat. In the merger cases, all cavities are assumed to nucleate at the same time. For bubble merger cases the initial total volume of vapor in the domain is larger than that for a single bubble case. Hence at 0 ms, the initial equivalent diameter is higher. Start of merger process has been indicated for the merger cases. The bubble diameters at departure and growth period for three bubble merger cases are smaller than those for single bubble or two bubble merger cases. However, the major effect is on the growth period. Figure 16(*b*) shows the equivalent bubble base diameters as a function of time. For all the merger cases, we note oscillations in the base diameter after merger. The bubbles depart when the base diameters approach zero.

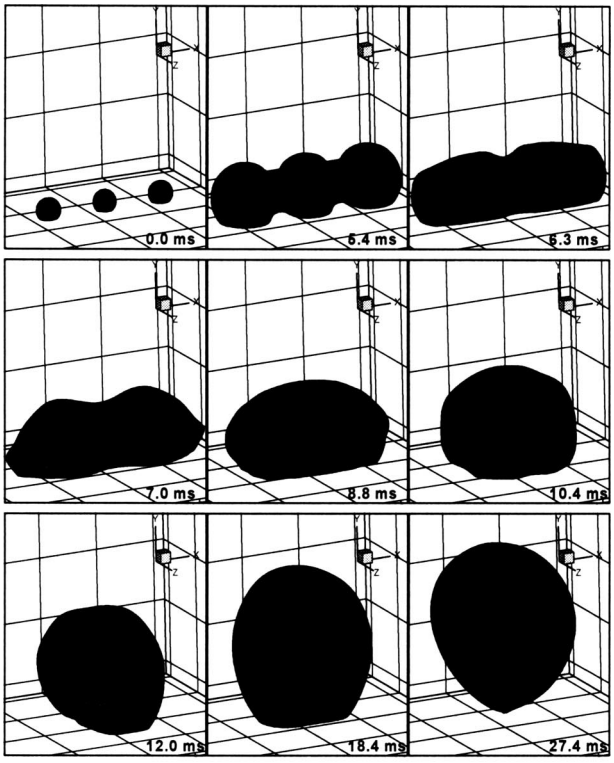

(a)

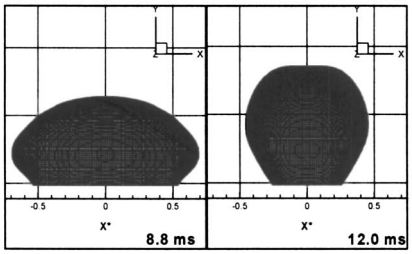

(b)

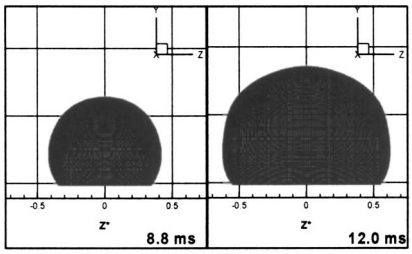

(c)

Fig. 11 Merger of three bubbles in a line for a wall superheat of 10°C

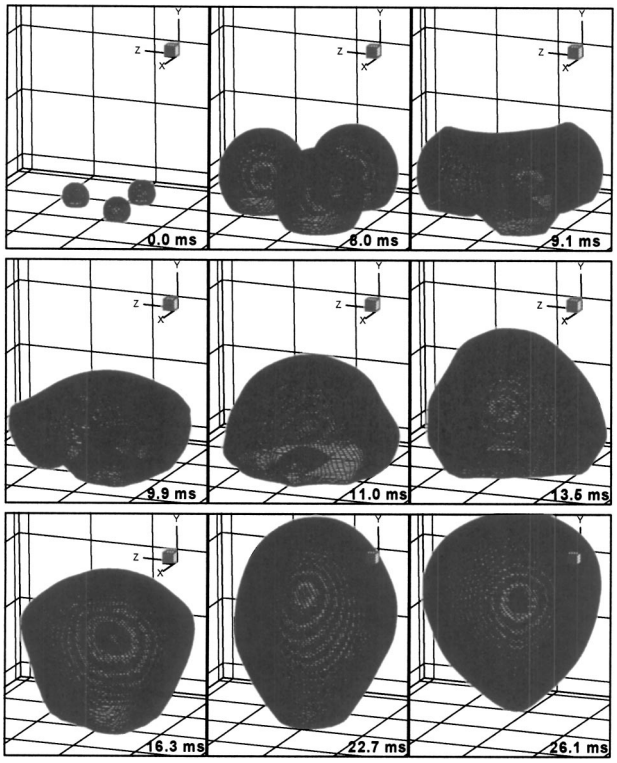

Fig. 12 Merger of three bubbles in a triangle for a wall superheat of 10°C

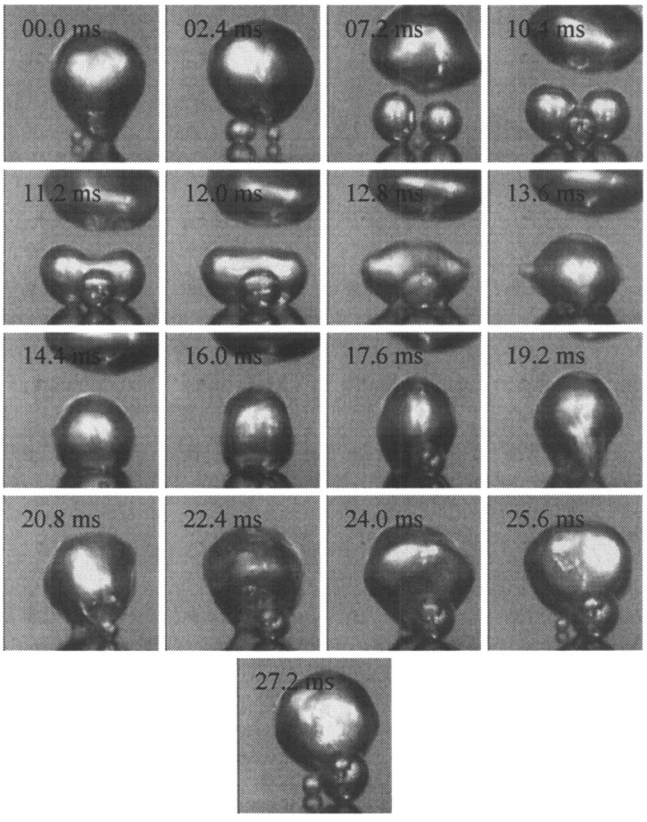

Fig. 13 Three-bubble merger in plane at 6°C superheat

The growth time of the two-bubble merger case is only about 2 ms earlier than that for the single bubble. However for the three-bubble cases both in plane and in line, the merged bubble departs much earlier (around 26 ms), leading to higher vapor removal rate. The time averaged vapor removal rate for single bubble is around 0.5 mm^3/ms whereas for the three-bubble merger in plane it increases to 0.8 mm^3/ms.

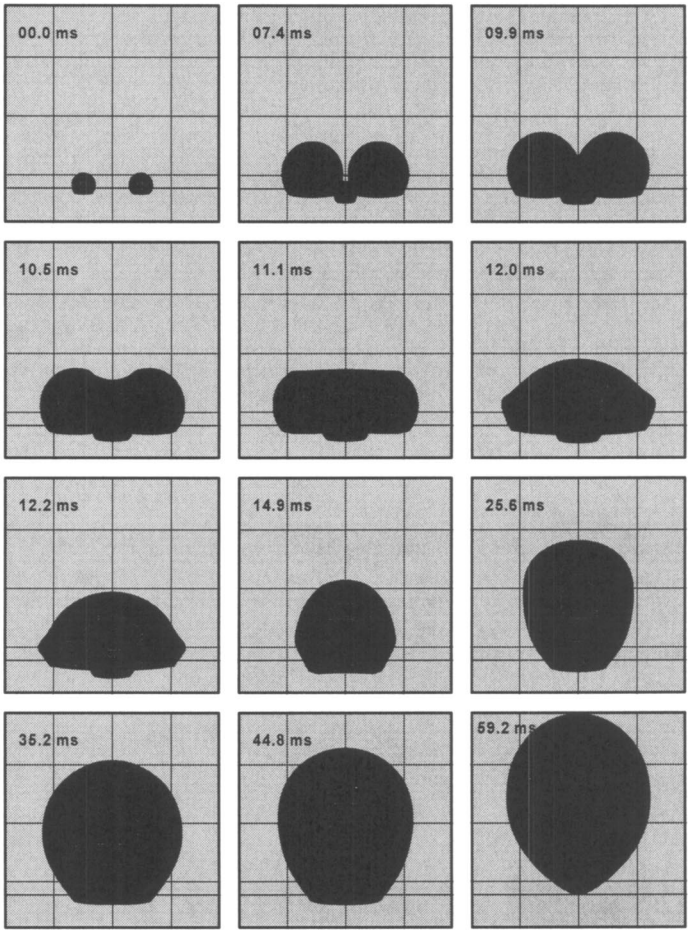

Fig. 14 Numerical simulation of three-bubble merger in plane at 6°C wall superheat

In the cases of single bubble and two-bubble merger, the base diameter shrinks continuously from 28 ms leading to departure around 46 ms. However, for the cases of three-bubble merger, the bases start to shrink much earlier which leads to early departure. Bubble departure is a complicated nonlinear process dependent on several variables such as bubble growth rate, contact angle, orientation, relative bubble sizes, bubble spacing, etc. The flow field around the bubbles caused by merger can also play a very important role. Ultimately it is the net force on the bubbles that determines the lift off. It is proposed that the flow field leads to addi-

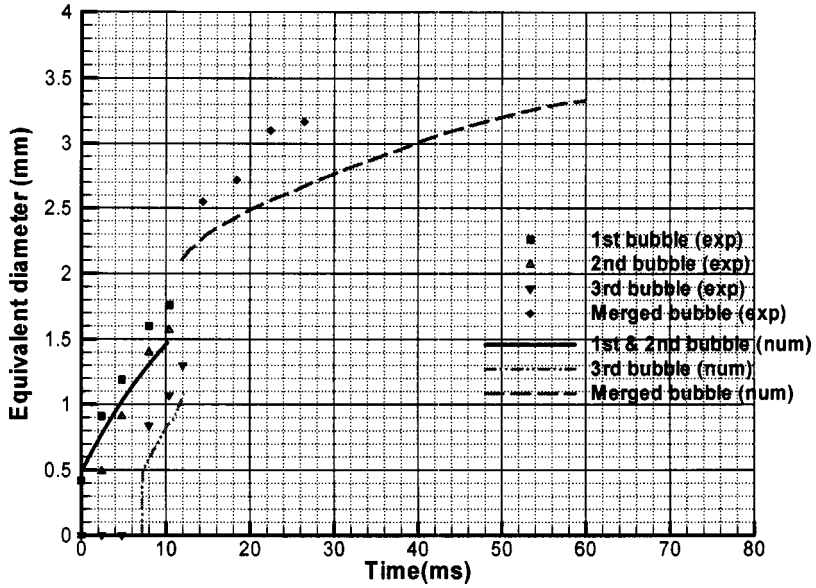

Fig. 15 Comparison of growth rate for three-bubble merger in plane at 6°C wall superheat with experimental data

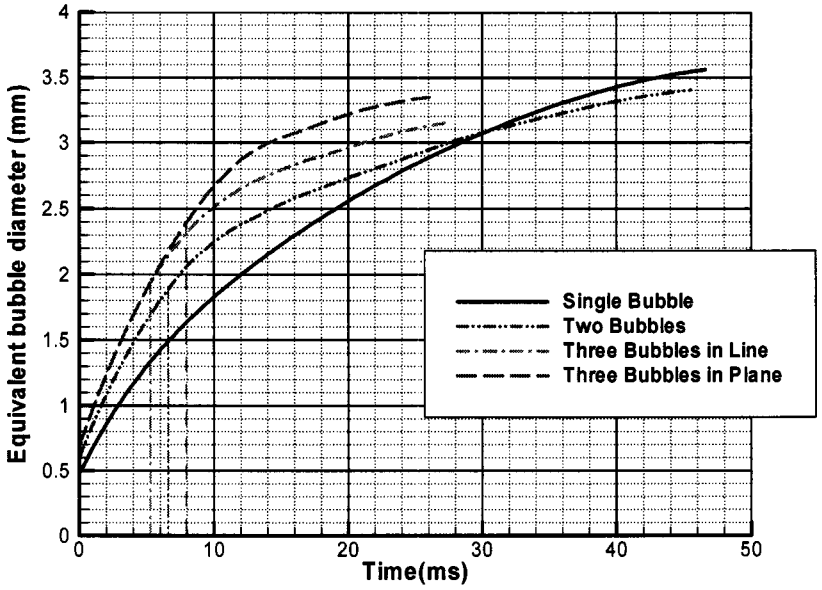

(a)

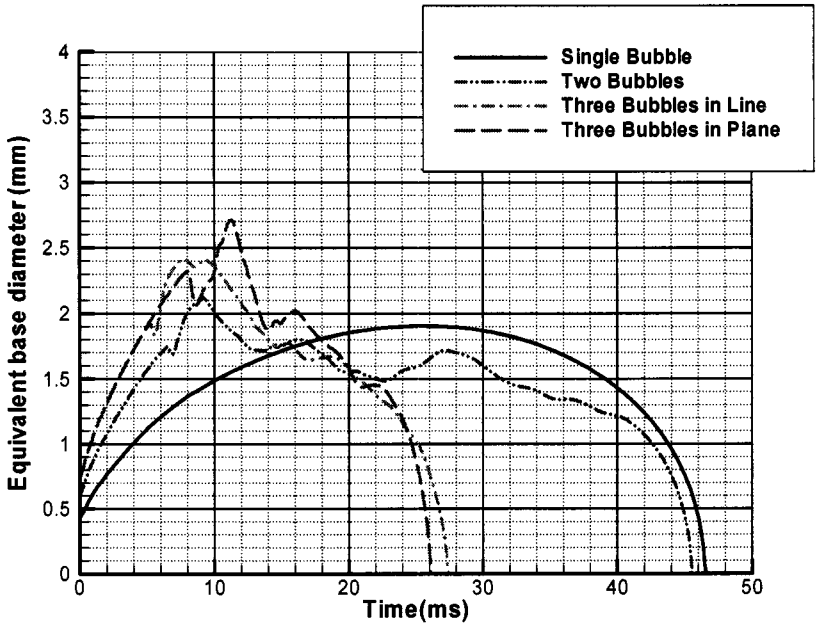

(b)

Fig. 16 Comparison of bubble growth at 10°C wall superheat

tional lift force that causes the bubble diameter at departure to be slightly smaller for three in-line and in-plane merger cases.

It should also be noted that for the three-bubble merger in a plane, the growth rate at about 12 ms is higher than that for the three in-line bubble merger. This is due to the difference in the heat transfer rate associated with the trapped liquid layers between the bubble bases that will be explained later.

The total wall heat transfer for all the cases are compared in Fig. 17. The Nusselt number (Nu) is calculated based on the area-averaged heat transfer coefficient (h) at the wall given by,

$$\overline{h} = \frac{1}{A}\int_0^A h dA \tag{23}$$

where A is the wall area and h is obtained from

$$h = \frac{-k_l \left.\dfrac{\partial T}{\partial y}\right|_{y=0}}{T_w - T_{\text{sat}}} \tag{24}$$

The wall Nusselt number is defined as,

$$\text{Nu} = \frac{\overline{h} l_0}{k_l} \tag{25}$$

At $t/t_0 = 0$, we see that the wall heat transfer is higher as the number of bubbles in the domain increases, since the contribution of microlayer evaporation at the bubble bases is more. The time-averaged value of Nusselt number computed for the four cases from Fig. 17 are 5.7, 6.6, 7.7, and 8.6, respectively. The corre-

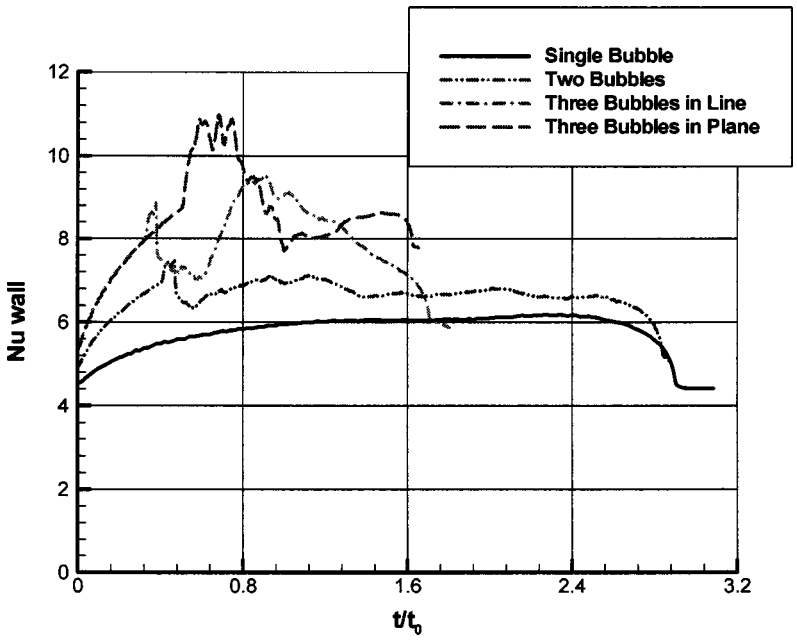

Fig. 17 Comparison of wall heat transfer at 10°C wall superheat

sponding dimensional values of wall heat transfer coefficient are 1553, 1798, 2097, and 2343 $W/m^2 K$. Thus the case of three bubbles merging in plane yields the highest time averaged wall heat transfer rate.

Figure 18 shows the temperature field around the single bubble at 12.8 ms ($t/t_0 = 0.8$) in three different planes. Isotherms are plotted at ten discreet intervals between nondimensional temperatures 0 and 1 corresponding to liquid pool and wall, respectively. The $y = d/2$ plane corresponds to the liquid layer next to the wall. The concentration of isotherms near the bubble base indicates high heat transfer into the vapor liquid interface.

For the two-bubble case, the bubbles start to merge at 6 ms,

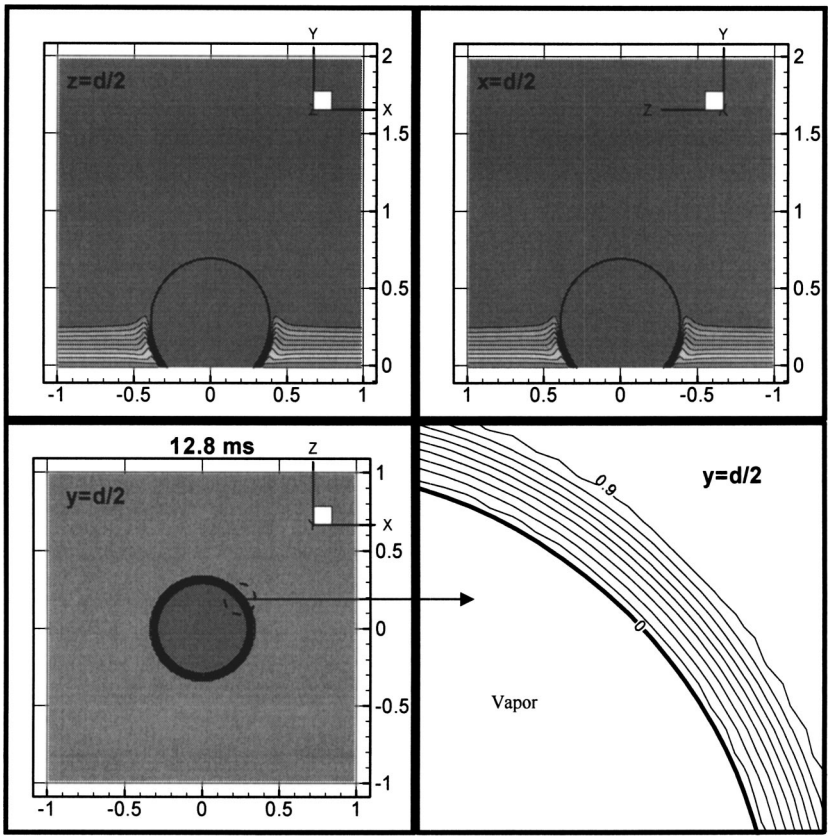

Fig. 18 Temperature field around single bubble at 12.8 ms

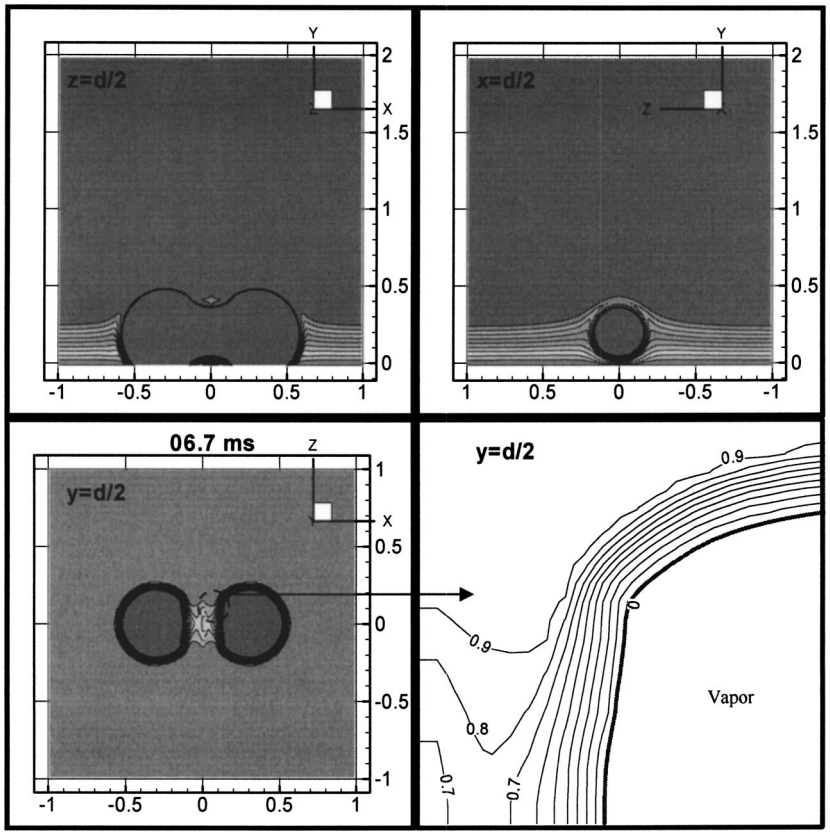

Fig. 19 Temperature field in two-bubble merger case at 6.7 ms

trapping liquid between the bubble bases. Figure 19 shows the temperature field in three different planes during two-bubble merger. A thin layer of superheated liquid can be seen trapped between the two bubble bases just after the bubbles merged at 6.7 ms ($t/t_0=0.42$). The enlarged view of $y=d/2$ plane shows temperature of liquid between the bubble bases. This view is zoomed over a small area and hence it shows variation of temperature over few grid points only. Hence the contour profiles do not appear smooth everywhere in this frame. Wall heat transfer in the region between the bubble bases is high due to presence of liquid at lower temperature near the wall as seen in the figure.

As the trapped liquid is pushed out around 7.5 ms ($t/t_0=0.47$), the overall wall heat transfer decreases and the bubble continues to grow thereafter just like a single bubble. However due the effect of merger, the wall heat transfer stays higher compared to the single bubble case (Fig. 17).

Figure 20 shows the temperature field around the merged bubble at 12.8 ms ($t/t_0=0.8$). As the merged bubble contracts in the *x*-direction, the fluid flows towards the wall causing crowding of isotherms and higher wall heat transfer. However, in the *z*-direction heat transfer did not change since the bubble expanded and pushed the liquid away from the wall. In the $z=d/2$ plane we can see thinning of thermal boundary layer at the two sides of the bubble base leading to higher wall heat transfer. The temperature field at $y=d/2$ plane also shows clearly, the regions of lower liquid temperatures and hence higher wall heat flux, on the two sides of the bubble base.

Comparing the isotherms at $y=d/2$ plane in Fig. 18 and Fig. 20 at 12.8 ms for the single bubble and the merged bubble, we can see additional areas of higher wall heat transfer around the bubble base caused by bubble merger.

In the case of three-bubble merger in a line, liquid gets trapped between the bases during the period from 5 to 6 ms ($t/t_0=0.31$ to 0.37). Figure 17 shows a jump in wall heat transfer during this time period. Figure 21 shows the corresponding temperature field around the merged bubbles at 5.4 ms. High wall heat flux region indicated by lower liquid temperature can be observed between the three bubble bases at the $y=d/2$ plane.

The heat transfer increases again at 10 ms as the merged bubble contracts under the influence of surface tension drawing saturated liquid towards the wall. Highest wall heat transfer occurs at 14 ms ($t/t_0=0.88$) and this magnitude is much higher in comparison to the two-bubble merger case (Fig. 17).

Figure 22 shows the temperature field for three in-line bubbles at 12.0 ms. As the three bubbles merge and contract, they influenced much bigger area on the wall compared to the two bubble merger case, which can be seen by comparing the isotherms in the $y=d/2$ plane in Figs. 20 and 22. Thus we see that in both cases, the bubble merger leads to thinning of thermal boundary layer near the bubble base, causing higher wall heat transfer.

For the growth of three bubbles in a plane, the bubbles start merging at 8 ms ($t/t_0=0.5$) and the trapped liquid layer stays on the wall until 13 ms ($t/t_0=0.81$). Thus we see that the duration of the trapped liquid layer is much higher compared to merger of three bubbles in line. High heat transfer rate from the wall when the trapped liquid layer exists was seen in Fig. 17. Figure 23 shows the temperature field around the merged bubble at 8.6 ms. A cross section at planes $x=d/2$ and $z=0.99-d/2$ plane shows the trapped liquid between the three bubbles. Vapor bridges can be observed connecting the three bubbles with each other. The areas of low liquid temperature and hence increased heat transfer at the wall can be seen, at the $y=d/2$ plane.

As the vapor bridges expand, the trapped liquid is pushed out, and the wall heat transfer decreases. However between 16 ms ($t/t_0=1.0$) and 24 ms ($t/t_0=1.5$), the wall heat transfer again increases, as the merged bubble base contracts, causing liquid to rush in from all sides. Interestingly, this increase in heat transfer is not as pronounced compared to the case of merger of three

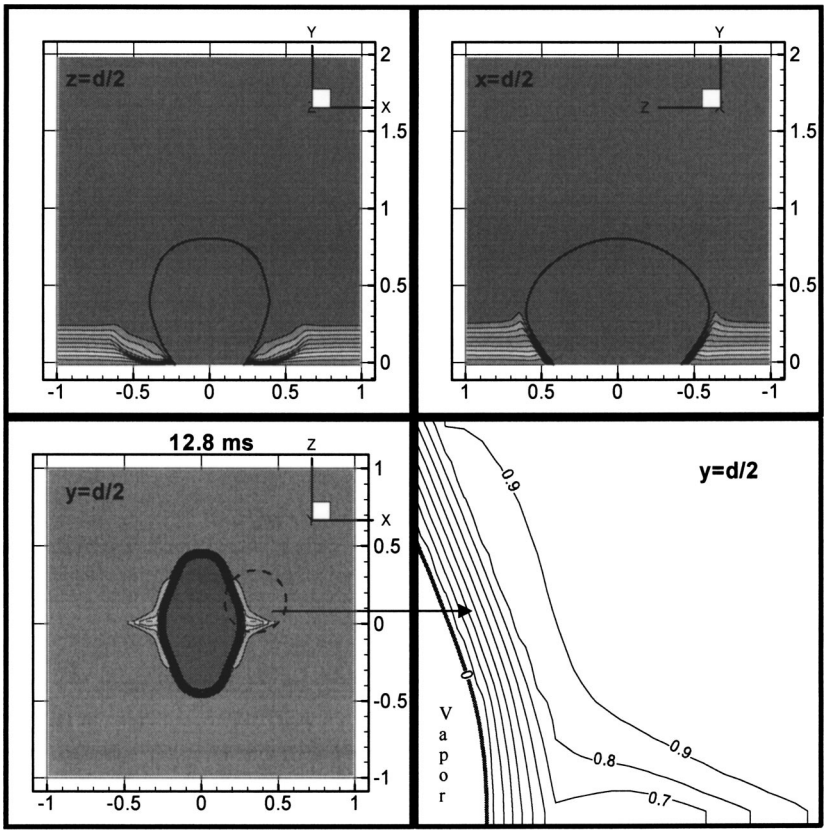

Fig. 20 Temperature field in two-bubble merger case at 12.8 ms

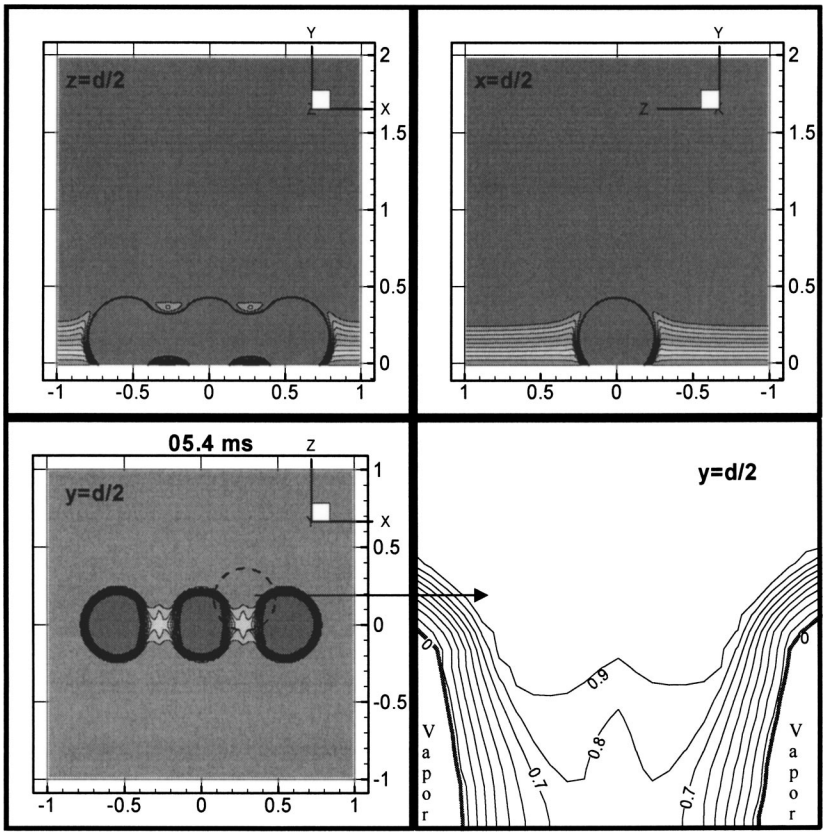

Fig. 21 Temperature field around merged three in-line bubbles at 5.4 ms

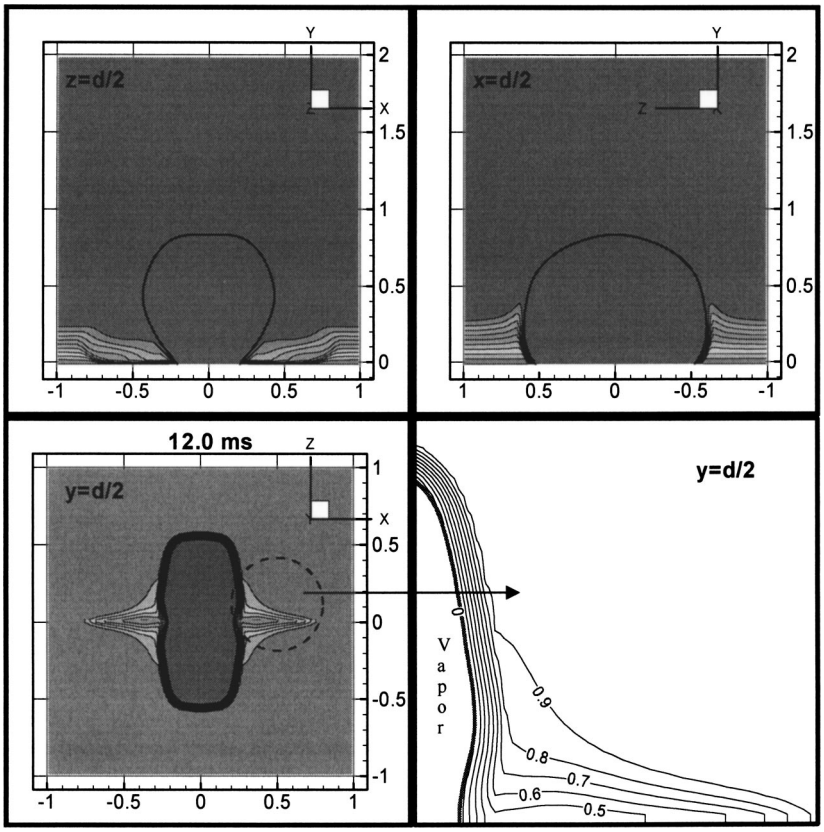

Fig. 22 Temperature field around merged three in-line bubbles at 12.0 ms

bubbles in line (Fig. 17). For three bubbles merging in line, the increase in heat transfer from 10 ms ($t/t_0=0.66$) to 14 ms ($t/t_0=0.88$) during contraction after merger is comparatively much higher.

Thus we see that in case of merger of three bubbles in line, the effect of the cooler liquid rushing towards the wall near the bubble base is the most significant reason for increase in wall heat transfer. In the case of merger of three bubbles in plane, the primary cause of this increase is the formation of trapped liquid layer that causes a high local temperature gradient at the wall. In the latter case, the trapped liquid layer is pushed against the wall and thins as the vapor bridges expand causing evaporation to take place from the upper interface of the film. This in turn leads to higher temperature gradient at the wall. The liquid layer present between the bubbles prior to merger is thicker and leads to lower heat transfer rate.

Figure 24 shows the area of influence around the bubbles for the two different orientations. The area of influence is defined by simply drawing tangents to the maximum diameter of two adjacent bubbles. When bubbles merge, the vapor bridges expand and try to align along the tangents. This can be seen from our numerical calculations e.g., at 7.3 ms in Fig. 7, at 6.3 ms in Fig. 11 and at 9.1 ms in Fig. 12. Hence the amount of liquid present between the bubbles that is enclosed by the tangents is influenced by the merger process. The shaded area in the figure is the area over which the trapped liquid can exist. When the bubbles contract under the influence of surface tension forces, the trapped liquid has to be pushed out from the sides. In case (a) the liquid trapped at the center has no direct escape route. Thus the trapped liquid exists on the wall for much longer time in the plane orientation compared to the in-line orientation.

In case (a), the distance between the center of the area of influence to the farthest point is 1.08D, whereas in case (b) the same distance is 1.5D. Thus when the bubbles contract just after merger, the length over which this contraction takes place is larger in the case of three bubbles merging in line, compared to three bubbles merging in triangle. As such the increase in wall heat transfer due to drawing of cooler liquid towards the wall is higher in the case of bubbles merging in line.

However, the total time averaged heat transfer is found to be higher for bubbles merging in plane, as mentioned earlier.

5 Conclusions

1. The process of horizontal bubble merger during bubble growth on a wall is numerically simulated for different bubble orientations.
2. The bubble merger process shows formation of vapor bridges with liquid trapped underneath the bridges and vapor tails during merger.
3. For in-line bubble merger, the merged bubble is found to oscillate in size prior to departure.
4. Merger of three bubbles is found to cause higher vapor removal rate compared to a single bubble.
5. The highest wall heat transfer is obtained for bubbles merging in a plane.
6. Bubble merger process increased the overall wall heat transfer by trapping a liquid layer between bubble bases and by drawing cooler liquid towards the wall during contraction.
7. Good agreement is observed when comparisons of bubble shapes and bubble growth rate are made between numerical calculations and experimental data.

Acknowledgments

This work received support from NASA under the Microgravity Fluid Physics Program.

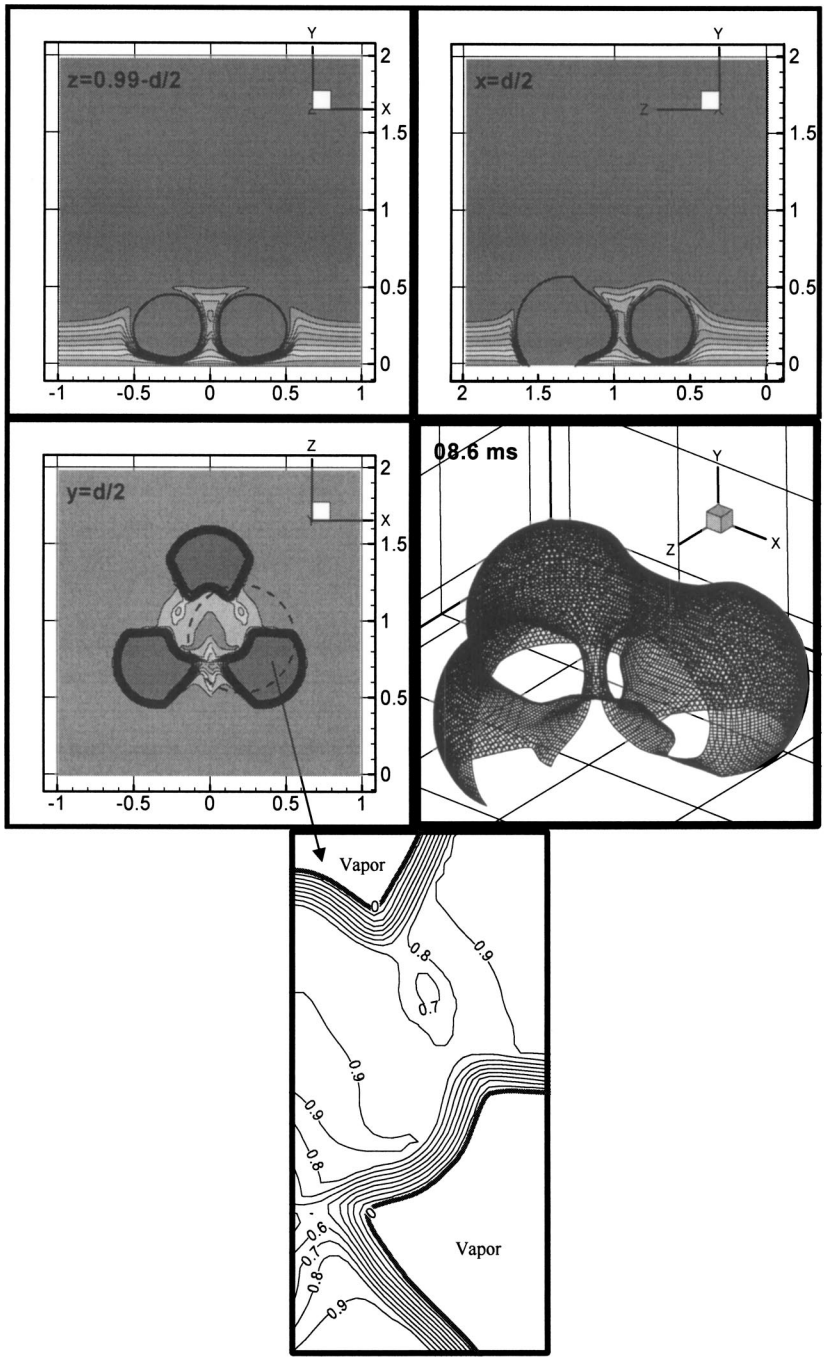

Fig. 23 Temperature field during merger of three bubbles in triangle at 8.6 ms

Nomenclature

A = wall area
C_p = specific heat at constant pressure
D = bubble diameter
d = grid spacing
exp = experimental
g = gravity vector
H = Heaviside function
h = heat transfer coefficient
h_{fg} = latent heat of evaporation
k = thermal conductivity
l_0 = characteristic length scale
m = mass transfer rate at interface
ms = milliseconds
Nu = Nusselt number
num = numerical
p = pressure
r = radius
T = temperature
ΔT = temperature difference, $T_w - T_{\text{sat}}$
t = time
t_0 = characteristic time scale
u_0 = characteristic velocity scale
u = x direction velocity
v = y direction velocity
$\dot{V}_{\text{micro}}$ = rate of vapor volume production from the microlayer
w = z direction velocity
α = thermal diffusivity

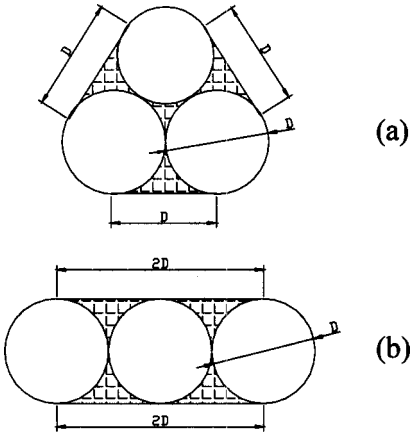

Fig. 24 Effect of bubble orientation on the area of influence

β_T = coefficient of thermal expansion
δ_T = thermal layer thickness
κ = interfacial curvature
μ = dynamic viscosity
ν = kinematic viscosity
ρ = density
σ = surface tension
ϕ = level set function
φ = contact angle

Subscripts

evp = evaporation
l = liquid
v = vapor
x = $\partial/\partial x$
y = $\partial/\partial y$
z = $\partial/\partial z$
sat = saturation
w = wall

Superscript

$*$ = nondimensional quantity
$-$ = area averaged

References

[1] Gaertner, R. F., 1965, ''Photographic Study of Nucleate Pool Boiling on a Horizontal Surface,'' ASME J. Heat Transfer, **87**, pp. 17–29.
[2] Mikic, B. B., and Rohsenow, W. M., 1969, ''A New Correlation of Pool-Boiling Data Including the Effect of Heating Surface Characteristics,'' ASME J. Heat Transfer, **9**, pp. 245–250.
[3] Yu, C. L., and Mesler, R. B., 1977, ''A Study of Nucleate Boiling Near the Peak Heat Flux Through Measurement of Transient Surface Temperature,'' Int. J. Heat Mass Transfer, **20**, pp. 827–840.
[4] Dhir, V. K., 1991, ''Nucleate and Transition Boiling Heat Transfer Under Pool and External Flow Conditions,'' Int. J. Heat Fluid Flow, **21**, pp. 290–314.
[5] Ramanujapu, N., and Dhir, V. K., 2000, ''On the Formation of Vapor Columns and Mushroom Type Bubbles During Nucleate Boiling on a Horizontal Surface,'' in Proceedings of NHTC'00, NHTC2000-12208, Pittsburgh, Pennsylvania.
[6] Chen, Tailian, and Chung, J. N., 2002, ''Coalescence of Bubbles in Nucleate Boiling on Microheaters,'' Int. J. Heat Mass Transfer, **45**, pp. 2329–2341.
[7] Chen, Tailian, and Chung, J. N., 2003, ''Heat Transfer Effects of Coalescence of Bubbles From Various Site Distributions,'' Proc. R. Soc. London, Ser. A, **459**, pp. 2497–2527.
[8] Son, G., Dhir, V. K., and Ramanujapu, N., 1999, ''Dynamics and Heat Transfer Associated With a Single Bubble During Nucleate Boiling on a Horizontal Surface,'' ASME J. Heat Transfer, **121**, pp. 623–631.
[9] Patankar, S. V., 1980, *Numerical Heat Transfer and Fluid Flow*, Hemisphere Publishing Company, Washington, D.C.
[10] Van Doormaal, J. P., and Raithby, G. D., 1984, ''Enhancements of the SIMPLE Method for Predicting Incompressible Fluid Flows,'' Numer. Heat Transfer, **7**, pp. 147–163.
[11] Patankar, S. V., 1981, ''A Calculation Procedure for Two-Dimensional Elliptic Situations,'' Numer. Heat Transfer, **4**, pp. 409–425.
[12] Sussman, M., Smereka, P., and Osher, S., 1994, ''A Level Set Approach for Computing Solutions to Incompressible Two-Phase Flow,'' J. Comput. Phys., **114**, pp. 146–159.
[13] Fedkiw, R. P., Aslam, T., Merriman, B., and Osher, S., 1998, ''A Nonoscillatory Eulerian Approach to Interfaces in Multimaterial Flows (The Ghost Fluid Method),'' UCLA CAM Report No. 98-17, Los Angeles, CA.
[14] Son, G., Ramanujapu, N., and Dhir, V. K., 2002, ''Numerical Simulation of Bubble Merger Process on a Single Nucleation Site During Nucleate Pool Boiling,'' ASME J. Heat Transfer, **124**, pp. 51–62.
[15] Kays, W. M., and Crawford, M. E., 1980, *Convective Heat and Mass Transfer*, McGraw–Hill, New York, p. 328.

An Improved Cluster-Renewal Model for the Estimation of Heat Transfer Coefficients on the Furnace Walls of Commercial Circulating Fluidized Bed Boilers

Animesh Dutta
Greenfield Research Incorporated, P.O. Box #25018, Halifax, NS, B3M 4H4, Canada

Prabir Basu
Mechanical Engineering Department, Dalhousie University, P.O. Box #1000, Halifax, NS, B3J 2X4, Canada

Using data from large CFB boilers, and taking average solids concentration, size and height of the boiler-furnace as variables, a correlation for fractional wall coverage has been developed. This correlation for wall coverage and several other refinements have been used to modify the cluster renewal model of heat transfer. Predicted heat transfer coefficients from this model, for a wide range of CFB boilers, show good agreements with those measured in these boilers. [DOI: 10.1115/1.1833360]

Introduction

Even though the cluster renewal model [1] is generally accepted as a good means for calculating heat transfer coefficients on water walls of a Circulating Fluidized Bed (CFB) boiler, certain parameters of this model such as thickness of the gas-gap between the wall and the particle suspension, wall coverage, thermal boundary layer, cluster concentration, cluster velocity, and dispersed phase convection lack reliable expressions. Reliable data and good correlations are available for most of these parameters, but no data for wall coverage in commercial boilers is available. According to the cluster renewal, on the other hand, the fractional wall coverage directly influences the heat transfer coefficient.

In this paper an effort is made to develop a correlation for the wall coverage using data from four commercial CFB boilers. Direct information on wall coverage in commercial boilers is lacking. Also the cluster renewal model was improved further using the derived correlation for wall coverage and other modified information.

Refinement of Existing Cluster Renewal Model

The process of heat transfer in a CFB boiler involves three mechanisms: gas convection, particle convection, and radiation, each of which makes some contribution to the total heat transfer. Contributions of these individual mechanisms are not strictly additive, but for most practical applications they can be treated separately and added. So the overall heat transfer coefficient, h_{tot} may be expressed as a function of *f*, which is the time average value of the fraction of the wall covered by clusters,

$$h_{\text{tot}} = f(h_{\text{con}} + h_{\text{rad}})_{\text{cluster}} + (1-f)(h_{\text{con}} + h_{\text{rad}})_{\text{dilute}} \tag{1}$$

Cluster Heat Transfer. The cluster convective and radiative heat transfer coefficients are estimated using Eqs. (2) and (3). The heat transfer from the cluster is:

$$(h_{\text{con}})_{\text{cluster}} = \frac{1}{\left[\frac{\pi t_c}{4k_c(\rho c)_c}\right]^{0.5} + \frac{\delta d_p}{k_g}} \tag{2}$$

$$(h_{\text{rad}})_{\text{cluster}} = \frac{\{\sigma(T_s^4 - T_w^4)\}}{\left(\frac{1}{e_c} + \frac{1}{e_w} - 1\right)}(T_s - T_w)^{-1} \tag{3}$$

The above equations are refined by incorporating new information on gas gap [2], cluster concentration [2], thermal boundary layer [3], and cluster velocity [4]. These refined values as found by a number of researchers [2,3,4] are listed in Eqs. (4)–(8).

The nondimensional gas layer thickness δ is the distance between the wall and the cluster. It is calculated by the expression given by Lints and Glicksman [2]:

$$\delta = 0.0282(1-\varepsilon_{\text{avg}})^{-0.59} \tag{4}$$

where ε_{avg} is cross section average voidage.

The specific heat of cluster, represented by a *lumped* property (heat capacity), is estimated as below [5]:

$$(\rho c)_c = (1-\varepsilon_c)\rho_p c_p + \varepsilon_c \rho_g c_g \tag{5}$$

where cluster voidage ε_c can be estimated by the equation given by Lints and Glicksman [2] as below:

$$\varepsilon_c = 1 - 1.23(1-\varepsilon_{\text{avg}})^{0.54} \tag{6}$$

The residence time for each cluster (t_c) at the wall surface would be given by:

$$t_c = \frac{L_c}{U_{\text{cl}}} \tag{7}$$

Where cluster velocity, U_{cl} can be estimated by the following correlation proposed by Noymer and Glicksmann [4]:

$$U_{\text{cl}} = 0.75\sqrt{\frac{\rho_p}{\rho_g} g d_p} \tag{8}$$

The temperature of solids near the wall is estimated by the following equation given by Borodulya and Teplitsky [3]:

$$T_s = T_w + 1.29\left(\frac{\rho_s}{\rho_p}\right)^{0.13}(T_b - T_w) \tag{9}$$

Dilute Phase Heat Transfer. For the dilute phase convection we used the heat transfer coefficient for longitudinal sweeping of a vertical wall proposed by Basu et al. [6] instead of using the modified equation of Wen and Miller [7] proposed earlier by Basu and Fraser [8] and the Dittus Boelter [9] equation proposed by Golriz and Grace [10].

Contributed by the Heat Transfer Division for publication in the JOURNAL OF HEAT TRANSFER. Manuscript received by the Heat Transfer Division June 3, 2003; revision received July 17, 2004. Associate Editor: S. Acharya.

Table 1 Selected valves of *F*

Flow condition	*F*
Fully developed velocity profile	1.4
Abrupt contraction entrance	6
90° right-angle bend	7
180° round bend	6

$$(h_{con})_{dilute} = 0.023 C C_l C_t \frac{k_g}{D_{eq}} \mathrm{Re}^{0.8} \mathrm{Pr}^{0.4} \tag{10}$$

where C_t is the correction factor for the temperature difference between the wall and the medium. It can be calculated as [6]:

$$C_t = \left(\frac{T_b}{T_w}\right)^{0.5} \tag{11}$$

The correction factor of tube length, $C_l = 1$ when $L/D_{eq} > 50$. When the entrance effect is predominant, the entrance effect is taken into account by the following equation [11]:

$$C_l = 1 + F\left(\frac{D_{eq}}{L}\right) \tag{12}$$

Some selected values of F are noted in Table I.

In this case, the correction factor, C for the presence of particles in the dilute phase is taken as [12]:

$$C = 1.1 \tag{13}$$

The radiation between the suspension (dilute phase) and a bare wall is estimated from the expression for parallel surfaces, i.e.

$$(h_{rad})_{dilute} = \frac{\{\sigma(T_b^4 - T_w^4)\}}{\left(\frac{1}{e_b} + \frac{1}{e_w} - 1\right)} (T_b - T_w)^{-1} \tag{14}$$

Development of a Correlation for Wall Coverage

Glicksman [13] proposed a correlation based on experimental data from his 20 cm diam experimental unit. Experimental data on the wall coverage, as plotted by him, shows a strong influence of the column diameter; and yet the correlation omits the dependence of the wall coverage on the column diameter. Therefore, this correlation is unsuitable for use in a large unit.

Golriz and Grace [10] proposed a correlation, as given below, to account for the size effect of the boiler:

$$f = 1 - \exp\left\{-25{,}000\left[1 - \frac{2}{e^{0.5D_{eq}} + e^{-0.5D_{eq}}}\right](1 - \varepsilon_{avg})\right\} \tag{15}$$

While applying Eq. (15) to a commercial unit of an equivalent diameter of 3 m and higher with a solid concentration of 0.0004 (suspension density of 2 kg/m^3) and higher, the wall coverage approaches 1.0. For all the commercial boilers listed in the Appendix, Eq. (15) predicts full wall coverage by cluster. This would suggest a minimal effect of the radiation on the total heat transfer to the walls of these commercial boilers.

A number of researchers (Divilio and Boyd [14], Baskakov et al. [15], Dutta and Basu [16]) reported that for a commercial boiler radiation (at least in the upper two thirds of the combustor) is the dominant factor in heat transfer. It is also the case for (suspension densities below 5 kg/m^3). Thus Eq. (15) fails to reasonably predict heat transfer coefficients for large CFB boilers. The above equation, however, can predict the wall coverage for small laboratory units like the one reported by Glicksman [13].

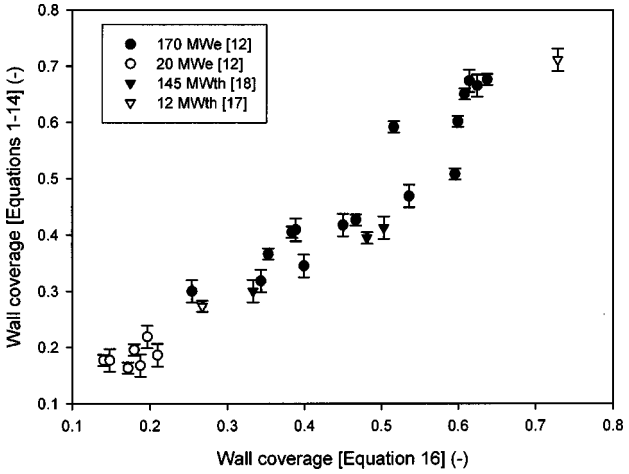

Fig. 1 Comparison of estimated [Eqs. (1)–(14)] versus predicted [Eq. (16)] wall coverage for a number of commercial boilers

Furthermore, for a CFB riser, the cross-section average solid concentration has a dominant influence on the wall coverage. As the average solid concentration (suspension density) varies exponentially with the height of the furnace, the wall coverage must, therefore, vary along the height. Considering the above, a correlation for estimating fractional wall coverage is proposed using the size and the height of the riser in a nondimensional form (D/H):

$$f = 1 - \exp\left(-a\{1 - \varepsilon_{avg}\}^b \left\{\frac{D_{eq}}{H}\right\}^c\right) \tag{16}$$

In commercial boilers the wall coverage, f, is never measured. Thus direct experimental values of this important parameter are unavailable in published literature. However, there is a well-defined relationship between the wall coverage, f, and the heat transfer coefficient on the wall. So, the data for fractional wall coverage, f, were derived from measured values of heat transfer coefficients on four specific commercial units of equivalent size of 1.6 m (12 MW$_{th}$) [17], 5.2 m (20 MW$_e$) [12], 6.2 m (145 MW$_{th}$) [18], and 10.6 m (170 MW$_e$) [12] having heights (above the secondary air supply) of 11.5 m, 25 m, 26 m, and 30 m. The values of f, thus derived, were used to find values of the coefficient of a, b, and c of Eq. (16). The coefficients, estimated using multiple regression analysis, were

$$a = 4300, \quad b = 1.39, \quad c = 0.22. \tag{17}$$

These values now make it possible to use Eq. (16) to compute the fractional wall coverage for any large CFB boiler which in turn allows determination of heat transfer coefficients for any range of CFB boilers using the cluster renewal model [Eqs. (1)–(14)].

Results and Discussion

Equations (1)–(14) were used to calculate the values of fractional wall coverages at different operating conditions for the four commercial CFB boilers in the Appendix. The values computed, are compared with the predicted ones from Eq. (16). Both values

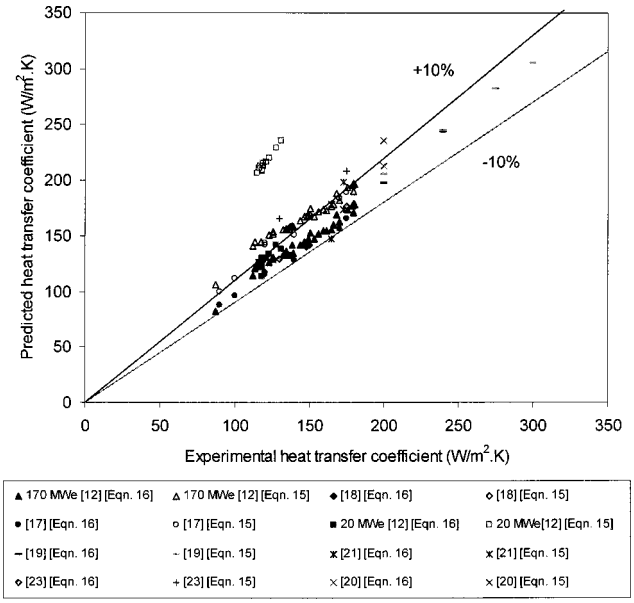

Fig. 2 Predicted heat transfer coefficient with measured heat transfer coefficient

are plotted in Fig. 1. The deviation from a perfect match is within ±10%. The values computed from equation (15) for all the four boilers are found to be 1.0, and hence could not be plotted here for the comparison.

Modification of Cluster Renewal Model. Now the cluster renewal model is modified using the new wall coverage Eqs. (16) and (17).

The modified cluster renewal model is now used to predict heat transfer coefficients for commercial CFB boilers other than those used to compute coefficients for wall coverage. Figure 2 plots the predicted heat transfer coefficients with experimental data (see Appendix) for the water walls as reported by different researchers for eight commercial boilers.

It may be noted that these data are for a wide range of operating conditions and they include data which were not used for the development of Eq. (16). It is clearly depicted in the graph that the new correlation predicts the heat transfer coefficient within ±10%.

For comparison it also plots the predicted heat transfer coefficient using the cluster renewal model with the old correlation of Golriz and Grace [10] for wall coverage [Eq. (15)]. It is seen from the graph that the old correlation [Eq. (15)] always overpredicts the heat transfer coefficient as it estimates full wall coverage by the cluster to the wall even at a lean phase for all the commercial boilers reported here. However, as expected, the old correlation can be used for higher solids concentration (suspension density of 10 kg/m^3 and higher) [19–21].

Conclusion

A correlation for fractional wall coverage of the water wall of commercial CFB boilers is developed. The cluster renewal model of Subbarao and Basu [1] is improved using this correlation and by using other improved expressions of thermal boundary, nondimensional gas gap, cluster velocity, etc. The following conclusions are drawn from this work:

1. The fractional wall coverage depends on the solids concentration, averaged over the height of the heat transfer surface and nondimensional diameter (hydraulic diameter/height of the furnace from secondary air supply). A correlation developed for this, shows a good agreement with the estimated values for a number of large boilers.
2. The modified cluster renewal model predicts within ±10% error the heat transfer coefficients for the water walls of different sizes of commercial boilers for a wide range of operating conditions.

Nomenclature

$(h_{con})_{cluster}$ = cluster convective heat transfer coefficient, W/m^2 K
$(h_{con})_{dilute}$ = dilute convective heat transfer coefficient, W/m^2 K
$(h_{rad})_{cluster}$ = cluster radiative heat transfer coefficient, W/m^2 K
$(h_{rad})_{dilute}$ = dilute radiative heat transfer coefficient, W/m^2 K
C = correction factor
C_c = specific heat of cluster in the dilute section, J/kg K
C_g = specific heat of gas, J/kg K
C_l = correction factor for length,
C_p = specific heat of particle, J/kg K
C_t = correction factor for temperature
D_{eq} = hydraulic diameter, m
d_p = diameter of particle, m
e_b = dilute phase emissivity
e_c = cluster emissivity
e_w = wall emissivity
f = fraction of wall covered by cluster
H = height from the secondary air supply to the top of the combustor in a commercial boiler, m
h_{tot} = total heat transfer coefficient, W/m^2 K
k_c = thermal conductivity of cluster in the dilute section, W/m K
k_g = thermal conductivity of gas, gas film, W/m K
L = length of heating susface
L_c = characteristic length, m
Pr = Prandtl number
Re = Reynold number
T_b = bed temperature, K
t_c = residence time of cluster with wall, s
T_s = first row of solids temperature (near the heat transfer surface), K
T_w = average wall temperature, K
U_{cl} = downwards velocity of cluster, m/s

Greek Symbols

δ = nondimensional gas layer thickness between wall and cluster
ε_{avg} = average voidage in the dilute section
ε_c = average voidage in the cluster
ρ_c = cluster density in the dilute section, kg/m^3
ρ_g = density of gas, kg/m^3
ρ_p = density of particle, kg/m^3
ρ_s = average suspension density, kg/m^3

Appendix. Measurement on heat transfer in different commercial units [12]

Unit, Reference	Plant Output	Size of the furnace (m)	Sus. density (kg/m^3)	Bed temp (^0C)	Wall Temp (^0C)	Particle size (μm)	HTC $W/m^2.K$
Chalmers University, Sweden [17]	12 MW_{th}	1.4×1.7×13.5	1.5-13	760-860	210	220	100-200
Jianjiang, China [19]	50 MW_{th}	3×6×20	14-52	920	290	400	200-300
Chatham, Canada [20]	72 MW_{th}	4×4×23	10.4	880	500	200	200
Flensburg, Germany [21]	109 MW_{th}	5.1×5.1×28	6.1-9.2	860	340	209	165-173
VW Wolfsburg [18]	145 MW_{th}	7.6×5.2×31	2.3-5.2	850	340	NS	110-150
Orebro [17]	165 MW_{th}	4.6×12×33.5	NS	700-860	360	280	NS
Duisberg, Germany [21]	226 MW_{th}	8(dia)×32 (Horizontal tube bank)	NS	850	650	177	445-596
Nucla, USA [22]	110 MW_e	6.9×7.4×34	NS	774-913	330	150	130-188
Emile Huchet, France [23]	125 MW_e	8.6×11×33	5-11	800-860	340	150	130-175
[1]Dutta [12]	170 MW_e	7.5×18×36	1.8-8.2	554-940	360	240	87-181
[2]Dutta [12]	20 MW_e	5.2×5.2×32	2.7-3.45	850-925	343	230	115-131

References

[1] Subbarao, D., and Basu, P., 1986, ''A Model for Heat Transfer in Circulating Fluidized Beds,'' Int. J. Heat Mass Transfer, **29**, pp. 487–489.

[2] Lints, Michael. C., and Glicksman, L. R., 1994, ''Parameters Governing Particle to Wall Heat Transfer in a Circulating Fluidized Bed,'' Circulating Fluidized Bed Technology IV, edited by A. A. Avidan, pp. 297–304.

[3] Borodulya, V. A., and Teplitsky, Yu. S., 1999, ''Prediction of Average Heat Transfer Coefficients Between a Riser's Wall and Circulating Fluidized Bed: Effect of Pressure and Temperature,'' *Circulating Fluidized Bed Technology VI*, edited by Werther, J., Dechema, Germany, pp. 379–384.

[4] Noymer, P. D., and Glicksman, L. R., 2000, ''Descent Velocities of Particle Clusters at the Wall of a Circulating Fluidized Bed,'' Chem. Eng. Sci., **55**, pp. 5283–5289.

[5] Breitholtz, C., 2000, ''Heat Transfer in Circulating Fluidized Bed Boilers,'' Ph.D. thesis, Chalmers University of Technology, Goteborg, Sweden.

[6] Basu, P., Kefa, C., and Jestin, L. 2000, *Boilers and Burners Design and Theory*, Springer, New York.

[7] Wen, C. Y., and Miller, E., 1961, ''Heat Transfer in Solid-Gas Transport Lines,'' J. Ind. Eng. Chem., **53**, pp. 51–53.

[8] Basu, P., and Fraser, S. A., 1991, *Circulating Fluidized Bed Boilers-Design and Operation*, Butterworths-Heinemann, Stoneham.

[9] Dittus, F. W., and Boelter, L. M. K., 1930, *Heat Transfer in Automobile Radiators of the Tubular Type*, University of California, pp. 13, 443.

[10] Golriz, M. R., and Grace, J. R., 2002, ''Predicting Heat Transfer in Large-Scale CFB Boilers,'' *Circulating Fluidized Bed Technology VII*, edited by Grace, J. R., Zhu, J., and Lasa, H. D., Niagara Falls, Canada, pp. 121–128.

[11] Perry, R. H., Green, D. W., and Maloney, J. O., 1984, ''Heat Transmission,'' in *Perry's Chemical Engineering Handbook*, 6th ed., pp. 10–17.

[12] Dutta, A., 2002, ''Heat Transfer in Circulating Fluidized Bed Boilers,'' Ph.D. thesis, Dalhousie University.

[13] Glicksman, L. R., 1997, ''Heat Transfer in Circulating Fluidized Beds,'' in *Circulating Fluidized Beds*, edited by Grace, J. R., Avidan, A. A., and Knowlton, T. M., Chapman & Hall, London, pp. 261–310.

[14] Divilio, R. J., and Boyd, T. J., 1994, ''Practical Implications of the Effect of Solids Suspension Density on Heat Transfer in Large-Scale CFB Boilers,'' in *Proceedings of the 4th International Conference Circulating Fluidized Beds*, Hidden Valley, PA, pp. 334–339.

[15] Baskakov, A., Leckner, B., and Breitholtz, K., 2001, ''Complex Heat Transfer Furnaces With a Circulating Fluidized Bed,'' Heat Transfer-Sov. Res., **32**, pp. 343–348.

[16] Dutta, A., and Basu, P., 2002, ''Overall Heat Transfer to Water-Walls and Wing-Walls of Commercial Circulating Fluidized Bed Boilers,'' J. Inst. Energy, **75**, pp. 85–90.

[17] Andersson, B.-A., 1996, ''Effect of Bed Particle Size on Heat Transfer in Circulating Fluidized Bed Boilers,'' Powder Technol., **87**, pp. 233–238.

[18] Blumel, W. P., Kaferstein, P., Rummel, A., and Morl, P., 1992, ''Wirbelschichtsysteme,'' VGB conference.

[19] Xiaozhong, J., Junfu, L., Qing, L., Yong, L., Jiansheng, Z., Xing, X., and Guangxi, Y., 1999, ''Investigation on the Heat Transfer in a CFB Boiler,'' in *Circulating Fluidized Bed Technology VI*, edited by J. Werther, pp. 355–360, Wurzburg, Germany.

[20] Couturier, M. F., Steward, F. R., and Poolpol, S., 1993, ''Experimental Determination of Heat Transfer Coefficients in a 72 MW_t Circulating Fluidized Bed Boiler,'' in *Proceedings of the 12th International Conference Fluidized Bed Combustion*, edited by L. Rubow and G. Commonwealth, ASME, pp. 1215–1222.

[21] Werdermann, C. C., and Werther, J., 1994, ''Heat Transfer in Large Scale Circulating Fluidized Bed Combustors of Different Sizes,'' in *Circulating Fluidized Bed Technology IV*, edited by Avidan, AIChE, New York, pp. 428–435.

[22] Boyd, T. J., and Friedman, M. A., 1991, ''Operation and Test Program Summary at the 110 MWe Nucla CFB,'' in *Circulating Fluidized Bed Technology III*, edited by P. Basu, M. Horio, and M. Hasatani, Pergamon Press, Oxford, pp. 297–312.

[23] Jestin, L., Meyer, P., Schmitt, C., and Morin, J. X., 1992, ''Heat Transfer in a 125 MWe CFB Boiler,'' presented at the Engineering Foundation Conf. Australia.

Assessment of Periodic Flow Assumption for Unsteady Heat Transfer in Grooved Channels

Yongmann M. Chung
e-mail: Y.M.Chung@warwick.ac.uk
School of Engineering and also the Centre for Scientific Computing, University of Warwick, Coventry CV4 7AL, United Kingdom

Paul G. Tucker
Civil and Computational Engineering Centre, University of Wales, Swansea, Swansea SA2 8PP, Wales, United Kingdom

Numerical studies of unsteady heat transfer in grooved channel flows are made. The flows are of special relevance to electronic systems. Predictions suggest a commonly used periodic flow assumption (for modeling rows of similar electronic components) may not be valid over a significant system extent. It is found that the downstream flow development is strongly dependent on geometry.
[DOI: 10.1115/1.1833371]

Keywords: Computational, Modeling, Heat Transfer, Laminar, Periodic, Unsteady

1 Introduction

With increasing power densities, the reliable computation of heat transfer in electronic systems is becoming ever more important [1–3]. The grooved channel flow (see Fig. 1), which simulates rows of integrated circuits (ICs) on a circuit board, is especially relevant to electronics cooling. At Reynolds numbers relevant to electronics, grooved channel flows can become unsteady. This can strongly affect heat transfer [1,2,4]. Here, the Reynolds number is defined as $\mathrm{Re}=U_c h/\nu$ where U_c is the centerline velocity and h the channel half height.

Ghaddar et al. [5] studied idealized two dimensional (2D) isothermal cyclic flow in channels with IC-like protrusions. For Reynolds numbers larger than a critical value (Re_c), cyclic flow oscillations which increase fluid transport are observed. Ghaddar et al. [6] use two dimensional nonisothermal predictions to illustrate the potential for naturally enhancing heat transfer using the unsteadiness observed by Ghaddar et al. [5]. Amon and Mikic [7], Amon [8], and Nigen and Amon [9–11] extend the above work, comparing heat transfer enhancement for flows where oscillations are induced passively and naturally when $\mathrm{Re}>\mathrm{Re}_c$. Wang and Vanka [12], Greiner et al. [13], and Nishimura and Kawamura [14] studied oscillatory flow in wavy-walled channels. They observed similar heat transfer enhancement.

Importantly, due to computational resource constraints, all of the above work assumes periodic flow. The question remains unanswered as to how realistic this assumption is in a practical electronics design context (i.e., over what percentage of a circuit board is the periodic flow assumption valid). Exploring this is the objective of the present work.

Contributed by the Heat Transfer Division for publication in the JOURNAL OF HEAT TRANSFER. Manuscript received by the Heat Transfer Division January 14, 2004; revision received September 16, 2004. Associate Editor: C. H. Oh.

2 Governing Equations and Numerical Method

The unsteady Navier–Stokes and continuity equations can be written in the following nondimensional incompressible flow form:

$$\frac{\partial u_i}{\partial x_i}=0, \tag{1}$$

$$\frac{\partial u_i}{\partial t}+\frac{\partial}{\partial x_j}(u_i u_j)=-\frac{\partial p}{\partial x_i}+\nu\frac{\partial^2 u_i}{\partial x_j^2}, \tag{2}$$

$$\frac{\partial T}{\partial t}+\frac{\partial T u_i}{\partial x_i}=-\frac{k}{\rho C_p}\frac{\partial^2 T}{\partial x_i^2}. \tag{3}$$

In the above, u_i is the instantaneous velocity in the x_i direction, t is time, p is the pressure, and T temperature. Here ρ is the fluid density, k thermal conductivity, and C_p the specific heat capacity.

2.1 Boundary Conditions. Parabolic inlet velocity profiles are used. At outflow boundaries, to suppress wave reflections, a convective boundary condition [15,16] is applied. At solid walls, the no-slip and impermeability conditions are used. The temperature of the incoming flow is constant at T_i. For relevance to heat transfer from ICs, the temperature of the block is $T_b>T_i$. The temperature of the other walls is constant at T_i.

2.2 Numerical Scheme. The governing equations are solved using a standard well-verified finite volume method (see Refs. [3,17]). Time integrations use a second-order Crank–Nicolson scheme for both the convective and viscous terms. For the spatial discretization, second-order central differences are

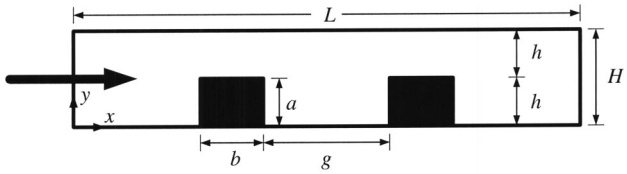

Fig. 1 Problem definition and computational domain. The temperature of the blocks is T_b and the temperature of the other walls is T_i.

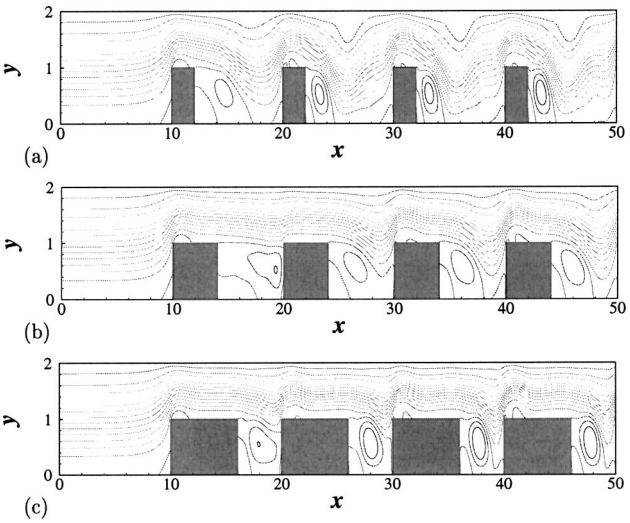

Fig. 2 Time-mean streamline contours. (*a*) $b/h=2$, (*b*) $b/h=4$ and (*c*) $b/h=6$.

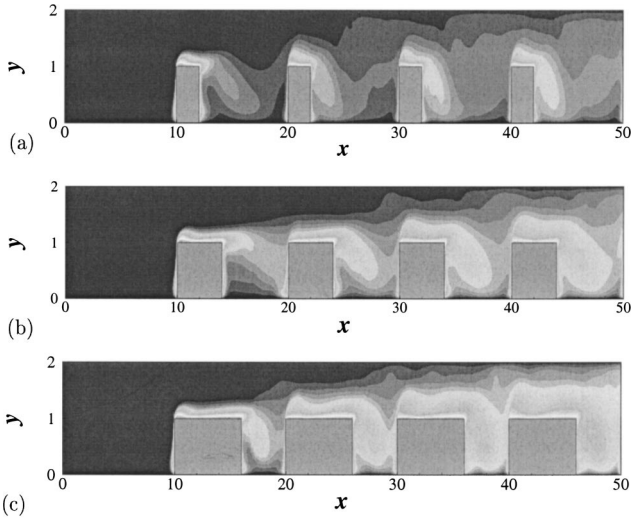

Fig. 3 Time-mean temperature contours. (*a*) $b/h=2$, (*b*) $b/h=4$ and (*c*) $b/h=6$.

used. Temporal resolution effects are investigated by successively halving time steps until no substantial differences are observed. To resolve high shear, a hyperbolic tangent grid stretching is used. Most simulations are run on a 1430×65 nonuniform grid. A grid independence study is made using a 2070×65 grid. Time steps of $\Delta t=0.02$ are used. Typically, simulations contain 10 blocks. A comparison has been made with the experimental data of Tropea and Gackstatter [18] for flow in a single groove channel. The present results are in good agreement with these measurements.

3 Results and Discussion

The block height is $a/h=1$ and the spacing between neighboring blocks $(b+g)/h=10$, where b is the block width and g the groove width. The first block is located at $x=10h$ (i.e., the upstream side of the block is located at $x=10h$ and the downstream at $x=10h+b$).

Preliminary simulations are used to determine Re_c. For this test, just $b/h=2$ and $g/h=8$ are considered, giving $\mathrm{Re}_c>155$. Therefore, to ensure unsteady flow for all geometries ($b/h=2$, 4 and 6) $\mathrm{Re}=500$ is used.

3.1 Mean Flow Distributions. For $b/h=2$, the recirculating flow region downstream the block is small compared to g. For $b/h=6$, g is too short for the recirculating flow to reattach on the lower channel surface between the blocks. For $b/h=4$, the recirculating region size is comparable to g. Time-mean streamline and temperature contours are shown in Figs. 2 and 3, respectively, for the three b/h values. As can be seen from Figs. 2 and 3, with increasing x the flow tends to a "periodic state." In this region, a single block could be considered with periodic streamwise boundaries.

For $b/h=2$ (see Figs. 2(*a*) and 3(*a*)), the flow development along the groove surface after the reattachment is quite independent of the recirculating flow upstream and the flow reaches a "periodic state" relatively quickly. After the first block, the flows become unsteady. This increases with x and eventually, the unsteady fluctuations become the same order of magnitude as U_m.

3.2 C_f and Nu Distributions. Figures 4 and 5 show the downstream development of C_f and Nu over block surfaces for $b/h=2$, 4, and 6. The definitions of C_f and Nu are:

$$C_f=\frac{dU}{dy}\mathrm{Re}, \tag{4}$$

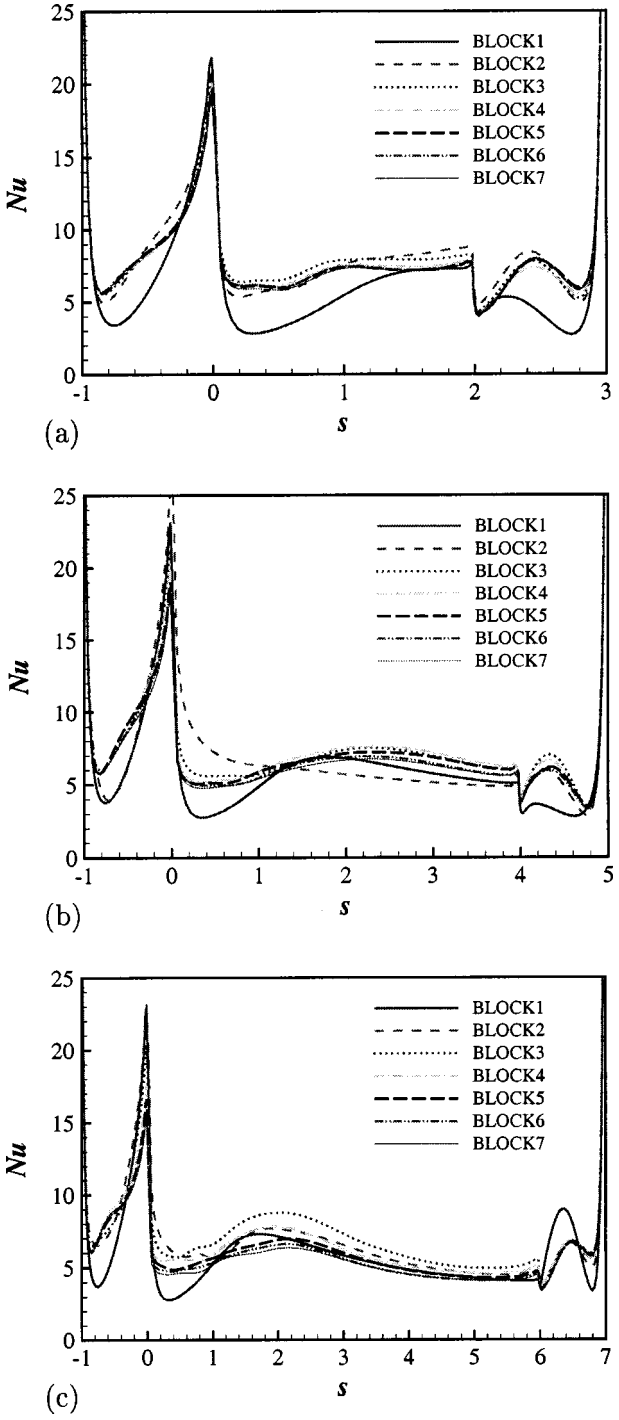

Fig. 4 C_f distributions around the blocks. (*a*) $b/h=2$, (*b*) $b/h=4$, and (*c*) $b/h=6$.

$$\mathrm{Nu}=\frac{h}{\Delta T}\frac{dT}{dy}, \tag{5}$$

where ΔT is the temperature difference, T_b-T_i. A new coordinate s is introduced such that $s=0$ indicates the upstream corner of each block. Note, for a fully developed plane channel flow $C_f=2$. The strong C_f singularities at $s=0$ are caused by the sharp groove edges. For all b/h values the C_f profiles change substantially with x for $x<30$ (the third block). The negative C_f peak has a fully developed value around the fifth groove. Fluctuating kinetic energy (k) against x is also examined (not shown here). The

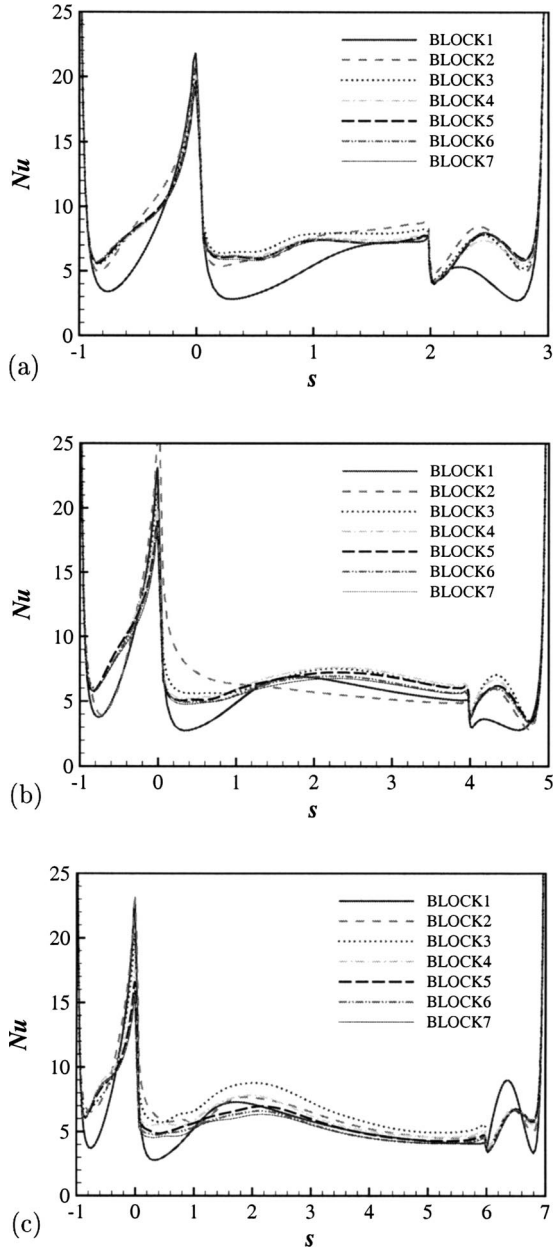

Fig. 5 Nu distributions around the blocks. (*a*) $b/h=2$, (*b*) $b/h=4$, and (*c*) $b/h=6$.

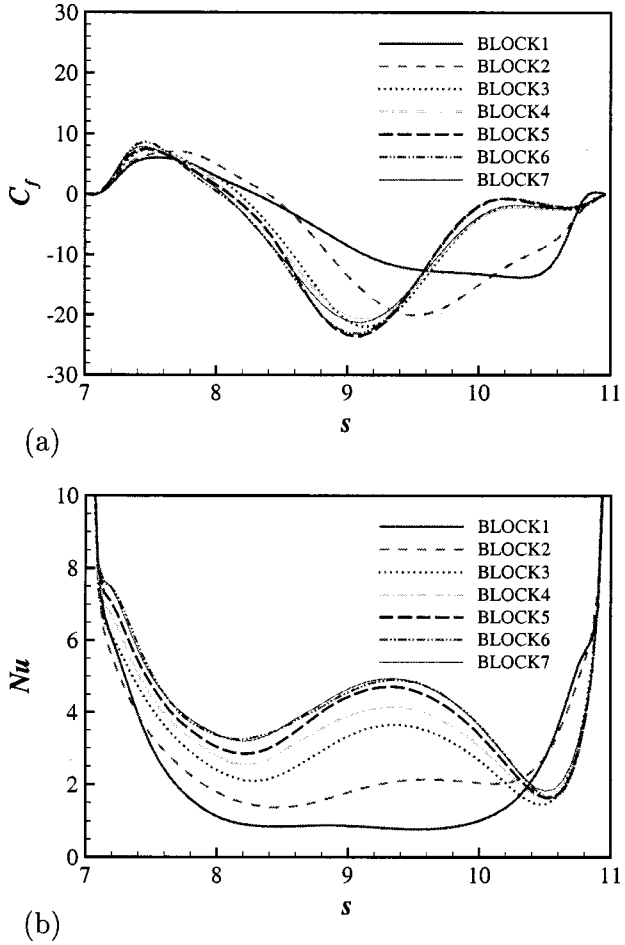

Fig. 6 Distributions between blocks for $b/h=6$: (*a*) C_f and (*b*) Nu

measuring points are $3h$ downstream of each block and at $y/h=1$. Consistent with the negative peak C_f evidence, after the fifth block, k reaches a quasifully developed value. After this $x>50$ region, flow periodicity could be assumed. Figure 5 shows that the heat transfer is much lower for the first few blocks, prior to reaching ''quasiperiodicity.''

Figure 6 shows the interblock C_f and Nu distributions for $b/h=6$. For this b/h, the recirculating flow impinges on the vertical upstream surfaces of the blocks (C_{f_U}). The flow development toward the ''quasiperiodic'' state is much slower between the block compared with over the block surface (shown in Figs. 4 and 5). A comparison of C_f and Nu suggests that the thermal boundary layer development is much slower than that of the flow field. The cases with $b/h=2$ and 4 show similar trends although the approach to the ''quasiperiodic'' state is slightly faster.

Figure 7 highlights the downstream development of the flow using averaged surface properties. The average C_f and Nu over block surfaces and between them is given. The subscript U represents upstream block face values, A a block surface average and I interblock values. Studying C_{f_U} shows that as b increases, the flow takes longer to develop. For $b/h=2$, C_{f_U} does not change much along the downstream direction while $b/h=4$ and 6 accompany significant changes. For example, for $b/h=6$, C_{f_U} attains a ''periodic value'' after block four. For $b/h=4$, the recirculating flow region downstream of the first block is as large as g, resulting in negative shear (see also Figs. 2(*b*) and 4(*b*)). Importantly, it takes longer distance for the actual velocity fluctuations to become periodic. Figures 7(*b*) and 7(*c*) indirectly give thermal field data. It is clear (cf. Figs. 7(*a*)–7(*c*)) that the periodic flow assumption can be more problematic for the thermal field. Figures 7(*b*) and 7(*c*) show that the thermal field develops more slowly with increasing b/h. For example, with $b/h=6$, Nu_A changes even after the sixth block.

4 Concluding Remarks

Numerical studies of unsteady laminar flow heat transfer in grooved channel flows of especial relevance to electronic systems are made. The validity of a commonly used periodic flow assumption is explored. Predictions for $\mathrm{Re}=500$ show the flow typically can become periodic by around the fifth groove. Hence, when modeling IC rows on circuit boards the popular periodic flow assumption might not be valid for a significant area.

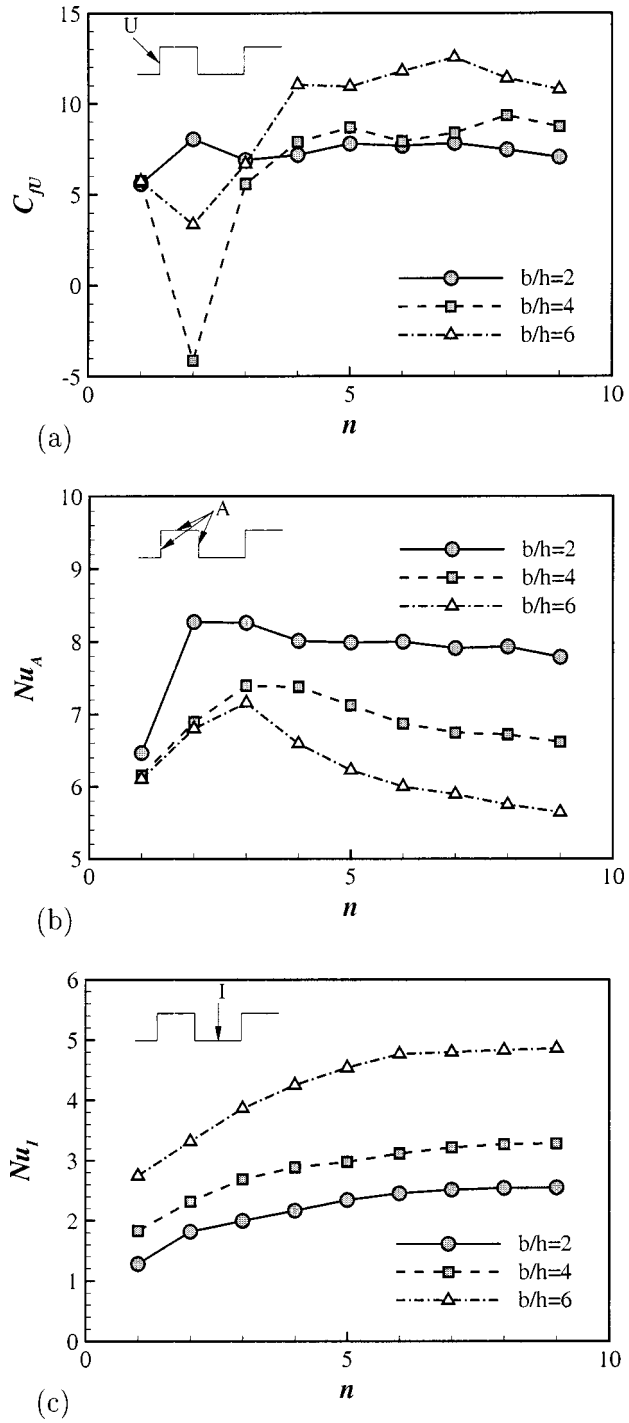

Fig. 7 Average C_f and Nu around the block: (*a*) C_{f_U}, (*b*) Nu_A, and (*c*) Nu_I

Acknowledgment

The support of the Engineering and Physical Sciences Research Council (EPSRC) of the United Kingdom under Grant No. GR/N05581 is gratefully acknowledged.

References

[1] Chung, Y. M., Tucker, P. G., and Luo, K. H., 2001, "Large-Eddy Simulation of Complex Internal Flows," in *Direct and Large-Eddy Simulation IV*, B. J. Geurts, R. Friedrich, and O. Mètais, eds., Kluwer Academic Publishers, The Netherlands, pp. 373–380.

[2] Chung, Y. M., Luo, K. H., and Sandham, N. D., 2002, "Numerical Study of Momentum and Heat Transfer in Unsteady Impinging Jets," Int. J. Heat Fluid Flow, **23**, pp. 592–600.

[3] Chung, Y. M., Tucker, P. G., and Roychowdhury, D. G., 2003, "Unsteady Laminar Flow and Convective Heat Transfer in a Sharp 180° Bend," Int. J. Heat Fluid Flow, **24**, pp. 67–76.

[4] Chung, Y. M., and Luo, K. H., 2002, "Unsteady Heat Transfer Analysis of an Impinging Jet," ASME J. Heat Transfer, **124**, pp. 1039–1048.

[5] Ghaddar, N. K., Karczak, K. Z., Mikic, B. B., and Patera, A. T., 1986a, "Numerical Investigation of Incompressible Flow in Grooved Channels, Part 1. Stability and Self-Sustained Oscillations," J. Fluid Mech., **163**, pp. 99–127.

[6] Ghaddar, N. K., Magen, M., Mikic, B. B., and Patera, A. T., 1986b, "Numerical Investigation of Incompressible Flow in Grooved Channels. Part 2. Resonance and Oscillatory Heat-Transfer Enhancement," J. Fluid Mech., **168**, pp. 541–567.

[7] Amon, C. H., and Mikic, B. B., 1990, "Numerical Prediction of Convective Heat Transfer in Self-Sustained Oscillatory Flows," J. Thermophys. Heat Transfer, **4**, pp. 239–246.

[8] Amon, C. H., 1992, "Heat Transfer Enhancement by Flow Destabilization in Electronic Chip Configurations," ASME J. Electron. Packag., **114**, pp. 35–40.

[9] Nigen, J. S., and Amon, C. H., 1993, "Forced Convective Cooling Enhancement of Electronic Package Configurations Through Self-Sustained Oscillatory Flows," ASME J. Electron. Packag., **115**, pp. 356–365.

[10] Nigen, J. S., and Amon, C. H., 1994, "Time-Dependent Conjugate Heat Transport Characteristics of Self-Sustained Oscillatory Flows in a Grooved Channel," ASME J. Fluids Eng., **116**, pp. 499–507.

[11] Nigen, J. S., and Amon, C. H., 1995, "Effect of Material Composition and Localized Heat Generation on Time-Dependent Conjugate Heat Transport," Int. J. Heat Mass Transfer, **38**, pp. 1565–1576.

[12] Wang, G., and Vanka, S. P., 1995, "Convective Heat Transfer in Periodic Wavy Passages," Int. J. Heat Mass Transfer, **38**, pp. 3219–3230.

[13] Greiner, M., Fischer, P. F., and Tufo, H., 2002, "Numerical Simulations of Resonant Heat Transfer Augmentation at Low Reynolds Numbers," ASME J. Heat Transfer, **124**, pp. 1169–1175.

[14] Nishimura, T., and Kawamura, Y., 1995, "Three-Dimensionality of Oscillatory Flow in a Two-Dimensional Symmetric Sinusoidal Wavy-Walled Channel," Exp. Therm. Fluid Sci., **10**, pp. 62–73.

[15] Pauley, L. R., Moin, P., and Reynolds, W. C., 1990, "The Structure of Two-Dimensional Separation," J. Fluid Mech., **220**, pp. 397–411.

[16] Chung, Y. M., Sung, H. J., and Boiko, A. V., 1997, "Spatial Simulation of the Instability of Channel Flow With Local Suction/Blowing," Phys. Fluids, **9**, pp. 3258–3266.

[17] Tucker, P. G., 2001, Computation of Unsteady Internal Flows, Kluwer Academic Publishers.

[18] Tropea, C. D., and Gackstatter, R., 1985, "The Flow Over Two-Dimensional Surface-Mounted Obstacles at Low Reynolds Numbers," ASME J. Fluids Eng., **107**, pp. 489–494.

Volume Scattering of Radiation in Packed Beds of Large, Opaque Spheres

Quinn Brewster
ASME Fellow, Department of Mechanical and Industrial Engineering, University of Illinois,
Urbana, IL 61801

A simple model is proposed for radiative properties of close-packed large, opaque spheres that accounts for nonvanishing volume of the particles, i.e., volume scattering as opposed to point scattering. It is based on the mean-beam-length concept applied to an assembly of particles, as illustrated by Mills. The resulting particle-scattering properties differ from those of classical pseudocontinuum theory based on point scattering by the simple factor of void fraction, and reduce to the point-scattering expressions in the limit of small particle volume fraction. The volume-scattering model matches detailed Monte Carlo results for extinction obtained by Kaviany and Singh and by Coquard and Baillis, which explicitly accounted for particle volume. The present model also confirms the Monte Carlo finding that the effects of nonvanishing particle volume are felt primarily in the extinction coefficient; albedo and phase function are relatively unaffected. These findings pertain only to the geometric optics regime where dependent scattering (wave coherence effects) are negligible.
[DOI: 10.1115/1.1795247]

Introduction

The classical pseudocontiuum theory for radiative transfer in particulate media that scatter and absorb radiative energy is based on the assumption that the particles act like point scatterers with negligible volume [1]. This theory works well for media in which the particle volume fraction is small ($f_v<0.1$) such that the assumptions of negligible shadowing and negligible multiple scattering within an optically thin, differential volume element are satisfied. Packed beds, however, which typically have particle volume fractions of about 0.6, do not satisfy these conditions. Nevertheless, it was suggested in 1982 by Brewster and Tien [2] that the assumption of point scattering might be just an artifice in deriving the theory, and that the radiative transfer equation with point-scattering properties was applicable in packed and fluidized beds with f_v as high as 0.7 as long as an independent scattering interparticle clearance-to-wavelength criterion (at that time taken to be $c/\lambda>0.3$) was satisfied, which is usually the case.

In the 1990s it was suggested by Singh and Kaviany that the idea of Brewster and Tien of extending point-scattering properties to f_v values as high as 0.7 was flawed, the experimental support for it having been based on special conditions such as nonopaque particles [3,4]. Using a Monte Carlo analysis, Singh and Kaviany showed that the nonvanishing particle volume in packed beds had an effect on the extinction coefficient of the bed, which effect was particularly evident for opaque particles and invalidated the use of the point-scattering extinction coefficient for $f_v>0.1$. They also obtained a polynomial curve fit by which the point-scattering extinction coefficient could be corrected for $f_v>0.1$. Various other studies have proposed other corrections for ''dependent'' (nonpoint) scattering in packed beds of opaque spheres [5]. A recent review of the current status of the theory for radiation in packed beds is given by Baillis and Sacadura [6]. Further experimental and modeling work by Baillis and Sacadura in isothermal [7] and nonisothermal [8] packed beds has supported the conclusions of Singh and Kaviany and the use of their extinction coefficient scaling correction. Thus there is both experimental and computational support for the concept of extinction coefficient scaling to account for nonvanishing (nonpoint), particle volume-scattering effects in packed beds of opaque spheres.

This Note proposes a new, simple, theoretically based model for the radiative properties of particulate media consisting of opaque, close-packed spheres in the geometric optics regime (c/λ large enough that interference or dependent scattering effects are not important). The model accounts for the nonvanishing volume of the particles. The resulting property expressions, though exceedingly simple, reduce to the classical point-scattering expressions in the limit of small f_v. Thus the theory is a generalization of the dilute limit and holds into the close-packed limit. The model also agrees with the numerical Monte Carlo results for close-packed opaque spheres of Singh and Kaviany. The model serves in essence (1) as a correction for the theoretical error overlooked in the original Brewster and Tien paper, (2) as a simple, theoretical justification for the close-packed correlation of Singh and Kaviany, and (3) as a basis for evaluating packed bed radiative properties in the framework of the continuum radiative transfer equation description. It is a pseudocontinuum theory for independent, volume (nonpoint) scattering in close-packed beds of opaque spheres.

Volume-Scattering Extinction Coefficient: Mean-Beam-Length Approach

The idea for this model comes from a textbook example problem that demonstrates calculation of mean beam length in an array of tubes [9] (see Fig. 1). That particular example problem is unique among textbook examples because it illustrates the case of a gas bordered by a noncontiguous surface. The surface is an array of long cylinders of diameter 4 units, with centers forming equilateral triangles of side length 7 units. The geometric mean beam length is found by the well-known formula for an isothermal gas surrounded by an isothermal, opaque surface:

$$L_{m_0}=\frac{4V_g}{A_s}=\frac{4[\frac{1}{2}(7)(7^2-3.5^2)^{1/2}-\frac{3}{6}(\pi/4)(4)^2](1)}{(3)(\pi/6)(4)(1)}=9.5. \tag{1}$$

Thus, the average path length traveled by a photon after leaving one tube in this array before interacting with another tube (under optically thin or nonabsorbing gas conditions) is 9.5 units.

The idea of the present model is to consider the array of tubes and surrounding gas in this example as a pseudocontinuous participating medium comprised of the absorbing/reflecting tubes and the nonabsorbing, nonemitting gas. In the array of tubes so considered the inverse of the mean free photon path length obtained from the geometric mean beam length is equivalent to the effective extinction coefficient of the medium. By adapting this idea to a participating medium consisting of scattering, absorbing particles surrounded by nonparticipating gas the effective bulk, volumetric radiative properties for a scattering, absorbing particle medium including the volume of the particles (nonpoint scattering) are obtained.

Consider an assembly of N identical spheres of diameter d surrounded by nonparticipating gas as shown in Fig. 2. The total, particle, and gas volumes, respectively, are V, $NV_p(=f_vV)$, and V_g. The geometric mean beam length of this participating medium, after the previous example, is as follows:

Contributed by the Heat Transfer Division for publication in the JOURNAL OF HEAT TRANSFER. Manuscript received by the Heat Transfer Division April 23, 2004; revision received April 30, 2004. Associate Editor: S. Thynell.

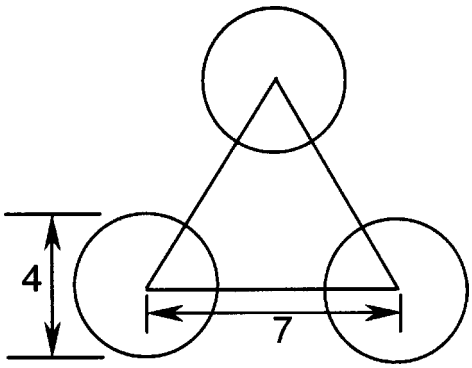

Fig. 1 Parallel cylinders in an equilateral triangle array (see Ex. 6.23 of Ref. [9])

$$L_{m_0}=\frac{4V_g}{A_s}=\frac{4(V-NV_p)}{NA_p}=\frac{4V}{N}\frac{(1-NV_p/V)}{A_p}$$
$$=\frac{4V_p}{f_v}\frac{(1-f_v)}{A_p}=\frac{4V_p}{A_p}\frac{(1-f_v)}{f_v}$$
$$=\frac{4(\pi/6)d^3}{\pi d^2}\frac{(1-f_v)}{f_v}$$
$$=\frac{(1-f_v)d}{1.5f_v}. \tag{2}$$

The inverse of L_{m_0} is the extinction coefficient.

$$K_e=\frac{1}{L_{m_0}}=\frac{1.5f_v}{(1-f_v)d} \quad \text{(volume scattering)}. \tag{3}$$

This familiar expression can be compared to with the usual expression [1] for point scattering:

$$K_e=\frac{1.5f_vQ_e}{d} \quad \text{(point scattering)}. \tag{4}$$

Assuming that a particle extinction efficiency of 1 ($Q_e=1$, for large particles) is implicit in the volume-scattering expression, the only difference between the point and volume-scattering expressions is the factor $(1-f_v)$. Since the derivation leading to the point-scattering expression [1] ignores particle volume by assuming negligible shadowing of particles by each other within a differential, single-scattering control volume, dV, it may therefore be concluded that the factor $(1-f_v)$ accounts for the nonvanishing volume of the particles.

If we write the scattering and absorption coefficients in a similar manner by including the void fraction factor $(1-f_v)$ the following properties are obtained:

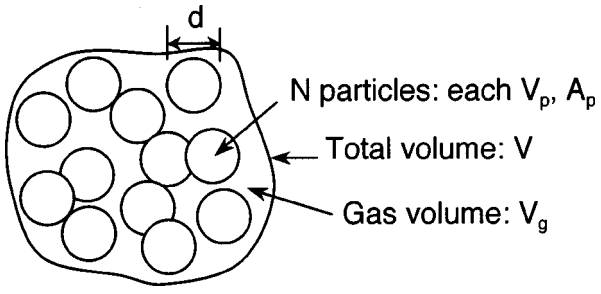

Fig. 2 Participating medium comprised of absorbing, reflecting spheres of nonvanishing volume (nonpoint scatterers) surrounded by nonparticipating gas

$$K_{e,s,a}=\frac{1.5f_vQ_{e,s,a}}{(1-f_v)d}, \tag{5}$$
$$Q_e=1, \quad Q_s=\rho=\omega_0, \quad Q_a=1-\omega_0 \quad \text{(volume scattering)}.$$

The phase function and single-scattering albedo (particle reflectivity) are unchanged from single-particle properties. These properties hold for nonpoint, volume scattering in the independent scattering regime for large particles ($d\gg\lambda$) such that electromagnetic wave interference or dependent scattering is negligible ($c/\lambda>0.5$) and diffraction can be treated as unscattered radiation ($Q_e=1$). (For dependent scattering effects see Refs. [10–13]. It can be seen that the volume-scattering expression reduces to the point-scattering result in the dilute limit ($f_v\ll1$). The difference would only be noticeable for particle volume fractions around 0.1 or larger where the void fraction factor $1/(1-f_v)$ would become significant. Thus the regime of interest for the more general volume-scattering theory is that of packed or fluidized beds. Next this simple volume-scattering model is compared with Monte Carlo simulations of multiple (independent) scattering in beds of close-packed spheres.

Comparison With Monte Carlo Calculations

Singh and Kaviany [3,4] performed Monte Carlo simulations of radiative transfer in packed beds of opaque spheres with particle volume fraction $0.008<f_v<0.7$. They found that volume-scattering effects became noticeable for volume fractions as small as 0.065. They concluded that the point-scattering recommendation of Brewster and Tien was erroneous because it had been based primarily on experiments with nonopaque particles, in which the nonvanishing volume fraction of the particles is compensated for by the non-negligible mean transport distance through a particle relative to the mean distance between particles. Based on their Monte Carlo results they proposed a point-scattering correction to account for "dependent" (nonvanishing particle volume) effects:

$$K_{e,s,a}=\frac{1.5f_vQ_{e,s,a}S_r}{d}, \tag{6}$$

$$S_r=1+1.84f_v-3.15f_v^2+7.20f_v^3, \quad f_v<0.7. \tag{7}$$

The phase function and albedo were found to be relatively unaffected by particle volume, similar to the assumptions noted above in connection with Eq. (5). It is of interest to compare the Singh-Kaviany scaling factor S_r to the factor $1/(1-f_v)$ from the volume-scattering result based on mean beam length. Figure 3 shows that the polynomial for S_r is actually a very good curve fit to the mean-beam-length, volume-scattering factor $1/(1-f_v)$. That is, the detailed numerical Monte Carlo simulation results of Singh and Kaviany are confirmed by the present, simple model:

$$\frac{1}{1-f_v}\cong1+1.84f_v-3.15f_v^2+7.20f_v^3, \quad f_v<0.7. \tag{8}$$

Figure 3 also illustrates how (as observed by Singh and Kaviany) volume scattering effects become noticeable at about $f_v\sim0.1$ by comparing the point-scattering factor f_v with the volume-scattering factor $f_v/(1-f_v)$.

Recently Coquard and Baillis revisited this problem using the Monte Carlo method [14]. They obtained results that essentially confirm the findings reported here and by Kaviany and Singh that (a) volume scattering (the effect of nonvanishing particle volume) is well represented by modifying only the point-scattering extinction coefficient via a factor of inverse porosity, Eq. (8), $1/\varepsilon$, where $\varepsilon=1-f_v$; (b) the effective scattering albedo is not much affected by volume scattering; and (c) the effective scattering phase function is also not much affected by volume scattering. On points (a) and (b) the present results and those of Coquard and Baillis agree with Kaviany and Singh but not with Kamiuto. [Kamiuto's results agree on point (c).] To compare the results of various investigators

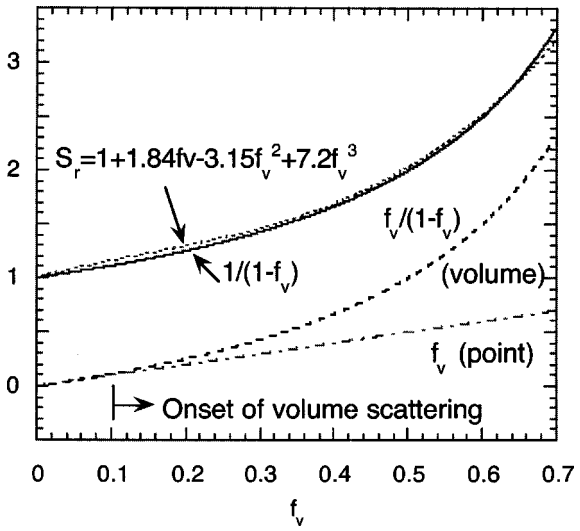

Fig. 3 Volume-scattering augmentation factor for extinction coefficient from mean beam length [$1/(1-f_v)$] and Monte Carlo simulation (S_r) in packed beds for opaque spheres [4]

Coquard and Baillis presented a plot of the extinction coefficient times particle radius ($K_e d/2$) versus void fraction or porosity ($\varepsilon = 1-f_v$). Figure 4 shows the same plot updated with the volume scattering prediction of Eq. (5): $K_e d/2 = 0.75(1-\varepsilon)/\varepsilon$. It can be seen that the simple, analytical mean-beam-length results of Eq. (5) are in good agreement with the Monte Carlo results of both Kaviany and Singh and Coquard and Baillis, while the results of Kamiuto and point-scattering theory [$K_e d/2 = 0.75(1-\varepsilon)$] show increasing deviation.

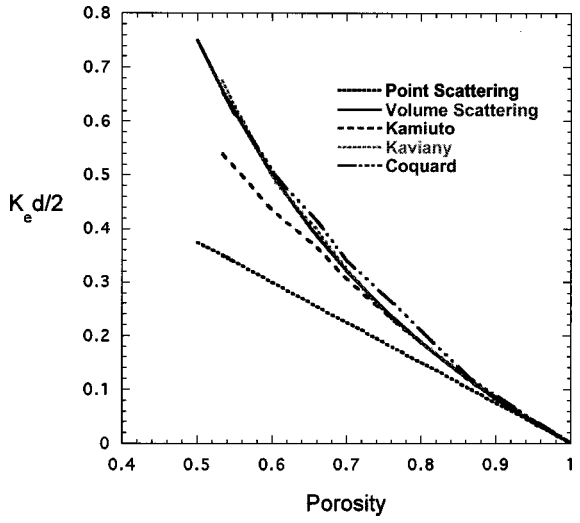

Fig. 4 Extinction coefficient times particle radius, after Fig. 5 of Ref. [14] for various numerical models [4,5,14] and two analytical models, point scattering [Eq. (4)] and volume scattering [Eq. (5)]

In summary, the agreement between Monte Carlo results for the effect of volume scattering by opaque spherical particles from two independent sets of investigators and a simple mean-beam-length model is very good. Both models suggest that the effect of nonvanishing particle volume for opaque particles is to increase the extinction, scattering, and absorption coefficients (relative to the point-scattering coefficients) as an increasing function of f_v [specifically $1/(1-f_v)$ with no significant particle emissivity dependence] such that albedo and phase function are unaffected. Finally it should be noted that these results apply to the geometric optics regime where particle size is much larger than wavelength such that interparticle clearance is sufficiently large to neglect dependent scattering effects. The effects discussed in this Note (and by Kaviany and Singh and by Coquard and Baillis for that matter) are not true dependent scattering effects but rather are simply nonvanishing particle volume effects.

Acknowledgments

The author gratefully acknowledges the mentoring of C.-L. Tien, under whose guidance this problem was originally investigated, the textbook *Heat and Mass Transfer* of Professor A. F. Mills, which inspired this little insight, and the *Radiation Heat Transfer Notes* of Professor D. K. Edwards, which have also been a source of inspiration.

References

[1] Brewster, M. Q., 1992, *Thermal Radiative Transfer and Properties*, Wiley, New York.
[2] Brewster, M. Q., and Tien, C. L., 1982, "Radiative Transfer in Packed and Fluidized Beds: Dependent Versus Independent Scattering," ASME J. Heat Transfer, **104**, pp. 573–579.
[3] Singh, B. P., and Kaviany, M., 1991, "Independent Theory Versus Direct Simulation of Radiation Heat Transfer in Packed Beds," Int. J. Heat Mass Transfer, **34**, pp. 2869–2882.
[4] Singh, B. P., and Kaviany, M., 1992, "Modelling Radiative Heat Transfer in Packed Beds," Int. J. Heat Mass Transfer, **35**, pp. 1397–1405.
[5] Kamiuto, K., 1992, "Radiative Properties of Packed-Sphere Systems Estimated by the Extended Emerging-Intensity Fitting Method," J. Quant. Spectrosc. Radiat. Transf., **47**, pp. 257–261.
[6] Baillis, D., and Sacadura, J. F., 2000, "Thermal Radiation Properties of Dispersed Media: Theoretical Prediction and Experimental Characterization," J. Quant. Spectrosc. Radiat. Transf., **67**, pp. 327–363.
[7] Lopes, R., Moura, L. M., Baillis, D., and Sacadura, J. F., 2001, "Directional Spectral Emittance of a Packed Bed Correlation Between Theoretical Prediction and Experimental Data," ASME J. Heat Transfer, **123**, pp. 240–248.
[8] Baillis, D., and Sacadura, J. F., 2002, "Directional Spectral Emittance of a Packed Bed—Influence of the Temperature Gradient in the Medium," ASME J. Heat Transfer, **124**, pp. 904–911.
[9] Mills, A. F., 1999, *Heat Transfer*, 2nd ed., Prentice-Hall, Upper Saddle River, NJ.
[10] Cartigny, J. D., Yamada, Y., and Tien, C. L., 1986, "Radiative Transfer With Dependent Scattering by Particles: Part I—Theoretical Investigation," ASME J. Heat Transfer, **108**, pp. 608–613.
[11] Yamada, Y., Cartigny, J. D., and Tien, C. L., 1986, "Radiative Transfer With Dependent Scattering by Particles: Part II—Experimental Investigation," ASME J. Heat Transfer, **108**, pp. 614–618.
[12] Drolen, B. L., and Tien, C. L., 1987, "Independent and Dependent Scattering in Packed-Sphere Systems," J. Thermophys. Heat Transfer, **1**, pp. 63–68.
[13] Kumar, S., and Tien, C. L., 1990, "Dependent Absorption and Extinction of Radiation by Small Particles," ASME J. Heat Transfer, **112**, pp. 178–185.
[14] Coquard, C., and Baillis, D., 2004, "Radiative Characteristics of Opaque Spherical Particle Beds: A New Method of Prediction," AIAA J. Thermophys. Heat Transfer, **18(2)**, 178–186.

Journal of Heat Transfer

Technology Review

Donald Q. Kern Lecture Award Paper

Odyssey of the Enhanced Boiling Surface

Ralph L. Webb
e-mail: RLWebb@psu.edu
Penn State University,
University Park, PA 16802

*This paper traces the evolution of enhanced boiling surfaces. Early work was highly empirical and done in industrial research. The 1968 Milton patent ["Heat Exchange System," U.S. Patent 3,696,861] described the first porous coated surface, and the 1972 Webb patent ["Heat Transfer Surface Having a High Boiling Heat Transfer Coefficient," U.S. Patent 3,521,708] described a "structured" tube surface geometry. The first fundamental understanding of the "pore-and-tunnel" geometry was published by Nakayama in 1980 [Nakayama, W., Daikoku, T., Kuwahara, H., and Nakajima, T. 1980, "Dynamic Model of Enhanced Boiling Heat Transfer on Porous Surfaces Part I: Experimental Investigation," J. Heat Transfer, **102**, pp. 445–450]. Webb and Chien's flow visualization allowed observation of the evaporation in the subsurface tunnels [Chien, L.-H., and Webb, R. L., 1998, "Visualization of Pool Boiling on Enhanced Surfaces," Exp. Fluid Thermal Sci., **16b**, pp. 332–341]. They also performed an experimental parametric study that defines the effect of pore diameter and pitch on the boiling performance. The progression of work on analytical boiling models is also reviewed.* [DOI: 10.1115/1.1834615]

Introduction

Tubular geometries having an enhanced outer boiling surface are now widely used in commercial applications. The surface enhancement contains a high area density of artificial nucleation sites and provides very high nucleate boiling performance. All refrigeration "water chillers" presently use such enhanced tubes. They are also used in some process applications. They were initially introduced about 1971 and are now made by a number of tube manufacturers. The technology has advanced through three generations of improvements. The purpose of this lecture is to document this important advancement in enhanced heat transfer technology.

Initial Efforts on Enhanced Boiling

The fact that "roughness" can improve nucleate boiling performance has been known since 1931. In 1931, Jakob and Fritz investigated the effect of surface finish on nucleate boiling performance, as reported by Jakob [1]. They boiled water from a sandblasted surface and a surface having a square grid of machined grooves (0.016 mm square with 0.48 mm spacing). The sandblasting provided no more than 15% improvement, which dissipated within a day. The grooved surface initially yielded boiling coefficients about three times higher than those of a smooth surface, but this performance also dissipated after several days. The observed performance decay in a short time was described as an "aging effect." Today, we would explain this by saying that the cavities formed by the roughening were not stable vapor traps and slowly degassed, eventually leaving no vapor to sustain the nucleation process. Until 1954, this "short-term" enhancement was regarded as an interesting, but commercially unusable concept because the heat transfer improvement lasted for only a matter of hours before "aging" caused the performance to decay to the plain surface value.

Interest in roughness was renewed in 1954, and between 1954 and 1962, three studies were performed using flat surfaces roughened with emery paper of different coarseness or lapping compounds. Berenson [2] observed nucleate boiling coefficient increases as large as 600% using lapped surfaces. The tests were not run long enough to establish the long-term aging performance, although the Corty and Foust [3] tests of grit-roughened surfaces did show some short-term aging. Kurihari and Myers [4] boiled water and several organic fluids on copper surfaces roughened with different grades of emery paper. Figure 1 shows their acetone results for the different grit sizes. They clearly established that the increased boiling coefficient results from an increased area density of nucleation sites. Their results for five test fluids showed that $h \propto n_s^{0.43}$. These works demonstrated that boiling enhancement will occur if the site density of stable nucleation sites can be increased. The artificially formed sites allowed incipience to occur at a lower $\Delta T_{ws} (= T_w - T_{sat})$ than for naturally occurring nucleation sites. These studies motivated later researchers to investigate other means of making artificial sites that show incipience at low ΔT_{ws} and function as stable vapor traps. This work "opened the door" to interest in the mechanism of nucleate boiling and many studies of nucleate boiling were subsequently performed.

Corty and Foust [3] and Bankoff [5] proposed that bubbles will emerge from cavities in which a gas or vapor phase pre-exists. The existence of a vapor–liquid interface in a small subsurface cavity is a metastable thermodynamic state. The liquid must be superheated for such a curved liquid–vapor interface to exist. The required liquid superheat for a convex interface of radius r is given by

$$T_l - T_{sat} = \frac{1}{m}\left(\frac{2\sigma}{r} - P_G\right) \tag{1}$$

where $m \equiv dp/dT \cong = \lambda / T_{abs} v_{fg}$ and p_G is the pressure of any noncondensible gas (e.g., air trapped in the cavity). When the vapor interface emerges from the surface of the cavity, the radius of the interface will equal the cavity radius (r_c). Hence, for no noncondensible gas at the cavity surface where $r = r_c$, one must have a minimum superheat of

Contributed by the Heat Transfer Division for publication in the JOURNAL OF HEAT TRANSFER. Manuscript received by the Heat Transfer Division September 10, 2004; revision received September 13, 2004.

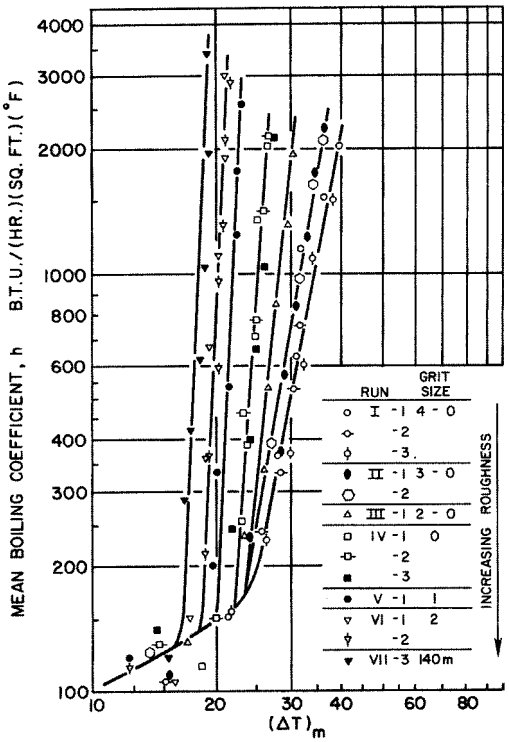

Fig. 1 Effect of emery paper roughening for acetone boiling on copper, Kurihari and Myers [4]

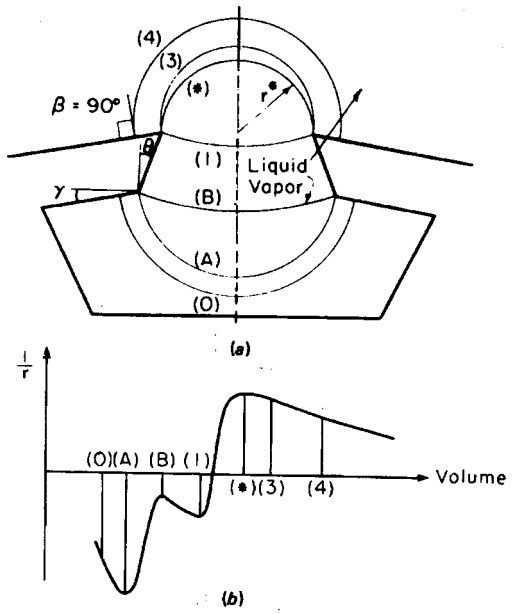

Fig. 2 (*a*) States of the liquid–vapor interface in a reentrant cavity. (*b*) Reciprocal radius (1/*r*) versus vapor volume for 90° contact angle, Griffith and Wallis [7].

$$T_l - T_{sat} = \frac{2\sigma}{mr_c} \tag{2}$$

Fundamental understanding of boiling on a ''smooth'' surface was advanced by the high-speed photography of Westwater and co-workers. For example, Clark et al. [6] identified naturally occurring pits and scratches between 8 and 80 μm widths as active boiling sites for pentane. Hence, one would expect a vapor bubble radius at the surface approximately half the observed pit diameter. Such small surface cavities will require quite high liquid superheat. A desirable characteristic for an artificial nucleation site is a larger pore diameter at the surface, so that small liquid superheat will be required for the site to be active.

The first fundamental understanding of how an artificial nucleation site may function was proposed by Griffith and Wallis [7], who showed that the cavity geometry is important in two ways. Figure 2 shows the reentrant cavity shape proposed by Griffith and Wallis. First, the mouth diameter determines the superheat needed to initiate boiling, and its shape determines its stability once boiling has begun. Figure 2 shows 1/*r* versus bubble volume. The term 1/*r* is proportional to the liquid superheat required to maintain a vapor nucleus. When the vapor radius of curvature becomes negative (concave curvature of the liquid–vapor interface), the vapor nucleus may still exist in the presence of subcooled liquid. Therefore, a reentrant cavity should be a very stable vapor trap. Benjamin and Westwater [8] were apparently the first to construct a reentrant cavity and demonstrate its superior performance as a vapor trap.

In the 1960s, researchers started to perform work on actually forming artificial nucleation sites. Among this was work of Marto and Rohsenow [9], who boiled sodium on a 75 mm diameter surface having 12 doubly reentrant cavities, as shown in Fig. 3. They found significant boiling enhancement. Although this work showed that it was possible to attain high performance via an artificial nucleation site, practical means to form a high area density of such sites in a tube walls was still unknown. Webb [10] provides a review of much of this early work on boiling enhancement.

Practical Enhanced Boiling Tubes

In the 1960s, large refrigeration water chillers used 19.5 mm diameter 748 or 1024 fins/m integral-fin tubes with 1.5 mm high fins in the condenser and evaporator. There was no water-side enhancement inside the tube. These tubes provided refrigerant-side enhancement by increasing the surface area. These tubes did not provide enhancement via artificial nucleation sites. Such water chillers in the early 1960's typically used R-11, and the controlling thermal resistance was on the refrigerant side. Hence, there

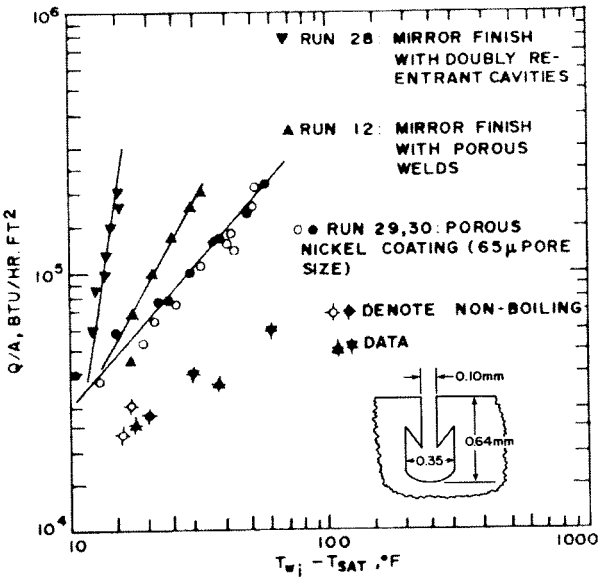

Fig. 3 (*a*) Effect of several surface treatments on sodium boiling at 65 mm Hg. (*b*) Cross section of doubly reentrant cavities tested, Marto and Rohsenow [9].

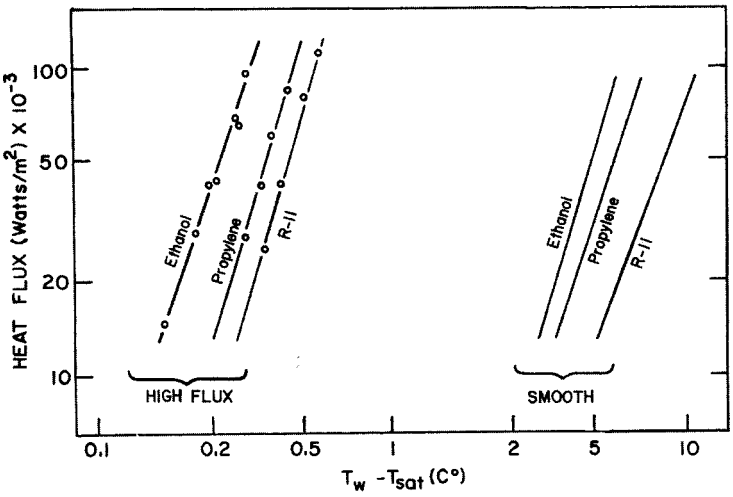

Fig. 4 (*a*) Enhancement by porous High-Flux™ surface for three fluids boiling at 101 kPa, Gottzmann et al. [14]

was high motivation to improve the boiling-side performance. However, the formation of discrete cavities is difficult and of limited practicality for thin wall, tubular heat exchanger surfaces. The new challenge was how to provide a high area density of nucleation sites on the tube's outer diameter.

In the mid-1960s, industrial research was underway to achieve the goal of a practical enhanced boiling surface for commercial application. Two different concepts were being investigated: (1) a porous coating and (2) cold reworking of the tube to form nucleation sites.

The results of this work are found in the patent literature. The Milton [11–13] patents achieved this goal by applying a 0.25 mm thick sintered copper coating to the surface of a plain tube. This tube is commercially known as the HIGH-FLUX™ tube. Figure 4 shows measured performance for plain and the HIGH-FLUX™ sintered coating tube reported by Gottzmann et al. [14].

Kun et al. [15] describe a method to score a flat aluminum plate with closely pitched parallel grooves (0.13 mm pitch) and 0.25 mm deep. The grooves are formed sequentially. The plate was then scored again (to a lesser depth) perpendicular to the first set of grooves. This formed subsurface cavities with restricted openings at the top. This surface showed very high performance for both water and liquid nitrogen.

An early concept that considerably improved the performance of integral-fin tubes is shown in Fig. 5 taken from the 1970 patent of Webb [16]. Nucleation sites were formed in the crevices between the wire wrap and the base of the fins. At a heat flux based on the nominal surface area of 50 kW/m^2, the boiling ΔT for R-11 was reduced from 4.2 to 1.3 K. However, a preferred approach would be to reconfigure the tube surface by cold metal working in some way to form nucleation sites. By 1967, we had achieved a practical means in the laboratory to attain this goal. This approach is the "bent fin" surface described by Webb [17] and shown in Fig. 6(*a*). The boiling ΔT for R-11 was reduced from 4.2 to 1.3 K at 50 kW/m^2. Following commercial introduction of the Fig. 6(*a*) bent fin surface by Trane, other refrigeration manufacturers developed competitive enhancement technologies, which are illustrated in Figs. 6(*b*)–6(*d*). These are the Hitachi Thermoexcel-E™ patented by Fujie et al. [18], the Wieland GEWA-T™ patented by Saier et al. [19], and the Furukawa ECR-40™ patented by Fujikake [20]. All of the Fig. 6 surfaces provide performance competitive with one another. The Figs. 6(*b*) and 6(*d*) geometries have gone through several periods of evolution since their initial introduction. The original Wolverine Turbo-B™ (Fig. 6*d*) had 1650 fins/m (40 fins/in.). The latest version, Turbo-BIII™, has 2362 fins/m (60 fins/in.) on the outer surface. These tubes also have internal helical grooves for water-side enhancement.

Figure 7, taken from the patent of Thors et al. [21], shows the performance improvements of the Wolverine Turbo-B™ tube to the current version, Turbo-B™III. The boiling data were taken for R-134a at 15°C. The figure shows that the highest performance tube (Turbo-BIII)™ gives 70% higher performance than the original Turbo-B™ tube for $(T_w - T_{sat}) = 0.55$ K (1.0 F).

Boiling Visualization in Tunnels

Although Griffith and Wallis [7] sought to explain boiling entrapment in reentrant cavities, this work does not explain the boiling mechanism in the structured surfaces illustrated in Fig. 6.

For descriptive purposes, we will call surfaces having surface pores and subsurface tunnels as "pore-and-tunnel" surface geometries. The first attempt to experimentally observe the boiling mechanism in the Fig. 6(*b*) pore-and-tunnel surface was by Nakayama et al. [22]. They performed flow visualization in a single tunnel having glass sidewalls and pores in the top surface. Heat was supplied at the base, between the glass walls. At moderate wall superheat, they observed a gas filled tunnel with menisci in the corners. Bubbles emerged from the pores. Nakayama et al.

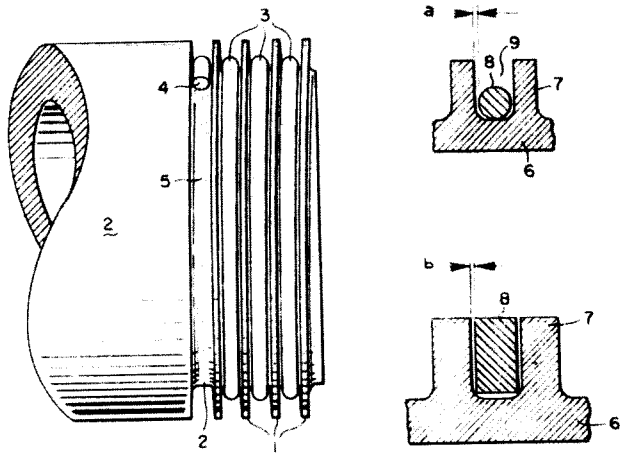

Fig. 5 Heat transfer surface which promotes nucleate boiling, [16]

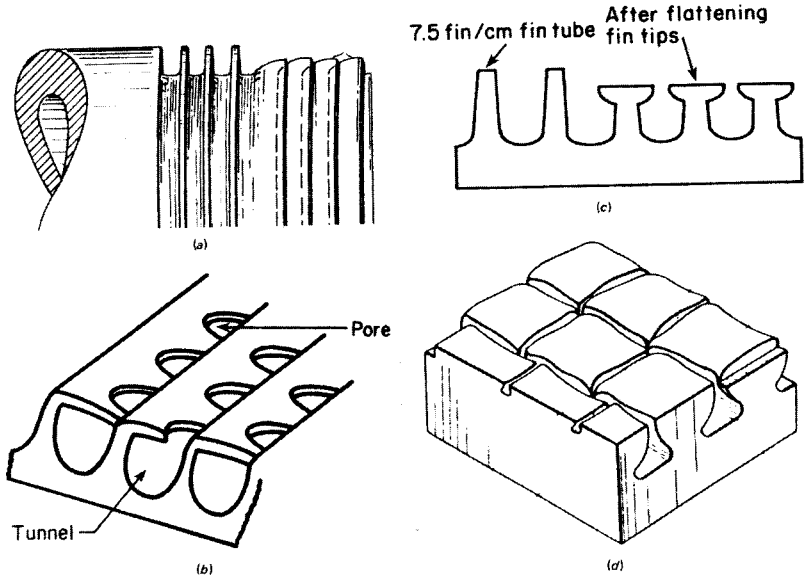

Fig. 6 Four patented structured boiling surfaces. (*a*) Webb [17] (*b*) Fujie et al. [18], (*c*) Saier et al. [19], and (*d*) Fujikake [20].

[23] hypothesized that three different modes of evaporation may occur in the tunnels, depending on the heat flux. Nakayama et al. [23] state that the ''flooded mode'' occurs at low heat flux, where most of the tunnel space is occupied by liquid, and an active pore acts as an isolated nucleation site. At higher heat flux, the ''suction-evaporation mode'' exists, where liquid is sucked in the tunnel space through inactive pores by the pumping action of bubbles growing at active pores. It then spreads along the tunnels and evaporates from menisci at the corners of the tunnel. With further heat flux increase, the ''dried-up mode'' exists, where the tunnel space is filled with vapor, and vaporization into bubbles takes place outside the tunnels. They envisioned that the ''suction-evaporation mode'' would exist at heat fluxes typical of that existing in a water-chiller evaporator.

Chien and Webb [24] performed visualization experiments on a finned tube geometry that closely simulates the actual tube geometry. The experiments viewed a 1575 fins/m, 19.5 mm diameter, copper, integral-fin tube having 0.8 mm fin height. A 20 μm thick, transparent plastic film was wrapped over the fins and 0.23 mm pores were made in the transparent film at 1.5 mm pore pitch using a heated needle. This allowed direct observation of the boiling process in the tunnels for methanol at $T_{sat}=64.5°C$. Data were taken for $2<q''<20\ \mathrm{kW/m^2}$. See details in their paper for discussion of their observations. Figure 8 shows methanol boiling at $q''=10\ \mathrm{kW/m^2}$. All bubbles emerged from vapor filled tunnels with menisci in the corners, which are annotated on the figure. Their observations conclusively proved the ''flooded mode'' and the ''suction evaporation'' mechanisms hypothesized by Nakayama et al. [23].

Effect of Pore Size and Pore Diameter

Chien and Webb [25,26] performed boiling tests to define the effect of the tunnel and pore dimensions on performance using an integral-fin tube wrapped with a 50 μm copper foil, which was soldered to the fin tips. R-11 or R-123 was used as the working

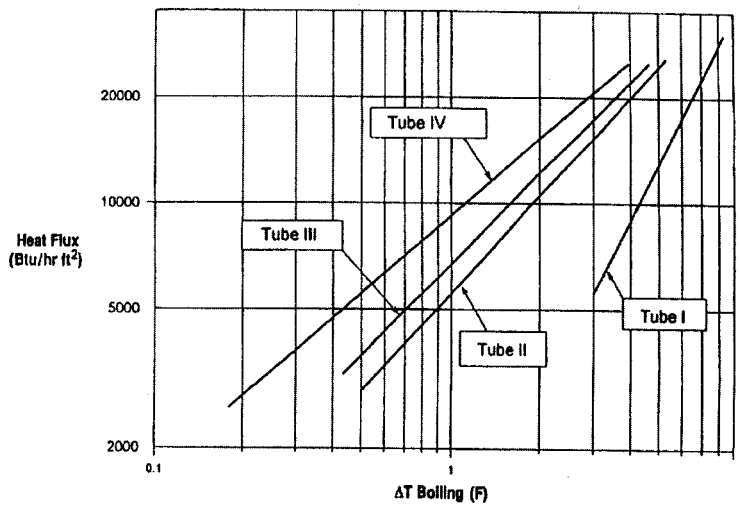

Fig. 7 R-134a at 5.0°C from Thors et al. [21] patent. Tube I (TurboChil™), Tube II (Turbo-B™), Tube III (Turbo-BII™), Tube IV (Turbo-BIII™).

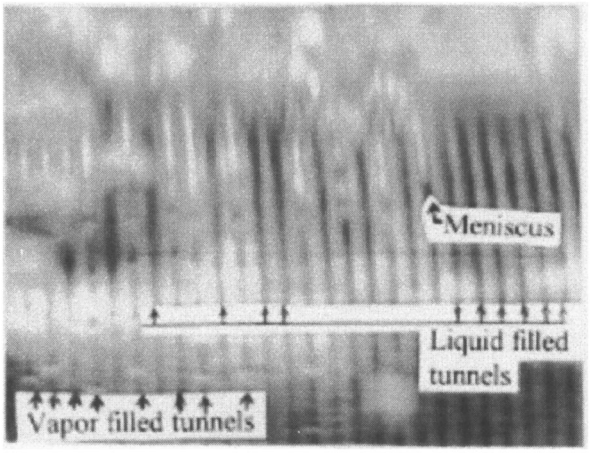

Fig. 8 Methanol boiling at 10 kW/m^2 on a horizontal 1574 fins/m tube having a transparent cover with pores, from Chien and Webb [24]

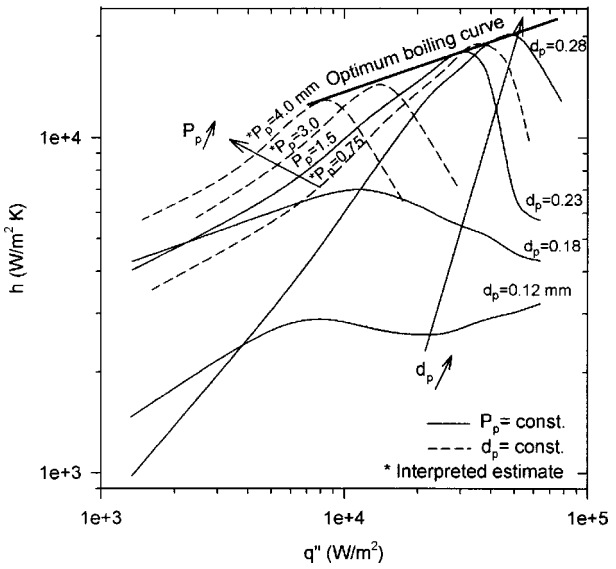

Fig. 9 Map showing combined effect of pore diameter (d_p) and pore pitch (P_p) for R-11 boiling on 1378 fins/m tube, from Chien and Webb [24]

fluid. Chien and Webb [27] provide additional data for R-134A and R-22. The pores were made by piercing the copper foil using a needle. The tunnel pitch and the tunnel height are equal to the fin pitch and height, respectively. Pores of specific diameters (d_p) were pierced in the foil at a specific pore pitch (P_p). The 50 μm copper foil was pierced to provide pore pitches of 0.75, 1.5, or 3.0 mm, and pore diameters of 0.12, 0.18, 0.23, or 0.28 mm. The tunnel dimensions were varied by using integral-fin tubes of different fin pitch and fin height. The tubes used were: 1378 fin/m having either 0.5 or 0.9 mm fin height, 1575 fins/m with 0.9 mm fin height, and 1969 fins/m with 0.9 mm fin height. A dimensional code was defined to describe the pore and tunnel dimensions. For example, code 1969-0.9-0.23-1.5 means a surface made on a 1969 fins/m and 0.9 mm fin height tube, having 0.23 mm diameter surface pores (d_p) on 1.5 mm pitch (P_p). Boiling occurred in 178 mm long cylindrical glass vessel having brass end flanges. The wall temperature was measured by 0.25 mm diameter iron-constantan sheathed thermocouples located below the tube wall at 180° opposite positions. The test tubes were 140 mm long, 9.53 mm inside diameter, and 18–19.5 mm outside diameter. Heat input was provided by a 9.52 mm diameter, 129 mm long, 500 W electric cartridge heater in the copper tube. Data were taken for 26.7°C saturation temperature using procedures described by Chien and Webb [25,26].

Figure 9 is a composite diagram showing the separate and combined effects of pore diameter (d_p) and pore pitch (P_p) for the 1378 fins/m tube having 0.9 mm fin height. This figure is based on detailed observations in [25,26]. Data were obtained only for the $d_p = 0.23$ mm, $P_p = 1.5$ and 3.0 mm cases. The dashed lines are the authors' qualitative estimates of the effect of pore pitch. There are two families of curves on Fig. 9. The solid lines are for fixed pore pitch ($P_p = 1.5$ mm) with increasing pore diameter (d_p). The dashed lines show the effect of pore pitch ($0.75 \leq P_p \leq 4.0$ mm) for fixed pore diameter ($d_p = 0.23$ mm). The salient features shown on Fig. 9 are:

1. As shown by the solid curves for fixed P_p, the DHF increases as the pore diameter increases. A lower DHF occurs for the smaller pore diameters, because they cannot supply enough liquid to the tunnel at high heat flux. Thus, the smaller pores become dry and the DHF occurs at a lower heat flux. Conceivably, a higher DHF would be observed for $d_p > 0.28$ mm. However, the maximum possible pore diameter is limited by the fin pitch, 0.5 mm.

2. For fixed P_p and heat fluxes, less than the DHF (e.g., 50% of the DHF), the heat transfer coefficient increases as d_p increases, except for the largest d_p (0.28 mm). The lower heat transfer coefficient for the largest d_p occurs because too much liquid is supplied to the tunnels, and floods the intermittent regions. Hence, there is an optimum pore diameter for operation at low-to-moderate heat flux.

3. For fixed d_p (0.23 mm), the DHF decreases as the P_p increases. This is because the tunnel needs greater liquid supply at the higher heat flux. However, the more widely spaced pores are unable to supply sufficient liquid.

4. For low heat flux at fixed d_p (0.23 mm), increasing P_p causes the heat transfer coefficient to increase. At lower heat flux, a smaller liquid supply to the tunnel will prevent tunnel flooding and result in a thin film in the tunnel.

Figure 9 clearly shows that there is a preferred combination of pore diameter and pore pitch for a specified design heat flux. The pore pitch/pore diameter combination influences the liquid supply rate to the tunnel via the total open pore area per unit tunnel length ($A_{pt} = \pi d_p^2 / 4P_p$). If the liquid supply rate exceeds the evaporation rate, the performance will be reduced, because of tunnel flooding. For fixed pore pitch, the highest boiling coefficient is obtained by use of the largest pore diameter. However, a smaller pore diameter is preferred for low heat fluxes. A large pore diameter may result in too much liquid supply to the tunnel at low heat flux and result in tunnel flooding.

One may use this information to select the preferred d_p and P_p combination for a specific design heat flux (e.g., an electronic heat sink). However, the heat flux significantly varies over the tube length in refrigerant water chillers. At the water inlet, a heat high flux exists and it may decrease by a factor of 5 over the tube length. According to the Fig. 9 boiling map, one would decrease A_{pt} over the tube length by appropriate selection of the d_p and P_p combination. Thus, it is possible to optimize the surface performance for operation within a specific heat flux range (below the DHF). This is equivalent to being able to change the slope of the boiling curve.

Fabrication of Pore-and-Tunnel Surfaces

Although tube manufacturers consider their enhanced boiling tube fabrication processes as proprietary, public knowledge exists on how to make such surfaces—either in flat plate or tubular form.

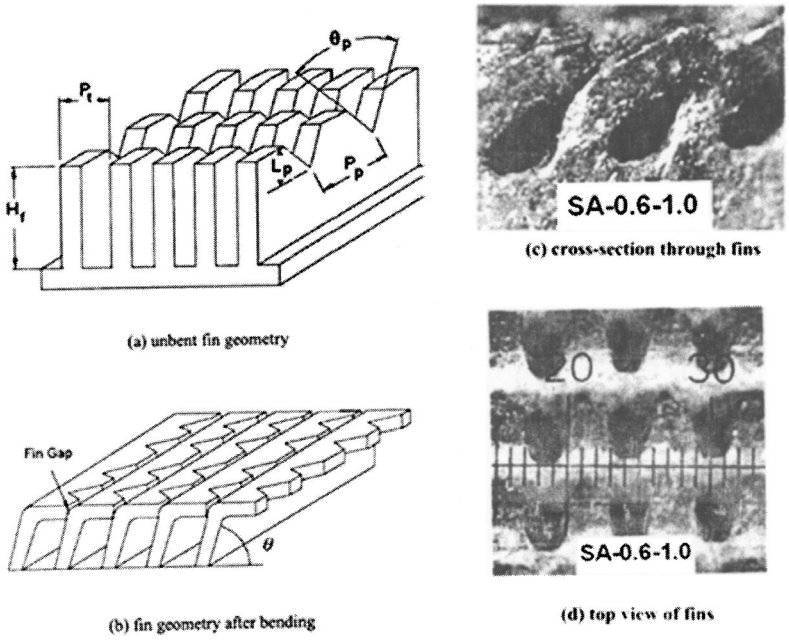

Fig. 10 Surfaces made by Chien and Chang [28]. (*a*) Illustration of unbent fins. (*b*) Illustration of bent fins. (*c*) Cross section through fins of surface (0.6 mm fin pitch and pore pitch with (*d*) 1.0 mm high fins).

Details on flat plate versions of the pore and tunnel surface are given in Nakayama et al. [22,23]. Such concepts may be highly applicable to cooling electronic devices.

Chien and Chang [28] made pore-and-tunnel surfaces, shown in Figs. 10(*c*) and 10(*d*), which are similar to Fig. 6(*b*). The enhanced surfaces were formed in flat plates, and were tested in the vertical orientation using water and HFC-4310. Triangular grooves 0.3 mm deep were cut in the fin tips (0.6 or 1.0 mm pitch) and then the fins were bent to form surface pores of triangular cross-section, as shown in Figs. 10(*a*) and 10(*b*). Kim and Choi [29] also made a tube having subsurface tunnels and surface pores similar to Fig. 6(*b*). They provide test results for different pore diameters using R-134A.

Analytical Models of Structured Surface

Nakayama et al. Model. Nakayama et al. [30] developed an analytically based model to predict boiling performance of the Fig. 6(*b*) Thermoexcel-E™ surface. Their model is based on the ''suction-evaporation'' mode. They assume that the total heat flux is the sum of a latent heat generated in the tunnel (q''_{tun}) and a single phase (external convection) heat flux. (q''_{ex}). This is expressed by

$$q'' = q''_{tun} + q''_{ex} \tag{3}$$

The model for q''_{tun} assumes that wetting occurs only in the corners of the tunnel. The model required six empirical constants for q''_{tun} and one for q''_{ex}.

Nakayama et al. [22] measured the latent heat flux (q''_{lat}) fraction of the total heat flux for boiling on a flat plate version of the Fig. 6(*b*) surface and on a plain surface. This was determined using the measured bubble departure diameter and the nucleation site density. Figure 11 shows that q''_{lat} contributes a much greater fraction of the total for the Thermoexcel-E™ enhanced surface than for a plain surface. Hence, a significant fraction of the total evaporation occurs in the subsurface tunnels. The major deficiency of the Nakayama et al. [20] model is that it requires seven empirical constants.

Chien and Webb Model. The flow visualization of Chien and Webb [24] confirm the Nakayama et al. [30] ''suction and evaporation'' model is correct for saturated boiling at typical operational heat fluxes. In the Nakayama et al. [30] model, the external convection heat flux does not include the bubble frequency and bubble departure diameter. Chien and Webb [31] provide an improvement over the Nakayama et al. [30] model. The Chien and Webb model has only two empirical constants compared to seven in the Nakayama et al. [30] model. The Chien and Webb model:

1. Accounts for the temporal evaporation rate variation inside tunnels by analyzing meniscus thickness, bubble departure diameter, and bubble growth.
2. The effect of bubble frequency and departure diameter for external the heat flux.

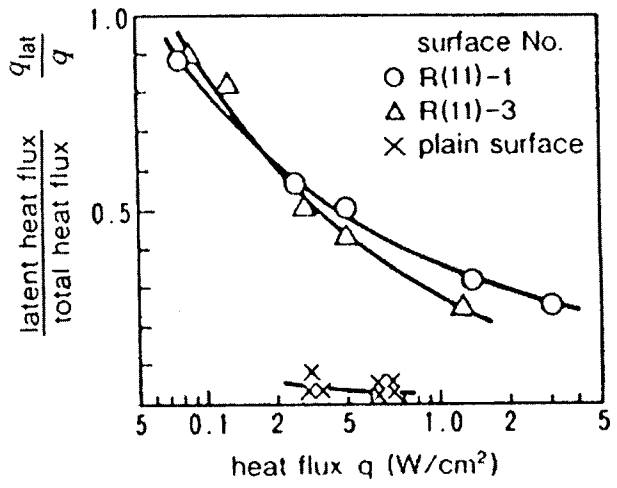

Fig. 11 Contribution of latent heat transport to the total heat flux on the Fig. 6(*b*) surface, from Nakayama et al. [22]

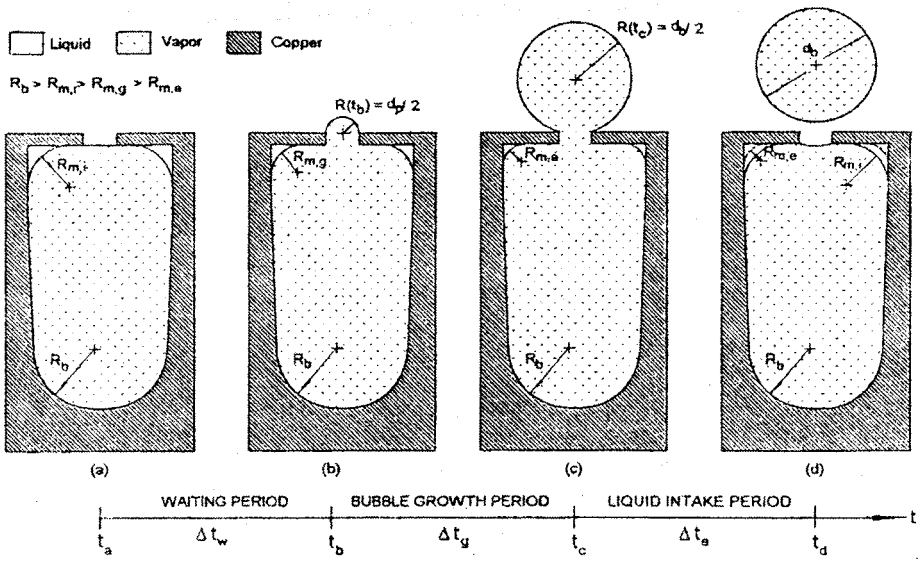

Fig. 12 Process of evaporation in the subsurface tunnel for one bubble cycle, from Chien and Webb [31]

As given by Eq. (3), the total heat flux is separated into two parts, tunnel heat flux (q''_{tun}) and external heat flux (q''_{ex}). The heat transfer rate in the tunnel is governed by evaporation of liquid menisci. The external heat flux is contributed by transient conduction and convection caused by the departing bubbles. The complete development of this model is given in Chien and Webb [31]. An overview of the model is given here. A bubble cycle includes three periods: waiting period (Δt_w), bubble growth period (Δt_g) and liquid intake period (Δt_e). Figure 12 shows the process of evaporation in the tunnel during one bubble cycle, which includes the following three periods:

1. Waiting period (Δt_w): In this period (Figs. 12(*a*) and 12(*b*)), liquid is evaporated in the tunnel. However, the vapor is constrained inside the tunnel by the surface tension on the pore, so that the pressure in the tunnel increases with time. A bubble embryo protrudes from a pore when $P_v - P_{sat} \equiv \Delta P_{br} = 4\sigma/d_p$.
2. Bubble growth period (Δt_g): Vapor passes through the surface pores and the bubble grows above the pore. The liquid in the tunnel continues to evaporate and the meniscus radius decreases. Meniscus evaporation stops when the elevation of saturation temperature, due to capillary pressure (σ/R) equals the wall superheat. At this point, the meniscus radius R_{ne} is

$$R_{ne} = \frac{\sigma}{\Delta T_{ws}} \left(\frac{dT}{dP} \right) \tag{4}$$

At time t_d (Fig. 12(*c*)) bubbles of diameter d_b depart from the surface pores.

Liquid intake period (Δt_e): After the bubble departs, the pressure in the tunnel is lower than that of the liquid pool, and liquid quickly flows into the tunnel, and is retained in the corners. At the end of the liquid intake period, the radius of the meniscus equals $R_{m,i}$ as shown on Fig. 12(*d*). The pore diameter and pitch control the amount of the liquid that flows into the tunnel.

The tunnel heat flux in Eq. (3) is the product of the latent heat transferred at the menisci during a bubble cycle and the bubble frequency, as given by

$$q''_{tun} A_{tun} = (Q_m) f \tag{5}$$

where Q_m is the latent heat from the menisci in one bubble cycle.

Figure 13 shows a meniscus existing at the top corner of the tunnel. Surface tension force acts to spread the entering liquid along the tunnel wall and pull it into the corners. Evaporation occurs only on the liquid menisci in the corners of the tunnel. A one-dimensional model is used to calculate the evaporation rate of this meniscus.

$$q'' = \frac{k_l}{\delta} (T_w - T_s) \tag{6}$$

The total latent heat (Q_{tun}) in the tunnel during one bubble cycle is obtained by integrating the heat transfer rate across menisci (dQ_m/dt) during a bubble cycle, and is given by

$$Q_{tun} = \int_0^{1/f} \left[\Delta T_{ws} \int_0^{A_m} \frac{k_l}{\delta_m(t,\phi)} dA \right] dt \tag{7}$$

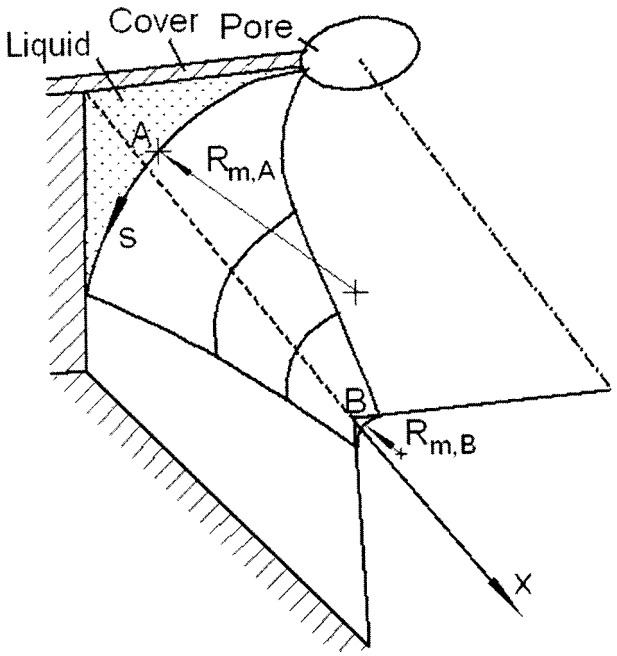

Fig. 13 Meniscus in the subsurface tunnel, from Chien and Webb [31]

where $\delta_m(t,\varphi)$ is the local thickness of the liquid meniscus, and A_m is the meniscus surface per unit tunnel length. For a given meniscus radius (R_m), $\delta_m(\varphi)=(R_m+\delta_{ne})\sec(\varphi)$ and R_m is a function of time given by

$$\delta_m(t,\phi)=[R_m(t)+\delta_{ne}]\sec(\phi)-R_m(t) \tag{8}$$

When the liquid meniscus becomes very thin, the saturation temperature elevates because of the disjoining pressure and capillary pressure (σ/R). When the elevated saturation temperature equals T_w, no further evaporation will occur. The integrations in Eq. (7) were numerically calculated using small increments of time (t) and angle (φ). Detailed methodology is given by Chien and Webb [31].

The sensible heat flux (q''_{ex}) term in Eq. (3) is due to the external convection induced by bubble agitation. The mechanism is similar to pool boiling on a plain surface in that the bubble evaporates into a superheated liquid layer above the base surface. The key difference between the present situation for q''_{ex} and boiling on a plain surface is that the nucleation site density, frequency, and bubble departure diameter are known.

An analytically based model developed by Haider and Webb [32] was used to predict the external heat flux. This model is based on an extension of the Mikic and Rohsenow [33] model. However, the Haider and Webb model includes the effects of transient convection to the liquid, caused by convection in the wake of the departing bubbles. Transient microconvection, rather than transient conduction, is the dominant heat transport mechanism.

The equations for prediction of q''_{tun} and q''_{ex} both require knowledge the active nucleation site density (n_s), bubble frequency (f), and bubble departure diameter (d_b). Nakayama et al. [30] used a force balance that included an empirical term to predict the bubble departure diameter. Chien and Webb [31] formulated the force balance using buoyancy and surface tension forces as a function of d_b, d_p, and contact angle (θ), which avoided an empirical constant. The bubble frequency is obtained from $1/f=\Delta t_w+\Delta t_g$. The waiting period and the bubble growth period were modeled separately and are given in Chien and Webb [31]. This work was supported by measurement of the bubble dynamic parameters by Chien and Webb [34].

The vapor generated in the tunnel is ejected through the surface pores. From an energy balance, $Q_{tun}=i_{fg}V_v\rho_v$, where V_v is the vapor volume. One obtains the nucleation site density (n_s) using the mass balance equation

$$n_s=\frac{q''_{tun}}{\rho_v i_{fg} f(\pi d_b^3)/6} \tag{9}$$

The model predicts the total heat flux (q'') for given wall superheat (ΔT_{ws}) and dimensions (d_b, P_p, P_f, H_t) using the detailed procedure given in Chien and Webb [31]. The model was used to predict the R-11, R-123, R-134a, and R-22 data of Chien and Webb [25,26] and Chien et al. [27]. The predictions were limited at the low end, because the model assumes the tunnels are vapor filled, which may not be true at low heat flux. These data include pool boiling data on tubular surfaces having a circular fin base for heat fluxes between 10 and 65 kW/m^2. The heat flux was predicted within 20% mean standard deviation.

Ramaswamy et al. Model. The 2003 Ramaswamy et al. [35] model is an update of the original Nakayama [30] model and is co-authored by Nakayama. The model parallels the Chien and Webb model with some key differences. One difference is in the model for the external heat flux. Whereas Chien and Webb used the Haider and Webb [32] model having a constant of 6.42, Ramaswamy et al. replaced the constant with a polynomial of (T_w-T_{sat}). They predicted their own data within $\pm 40\%$.

Jiang et al. Model. Similar to the suction-evaporation boiling model of Nakayama et al. [30] and the Chien and Webb [31] model, Jiang et al. [36] also assumed that evaporation occurs on liquid meniscus in the tunnel corners. The evaporation rate of the menisci was taken from Khrustalev and Faghri [37], who modeled evaporation in a heat pipe having microgrooves. The model contains an empirical constant (c_f) that was adjusted to fit the nucleation site density data. The Jiang et al. [36] model assumed $q''_{ex}=0$. This assumption is contrary to the measurements of Nakayama [30], as shown in Fig. 11. Further, they obtained the initial meniscus radius by solving the momentum equation for the liquid volume during the intake period. They set the boundary condition on the pores using a correlation of others to account for the pressure drop of the liquid flowing through inactive pores.

Conclusions

This paper traces the evolution of enhanced boiling surfaces. The early work was highly empirical and done in industrial research. Between 1968 and 1972, the first three patents on commercially viable enhanced surfaces [11,15,18] were issued. The first fundamental understanding of the ''pore-and-tunnel'' geometry was published by Nakayama [22,30], who formulated an analytically based model having seven empirical constants. Chien and Webb [24] performed flow visualization that allowed observation of the evaporation in the tunnels and validated the suction-evaporation model of Nakayama [30]. Chien and Webb [31] formulated an advanced version of the Nakayama [30] model, which had only two empirical constants. Chien and Webb [25,26] performed an experimental parametric study that defines the effect of pore diameter and pitch on the boiling performance. Industrial companies have continued to evolve higher performance versions of the pore-and-tunnel geometry.

Nomenclature

A = Surface area, m^2
A_m = Meniscus surface area, m^2
A_{tun} = Total surface area inside tunnels
c_p = Heat capacity, J/g K
d_b = Bubble departure diameter
DHF = Dry-out heat flux, kW/m^2
d_p = Pore diameter, m
f = Bubble frequency, l/s
h = Heat transfer coefficient, W/m^2 K
H_f = Fin height or tunnel height $(H_t=H_f)$, mm
i_{fg} = Latent heat, J/kg
k = Thermal conductivity, k_1 (of liquid), W/m K
m_v = Vapor mass, kg
n_s = Nucleation site density, l/m^2
P = Pressure, P_1 (liquid), P_s (sat), P_v (vapor), P_G (of noncondensible), Pa
P_p = Pore pitch, m
P_t = Tunnel pitch, m
Q = Heat, Q_m (meniscus), Q_{bub} (bubble), Q_{tun} (tunnel), J
q'' = Heat flux based on projected area, kW/m^2
Q_m = Heat evap from liquid menisci in bubble cycle, J
r = Radius of meniscus interface curvature, m
R = R_b (tunnel base), R_m (meniscus), m
R_{ne} = meniscus radius when evaporation stops, m
t = Time, t_a, t_b, t_c, t_d (times during bubble growth), s
T = Temperature, T_1 (liq), T_{sat} (sat), T_v (vap), K
u = Velocity of the liquid in the tunnel, m/s
V_v = Vapor volume, V_b (bubble), m^3
V_t = Tunnel volume, $(V_t=L\times W_t\times H_t)$, m^3
W_t = Tunnel width, m
δ = Liquid film thickness, δ_m (local meniscus thickness), m
δ_{ne} = Non-evaporation liquid film thickness, m
ΔP_{br} = Break through pressure $(\Delta P_{br}=4\sigma/d_p)$, Pascal
Δt = Diff. of time, Δt_e (liquid intake), Δt_g (bubble growth), t_w (bubble waiting period), s
ΔT = $\Delta T_{vs}=(T_v-T_s)$, $\Delta T_{ws}=(T_w-T_{sat})$, K

μ = Viscosity, μ_l (of the liquid), kg/m^2 s
ρ = Density, ρ_l (liquid), ρ_v (vapor), kg/m^3
σ = Surface tension, N/m

References

[1] Jakob, M., 1949, *Heat Transfer*, John Wiley & Sons, New York, pp. 636–638.
[2] Berenson, P. J., 1962, ''Experiments on Pool Boiling Heat Transfer,'' Int. J. Heat Mass Transfer, **5**, pp. 985–999.
[3] Corty, C., and Foust, A. S., 1955, ''Surface Variables in Nucleate Boiling,'' Chem. Eng. Prog., Symp. Ser., **51**, No. 17, pp. 1–12.
[4] Kurihari, H. M., and Myers, J. E., 1960, ''Effects of Superheat and Roughness on the Boiling Coefficients,'' AIChE J., **6**, pp. 83–91.
[5] Bankoff, S. G., 1959, ''Entrapment of Gas in the Spreading of a Liquid Over a Rough Surface,'' AIChE J., **4**, pp. 24–26.
[6] Clark, H. B., Strenge, P. H., and Westwater, J. W., 1959, ''Active Sites for Nucleate Boiling,'' Chem. Eng. Prog., Symp. Ser., **55**, No. 29, pp. 103–110.
[7] Griffith, P., and Wallis, J. D., 1960, ''The Role of Surface Conditions in Nucleate Boiling,'' Chem. Eng. Prog., Symp. Ser., **56**, No. 49, pp. 49–63.
[8] Benjamin, J. E., and Westwater, J. W., 1961, ''Bubble Growth in Nucleate Boiling of a Binary Mixture,'' *International Developments in Heat Transfer*, ASME, New York, pp. 212–218.
[9] Marto, P. J., and Rohsenow, W. M., 1966, ''Effects of Surface Conditions on Nucleate Pool Boiling of Sodium,'' J. Heat Transfer, **88**, pp. 196–204.
[10] Webb, R. L., 1981, ''The Evolution of Enhanced Surface Geometries for Nucleate Boiling,'' Heat Transfer Eng., **2**, pp. 46–69.
[11] Milton, R. M., 1968, ''Heat Exchange System,'' U.S. Patent 3,384,154.
[12] Milton, R. M., 1970, ''Heat Exchange System,'' U.S. Patent 3,523,577.
[13] Milton, R. M., 1971, ''Heat Exchange System With Porous Boiling Layer,'' U.S. Patent 3,587,730.
[14] Gottzmann, C. F., O'Neill, P. S., and Minton, P. E., 1973, ''High Efficiency Heat Exchangers,'' Chem. Eng. Prog., **69**(7), pp. 69–75.
[15] Kun, L. C., and Czikk, A. M., 1969, ''Surface for Boiling Liquids,'' U.S. Patent 3,454,081 (Reissued August 21, 1979 Re. 30,077).
[16] Webb, R. L., 1970, ''Heat Transfer Surface Which Promotes Nucleate Boiling,'' U.S. Patent 3,521,708.
[17] Webb, R. L., 1972, ''Heat Transfer Surface Having a High Boiling Heat Transfer Coefficient,'' U.S. Patent 3,696,861, assigned to The Trane Co.
[18] Fujie, K., Nakayama, W., Kuwahara, H., and Kakizakci, K., 1977, ''Heat Transfer Wall for Boiling Liquids,'' U.S. Patent 4,060,125.
[19] Saier, M., Kastner, H. W., and Klockler, R., 1979, ''Y- and T-Finned Tubes and Methods and Apparatus for Their Making,'' U.S. Patent 4,179,911.
[20] Fujikake, J., 1980, ''Heat Transfer Tube for Use in Boiling Type Heat Exchangers and Method of Producing the Same,'' U.S. Patent 4,216,826.
[21] Thors, P., Clevinger, N. R., Campbell, B. J., and Tyler, J. T., 1997, ''Heat Transfer Tubes and Methods of Fabrication Thereof,'' U.S. Patent 5,697,430.
[22] Nakayama, W., Daikoku, T., Kuwahara, H., and Nakajima, T., 1980, ''Dynamic Model of Enhanced Boiling Heat Transfer on Porous Surfaces Part I: Experimental Investigation,'' J. Heat Transfer, **102**, pp. 445–450.
[23] Nakayama, W., Daikoku, T., and Nakajima, T., 1982, ''Effects of Pore Diameters and System Pressure on Saturated Pool Nucleate Boiling Heat Transfer From Porous Surfaces,'' J. Heat Transfer, **104**, pp. 286–291.
[24] Chien, L.-H., and Webb, R. L., 1998, ''Visualization of Pool Boiling on Enhanced Surfaces,'' Exp. Fluid Thermal Science, **16**, pp. 332–341.
[25] Chien, L.-H., and Webb, R. L., 1998, ''Parametric Studies of Nucleate Pool Boiling on Structured Surfaces, Part I: Effect of Tunnel Dimensions and Comparison of R-11,'' J. Heat Transfer, **120**, pp. 1042–1048.
[26] Chien, L.-H., and Webb, R. L., 1998, ''Parametric Studies of Nucleate Pool Boiling on Structured Surfaces, Part II: Effect of Pore Diameter and Pore Pitch,'' J. Heat Transfer, **120**, pp. 1048–1054.
[27] Chien, L.-H., and Webb, R. L., 2001, ''Effect of Geometry and Fluid Property Parameters on Performance of Tunnel and Pore Enhanced Boiling Surfaces,'' J. Enhanced Heat Transfer, **8**, pp. 329–340.
[28] Chien, L.-H., and Chang, C.-C., 2003, ''Enhancement of Pool Boiling on Structured Surfaces Using HFC-4310 and Water,'' J. Enhanced Heat Transfer, **11**, pp. 23–44.
[29] Kim, N.-H., and Choi, K.-K., 2001, ''Nucleate Pool Boiling on Structured Enhanced Tubes Having Pores With Connecting Gaps,'' Int. J. Heat Mass Transfer, **44**, pp. 17–28.
[30] Nakayama, W., Daikoku, T., Kuwahara, H., and Nakajima, T., 1980, ''Dynamic Model of Enhanced Boiling Heat Transfer on Porous Surfaces Part II: Analytical Modeling,'' J. Heat Transfer, **102**, pp. 451–456.
[31] Chien, L.-H., and Webb, R. L., 1998, ''A Nucleate Boiling Model for Structured Enhanced Surfaces,'' Int. J. Heat Mass Transfer, **41**, pp. 2183–2195.
[32] Haider, S. I., and Webb, R. L., 1997, ''A Transient Micro-Convection Model of Nucleate Pool,'' Int. J. Heat Mass Transfer, **40**, pp. 3675–3688.
[33] Mikic, B. B., and Rohsenow, W. M., 1969, ''A New Correlation of Pool-Boiling Data Including the Effect of Heating Surface Characteristics,'' J. Heat Transfer, **91**, pp. 245–250.
[34] Chien, L.-H., and Webb, R. L., 1998, ''Measurement of Bubble Dynamics on an Enhanced Boiling Surface,'' Exp. Fluid Thermal Science, **16**, pp. 177–186.
[35] Ramaswamy, C., Joshi, Y., Nakayama, W., and Johnson, W. B., 2003, ''Semi-Analytical Model for Boiling From Enhanced Structures,'' Int. J. Heat Mass Transfer, **46**, pp. 4257–4269.
[36] Jiang, Y. Y., Wang, W. C., Wang, D., and Wang, B. X., 2001, ''Boiling Heat Transfer on Machined Porous Surfaces With Structural Optimization,'' Int. J. Heat Mass Transfer, **44**, pp. 443–456.
[37] Khrustalev, D., and Faghri, A., 1994, ''Thermal Analysis of a Micro Heat Pipe,'' J. Heat Transfer, **116**, pp. 189–198.

Journal of Heat Transfer

Discussion

Discussion: "A Numerical Study of Thermal Dispersion in Porous Media" and "Numerical Determination of Thermal Dispersion Coefficients Using a Periodic Porous Structure"

Boming Yu[1,2]

In the two papers [1–2], Kuwahara et al. investigated thermal dispersion in convective flow in porous media by using a two-dimensional periodic model of porous structure. In their study, a macroscopically uniform flow is assumed to pass through a collection of square rods placed regularly in an infinite space, where a macroscopic temperature gradient is imposed perpendicularly and in parallel to the macroscopic flow direction, respectively. Due to the periodicity of the model, only one structure unit is taken for a calculation domain to resolve an entire domain of porous medium. Exhaustive numerical computations were conducted for thermal dispersion conductivity. The transverse thermal dispersion conductivity results were correlated as the following expression [1]:

$$\frac{(k_{dis})_{yy}}{k_f}=0.022\frac{\mathrm{Pe}_D^{1.7}}{(1-\varepsilon)^{1/4}}\quad \text{for } (\mathrm{Pe}_D<10) \tag{26a}$$

and the longitudinal thermal dispersion conductivity results were correlated as [2]

$$\frac{(k_{dis})_{xx}}{k_f}=0.022\frac{\mathrm{Pe}_D^{2}}{(1-\varepsilon)}\quad \text{for } (\mathrm{Pe}_D<10) \tag{16a}$$

$$\frac{(k_{dis})_{xx}}{k_f}=2.7\frac{\mathrm{Pe}_D}{\varepsilon^{1/2}}\quad \text{for } (\mathrm{Pe}_D>10) \tag{16b}$$

where $\mathrm{Pe}_D=\mathrm{Pe}(1-\varepsilon)^{1/2}$. Equation (26*a*) was also summarized together with their longitudinal thermal dispersion conductivity results, Eq. (16), in their later paper [2]. The parameters used in this discussion are defined as the same as those applied by Ref. [1–2]; see also the *Nomenclature* in this discussion.

However, correlations (26*a*), (16*a*) and (16*b*) are questionable. Here is my detailed analysis.

According to the definition on the Peclet number given by Refs. [1–2], the Peclet number Pe should be expressed as

$$\mathrm{Pe}=(\rho C_p)_f u_m H/k_f \tag{D1}$$

However, the generally applied definition on the Peclet number is [3–7]

$$\mathrm{Pe}_g=(\rho C_p)_f u_m D/k_f \tag{D2}$$

If the generally applied definition on the Peclet number, Eq. (*D*2), is applied to Eqs. (26*a*), (16*a*) and (16*b*), Eqs. (26*a*), (16*a*) and (16*b*) will present the unreasonable results due to the structural unit applied by Kuwahara et al. [1–2]. The structural unit applied by Kuwahara et al. [1–2] in their numerical experiments is shown in Fig. 1.

According to Fig. 1, the total volume of the structural unit is

$$V_t=H^2 \tag{D3}$$

The pore volume of the unit is

$$V_p=H^2-D^2 \tag{D4}$$

So, the porosity of the unit can be expressed as

$$\varepsilon=V_p/V_t=1-D^2/H^2 \tag{D5}$$

From Eq. (*D*5), we have

$$D/H=(1-\varepsilon)^{1/2} \tag{D6}$$

or

$$H=D/(1-\varepsilon)^{1/2} \tag{D7}$$

Equation (*D*7) indicates that H is a function of porosity. Inserting Eq. (*D*7) into Eq. (*D*1) yields

$$\mathrm{Pe}=(\rho C_p)_f u_m D/[k_f(1-\varepsilon)^{1/2}] \tag{D8}$$

Due to the generally applied definition for the Peclet number Eq. (*D*2), Eq. (*D*8) can be written as

$$\mathrm{Pe}=\mathrm{Pe}_g/(1-\varepsilon)^{1/2} \tag{D9}$$

Equation (*D*9) establishes the relation between the Peclet number, Eq. (*D*1), defined by Refs. [1–2] and the generally applied Peclet number, Eq. (*D*2) [3–7].

According to $\mathrm{Pe}_D=\mathrm{Pe}(1-\varepsilon)^{1/2}$ (defined by Refs. [1–2]) and $\mathrm{Pe}=\mathrm{Pe}_g/(1-\varepsilon)^{1/2}$ (i.e. Eq. (*D*9)), we obtain

$$\mathrm{Pe}_D=\mathrm{Pe}_g \tag{D10}$$

Inserting Eq. (*D*10) into Eqs. (26*a*), (16*a*) and (16*b*) results in

$$\frac{(k_{dis})_{yy}}{k_f}=0.022\frac{\mathrm{Pe}_g^{1.7}}{(1-\varepsilon)^{1/4}}\quad \text{for } (\mathrm{Pe}_D<10) \tag{D11}$$

$$\frac{(k_{dis})_{xx}}{k_f}=0.022\frac{\mathrm{Pe}_g^{2}}{(1-\varepsilon)}\quad \text{for } (\mathrm{Pe}_D<10) \tag{D12a}$$

$$\frac{(k_{dis})_{xx}}{k_f}=2.7\frac{\mathrm{Pe}_g}{\varepsilon^{1/2}}\quad \text{for } (\mathrm{Pe}_D>10) \tag{D12b}$$

where $\mathrm{Pe}_g=(\rho C_p)_f u_m D/k_f$ is the generally defined definition for the Peclet number given by Eq. (*D*2).

From the above analysis, it is seen that the equations (*D*11), (*D*12*a*) and (*D*12*b*) are equivalent to Eqs. (26*a*) and (16*a*) and (16b). Equations (*D*11) and (*D*12) are transverse and longitudinal thermal dispersion conductivities, respectively, which are ex-

[1]Department of Physics and the State Key Laboratory of Plastic Forming and Die & Mold Tech., Huazhong University of Science and Technology, Wuhan, 430074, P. R. China. E-mail: yuboming2003@yahoo.com.cn, Fax: 86-27-87542153.

[2]The State Key Laboratory of Nonlinear Mechanics (LNM), Institute of Mechanics, Chinese Academy of Science, Beijing, 100080, China.

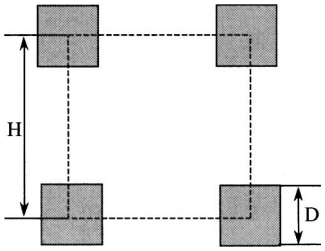

Fig. 1 The structural unit applied by Refs. [1–2] in their numerical experiments

pressed in terms of porosity and generally defined Peclet number Pe_g. However, Eqs. (*D*11) and (*D*12) present unreasonable results. For example, the thermal dispersion conductivities given by Eqs. (*D*11) and (*D*12*a*) increase with the increase of porosity. If porosity is 1, Eqs. (*D*11) and (*D*12*a*) present the infinite values for transverse and longitudinal thermal dispersion conductivities, while Eq. (*D*12*b*) presents nonzero longitudinal thermal dispersion conductivity. These are inconsistent with physical situation because the thermal dispersion should be reduced with the increase of porosity, and when porosity is 1, there is no dispersion and thermal dispersion conductivity should be zero.

In conclusion, it seems to me that the transverse and longitudinal thermal dispersion conductivity correlations, Eq. (26*a*), Eq. (16*a*) and (16b) given by Refs. [1–2], are questionable because they present unreasonable results.

Acknowledgment

This work was supported by the National Natural Science Foundation of China through Grant No. 10272052.

Nomenclature

D = size of square rod or size of particle
H = size of structural unit
k = thermal conductivity
Pe = Peclet number based on H and the macroscopically uniform velocity defined by Refs. [1–2]
Pe_g = generally defined Peclet number given by Eq. (*D*2)
u_m = the macroscopically uniform velocity
V = volume
ε = porosity

Subscripts

dis = dispersion
f = fluid
xx = longitudinal direction
yy = transverse direction
g = generally applied
t = total
p = pore

References

[1] Kuwahara, F., Nakayama, A., and Koyama, H., 1996, ''A Numerical Study of Thermal Dispersion in Porous Media,'' ASME J. Heat Transfer, **118**, pp. 756–761.
[2] Kuwahara, F., and Nakayama, A., 1999, ''Numerical Determination of Thermal Dispersion Coefficients Using a Periodic Porous Structure,'' ASME J. Heat Transfer, **121**, pp. 160–163.
[3] Cheng, P., and Vortmeyer, D., 1988, ''Transverse Thermal Dispersion and Wall Channeling in a Packed Bed With Forced Convective Flow,'' Chem. Eng. Sci., **43**, pp. 2523–2532.
[4] Hsu, C. T., and Cheng, P., 1990, ''Thermal Dispersion in Porous Media,'' Int. J. Heat Mass Transfer, **33**, pp. 1587–1597.
[5] Hunt, M. L., 1990, ''Comparison of Convective Heat Transfer in Packed Beds and Granular Flows,'' Annu. Rev. Heat Transfer, **3**, pp. 163–193.
[6] Cheng, P., Chowdhury, A., and Hsu, C. T., 1991, ''Forced Convection in Packed Tubes and Channels With Variable Porosity and Thermal Dispersion Effects,'' in *Computer Applications in Production Engineering*, S. Kakc, B. Kikic, F. A. Kulacki, and F. Arinc, eds., Kluwer Academic Pub., Dordrecht, The Netherlands, pp. 625–653.
[7] Adnani, P., Catton, I., and Abdou, M. A., 1995, ''Non-Darcian Forced Convection in Porous Media With Anisotropic Dispersion,'' ASME J. Heat Transfer, **117**, pp. 447–451.

Closure to Discussion: "A Numerical Study of Thermal Dispersion in Porous Media" (Kuwahara, F., Nakayama, A., and Koyama, H., 1996, ASME J. Heat Transfer, 118, pp. 756–761) and "Numerical Determination of Thermal Dispersion Coefficients Using a Periodic Porous Structure" (Kuwahara, F., and Nakayama, A., 1999, ASME J. Heat Transfer, 121, pp. 160–163)

A. Nakayama

F. Kuwahara
Dept. of Mechanical Engineering, Shizuoka University, 3-5-1 Johoku, Hamamatsu, 432-8561 Japan

We thank Dr. Yu for his discussion on two papers [1,2] of ours on thermal dispersion in porous media that appeared in the Journal of Heat Transfer. Dr. Yu rewrites our correlations established performing a series of numerical experiments as follows:

For the transverse dispersion:

$$\frac{(k_{dis})_{yy}}{k_f} = 0.022\frac{\mathrm{Pe}_D^{1.7}}{(1-\varepsilon)^{1/4}} \quad \text{for } (\mathrm{Pe}_D < 10) \tag{26a}$$

$$\frac{(k_{dis})_{yy}}{k_f} = 0.052(1-\varepsilon)^{1/2}\,\mathrm{Pe}_D \quad \text{for } (\mathrm{Pe}_D > 10) \tag{26b}$$

For the longitudinal dispersion:

$$\frac{(k_{dis})_{xx}}{k_f} = 0.022\frac{\mathrm{Pe}_D^2}{(1-\varepsilon)} \quad \text{for } (\mathrm{Pe}_D < 10) \tag{16a}$$

$$\frac{(k_{dis})_{xx}}{k_f} = 2.7\frac{\mathrm{Pe}_D}{\varepsilon^{1/2}} \quad \text{for } (\mathrm{Pe}_D > 10) \tag{16b}$$

Dr. Yu assumes that the thermal dispersion decreases with the increase in the porosity, for it vanishes when the porosity asymptotically approaches unity. (Incidentally, he did not give Eq. (26*b*) in his discussion, perhaps because it satisfies the foregoing asymptotic behavior with which he is concerned.) He is correct for the case of a high Peclet number since it should decrease with the increase in ε (see Eqs. (26*b*) and (16*b*)), but incorrect for the case of low Peclet number. Dr. Yu should note that our low Peclet number correlations given by (26*a*) and (16*a*) are consistent with the following analytical expressions reported by Koch and Brady [3] for the dispersion in fixed beds (also see Kaviany [4]):

For the transverse dispersion:

$$\frac{(k_{dis})_{yy}}{k_f} = \frac{\sqrt{2}}{240}\frac{\mathrm{Pe}_D^2}{(1-\varepsilon)^{1/2}} \quad \text{for } (\mathrm{Pe}_D \ll 1)$$

For the longitudinal dispersion:

$$\frac{(k_{dis})_{xx}}{k_f} = \frac{\sqrt{2}}{60}\frac{\mathrm{Pe}_D^2}{(1-\varepsilon)^{1/2}} \quad \text{for } (\mathrm{Pe}_D \ll 1)$$

Kaviany [4] explains the denominator $(1-\varepsilon)^{1/2}$, stating that, for the case of sufficiently low Peclet number, convection extends a distance of $D/3\sqrt{2}(1-\varepsilon)^{1/2} \sim H$, resulting in the spread of the heat much beyond a distance of a particle diameter associated with the pure conduction contribution.

Like these expressions, our expressions (26*a*) and (16*a*) fail as the porosity approaches unity. They may also fail under the other limiting condition, namely, $\varepsilon \to 0$, since the permeability–porosity relationship is different there. The porosity range in which our correlations are valid may be judged by reexamining Fig. 8 in our paper [1], where the coefficients are plotted against the abscissa variable $(1-\varepsilon)$ to find possible correlations. The errors become large as the porosity approaches zero. Also, in the range close to the origin (i.e. $\varepsilon = 1$), the coefficients reduce to values too small to elucidate a functional relationship. Thus, we presume that our correlations given by (26*a*), (26*b*), (16*a*) and (16*b*) are valid only for a limited porosity range, say, $0.2 < \varepsilon < 0.8$. It should also be noted that neither (26*b*) nor (16*b*) can be used beyond this range, since neither of them has been designed to account for the asymptotic behavior that Dr. Yu presumed in his discussion.

As in Figs. 9 in Ref. [1] and Fig. 4 in Ref. [2], the high Peclet number correlations are found in good accord with available experimental data. This substantiates the validity of our correlations. However, sufficient experimental data are not available for the low Peclet number range with which Dr. Yu is mostly concerned. For this range, we simply repeat that the correlations are consistent with those for packed beds reported by Koch and Brady [3].

References

[1] Kuwahara, F., Nakayama, A., and Koyama, H., 1996, "A Numerical Study of Thermal Dispersion in Porous Media," ASME J. Heat Transfer, **118**, pp. 756–761.
[2] Kuwahara, F., and Nakayama, A., 1999, "Numerical Determination of Thermal Dispersion Coefficients Using a Periodic Structure," ASME J. Heat Transfer, **121**, pp. 160–163.
[3] Koch, D. L., and Brady, J. F., 1985, "Dispersion in Fixed Beds," J. Fluid Mech., **154**, pp. 399–427.
[4] Kaviany, M., 1995, *Principles of Heat Transfer in Porous Media*, 2nd edition Springer-Verlag, New York, p. 209.

Erratum: "Duality of Heat Exchanger Performance in Balanced Counter-Flow Systems" (ASME J. Heat Transfer, 2003, 125, pp. 530–532)

Ken Ogiso

Eq. (1) should be:

$$N_S = \dot{S}_{gen}/C_{\min} = \ln\{[1-\varepsilon(1-T_2/T_1)][1+\varepsilon(T_1/T_2-1)]\} \quad (1)$$

